**University of Alberta**

# Structure and Catalytic Properties of Chabazite-Supported Nickel and Molybdenum

by

Brian R. Greenhalgh ©

A thesis submitted to the Faculty of Graduate Studies and Research
in partial fulfillment of the requirements for the degree of

Doctor of Philosophy

In

Chemical Engineering

Department of Chemical and Materials Engineering

Edmonton, Alberta
Fall 2007

Library and
Archives Canada

Published Heritage
Branch

395 Wellington Street
Ottawa ON K1A 0N4
Canada

Bibliothèque et
Archives Canada

Direction du
Patrimoine de l'édition

395, rue Wellington
Ottawa ON K1A 0N4
Canada

*Your file Votre référence*
*ISBN: 978-0-494-32965-8*
*Our file Notre référence*
*ISBN: 978-0-494-32965-8*

NOTICE:
The author has granted a non-exclusive license allowing Library and Archives Canada to reproduce, publish, archive, preserve, conserve, communicate to the public by telecommunication or on the Internet, loan, distribute and sell theses worldwide, for commercial or non-commercial purposes, in microform, paper, electronic and/or any other formats.

The author retains copyright ownership and moral rights in this thesis. Neither the thesis nor substantial extracts from it may be printed or otherwise reproduced without the author's permission.

AVIS:
L'auteur a accordé une licence non exclusive permettant à la Bibliothèque et Archives Canada de reproduire, publier, archiver, sauvegarder, conserver, transmettre au public par télécommunication ou par l'Internet, prêter, distribuer et vendre des thèses partout dans le monde, à des fins commerciales ou autres, sur support microforme, papier, électronique et/ou autres formats.

L'auteur conserve la propriété du droit d'auteur et des droits moraux qui protège cette thèse. Ni la thèse ni des extraits substantiels de celle-ci ne doivent être imprimés ou autrement reproduits sans son autorisation.

---

In compliance with the Canadian Privacy Act some supporting forms may have been removed from this thesis.

While these forms may be included in the document page count, their removal does not represent any loss of content from the thesis.

Conformément à la loi canadienne sur la protection de la vie privée, quelques formulaires secondaires ont été enlevés de cette thèse.

Bien que ces formulaires aient inclus dans la pagination, il n'y aura aucun contenu manquant.

Canada

# Abstract

Supported mixed metal clusters of nickel and molybdenum on chabazite (CHA) show novel activity and resistance to sulfur poisoning in hydrogenation catalysis. Two distinct approaches of preparation were employed. Series 1 was prepared via high temperature reflux, while Series 2 was prepared in a constant concentration exchange column. In each series, three systems were prepared. Aqueous reflux of the sodium form of chabazite in chloride salts of Ni and Mo resulted in Ni-CHA, Mo-CHA, and NiMo-CHA (Series 1), while passing solutions of the metal chlorides through a bed of acidified chabazite in the exchange column produced NiHCHA, MoHCHA and NiMoHCHA (Series 2). Additional preparation studies focused on increasing the acidity of the metal loaded chabazites, both before and after metal incorporation. The metal loaded chabazites produced were characterized by instrumental neutron activation analysis (INAA), x-ray photoelectron spectroscopy (XPS), transmission electron microscopy (TEM), x-ray diffraction (XRD) and $NH_3$ temperature programmed desorption (TPD) in order to give insight into the structure of the supported phases. Ethylene hydrogenation was used as a probe reaction, in both the presence and absence of $H_2S$, as a measure of the activity, selectivity and deactivation characteristics of these systems. Characterization studies indicate that Series 1 is characterized by a strong interaction with the support, and consequently cluster sizes which grow controllably in response to reduction and sulfidation. Contrastingly, Series 2 was characterized by a weaker interaction between the metals and the support, leading to clusters which grow significantly under reduction and sulfidation. A key finding in this study was the observation, by TEM, of $MoS_2$ type clusters in both the MoHCHA and the NiMoHCHA samples. XPS studies indicate that

the NiMo catalysts (NiMo-CHA and NiMoHCHA) show enhanced Ni metallic character over their Ni analogues. This was evidenced by a greater degree of reduction/sulfidation of Ni within the NiMo chabazites compared to that within the Ni chabazite. These and other findings of the characterization studies complement the catalytic properties of the bimetallic systems, which show unique resistance to sulfur poisoning relative to the monometallic systems.

# Dedication

To my father, James Ronald Greenhalgh.

"………….this too shall pass."

# Acknowledgement

At the conclusion of this research project, I find myself looking back over the five years between taking my first graduate course, and checking the margins one last time before hitting the print button. In doing so, I have come to the realization that, with the exception of the author, none of the main characters in this episode were present from *day one* to *day done*. There are those who were there in the beginning; supervisors who came and went, friends who did the same, as well as peer students with whom contact was lost upon conclusion of the final exam in the course that made us colleagues for such a short while. As well, those who played such a major role towards the end were not actually there in the beginning. It is, therefore, with all requisite humility and measure that I will first congratulate myself, for staying the course.

Next, I thank my wife Claudia, who not only provided me an example to follow, but was the most significant source of encouragement and support during those times when the task seemed too much. "I couldn't have done it without you." is an understatement. With love, thank you.

With struggle comes sacrifice, and I was willing to trade more than a few evenings locked up in the lab for this degree. My two faithful pugs Diesel and Portia spent those same evenings locked up too. Yet even at the latest of hours, I was always greeted affectionately, no questions asked. I'm sure only the dog lovers out there will truly understand, but some serious cookies are in order.

The support of my family played a key role in my completion of this degree. My mom's unconditional love, my brother's advice on navigating the various situations I encountered along the way, and of course, I never would have signed up for a Ph.D. if my sister hadn't raised the bar by earning her Masters degree. A certain aunt also shares the credit for driving me to this. Hopefully my grammar and word selection requires no further revision.

It's been said that research is a group effort, and I have no argument there. I'd like to thank Walter Boddez, Dr. John Duke, Dimitre Karpuzov, Andreé Koenig, Tuyet Le, Wayne Moffet, Dave Parin, Greg Popowich , Dr. Peter Unwin and Dr. Long Wu. These people literally helped me get the data into my lab book, whether it was running analyses for me, teaching me how to get that data myself, fixing things, or simply having useful supplies to steal. In addition, to all my labmates past and present, thanks for making the whole thing fun.

Finally, I thank my supervisors. You were there for me when I needed you. The three of us are very different people, and at times I wasn't sure that having us together in one room was the wisest course of action, but here we are.

## Table of Contents

Chapter 1: Introduction 1
    1.1: Background and Motivation 1
    1.2: Research Objectives 3

Chapter 2: Overview of Zeolites and Zeolite-Supported Ni, Mo, NiMo Catalysts 6
    2.1 Introduction to Zeolites 6
    2.2 Zeolite Structure 6
    2.3 Zeolite Acidity 8
    2.4 Applications of Zeolites 12
    2.5 Preparation of Zeolite Supported Catalysts 12
    2.6 Zeolites in Catalysis 17
    2.7 The Use of Chabazite in Catalysis and Research 20
    2.8 Ethylene Hydrogenation 21
    2.9 Introduction to Metal Sulfide Hydrotreating Catalysts 23

Chapter 3: Experimental Methods and Procedures 26
    3.1 Materials Preparation 26
    3.2 Characterization Methods 38

Chapter 4: Results and Discussion 47
    4.1: Composition of Supports and Catalysts (XPS and INAA) 48
    4.2: Structure of Supports and Catalysts (TEM, XRD and Surface Area) 72
    4.3: Acidity of Supports and Catalysts ($NH_3$-TPD) 101
    4.4: Summary of Characterization Results 108
    4.5: Ethylene Hydrogenation Activities 110

Chapter 5: Summary and Conclusions 120

Chapter 6: Recommendations and Future Work 121

References 123

Appendices 129

- A. XPS Results 129
- B. TEM Results 138
- C. $NH_3$-TPD Results 280
- D. Ethylene Hydrogenation Results 290

## List of Tables

Table 3.1: Effluent conditions during the Ni exchange into HCHA. 32

Table 3.2: Effluent conditions during the further Mo exchange into MoHCHA. 35

Table 3.3: Effluent conditions during the Ni exchange into MoHCHA. 37

Table 3.4: Demonstration of composition calculation in the hydrogenation study. 45

Table 4.1: Definition of catalyst materials studied. 47

Table 4.2a: Mass percentages from wide scans of as made and reduced Ni-CHA. 50

Table 4.2b: Mass percentages from wide scans of as made and reduced NiMo-CHA. 51

Table 4.3a: Wide scan 'Per silicon' concentrations of as made and reduced Ni-CHA. 52

Table 4.3b: Wide scan 'Per silicon' concentrations of as made and reduced NiMo-CHA. 53

Table 4.4a: Mass percentages from wide scans of as made and sulfided Ni-CHA. 60

Table 4.4b: Mass percentages from wide scans of as made and sulfided Ni-CHA. 60

Table 4.5a: 'Per silicon' concentrations wide scans of as made and sulfided Ni-CHA. 61

Table 4.5b: 'Per silicon' concentrations wide scans of as made and sulfided NiMo-CHA. 61

Table 4.6a: INAA mass percentages of as made Series 1 catalysts. 71

Table 4.6b: INAA 'Per silicon' concentrations of as made Series 1 catalysts. 71

Table 4.7: Parameters and results of the Scherrer equation applied to Series 1. 94

Table 4.8: Parameters and results of the Scherrer equation applied to Series 2. 97

Table 4.9: Surface area data from selected samples. 100

Table 4.10: Heats of adsorption of $NH_3$ on samples from Series 1. 103

Table 4.11: $NH_3$ heats of adsorption for sequential exchange of $NH_4^+$ into Na-CHA. 104

Table 4.12: Heats of adsorption of $NH_3$ on samples from Series 2. 108

Table A.1a: Compositions of the Series 2 catalysts in the as made state in the R200 experiment. 131

Table A.1b: Compositions of the Series 2 catalysts reduced at 200°C in the R200 experiment. 132

Table A.1c: Compositions of the Series 2 catalysts in the as made state in the R300 experiment. 132

Table A.1d: Compositions of the Series 2 catalysts reduced at 300°C in the R300 experiment. 133

Table A.1e: Compositions of the Series 2 catalysts in the as made state in the R340 experiment. 133

Table A.1f: Compositions of the Series 2 catalysts reduced at 340°C state in the R340 experiment. 134

Table A.2a: 'Per silicon' compositions of the Series 2 catalysts in the as made state in the R200 experiment. 134

Table A.2b: 'Per silicon' compositions of the Series 2 reduced at 200°C in the R200 experiment. 135

Table A.2c: 'Per silicon' compositions of the Series 2 in the as made state in the R300 experiment. 135

Table A.2d: 'Per silicon' compositions of the Series 2 reduced at 300°C in the R300 experiment. 136

Table A.2e: 'Per silicon' compositions of the Series 2 in the as made state in the R340 experiment. 136

Table A.2f: 'Per silicon' compositions of the Series 2 reduced to 340°C in the R340 experiment. 137

## List of Figures

Figure 1.1: Schematic diagram of bulk (left) and supported (right) catalysts. 1

Figure 2.1: Pore structure of zeolite X and Y. 8

Figure 2.2: Schematic diagram of NiMoS. 13

Figure 2.3: Graphical depiction of shape selection between 2,6- and 2,7-DIPN on H-Mordenite. DIPN = Diisopropylnaphthalene. 18

Figure 2.4: The sodalite cage structure of chabazite. 21

Figures 2.5a-d: Horiuti-Polanyi mechanism of Ethylene Hydrogenation. 22

Figure 3.1: Schematic of the reflux system. 26

Figure 3.2: Setup of the exchange column. 31

Figure 3.3: Flow Rate versus volume eluted during the Ni exchange into HCHA. 33

Figure 3.4: Flow rate versus volume eluted during the Ni exchange into MoHCHA. 38

Figure 3.5: The quartz U-tube used in Ammonia TPD experiments. 39

Figure 3.6: Schematic of a four-well sample holder. 40

Figure 3.7: Diagram of the in-situ TPR-XPS setup. 41

Figure 4.1a: Wide scan of as made Ni-CHA showing the various components of the sample. 48

Figure 4.1b: Wide scan of as made NiMo-CHA showing the various components of sample. 49

Figure 4.2: Overlap of Al 2p, Ni 3p and Na 2s features affecting the value of Si/Al. 54

Figure 4.3a: Narrow scans of the Ni 2p feature within as made and reduced Ni-CHA. 55

Figure 4.3b: Narrow scans of the Ni 2p feature within as made and reduced NiMo-CHA. 56

Figure 4.4: Quantified extent of reduction of Ni-CHA and NiMo-CHA. 57

Figure 4.5: Narrow scans of the Mo 3d feature within as made and reduced NiMo-CHA. 58

Figure 4.6a: Wide scan of Ni-CHA sulfided at 265°C. 59

Figure 4.6b: Wide scan of NiMo-CHA (lower) sulfided at 265°C. 59

Figure 4.7a: Narrow scans of the Ni 2p feature within as made and sulfided Ni-CHA. 62

Figure 4.7b: Narrow scans of the Ni 2p feature within as made and sulfided NiMo-CHA. 62

Figure 4.8: Quantified extent of sulfidation of Ni-CHA and NiMo-CHA. 63

Figure 4.9: Narrow scans of the Mo 3d feature within as made and sulfided NiMo-CHA. 64

Figure 4.10a: Narrow scans of the Ni 2p feature within as made and reduced NiHCHA. 66

Figure 4.10b: Narrow scans of the Ni 2p feature within as made and reduced NiMoHCHA. 67

Figure 4.11: Quantified extent of reduction of NiHCHA and NiMoHCHA. 68

Figure 4.12a: Narrow scans of the Mo 3d feature within as made and reduced NiMoHCHA. 69

Figure4.12b: Narrow scans of the Mo 3d feature within as made and reduced MoHCHA. 69

Figure 4.13: Effect of exposure upon reduced NiHCHA (Ni) and NiMoHCHA (NiMo). 70

Figure 4.14: TEM image of Na-CHA reduced at 350ºC. 73

Figure 4.15: TEM image of Ni-CHA reduced at 275ºC. 74

Figure 4.16: TEM image of Ni-CHA reduced at 450ºC. 75

Figure 4.17: TEM image of Ni-CHA sulfided at 250ºC. 76

Figure 4.18: TEM image of as made Mo-CHA. 77

Figure 4.19: TEM image of Mo-CHA reduced at 450ºC. 78

Figure 4.20: TEM image of Mo-CHA sulfided at 350ºC. 79

Figure 4.21: TEM image of NiMo-CHA reduced at 450ºC. 80

Figure 4.22: TEM image of NiMo-CHA sulfided at 350°C. 81

Figure 4.23: TEM image of NiHCHA reduced at 200°C. 82

Figure 4.24: TEM image of NiHCHA reduced at 400°C. 83

Figure 4.25: TEM image of NiHCHA sulfided at 300°C. 84

Figure 4.26: MoHCHA reduced at 200°C. 85

Figure 4.27: TEM image of MoHCHA reduced at 400°C. 86
Figure 4.28: TEM image of MoHCHA sulfided at 400°C. 87
Figure 4.29: TEM image of NiMoHCHA reduced at 400°C. 89
Figure 4.30a: TEM image of NiMoHCHA sulfided at 300°C. 90
Figure 4.30b: TEM image of NiMoHCHA sulfided at 300°C with contrast and brightness adjustment. 91
Figure 4.31: Wide scans of the as made catalysts in Series 1. 92
Figure 4.32: Emergence of Ni (111) line upon hydrogen reduction of Ni-CHA. 93
Figure 4.33: Wide scans of the as made catalysts in Series 2. 95
Figure 4.34a: Emergence of Ni (111) line upon hydrogen reduction of NiHCHA. 96
Figure 4.34b: Emergence of Ni (111) line upon hydrogen reduction of NiMoHCHA. 96
Figure 4.35a: Wide scans of sulfided NiHCHA. 98
Figure 4.35b: Wide scans of sulfided NiMoHCHA. 99
Figure 4.35c: Wide scans of sulfided MoHCHA. 99
Figure 4.36a: $NH_3$-TPD Spectrum for Na-CHA. 102
Figure 4.36b: First order plot of the peak temperature (Tp) data for Na-CHA. 102
Figure 4.37a: $NH_3$ TPD spectra for NiMo-CHA prior to exchange with $NH_4^+$. 104
Figure 4.37b: First order plot of the peak temperature (Tp) data for NiMo-CHA prior to exchange with $NH_4^+$. 105
Figure 4.38a: $NH_3$ TPD spectra for NiMo-CHA following exchange with $NH_4^+$. 105
Figure 4.38b: First order plot of the peak temperature (Tp) data for NiMo-CHA following exchange with $NH_4^+$. 106
Figure 4.39a: $NH_3$ TPD spectra for NiHCHA. 107
Figure 4.39b: First order plot of the peak temperature (Tp) data of SI and SII for NiHCHA. 108
Figure 4.50: Reactor effluent compostion (excluding $H_2$ and Ar ) from ethylene hydrogenation over NiMo-CHA reduced at 450°C. 110
Figure 4.51: Steady state ethane mole fraction (excluding $H_2$, $H_2S$ and Ar) in reactor effluent over Ni-, Mo- and NiMo-CHA sulfided at 450°C. 111
Figure 4.52a: Catalytic results for NiMoHCHA reduced at 300°C. 112
Figure 4.52b: Catalytic results for NiHCHA reduced at 300°C. 113

Figure 4.52c: Catalytic results for MoHCHA reduced at 300°C. 113
Figure 4.52d: Methane generation over metal loaded chabazites reduced at 300°C. 114
Figure 4.53a: Catalytic results NiMoHCHA sulfided at 300°C. 115
Figure 4.53b: Catalytic results NiHCHA sulfided at 300°C. 116
Figure 4.53c: Catalytic results MoHCHA sulfided at 300°C. 116
Figure 4.53d: Ethane generation over metal loaded chabazites reduced at 300°C. 117
Figure A.1a: Wide scan of as made HCHA. 129
Figure A.1b: Wide scan of as made NiHCHA. 130
Figure A.1c: Wide scan of as made NiMoHCHA. 130
Figure A.1d: Wide scan of as made MoHCHA. 131
Figure B.1 – B.142: TEM images of Series 1 and Series 2. 138
Figure C.1 – C.19: $NH_3$-TPD Spectra of various exchanged chabazites. 280
Figure D.1: Catalytic results for the metal loaded acidified chabazites reduced at 200°C. 290
Figure D.2: Catalytic results for the metal loaded acidified chabazites reduced at 300°C. 291
Figure D.3: Catalytic results for the metal loaded acidified chabazites reduced at 400°C. 292
Figure D.4: Catalytic results for the metal loaded acidified chabazites sulfided at 200°C. 293
Figure D.5: Catalytic results for the metal loaded acidified chabazites sulfided at 300°C. 294
Figure D.6: Catalytic results for the metal loaded acidified chabazites sulfided at 400°C. 295

## List of Equations

| | | |
|---|---|---|
| Equation 2.1 | Structural formula of aluminosilicates | 6 |
| Equation 2.2 | Acidification through ammonium exchange | 9 |
| Equation 2.3 | Direct acifidification of zeolites | 9 |
| Equation 2.4 | Hirschler-Plank Scheme for multivalent cation acidification | 9 |
| Equation 2.5 | Hirschler-Plank Scheme for multivalent cation acidification | 9 |
| Equation 2.6 | Hirschler-Plank Scheme for multivalent cation acidification | 9 |
| Equation 2.7 | Reduction of ion-exchanged metals within zeolites | 11 |
| Equation 4.1 | Computation of surface atomic composition from XPS data | 49 |
| Equation 4.2 | Computation of surface mass composition from surface atomic composition | 50 |
| Equation 4.3a | Computation of surface mass composition normalized to silicon surface mass composition | 52 |
| Equation 4.3b | Computation of surface atomic ratios normalized to silicon | 52 |
| Equation 4.4 | Computation of extent of reduction from XPS data | 56 |
| Equation 4.5 | Scherrer equation for calculation of crystallite size from XRD data | 93 |

## List of Nomenclature

| Symbol | Meaning | Unit |
|---|---|---|
| B | Angular full width at half max ($2\theta$) | radians |
| BASF | Badische Anilin und Sodafabrik | |
| CEC | Cation exchange capacity | mmole/g |
| CHA | Chabazite | |
| DIPN | Diisopropylnaphthalene | |
| D.I. $H_2O$ | De-ionized water | |
| $E_{Red}$ | Extent of reduction | no unit |
| FCC | Fluidized catalytic cracking | |
| HDN | Hydrodenitrogenation | |
| HDS | Hydrodesulfurization | |
| INAA | Instrumental neutron activation | |
| M | Metal exchanged into zeolite framework | |
| M | Mordenite | |
| $M_{Atomic}$ | Atomic Mass | g/atom |
| MTG | Methanol to gasoline | |
| $M^0$ | Metal within zeolite framework | |
| $M^{2+}$ | Metal cation within zeolite framework | |
| $NH_3$-TPD | Ammonia temperature programmed desorption | |
| RC | Ring contraction | |
| S | Site within faujasite structure | |
| SAPO | Silicoaluminophosphates | |
| Si/Al | Silicon to aluminum ratio | (mole/mole) |
| t | Crystallite size as measured by the Scherrer equation | nm |
| TEM | Transmission electron microscopy | |
| Tp | Peak temperature in $NH_3$-TPD data | °C or K |
| TPR | Temperature programmed reduction | |
| TPS | Temperature programmed sulfidation | |
| USD | U.S. dollars | |

| | | |
|---|---|---|
| X | Zeolite X | |
| $X_{Atomic}$ | Surface atomic composition | no unit |
| $X_{Mass}$ | Surface mass composition | no unit |
| $X_{Mass, Si}$ | Surface mass composition normalized to Si mass composition | no unit |
| XPS | X-ray photoelectron spectroscopy | |
| XRD | X-ray diffraction | |
| $x_{Si}$ | Surface mass composition of Si | no unit |
| x/y | Molar silicon to aluminum ratio | no unit |
| Y | Zeolite Y | |
| $y_{Al}$ | Surface mass composition of Al | no unit |
| $Y_{j,Si}$ | Surface atomic ratio normalized to Si | no unit |
| Z | Zeolite | |
| ZSM-5 | Zeolite Scony Mobile number 5 | |
| $\beta$ | Ramp rate in $NH_3$-TPD experiments | °C/min or K/min |
| $\Delta H_{Ads}$ | Enthalpy of $NH_3$ adsorption in $NH_3$-TPD experiments | kJ/mole |
| $\lambda$ | Wavelength Cu Kα radiation (0.154) | nm |
| $\theta$ | Diffraction angle | radians, degrees |

# CHAPTER 1

# Introduction

## 1.1 Background and Motivation

Supported metal catalysts have been widely employed in academic and industrial settings for many years. The use of bulk catalysts is usually cost prohibitive because the metals responsible for the catalytic activity are typically too expensive to employ in such quantities. Through the use of a catalyst support, equivalent or higher activity can be achieved using less of the active metal, because of the high degree of dispersion that can be achieved. This results because in a bulk catalyst, the portion of the active metal below the external surface cannot be reached easily by the reactants, and is therefore of little catalytic use (Figure 1.1).

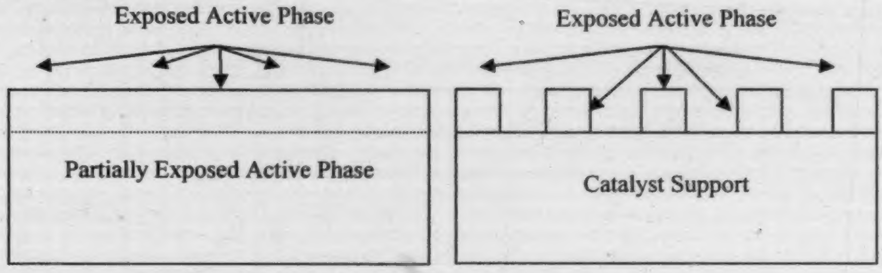

Figure 1.1: Schematic diagram of bulk (left) and supported (right) catalysts.

While conventional hydrogenation catalysts can be employed much more economically in supported form, another advantage to supported metal catalysts is realized in applications requiring bifunctional catalysis. An example is ring opening, which in addition to strong metallic (hydrogenation) activity, also requires strong acid (isomerisation) sites [1]. In such applications, the chemistry of the support itself becomes relevant, and as a result, the overall chemistry of the support and the metal phase must be simultaneously considered.

Another important consideration is the means by which the metal phase is incorporated within the support. Common methods include impregnation and ion-exchange. The former typically involves evaporating a solution or suspension of the active phase on the support, the resulting dispersion of which depends on factors such as metal-support interactions, drying rates, solution loading and support morphology. As metals readily form cations in aqueous solution, a support featuring ion exchange capacity can lead to vast improvements in the dispersion of the active phase.

With these two support characteristics in mind, zeolites make ideal supports for metals (or metal sulfides, oxides etc.) as they are renowned for both their acidic properties and their ion exchange capacities [2]. In addition, zeolites offer the advantage of uniform pore size, which in many cases can be tailored through adjustment of zeolite structural parameters such as the Si/Al ratio, in the case of the most common zeolites, aluminosilicates.

As stated above, supported metal catalysts are not always employed in their metallic state. In real world applications, catalysts must be able to maintain their activity in the presence of catalytic poisons such as heteroatomic species containing sulfur and nitrogen. As legislation regulating the sulfur and nitrogen content in transportation fuels becomes ever more stringent in response to the protection of the environment [3], hydrotreating catalysts are typically employed in the sulfide form, in order to process such refractory species.

Despite their resistance to sulfur and nitrogen, sulfide catalyst can undergo severe deactivation in the presence of other poisons such as arsenic. Also, reactions taking place simultaneously on the catalyst surface, such as hydrodesulfurization (HDS) and hydrodenitrogenation (HDN), demand a high degree of site dispersion in order to achieve high reaction rates in the processing of low concentrations of sulfur and nitrogen species.

It is for this reason that a prime motivation of this project was to prepare highly dispersed metal phases in both the metallic and sulfide form. As an exploratory goal, the preparation of NiMoS type catalytic sites on the surface of a zeolite support was adopted.

This is an active area of research, which was recently reviewed by Hensen and van Veen in 2003 [4]. The zeolite chosen was chabazite, an aluminosilicate with a faujasite-like structure that has recently shown promise in its ability to act as a hydrogen storage material [5, 6] and to stabilize small clusters of metal on its external surface [7]. In addition, owing to its layered structure, chabazite is believed to have a high external surface area compared to other zeolites. Finally, at the time of this research, there were no known publications on the use of chabazite as a support for Ni and Mo, typical metals used in the sulfide phase as hydrogenation catalysts. For these reasons, chabazite was seen as an ideal candidate for development as a hydrogenation catalyst support.

## 1.2 Research Objectives

The objectives of this study can be summarized into the following;

1) The determination of factors which affect the structure and stability of supported Ni, Mo and NiMo catalysts. The proposed means of achieving this was through variations of the ion-exchange technique used to introduce Ni (as $NiCl_2$) and Mo (as $MoCl_3$) into the sodium form of chabazite, Na-CHA. The first series of materials was produced through a high temperature batch reflux, while the second was produced through the use of a lower temperature exchange column, through which aqueous solutions of the metal chlorides to be exchanged were contacted with pre-acidified chabazite, (HCHA). In addition, post-treatment techniques, such as reduction in hydrogen and sulfidation using hydrogen sulfide, were used to generate active sites in both the metallic and the sulfide state. Modification of the support, through $NH_4^+$ exchange and direct acidification, was attempted in order to gauge how the properties of the support affect the dispersion and size of the supported clusters. Insight into the combined structure of the chabazite support and the incorporated metal phases was pursued through the use of the following characterization techniques;

- Instrumental Neutron Activation (INAA)
  This technique, based on the emission of excited state neutrons, provides compositional information of solid samples without requiring dissolution or significant sample processing.

- X-Ray Photoelectron Spectroscopy (XPS)
  Based on the photoelectric effect, XPS provides not only surface compositional information, but can also identify the oxidation state and chemical state of the components of the surface of the sample.

- Transmission Electron Microscopy (TEM)
  This technique provides nanometer scale images of the surface of a sample, allowing measurement of cluster size and morphology.

- $NH_3$ Temperature Programmed Desorption ($NH_3$-TPD)
  This technique provides the enthalpy of $NH_3$ adsorption on the acid sites of the catalyst, which can be taken as a measure of the acidity of the sample.

- X-Ray Diffraction (XRD)
  This technique provides structural information on the support, as well as cluster size of the supported phase.

2) The determination of hydrogenation activity in both the presence and absence of $H_2S$, using ethylene hydrogenation as a probe reaction. This extensively studied reaction has been described as structure insensitive, while ethane hydrogenolysis is believed to be structure senstive [8], while less complex than the typical model compounds of HDS and HDN reactions, (such as thiophene or pyrrole, respectively), offers a comparatively simple product spectrum, consisting of ethane (hydrogenation) or methane (hydrogenolysis).

Chapter 2 of this thesis consists of an overview of zeolites, the preparation of transition metal zeolite catalysts, and catalytic properties. Chapter 3 contains descriptions of the experimental methods used, and in Chapter 4 the results of the study are presented and discussed. Chapter 5 contains a summary of the study, and general conclusions are drawn. Recommendations for further study in this area of research are presented in Chapter 6. There are several appendices included at the end of this thesis, which contain a much wider set of results of the various endeavours undertaken.

# Chapter 2

# Overview of Zeolites and Zeolite-Supported Ni, Mo and NiMo Catalysis

## 2.1 Introduction to Zeolites

The word *zeolite* has been in use since 1756, when the Swedish mineralogist Crönstead discovered Stilbite, a mineral that upon heating exhibits *intumescence*, which is an expansion of the crystallite size often accompanied by release of water [9]. Crönstead coined the term *zeolite*, derived from the Greek words *zein* (to boil) and *lithos* (stone), due to the observation that some zeolites appear to boil as they melt (the release of water).

## 2.2 Zeolite Structure

The structure of a zeolite can be described as a large extended framework that is essentially a crystalline polymer arrangement of groups such as tetrahedral $AlO_4$ and $SiO_4$ units sharing corner oxygen atoms. While not unique among porous media, zeolites are unique in that they feature uniform pore dimensions, which are on the order of molecular sizes [2]. The earliest known zeolites, aluminosilicates, are by far the most common, (both naturally and synthetically). These have the structural formula [10];

$$M_{x/n}(AlO_2)_x(SiO_2)_y \qquad \textbf{2.1}$$

where $n$ is the valence of the cation, M,
$x + y$ is the number of tetrahedra within the unit cell,
$y/x$ is the Si/Al ratio, a key parameter in zeolites.

As discussed above, there are zeolites which are not aluminosilicates, such as silicoaluminophosphates, (SAPO), which can take on structures which do not exist as aluminosilicates [2]. Zeolite structures with framework titanium, (titanosilicates) vanadium, iron etc. have also been developed and are used in areas such as oxidation catalysis [2].

The value of Si/Al takes a minimum value of unity, as stated by Lowenstein's rule; there cannot be two adjacent $AlO_4$ groups. It should be noted that a given zeolite structure does not necessarily imply a composition. Many zeolite structures can exist over a range of Si/Al values. Post-synthetic treatments such as addition or removal of aluminum (dealumination) in acidic media, and the addition of silicon via silicon halides or hexafluorosilicates, are all documented in the literature. While these treatments may not change the essential structure of the zeolite in question, framework charge density, acidity, cation exchange capacity, hydrophobicity and unit cell dimensions often change significantly as a result [2].

In aluminosilicates, the aluminum atoms are in a (+3) oxidation state, while the silicon atoms are in a (+4) state. As both are present within tetrahedra of shared oxygen atoms, the silica groups are electronically neutral, while the alumina groups have a net charge of (–1). These charges must be balanced, and this is typically achieved by ionically bound cations, and as a result, zeolites are well known for their remarkable ion-exchange properties. In the common case of zeolites in either the Na or H form, (charges balanced by either $Na^+$ or $H^+$), exchange with divalent metals such as $Ni^{2+}$ or $Co^{2+}$ is also well established [9]. For illustrative purposes, the structure of faujasite is shown in Figure 2.1. This is the parent structure of the common zeolites X and Y, which are commonly used in both computational and experimental research into zeolite catalysis. Each vertex represents either Si or Al atoms, with the bridging O atoms omitted for clarity. As shown, there are multiple locations (I, I', II, II') at which a cation can reside.

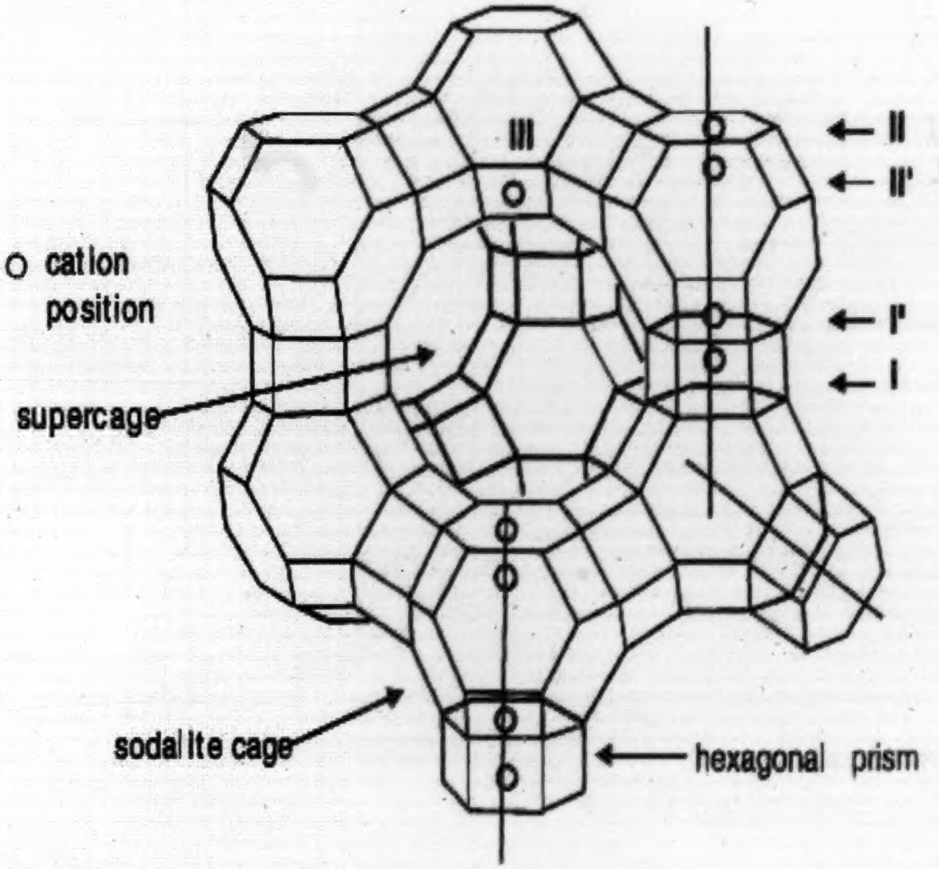
III
II
II'
o cation position
I'
I
supercage
sodalite cage
hexagonal prism

Figure 2.1: Pore structure of zeolite X and Y (Faujasite) [11] .

The crystal size of many zeolites is on the micron scale, although synthetic zeolites which feature crystal sizes on the nm scale, which appear amorphous by XRD, have been synthesized [2].

### 2.3 Zeolite Acidity

As is the case with other aluminosilicates supports, zeolites show an inherent acidity. This acidity is due to both Brønsted (proton donor) and Lewis (electron pair acceptor) sites. The fact that this acidity can be tuned is one of the most valuable traits of zeolite supports.

Brønsted acidity within zeolites can be introduced by ion-exchanging ammonium ions, followed by heat treatment (liberating free ammonia, leaving the zeolite in the protonated state) [2].

$$NH_4^+ + Na^+Z^- \xrightarrow[-Na^+]{} NH_4^+Z^- \xrightarrow[\sim 350^\circ C, -NH_3]{} H^+Z^- \qquad 2.2$$

Direct acid exchange, represented by the following reaction [2],

$$H^+ + Na^+Z^- \xrightarrow[-Na^+]{} H^+Z^- \qquad 2.3$$

is less favoured, due to the risk of dealumination or even complete framework collapse, as would likely occur in aluminum-rich structures [2]. Multivalent cations exchanged into the zeolite behave similarly to incorporated $NH_4^+$, (discussed above), according to the so-called *Hirschler-Plank* scheme [2];

$$[La(H_2O)_n]^{3+} + 3Na^+Z^- \xrightarrow[-3Na^+]{} [La(H_2O)_n]^{3+}(Z^-)_3 \qquad 2.4$$

$$[La(H_2O)_n]^{3+}(Z^-)_3 \xrightarrow[\sim 300^\circ C, -(n-2)H_2O]{} [(LaOH)(H_2O)]^{2+}H^+(Z^-)_3 \qquad 2.5$$

$$[(LaOH)(H_2O)]^{2+}H^+(Z^-)_3 \longrightarrow [La(OH)_2]^+(H^+)_2(Z^-)_3 \qquad 2.6$$

The protons of the Brønsted acid sites, regardless of the method of generation, take the form of bridging hydroxyl groups between $AlO_4$ and $SiO_4$ groups, (or such analogues in other structures) [2]. As Brønsted acidity is related intimately to ion-exchange, the maximum number of such protons results from the minimization of the Si/Al ratio, which takes its lowest value of unity (Lowenstein's rule). According to the structural formula given previously, the maximum number of such Brønsted acid sites is theoretically 8.33 mmol $g^{-1}$. However, complete protonation is generally unattainable due to steric effects, competing ions, and the loss of crystallinity that can occur with certain structures at high acidity [2, 9]. The Brønsted acidity of a zeolite can be reduced by calcining at elevated temperatures, whereby bridging hydroxyl groups are eliminated from the framework as liberated water molecules. This is often referred to as dehydroxylation. Some structures, such as chabazite and clinoptilolite, may suffer framework collapse as a result, while others, such as erionite and zeolite Y, retain their crystallinity at low to moderate dehydroxylation [12].

Another key concept related to the Brønsted acidity of zeolites is the required distinction between the number of such sites (i.e. acid site density) and the strength of such sites. While it is true that minimizing the Si/Al ratio maximizes the number of Al atoms in the structure, and therefore the number of Brønsted acid sites, the strength of a given acid site is reduced with increasing Al content [13]. In this way, Brønsted site density and site strength have an inverse relationship to each other within zeolites. As a result of this, zeolite catalysts employed for their acidic properties often take on a maximum activity at relatively small Si/Al values, above which higher site strength is achieved at the expense of site density. For example, dealuminated zeolite Y employed as a cracking catalyst achieves maximum activity at Si/Al approximately 10. This observation has also been supported by quantum mechanical calculations [2].

Lewis acid sites also contribute to the acidity of zeolites. However, there is some contention in the literature as to the exact nature of these sites within zeolites. For example, it has been shown that silicon remains tetracoordinated upon dehydroxlation, which results in so-called extra-framework aluminum species [14]. These charged $AlO_x$ structures are believed to act as Lewis (electron pair accepting) acid sites [2]. Another possibility is the presence of highly charged (multivalent) ions within the support which may act as electron pair acceptors in their own right. Literature sources draw a distinction between incorporated cations and extra-framework alumina species, the latter of which are often referred to as 'true Lewis sites'.

Worth noting is that within zeolites, the Brønsted and Lewis modes of acidity are not truly independent [2, 15]. It has been reported that Brønsted acid sites play a stronger role in catalytic activity than Lewis sites, but that presence of Lewis acid sites may enhance the strength of local Brønsted sites [2] .

Not only do the Brønsted and Lewis sites differ in strength, but sites of either type at different locations within the zeolite (see Figure 2.1) may also differ significantly in their acidity [2]. It is therefore common research practice to determine the distribution of the acid sites present. To determine the strength distribution, (the number of sites of a given strength), one can resort to calorimetric, spectroscopic or temperature programmed techniques, each with its own associated advantages and disadvantages [2]. For example, acid site density can be determined spectroscopically, through techniques like $^1$H-NMR or IR. Although these experiments are simple enough to perform, quantification requires knowledge of parameters such as extinction coefficients, which are not readily available [2]. A more difficult experiment to perform, but one requiring less literature parameters is the use of techniques such as ammonia temperature programmed *desorption* or propylamine temperature programmed *decomposition*. Note that the acronym 'TPD' is often misleadingly applied to both of these techniques. Ammonia adsorbs onto and desorbs from both Brønsted and Lewis sites alike, therefore ammonia temperature programmed desorption gives a convolution of the two types of sites within the support. The decomposition of propylamine or other alkylamines (alkylamine temperature programmed decomposition) is a proton-catalyzed reaction, and therefore only sensitive to Brønsted acid sites. Performed together, ammonia and alkylamine temperature programmed studies allow the calculation of both the Brønsted and Lewis site densities.

Despite being an inherent property of the support, acidity can also be affected by the incorporation and post-treatment of a secondary phase within the pore structure of the zeolite. A very relevant example to this discussion is the reduction of ion-exchanged catalytic metals. As discussed by Weitkamp (2000), the following reaction is plausible [2];

$$M^{2+}\left(Z^-\right)_2 \xrightarrow[H_2]{} M^0\left(H^+\right)_2\left(Z^-\right)_2 \qquad \textbf{2.7}$$

Published reports of this concept can be found in the work of Shil et al. [16], who found an increase in Brønsted acidity upon the reduction of NiCa-Y.

## 2.4 Applications of Zeolites

Although on a tonnage basis, zeolites find their widest use in the detergents industry, the greatest sector in terms of total value of zeolites is in the field of catalysis [2].

Zeolites have been used in industrial catalytic processes for many years, beginning in the 1950s with the use of zeolite Y in isomerization reactions and other applications by Union Carbide [17, 18]. Zeolites began to play a more significant role in catalysis with the development of synthetic zeolite X and Y for use in fluidized catalytic cracking (FCC) processes in 1962 [2]. Previous FCC catalysts had the tendency to 'overcrack', whereas synthetic zeolites offer a more uniform acidity. In applications where high acidity is required, zeolite-based catalysts offer significantly higher acidity than their industrial forerunners [2]. It is not surprising then that reports as of the year 2000 state that use of zeolites in petroleum refining has led to a savings of approximately 10 billion USD worldwide [2]. An important sector of petroleum refining focuses on raising the octane number of fuels. It is known that low temperatures favour the type of isomerisation reactions needed to raise octane numbers, and chlorinated aluminas are well-suited as bifunctional catalysts for these processes. However, they suffer from drawbacks such as problems with equipment corrosion and the need for feedstock pre-treatment to avoid deactivation, (i.e. they are sensitive to poisoning by sulfur and nitrogen compounds in the feed). Noble metal zeolite catalysts are attractive alternatives in this case, and have been widely reviewed in literature [16] .

## 2.5 Preparation of Zeolite Supported Catalysts

In contrast to alumina and silica, zeolites are highly crystalline materials with tremendous potential for adsorption and cationic exchange due to their highly ordered pore structure. By making use of these properties, catalytically active metals such as Ni and Mo can be incorporated into zeolite supports in a number of ways. One of the most common methods found in the literature is broadly termed *impregnation.* A less common approach, but of wide use in the preparation of zeolite catalysts is *ion exchange*. This report will focus primarily on the preparation of sulfur resistant transition metal, (such as widely known NiMo or CoMo type) zeolite catalysts, for use in hydrogenation applications such as hydrodsulfurization, (HDS).

### 2.5.1 Impregnation

The success of NiMoS type catalysts has motivated the incorporation of bimetallic clusters, specifically because of the knowledge that formation of NiMoS type structures requires close proximity of the two metals [11]. In such a phase, represented schematically below in Figure 2.2, nickel decorates the edge of $MoS_2$ slabs, and it is this promoter effect that is believed to be the source of this material's catalytic activity.

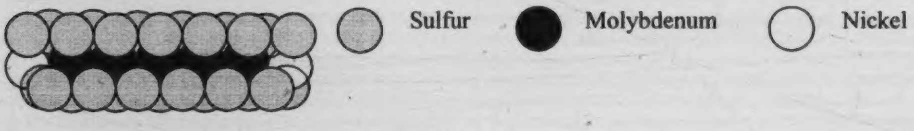

Figure 2.2: Schematic diagram of NiMoS.

This unique metal sulfide has a distinct advantage over discreet metal sulfides, in that the nickel is four coordinate with sulfur, (and thus 'fully sulfided'), and yet it is still accessible as a catalytic site, due to the square planar (as opposed to tetrahedral) arrangement of the sulfur around the nickel. More recent works have refined this postulate, referring to 'brim sites' near the edge of the NiMoS structure as showing unique catalytic activity [19] .

The incorporation of bimetallic oxide clusters is exemplified by the work of Plaznet et al. [20] who attempted the incorporation of $[CoMo_6O_{24}H_6]^{3-}$ into zeolite Y. While they were successful in preserving the complex within the support, thermal decomposition proved to be problematic. Taniguchi et al. [21] investigated the incorporation of $[Mo_3NiS_4Cl(H_2O)_9]^{3+}$, which technically represents an ion exchangeable cluster, but is more appropriately discussed here in the sense that the Ni and Mo are not introduced as separate ions. Also, note that this attempt made use of a presulfided cluster. These authors report the successful incorporation of the complex, as well as a synergic affect relative to the separate introduction of Ni and Mo, although it should be noted that their synthesis of the Ni-Mo catalyst did not include a calcination step, thereby avoiding thermal decomposition issues. However, there may be limitations to this approach, due to the narrow thermal stability of such supported systems.

Work on transition metal carbonyls is also widely reported in literature. Okamoto and Katsuyama [22] studied the incorporation of $Mo(CO)_6$ and subsequent sulfidation within zeolite Y. They report a highly dispersed molybdenum sulfide phase with high thermal stability and HDS activity toward thiophene. While studies involving $Ni(CO)_4$ are obviously limited due to reasons of toxicity, examples can be found in the literature [23, 24]. A general conclusion in all of such studies is that intrazeolite water reduces the amount of metal carbonyl incorporated, and that the strength of the support-carbonyl interaction is a function of the Si/Al ratio of the support [11].

### 2.5.2 Ion Exchange

Ion exchange with divalent metals is well established [9]. Typically, the Na or H form of the support (that is, with $Na^+$ or $H^+$ ions balancing charge) is suspended in an aqueous solution of the metal ions to be exchanged. In the event that the cation to be exchanged is too large (particularly in its solvated form), procedures for solid state ion exchange are published in the literature [2]. Depending on the desired extent of exchange, this process may be carried out at elevated temperatures and/or repeated with fresh metal solution. The exchange capacity of a zeolite is governed by the Si/Al ratio (i.e. the Al content), and thus, the metal loading through ion-exchange is similarly bounded [25]. After collecting the solids on a Buchner funnel, washing with D.I. water to remove free ions and drying the solids, the resulting product can be calcined at elevated temperatures (within the thermal stability limit of the support and with regard for support acidity, as discussed earlier). Such calcinations in air may result in partial oxidation of the metal phase.

Just as there are variations in acid site strengths, the various ion-exchange sites are not equivalent either. As found in Shil et al. [16], the XRD work of Olson [26] and Gallezot et al. [27] on Ni within zeolite Y showed that two thirds of the $Ni^{2+}$ ions incorporated reside in $S_I$ (hexagonal prism) sites, with the balance in the $S_{II}$, $S_{II}$' and $S_I$' sites (see Figure 2.1). Combining this with the findings of Egerton et al. [28], that $Ca^{2+}$ preferentially exchanges at $S_I$ sites, at which the reduction of $Ni^{2+}$ has a high activation energy barrier [29], it is clear that competitive exchange would result in a higher population of $Ni^{2+}$ in sites other than $S_I$, (i.e. in sites at which it is more easily reduced), thereby producing Ni clusters of larger size, as outlined by Shil et al. [16]. Upon review of their data, it does appear that crystallite size does indeed seem to increase with increasing Ca loading.

The method of ion exchange also allows for more control over the dispersion of the incorporated phase, leading to changes in characteristics such as activity and selectivity. As reported in the literature, [11, 25, 30], ion-exchange results in more regular metal dispersion, owing to a more pronounced metal-support interaction. This results in smaller metal clusters on the support, favouring isomerisation over hydrogenation. However, in their study of Ni supported on H-Mordenite, Cañizares et al. [25] found little difference in the TEM clusters size of Ni incorporated through ion-exchange versus impregnation. However, the 'anchoring effect' with ion-exchange was observed in the case of Pd on H-Mordenite.

### 2.5.3 Post-treatment Techniques

The reduction of the incorporated metal phase in flowing hydrogen is well established [16, 29, 30]. By monitoring hydrogen consumption as a function of temperature, one can determine the quantity of metal sites incorporated into the support, as well as track stepwise reductions in the case of multivalent metals. This technique is commonly referred to as temperature-programmed reduction (TPR). Incorporated metals are analogously converted to the sulfide form via temperature-programmed sulfidation (TPS) in which $H_2S$ (or a blend of $H_2S$ / $H_2$) is used in place of $H_2$. In their study on zeolite/alumina mixtures, Ding et al. [31] concluded that the length and stacking height of $MoS_2$ slabs increased with increased Si/Al. Also noted was that an effect of sulfidation was to cause migration of Mo and Ni into the bulk, an effect more pronounced in the case of Mo than for Ni.

While methods do exist for the determination of the location of such incorporated species [28], there is some disagreement in literature sources on their precise location within the zeolite framework. For example, in zeolite X and Y, it has been reported that $Ni^{2+}$ occupies primarily $S_I$ and $S_{II}$ sites [9], yet other authors [11, 32] report more generally that cations are found in all cages of faujasite (hexagonal prism, sodalite cage and supercage) and the corresponding sulfides are usually restricted to the supercage (see Figure 2.1). This presents an interesting question, namely whether there is a migration upon sulfidation [33, 34] or if this 'selective sulfidation' is similar to the question of variation in metal reducibility among different cation locations [16, 29, 35].
There are reports in the literature describing the effect of secondary ions on the incorporation of catalytically active metal ions. For example, $Ca^{2+}$ has been shown to affect the reduction temperature of incorporated $Ni^{2+}$ [16]. In addition, the order of metal incorporation can lead to different structures and stabilities. For example, the incorporation of $Co^{2+}$ prior to incorporation of $MoO_3$ leads to a stabilization of the support against acidic breakdown [36]. Thiophene HDS studies by de Bont et al. [37] report a synergic effect between sulfided Co and Mo supported on zeolite Y. However, the authors explain this effect more in terms of stabilization of the 'Co-sulfide' by the presence of Mo, rather than the formation of true Co-Mo-S type species.

It is widely known that intrazeolite water interferes with the interaction between the support and the metal sulfide, and that the presence of such water is therefore detrimental to the formation of stable metal sulfides [11, 30, 37]. Futhermore, the strength of interaction between the metal sulfide and the zeolite support, which is tunable in terms of the Si/Al ratio, has been reported to influence which phase of metal sulfide is stabilized on the support. It has been suggested [30] that the stronger the metal sulfide to zeolite interaction, the higher the stability of NiS over $Ni_3S_2$. Also reported is the role of surface Brønsted groups which affect the stability of metal/metal sulfides [4].

## 2.6 Zeolites in Catalysis

### 2.6.1 Zeolites as Shape Selective Catalysts

In addition to ion-exchange, zeolites are widely known for their size exclusion properties, hence their alternate name *molecular sieves*. This term originates from the ability of zeolites to admit one molecule into their pore systems while rejecting others of only slightly larger size, or confirmation, in the case of isomers. There is some distinction in the literature between the terms zeolite and molecular sieve, focusing on the framework composition [17], although the terms are widely used synonymously. As summarized by Weitkamp [2] the shape selectivity effect of zeolites can be described in terms of the following classifications:

1) Reactant Shape Selectivity
   The admission of reactant molecules into the catalyst is selective, based on differences in size, adsorption, etc, leading to differences in diffusion rates.

2) Product Shape Selectivity
   Product formation is selective based on size, so that less hindered molecules preferentially form over more sterically hindered ones.

3) Restricted Transition State Shape Selectivity
   The formation of different transition states (leading to different products) is selective based on size constraints within pores. Although seemingly unlikely, a plausible example of such selectivity would be the restriction of a transition state resulting from a bimolecular reaction, while that from a monomolecular transition was permitted.

An illustration of this property is the shape selectivity of H-mordenite, (an aluminosilicate), toward substituted naphthalenes. The work of Horsely et al. [38] has shown clear differences in the pore diffusion rates between 2,6-DIPN and 2,7-DIPN, (DIPN = Diisopropylnaphthalene). See Figure 2.3.

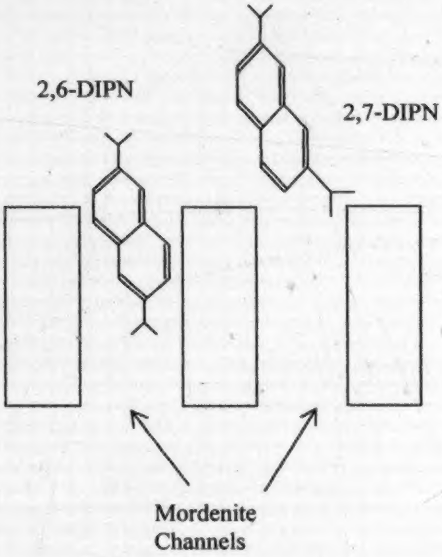

Figure 2.3: Graphical depiction of shape selection between 2,6- and 2,7-DIPN on H-Mordenite.

In an attempt to exploit this selectivity, Kim et al. [39] focused on the intentional deactivation of the external surface acid sites while preserving this functionality within the pores and channels of mordenite. In the isopropylation of naphthalene, it was found that dispersion of ceria on the external surface led to increased selectivity toward 2,6-DIPN over 2,7-DIPN.

The most well-known zeolite exploited for its shape-selectivity is ZSM-5, a pentasil based system consisting of intersecting 10-membered rings. Uses of this zeolite include the synthesis of ethylbenzene, xylene isomerisation, and the disproportionation of toluene to benzene and xylenes [2], as well as dewaxing applications.

### 2.6.2 Zeolites as Ring Opening Catalysts

The use of zeolites as ring opening catalysts has been studied extensively. The work of Corma et al. [40] examined the reaction of decalin and tetralin on various zeolites with varying pore size and topology. Their results show that the product distribution is determined significantly by the pore size of the zeolite support, with large pore zeolites preferred in order to facilitate diffusion of the probe molecules into the pores of the zeolite itself. The work of Kubička et al. [41] reports that ring opening of decalin over acidic zeolites proceeds through a ring contraction (RC) mechanism, requiring the presence of strong Brønsted acid function within the zeolite. Furthermore, these authors have found variations in deactivation due to zeolite pore size as a result of the formation of pore blocking intermediates. As noted by Weisser et al. [42], a balance between residence time within the pore structure and blockage of the pores by intermediates and/or products must be found. The work of McVicker et al. [43] has emphasized the important role played by metal function in ring opening catalysis. Aside from the limited case of cyclohexanes, it is generally accepted that ring opening catalysis proceeds through a combination of metal and acidic function [1]. Zeolite supported metal catalysts offer both catalyst functions, and thus find wide use in this field of catalysis.

### 2.6.3 Zeolite Supported Transition Metals in Hydrotreating Catalysis

Metal sulfides are rarely used in catalysis as pure substances. Similar to metallic catalysts, supports such as alumina or zeolites are used which impart their own influence on the over all catalysis. A common question addressed in the literature is whether or not the support can affect the properties of the metal phase. For example, the review by Hensen and van Veen [11] addressed whether or not there was an optimal size of transition metal sulfide clusters for use in hydrotreating. The essential conclusion of the review was that such an optimum may exist, but that maintenance of such highly dispersed phases within the pores of a zeolite would be industrially quite challenging. According to Ross [44], there are two types of Ni clusters when supported on zeolite Y; large clusters with properties similar to bulk metal which facilitate hydrogenolysis, and finely dispersed clusters which facilitate isomerisation and cracking. However, in their study of n-hexane isomerisation over Ni zeolites, Shil et al. [16] found little variation in activity with changing cluster size, both in the case of NiCa-Y and NiH-M. Welters et al. [30] studied the dispersion of nickel sulfides (both as NiS and $Ni_3S_2$), and found the dominant fraction of the sulfide phase was on the external surface, with a smaller fraction of highly dispersed, highly active sulfide clusters in the pores.

## 2.7 The Use of Chabazite in Catalysis and Research

Natural zeolites are often considered to have the disadvantage of trace impurities, phase impurity, variation in composition, and they are not optimized catalytically (Si/Al ratio, pore size, etc) [30]. However, the use of a natural zeolite such as chabazite offers the additional advantage of having small, 0.4 nm pore diameters, while synthetic zeolites such as zeolite X and Y have large pore diameters of approximately 0.8 nm or larger. In addition, chabazite (CHA) is available from natural deposits and the costs of using such a material in an industrial process are much lower than those of synthetic zeolites used today.

### 2.7.1 Ion-exchange Properties of Chabazite

Beyer [12] reported on the thermal stability of $NH_4$-CHA, stating that dehydroxylation results in framework collapse, but that thermally induced dehydration, deammoniation, and dehydroxylation are all well resolved in temperature. As stated by Mortier et al. [45], this allows for the preparation of the protonic form of chabazite without concern for structural losses accompanying dehydroxylation. Querol et al. [46] reported a high *cation exchange capacity (CEC)* of chabazite, and commented on its potential use as a wastewater sorbent. Shipikin et al. [47] discussed the use of chabazite as geometrically selective catalysts which can be made bifunctional (incorporation of a hydrogenation function) through the reduction of incorporated $MoO_3$.

### 2.7.2 The Use of Chabazite in Catalysis and Research

The work of Lo et al. [48] has studied chabazite as a potential solid acid in such applications at methanol to gasoline (MTG). The bulk of the available literature on zeolite catalysts involves studies on faujasite (zeolite X and Y), mordenite, ZSM-5 etc. Very few studies in the literature report findings on chabazite, despite its high adsorption potential [5]. With its enlarged sodalite cages (Figure 2.4) relative to those of faujasite (Figure 2.1), chabazite has proven hydrogen storage potential [6] which in turn may facilitate what is known as ideal hydrotreating [4] in the vicinity of the active site.

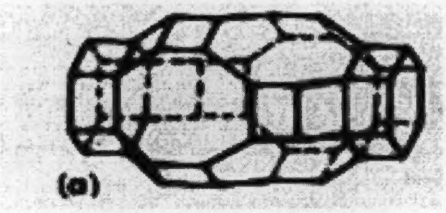

Figure 2.4: The sodalite cage structure of chabazite. Figure taken from Anderson [9].

## 2.8 Ethylene Hydrogenation

Ethylene hydrogenation has been used as a model reaction for olefin and aromatic hydrogenation reactions for many years, yet the mechanistic details of this comparatively simple reaction are not precisely known [49]. Mechanistic descriptions include dehydrogenation preceding hydrogenation, intramolecular hydrogen transfer between different adsorbed species of ethylene, yet the bulk of available kinetic data agrees with classical Horiuti-Polanyi mechanism [49]. Hydrogenation according to this mechanism, first postulated in 1934, can be summarized in terms of the following steps (Figures 2.5a through 2.5d),

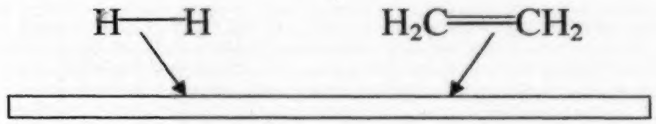

Figure 2.5a: Chemisorption of hydrogen and ethylene onto the catalyst surface.

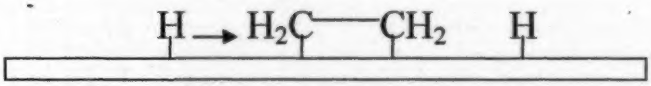

Figure 2.5b: Transfer of atomic hydrogen to di-sigma bound ethylene.

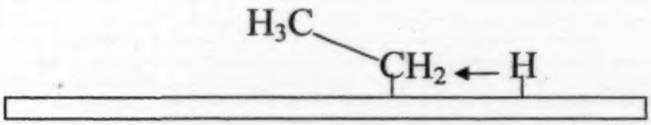

Figure 2.5c: Transfer of second atomic hydrogen to bound ethyl fragment.

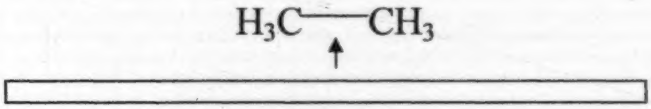

Figure 2.5d: Release of ethane from catalyst surface.

Ethylene hydrogenation over nickel catalysts is reported in literature to be well described by this mechanism [50]. In addition, the selectivity studies between ethylene hydrogenation/ethane hydrogenolysis is known to be a useful probe in determining site densities on catalyst surfaces. Specifically, it is reported that while ethylene hydrogenation is structure insensitive, ethane hydrogenolysis is a much more demanding reaction, requiring an ensemble of sites in close proximity [8].

## 2.9 Introduction to Metal Sulfide Hydrotreating Catalysts

Much of the development of hydrotreating catalysis took place in Germany. The following timeline of the development of sulfide catalysts, (adapted from Weisser et al. [42] ) summarizes the milestones of development.

- 1869: Bertholot reduces coal with hydroiodic acid
- 1906: Demonstration of the catalytic behaviour of platinum and palladium in hydrogenation of petroleum distillates by Day.
- 1910: Bergius made use of molecular hydrogen in the cracking of heavy petroleum distillates, producing gasoline fractions.
- 1912: Theodorin reported the hydrocracking of petroleum over iron and nickel catalysts.
- 1913 Bergius and Billwiller develop further coal hydrogenation, achieving 80% conversion to useful fractions. Further studies achieved breakthroughs in the hydrogenation of tar and heavy oils. Owing to the fact that their process was non-catalytic, the hydrogenation products were of excessively high molecular weight for use in motor fuels, as well as containing high amounts of sulfur, oxygen and nitrogen compounds. It was known at the time the presence of oxides, such as iron oxide, was beneficial to hydrogenation. For example, in the presence of iron oxide, 85% liquefaction of coal could be achieved. Bergius (erroneously) postulated that such high molecular weights resulted from sulfur acting to facilitate polymerization, but that oxides bind with sulfides, eliminating the sulfur's inhibitory effects. Carpenter reported the use of nickel subsulfide ($Ni_3S_2$) in the hydrodesulfurization of carbonization gases from coking processes.

- 1920s: Fischer develops alternate sources of hydrogen in Bertholot's work, such as sodium formate/water mixtures and carbon monoxide/steam. Scientists at I.G. Farbenindustrie A.G. as well as Varga showed that iron oxide acted as a catalyst for hydrocleavage products, as well as desulfurization, (the cleaving of carbon-sulfur bonds through the addition of hydrogen). It was also found that iron sulfide behaves similarly.

- 1921: Klever reports the catalytic properties of Ag, Zn, Cd Pb, Cu. etc. and compounds thereof in the hydrocracking of petroleum residues, tars and bitumen, as well as the possibility of simultaneous hydrodesulfurization within these processes. McComb employed molybdenum and nickel in the hydrogenation of oils.

- 1924: Research into synthetic methane and ammonia production at the Badische Anilin und Sodafabrik (BASF) in Ludwigshaben revealed the need for poison resistant catalysts for processing complex mixtures such as coal and tar. Krauch and Pier developed molybdenum and tungsten sulfide catalyst for exactly this reason.

- 1929: Howard patented the use of molybdenum and chromium oxides, as well as cadmium sulfide in the hydrogenation of coal paste.

- 1929: Early publications such as the work of Pier [51] revealed the shift from applied industrial research to fundamental studies of sulfided hydrotreating catatlysts.

- 1930: Fundamental research into sulfide catalysts develops outside Germany, particularly in the Soviet Union. This research continued the trend in fundamental studies on pure compounds, as opposed to industrial development focusing on mixtures. Further studies began in countries such as the U.S., Japan and Italy, before, during and especially after the Second World War

While not exhaustive, the preceding development milestones showed the importance of the development of sulfided hydrotreating catalysts. In contemporary hydrotreating catalysis, many applications which must deal with sulfur containing feedstocks make use of sulfide catalysts as a compromise between higher activity and resistance to sulfur poisoning. Interestingly, not only are sulfide catalysts resistant to poisoning by sulfur, but they actually require the presence of sulfur in the feed to maintain their sulfided state. However, despite their resistance to sulfur and nitrogen, sulfide catalysts undergo severe deactivation in the presence of arsenic.

As discussed in Weisser et al. [42], metal sulfides are intermediates between metals and insulators, due to their semiconductor properties. As a result, they not only facilitate redox reactions, but also show acid-base functionality, thereby increasing the rate of isomerization reactions. Also, while purely metallic catalysts show high activity even at room temperature, the activity of common sulfide catalysts typically requires higher temperatures, (e.g. exceeding 250°C). However, the activity of metal sulfide catalysts is very sensitive to temperature. Thus, while of lower activity than a metal catalyst in low temperature applications, the activity of metal sulfides can exceed that of metallic catalysts in high temperature conditions. Natural sulfide minerals are generally of low activity, so special means of preparation are required for highly active sulfide catalysts. Like their metallic counterparts, metal sulfides show a high adsorption capacity for hydrogen and unsaturated hydrocarbons.

# Chapter 3

# Experimental Methods and Procedures

## 3.1 Materials Preparation

This section details the preparation of the metal loaded chabazites used in this study.

### 3.1.1 Preparation of Ni-CHA

Approximately 7.2 g of Na-CHA from the well-known Bowie deposit (GSA resources, Tucson Arizona), 5.8 g of $NiCl_2$ (Aldrich), 100 mL of D.I. $H_2O$ and a small Teflon stirbar were placed in a 500 mL round bottom flask fitted with a pyrex Liebig condenser (400 mm Std. Taper Joints 24/40), and refluxed for 24 h. Figure 3.1 shows the details of the reflux system used.

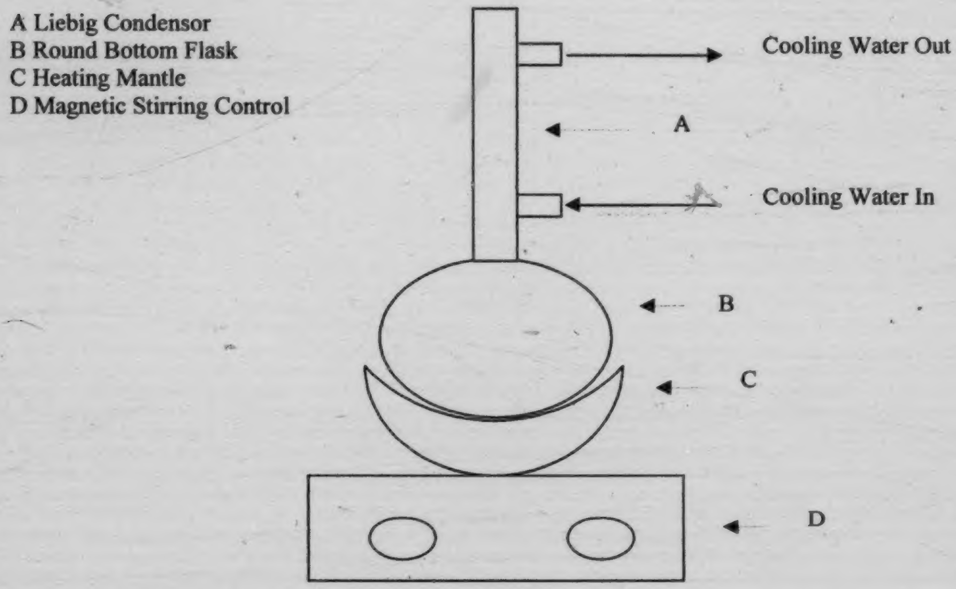
A Liebig Condensor
B Round Bottom Flask
C Heating Mantle
D Magnetic Stirring Control
Cooling Water Out
A
Cooling Water In
B
C
D

Figure 3.1: Schematic of the reflux system.

The solids were then collected on a Buchner funnel, and washed twice with 100 mL of boiling D.I. $H_2O$ to remove free metal chlorides. After drying in air at 100°C for 2 h, the solids were calcined in air for 24 h at 450°C. The amount of Ni added was equivalent a 4.6 times excess exchange loading of Ni on Na CHA, (assuming a Na-CHA exchange capacity of 2.7 mmole of charge/g).

### 3.1.2 Preparation of NiMo-CHA

5.0 g of Na-CHA from the well-known Bowie deposit (GSA resources, Tucson Arizona), 1.0 g of $NiCl_2$ (98% Aldrich), 1.0 g of $MoCl_3$ (Aldrich), 100 mL of D.I. $H_2O$ and a small Teflon stirbar were placed in a 500 mL round bottom flask fitted with a pyrex Liebig condenser (400 mm Std. Taper Joints 24/40), and refluxed for 24 h (see Figure 3.1).

The solids were then collected on a Buchner funnel, and washed twice with 100 mL of boiling D.I. $H_2O$ to remove free metal chlorides. After drying in air at 100°C for 2 h, the solids were calcined in air for 24 h at 450°C. The amounts of metals added corresponded to a 1.2 times excess exchange capacity for Ni and a 1.1 times excess exchange capacity for Mo on Na CHA, (assuming a Na-CHA exchange capacity of 2.7mmole of charge/g).

### 3.1.3 Preparation of Mo-CHA

5.1 g of Na-CHA from the well-known Bowie deposit (GSA resources, Tucson Arizona), 1.1 g of $MoCl_3$ (Aldrich), 100 mL of D.I. $H_2O$ and a small Teflon stirbar were placed in a 500 mL round bottom flask fitted with a pyrex Liebig condenser (400 mm Std. Taper Joints 24/40), and refluxed for 24 h, (see Figure 3.1).

The solids were then collected on a Buchner funnel, and washed twice with 100 mL of boiling D.I. $H_2O$ to remove free metal chlorides. After drying in air at 100°C for 2 h, the solids were calcined in air for 24 h at 450°C. The amount of Mo added was equivalent to 1.1 times the excess exchange capacity of Mo on Na CHA, (assuming a Na-CHA exchange capacity of 2.7mmole of charge/g).

### 3.1.4 Preparation of $NH_4$-CHA

6.1 g of Na-CHA from the well-known Bowie deposit (GSA resources, Tucson Arizona), 22.7 g of $NH_4Cl$ (Fluka), 200 mL of D.I. $H_2O$ and a small Teflon stirbar were placed in a 500 mL round bottom flask, and stirred for 2 h at room temperature. The solids were then collected on a Buchner funnel, and washed twice with 200 mL aliquots of D.I. $H_2O$. Approximately one third of the wet solids were dried in air for 2 h at 100°C, then were transferred to a glass vial. These solids were referred to as $NH_4$-CHA(1). The remaining wet solids were combined with 15.1 g of $NH_4Cl$ (Fluka), 133 mL of D.I. $H_2O$ in order to affect a second exchange, as above. After collecting and washing the wet solids on the Buchner funnel as above, one half was dried in air for 2 h at 100°C. These solids were transferred to a glass vial, and referred to as $NH_4$-CHA(2). The remaining wet solids were combined with 7.5 g of $NH_4Cl$ (Fluka) and 60 mL of D.I. $H_2O$ in order to affect a third exchange. After collecting and washing the wet solids on the Buchner funnel as above, these solids were dried in air for 2 h at 100°C. These solids were transferred to a glass vial, and referred to as $NH_4$-CHA(3).

### 3.1.5 Exchange of $NH_4$ into NiMo -CHA

NiMo-CHA was prepared by stirring 0.4 g of $NiCl_2$ (Aldrich) and 0.6 g of $MoCl_3$ (Aldrich) in 200 mL of D.I. $H_2O$ in a large Erlenmeyer flask. After adding 1.9 g Na-CHA, the suspension was stirred at room temperature for 2 h. Following 2 h of drying at 200°C in air, these solids were stored in a glass vial. Next, 1g of this NiMo-CHA was combined with 3 g of $NH_4Cl$ and 33 mL of D.I. $H_2O$. Following 3 h of stirring at room temperature, filtering and washing on a Buchner funnel, the solids were dried for 2 h in air at 100°C.

### 3.1.6 Exchange of NiMo into $NH_4$-CHA

$NH_4$-CHA was prepared by combining 3 g of Na-CHA from the well-known Bowie deposit (GSA resources, Tucson Arizona), 11.3 g of $NH_4Cl$ (Fluka), 100 mL of D.I. $H_2O$ and a small Teflon stirbar in a 500 mL round bottom flask. After stirring for 2 h at room .

temperature, the solids were then collected on a Buchner funnel, and washed twice with 200 mL aliquots of D.I. $H_2O$. The wet solids were dried in air for 2 h at 100°C. Next, 0.4 g of $NiCl_2$ (Aldrich), 0.6 g of $MoCl_3$ (Aldrich), and 200 mL of D.I. $H_2O$ were combined in a large Erlenmeyer flask in order to dissolve the metal chlorides. The above $NH_4$-CHA was combined with 100 mL of this solution, and stirring continued for 2 h at room temperature. After collecting the solids on a Buchner funnel, the wet solids were recombined with the remaining 100 mL of the metal chloride solution. After stirring at room temperature for 2 h, the solids were collected on a Buchner funnel, washed twice with 100 mL aliquots of D.I. $H_2O$. After drying in air at 100°C for 2 h, the solids were placed in a glass vial.

### 3.1.7 Preparation of HCHA

The sodium form of chabazite (Thermally Activated Chabazite Test #2 from GSA Resources) was lightly ground in a mortar and pestle, and then sieved between 50 and 20 mesh grids. Approximately 150 g of this solid, referred to as 20-50 Na-CHA, was recovered and stored in an airtight glass jar.

125 g of 20-50 Na-CHA was immersed in 500 mL of de-ionized $H_2O$ in a 1 L Erlenmeyer flask. This resulted in pronounced effervescene, and a pH of 10.3. This pH measurement, as well as all subsequent measurements, were acquired using an Accumet AB15 fitted with a temperature probe.

Next, the pH was adjusted to pH 5 using 1 M HCl (aq), (dropwise from a pasteur pipette). The suspension was then warmed to 60°C on a hotplate. After 15 min, the pH of the solution was 5.3, and after 30 min, the pH was found to be 7.3. The solution was decanted off, and replaced with fresh D.I. $H_2O$. The pH of this new suspension was found to be 7.9. Via dropwise addition of 1 M HCl (aq), the pH was re-adjusted to 5.0, and the suspension was returned to the hotplate. After 90 minutes with occasional manual agitation of the flask, the solution stabilized at a pH of about 6. Once again the liquid was decanted, replaced with fresh D.I. $H_2O$, acidified to pH 5.0 with 1 M HCl (aq). The suspension was covered and left on the bench top overnight.

The next morning, (15 h later), the pH of the suspension was found to be 7.50. After adjusting the pH to 4.0, the flask was placed on the hotplate and warmed to 40°C. After 2 h, the pH stabilized at 6.5. The solids were then collected on a Buchner funnel and wished with two, 500 mL portions of D.I. $H_2O$. The wet solids, weighing approximately 165 g were collected in a large metal pan, and transferred to a 60°C drying oven. After 4 h, the mass of dried solids was found to be 118 g. This resulting solid was sieved between 50 mesh and 20 mesh grids. The resulting solids, referred to as 20-50 H-CHA, weighed approximately 108 g.

### 3.1.8 Preparation of NiHCHA

A rubber bung (triple zero, (000), size) was drilled through with a 3 mm hole, into which a small amount of quartz wool was loosely packed. This was then press-fit into the top of the inner tube of a glass jacketed condenser (pyrex Liebig condenser 400 mm Std. Taper Joints 24/40). The condenser was then inverted and mounted in a laboratory clamp stand. A powder funnel was used to transfer 19 g of H-CHA to the inner tube of the condenser, leaving about 5 cm of empty space at the top of the bed. Using a ring clamp attached to the above lab stand, a 1 L separation funnel was supported above the inverted condenser, with the outlet of the funnel placed inside the condenser's inner tube. A recirculating heater filled with water was attached to the jacket of the condenser, maintaining the bed at 60°C. The setup is shown schematically in Figure 3.2 below.

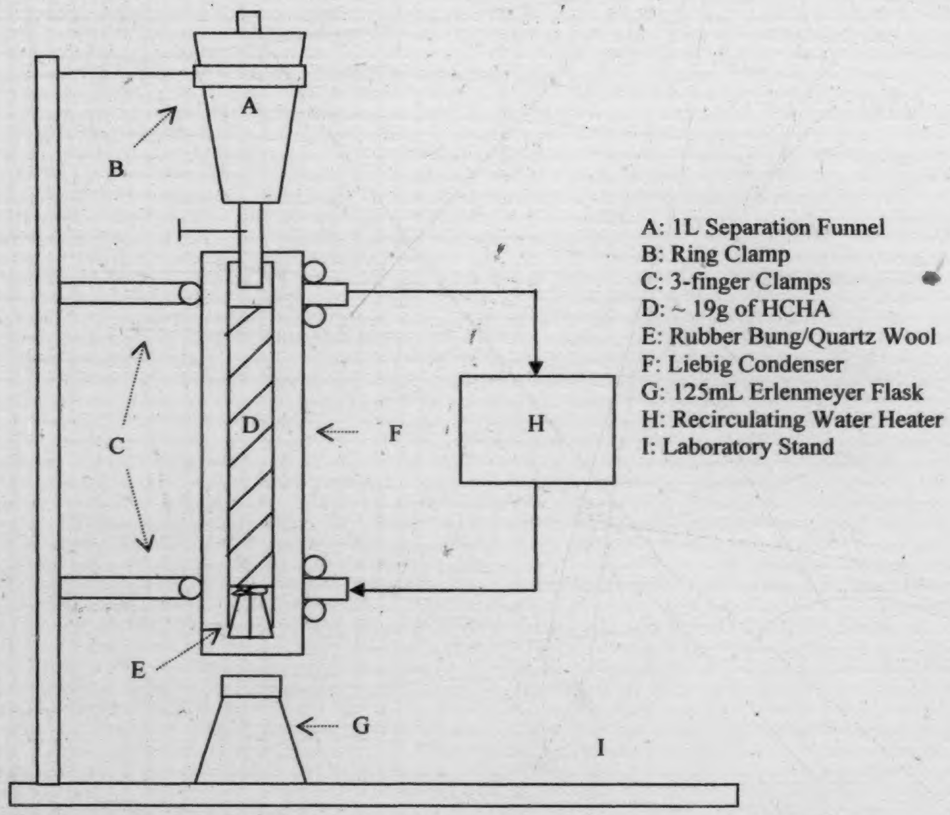
A
B
C
D
E
F
G
H
I
A: 1L Separation Funnel
B: Ring Clamp
C: 3-finger Clamps
D: ~ 19g of HCHA
E: Rubber Bung/Quartz Wool
F: Liebig Condenser
G: 125mL Erlenmeyer Flask
H: Recirculating Water Heater
I: Laboratory Stand

Figure 3.2: Setup of the exchange column.

13 g of $NiCl_2$ were weighed into a 2 L Erlenmeyer flask, and dissolved in 1.6 L of D.I. $H_2O$. The pH of this solution was found to be 7.4. After filling the separation funnel with $NiCl_2$ (aq) solution, stopcock of the funnel was opened and adjusted to maintain a constant level of solution above the bed. Aliquots of column effluent were collected in Erlenmeyer flasks. The volume and time required to collect it, along with the pH, temperature, descriptions of the colour of the aliquot and any other observations were recorded. This data is listed in Table 3.1 and Figure 3.3.

Table 3.1: Effluent conditions during the Ni exchange into HCHA.

| Elapsed Time (min) | Vol. (mL) | Sum Vol mL | Description | pH | Temp. (°C) | Flow Rate (mL/min) |
|---|---|---|---|---|---|---|
| 4 | 50 | 50 | Cloudy-Clear | 6.74 | 45.7 | 13 |
| 5 | 50 | 100 | Faint Green | 6.75 | 43.1 | 10 |
| 15 | 50 | 150 | green | 6.76 | 40 | 3 |
| 10 | 50 | 200 | Light Green | 6.38 | 40 | 5 |
| 14 | 50 | 250 | Light Green | 6.53 | 40 | 4 |
| 16 | 50 | 300 | Light Green | 6.40 | 40 | 3 |
| 11 | 50 | 350 | Light Green | 5.80 | 40 | 5 |
| 10 | 50 | 400 | As inlet | 6.20 | 39 | 5 |
| 14 | 50 | 450 | " | 6.40 | 39 | 4 |
| 14 | 50 | 500 | " | 6.42 | 39 | 4 |
| 36 | 100 | 600 | " | 6.18 | 39 | 3 |
| 35 | 100 | 700 | " | 6.24 | 39 | 3 |
| 37 | 100 | 800 | " | 6.05 | 39 | 3 |
| 6 | 100 | 900 | " | 5.69 | 39 | 17 |
| 6 | 100 | 1000 | " | 5.64 | 39 | 17 |
| 7 | 100 | 1100 | " | 5.54 | 39 | 14 |
| 7 | 100 | 1200 | " | 6.69 | 39 | 14 |
| 8 | 100 | 1300 | " | 5.71 | 39 | 13 |
| 8 | 110 | 1410 | " | 5.77 | 39 | 14 |
| 11 | 100 | 1510 | " | 5.74 | 39 | 9 |
| 7 | 100 | 1610 | " | 6.00 | 39 | 14 |
| 9 | 100. | n.a. | Clear | 6.98 | n.a. | n.a |

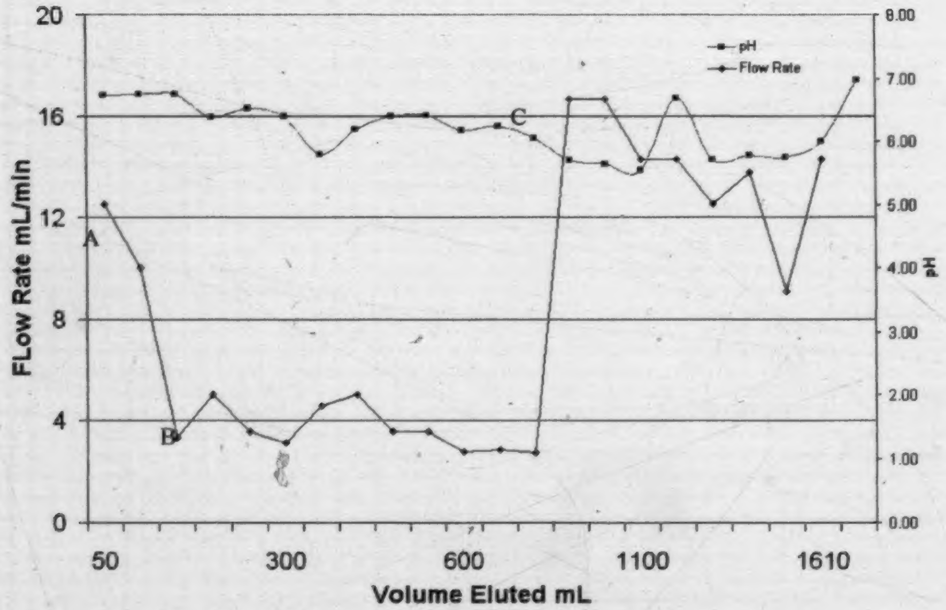

Figure 3.3: Flow rate versus volume eluted during the Ni exchange into HCHA.

A: Noticed the formation of a precipitate on the top of the bed and in the $NiCl_2$ (aq). Flow eventually stopped completely.

B: Acidified the $NiCl_2$ (aq) solution to pH 3.5 with 1 M HCl, then filtered it through a Buchner funnel back into the separation funnel. Flow eventually resumed.

C: Added an extension to the condenser, to increase the pressure on the bed. Flow increased dramatically.

The column was then allowed to drip dry for 15 min, then the bed was knocked into a large metal pan. After pipetting away the free liquid, the mass of wet solids was found to be 35.1 g. After drying at 68°C for 18 h, the mass of the dry solid, (referred to as NiHCHA) was found to be 15.1 g. Subsequently, 9.5 g of NiHCHA was placed in a crucible and calcined at 400°C for 80 min. The mass of solid, referred to as calicined NiHCHA was found to be 8.6 g.

### 3.1.9 Preparation of MoHCHA

4.1 g of $MoCl_3$ (Aldrich), 40.1 g of HCHA, 250 mL of D.I. $H_2O$ and a small Teflon stirbar were placed in a 500 mL round bottom flask fitted with a pyrex Liebig condenser (400 mm Std. Taper Joints 24/40), and refluxed for 3 h. The pH was monitored throughout (using an Accumet AB15 fitted with a temperature probe) and was found to be roughly constant at about 4.7. The details of the reflux system used are shown in Figure 3.1.

When the solids were collected on a Buchner funnel, it appeared that there was a significant amount of undissolved $MoCl_3$ in the flask. The solids were therefore liberally washed with D.I. $H_2O$, until the wash water appeared clear. Between 2 and 3 L of D.I. $H_2O$ was required. The wet solid, (MoHCHA), had a mass of 54.7 g before drying at 60°C for 18 h, after which the mass was found to be 31.5 g. Also, a few small black solids, (resembling black pepper in color), were observed evenly distributed through the MoHCHA. An attempt was made to remove as many of these as possible, and it was noted that they were completely insoluable in water, making it unlikely that they were excess $MoCl_3$.

15 g of dried MoHCHA was loaded into the exchange column as described in the preparation of NiHCHA. An aqueous solution of $MoCl_3$ (aq) was prepared by stirring 1.88 g of $MoCl_3$ (Aldrich) in 1.4 L D.I. $H_2O$ in a vented fumehood. After filtering out the small amount of visible sediment, a dark burgundy solution of pH 2.5 resulted. This was poured through the exchange system described in the preparation of NiHCHA, see Figure 3.2. Observations were made of the colour, pH, temperature and flow rate of the effluent, and are shown in Table 3.2.

Table 3.2: Effluent conditions during the further Mo exchange into MoHCHA.

| Elapsed Time (min) | Vol. (mL) | Sum Vol (mL) | Description | pH | Temp. (°C) | Flow Rate (mL/min) |
|---|---|---|---|---|---|---|
| 6 | 50 | 50 | Brown | 4.60 | 45.7 | 8 |
| 12 | 50 | 100 | Light Brown | 4.70 | 43.1 | 4 |
| 18 | 50 | 150 | Darker Brown | 4.80 | 40 | 3 |
| 24 | 65 | 215 | Lighter Brown | 4.80 | 40 | 3 |
| 32 | 75 | 290 | Similar to feed | 4.80 | 40 | 2 |
| 39 | 65 | 355 | Similar to feed | 4.80 | 40 | 2 |
| 49 | 110 | 465 | Similar to feed | 4.80 | 40 | 2 |
| 60 | 125 | 590 | Similar to feed | 4.60 | 39 | 2 |
| 75 | 125 | 715 | Similar to feed | 4.60 | 39 | 2 |
| 82 | 75 | 790 | Similar to feed | 4.60 | 39 | 1 |
| 94 | 110 | 900 | Similar to feed | 4.60 | 39 | 1 |
| 110 | 125 | 1025 | Similar to feed | 4.60 | 39 | 1 |
| 125 | 125 | 1150 | Similar to feed | 4.60 | 39 | 1 |
| 148 | 150 | 1300 | Similar to feed | 4.60 | 39 | 1 |

125 mL of D.I. $H_2O$ was rinsed through the bed as the last of the $MoCl_3$ (aq) solution entered the bed. This wash water effluent was red in colour, and the pH was measured to be 4.9.

The wet solids were knocked into a small glass beaker, and had a mass of 26.4 g. After drying at 60°C for 18 h, the dried exchanged MoHCHA was found to be 11.5 g. Into a crucible was placed 8.8571 g of dried exchanged MoHCHA. After 2 h at 400°C in a drying oven, the mass of this calcined MoHCHA was 7.5 g.

Simultaneously, some of the black solids which had been removed during the reflux step were also placed in the oven. The colour of these solids was found to have changed from black to green-white upon calcination. There was no colour change observed in the calcined MoHCHA.

### 3.1.10 Preparation of NiMoHCHA

14.4 g of dried refluxed MoHCHA was loaded into the setup as described in the preparation of NiHCHA, (See Figure 3.2).

8.16 g of $NiCl_2$ (Aldrich) was dissolved in 400mL of D.I. $H_2O$ in a 2 L Erlenmeyer flask. There was an obvious cloudiness to the solution, even after diluting the solution to 1.6L and stirring, this cloudiness did not clear. After acidifying to pH 2.5, the solution was observed to be clear and free of precipitates. This solution was then poured through the exchange system.

13 g of $NiCl_2$ was weighed into a 2 L Erlenmeyer flask, and dissolved in 1.6 L of D.I. $H_2O$. The pH of this solution was found to be 7.4. After filling the separation funnel with $NiCl_2$ (aq) solution, the stopcock of the funnel was opened and adjusted to maintain a constant level of solution above the bed. The volume and collection time, along with the pH and a description of the colour of the aliquot were recorded. This data is shown in Table 3.3 and Figure 3.4.

Table 3.3 Effluent conditions during the Ni exchange into MoHCHA.

| Elapsed (min) | Vol. (mL) | Sum Vol (mL) | Description | pH | Description | Flow Rate (mL/min) |
|---|---|---|---|---|---|---|
| 4.5 | 50 | 50 | Brown | 3.47 | Black-Green | 11.1 |
| 9.0 | 50 | 100 | Light Brown | 3.53 | Lighter than prev. | 5.6 |
| 14.0 | 50 | 150 | Darker Brown | 3.56 | Avg. of prev. two | 3.6 |
| 19.3 | 50 | 200 | Lighter Brown | 3.62 | " | 2.6 |
| 30.5 | 75 | 275 | Similar to feed | 3.65 | Darker than prev. | 2.5 |
| 41.3 | 75 | 350 | Similar to feed | 3.70 | " | 1.8 |
| 50.5 | 75 | 425 | Similar to feed | 3.75 | " | 1.5 |
| 70.5 | 135 | 560 | Similar to feed | 3.78 | Darker than prev.7 | 1.9 |
| 90.5 | 135 | 695 | Similar to feed | 3.81 | " | 1.5 |
| 103.0 | 100 | 795 | Similar to feed | 3.80 | " | 1.0 |
| 122.0 | 125 | 920 | Similar to feed | 3.75 | " | 1.0 |
| 141.0 | 125 | 1045 | Similar to feed | 3.74 | " | 0.9 |
| 160.0 | 125 | 1170 | Similar to feed | 3.70 | " | 0.8 |
| 171.0 | 80 | 1250 | Similar to feed | 3.71 | " | 0.5 |

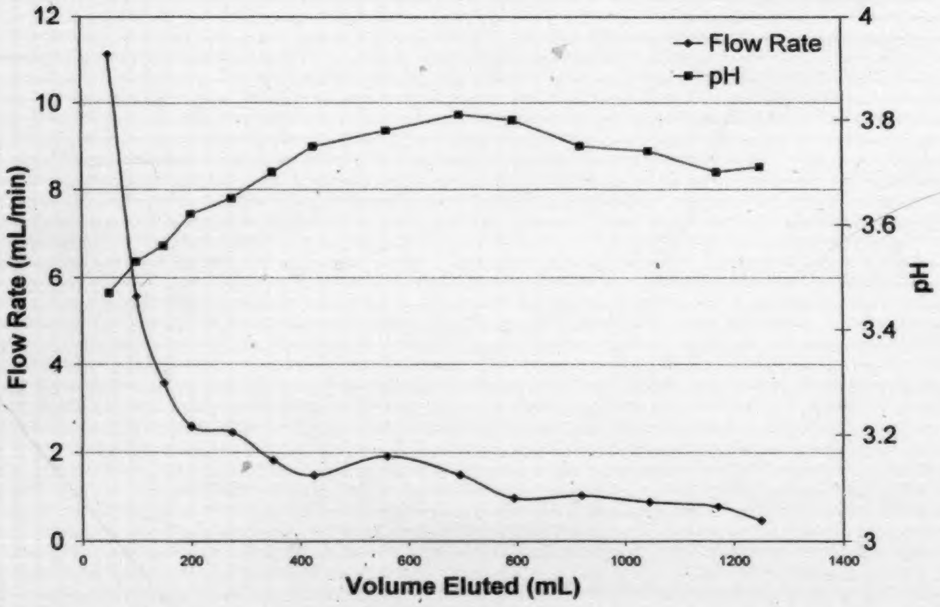

Figure 3.4: Flow rate versus volume eluted during the Ni exchange into MoHCHA.

As the last of the $NiCl_2$ (aq) solution entered the bed, D.I. $H_2O$, (pH = 6.17) was poured through the bed. 50 mL of this wash were collected and it was noted that this solution, faint green in color, had a pH of 4.0. The column was then allowed to drip dry, after which the bed was knocked into a large metal pan. After pipetting away the free liquid, the mass of wet solids was found to be 29.0 g. After drying at 60°C for 18 h, the mass of the dry solid, (referred to as NiMoHCHA) was found to be 11.7 g. Subsequently, 10.80 g of NiHCHA was placed in a crucible and calcined at 400°C for 2 h. The mass of solid, referred to as calicined NiMoHCHA was found to be 9.0 g.

## 3.2 Characterization Methods

### 3.2.1 Transmission Electron Microscopy (TEM)

The morphology of each metal-chabazite sample was characterized using transmission electron microscopy (TEM). Prior to analysis, each sample was ground to a fine powder using a mortar and pestle, then dispersed in methanol. A 200 mesh C-coated Cu grid, (SPI Inc.) was held in a pair of self-closing tweezers, while a second pair of tweezers was used, with the aid of a compound light microscope, to create a hole in the C coating of the grid near its centre (in order to acquire a background for the analysis). After the grid was dipped into the suspension, it was viewed under the light microscope to confirm the transfer of particles from the suspension. The grid was then loaded into the JEOL 2010 (JEOL Corp. Japan) microscope, which employed a 200 kV accelerating voltage and magnification factors ranging from $10^2$ to $10^6$. On the order of 20 images of each sample were captured, using a Hamamatsu CCD camera.

### 3.2.2 Ammonia Temperature Programmed Desorption

Approximately 100 mg of sample was loaded into a quartz U-tube sample holder of a Micromeritics Autochem II Chemisorption Analyzer. This holder is shown schematically in Figure 3.5.

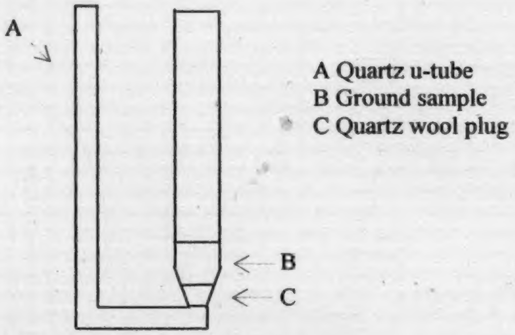

Figure 3.5: The quartz U-tube used in Ammonia TPD experiments.

Pretreatment consisted of heating to 450°C at a ramp rate of 10°C/min in flowing He, with a hold time of 2 h. The sample was then cooled to 120°C and dosed with 15 % $NH_3$/He (Praxair) for 30 min. After removing excess $NH_3$ in flowing He (5.0 Praxair) for 1 h at 120°C, the temperature was ramped to 450°C. This desorption process was carried out at varying ramp rates of $\beta = 5, 10, 15, 20$ and 30°C/min. Ammonia desorption peak temperatures ($Tp$) were determined for each value of $\beta$, and a plot of $\ln(Tp^2/\beta)$ vs $1/Tp$

was constructed in order to extract the activation energy of desorption and, by assumption, the heat of adsorption [52] .

### 3.2.3 Temperature Programmed Reduction: X-Ray Photoelectron Spectroscopy (TPR:XPS)

Various sample holders were fabricated for these studies. A four-well holder is shown schematically below in Figure 3.6.

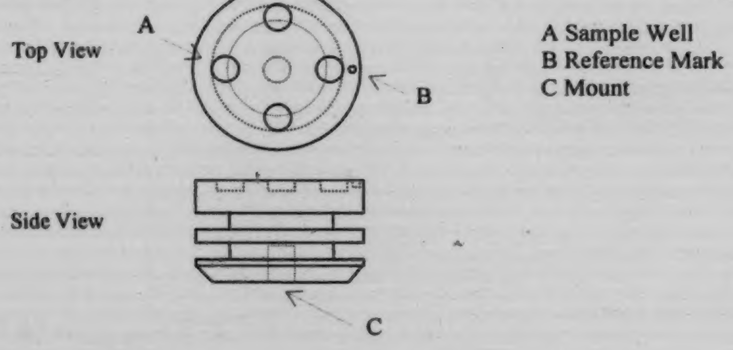

Figure 3.6: Schematic of a four-well sample holder.

Holders were either made from quartz (Chemistry Glassblowers, University of Alberta), from stainless steel or brass (both made by the Chemical and Materials Engineering Machine Shop, University of Alberta). The brass holder featured only two sample wells, while the quartz and stainless steel versions had four wells. Otherwise, the holders were geometrically identical. The use of at least two ports allowed the simultaneous treatment of samples, thereby eliminating any differences in variables such as temperature of time of reduction in comparative studies. This is primarily important when comparing Ni and NiMo containing samples. The holders featured a reference mark for distinguishing samples on the black and white monitor of the XPS system and a mount for securing the sample within the catalytic cell (Cat Cell). More information on the Cat Cell can be found in the document entitled "Catalyst Reaction Cell User Manual", published by Kratos Analytical LTD 1999. It was found that loading samples into the wells in powder form resulted in cross-contamination or in some cases the total loss of samples under the flowing gases of the Cat Cell. In later experiments, wafers were prepared using a hydraulic press in much the same way IR samples are prepared, although no KBr or similar binding materials were used. These wafers were then carefully cut to size with a laboratory spatula so that they would fit tightly in the sample wells. In some experiments, powders were hand pressed into the sample wells using the stainless steel ram from the IR wafer preparation jig.

After the stub was loaded with samples, it was pumped down to $10^{-9}$ torr in the load-lock of an Axis 165 Hi instrument (Kratos Scientific, UK) equipped with Mg $K_\alpha$ (1253.6 eV) and monochromatic Al $K_\alpha$ (1486.6 eV) sources. After degassing for several hours, survey scans between 1100 and 0 eV were collected at a pass energy of 120 eV, a step size of 0.3 eV, a dwell time of 60 ms and 2 sweeps per sample. Narrow elemental scans were collected at 20 eV pass energy, 0.1 eV step size, 100 ms dwell time and 8 sweeps per element. Following initial this sample characterization, the sample holder was transferred to the Cat Cell without exposure to air. For clarity, the experimental setup is diagrammed below in Figure 3.7.

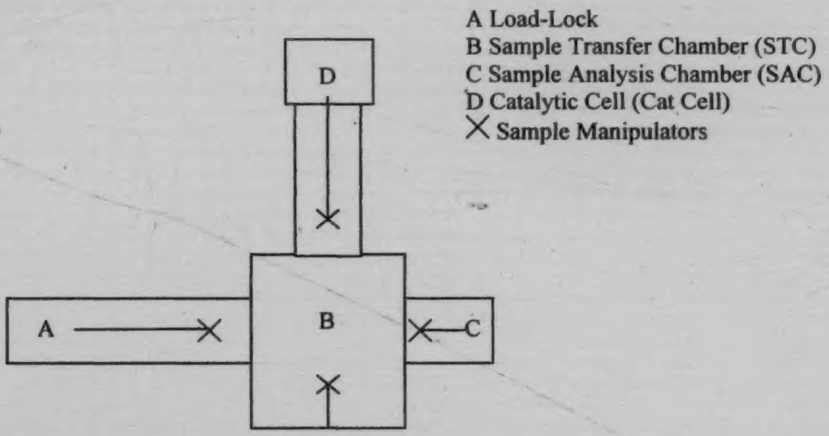
A Load-Lock
B Sample Transfer Chamber (STC)
C Sample Analysis Chamber (SAC)
D Catalytic Cell (Cat Cell)
× Sample Manipulators
D
A
B
C

Figure 3.7: Diagram of the in-situ TPR-XPS setup.

Reduction was carried out at the desired temperature and ambient pressure for 1 h in flowing hydrogen (5.0 Praxair) at a flow rate of 30 mL/min. The flow rate was determined by attaching a soap bubbler to the exhaust line of the reactor. After the flow rate was established, the bubbler was removed and the exhaust was directed to the vent.

Following the reduction, the reaction cell was allowed to cool to below 100°C, purged with $N_2$ (5.0 Praxair) to remove $H_2$, and then pumped down to a pressure of $1x10^{-9}$ Torr. The sample holder was then transferred back to the analyzer where the survey and element scans were recorded in the manner described above.

As part of a related study, following post-reduction XPS, some experiments included the deliberate exposure of the samples to the laboratory environment in order to gauge the necessity of the *in-situ* treatments. The exposure consisted of transferring the sample stub to the loadlock, then slowly venting to ambient pressure, where it remained for 1 h in the ambient laboratory air. The stub sample was then returned to the analysis chamber and the XPS analysis was repeated, in the manner described above. Subsequently, the stub was removed to the laboratory benchtop, where it was exposed for 10 h. Upon return to the analysis chamber, the samples were analyzed once more in the manner described above.

Peak assignments were calculated using CasaXPS software v2.3.5 and all spectra were referenced to O 1s binding energy of values of 532.0 eV. This was chosen over the typical C 1s values of 285.0 eV due to the occurrence of shake-ups or other such ambiguities, making assignments of binding energies difficult in some samples. Peaks were fitted using either a Shirley or Linear baseline, chosen on which gave a better fit of the data, and a symmetric Gaussian-Lorentzian peak shape of the form GL(30), with the exception of the nickel feature that emerged upon reduction, which was fit with an asymmetric lines shape of the form A(0.2,0.9,30)GL(30). This was suggested by A. Grosvenor, who is active in the field of Ni analysis by XPS [53], [54]. Also, the satellite feature of the emerging Ni feature was also omitted, based on discussions with D. Karpuzov who has found the contribution of the satellite to metallic Ni to be very small in Ar sputtering experiments. This was also confirmed by A. Grosvenor. These refinements led to much more satisfactory peak fits than the use of purely symmetric line shapes and satellite features for both the Ni oxide and Ni metal states.

### 3.2.4 Temperature Programmed Sulfidation: X-Ray Photoelectron Spectroscopy (TPS:XPS)

The sample holders employed in these studies were identical to those employed in the TPR:XPS studies, (see Figure 3.6). The sample loading procedure was also identical, as were the experimental setup (Figure 3.7) and the parameters used in data acquisition.

Sulfidation was carried out at the desired temperature and ambient pressure for 1 h in a flowing blend of 10% $H_2S$ in $H_2$ (Praxair) at a flow rate of 30 mL/min. The flow rate was determined by attaching a soap bubbler to the exhaust line of the reactor. After the flow rate was established, the bubbler was removed and the exhaust was directed to the vent. Following sulfidation, the reaction cell was allowed to cool to below 100°C, purged with $N_2$ (5.0 Praxair) to remove $H_2S/H_2$, and then pumped down to a pressure of $1 \times 10^{-9}$ Torr. The sample holder was then transferred back to the analyzer where the survey and element scans were recorded in the manner described above.

Peak assignments and data processing were as discussed in the TPR:XPS section of this thesis, including the use of asymmetric line features to fit the nickel feature which emerged upon sulfidation, and the omission of satellite features for the emerging Ni feature upon sulfidation. As in the reduction studies, refinements led more satisfactory peak fits than the use of purely symmetric line shapes and satellite features for both the Ni oxide and Ni the metal/sulfide states.

Due to equipment maintenance requirements, the TPS-XPS system was only available during the Series 1 study. No results for the sulfidation of the acidified, (Series 2), chabazites are available.

### 3.2.5 X-ray Diffraction (XRD)

X-ray diffraction (XRD) spectra were recorded on a Philips diffractometer, equipped with a PW1730/10 generator and PW1050/70 vertical goniometer. The source was a PW2233/20 tube with a copper anode. The diffracted beam was passed through an

AMRAY Model E3-202 GVW-7794 graphite monochromator before reaching a PW1965/60 proportional detector. Samples were scanned from 0 to 80 °2θ, with 4 second dwell time and 0.1 °2θ step size. Narrow scans of Ni and Mo regions of interest were carried out with a 20 s dwell time and a 0.01 °2θ step size.

### 3.2.6 BET Surface Area

Brunauer, Emmet and Teller (BET) surface areas were measured using an Omnisorb 360 surface area analyzer. Approximately 50 mg of sample was placed in the sample holder and degrassed at 350°C for 4 h. The sample holder was then immersed in liquid $N_2$, and exposed to varying pressures, of $N_2$. At each pressure, P, the amount of $N_2$ adsorbed by the sample was measured. Simultaneously, the saturation pressure of $N_2$, Po, was measured. According to the theory of BET analysis [55], the data were plotted in the form of 1/[V(Po/P-1)] against P/Po, giving a straight line with with slope $(c-1)/v_m c$ and intercept $1/v_m c$. From values of the slope and intercept, the values of these two parameters, the monolayer volume, $v_m$, and an enthalpy related parameter c, can be determined. Taking the $N_2$ molecular cross section to be 0.162 $nm^2$, the value of $v_m$ was used to calculate the area of the monolayer [56]. Also, through the method of t-plot analysis [57], the external surface area and the micropore volume was determined.

### 3.2.7 Ethylene Hydrogenation Studies

Approximately 150 mg of catalyst was finely ground using a mortar and pestle, then weighed into a quartz U-tube of a Micromeritics Autochem II 2920, fitted with a quart wool plug. This is identical to the U-tube holder used in the Ammonia TPD studies detailed above, (See Figure 3.5).

After installing the U-tube inside the furnace of the Autochem II 2920, the sample temperature was ramped at 10°C/min from room temperature to 400°C, with a 1 h hold in 30 mL/min He 5.0 (Praxair), followed by a quick cooling step to room temperature. The He was then replaced with $H_2$ 5.0 (Praxair), and the sample was reduced at 10°C/min up to the desired reduction temperature, (between room temperature and 400°C), with a 1 h hold, then quickly cooled to room temperature. Next, a blend of 10 mL/min of 10% $C_2H_4$ in Ar (Praxair) and 10 mL/min $H_2$ 5.0 (Praxair) was directed through the catalyst at room temperature, with the exhaust directed to a modified HP 5890 Gas Chromatograph (GC) fitted with a Carboxen 1010 capillary column (Supelco) and a Valco 6 port gas sampling valve and a flame

ionization detector (FID). The setup of the GC consisted of a He 5.0 (Praxair) carrier flow of 9.5 mL/min through the column, with 360 mL/min of extra dry air (Praxair) and 32 mL/min $H_2$ 5.0 (Praxair) to the FID. All flows were measured by a soap bubbler operated at ambient temperature (~298 K) and pressure (~93 kPa) After 30 minutes, the exhaust gas was sampled by the actuating the sampling valve on the GC. The chromatogram was recorded via an HP 3393A Integrator on thermal paper. Using this setup, the retention times of $CH_4$, $C_2H_4$ and $C_2H_6$ were approximately 0.86, 4.8 and 7.6 min, respectively. These times were confirmed by the introduction of standard sources of these gases through the reaction system with a blank U-tube in place. In all of the reaction data recorded, there were no other peaks of significant area. Composition data was determined directly from the peak areas, compensating for the methane by a weighting factor of two. This procedure is demonstrated below in Table 3.4.

Table 3.4: Demonstration of composition calculation in the hydrogenation study.

| RT (min) | Area (-) | Area Percent (-) | Adjusted Area (-) | Adjusted Area Percents (-) |
|---|---|---|---|---|
| 0.86 | 100 | 11 | 200 | 20 |
| 4.2 | 500 | 55 | 500 | 50 |
| 7.6 | 300 | 33 | 300 | 30 |

Once the sampling had been repeated to ensure that the reaction had stabilized, the furnace was increased to the next temperature, up to a maximum of 400°C, (the calcination temperature). Typical reaction temperatures were 30, 200, 300 and 400°C. At each temperature, the adjusted area percentages were averaged in the final analysis, although there was no significant deviation from the average.

In a separate series of experiments, the effects of sulfur on the reactivity of the catalyst was studied. This consisted of replacing the $H_2$ with 10% $H_2S/H_2$ (Praxair) in both the pre-treatment, (the catalyst were sulfided to a temperature less than or equal to 400°C), and the reaction feed. As above, the only peaks visible in the chromatogram where those of $CH_4$, $C_2H_4$ and $C_2H_6$, and there were no significant changes in the retention times.

# Chapter 4

## Results and Discussion

For clarity, the abbreviated names for the different catalyst materials studied are defined in Table 4.1, which also includes notes on any relevant treatments done during preparation.

Table 4.1: Definition of catalyst materials studied.

| **Name:** | **Description:** | **Notes:** |
|---|---|---|
| Na-CHA | Chabazite starting material, in the sodium form | n.a. |
| Ni-CHA | Na-CHA ion exchanged with $NiCl_2$ | Dried at 100°C and calcined at 450°C in air |
| Mo-CHA | Na-CHA ion exchanged with $MoCl_3$ | Dried at 100°C and calcined at 450°C in air |
| NiMo-CHA | Na-CHA simultaneously ion exchanged with $NiCl_2$ and $MoCl_3$ | Dried at 100°C and calcined at 450°C in air |
| $NH_4$-CHA(x) | Na-CHA ion exchanged with $NH_4Cl$, x times | Dried at 100°C in air |
| $NH_4^+$ exchanged into NiMo-CHA | NiMo-CHA ion exchanged with $NH_4Cl$ | Dried at 100°C in air |
| NiMo exchanged into $NH_4$-CHA | $NH_4$-CHA simultaneously ion exchanged with $NiCl_2$ and $MoCl_3$ | Dried at 100°C in air |
| HCHA | Na-CHA ion exchanged with HCl | Dried at 60°C in air |
| NiHCHA | HCHA ion exchanged with $NiCl_2$ | Dried at 68°C and calcined at 400°C in air |
| MoHCHA | HCHA ion exchanged with $MoCl_3$ | Dried at 60°C and calcined at 400°C in air |
| NiMoHCHA | MoHCHA ion exchanged with $NiCl_2$ | Dried at 60°C and calcined at 400°C in air |

Elsewhere in this text, there are other statements of such treatments carried out during the course of experimentation.

## 4.1 Composition of Supports and Catalysts

### 4.1.1 XPS

*Series 1*

Wide scans of the catalysts confirm the presence of nickel and molybdenum within the respective samples. In addition to the components of the chabazite (Si, Al and O), a number of metal species such as Na, Mg and Fe were also detected, (See Figures 4.1a and 4.1b).

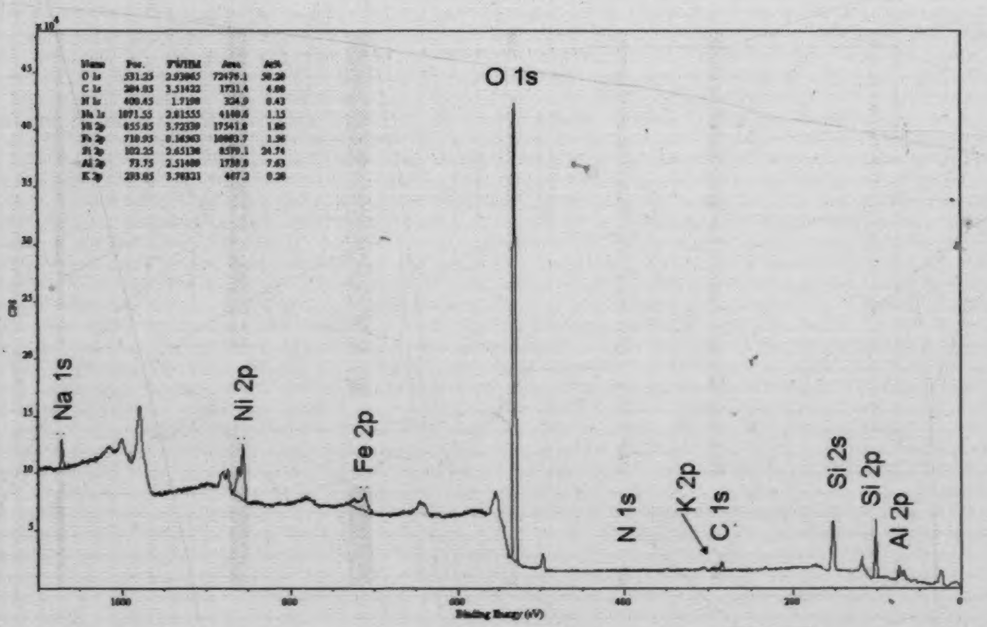

| Name | Pos. | FWHM | Area | At% |
|---|---|---|---|---|
| O 1s | 531.25 | 2.93865 | 72476.1 | 58.20 |
| C 1s | 284.85 | 3.51422 | 1731.4 | 4.08 |
| N 1s | 400.45 | 1.7190 | 324.9 | 0.43 |
| Na 1s | 1071.55 | 2.81555 | 4100.6 | 1.15 |
| Ni 2p | 855.85 | 3.72330 | 17541.8 | 1.86 |
| Fe 2p | 710.95 | 0.16963 | 10003.7 | 1.56 |
| Si 2p | 102.25 | 2.65138 | 8579.1 | 24.74 |
| Al 2p | 73.75 | 2.51400 | 1730.0 | 7.63 |
| K 2p | 293.05 | 3.70321 | 407.2 | 0.28 |

Figure 4.1a: Wide scan of as made Ni-CHA showing the various components of the sample.

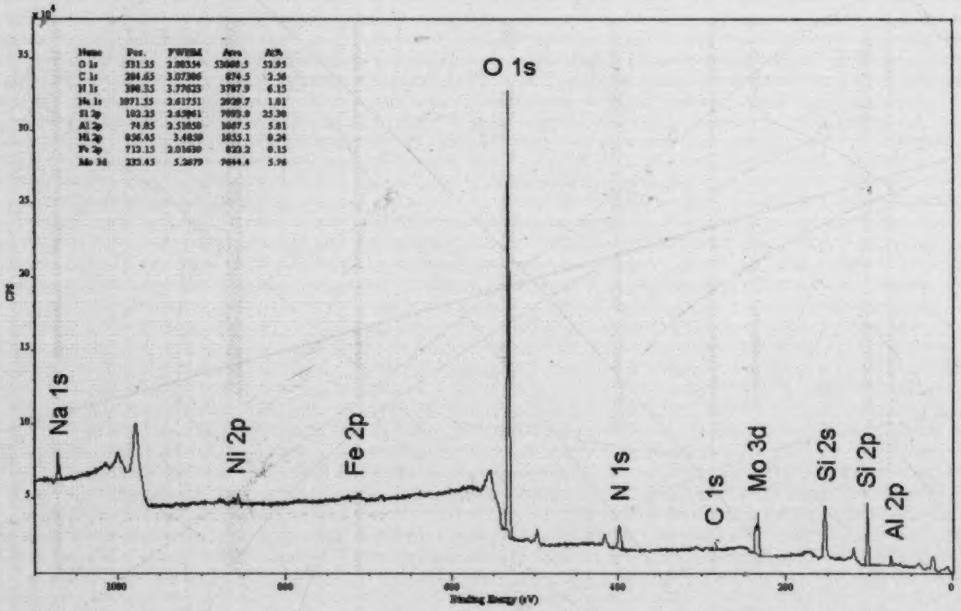

Figure 4.1b: Wide scan of as made NiMo-CHA showing the various components of the sample.

While useful in identifying the components of solid samples, and in particular the oxidation states of the elements present, XPS analysis can also be used for composition analysis of the top few atomic layers, although the accuracy is limited to within a few percent. Using the wide scan data, along with relative sensitivity factors, the surface composition of the samples was calculated, according to the following formula [58] :

$$(X_{atomic})_i = 100\,\% \frac{A_i \big/ (R.S.F.)_i}{\sum_j \left( A_j \big/ (R.S.F.)_j \right)} \qquad \textbf{4.1}$$

where $A_i$ and $(R.S.F.)_i$ are the area and relative sensitivity factor of the i<sup>th</sup> element, respectively. $A_i$ was determined through use of the software package CasaXPS v2.3.5, and the (R.S.F.) values were taken from its library files.

The mass percents were then calculated from the atomic masses of the elements detected in the survey scans, according to the following formula;

$$(X_{mass})_i = 100\% \frac{(X_{Atomic})_i (M_{Atomic})_i}{\sum_j (X_{Atomic})_j (M_{Atomic})_j} \tag{4.2}$$

where $X_{Atomic}$ and $M_{Atomic}$ are the atomic percentage and atomic mass of the $i^{th}$ species, respectively. The mass percent data is summarized in Tables 4.2a and 4.2b.

Table 4.2a: Mass percentages from wide scans of as made and reduced Ni-CHA.

| Name | Elemental Composition from XPS, $(X_{mass})_i$ | | | | |
|---|---|---|---|---|---|
| | Ni-CHA As Made | Ni-CHA R275 | Ni-CHA R400 | Ni-CHA R500 | Ni-CHA R650 |
| Na 1s | 1.2 | 1.0 | 1.1 | 1.0 | 1.1 |
| K 2p | 0.5 | 0.0 | 0.0 | 0.0 | 0.0 |
| Ni 2p | 5.2 | 5.0 | 3.1 | 3.0 | 1.5 |
| Fe 2p | 4.1 | 2.2 | 1.3 | 1.0 | 0.5 |
| O 1s | 43.9 | 43.7 | 44.9 | 45.4 | 46.1 |
| N 1s | 0.3 | 0.1 | 0.0 | 0.0 | 0.0 |
| C 1s | 2.3 | 2.4 | 2.2 | 1.5 | 1.7 |
| Si 2p | 32.8 | 35.4 | 37.9 | 38.1 | 36.0 |
| Mg 2s | 0.0 | 0.3 | 0.0 | 0.0 | 0.0 |
| Al 2p | 9.7 | 9.8 | 9.5 | 9.9 | 13.0 |
| Si/Al mol/mol | 3.2 | 3.5 | 3.9 | 3.7 | 2.8 |

Table 4.2b: Mass percentages from wide scans of as made and reduced NiMo-CHA.

| Name | Elemental Composition from XPS, $(X_{mass})_i$ | | | | |
|---|---|---|---|---|---|
| | NiMo-CHA As Made | NiMo-CHA R275 | NiMo-CHA R400 | NiMo-CHA R500 | NiMo-CHA R650 |
| Na 1s | 1.1 | 1.0 | 1.1 | 1.4 | 1.6 |
| Ni 2p | 0.7 | 0.2 | 0.6 | 0.7 | 0.6 |
| Fe 2p | 0.4 | 0.8 | 0.6 | 0.6 | 0.1 |
| O 1s | 40.2 | 39.9 | 40.7 | 40.6 | 40.0 |
| N 1s | 4.1 | 3.8 | 3.1 | 2.9 | 3.2 |
| C 1s | 1.5 | 3.0 | 1.5 | 1.0 | 1.2 |
| Mo 3d | 10.7 | 9.9 | 9.3 | 8.8 | 8.6 |
| Si 2p | 33.9 | 33.6 | 34.5 | 35.5 | 35.6 |
| Mg 2s | 0.0 | 0.0 | 0.0 | 0.0 | 0.4 |
| Al 2p | 7.5 | 7.9 | 8.6 | 8.4 | 8.7 |
| Si/Al mol/mol | 4.4 | 4.1 | 3.8 | 4.1 | 3.9 |

According to Table 4.2a, the as made Ni-CHA has a Ni loading of approximately 5%, while NiMo-CHA has a Ni loading of 0.7%. Reduction would not be unexpected to result in variations in the composition of the samples, other than perhaps that of oxygen. Yet, a review of the composition data among reduced samples (Tables 4.2a and 4.2b) does indeed show variation in components such as Na, K, Ni, Fe, N, C, Al in the Ni-CHA samples, and Na, Ni, Fe, N, C, Mo, Mg, Al in the NiMo-CHA samples. In particular, the Ni concentration within Ni-CHA undergoes a decreasing trend upon reduction. One possible reason for this is that even at the low operating pressures ($10^{-9}$ torr) employed in the XPS analysis, there remains adsorbed species such as CO, $CO_2$, $N_2$ and $O_2$ on the surface of the samples, which can vary between analysis (i.e. between the 'as made' state and reduced states), thus skewing the percent composition data. In order to investigate this, the composition data was recalculated on a 'per silicon' basis according to the following formula:

$$\left(X_{Mass,Si}\right)_i = 10\frac{\left(X_{Mass}\right)_i}{\left(X_{Mass}\right)_{Si}} \qquad \textbf{4.3a}$$

Also, the atomic ratios of Ni and Mo to Si are calculated as follows:

$$\left(Y_{j,Si}\right) = 10\frac{\left(X_{Mass,Si}\right)_j}{\left(M_{Atomic}\right)_j}\left(M_{Atomic}\right)_{Si} \qquad \textbf{4.3b}$$

Equation 4.3b can be interpretted as the number of atoms of type j, (j = Ni, for example), per 100 atoms of Si, as detected on the surface by XPS.

The 'per silicon' compositions of Ni-CHA and NiMo-CHA are shown in Tables 4.3a and 4.3b.

Table 4.3a: Wide scan 'Per silicon' concentrations of as made and reduced Ni-CHA..

| Name | Composition normalized with respect to Si content; $(X_{Mass,\ Si})_i$ | | | | |
|---|---|---|---|---|---|
| | Ni-CHA As Made | Ni-CHA R275 | Ni-CHA R400 | Ni-CHA R500 | Ni-CHA R650 |
| Na 1s | 0.4 | 0.3 | 0.3 | 0.3 | 0.3 |
| K 2p | 0.2 | 0.0 | 0.0 | 0.0 | 0.0 |
| Ni 2p | 1.6 | 1.4 | 0.8 | 0.8 | 0.4 |
| Fe 2p | 1.3 | 0.6 | 0.3 | 0.3 | 0.1 |
| O 1s | 13.4 | 12.3 | 11.8 | 11.9 | 12.8 |
| N 1s | 0.1 | 0.0 | 0.0 | 0.0 | 0.0 |
| C 1s | 0.7 | 0.7 | 0.6 | 0.4 | 0.5 |
| Si 2p | 10.0 | 10.0 | 10.0 | 10.0 | 10.0 |
| Mg 2s | 0.0 | 0.1 | 0.0 | 0.0 | 0.0 |
| Al 2p | 3.0 | 2.8 | 2.5 | 2.6 | 3.6 |
| $Y_{Ni,Si}$ | 7.7 | 6.7 | 3.8 | 3.8 | 1.9 |

Table 4.3b: Wide scan 'Per silicon' concentrations of as made and reduced NiMo-CHA.

| Name | Compostion normalized with respect to Si content; $(X_{Mass,\ Si})_i$ | | | | |
|---|---|---|---|---|---|
| | NiMo-CHA As Made | NiMo-CHA R275 | NiMo-CHA R400 | NiMo-CHA R500 | NiMo-CHA R650 |
| Na 1s | 0.3 | 0.3 | 0.3 | 0.4 | 0.4 |
| Ni 2p | 0.2 | 0.1 | 0.2 | 0.2 | 0.2 |
| Fe 2p | 0.1 | 0.2 | 0.2 | 0.2 | 0.0 |
| O 1s | 11.9 | 11.9 | 11.8 | 11.4 | 11.2 |
| N 1s | 1.2 | 1.1 | 0.9 | 0.8 | 0.9 |
| C 1s | 0.4 | 0.9 | 0.4 | 0.3 | 0.3 |
| Mo 3d | 3.2 | 2.9 | 2.7 | 2.5 | 2.4 |
| Si 2p | 10.0 | 10.0 | 10.0 | 10.0 | 10.0 |
| Mg 2s | 0.0 | 0.0 | 0.0 | 0.0 | 0.1 |
| Al 2p | 2.2 | 2.4 | 2.5 | 2.4 | 2.4 |
| $Y_{Ni,Si}$ | 1.0 | 2.9 | 2.9 | 1.0 | 1.0 |
| $Y_{Mo,Si}$ | 9.3 | 8.5 | 7.8 | 7.3 | 7.0 |

The elements K, Ni, Fe, O, N, C, Mg, Al are still seen to vary across reduction in the Ni-CHA (see Tables 4.3a and b). Of these, we need not concern ourselves with O, N or C, as the composition of these elements will be skewed by adsorbed species regardless of whether the data is plotted on a per silicon basis, (especially since the Si concentrations were not found to vary significantly). Mg can be omitted as well from consideration, as it was only detected in very low concentrations, or not at all. What is relevant is the trend of decreasing Ni concentration with increasing reduction temperature. It is possible that as cluster size increases, (as was observed by TEM and XRD), an increasing fraction of the metal is shielded from the XPS beam, the escape depth of which is limited to a few nanometers. It is not surprising that this would manifest itself in the case of clusters known to be up to 20 nm in size under such reducing conditions. The compositions within NiMo-CHA (Table 4.3b) are more consistent across reduction, including that of Ni, which provides further support to the above arguments of Ni shielding upon agglomeration, as NiMo-CHA was found to have metal cluster sizes of approximately 2 nm by TEM, which were relatively stable under reduction.

Another feature to consider in the data is the variation in the Si/Al values in both the Ni-CHA and NiMo-CHA samples across reduction. A possible cause of this is the interference from the Ni 3p and Na 2s lines close to the Al 2p, which is used in the calculation of the Si/Al ratio. This is illustrated in below in Figure 4.2.

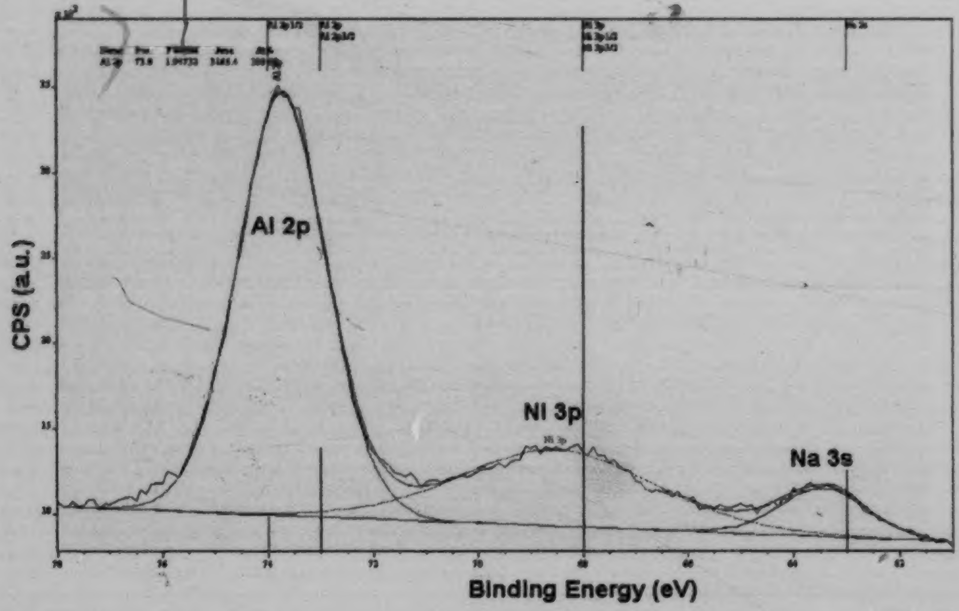

Figure 4.2: Overlap of Al 2p, Ni 3p and Na 2s features affecting the value of Si/Al.

Although accurate deconvolution of these peaks can be done in narrow scans such as the one shown above, this is not possible in the wide scans. Any errors in measuring the area of the Al 2p feature would result in noticeable discrepancies in the value of Si/Al. While interference from the Ni 3p and Na 2s may partially explain this in the case of Ni containing samples, there was also variation among Si/Al ratios in the corresponding Ni-free samples. Another point to consider is the compounding of errors which results in inaccuracies in the concentration of Si and Al. Consider the following example (using data from NiMo-CHA R400, Table 4.2b);

$$x_{Si} = 34.5 \pm 1, y_{Al} = 8.6 \pm 1$$

$$f(x,y) = \frac{(M_{Atomic})_{Al}}{(M_{Atomic})_{Si}} \frac{x_{Si}}{y_{Al}} = \frac{26.98}{28.09} \frac{34.5}{8.6} = 3.8$$

$$f_{\min} = \frac{26.98}{28.09} \frac{33.5}{9.6} = 3.4, f_{\max} = \frac{26.98}{28.09} \frac{35.5}{7.6} = 4.5$$

$$Si/Al = [3.4 \ldots 4.5]$$

The above example illustrates that interpretation of variations in Si/Al values must be done with caution.

Narrow scans of the Ni 2p region in the Ni-CHA and NiMo-CHA samples show an increasing emergence of what appears to be metallic Ni. In all but the 400°C reduction sample, referencing to O 1s at 532.0 eV produces a progressive series of metallic Ni with a binding energy of approximately 853 eV. Furthermore, the extent of reduction appears to be higher in NiMo-CHA than in Ni-CHA (See Figures 4.3a and 4.3b).

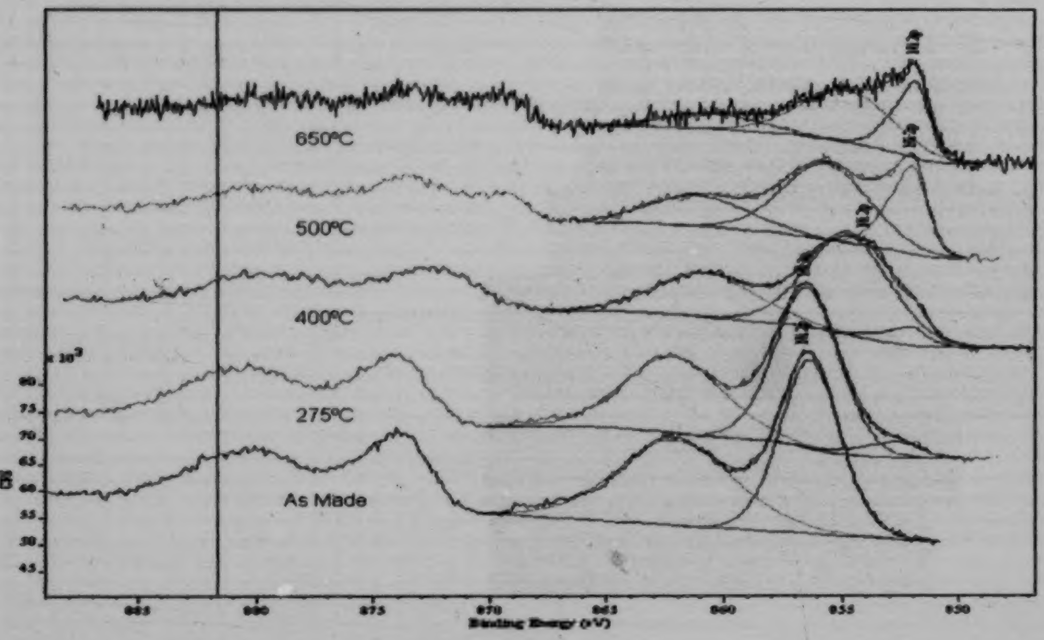

Figure 4.3a: Narrow scans of the Ni 2p feature within as made and reduced Ni-CHA.

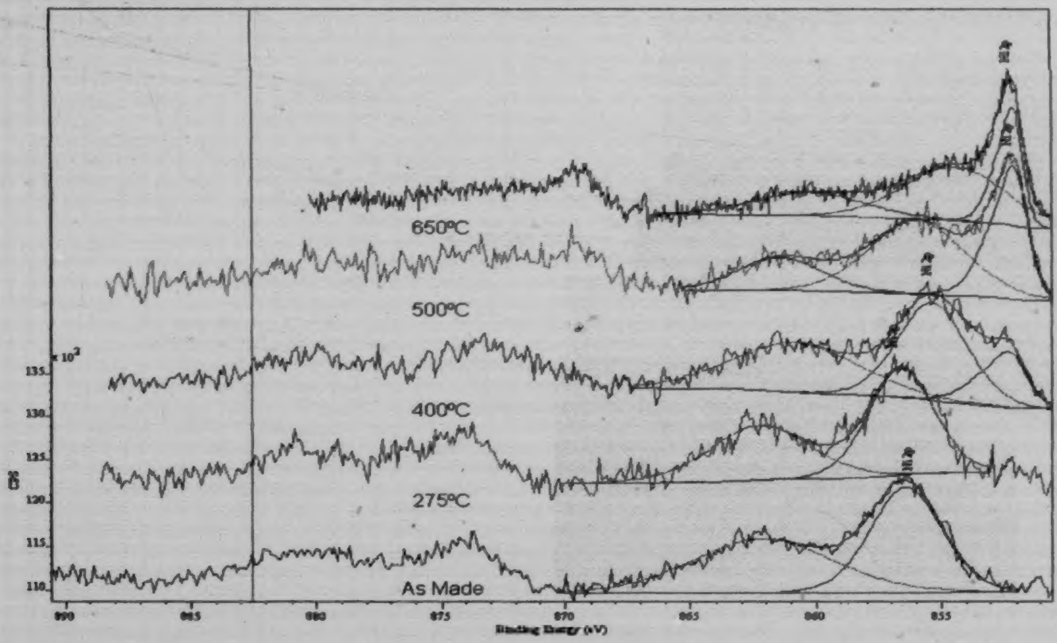

Figure 4.3b: Narrow scans of the Ni 2p feature within as made and reduced NiMo-CHA.

The extent of reduction can be quantified through the use of the following relationship;

$$E_{Red} = 100 \times \frac{\left(A_{Ni(Metal)}\right)}{\left(A_{Ni(Metal)} + A_{Ni(Oxide)}\right)} \% \qquad \mathbf{4.4}$$

where $A_{Ni(Metal)}$ and $A_{Ni(Oxide)}$ are the areas of the metallic and oxide peaks respectively, as determined through the use of CasaXPS software. No R.S.F. value is required because only Ni features are being compared. Applying the above formula to the narrow scan data for both Ni-CHA and NiMo-CHA, the two can be compared in terms of extent of reduction (See Figure 4.4).

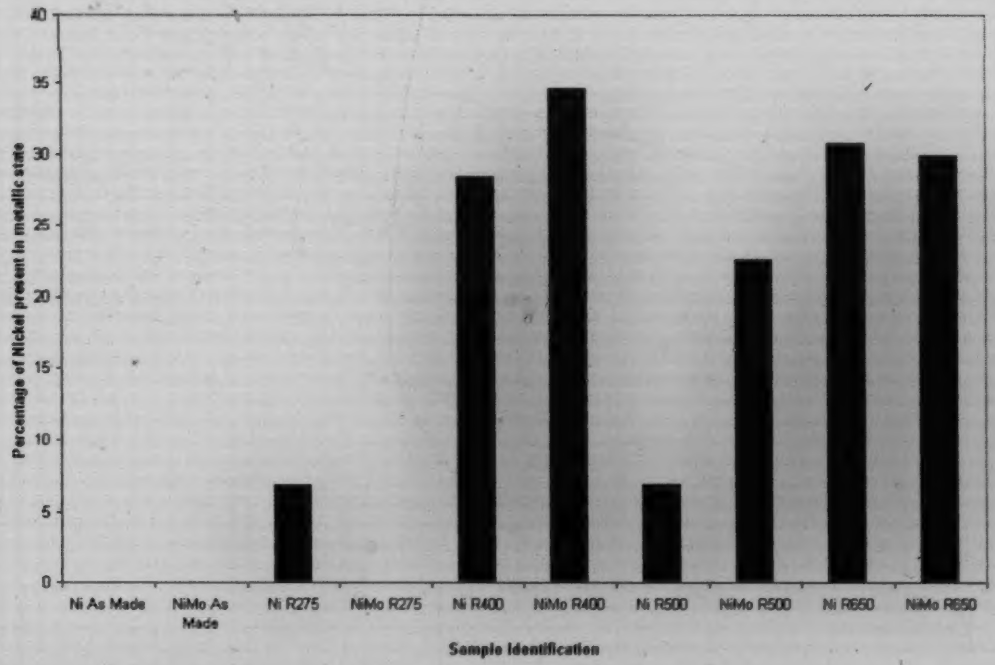

Figure 4.4: Quantified extent of reduction of Ni-CHA and NiMo-CHA.

Other than the anomalously high extent in the R400 experiment, there is a clear trend of increasing extent of reduction with increasing temperature.

Limited analysis of the Mo 3d feature within NiMo-CHA across reduction reveals the emergence of multiple oxidation states (Figure 4.5).

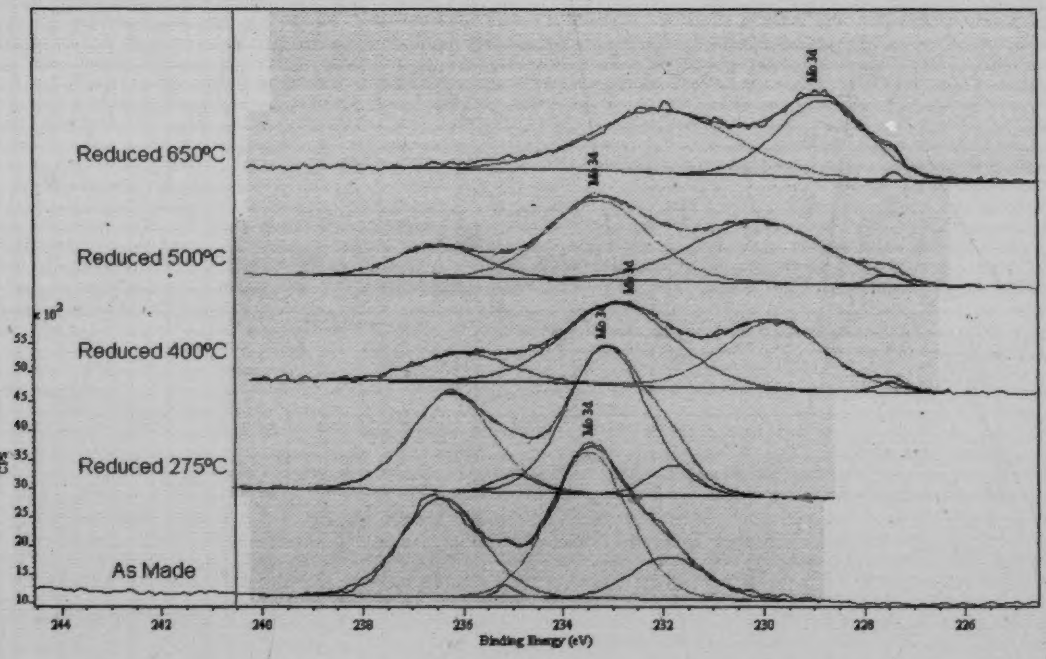

Figure 4.5: Narrow scans of the Mo 3d feature within as made and reduced NiMo-CHA. Reduction seems to result in the observation of multiple oxidation states.

As molybdenum can take on oxidation states of 2, 3, 4, 5 and 6, a precise resolution of the complex Mo 3d features observed would be difficult. However, the data does show that Mo undergoes reduction to some extent under the conditions studied, although not necessarily to a zero valence state.

In the TPS:XPS study, wide scans confirmed the presence of nickel, molybdenum as well as sulfur within the respective samples (See Figures 4.6a and 4.6b).

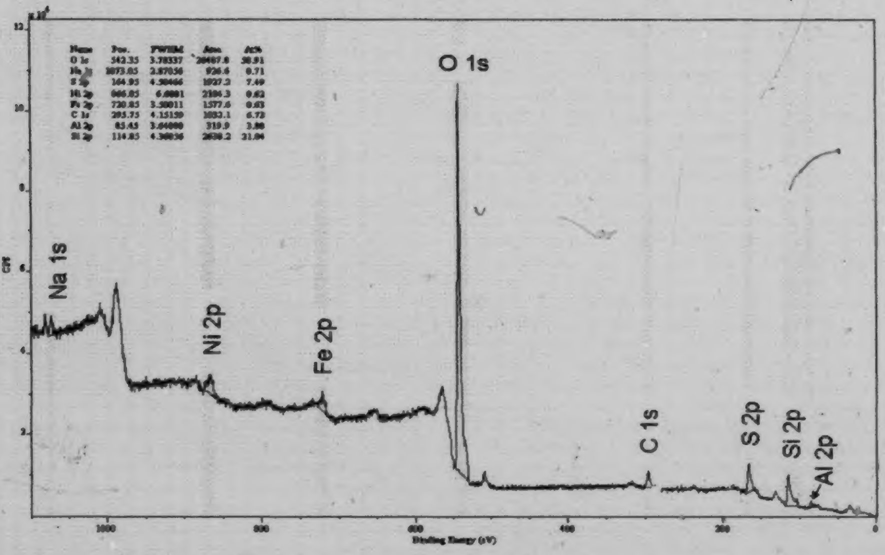

Figure 4.6a: Wide scan of Ni-CHA sulfided at 265°C.

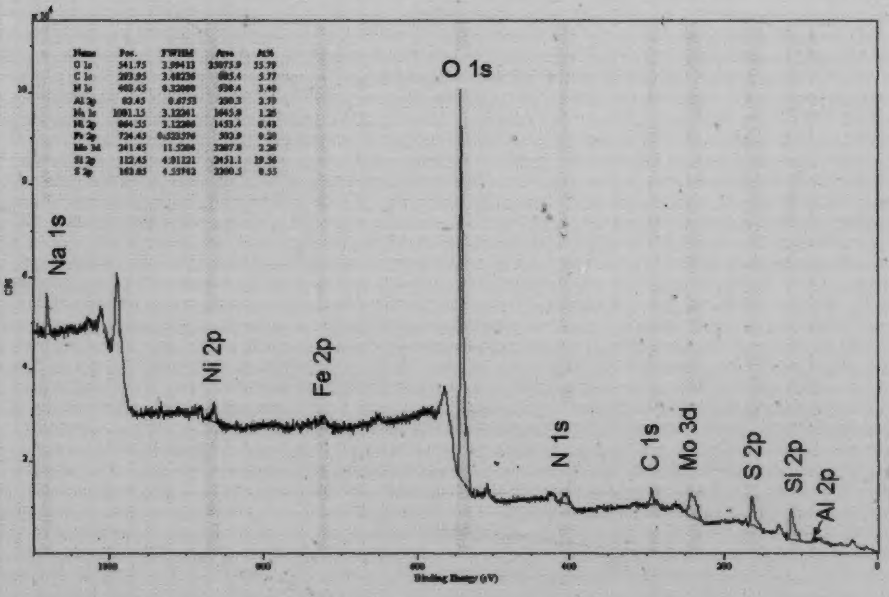

Figure 4.6b: Wide scan of NiMo-CHA (lower) sulfided at 265°C.

Using the wide scan data and Equations 4.1 and 4.2, the composition of Ni-CHA and Ni-CHA in the as made and reduced states was calculated, (See Tables 4.4a and 4.4b).

Table 4.4a: Mass percentages from wide scans of as made and sulfided Ni-CHA.

| Name | Elemental Composition from XPS, $(X_{mass})_i$ | | | |
|---|---|---|---|---|
| | Ni-CHA As made | Ni-CHA S23 | Ni-CHA S200 | Ni-CHA R265 |
| Na 1s | 1.3 | 1.5 | 0.9 | 0.7 |
| S 2p | 0.0 | 0.0 | 2.7 | 18.3 |
| Ni 2p | 2.8 | 2.4 | 1.7 | 1.4 |
| Fe 2p | 1.1 | 0.0 | 1.3 | 0.3 |
| O 1s | 43.2 | 44.0 | 41.8 | 39.1 |
| C 1s | 4.3 | 9.3 | 7.4 | 7.8 |
| Si 2p | 37.3 | 34.2 | 35.6 | 28.0 |
| Al 2p | 10.1 | 8.7 | 8.7 | 4.4 |
| Si/Al mol/mol | 3.6 | 3.8 | 3.9 | 5.4 |

Table 4.4b: Mass percentages from wide scans of as made and sulfided Ni-CHA.

| Name | Elemental Composition from XPS, $(X_{mass})_i$ | | | |
|---|---|---|---|---|
| | NiMo-CHA As Made | NiMo-CHA S23 | NiMo-CHA S200 | NiMo-CHA R265 |
| Na 1s | 1.4 | 0.9 | 0.9 | 1.3 |
| S 2p | 0.0 | 0.0 | 2.4 | 12.5 |
| Ni 2p | 0.9 | 0.7 | 0.4 | 1.1 |
| Fe 2p | 0.0 | 0.0 | 0.0 | 0.5 |
| O 1s | 37.4 | 39.0 | 37.4 | 40.8 |
| N 1s | 3.7 | 4.3 | 3.7 | 2.2 |
| C 1s | 5.8 | 7.4 | 6.2 | 3.2 |
| Mo 3d | 10.0 | 10.6 | 10.6 | 9.9 |
| Si 2p | 30.5 | 30.3 | 31.5 | 25.1 |
| Al 2p | 10.3 | 6.9 | 7.0 | 3.4 |
| Si/Al mol/mol | 2.6 | 4.2 | 4.3 | 7.0 |

As in the case of the reduction study discussed above, there is significant variation in the concentration of sample components across sulfidation. Upon further inspection of the mass percent data, a clear decreasing trend is seen in the concentration of Si and even more so Al, in both the Ni-CHA and NiMo-CHA samples upon sulfidation. Accompanying these decreases is the pronounced increase in the concentration of sulfur, at and above 200°C. It is unclear whether or not these phenomena are related. Note that although the mass percent of sulfur takes on higher values in the Ni-CHA than in the NiMo-CHA, consideration of the relative metal loadings of these two samples, the extent of sulfidation appears more pronounced in the NiMo sample. Looking at the data on a per silicon basis, there is less variation in the Ni concentration in Ni-CHA, but still significant variation within NiMo-CHA (Table 4.5a and 4.5b).

Table 4.5a: 'Per silicon' concentrations wide scans of as made and sulfided Ni-CHA

| Name | Composition normalized with respect to Si content; $(X_{Mass,\ Si})_i$ | | | |
|---|---|---|---|---|
| | Ni-CHA As Made | Ni-CHA S23 | Ni-CHA S200 | Ni-CHA S265 |
| Na 1s | 0.3 | 0.4 | 0.3 | 0.3 |
| S 2p | 0.0 | 0.0 | 0.8 | 6.5 |
| Ni 2p | 0.8 | 0.7 | 0.5 | 0.5 |
| Fe 2p | 0.3 | 0.0 | 0.4 | 0.1 |
| O 1s | 11.6 | 12.9 | 11.7 | 14.0 |
| C 1s | 1.2 | 2.7 | 2.1 | 2.8 |
| Si 2p | 10.0 | 10 | 10 | 10 |
| Al 2p | 2.7 | 2.5 | 2.4 | 1.6 |
| $Y_{Ni,Si}$ | 3.8 | 3.4 | 2.4 | 2.4 |

Table 4.5b: 'Per silicon' concentrations wide scans of as made and sulfided NiMo-CHA.

| Name | Composition normalized with respect to Si content; $(X_{Mass,\ Si})_i$ | | | |
|---|---|---|---|---|
| | NiMo-CHA As Made | NiMo-CHA S23 | NiMo-CHA S200 | NiMo-CHA S265 |
| Na 1s | 0.5 | 0.3 | 0.3 | 0.5 |
| S 2p | 0.0 | 0.0 | 0.8 | 5.0 |
| Ni 2p | 0.3 | 0.2 | 0.1 | 0.4 |
| Fe 2p | 0.0 | 0.0 | 0.0 | 0.2 |
| O 1s | 12.3 | 12.9 | 11.8 | 16.3 |
| N 1s | 1.2 | 1.4 | 1.2 | 0.9 |
| C 1s | 1.9 | 2.4 | 2.0 | 1.3 |
| Mo 3d | 3.3 | 3.5 | 3.4 | 3.9 |
| Si 2p | 10.0 | 10.0 | 10.0 | 10.0 |
| Al 2p | 3.4 | 2.3 | 2.2 | 1.4 |
| $Y_{Ni,Si}$ | 1.4 | 1.0 | 0.5 | 1.9 |
| $Y_{Mo,Si}$ | 9.7 | 10.3 | 10.0 | 11.4 |

By analyzing the Ni 2p spectra of the Ni-CHA and NiMo-CHA, the effects of sulfidation upon the Ni species were studied more closely (Figures 4.7a and 4.7b).

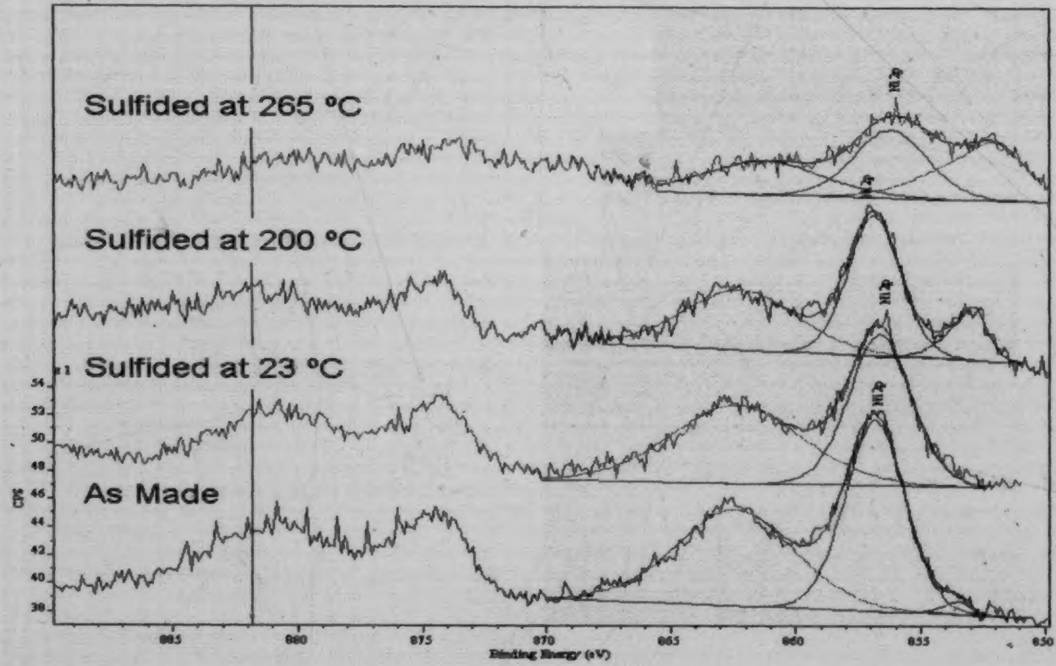

Figure 4.7a: Narrow scans of the Ni 2p feature within as made and sulfided Ni-CHA.

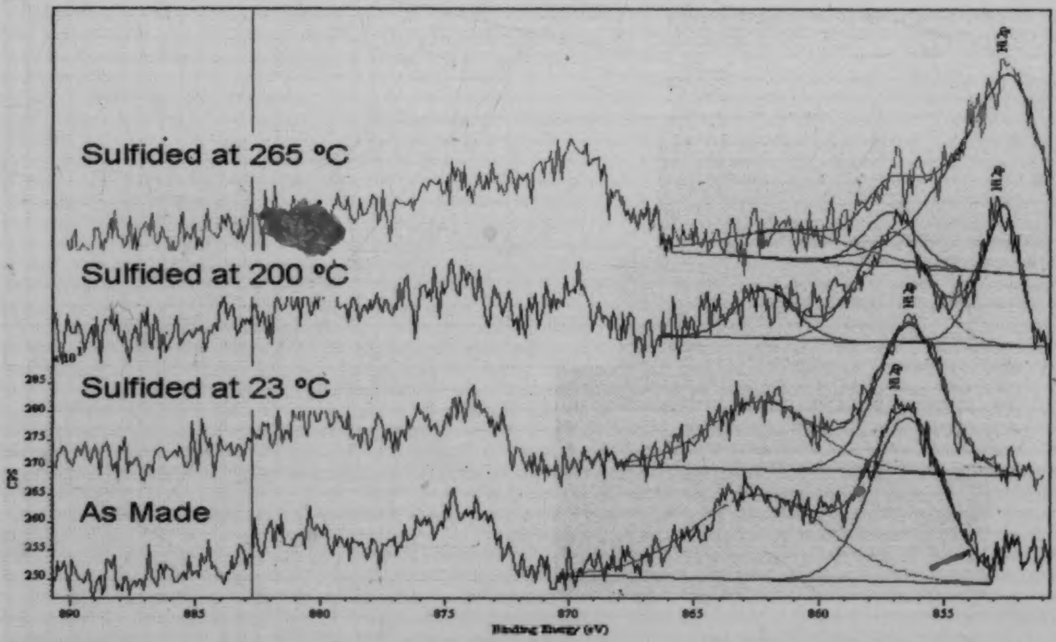

Figure 4.7b: Narrow scans of the Ni 2p feature within as made and sulfided NiMo-CHA.

The results appear very similar to those of the reduction study. In fact, it is difficult to discriminate between the Ni(metal) peaks seen in the hydrogenation study, and the novel features arising here, which after scaling to O 1s 532.0 eV, appear to have the same binding energy. Also, as observed in the hydrogenation study, it would appear that the effect of sulfidation is more pronounced in the NiMo-CHA samples than in Ni-CHA, at a given treatment temperature. This is shown quantitatively in Figure 4.8, through the analogous use of Equation 4.4 above.

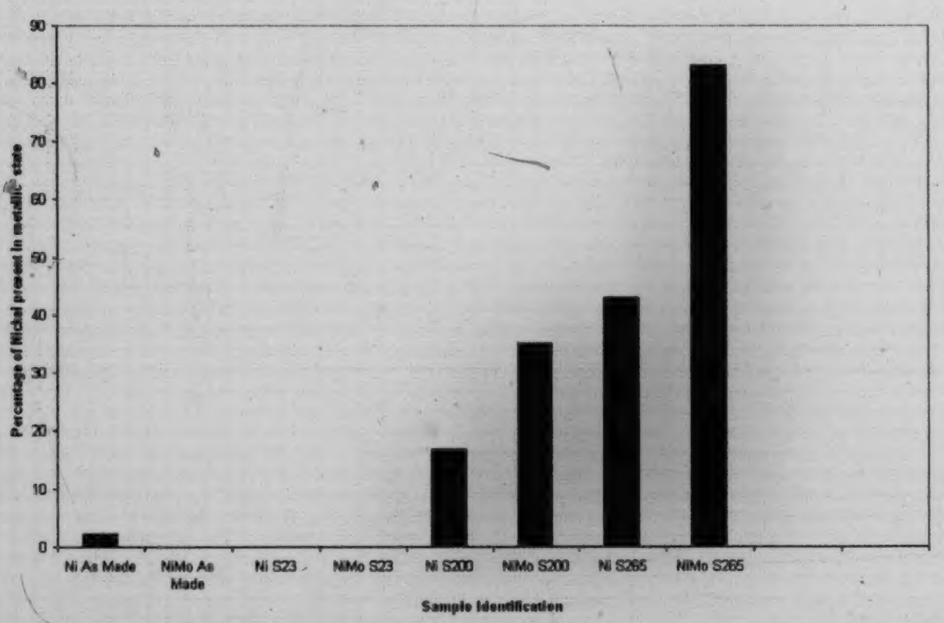

Figure 4.8: Quantified extent of sulfidation of Ni-CHA and NiMo-CHA.

The term metallic* extent is used with caution in the above figure, (Figure 4.8), as the XPS studies were not able to confirm whether a true sulfide or zero valent Ni state was observed under treatment with 10% $H_2S/H_2$. Nonetheless, this finding confirms that, at a given sulfidation temperature, the effect of sulfidation of NiMo-CHA exceeds that of Ni-CHA, under the conditions studied.

Examining the evolution of the Mo 3d feature within NiMo-CHA upon sulfidation, we see the emergence of multiple oxidation states (Figure 4.9).

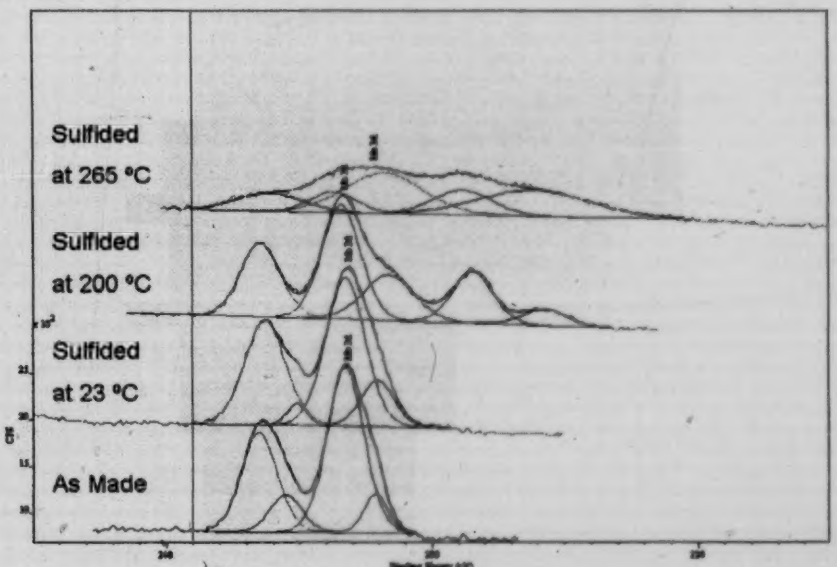

Figure 4.9: Narrow scans of the Mo 3d feature within as made and sulfided NiMo-CHA. (Note that multiple oxidation states are detected.)

In comparison with the analogous data from the reduction studies, features of even lower binding energy are observed in the 265°C sulfidation. It is tempting to attribute the structure of the Mo 3d spectra to the formation of $MoS_2$. Yet, published work on $MoS_2$ such as that of Iranmahboob et al. [59] indicates that such a low binding energy feature is likely that of the S 2s peak. Therefore, it cannot be said with certainty that XPS has detected the presence of $MoS_2$.

*Series 2*

As in Series 1, the initial wide scans indicated the presence of sodium, zinc, iron, calcium and carbon, in addition to the silicon, aluminum and oxygen expected to be present within chabazite. The presence of the supported metals, (nickel and molybdenum) was also confirmed within the respective samples (See Figure A.1a –A.1d, Appendix A). As in the Series 1 study, XPS wide scans and Equations 4.1 and 4.2 were used to compute the mass percentage compositions of the samples. This data is shown in Table A.1a - A.1f, Appendix A). Also evident from the compositional data is the same type of variation across reduction, as discussed in Series 1. Additionally, in Series 2, every TPR:XPS experiment consisted of scan of the as made catalyst before reduction and subsequent reanalysis. For this reason, the data set contains multiple analyses of the catalysts in the as made states. For example, XPS analyses of NiHCHA in the AMR200, AMR300 and AMR400 studies can be considered replicate analyses of the as made (AM) materials. Such variations are most significant in terms of the adsorbed species, (O, C, N) as discussed above. While differing across the various as made experiments, the Ni content of NiHCHA and NiMoHCHA appears to be 2% and 1% respectively. There is considerable disagreement between the as made and reduced samples. Using Equation 4.3, compositions were generated on a 'per silicon' basis. These compositions are listed in Tables A.2a - A.2f, Appendix A. When calculated on a per silicon basis, there is very little variation in the composition of the relevant species. However, it can be argued that the concentration of Ni within both NiHCHA and NiMoHCHA decreases upon reduction. This is likely due to the growth of large clusters, leading to 'shielding' of the relatively shallow penetrating XPS beam, as found and discussed in the Series 1 reduction studies. This explanation is substantiated by the Series 2 TEM data, which detected significant growth in cluster size in both NiHCHA and NiMoHCHA.

As in Series 1, there is significant variation in the Si/Al ratios. The effects of the Ni 3p and Na 2s features on the Al 2p feature, as discussed above, surely contribute to errors in the measurement of the Si/Al ratio by XPS. The limitations in calculating Si/Al ratio by XPS, as discussed in Series 1, apply equally here.

By analyzing the Ni 2p spectra of the NiHCHA and NiMoHCHA, the effects of hydrogen reduction upon the Ni species could be studied in detail. It is clear that in both NiHCHA and NiMoHCHA, significant reduction takes place under the conditions studied, as shown in Figures 4.10a and 4.10b.

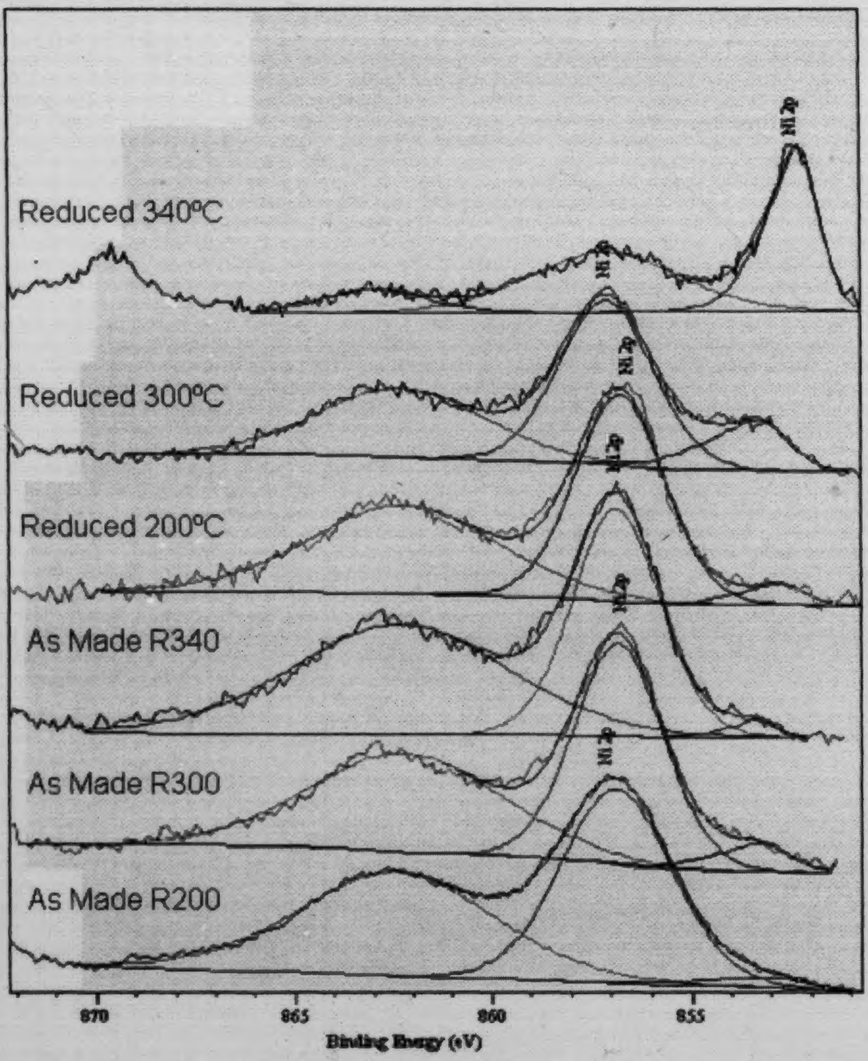

Figure 4.10a: Narrow scans of the Ni 2p feature within as made and reduced NiHCHA.

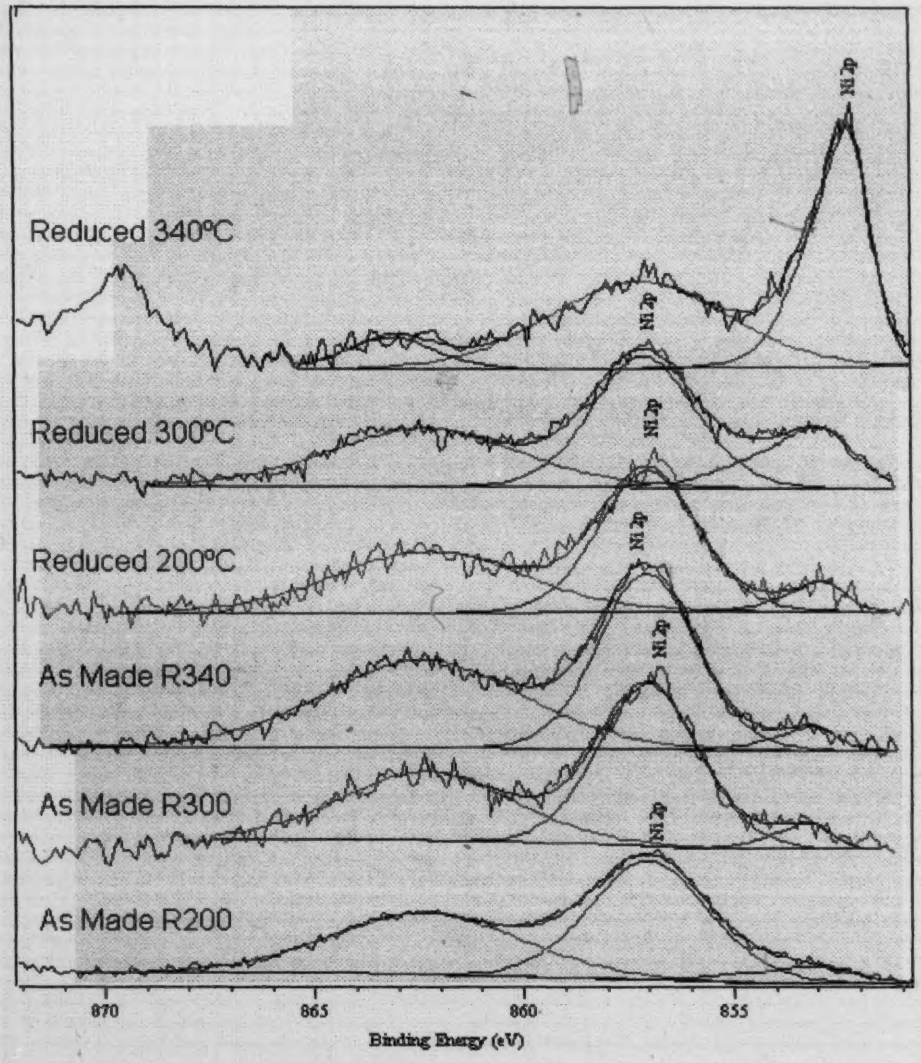

Figure 4.10b: Narrow scans of the Ni 2p feature within as made and reduced NiMoHCHA.

A plot of the extent of reduction versus reduction temperature (Figure 4.11) quantifies the results of Figures 4.10a and 4.10b.

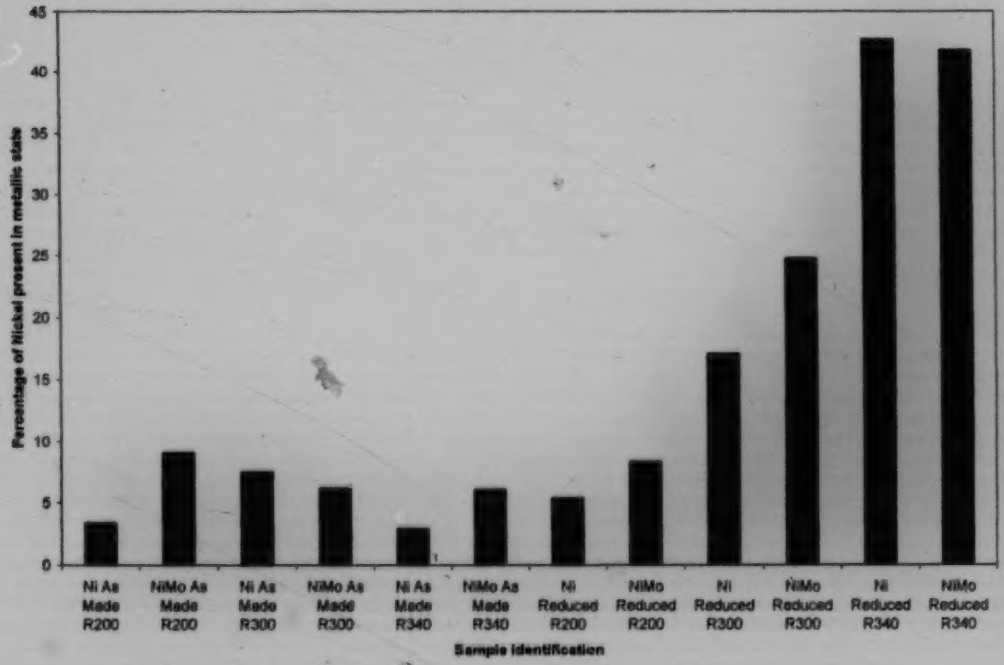

Figure 4.11: Quantified extent of reduction of NiHCHA and NiMoHCHA.

The plot (Figure 4.11) clearly shows the increasing trend of the extent of reduction with reduction temperature. Also evident is the higher extent of reduction in NiMoHCHA than in NiHCHA, as seen in Series 1. Another point to consider is that proper fitting of the as made spectra required the inclusion of small Ni(metal) features. Although this was also required in Series 1, the as made catalysts of Series 2 required a much more significant Ni(metal) contribution to the convolution of the spectra. It is not clear whether or not the as made materials actually contained any Ni in the metallic state.

Examining the evolution of the Mo 3d feature within NiMoHCHA and MoHCHA across reduction, we see little difference between the two, (Figures 4.12a and 4.12b).

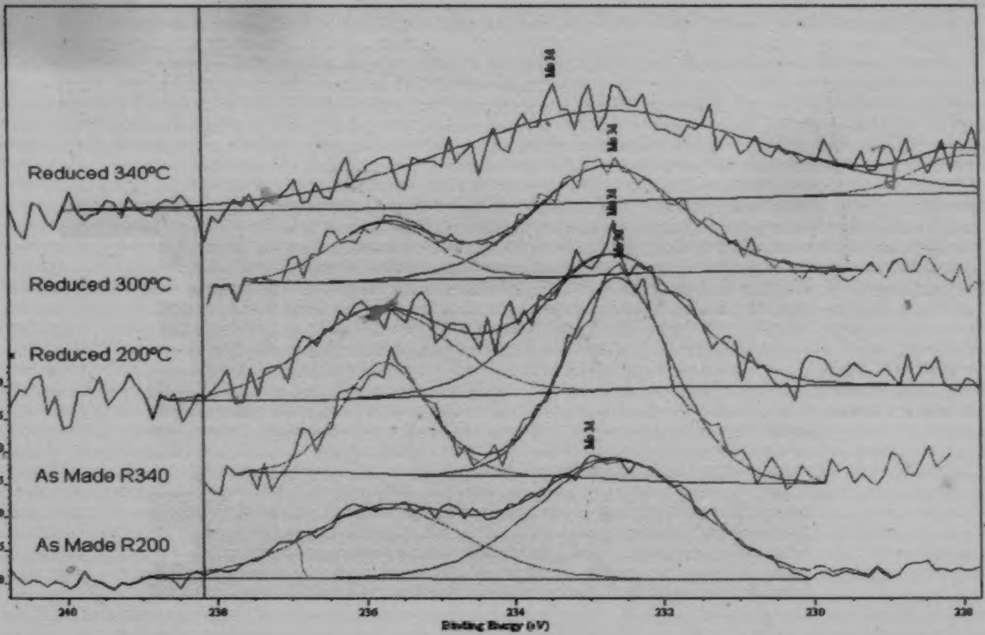

Figure 4.12a: Narrow scans of the Mo 3d feature within as made and reduced NiMoHCHA.

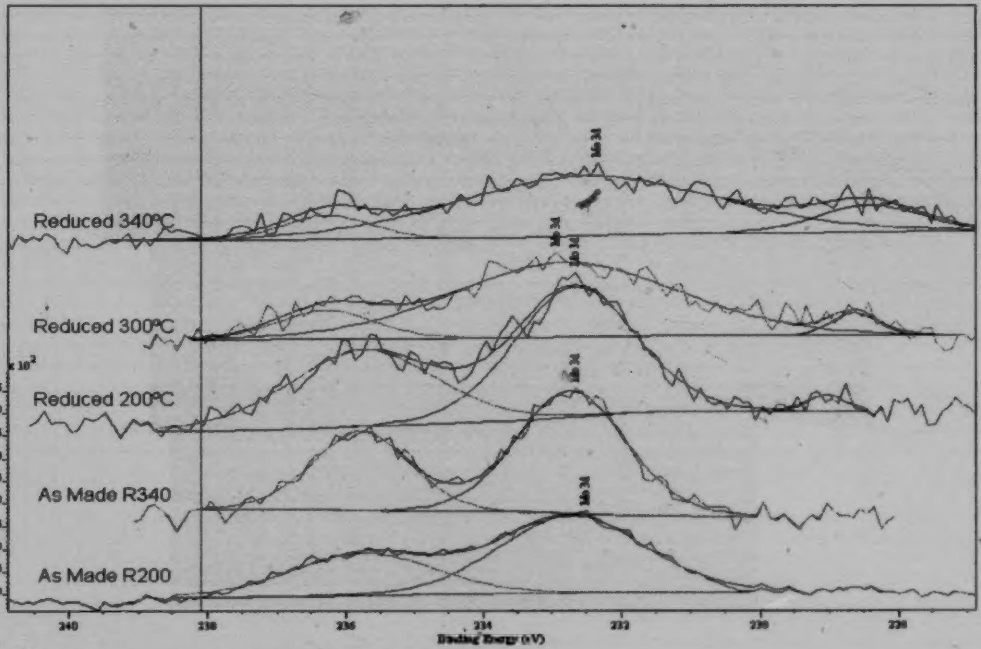

Figure 4.12b: Narrow scans of the Mo 3d feature within as made and reduced MoHCHA.

There is some evidence of multiple oxidation states in both sets of spectra. One could argue that the Mo 3d feature in Series 1 NiMo-CHA shows a more pronounced reduction feature (~229 eV) at 275°C than does the analogous feature in Series 2 NiMoHCHA at 300°C, yet this would likely be an over-interpretation of the data.

As discussed in section 3.2.3, the effects of ambient exposure on freshly reduced samples was studied in order to determine the necessity of *in-situ* XPS studies. The data from this investigation is shown in Figure 4.13.

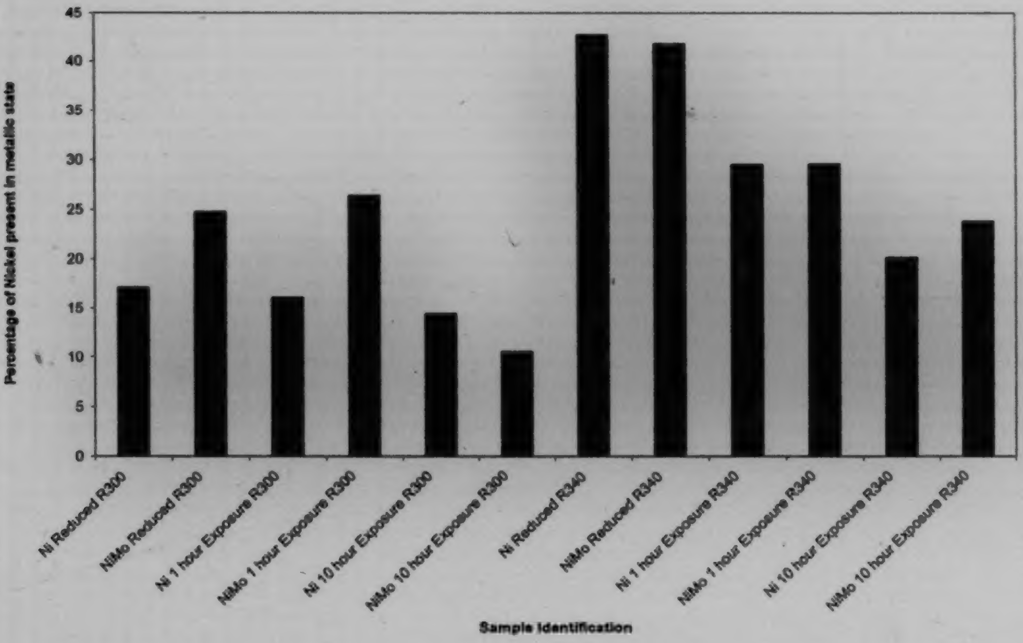

Figure 4.13: Effect of exposure upon reduced NiHCHA (Ni) and NiMoHCHA (NiMo).

At low temperatures of reduction (300°C), a brief exposure results in very little oxidation of the Ni components of the two samples, between which there is little difference. After longer exposure, both samples show significant oxidation, with a more pronounced effect on the NiMoHCHA than on NiHCHA. At higher temperatures, even brief exposure leads to significant oxidation. So severe is the effect that further exposure results in only minor losses beyond that sustained in the brief exposure. We can infer that at low extent of reduction, a significant exposure is required in order to affect the extent of reduction as measured by XPS, and there is variation in the magnitude of the effect of exposure between the samples, although this is not surprising based on the observed variation in the extent of reduction observed in the study. We can also infer that at higher degrees of reduction, even a brief exposure to the ambient air will result in erroneous measurements of the extent of reduction as measured by XPS. At such high degrees of reduction, there is less of a distinction between the samples. This is likely due to the fact that the focus of the analyses in both samples was Ni. Perhaps studies on a less easily oxidized metal would reveal differences in the extent of oxidation under longer periods of exposure.

### 4.1.2 INAA

The limited amount of INAA data gathered provides a measure of agreement with the XPS results. The data indicate that the Si, Al, Na, Ni, and Mo concentrations for the as made Ni- and NiMo-CHA agree within an order of magnitude with the findings of the XPS study. The agreement is perhaps superior on a 'per silicon' basis, (See Tables 4.6a and 4.6b).

Table 4.6a: INAA mass percentages of as made Series 1 catalysts.

| | Na-CHA | Ni-CHA | Mo-CHA | NiMo-CHA |
|---|---|---|---|---|
| Name | mass % | mass % | mass % | mass % |
| Si | 25.0 | 27.1 | 22.1 | 22.0 |
| Al | 7.7 | 8.0 | 8.0 | 7.6 |
| Na | 6.1 | 2.6 | 3.2 | 2.5 |
| Ni | 0.0 | 4.7 | 0.0. | 2.8 |
| Mo | 0.0 | 0.0 | 9.2 | 9.9 |
| Si/Al mol/mol | 3.1 | 3.3 | 2.7 | 2.8 |

Table 4.6b: INAA 'Per silicon' concentrations of as made Series 1 catalysts.

| | Na-CHA | Ni-CHA | Mo-CHA | NiMo-CHA |
|---|---|---|---|---|
| Name | mass % | mass % | mass % | mass % |
| Si | 10.0 | 10.0 | 10.0 | 10.0 |
| Al | 3.1 | 3.0 | 3.6 | 3.5 |
| Na | 2.4 | 1.0 | 1.4 | 1.1 |
| Ni | 0.0 | 1.7 | 0.0 | 1.3 |
| Mo | 0.0 | 0.0 | 4.1 | 4.5 |
| $Y_{Ni,Si}$ | 0.0 | 8.1 | 0.0 | 6.2 |
| $Y_{Mo,Si}$ | 0.0 | 0.0 | 12.0 | 13.0 |

There is variation in terms of the Si/Al ratio as measured by INAA, which appears more pronounced in the Mo containing samples. This coincides with the observation of baseline broadening observed in the XRD, which was pronounced in the Mo containing samples as well. Further experimentation into structural changes in the chabazite which may take place upon metal incorporation is required.

Unfortunately, no INAA results were available for Series 2 at the completion of this thesis.

## 4.2 Structure of Supports and catalysts

TEM and XRD were employed in order to characterize the structure of the bare and metal-loaded chabazite. Additionally, the formation of clusters upon reduction and sulfidation was of primary interest. A wide array of the results of these studies can be found in Appendix A, while representative excerpts are included below. BET surface area was employed to provide additional information on the support/supported metal structure, and to provide insight into the effects of metal incorporation.

### 4.2.1 Transmission Electron Spectroscopy

*Series 1*

Imaging the bare support (Na-CHA) reduced at 350°C reveals a layered structure, with no significant regions of high contrast (Figure 4.14).

Figure 4.14: TEM image of Na-CHA reduced at 350°C. There are no visible clusters detected in the image.

This confirms the utility of TEM in imaging the metal clusters on the surface of the support. Imaging of Ni-CHA at low degrees of reduction (50°C - 275°C) shows highly dispersed, circularly shaped Ni clusters. An example of such clusters is shown in Figure 4.15.

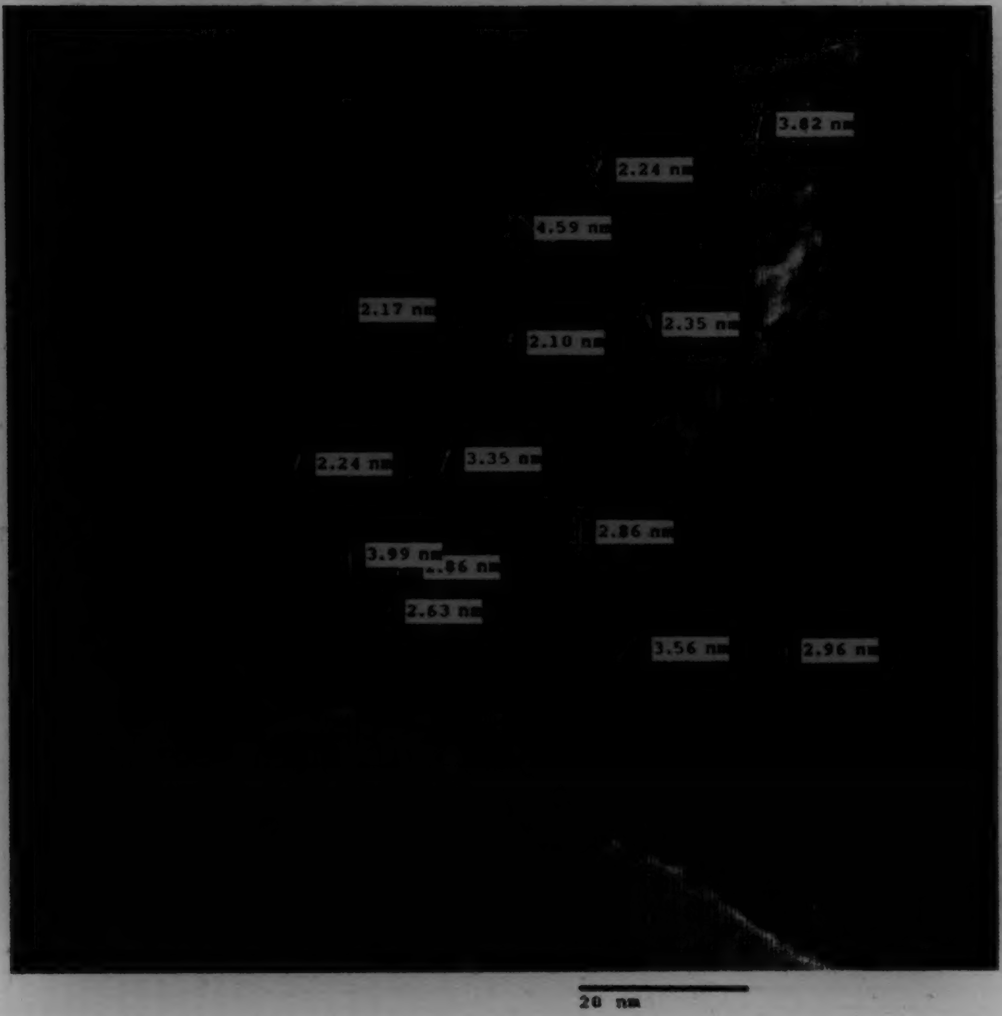
3.82 nm
2.24 nm
4.59 nm
2.17 nm
2.35 nm
2.10 nm
2.24 nm
3.35 nm
2.86 nm
3.99 nm
.86 nm
2.63 nm
3.56 nm
2.96 nm
20 nm

Figure 4.15: TEM image of Ni-CHA reduced at 275°C. The figure clearly shows well dispersed Ni clusters.

The majority of the clusters are on the order of 3 to 4 nm in size, yet between 275°C and 350°C, cluster growth clearly takes place, as images of the 350°C sample show clusters from 7 to 14 nm in size. This trend continues with increasing severity of reduction, as shown in the 450°C sample. The clusters imaged in this sample are on the order of 20 nm in size, and non-circular in shape, (see Figure 4.16). It appears that some of the clusters shown appear to be the merger of two clusters of differing size. The mechanism of such merging would need further investigation in order to substantiate it.

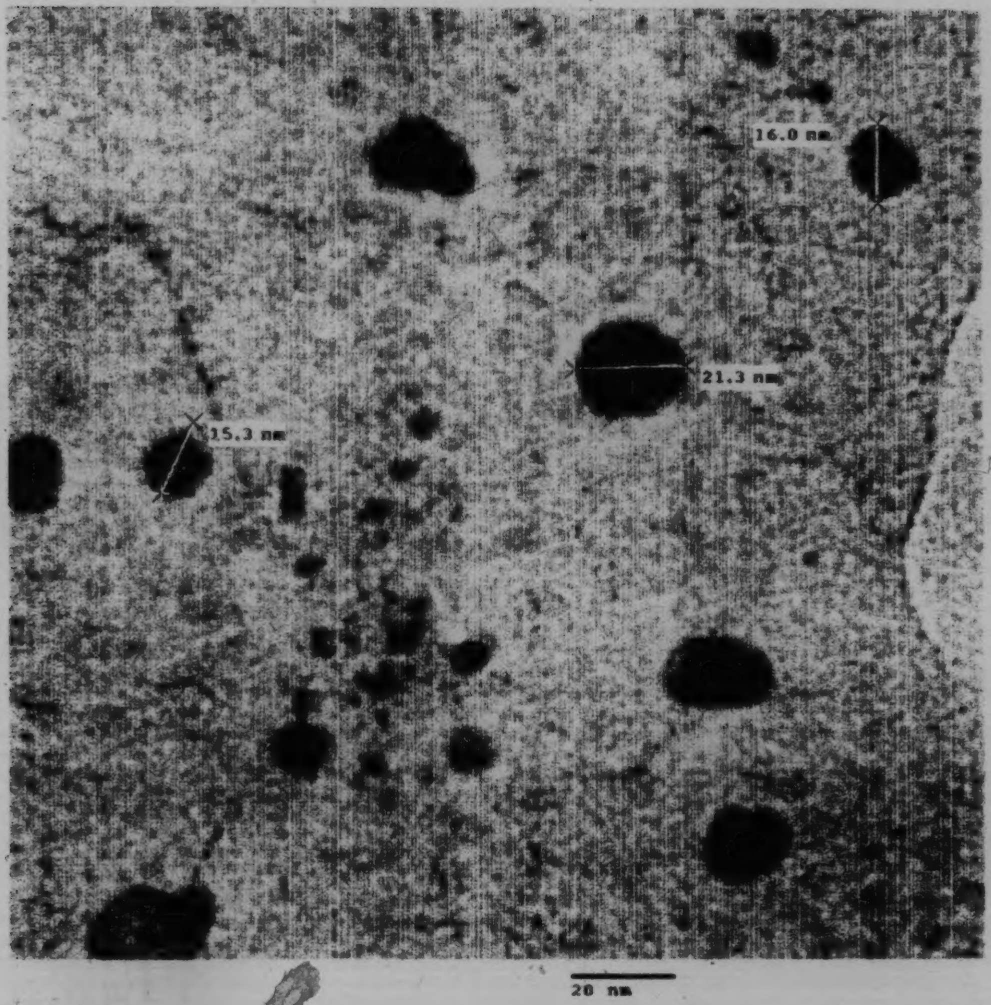

Figure 4.16: TEM image of Ni-CHA reduced at 450°C. The increased size of the clusters with increased temperature of reduction is obvious.

At 550°C, (conditions which exceed the 450°C calcination of the support), pronounced growth and distortion of the Ni clusters is obvious, (Figure B.18-B.21, Appendix B).

When treated with 10% H2s/$H_2$, Ni-CHA behaves as in pure $H_2$, with cluster size increasing monotonically with treatment temperature. At 150 °C, the clusters observed, (Figures B.22 – B.23, Appendix B), while well-dispersed, show a slightly larger (3 to 4 nm) nominal size when treated at 150°C in 10% H2s/$H_2$ than observed at the same temperature in hydrogen (3 nm). This growth continues at 250°C, where 6 nm clusters can be seen (Figure 4.17). Comparing this with 4 nm clusters observed in the 275°C reduction study (Figure 4.15), it appears that sulfidation leads to a larger cluster growth than reduction, at a given treatment temperature.

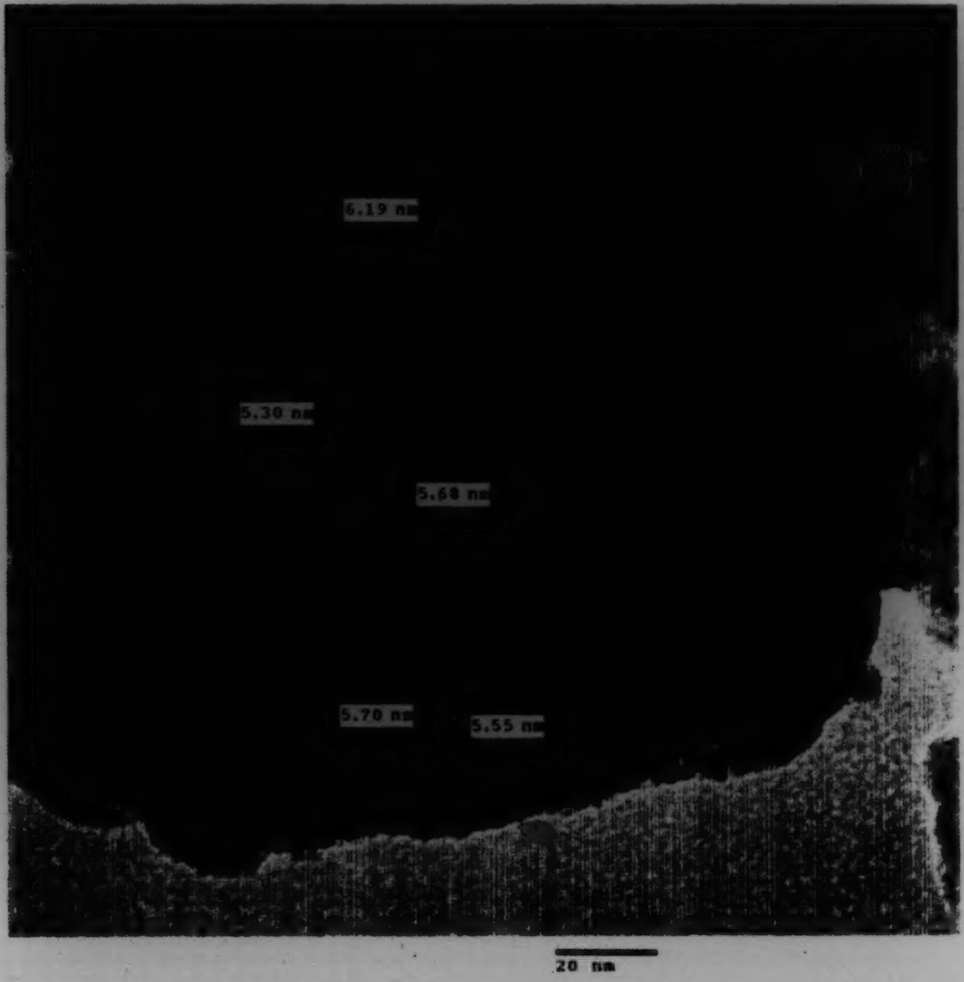

Figure 4.17: TEM image of Ni-CHA sulfided at 250°C. Clusters larger in size (~6 nm) than those seen under reduction at 275°C are evident.

At 350°C, there is clear evidence of sintering (reduced dispersion) such as uneven spacing between adjacent clusters as well as misshapen clusters 3 to 8 nm in size (See Figures B.28 – B.31, Appendix B). Treatment at 450°C shows a very slight increase in cluster size (4 to 9 nm). It is interesting to note that these sizes are smaller than the corresponding sizes observed under reduction, (Figures B.32 – B.35, Appendix B).

*Mo-CHA*

In the as made state, the clusters were found to be well dispersed in the 3 nm range, (See Figure 4.18).

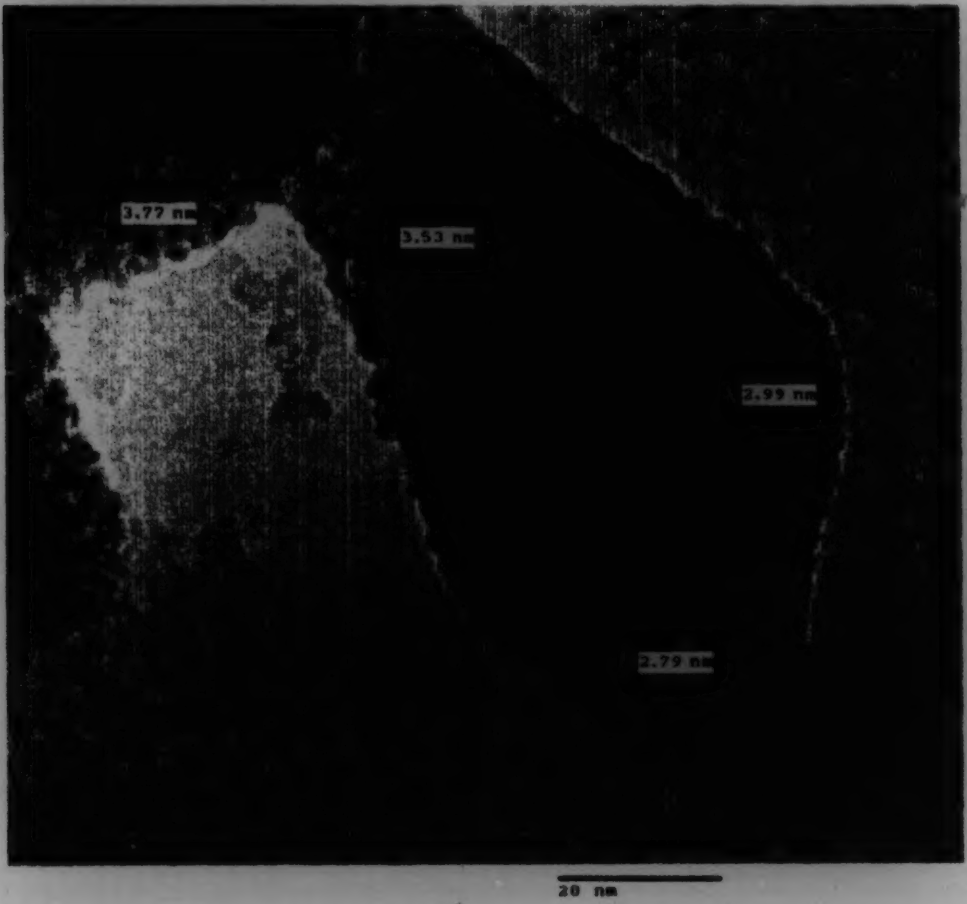

Figure 4.18: TEM image of as made Mo-CHA.

Under reduction at 150, 425 and 450°C, there was little difference in the TEM cluster size, suggesting a strong anchoring of the Mo clusters to the support (Figure 4.19).

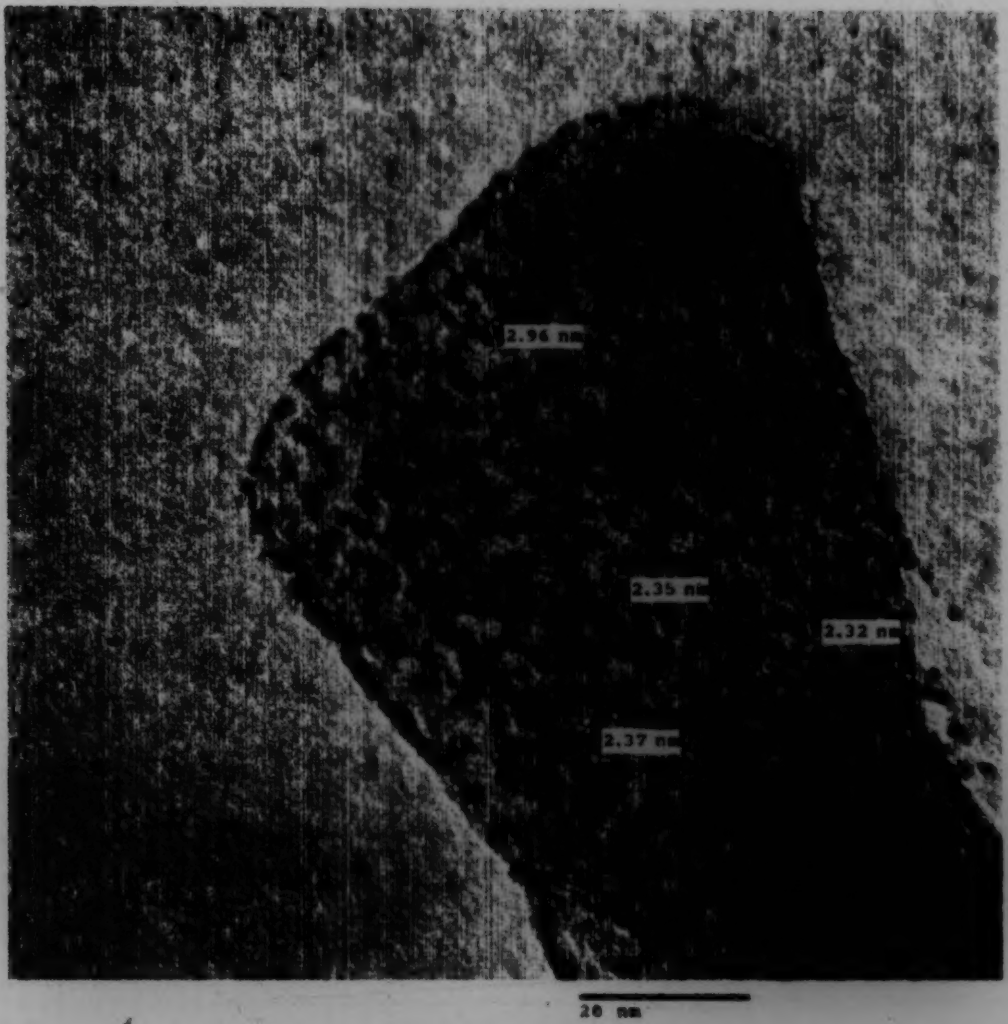

Figure 4.19: TEM image of Mo-CHA reduced at 450°C. The heavily reduced clusters shown here are similar in size to those seen in the as made state.

In the presence of 10% H2s/$H_2$, the behaviour of Mo-CHA was much the same as it was under reduction. Treatment at 250°C and 350°C both resulted in well dispersed 2 nm clusters (Figure 4.20).

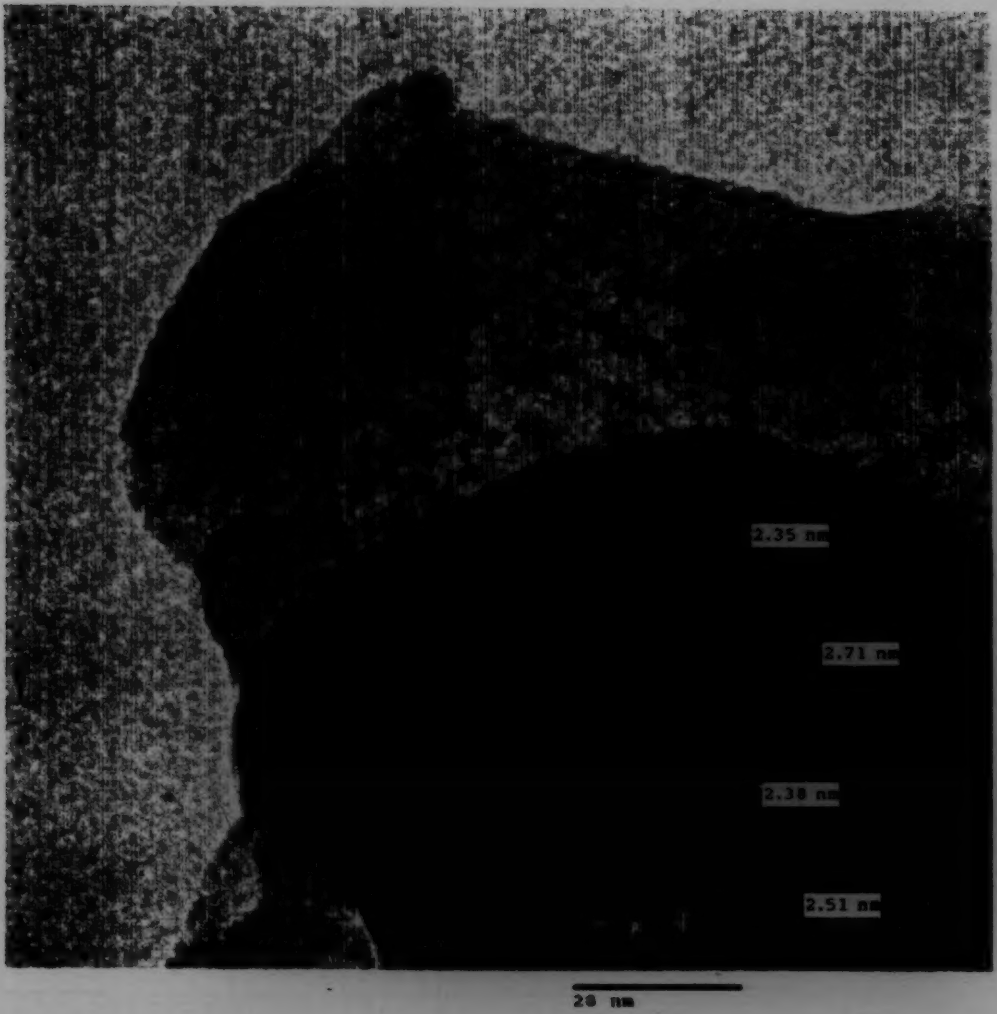

Figure 4.20: TEM image of Mo-CHA sulfided at 350°C. As in the reduction studies, the sulfided clusters of Mo are approximately the same size as those of the as made Mo-CHA.

*NiMo-CHA*

While the surface of as made NiMo-CHA appears to be very similar to that of the Ni-CHA at low severity of reduction, it was found that NiMo-CHA behaves more like Mo-CHA as there was little change in the dispersion/clusters size upon reduction. The clusters appear to be well-dispersed, with a cluster size just below 2 nm, and even under reduction at 450°C, there is little change in size and appearance of the clusters visible by TEM (Figure 4.21).

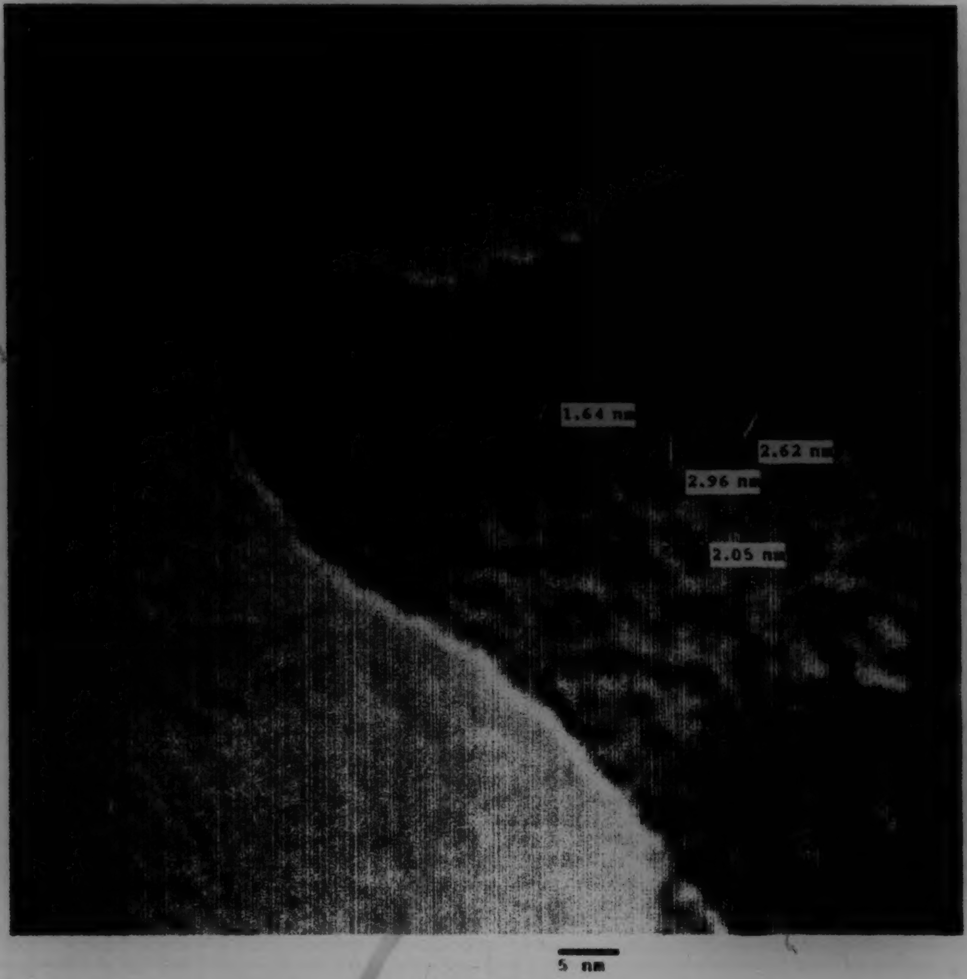

Figure 4.21: TEM image of NiMo-CHA reduced at 450°C. The clusters do not appear to increase in size upon reduction.

Recall that the clusters imaged in Ni-CHA underwent agglomeration up to 20 nm in size under these same conditions. This indicates that in the NiMo system, Ni and Mo appear to associate into a 'NiMo' type cluster, evidenced by the suppression of the growth/irregularity observed in Ni study.

When treated with 10% H2s/$H_2$ at 250°C, NiMo-CHA behaved similar to Mo-CHA in that well dispersed 2 nm clusters were observed as opposed to the 6 nm clusters observed in Ni-CHA treated under the same conditions. At 350°C, clusters in the 1.5 to 3 nm range are observed (Figure 4.22).

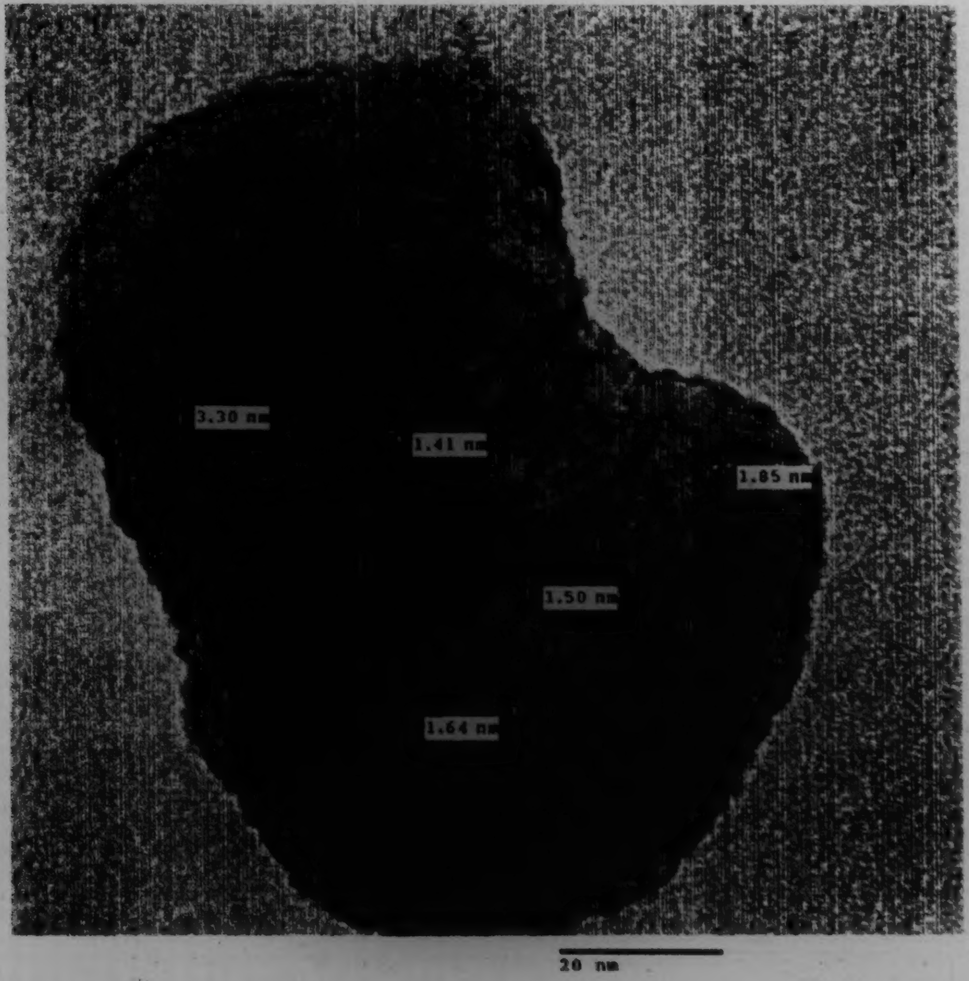

Figure 4.22: TEM image of NiMo-CHA sulfided at 350°C. As in the reduction study, there is little growth in the cluster size upon reduction.

This is further evidence of the Ni/Mo interplay, as Ni-CHA treated under the same conditions showed 8 nm 'dumbbell' shaped clusters.

### *Series 2*

*NiHCHA*

Imaging of the as made NiHCHA shows many high contrast regions of Ni, with most of the clusters on the order of 2 nm in size. However, even mild reduction at 200°C results in both large (20 nm) and remaining small (2 nm) clusters (Figure 4.23).

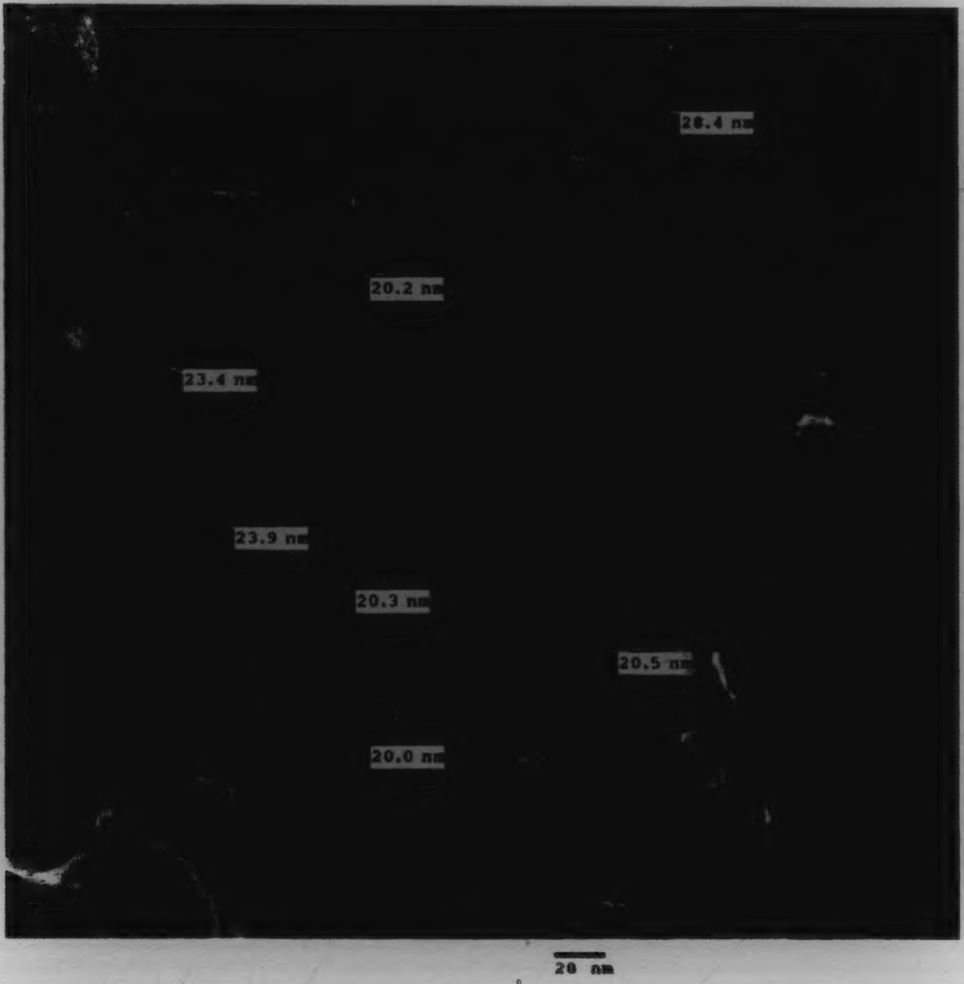

Figure 4.23: TEM image of NiHCHA reduced at 200°C.

At 300°C the images are similar to those at 200°C, with perhaps a slight increase in the size of the small fractions, (slightly larger than 2 nm). Again, there are large clusters among the smaller ones. At 400°C, growth of large clusters (~30 nm) among the smaller fractions can clearly be seen. Also evident is the presence of clusters which are slightly non-spherical in shape, with uneven spacing between them, indicating a lack of dispersion (Figure 4.24).

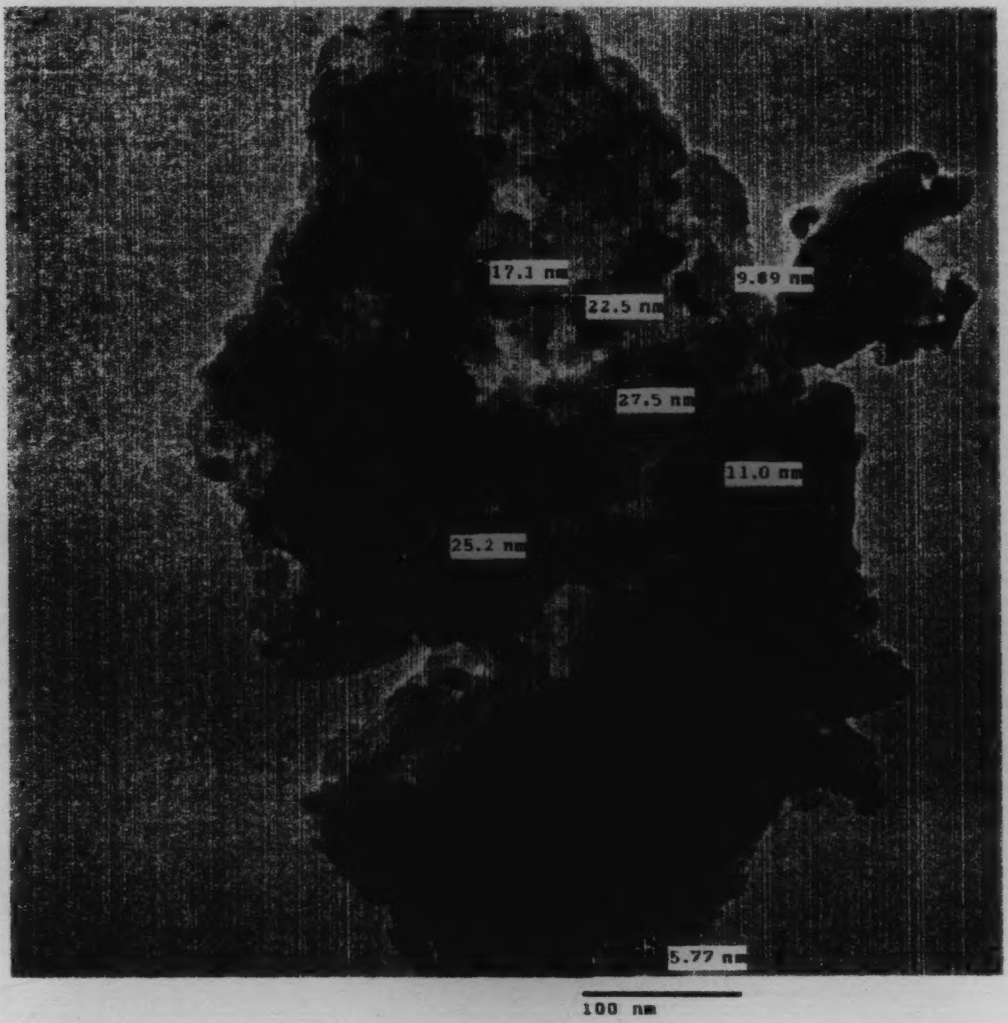

Figure 4.24: TEM image of NiHCHA reduced at 400°C. Note the variations in the cluster sizes.

A 200°C treatment in 10% $H_2S/H_2$ resulted in well dispersed clusters, the sizes of which are difficult to determine. At higher degrees of sulfidation, (300°C and 400°C), small clusters (~2 nm) are visible (Figure 4.25). They are well dispersed with less large fractions than were observed in NiHCHA reduced at such temperatures.

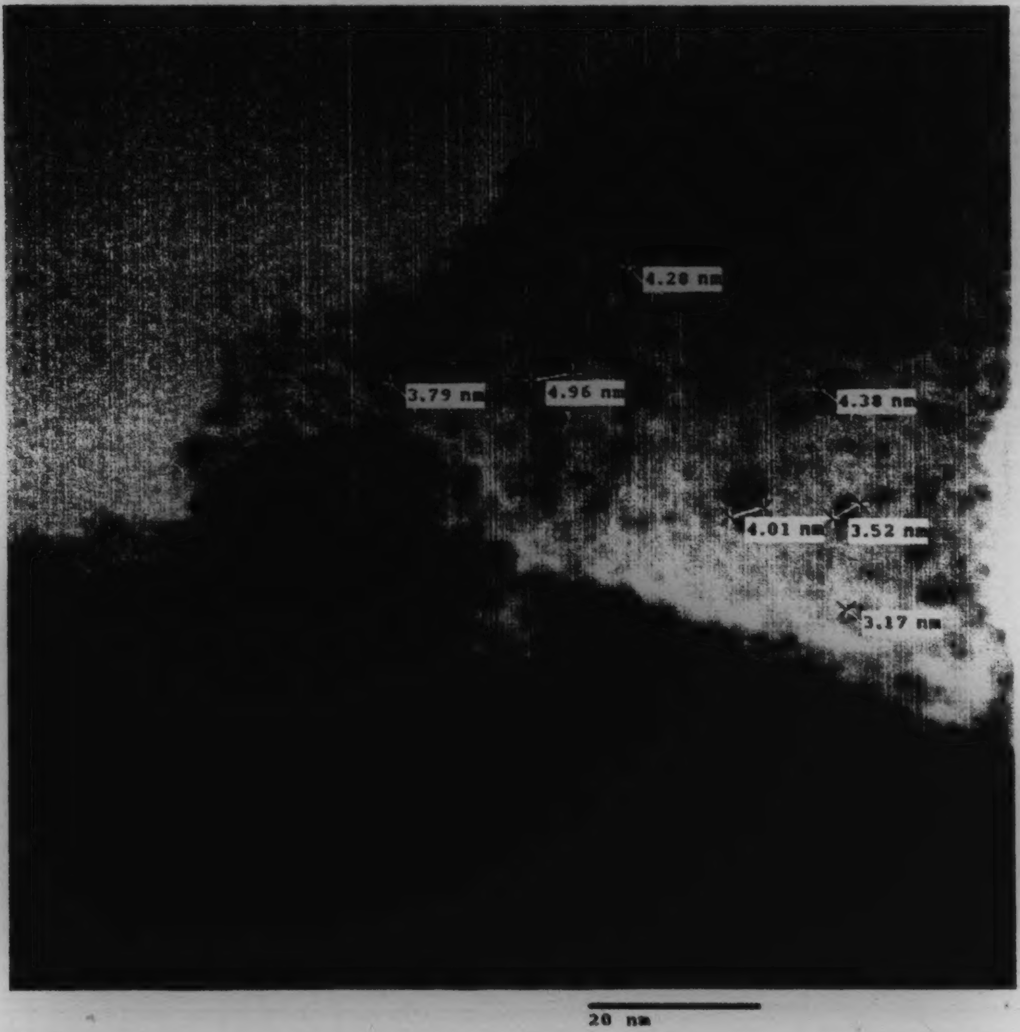

Figure 4.25: TEM image of NiHCHA sulfided at 300°C. The effects of sulfidation shown here indicate a smaller cluster size and better dispersion than that observed under reduction at the same temperature.

It should be noted that in the 400°C sulfidation study of NiHCHA (Figure B.83 – B.86, Appendix B), the two small ovals (black and white pair) which can be seen in the micrographs are believed to be anomalous material on the optics of the microscope, and not associated with the sample.

### *MoHCHA*

In the as made MoHCHA, only very small regions of high contrast, and they are not as well defined as the NiHCHA samples. Reduction at 200°C results in contrast regions, some of which showed an interesting structure, although such regions were not homogenously present (Figure 4.26).

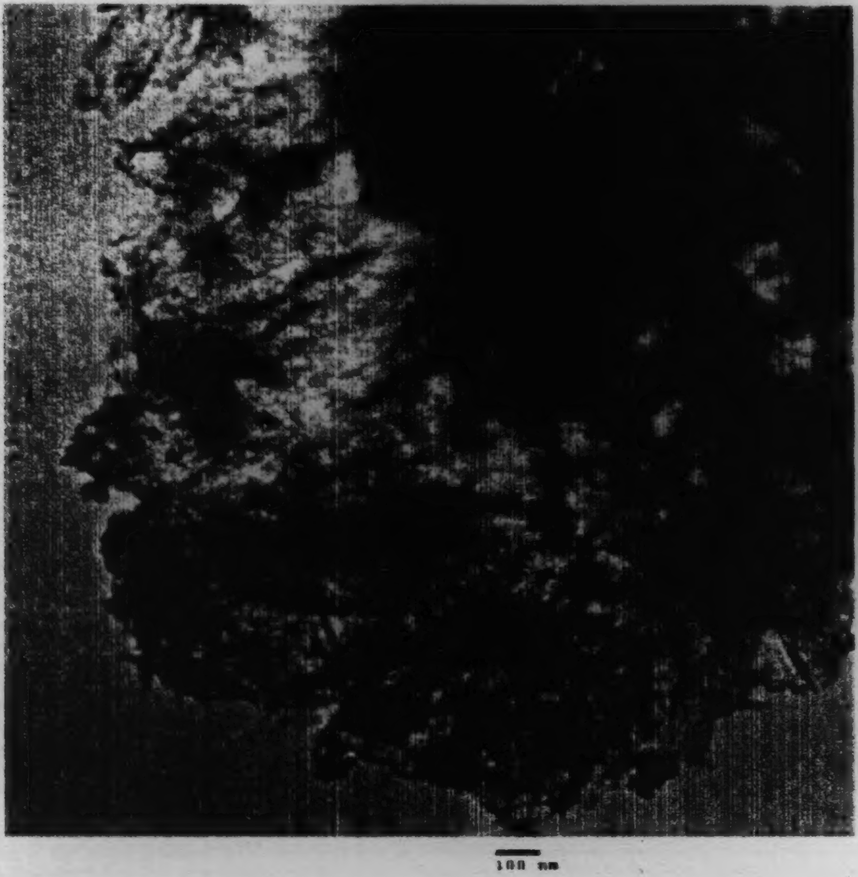

Figure 4.26: MoHCHA reduced at 200°C. The structures observed contrast with the circular clusters observed in the Series 1 (Mo-CHA) studies.

Further growth of high contrast particles are visible upon reduction at 300°C, as well as regions of similar structure to the anomalous region found in the 200°C reduction of MoHCHA. 400°C reduction results in large (60 nm) cluster growth, accompanied by reasonably well dispersed small clusters (Figure 4.27). Such cluster growth upon reduction in MoHCHA contrasts sharply with the findings on Mo-CHA. At 400°C, no evidence of the anomalous regions detected in MoHCHA reduced to 200 and 300°C was observed.

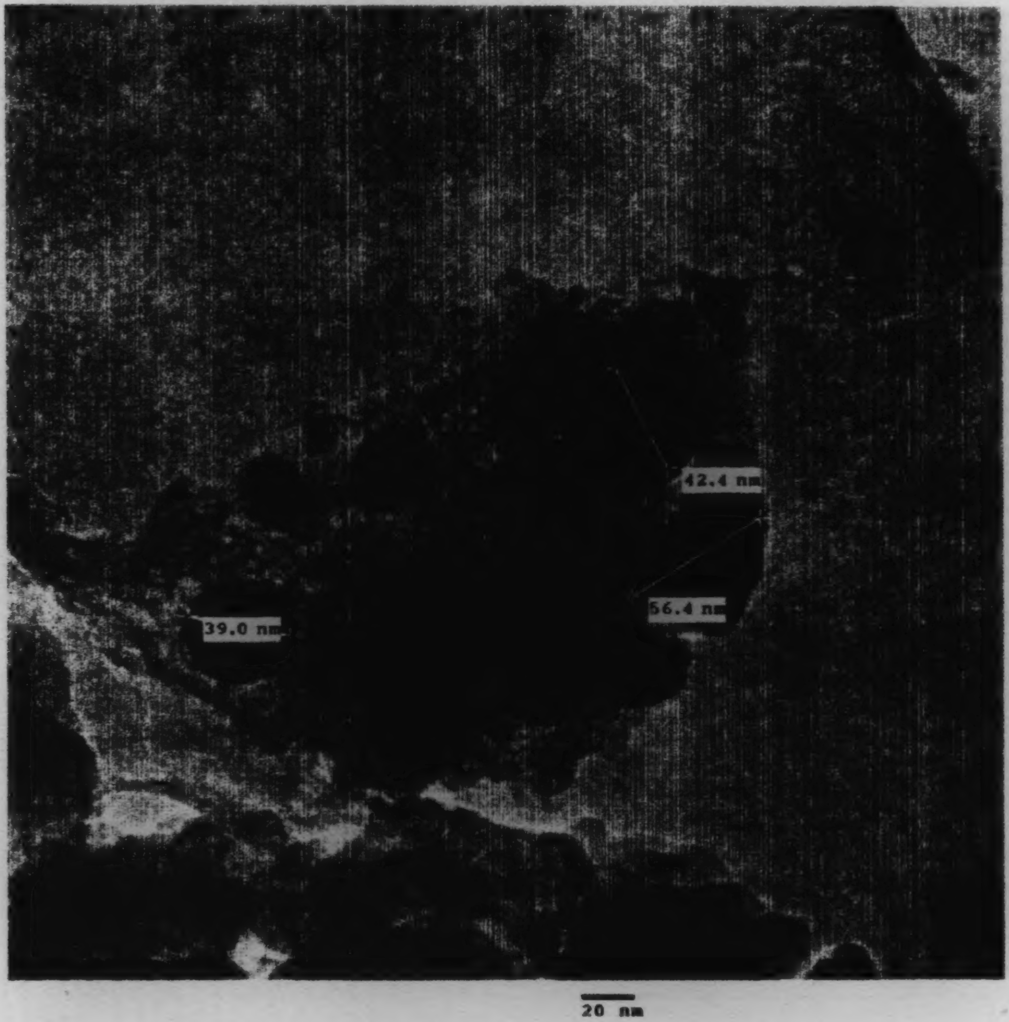

Figure 4.27: TEM image of MoHCHA reduced at 400°C. Reduction results in the familiar cluster shapes, albeit with a much higher nominal size.

In the presence of 10% $H_2S/H_2$ at 200°C, small 2 nm clusters are observed. However, at 300°C sulfidation, anomalous regions with a clear 'herring bone' structures were observed. These structures, scattered among clusters 2 nm in size, appear similar to $MoS_2$ structures, with line spacings (Mo-Mo) of approximately 1 nm. Sulfidation at 400°C appears increase the occurrence of such $MoS_2$ slabs, although there are still regions of the sample which do not contain such slabs, populated by clusters 3 to 10 nm in size. The slabs, which are much larger in size than those observed at 300°C, show a stacking lengths of 15 to 25 line spacings (Mo-Mo), again with spacings on the order of 1 nm (Figure 4.28).

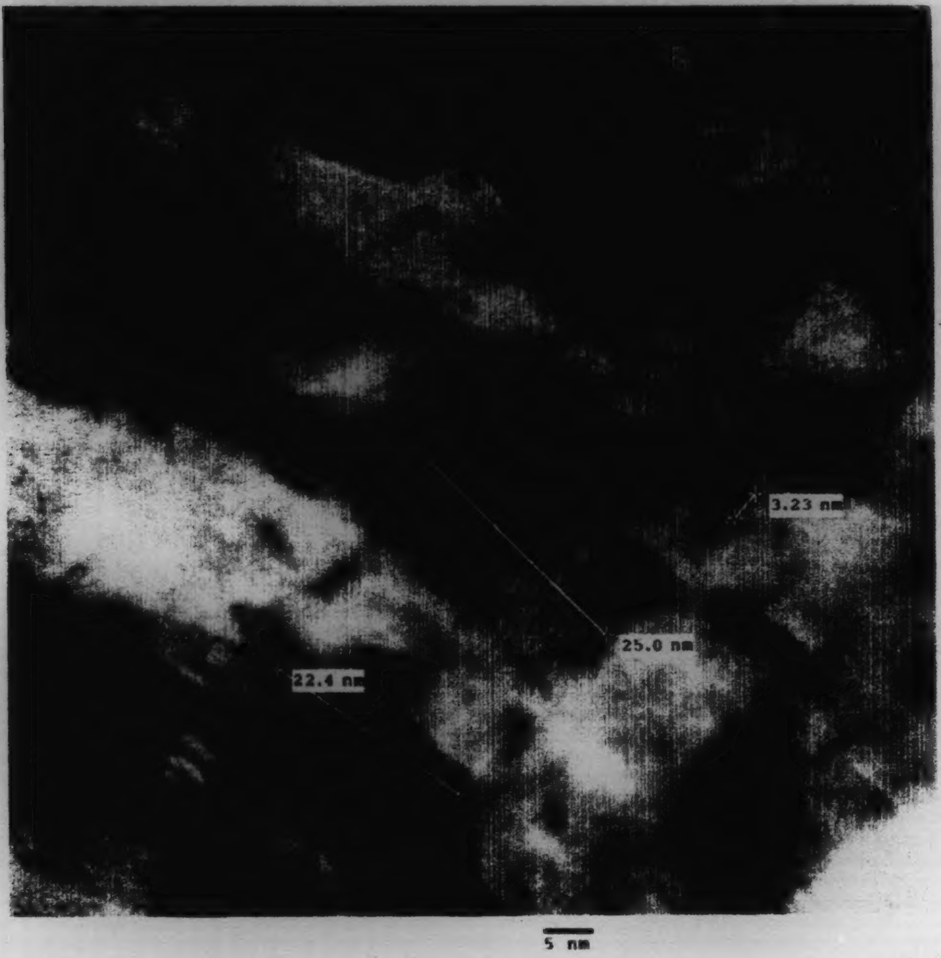

Figure 4.28: TEM image of MoHCHA sulfided at 400°C. The stacked structures are believed to be $MoS_2$.

The spacings of 1mm between shown agree with other publications of TEM imaged $MoS_2$ [3, 60]. These studies show the same 'herring bone' structures with similar spacing between the dark lines.

*NiMoHCHA*

Clusters ranging in size from 2 to 20 nm are visible in the as made NiMoHCHA. This is very different behaviour than what was observed for NiMo-CHA (Series 1). There was a single region of the sample showing large (2 to 14 nm), well defined clusters. This structure was only observed in this sample and only in one particular region of the grid, and therefore cannot be taken as representative of the sample. At 200°C reduction, well dispersed clusters, ranging between 2 and 10 nm in size can be seen. In addition, a region of similar structure to the interesting regions seen in MoHCHA was observed. At 300°C, clusters 3 to 9 nm in size can be seen, with perhaps an increasing distance between the clusters, indicating a loss of dispersion, although this interpretation may be beyond the resolution of the technique. At 400°C reduction, large (20 nm) clusters can be seen with increased spacings (relative to lower reduction temperatures) between them. This indicates a lost of dispersion through sintering, which contrasts strongly with the TEM findings on NiMo-CHA (see Figure 4.29).

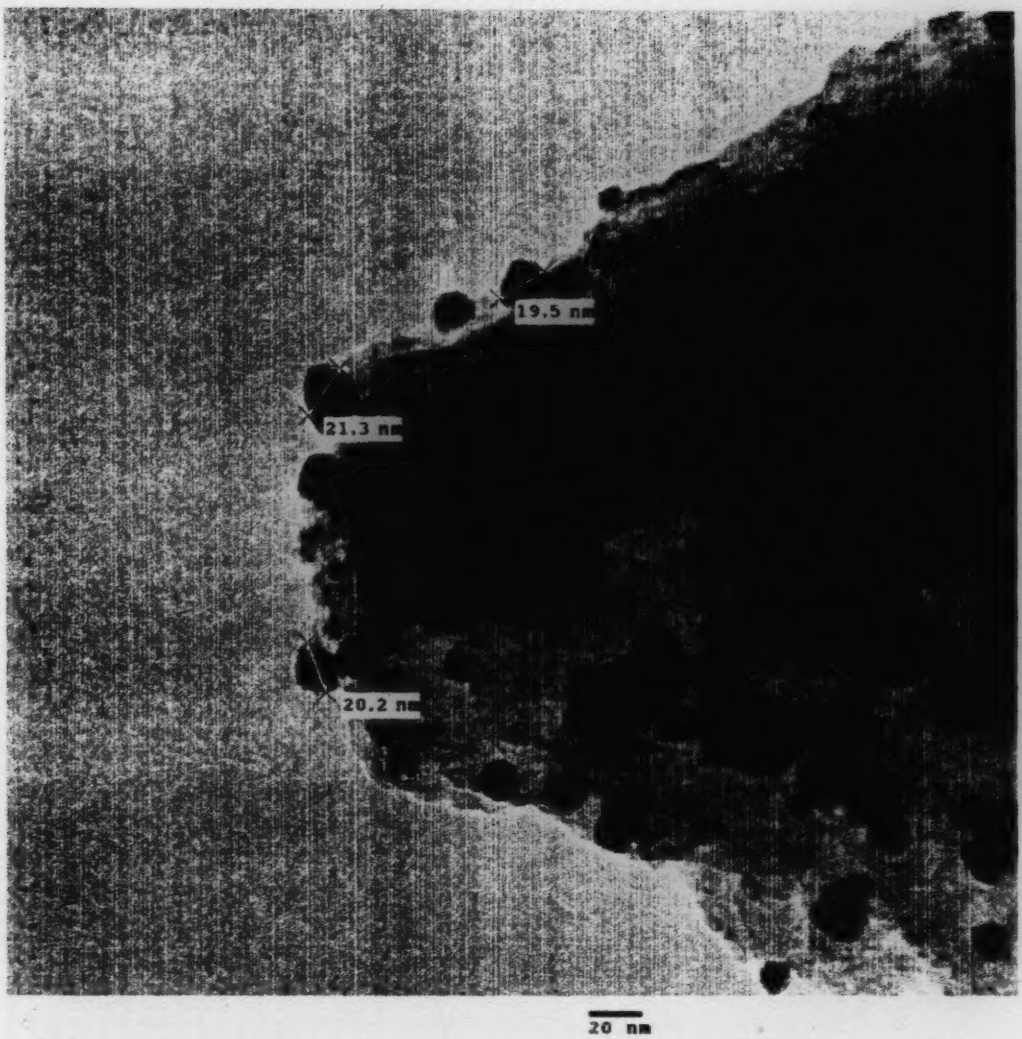

Figure 4.29: TEM image of NiMoHCHA reduced at 4[illegible]0°C. Much larger clusters than were observed in the study of NiMo-CHA under similar reduction conditions can be seen in the figure.

Upon sulfidation at 200°C, NiMoHCHA shows clusters similar in size to those observed under the same temperature of reduction. At 300°C, although limited in number, $MoS_2$ type slabs are clearly visible, raising the possibility of $NiMoS_2$ type structures present on the catalyst surface (Figure 4.30a).

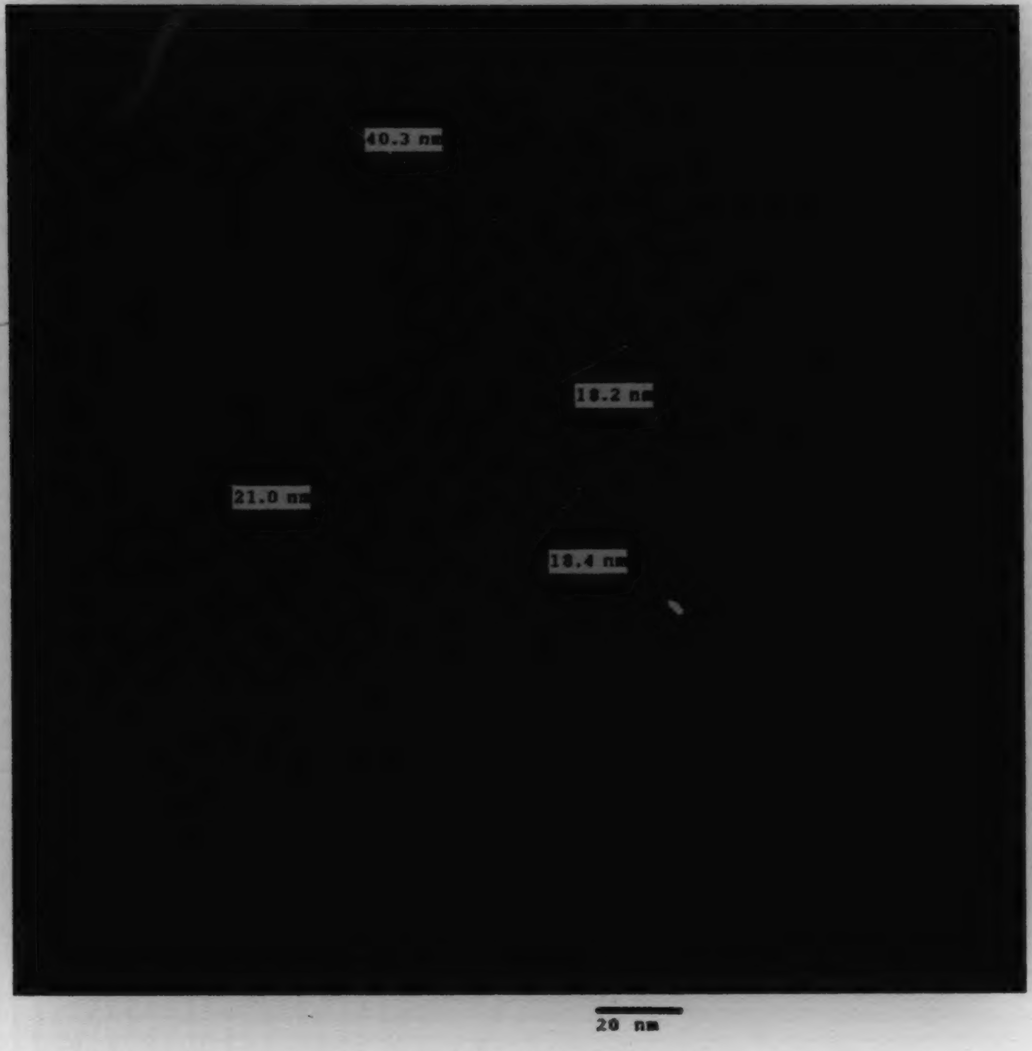

Figure 4.30a: TEM image of NiMoHCHA sulfided at 300°C.

Here as well, the anomalous white oval is believed to be an artifact of the instrument, and is in no way believed to be associated with the sample.

Figure 4.30b shows the results of adjusting the contrast and brightness of the original image (Figure 4.30a). The features of interest (the herring-bone dark lines) are clearly shown in Figure 4.30b. Note that the measurement scales shown in Figure 4.30a apply directly to Figure 4.30b.

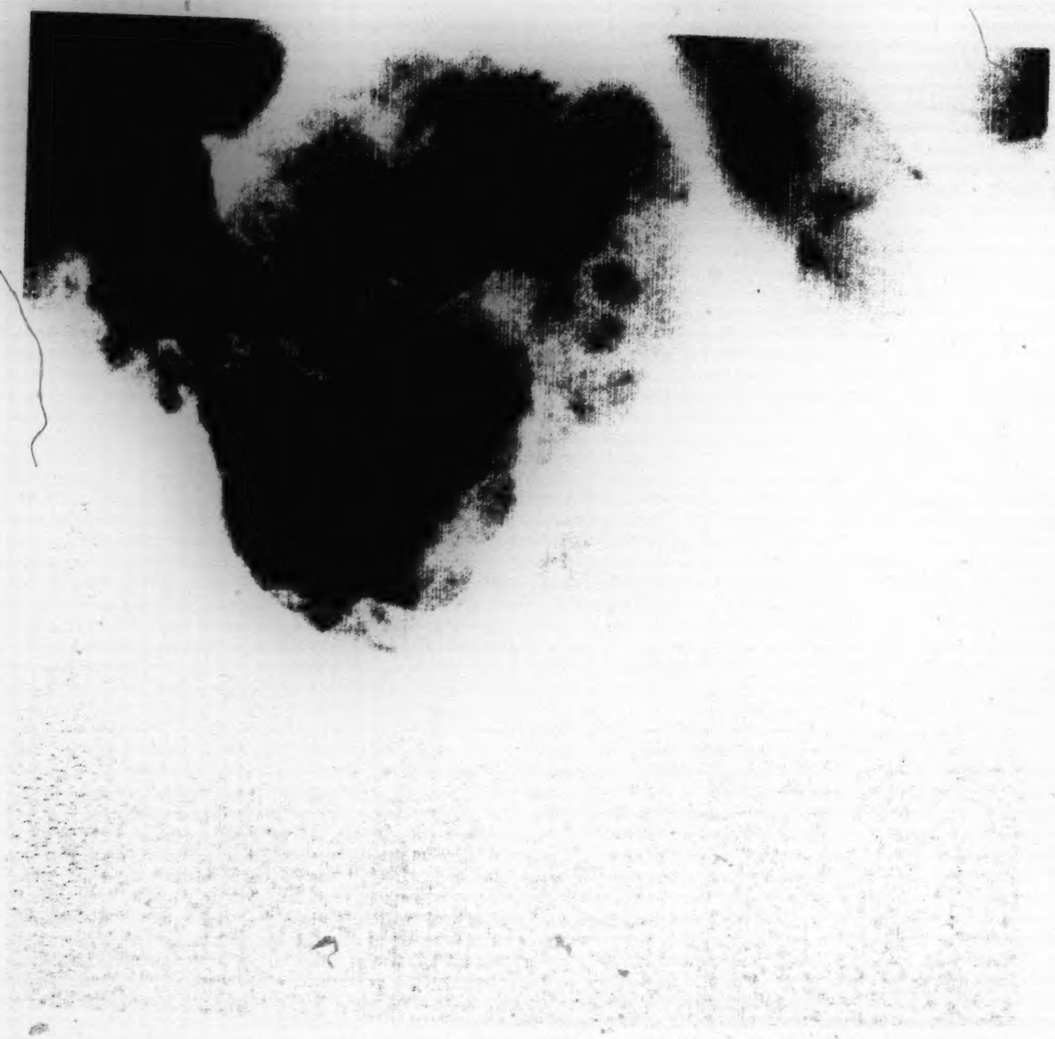

Figure 4.30b: TEM image of NiMoHCHA sulfided at 300°C with contrast and brightness adjustment.

At higher temperature, (400°C), no evidence of slabs were seen, but rather pronounced agglomeration, with clusters 4 through 24 nm clearly visible.

In summary, the metals on the bare support (Ni-, Mo- and NiMo-CHA) appear to be strongly bound, as they either undergo no significant agglomeration upon reduction/sulfidation (NiMo and Mo-CHA) or only at elevated temperatures (Ni-CHA). In contrast, the metals on the acidified support (Ni, Mo, and NiMoHCHA) appear to be weakly held, showing significantly higher agglomeration than on the bare support. The observation of $MoS_2$ slabs on the surface of MoHCHA and NiMoHCHA further substantiates this, as the metals are free to associate into the layered structures of the sulfide when not strongly bound to the zeolite framework.

### 4.2.2 XRD

*Series 1*

The wide scans of the made catalysts show a broadening of the baseline upon incorporation of Ni and Mo, particularly in the Mo containing samples (Figure 4.31).

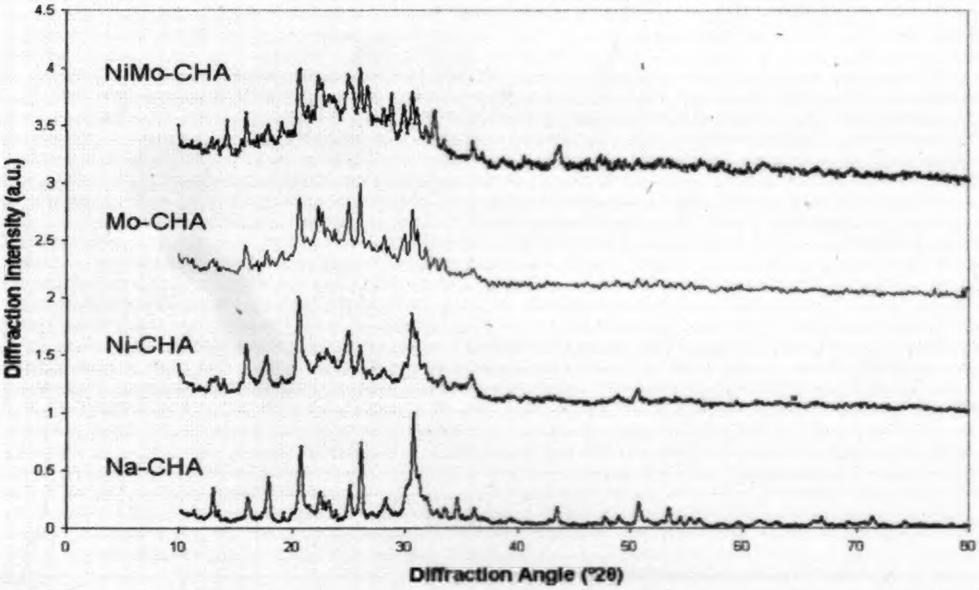

Figure 4.31: Wide scans of the as made catalysts in Series 1. The broadening of the baseline accompanying metal incorporation is of interest here.

This broadening has been reported in literature, particularly in the case of Mo incorporation into zeolites [61]. Nonetheless, the structural features of the support are otherwise retained upon incorporation, indicating that the framework integrity of the support has been preserved. Subsequent hydrogen reduction of Ni-CHA resulted in the emergence of a Ni (111) feature at and above 350°C. This can be seen at approximately 44.5 °2θ in Figure 4.32.

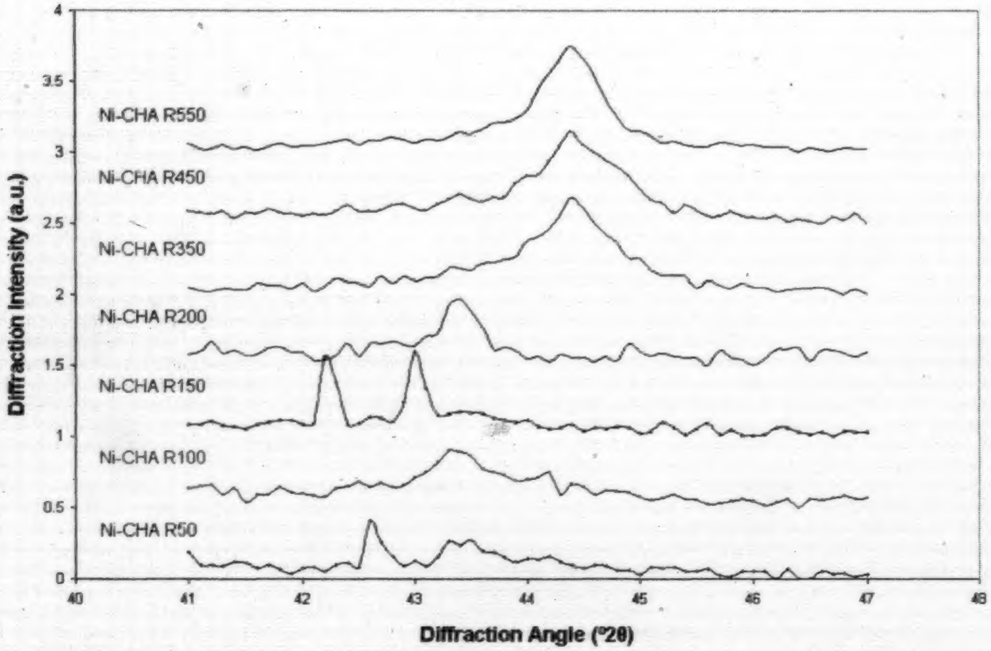

Figure 4.32: Emergence of Ni (111) line upon hydrogen reduction of Ni-CHA. The feature of narrowing width and increasing height at approximately 44.5 °2θ is characteristic of the formation of metallic Ni clusters [62]. The features found between 42 and 43 °2θ in R50, R100 and R150 are believed to be anomalous in nature, as they do not correspond to known features of the metal-support system.

The Scherrer equation, given below, was used to calculate the crystallite size corresponding to the observed Ni features.

$$t = \frac{0.9\lambda}{B\cos\theta} \qquad 4.5$$

where $t$ = crystallite size (nm)

$\lambda$ = wavelength Cu K$\alpha$ radiation, (0.154 nm)

$B$ = angular full width at half max ($2\theta$, radians)

$\theta$ = diffraction angle, radians

The required parameters for the 350, 450 and 550 °C reductions are summarized below in Table 4.7.

Table 4.7: Parameters and results of the Scherrer equation applied to Series 1.

| Reduction Temperature (°C) | B ($2\theta$, radians) | $\theta$ (radians) | t (nm) |
|---|---|---|---|
| 350 | 0.014 | 0.39 | 11 |
| 450 | 0.014 | 0.39 | 11 |
| 550 | 0.010 | 0.39 | 14 |

The feature of increasing height and decreasing width is characteristic of increasing crystallite size, which is reflected in the t values calculated above. However, these values are lower than the cluster sizes measured by TEM. As is known from literature sources [63], XRD detects the size of crystallites, and not necessarily the size of clusters. The latter can often result from aggregates of the former, leading to a smaller size measured by XRD than that measured by TEM. Recall that the TEM data indicated clusters sizes between 7 and 14 nm at 350°C, and 20 nm at 450°C and 550°C. Note also these clusters were misshapen, and perhaps slightly polycrystalline. This may explain why they appear smaller by XRD than by TEM. Reduction studies on Mo-CHA show no emergence of Mo features near the expected 40.45 °2θ, nor were any sulfide features of either Ni or Mo detected in any of the samples.

*Series 2*

As made scans in Series 2 shows significantly less baseline broadening than that seen in the as made samples in Series 1 (Figure 4.33).

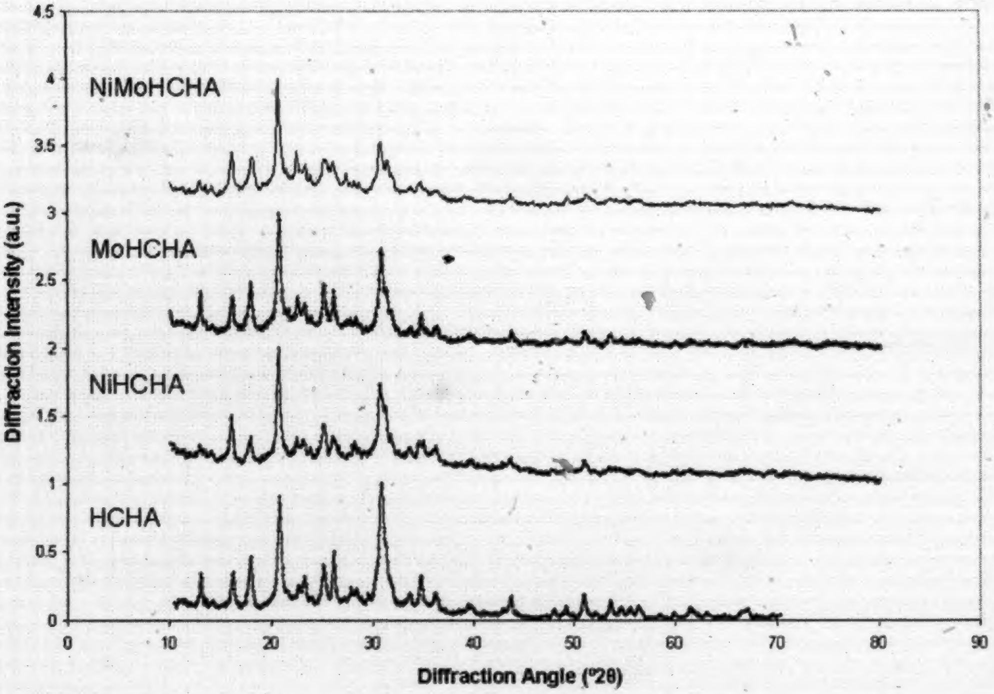

Figure 4.33: Wide scans of the as made catalysts in Series 2. There is considerably less broadening of the baseline shown here in Series 2 than was observed in Series 1.

This observation supports the interpretation of the TEM data; that the incorporated Ni and Mo are less strongly interacting with the support in Series 2 than in Series 1. Narrow scans of the Ni (111) feature within reduced NiHCHA and NiMoCHA shows the emergence of such a feature at 400°C, (Figures 4.34a and 4.34b).

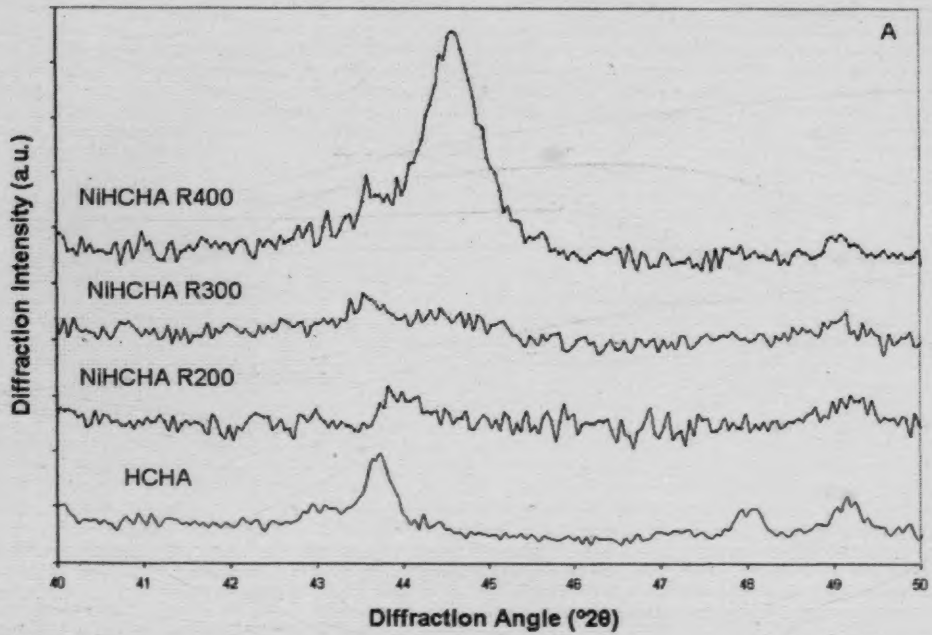

Figure 4.34a: Emergence of Ni (111) line upon hydrogen reduction of NiHCHA.

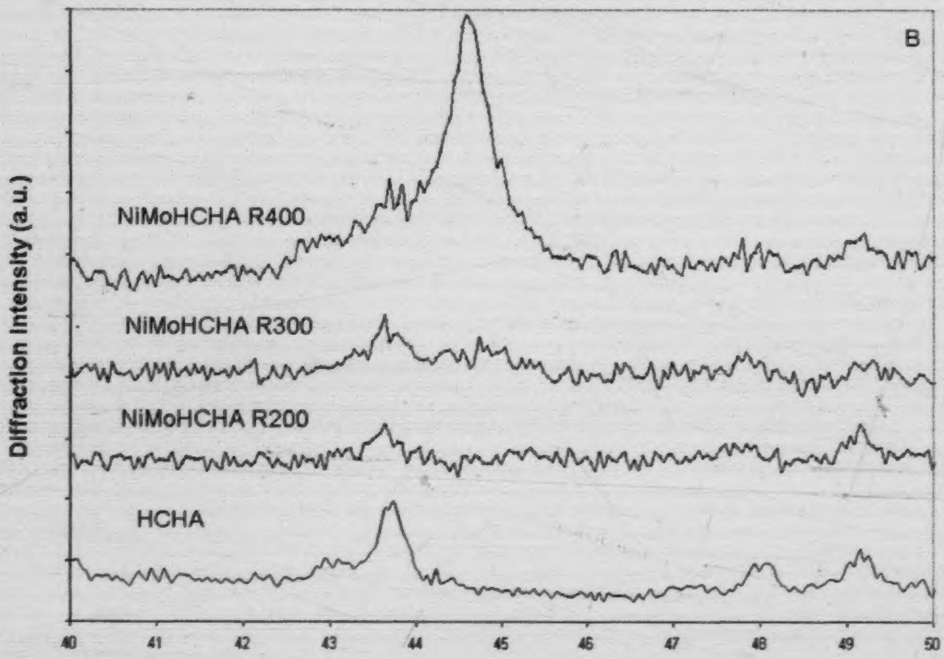

Figure 4.34b: Emergence of Ni (111) line upon hydrogen reduction of NiMoHCHA.

The Scherrer equation (Equation 4.5) was applied to the Ni (111) feature observed at 400°C, (see Table 4.8).

Table 4.8: Parameters and results of the Scherrer equation applied to Series 2.

| Sample | B<br>(2θ, radians) | θ<br>(radians) | t<br>(nm) |
|---|---|---|---|
| NiHCHA<br>R400°C | 0.013 | 0.39 | 11 |
| NiMoHCHA<br>R400°C | 0.010 | 0.39 | 14 |

It is interesting to note that TEM imaging of NiHCHA indicated the presence of 20 nm clusters at 200°C and 300°C reductions, while 400°C reduction led to 30 nm clusters. Here, the XRD data shows only 11 nm clusters at 400°C reduction, and little evidence of any Ni crystallites below this temperature. Corresponding TEM data on NiMoCHA showed 10 nm clusters at 200°C and 300°C reductions, and 20 nm clusters at 400°C, while the above XRD data only revealed the presence of 14 nm crystallites at 400°C reduction. Again, there was little evidence of any Ni crystallites below this temperature. The formation of polycrystalline clusters may again explain this, as the TEM data for Series 2 clearly showed non-circular (misshapen) clusters. However, another important observation made during TEM analysis, that there were a range of cluster sizes observed, is relevant here. While 10 and 20 nm clusters were observed in Series 2, so were 2 nm clusters. As XRD is a bulk technique, (giving a volume average of crystallite sizes), and TEM gives more a less a projection of a thin surface of the sample, the single value which results from application of the Scherrer equation may not represent the distribution of clusters sizes on the support, (although volume averaging would tend to favour the large fraction of the distribution). Another point to consider is that the resolution limit of XRD crystallite sizes is on the order of between 2 and 3 nm. Therefore a direct, quantitative comparison of TEM and XRD data is difficult. However, there is agreement between them, as both techniques indicate the growth of metallic Ni upon reduction in the materials analyzed.

No evidence of metallic Mo, or sulfide features of Ni or Mo were detected by XRD in any of the samples, similar to the findings in Series 1. Particularly, no evidence of $MoS_2$ type structures, expected near 14.33 °2θ was observed, although admittedly, such features may be concealed by feature corresponding to the support, (See Figure 4.35a-4.35c).

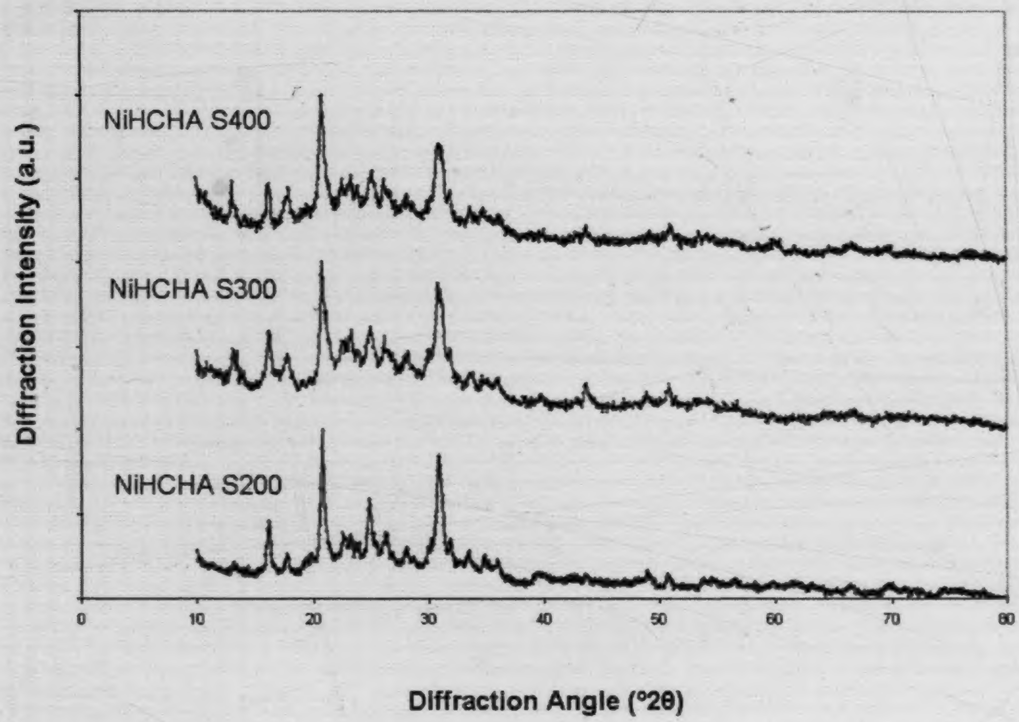

Figure 4.35a: Wide scans of sulfided NiHCHA.

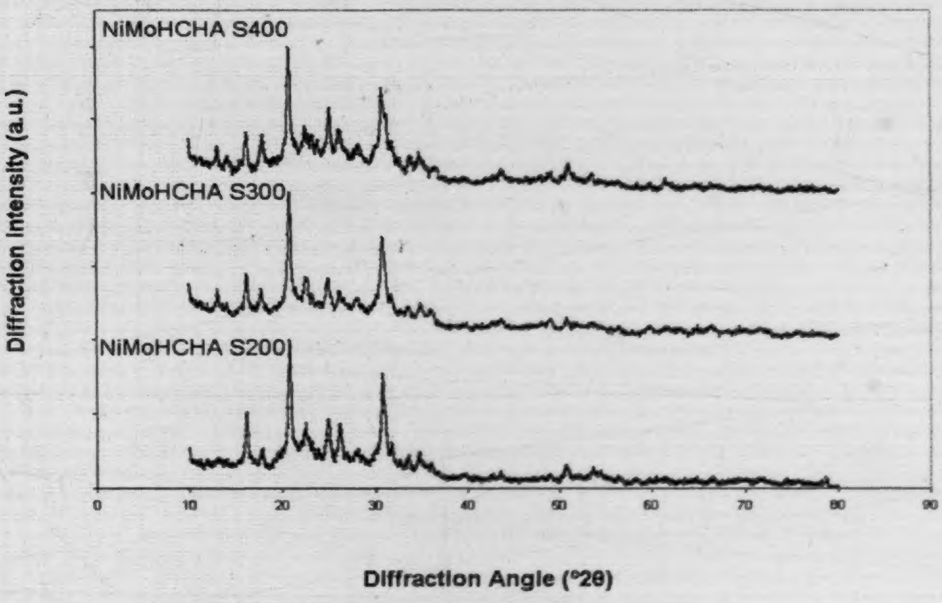

Figure 4.35b: Wide scans of sulfided NiMoHCHA.

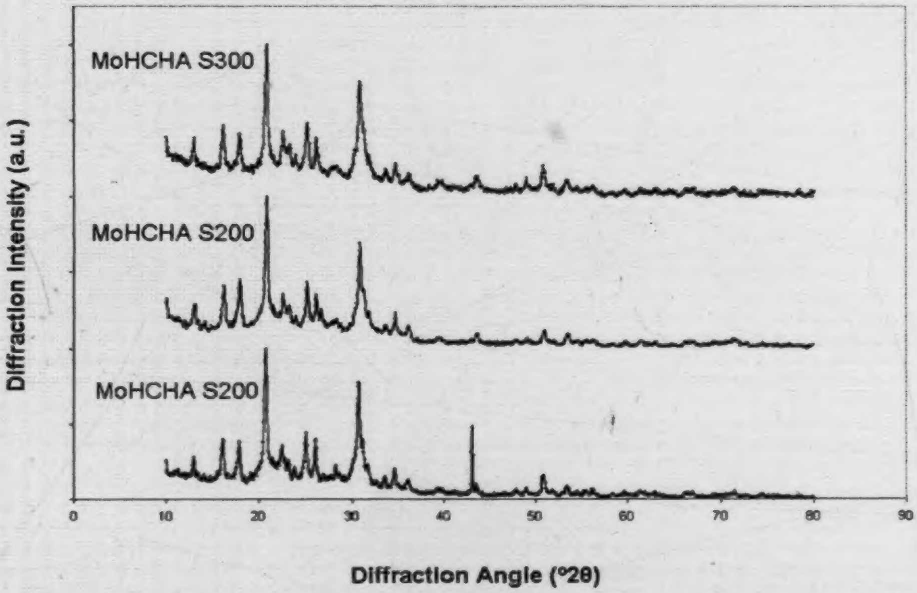

Figure 4.35c: Wide scans of sulfided MoHCHA. The feature at approximately 44 °2θ in the MoHCHA S200 run was found to be anomalous when this region was rescanned.

In summary, XRD indicates that the incorporation of Mo into Series 1, (Mo-CHA and NiMo-CHA) leads to baseline broadening, which is likely due to a loss of crystallinity. This was not observed to such a degree in Series 2. Recall the findings of the TEM study, which indicated a strong interaction between the incorporated metal phase and the support in Series 1, and a weak interaction in Series 2. It is therefore not surprising that the XRD study suggests a higher degree of crystallinity loss was observed in Series 1, while a lower degree was observed in Series 2. XRD also confirms that clusters of metallic Ni form upon reduction. However, no evidence of Ni in the metallic or sulfide state was detected upon treatment with 10% $H_2S/H_2$.

### 4.2.3 BET Surface Area

Surface area results from selected samples are shown below in Table 4.9.

Table 4.9: Surface area data from selected samples.

| Sample Identification | BET Area ($m^2/g$) | External Area ($m^2/g$) | Micropore Volume (mL/g) |
|---|---|---|---|
| Na-CHA | 395 | 45 | 0.142 |
| HCHA | 498 | 78 | 0.171 |
| NiHCHA | 364 | 72 | 0.120 |
| NiHCHA R200 | 329 | 83 | 0.101 |
| NiHCHA R300 | 321 | 65 | 0.104 |
| NiHCHA R400 | 277 | 62 | 0.087 |
| MoHCHA | 400 | 73 | 0.133 |
| NiMoHCHA | 329 | 72 | 0.105 |

While the surface areas of the different samples do change with metal incorporation and reduction, external surface areas remain remarkably high. Other common zeolites have considerably lower external surface areas. For example, ZSM-5, unless prepared with extremely small particle sizes, typically has an external surface area in the 30 to 50 $m^2/g$ [64,65], while Trigueiro et al. report the external surface area of zeolite Y to be in the 50 $m^2/g$ range with little change upon metal incorporation [66]. The data reported in Table

4.9 is significant, because even with large particle sizes, the chabazites show high external surface areas, (up to 83 $m^2/g$). This is likely due to the layered, or 'sheet-like' structure observed in the TEM studies. Further examination of Table 4.9 reveals that surface area changes upon reduction, for example, seem to correspond to changes in micropore volume, as opposed to external surface area. This means that these metal containing chabazites maintain high external surface areas under such treatments, making them ideal catalysts supports.

## 4.3 Acidity of Supports and Catalysts

### 4.3.1 NH3-TPD

In order to further characterize the incorporation of metals into chabazite, the acidity of the bare and metal loaded supports was measured by $NH_3$-TPD.

*Series 1*

TPD spectra for all the samples showed a series of broad desorptions, typified by the results for Na-CHA, shown in Figures 4.36a and 4.36b. Ammonia desorption peak temperatures ($Tp$) were determined for each value of the ramp rate ($\beta$), and a plot of $\ln(Tp^2/\beta)$ vs $1/Tp$ was constructed in order to extract the heat of adsorption, assuming that the adsorption was not an activated process, and that the desorption rate is first order [52].

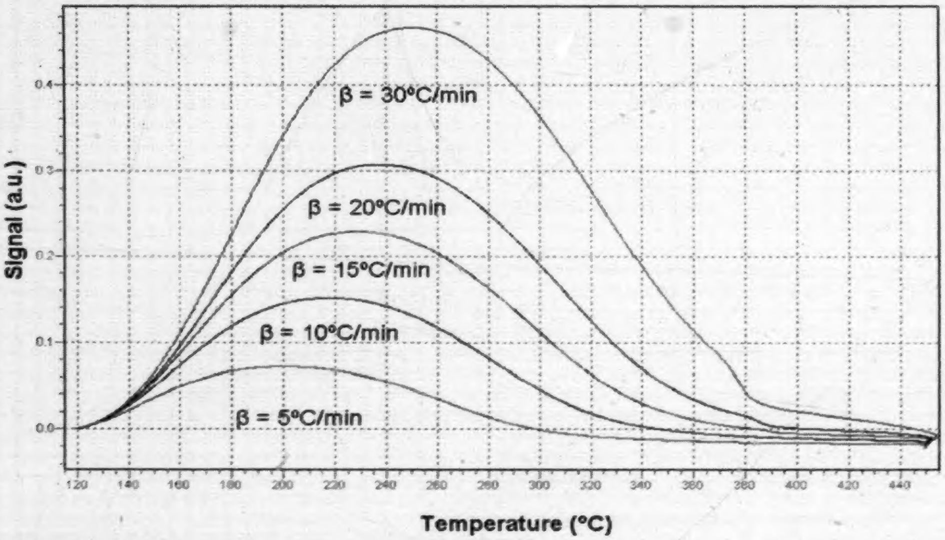

Figure 4.36a: $NH_3$-TPD Spectrum for Na-CHA.

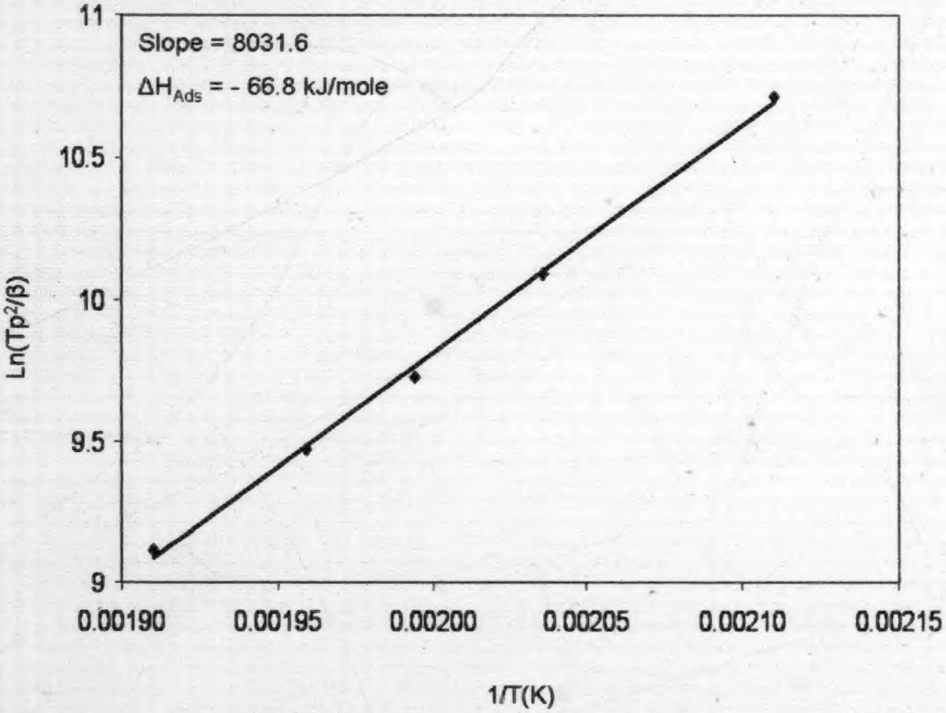

Figure 4.36b: First order plot of the peak temperature (Tp) data for Na-CHA. The data is well fit by the first order model applied.

TPD results for the blank support are compared with those for Ni-, Mo- and NiMo-CHA in Table 4.10. The spectra and data plots for these experiments are found in Figures C.1 – C.5 Appendix C.

Table 4.10: Heats of adsorption of $NH_3$ on samples from Series 1.

| Sample | Heat of Adsorption (kJ/mol) |
|---|---|
| Na-CHA | 66.8 |
| Ni-CHA | 72.3 |
| NiMo-CHA | 86.7 |
| NiMo-CHA reduced at 400°C | 85.4 |
| Mo-CHA | 87.2 |

It clear that metal incorporation leads to increases in acidity. Perhaps the increase in the heat of adsorption follows the increase in the valence of the exchanged cations, ($Na^+$, $Ni^{2+}$, $Mo^{3+}$), as this would be predicted by literature reports which detail mechanisms on the incorporation of multivalent ions and subsequent changes in Brønsted acidity [2]. Also, with regard to the possibility that free ions (i.e. weakly bound to the framework of the support) can act as Lewis acid (electron pair accepting) sites, it is important to note that reduction of NiMo-CHA showed essentially no change in the heat of adsorption upon reduction. This data indicates that the observed acidity is largely due to Brønsted acid sites. This finding agrees with the results of the TEM study, showing a strong interaction between the support and the incorporated metals, (i.e. no evidence of weakly bound ions).

Multiple exchange of $NH_4^+$ into Na-CHA yielded $NH_4$-CHA(X), with X = 1, 2 or 3; the spectra and data plots of which can be found in Figures C.6 – C.8 Appendix C. As shown in Table 4.11, there is a general increase in the measured heat of adsorption with increasing exchange. Comparing this with Na-CHA, (with a heat of 66.8 kJ/mole), it is clear that such treatments yield an increase in acidity.

Table 4.11: $NH_3$ heats of adsorption for sequential exchange of $NH_4^+$ into Na-CHA.

| Sample | Heat of Adsorption (kJ/mol) |
|---|---|
| $NH_4$-CHA(1) | 74.3 |
| $NH_4$-CHA(2) | 78.2 |
| $NH_4$-CHA(3) | 87.2 |

$NH_3$-TPD experiments on NiMo-CHA specifically prepared for subsequent incorporation of $NH_4^+$ revealed a heat of adsorption of 75.4 kJ/mol. This differs significantly from the result measured on the Series 1 NiMo-CHA, but it should be noted that this intermediate was not calcined, while the Series 1 material was. This illustrates the relevance of calcination in the preparation methods. Subsequent exchange with $NH_4^+$ leads to a heat of adsorption of 81.0 kJ/mol, as well as evidence of higher strength acidity. The two sets of spectra and data plots are shown in Figures 4.37a, 4.37b, 4.38a and 4.38b.

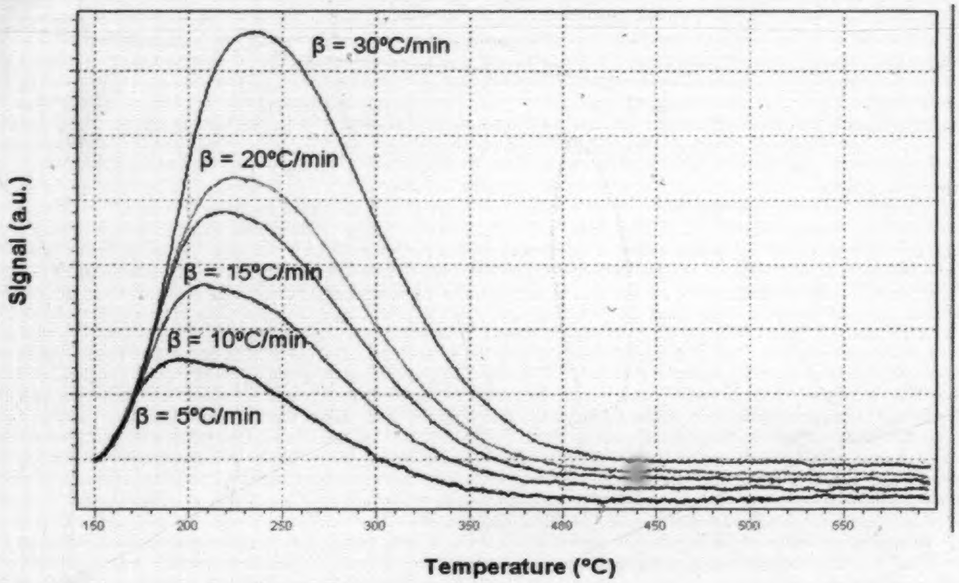

Figure 4.37a: $NH_3$ TPD spectra for NiMo-CHA prior to exchange with $NH_4^+$.

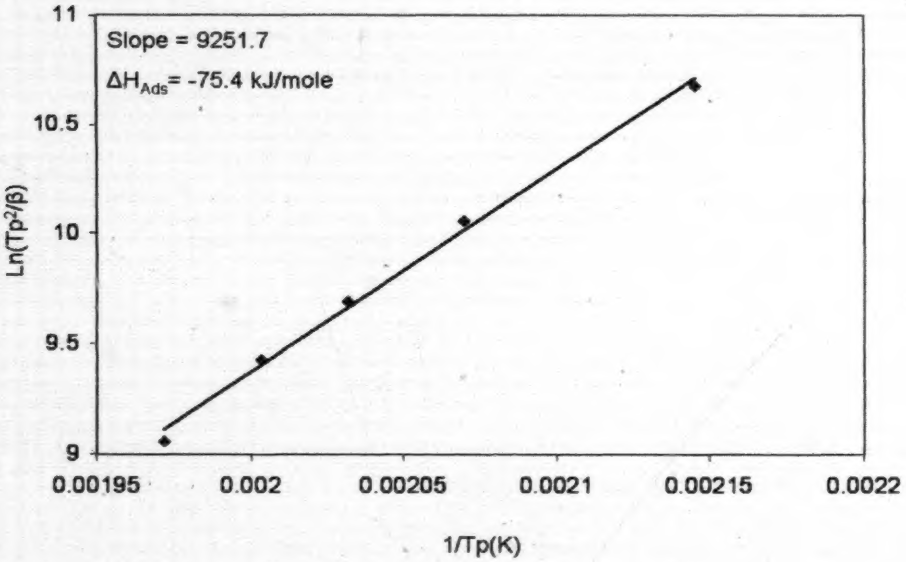

Figure 4.37b: First order plot of the peak temperature (Tp) data for NiMo-CHA prior to exchange with $NH_4^+$.

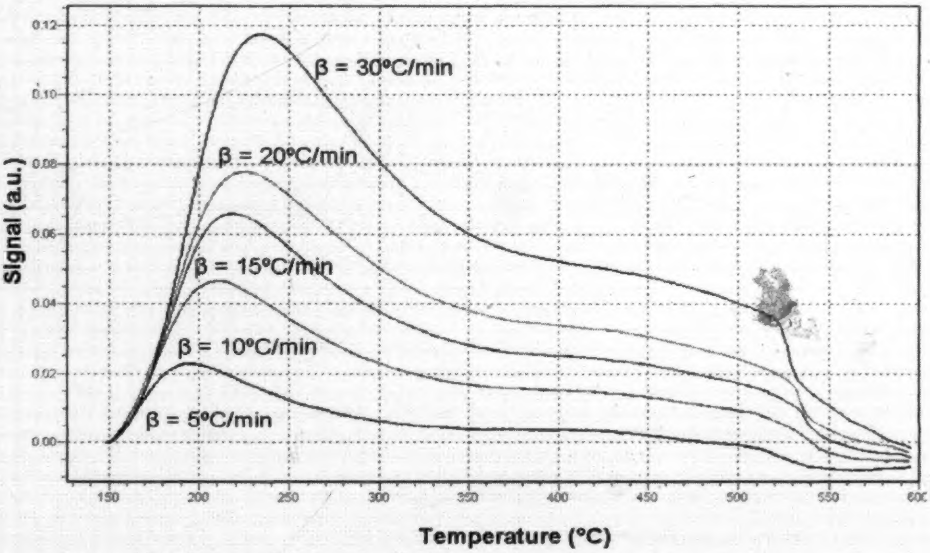

Figure 4.38a: $NH_3$ TPD spectra for NiMo-CHA following exchange with $NH_4^+$.

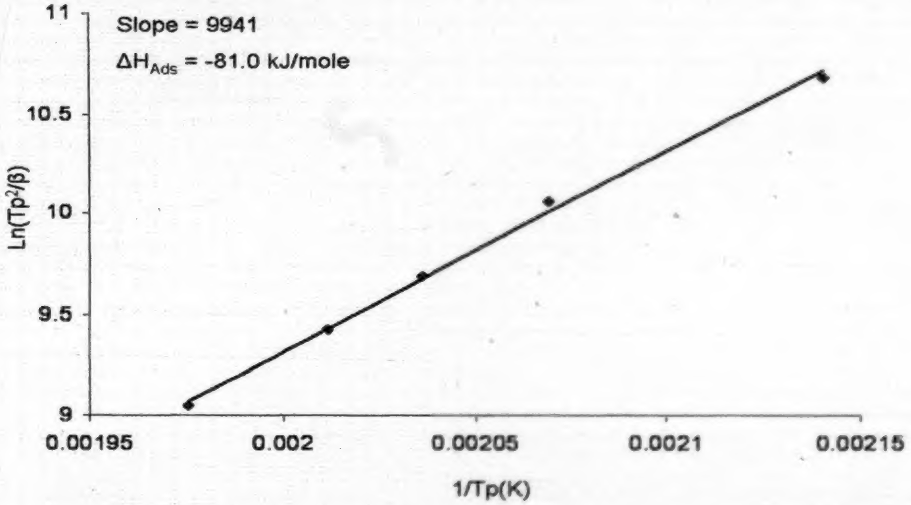

Figure 4.38b: First order plot of the peak temperature (Tp) data for NiMo-CHA following exchange with $NH_4^+$.

Reversing the order of exchange, the simultaneous incorporation of Ni and Mo into $NH_4$-CHA produced a heat of adsorption of 63.5 kJ/mole (Figure C.11, Appendix C). This is even lower than the heat of adsorption of the starting material ($NH_4$-CHA(1)) as reported above to be 74.3 kJ/mol. Also evident in Figure C.11 is a much more pronounced higher strength acidic feature than the opposite order of exchange. While calcination at 400°C and 600°C eliminated this high strength feature, (see Figures C.12 and C.13, Appendix C), there was also significant broadening of the primary desorption spectra, and consequently an increase in the calculated heat of adsorption, (109.2 kJ/mol for the 400°C calcination and 84.3 kJ/mol for the 600°C calcination). However, reduction appeared to have no effect on this high strength feature, (Figure C.14, Appendix C). Perhaps this feature was due to extra-framework alumina species, ($AlO_x$), acting as Lewis sites. More research into this area is required to investigate this matter further.

In the study of the pre-acidified samples, a clear improvement in the acid strength over Series 1 was observed. While studies on the acidified support showed similar spectra to the Na-CHA shown in Figure 4.36a, a higher heat of adsorption was noted. In addition, the metal loaded chabazites showed clear evidence of multiple sites (Figures 4.39a and 4.39b).

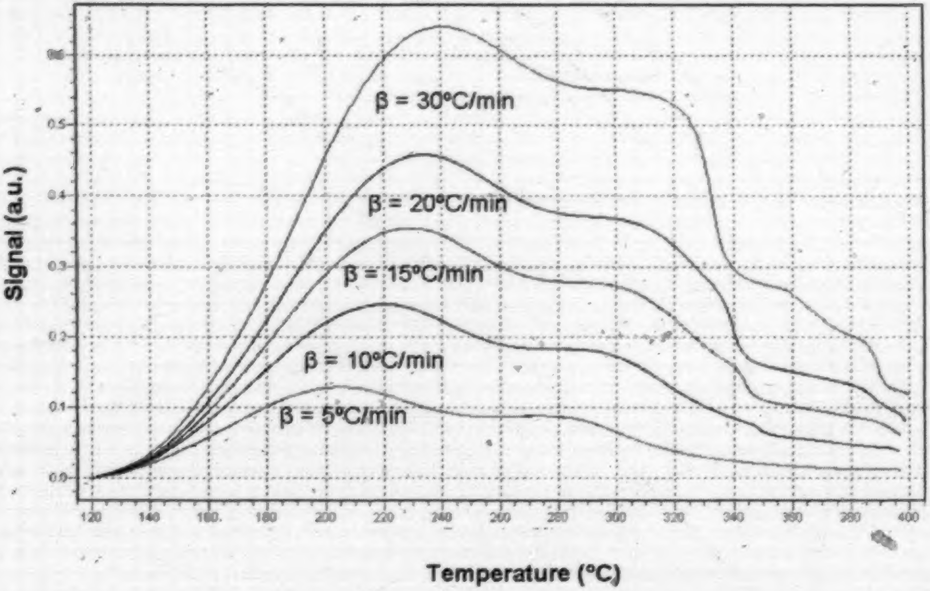

Figure 4.39a: $NH_3$ TPD spectra for NiHCHA. The peaks in the 200 to 240°C range were fit to one feature (S1), while the peaks in the 280 to 320°C range were fit to a second feature (S2).

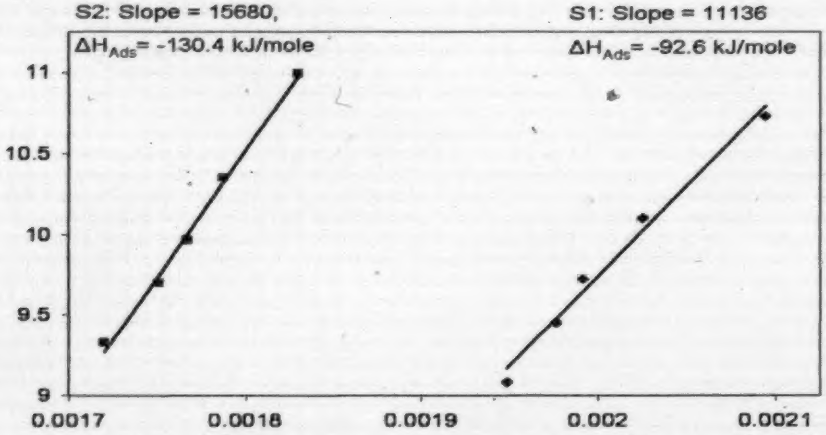

Figure 4.39b: First order plot of the peak temperature (Tp) data of SI and SII for NiHCHA.

Attempts to fully deconvolute the spectra were unsuccessful. In some cases, two site strengths were able to be fit with reasonable consistency, (resulting in a linear relationship in the data). The spectra and data plots for Series 2 can be found in Appendix C, while Table 4.12 contains the heats of adsorption extracted from the data.

Table 4.12: Heats of adsorption of $NH_3$ on samples from Series 2.

| Sample | Heat of Adsorption (kJ/mole) |
|---|---|
| HCHA | 87.3 |
| NiHCHA | 92.6, 130.4 |
| NiHCHA Reduced to 400°C | 73.7 |
| NiMoHCHA | 96.3, 129.8 |
| MoHCHA | 94.0 |

Inspection of the metal loaded samples reveals that there is not a great deal of variation among the samples. A possible explanation is that the incorporated metals are weakly bound, acting primarily as higher strength Lewis sites. This is supported by the observation of the higher strength features for which heats of adsorption were able to be extracted in the case of NiHCHA and NiMoHCHA. The presence of such higher strength features in the TPD spectra would lead to a shift to the right in the calculated heats of desorption values. A further justification of this interpretation is the fact that hydrogen reduction significantly suppresses these features, (as shown in the case of NiCHA in Table 4.12). These results are not surprisingly, based on the TEM findings that the metals agglomerate significantly under reduction and sulfidation, indicating a weak interaction with the support.

### 4.4 Summary of Characterization Results

Through the previous discussion of the characterization results, a recurring theme is self-evident; the interaction between the metals (Ni and Mo) and the support is considerably stronger in Series 1 than in Series 2.

Beginning with the XPS (section 4.11) and the INAA (4.12) compositional results, we see a much higher degree of exchange in Series 1 and than in Series 2. It is likely that the high temperature exchange conditions employed in the Series 1 synthesis allows for cation exchange at sites with high activation energies. The Series 2 synthesis, with its lower temperature and shorter contact time likely does not result in exchange at such 'hard to reach' sites. The results of the TEM and XRD studies found in Section 4.2 agree with the hypothesis of differening strengths of interaction between the two series. The Series 1 TEM results clearly indicate slight cluster growth under reduction and/or sulfidation, (Ni-CHA), or stable clusters, (Mo-CHA and NiMo-CHA), which do not sinter to any significant extent under such treatments. Strongly contrasting these results are those of Series 2, wherein it is found that all of the incorporated metals, (Ni, Mo, and NiMo), grow considerably under reduction and sulfidation. In addition, sulfidation of MoHCHA leads to $MoS_2$, and such structures are found in the sulfided NiMoHCHA samples as well. This is a further testamony to the weak interaction found in Series 2. It can be imagined that the interaction between the metals and the support is of such limited strength that metals such as Mo are free to associate into more complex, surface independent structures such as $MoS_2$, and that Ni may be free to incorporate within such structures, in a promoting or decorating fashion, (NiMoS). The XRD results of Section 4.2 also clearly shows a different strength of interaction between the two series. In Series 1, the pronounced baseline broadening, (amorphous halo), is a clear indication of the strong interaction between the chabazite framework and the incorporated cations, while the absence of this effect confirms the weaker interaction observed thus far in Series 2. Finally, the $NH_3$-TPD results presented in Section 4.3 clearly show single desporption spectra from Series 1, which are not affected by reduction, while Series 2 shows mult-site desporption. Reduction had no effect on the Series 1 catalysts, while reduction of the Series 2 catalysts resulted in only single site desorptions. The multiple sites observed in Series 2 can be explained in terms of the support acidity, (as observed in Series 1), plus a Lewis type acidity due to partially (i.e. weakly) bound ions. Upon reduction, these weakly bound ions are either in the metallic state, or of such low ionic character that they do not retain any sufficient Lewis acid characteristics. These observations further support the variation in interaction strength between the metals and the support found in Series 1 and Series 2.

## 4.5 Ethylene Hydrogenation Activities

*Series 1*

Control experiments with Na-CHA showed little or no ethylene hydrogenation activity, while comparative studies using Ni-CHA and Mo-CHA showed high activity toward ethylene hydrogenation, with Ni-CHA showing the highest activity of the supported metals. An illustrative example of the effluent composition during hydrogenation is found in Figure 4.40. (Note that in Figure 4.50 and subsequent figures, the mole fractions and mole percents, indicated by an asterisk, are on an $H_2$, $H_2S$ and Ar free basis).

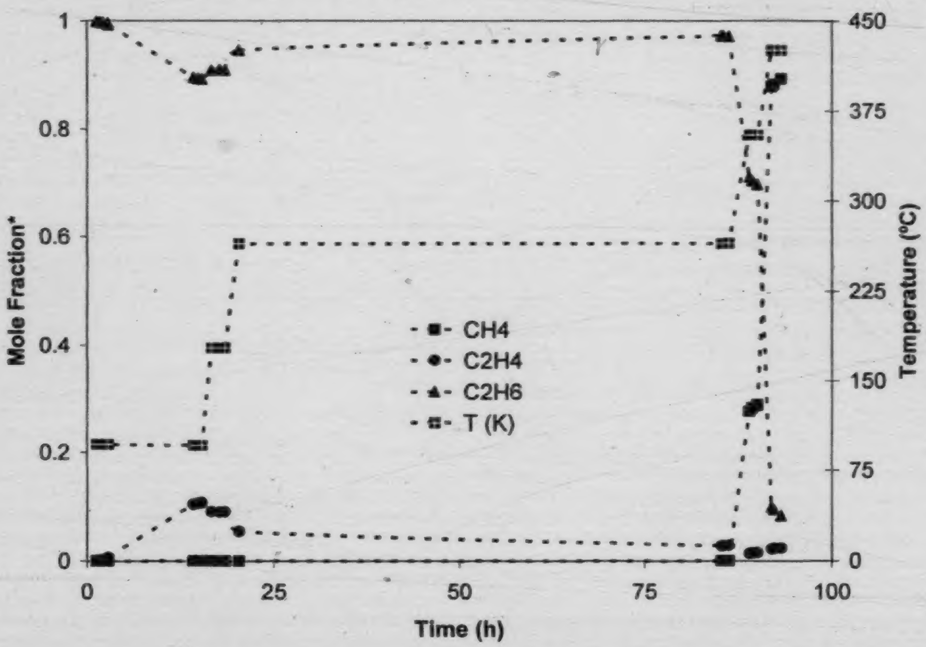

Figure 4.50: Reactor effluent composition (excluding $H_2$ and Ar) from ethylene hydrogenation over NiMo-CHA reduced at 450°C. (Figure adapted from Greenhalgh et al. [67]).

While initially there was some instability in the activity, at higher values of temperature and *time-on-stream* it was found that NiMo-CHA facilitates the near complete conversion of ethylene to ethane. Interestingly, there was a sharp change in selectivity toward methane at approximately 350 °C over NiMo-CHA. None of the monometallic systems showed any such selectivity toward methane in this experiment, yet follow up work did show $CH_4$ generation over Ni-CHA.

In the presence of sulfur, there was clear evidence of severe and rapid deactivation of the discrete metals, particularly in the case of Ni-CHA. While NiMo-SCHA was also deactivated in the presence of $H_2S$, it retains significant activity compared to the Ni- and Mo-SCHA, (Figure 4.51).

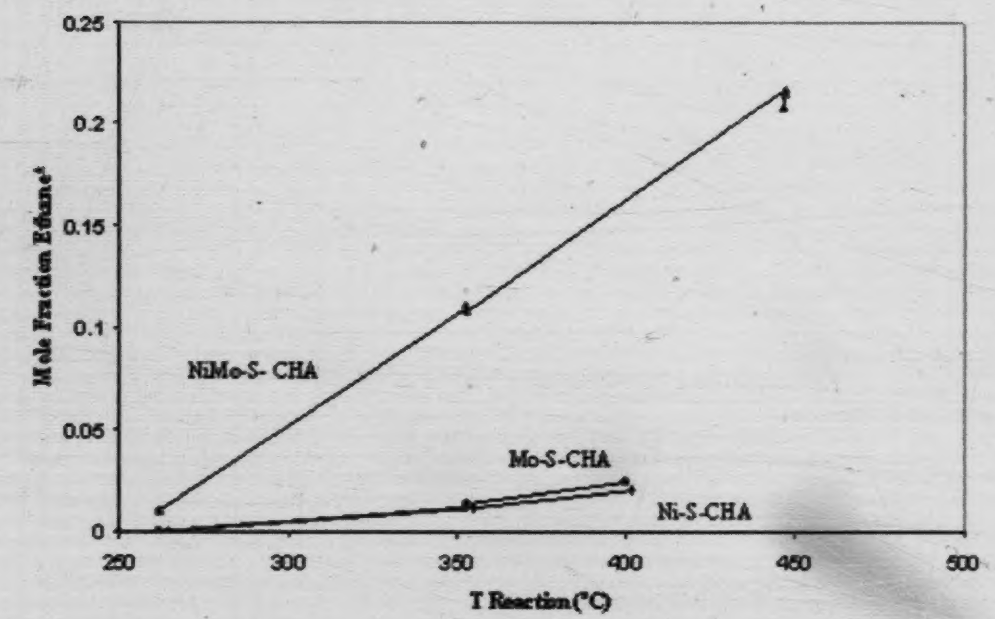

Figure 4.51: Steady state ethane mole fraction (excluding $H_2$, $H_2S$ and Ar) in reactor effluent over Ni-, Mo- and NiMo-CHA sulfided at 450°C. (Figure taken from B.R. Greenhalgh et al. [67] ).

This result is in agreement with the findings of the XPS studies, wherein in NiMo-CHA was found to have a more metallic character than Ni-CHA in the presences of $H_2S/H_2$. No evidence of selectivity toward methane for any of the metal chabazites was observed in the presence of sulfur.

*Series 2*

The catalytic studies in Series 2 were much more detailed and systematic than those of Series 1. The following discussion makes reference to a wider collection of figures which can be found in Appendix E. Where relevant to this discussion, selected figures are presented.

In the R200 study, NiHCHA shows appreciable activity near room temperature, while MoHCHA and NiMoHCHA do not show any significant conversion of ethylene. This data along with a comparison plot on the basis of ethane generation is shown in Figure D.1, Appendix D. On the basis of methane generation, the data collected shows essentially no activity for MoHCHA, with Ni and NiMo both showing small activity. When reduced at 300°C, all catalysts show an increased activity relative to the R200 data. A notable observation is that NiHCHA shows complete ethylene conversion near room temperature, while NiMoHCHA show about 35%, and MoHCHA appears inactive (Figures 4.52a – 4.52d).

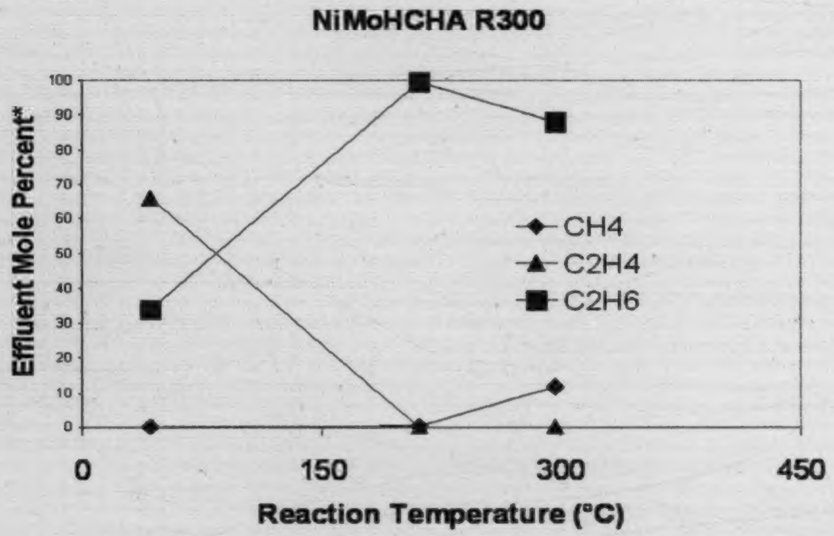
NiMoHCHA R300

Figure 4.52a: Catalytic results for NiMoHCHA reduced at 300°C.

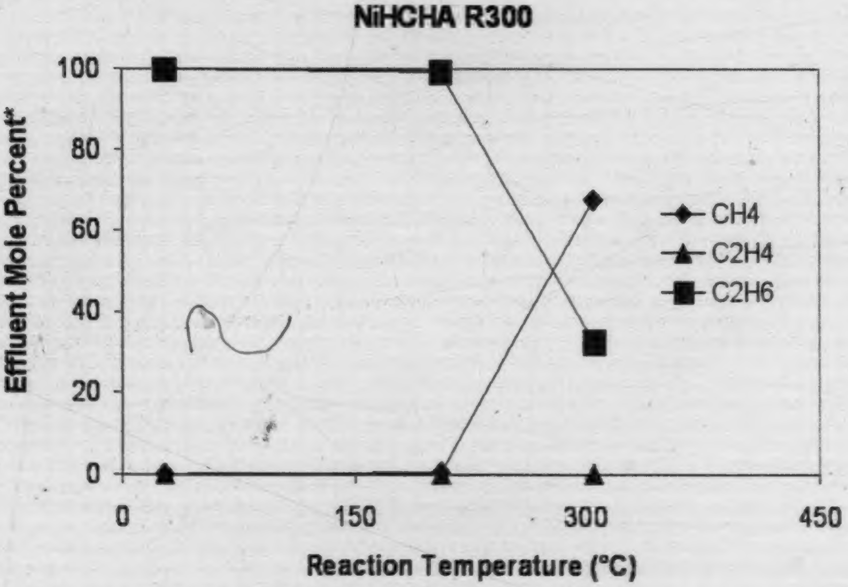

Figure 4.52b: Catalytic results for NiHCHA reduced at 300°C.

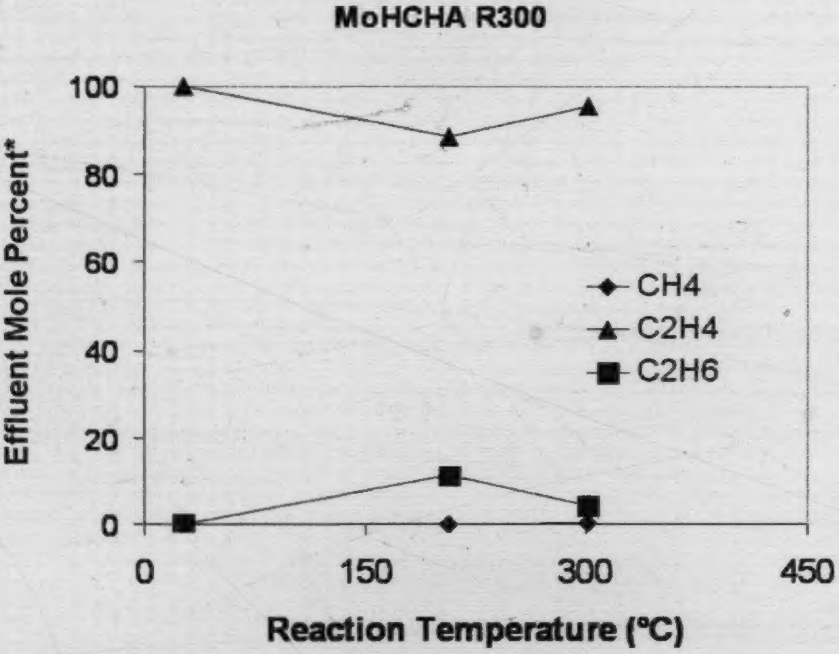

Figure 4.52c: Catalytic results for MoHCHA reduced at 300°C.

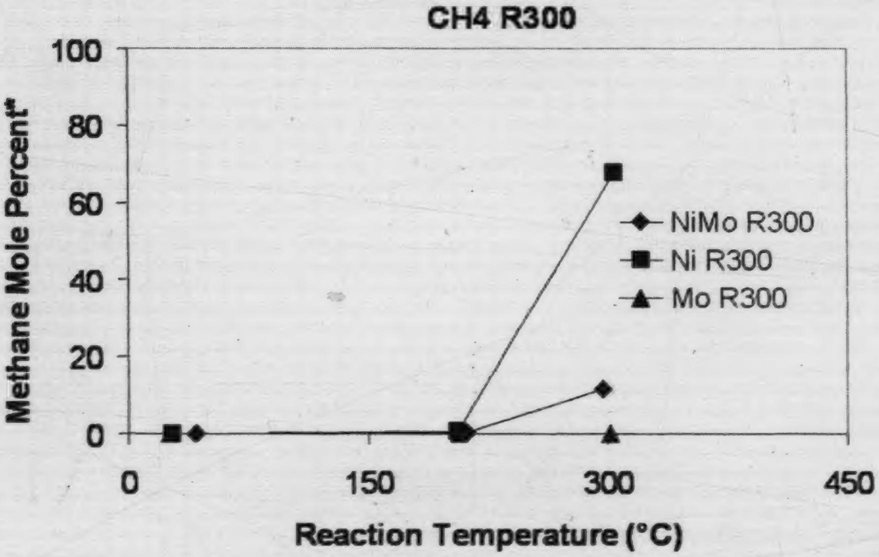

Figure 4.52d: Methane generation over metal loaded chabazites reduced at 300°C.

Methane generation was observed at 300°C for both Ni and NiMoHCHA, but the NiHCHA catalyst is clearly more active. Also of interest is the apparent maximum in the activity of MoHCHA near 200°C. On the basis of methane generation, NiHCHA is clearly the most active catalyst at this temperature. As found in Figure D.3, Appendix D, the R400 study reveals again that NiHCHA shows complete ethylene conversion near room temperature, yet neither NiMoHCHA nor MoHCHA show any conversion in the low temperature region. Methane generation is again observed at 300°C for both NiHCHA and NiMoHCHA, and the former is again clearly more active than the latter. The apparent maximum in the activity of MoHCHA observed near 200°C in the R300 study is observed again here in the R400 study. As in the R300 study, the R400 study shows that NiHCHA is clearly the most active catalyst in terms of methane generation.

All of the catalyst exhibit low activity toward ethylene hydrogenation in the S200 series (Figure D.4, Appendix D), with NiHCHA and NiMoHCHA showing distinctly higher activity than MoHCHA on the basis of ethane generation, (ethane was chosen at the basis of comparison because none of the catalysts showed any appreciable selectivity toward methane in the presence of sulfur).

Although all of the catalyst studied show an improvement in activity in the S300 study, NiMoHCHA clearly maintains a higher activity than NiHCHA or MoHCHA in the presence of sulfur (Figure 4.53a – 4.53d).

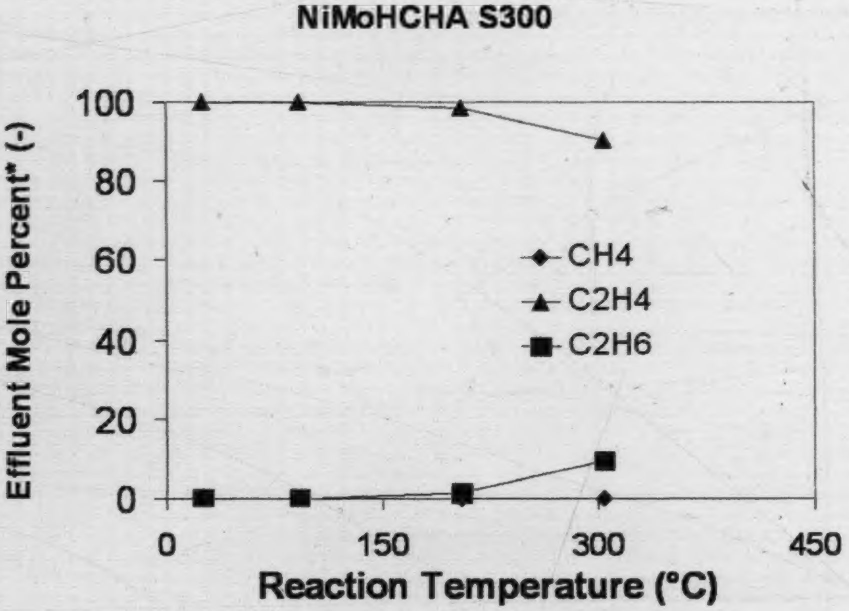

Figure 4.53a: Catalytic results NiMoHCHA sulfided at 300°C.

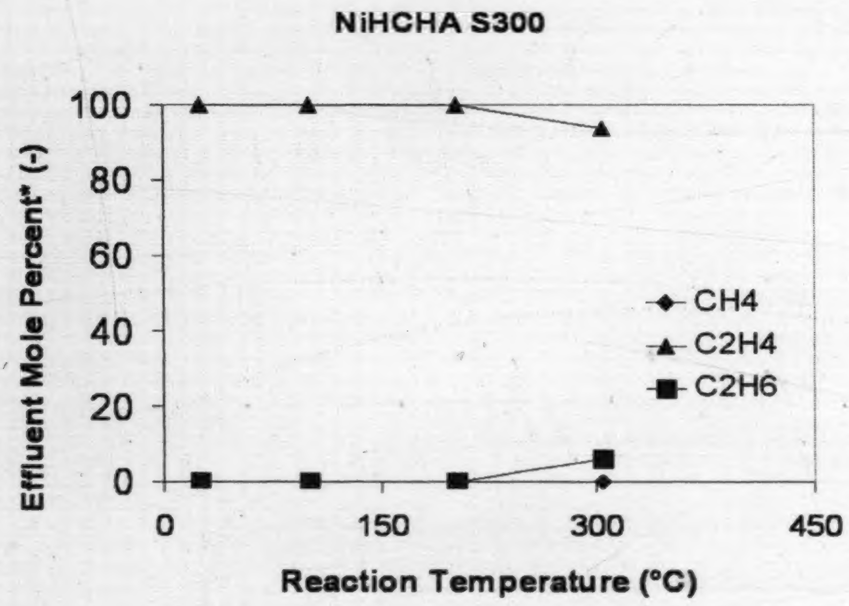

Figure 4.53b: Catalytic results NiHCHA sulfided at 300°C.

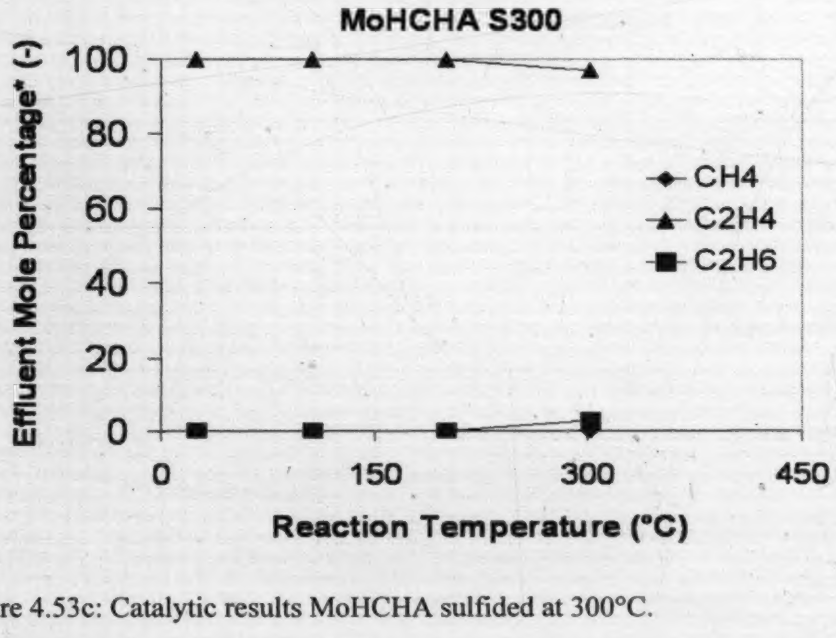

Figure 4.53c: Catalytic results MoHCHA sulfided at 300°C.

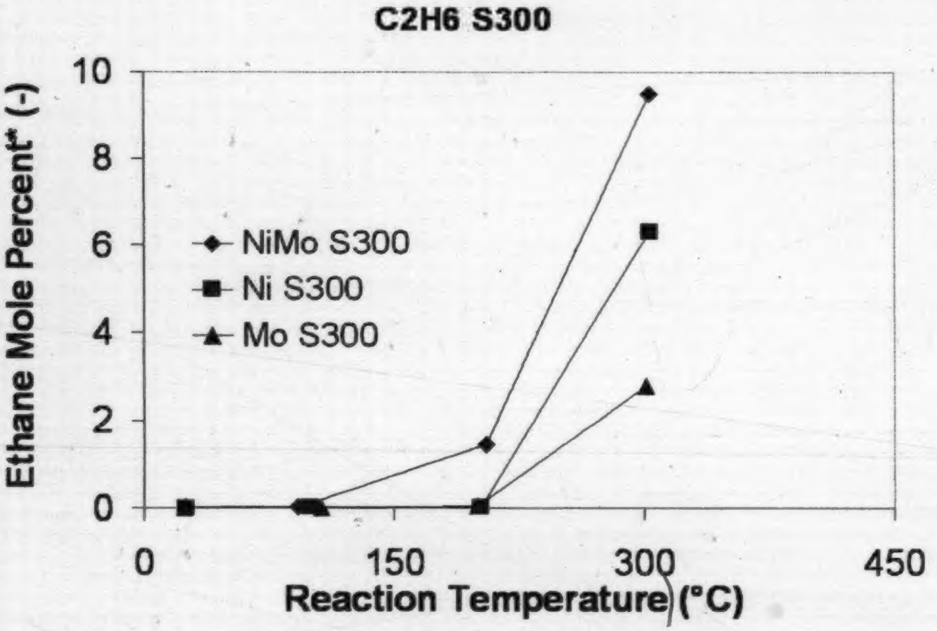

Figure 4.53d: Ethane generation over metal-loaded chabazites reduced at 300°C.

The S400 study shows a further distinction in the activity of NiMoHCHA over that of NiHCHA and MoHCHA (Figure D.6, Appendix D). Although the increased temperature leads to increased activity, it should be noted that a higher activity of NiMoHCHA occurred at 300°C in the S300 series than in the S400 series. This is interesting because the S300 TEM study revealed $MoS_2$ type structures in both MoHCHA and NiMoHCHA, (leading to the possibility of NiMoS type sites), whereas no such sites were observed in the NiMoHCHA within the S400 study. However, the nature of TEM imagery is such that the failure to observe a given feature does not mean that such a feature is not present in the sample. Nonetheless, these observations constitute a plausible structure-property relationship.

Recall the findings of the XPS studies on NiMo-CHA; that it is of a more highly metallic character than Ni-CHA. Coupling this with the TEM results which show well-dispersed, uniform clusters sizes as opposed to large Ni and small Mo clusters, (as shown to be the case in the respective mono-metallic studies), it is very likely that the surface of NiMo-

CHA consists of metallic (NiMo) sites in close proximity to acid (CHA) sites. This may explain why C-C bond scission is active in the NiMo system. However, looking at the Series 2 TEM data, we see essentially unrestricted cluster growth in both NiHCHA and NiMoHCHA, and both materials show activity in hydrogenation and hydrogenolysis (generation of methane).

Perhaps the generation of methane can be explained in terms of a sequential reaction, one in which ethylene is hydrogenated to ethane, which then in turn yields methane. Such a mechanism has been proposed in the literature, such as the work of Morikawa et al [68] on the reaction between propane and hydrogen over a Ni-Kieselguhr catalyst. These authors proposed the following reaction scheme, which suggests that ethane can react further with the catalyst to produce methane (Equations 4.5a and 4.5b);

$$C_3H_8 + H_2 \longrightarrow C_2H_6 + CH_4$$

**4.5a**

$$C_2H_6 + H_2 \longrightarrow 2CH_4$$

**4.5b**

It is interesting to note that the above work by Morikawa et al. [68] also examined the hydrogenation of ethylene over the same Ni catalysts, and yet no methane was observed. However, their experiment employed reaction temperatures not exceeding 138°C. The results presented here do not contain any observation of methane below 200°C, thus direct comparisons on the basis of methane generation is difficult. However, their studies on the hydrogenation decomposition of propane revealed the generation of methane under reaction temperatures as low as 157°C. Another important consideration is that the kinetic studies employed by Morikawa et al. [68] were carried out in a batch reactor, whereas the results presented here were acquired in a flow reactor. Nonetheless, such a sequential reaction would be in keeping with the observed hierarchy of reactivity, in that the NiHCHA showed the highest activity in the hydrogenation of ethylene, and also showed the highest selectivity to methane. Such reactivity would be required if ethane generated from ethylene is to subsequently react with the catalysts to form methane.

It is the in the presence of sulfur that a distinction between the catalysts becomes clear. In both Series 1 and Series 2, the NiMo catalysts retained the highest activity among the sulfided catalysts. TEM studies revealed the presence of $MoS_2$ type clusters within NiMoHCHA, yet no such structures were observed in NiMo-CHA. However, throughout this entire study, there is a great body of evidence showing a strong interaction between the chabazite support and the metals, while the acidified chabazite was characterized by a weaker interaction. It can therefore be argued that if any $MoS_2$ type clusters do form on the chabazite, (i.e. NiMo-CHA), they would likely be sufficiently restricted in size as to remain largely undetected by TEM and XRD, (as even the $MoS_2$ like structures seen by TEM in NiMoHCHA and MoHCHA were not detected by XRD). While MoHCHA clearly developed $MoS_2$ type sites in the presence of sulfur, it was essentially inactive in hydrogenation under these conditions. This underlines the interplay between Ni and Mo supported on chabazite, further strengthening the argument that a NiMoS type site forms on the surface of Ni and Mo exchanged chabazite upon sulfidation. If the mechanism of Morikawa et al. [68] given above in Equations 4.6a and 4.6b is applicable to the results here, it is not surprising that no methane was observed in the presence sulfur, owing to the low activity observed in all catalysts compared to the sulfur free experiments. The work of Goodman [69] reveals the inhibitory effects of sulfidation on the hydrogen absorption characteristic of single crystal Ni. These findings indicate that sulfidation of Ni results in significant depressions of the steady state atomic hydrogen surface of the catalyst. This may further explain why no methane was observed over the sulfided catalysts. Additionally, the work of Vang et al. [70] discusses the superior reactivity toward C-C bond scission of step sites over terrace sites within Ni(111) crystallites. Their investigation of the effects of dopants such as Ag reveals that such step sites are much more highly deactivated than terrace sites. Perhaps the observed deactivation of Ni-CHA and NiHCHA in the presence of sulfur is analogous to such findings for Ag, while the resistance to sulfur poisoning in the NiMo catalysts (NiMo-CHA and NiMoHCHA) is due the formation of NiMoS type sites, as argued above.

# Chapter 5

## Summary and Conclusions

In summarizing the findings of this work, a number of conclusions come to light. The method of catalyst preparation clearly plays a role, in which high temperature reflux exchange results in a strong binding of the metal to the support, while the exchange column method, characterized by contacting the pre-acidified support with a solution of constant concentration, appears to lead to a weaker interaction. The former leads to either stable clusters or at least clusters of predictable, uniform growth, (depending on the supported metal), while the latter results in higher Brønsted acidity (as found in the $NH_3$-TPD studies) and clusters which seem to be under little or no influence from support interactions. An example of this is the formation of $MoS_2$-like structures, observed in the TEM studies of MoHCHA and NiMoHCHA. Beyond this is the observed synergy between Ni and Mo. This manifests itself across a wide range of observables, such as the apparent alloying of Ni and Mo which leads to interdependent cluster growth, (confirmed by both TEM and XRD), and the apparent promoting effect of Ni within NiMo type clusters, as shown in the XPS studies. In-situ XPS studies also revealed the effects of ambient exposure on the analysis of reduced samples. In terms of reactivity, these materials show novel activity as metallic catalysts, along both hydrogenation and hydrogenolysis pathways. The resistance of the NiMo clusters to sulfur poisoning provides a final testament to the synergy between Ni and Mo, suggesting that true NiMoS type catalytic sites develop on the surface of chabazite under the conditions studied.

# Chapter 6

## Recommendations and Future Work

This research program, owing to its exploratory nature, was considerably broad in its scope. Owing to limits of equipment access, scheduling and time constraints, some of the more interesting areas of the research were not as deeply investigated as I would have liked. In order to complete the spectrum of experiments required to bring this project to an endpoint suitable for graduate studies, some of the more fascinating aspects of the project were given only passing consideration. In other cases, limited use and maintenance requirements of key instruments did not allow deeper examination of the some areas of the research. This is of course typical for any such project, as scientific research is an ongoing process, and rarely comes to an absolutely final stage of completion. It is my genuine hope that this research will be resumed by future investigators, whether they be students or professional researchers, and to this end, I recommend the following areas of further study.

### *Hydrogen Adsorption Studies:*

During the latter part of my research, a significant amount of time was devoted to measuring the dispersion of Ni on the external surface of the chabazite supports. Both static and pulse adsorption methods were attempted, with little success in terms of consistent results. The studies of cluster growth upon reduction would be well complemented by a quantitative measure of the metal dispersion by hydrogen adsorption.

### *Further development of the TPR/TPS-XPS studies:*

The setup employed in this study was quite sophisticated in terms of transfer mechanism and UHV capabilities, yet the temperature control system was rather crude. If improved heating rates and temperature control were available, a much more detailed study of the reduction and sulfidation behaviour of these catalysts would be rewarding. Also, due to equipment maintenance requirements, the TPS-XPS system was only available during the Series 1 study. While kinetic measurements confirmed that both Series 1 and Series 2 indicated a synergic effect between Ni and Mo in the NiMo systems, (NiMo-CHA and NiMoHCHA), no results for the sulfidation of the Series 2 chabazites were available. It would have been interesting to examine the results of such an experiment within the context of the TEM findings, which observed $MoS_2$ like structures.

*Further development of the activity studies:*

In order to further develop this project, reactions involving more complex molecules such as larger hydrocarbons would be a natural extension of this research. Considering the proven sulfur resistance of the NiMo chabazites, HDS reactions involving Thiophene and/or its derivatives would likely also yield interesting results. Mechanistic studies would also be rewarding, as part of a further attempt to explain the kinetic behaviour of these systems, particularly the mechanism of methane formation, and its absence in the presence of sulfur. In addition, making use of the size exclusion properties of zeolites, ring opening/cetane number improvement studies on such chabazite supported catalysts would likely be rewarding. As shown throughout this thesis, these materials not only have large external surface areas which facilitates contact between probe molecules and the catalytic sites, but they also exhibit proven hydrogenation activity and acidity characteristics, which are prerequisite for ring opening activity [1].

*Further study of the formation of $MoS_2$ type structures on chabazite:*

The observation of $MoS_2$ like structures in the TEM studies was truly a highlight of this research. Investigation into factors which govern the formation of these structures, such as support acidity, metal loading, $H_2S$ concentration, temperature ramp and hold times, etc., would likely prove very interesting within both academic and industrial research circles.

## References

[1] M. Santikunaporn, J.E. Herrera, S. Jongpatiwut, D.E. Resasco, W.E. Alvarez and E.L. Sughrue, J. Catal. 228 (2004) 100.

[2] J. Weitkamp, Solid State Ionics 131 (2000) 175.

[3] T. Fujikawa, Catal. Surv. Asia 10 (2006) 89.

[4] J.A.R. van Veen, in: Guisnet, M. Gilson, J.-p (Ed.), Imperial College Press, London, 2002, pp. 136.

[5] A. Zecchina, S. Bordiga, J.G. Vitillo, G. Ricchiardi, C. Lamberti, G. Spoto, M. Bjørgen and K.P. Lillerud, J. Am. Chem. Soc. 127 (2005) 6361.

[6] L. Regli, A. Zecchina, J.G. Vitillo, D. Cocina, G. Spoto, C. Lamberti, K.P. Lillerud, U. Olsbye and S. Bordiga, Phys. Chem. Chem. Phys. 7 (2005) 3197.

[7] S.M. Kuznicki, D.J.A. Kelly, J. Bian, C.C.H. Lin, Y. Liu, J. Chen, D. Mitlin and Z. Xu, Microporous and Mesoporous Materials 103 (2007) 309-315.

[8] M. Neurock, J. Catal. 216 (2003) 73-88.

[9] J.R. Anderson, Structure of Metallic Catalysts, Academic Press, London, 1975.

[10] D.W. Breck, Zeolite Molecular Sieves, Wiley, New York, 1974.

[11] E.J.M. Hensen and J.A.R. Van Veen, Catal. Today 86 (2003) 87.

[12] H.K. Beyer, J. Chem. Soc., Faraday Trans. I 73 (1976) 1111.

[13] W.E. Farneth and R.J. Gorte, Chem. Rev. 95 (1995) 615.

[14] M. Gutjahr, R. Böttcher and A. Pöppl, J. Phys. Chem. B 106 (2002) 1345.

[15] K. Wilson and J.H. Clark, Pure Appl. Chem. 72 (2000) 1313.

[16] L.N. Shil and S. Bhatia, Ind. Eng. Chem. Prod. RD. 25 (1986) 530.

[17] M. Pan, Micron 27 (1996) 219.

[18] M. Guisnet and J.-. Gilson, Zeolites for Cleaner Technologies, Imperial College Press, London, (2002).

[19] H. Topsøe, B. Hinnemann, J.K. Nørskov, J.V. Lauritsen, F. Besenbacher, P.L. Hansen, G. Hytoft, R.G. Egeberg and K.G. Knudsen, Catal. Today 107-108 (2005) 12.

[20] G. Plazenet, E. Payen and J. Lynch, Phys. Chem. Chem. Phys. 4 (2002) 3924.

[21] M. Taniguchi, D. Imamura, H. Ishige, Y. Ishii, T. Murata, M. Hidai and T. Tatsumi, J. Catal. 187 (1999) 139.

[22] Y. Okamoto and H. Katsuyama, Ind. Eng. Chem. Res. 35 (1996) 1834.

[23] N.K. Indu, H. Hobert, I. Weber and J. Datka, Zeolites 15 (1995) 714.

[24] K.M. Rao, G. Spoto and A. Zecchina, Langmuir 5 (1989) 319.

[25] P. Cañizares, A. De Lucas, F. Dorado, A. Durán and I. Asencio, Appl. Catal., A 169 (1998) 137.

[26] D.H. Olson, J. Phys. Chem. 72 (1968) 4366.

[27] P. Gallezot, Y. Ben Taarit and B. Imelik, J. Catal. 26 (1972) 481.

[28] T.A. Egerton and F.S. Stone, Trans. Faraday Soc. 66 (1970) 2364.

[29] M. Briend-Faure, J. Jeanjean, M. Kermarc and D. Delaflosse, J. Chem. Soc., Faraday Trans. I 74 (1978) 1538.

[30] W.J.J. Welters, G. Vorbeck, H.W. Zandbergen, J.W. Dehaan and V.H.J. Debeer, J. Catal. 150 (1994) 155.

[31] L. Ding, Y. Zheng, Z. Zhang, Z. Ring and J. Chen, Appl Catal A Gen 319 (2007) 25-37.

[32] A.C. Herd and C.G. Pope, J. Chem. Soc., Faraday Trans. I 69 (1973) 833.

[33] S. Bendezú, R. Cid, J.L.G. Fierro and A. López Agudo, Appl. Catal., A 197 (2000) 47.

[34] L. Ding and Y. Zheng, Catal. Commun. 7 (2006) 1035.

[35] M. Suzuki, K. Tsutsumi and H. Takahashi, Zeolites 2 (1982) 51.

[36] R. Cid, F. Orellana and A.L. Agudo, Appl. Catal. 32 (1987) 327.

[37] P.W. De Bont, M.J. Vissenberg, E.J.M. Hensen, V.H.J. De Beer, J.A.R. Van Veen, R.A. Van Santen and A.M. Van der Kraan, Appl. Catal., A 236 (2002) 205.

[38] J.A. Horsely, J.D. Fellmann, E.G. Derouane and C.M. Freeman, J. Catal. 147 (1994) 231.

[39] J.-. Kim, Y. Sugi, T. Matsuzaki, T. Hanaoka, Y. Kubota, X. Tu, M. Matsumoto, S. Nakata, A. Kato and Seo, G. Pak, C., Appl. Catal., A 131 (1995) 15.

[40] A. Corma, V. González-Alfaro and A.V. Orchillés, J. Catal. 200 (2001) 34.

[41] D. Kubička, N. Kumar, P. Mäki-Arvela, M. Tiitta, V. Niemi, T. Salmi and D.Y. Murzin, J. Catal. 222 (2004) 65.

[42] O. Weisser and S. Landa, Sulfide Catalysts, Their Properties and Applications, Pergamon, Czechoslovakia, 1973.

[43] G.B. McVicker, M. Daage, M.S. Touvelle, C.W. Hudson, D.P. Klein, W.C. Baird Jr., B.R. Cook, J.G. Chen, S. Hantzer, D.E.W. Vaughan, E.S. Ellis and O.C. Feeley, J. Catal. 210 (2002) 137.

[44] J.R.H. Ross, Structure and Defect Properties of Solids, Chemcial Society, London, 1975.

[45] W.J. Mortier, G.S.D. King and L. Sengier, J. Phys. Chem. 83 (1979) 2263.

[46] X. Querol, J.C. Umaña, F. Plana, A. Alastuey, A. Lopez-Soler, A. Medinaceli, A. Valero, M.J. Domingo and E. Garcia-Rojo, Fuel 80 (2001) 857.

[47] V.V. Shipikin, V.Y. Georgievskii, V.N. Brovko, A.B. Rozenblut and I.N. Tolkacheva, Chem. Technol. Fuels Oils 18 (1982) 266.

[48] C. Lo, C.A. Giurumescu, R. Radhakrishnan and B.L. Trout, Mol. Phys. 102 (2004) 281.

[49] M. Neurock and R.A. Van Santen, J Phys Chem B 104 (2000) 11127-11145.

[50] H. Ehwald, A.A. Shestov and V.S. Muzykantov, Catal. Lett. 25 (1994) 149.

[51] M. Pier, Z. Elektrochem. 53 (1949) 291.

[52] J.M. Thomas and W.J. Thomas, Principles and practice of heterogeneous catalysis, VCH, New York, 1997.

[53] A.P. Grosvenor, M.C. Biesinger, R.S.C. Smart and N.S. McIntyre, Surf Sci 600 (2006) 1771-1779.

[54] B.P. Payne, A.P. Grosvenor, M.C. Biesinger, B.A. Kobe and N.S. McIntyre, surf. interface anal. 39 (2007) 582-592.

[55] S. Brunauer, P.H. Emmett and E. Teller, J. Am. Chem. Soc. 60 (1938) 309.

[56] P.W. Atkins, in: Anonymous Physical Chemistry, 5th ed., Oxford University Press, Oxford, 1994, pp. 961.

[57] R. Hogg, in: M.C. Fuerstenau and K.N. Han (Eds.), Principles of Mineral Processing, SME, Colorado, 2003, pp. 29.

[58] J.F. Moulder, W.F. Stickle, P.E. Sobol and K. Bomben, Handbook of X-ray Photoelectron Spectroscopy, 2nd ed., Perkin-Elmer Corporation (Physical Electronics), 1992.

[59] J. Iranmahboob, S.D. Gardner, H. Toghiani and D.O. Hill, Journal of Colloid and Interface Science 270 (2004) 123-126.

[60] C.T. Tye and K.J. Smith, Catal Today 116 (2006) 461-468.

[61] M.O. de Souza, F.M.T. Mendes, R.F. de Souza and J.H.Z. dos Santos, Microporous Mesoporous Mater. 69 (2004) 217.

[62] X-Ray Powder Diffraction File, Sets 1-5 Inorganic, ASTM, 1965.

[63] C.R. Adams, H.A. Benesi, R.M. Curtis and R.G. Meisenheimer, J. Catal. 1 (1962) 336.

[64] F. Hernández, React Kinet Catal Lett 63 (1998) 165-170.

[65] A. Sayari, E. Crusson, S. Kaliaguine and J.R. Brown, Langmuir 7 (1991) 314-317.

[66] F.E. Trigueiro, D.F.J. Monteiro, F.M.Z. Zotin and E. Falabella Sousa-Aguiar, J. Alloy Compd 344 (2002) 337-341.

[67] B.R. Greenhalgh, S.M. Kuznicki and A.E. Nelson, Applied Catalysis A: General 327 (2007) 189-196.

[68] K. Morikawa, N.R. Trenner and H.S. Taylor, J. Am. Chem. Soc. 59 (1937) 1103.

[69] D.W. Goodman, Applications of surface science 19 (1983) 1-13.

[70] R.T. Vang, K. Honkala, S. Dahl, E.K. Vestergaard, J. Schnadt, E. Lægsgaard, B.S. Clausen, J.K. Nørskov and F. Besenbacher, Surface Science 600 (2006) 66-77.

# Appendecies

## Appendix A

## XPS Results

This Appendix contains a wide array of XPS results of Series 1, (Na-, Ni-, Mo- and NiMo-CHA) and Series 2 (Ni-, Mo- and NiMoHCHA), in the as made, reduced and sulfided states. This data was the basis for the discussion of the XPS results found in "Composition of supports and catalysts (XPS and INAA)", in Chapter 4. Results and Discussion, which contains excerpts from this appendix.

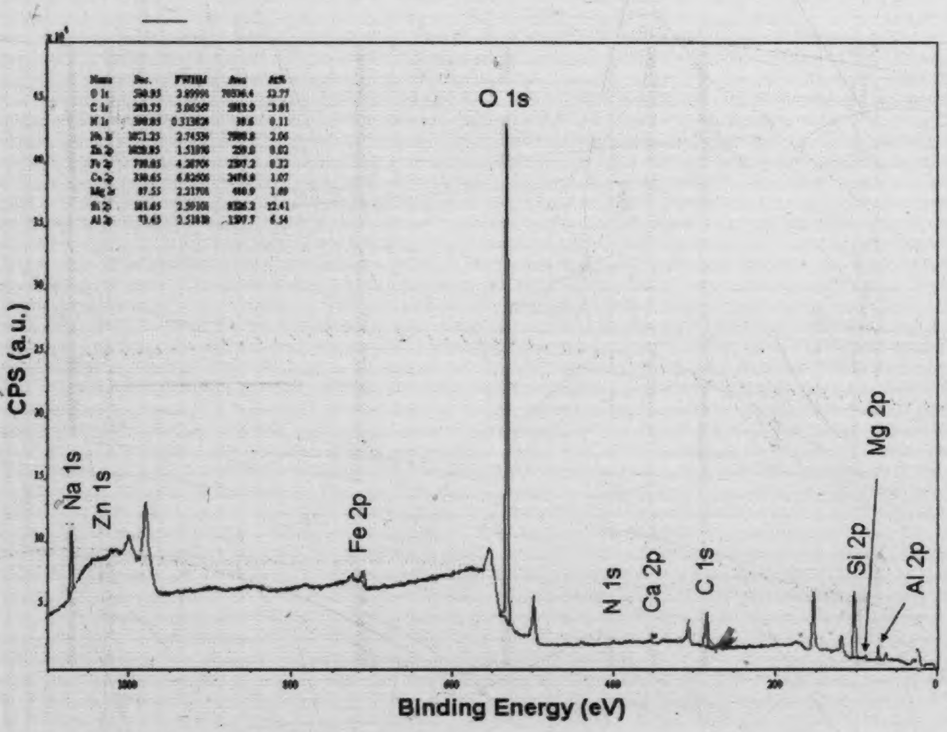

Figure A.1a: Wide scan of as made HCHA.

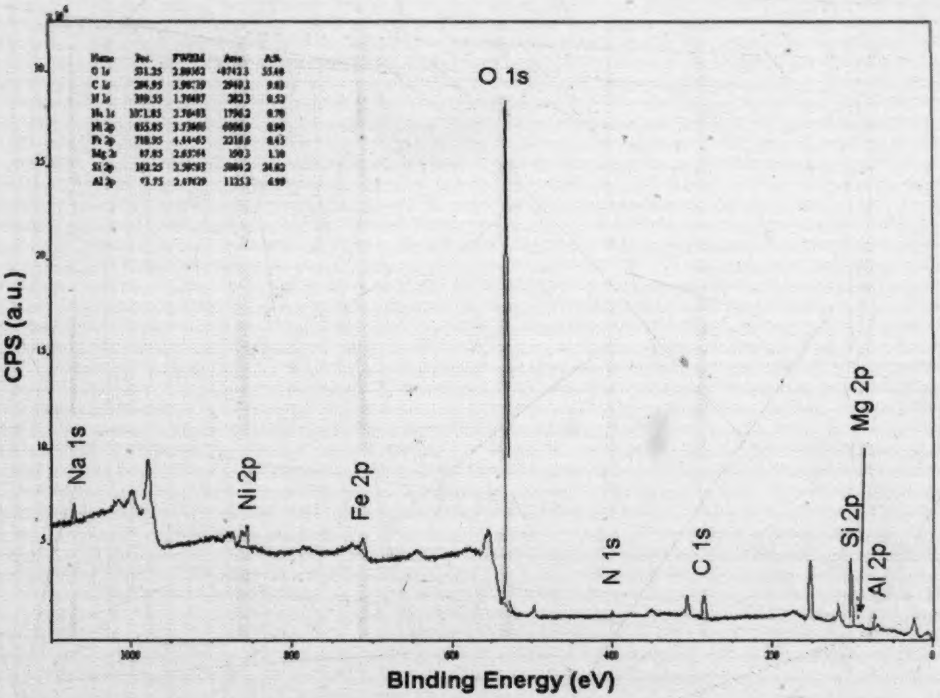

| Name | Pos. | FWHM | Area | At% |
|---|---|---|---|---|
| O 1s | 531.25 | 2.88062 | 48742.3 | 55.48 |
| C 1s | 284.95 | 3.98739 | 2940.2 | 9.83 |
| N 1s | 399.55 | 1.78487 | 382.3 | 0.52 |
| Na 1s | 1071.85 | 2.78483 | 1796.2 | 0.70 |
| Ni 2p | 855.85 | 3.73480 | 6886.9 | 0.90 |
| Fe 2p | 710.95 | 4.44463 | 2216.6 | 0.43 |
| Mg 2s | 87.85 | 2.65784 | 190.3 | 1.30 |
| Si 2p | 102.25 | 2.58583 | 5084.2 | 24.82 |
| Al 2p | 73.75 | 2.67029 | 1125.3 | 4.99 |

Figure A.1b: Wide scan of as made NiHCHA.

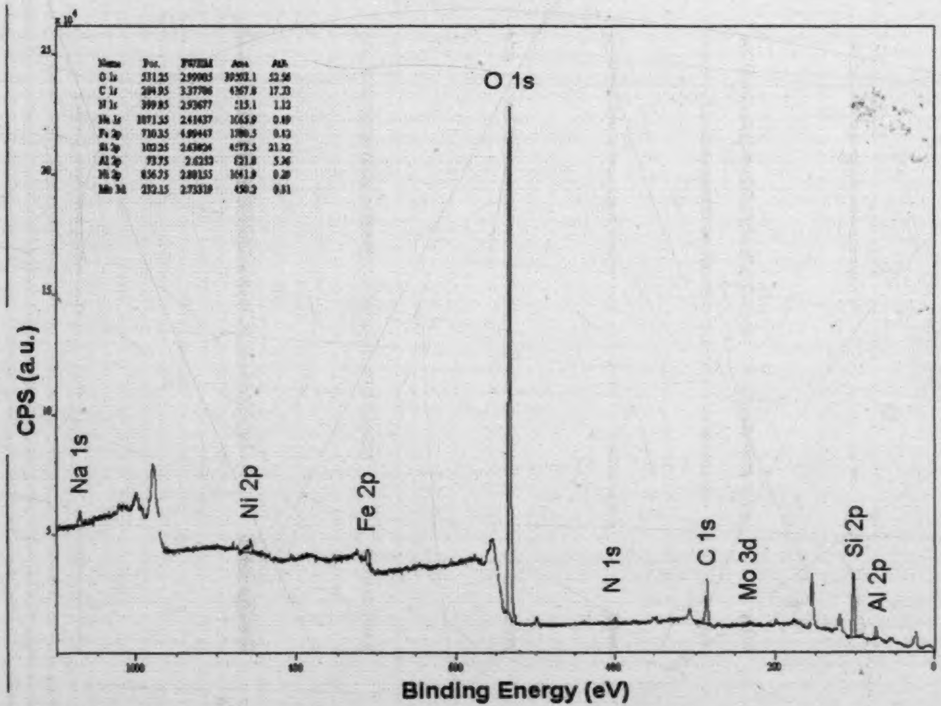

| Name | Pos. | FWHM | Area | At% |
|---|---|---|---|---|
| O 1s | 531.25 | 2.99985 | 39302.1 | 52.56 |
| C 1s | 284.95 | 3.37706 | 4367.8 | 17.33 |
| N 1s | 399.85 | 2.93677 | 215.1 | 1.12 |
| Na 1s | 1071.55 | 2.41437 | 1065.9 | 0.49 |
| Fe 2p | 710.35 | 4.99447 | 1780.5 | 0.43 |
| Si 2p | 102.25 | 2.63024 | 4573.5 | 21.32 |
| Al 2p | 73.75 | 2.6232 | 521.8 | 5.36 |
| Ni 2p | 856.75 | 2.80155 | 1041.9 | 0.29 |
| Mo 3d | 232.15 | 2.73319 | 450.2 | 0.31 |

Figure A.1c: Wide scan of as made NiMoHCHA.

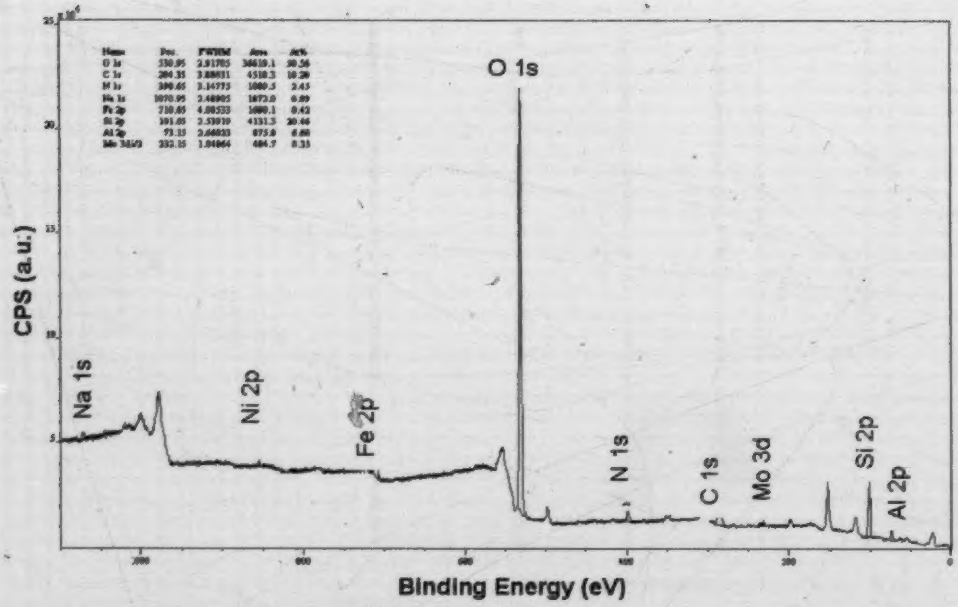

Figure A.1d: Wide scan of as made MoHCHA.

Table A.1a: Compositions of the Series 2 catalysts in the as made state in the R200 experiment.

| AMR200 | Elemental Composition from XPS, $(X_{mass})_i$ | | | |
|---|---|---|---|---|
| Name | HCHA | NiHCHA | NiMoHCHA | MoHCHA |
| Na 1s | 2.4 | 0.8 | 0.6 | 1.1 |
| Zn 2p | 0.1 | 0.0 | 0.0 | 0.0 |
| Ni 2p | 0.0 | 2.7 | 0.9 | 0.0 |
| Fe 2p | 0.9 | 1.3 | 1.2 | 1.2 |
| O 1s | 43.1 | 44.4 | 44.2 | 43.0 |
| N 1s | 0.1 | 0.4 | 0.8 | 1.8 |
| Ca 2p | 2.2 | 0.0 | 0.0 | 0.0 |
| C 1s | 8.0 | 5.9 | 10.7 | 11.7 |
| Mo 3d | 0.0 | 0.0 | 0.9 | 1.1 |
| Si 2p | 32.1 | 33.8 | 32.2 | 30.6 |
| Mg 2s | 2.1 | 1.3 | 0.0 | 0.0 |
| Al 2p | 9.0 | 9.4 | 8.5 | 9.5 |
| Si/Al mol/mol | 3.4 | 3.4 | 3.7 | 3.1 |

Table A.1b: Compositions of the Series 2 catalysts reduced at 200°C in the R200 experiment.

| RR200 | Elemental Composition from XPS, $(X_{mass})_i$ | | | |
|---|---|---|---|---|
| Name | HCHA | NiHCHA | NiMoHCHA | MoHCHA |
| Na 1s | 2.9 | 0.4 | 0.3 | 1.0 |
| Zn 2p | 0.0 | 0.0 | 0.0 | 0.0 |
| Ni 2p | 0.0 | 2.0 | 1.1 | 0.0 |
| Fe 2p | 1.1 | 2.1 | 1.9 | 2.2 |
| O 1s | 45.8 | 45.6 | 43.2 | 43.6 |
| N 1s | 0.6 | 0.5 | 0.7 | 1.6 |
| Ca 2p | 2.3 | 0.0 | 0.0 | 0.0 |
| C 1s | 8.4 | 8.4 | 8.9 | 8.9 |
| Mo 3d | 0.0 | 0.0 | 0.7 | 2.4 |
| Si 2p | 29.3 | 29.1 | 31.0 | 29.1 |
| Mg 2s | 1.7 | 1.2 | 0.9 | 0.0 |
| Al 2p | 8.0 | 10.9 | 11.4 | 11.2 |
| Si/Al mol/mol | 3.5 | 2.6 | 2.6 | 2.5 |

Table A.1c: Compositions of the Series 2 catalysts in the as made state in the R300 experiment.

| AMR300 | Elemental Composition from XPS, $(X_{mass})_i$ | | | |
|---|---|---|---|---|
| Name | HCHA | NiHCHA | NiMoHCHA | MoHCHA |
| Na 1s | 2.9 | 0.8 | 0.4 | 1.0 |
| Zn 2p | 0.2 | 0.1 | 0.1 | 0.0 |
| Ni 2p | 0.0 | 2.2 | 1.3 | 0.0 |
| Fe 2p | 1.1 | 1.3 | 1.0 | 0.9 |
| O 1s | 41.2 | 42.8 | 43.4 | 42.7 |
| N 1s | 0.6 | 0.6 | 0.9 | 0.7 |
| Ca 2p | 2.0 | 1.4 | 0.0 | 1.3 |
| C 1s | 9.0 | 9.7 | 10.5 | 7.9 |
| Mo 3d | 0.0 | 0.0 | 0.9 | 0.9 |
| Si 2p | 32.8 | 30.1 | 29.6 | 33.9 |
| Mg 2s | 1.8 | 1.9 | 0.0 | 1.0 |
| Al 2p | 8.5 | 9.1 | 12.0 | 9.6 |
| Si/Al mol/mol | 3.7 | 3.2 | 2.4 | 3.4 |

Table A.1d: Compositions of the Series 2 catalysts reduced at 300°C in the R300 experiment.

| RR300 | Elemental Composition from XPS, $(X_{mass})_i$ | | | |
|---|---|---|---|---|
| Name | HCHA | NiHCHA | NiMoHCHA | MoHCHA |
| Na 1s | 2.6 | 0.7 | 0.3 | 1.0 |
| Zn 2p | 0.1 | 0.0 | 7.0 | 0.0 |
| Ni 2p | 0.0 | 1.6 | 0.7 | 0.0 |
| Fe 2p | 1.7 | 2.2 | 1.6 | 1.5 |
| O 1s | 43.7 | 44.3 | 45.0 | 43.5 |
| N 1s | 0.0 | 0.1 | 0.8 | 0.3 |
| Ca 2p | 2.0 | 0.0 | 1.1 | 0.9 |
| C 1s | 4.5 | 6.3 | 0.0 | 5.4 |
| Mo 3d | 0.0 | 0.0 | 0.9 | 0.9 |
| Si 2p | 33.6 | 31.7 | 30.0 | 36.1 |
| Mg 2s | 2.1 | 1.6 | 0.0 | 0.0 |
| Al 2p | 9.8 | 11.5 | 12.7 | 10.4 |
| Si/Al mol/mol | 3.3 | 2.7 | 2.3 | 3.3 |

Table A.1e: Compositions of the Series 2 catalysts in the as made state in the R340 experiment.

| AMR340 | Elemental Composition from XPS, $(X_{mass})_i$ | | | |
|---|---|---|---|---|
| Name | HCHA | NiHCHA | NiMoHCHA | MoHCHA |
| Na 1s | 2.9 | 0.8 | 0.4 | 1.2 |
| Zn 2p | 0.0 | 0.0 | 0.0 | 0.0 |
| Ni 2p | 0.0 | 2.3 | 0.9 | 0.0 |
| Fe 2p | 1.0 | 1.2 | 0.8 | 1.0 |
| O 1s | 41.8 | 43.4 | 47.1 | 46.4 |
| N 1s | 0.0 | 0.5 | 0.5 | 0.4 |
| Ca 2p | 2.2 | 1.5 | 1.1 | 1.0 |
| C 1s | 6.5 | 9.2 | 8.6 | 5.4 |
| Mo 3d | 0.0 | 0.0 | 0.9 | 0.7 |
| Si 2p | 33.7 | 32.1 | 30.2 | 34.5 |
| Mg 2s | 2.4 | 1.2 | 0.0 | 0.7 |
| Al 2p | 9.6 | 8.0 | 9.4 | 8.6 |
| Si/Al mol/mol | 3.4 | 3.9 | 3.1 | 3.8 |

Table A.1f: Compositions of the Series 2 catalysts reduced at 340°C state in the R340 experiment.

| RR340 | Elemental Composition from XPS, $(X_{mass})_i$ | | | |
|---|---|---|---|---|
| Name | HCHA | NiHCHA | NiMoHCHA | MoHCHA |
| Na 1s | 2.5 | 0.4 | 0.2 | 1.2 |
| Zn 2p | 0.0 | 0.0 | 0.0 | 0.0 |
| Ni 2p | 0.0 | 0.9 | 0.6 | 0.0 |
| Fe 2p | 1.4 | 1.7 | 1.6 | 1.1 |
| O 1s | 45.3 | 45.7 | 44.2 | 45.9 |
| N 1s | 0.0 | 0.4 | 0.7 | 0.0 |
| Ca 2p | 2.3 | 1.4 | 0.9 | 1.1 |
| C 1s | 4.4 | 5.1 | 5.1 | 4.3 |
| Mo 3d | 0.0 | 0.0 | 0.8 | 0.7 |
| Si 2p | 33.3 | 31.5 | 32.6 | 36.2 |
| Mg 2s | 1.6 | 1.4 | 0.0 | 0.0 |
| Al 2p | 9.3 | 11.4 | 13.4 | 9.5 |
| Si/Al mol/mol | 3.4 | 2.6 | 2.3 | 3.7 |

Table A.2a: 'Per silicon' compositions of the Series 2 catalysts in the as made state in the R200 experiment.

| AMR200 | Composition normalized with respect to Si content; $(X_{Mass,\ Si})_i$ | | | |
|---|---|---|---|---|
| Name | HCHA | NiHCHA | NiMoHCHA | MoHCHA |
| Na 1s | 0.7 | 0.2 | 0.2 | 0.4 |
| Zn 2p | 0.0 | 0.0 | 0.0 | 0.0 |
| Ni 2p | 0.0 | 0.8 | 0.3 | 0.0 |
| Fe 2p | 0.3 | 0.4 | 0.4 | 0.4 |
| O 1s | 13.4 | 13.1 | 13.7 | 14.0 |
| N 1s | 0.0 | 0.1 | 0.2 | 0.6 |
| Ca 2p | 0.7 | 0.0 | 0.0 | 0.0 |
| C 1s | 2.5 | 1.7 | 3.3 | 3.8 |
| Mo 3d | 0.0 | 0.0 | 0.3 | 0.4 |
| Si 2p | 10.0 | 10.0 | 10.0 | 10.0 |
| Mg 2s | 0.7 | 0.4 | 0.0 | 0.0 |
| Al 2p | 2.8 | 2.8 | 2.6 | 3.1 |
| $Y_{Ni,Si}$ | 0.0 | 3.8 | 1.4 | 0.0 |
| $Y_{Mo,Si}$ | 0.0 | 0.0 | 0.9 | 1.2 |

Table A.2b: 'Per silicon' compositions of the Series 2 reduced at 200°C in the R200 experiment.

| RR200 | Composition normalized with respect to Si content; $(X_{Mass,\ Si})_i$ | | | |
|---|---|---|---|---|
| Name | HCHA | NiHCHA | NiMoHCHA | MoHCHA |
| Na 1s | 1.0 | 0.1 | 0.1 | 0.3 |
| Zn 2p | 0.0 | 0.0 | 0.0 | 0.0 |
| Ni 2p | 0.0 | 0.7 | 0.4 | 0.0 |
| Fe 2p | 0.4 | 0.7 | 0.6 | 0.8 |
| O 1s | 15.6 | 15.7 | 13.9 | 15.0 |
| N 1s | 0.2 | 0.2 | 0.2 | 0.5 |
| Ca 2p | 0.8 | 0.0 | 0.0 | 0.0 |
| C 1s | 2.9 | 2.9 | 2.9 | 3.1 |
| Mo 3d | 0.0 | 0.0 | 0.2 | 0.8 |
| Si 2p | 10.0 | 10.0 | 10.0 | 10.0 |
| Mg 2s | 0.6 | 0.4 | 0.3 | 0.0 |
| Al 2p | 2.7 | 3.7 | 3.7 | 3.8 |
| $Y_{Ni,Si}$ | 0.0 | 3.4 | 1.9 | 0.0 |
| $Y_{Mo,Si}$ | 0.0 | 0.0 | 0.6 | 2.3 |

Table A.2c: 'Per silicon' compositions of the Series 2 in the as made state in the R300 experiment.

| AMR300 | Composition normalized with respect to Si content; $(X_{Mass,\ Si})_i$ | | | |
|---|---|---|---|---|
| Name | HCHA | NiHCHA | NiMoHCHA | MoHCHA |
| Na 1s | 0.9 | 0.3 | 0.1 | 0.3 |
| Zn 2p | 0.1 | 0.0 | 0.0 | 0.0 |
| Ni 2p | 0.0 | 0.7 | 0.4 | 0.0 |
| Fe 2p | 0.3 | 0.4 | 0.3 | 0.3 |
| O 1s | 12.6 | 14.2 | 14.7 | 1.4 |
| N 1s | 0.2 | 0.2 | 0.3 | 0.2 |
| Ca 2p | 0.6 | 0.5 | 0.0 | 0.4 |
| C 1s | 2.7 | 3.2 | 3.5 | 2.3 |
| Mo 3d | 0.0 | 0.0 | 0.3 | 0.3 |
| Si 2p | 10.0 | 10.0 | 10.0 | 10.0 |
| Mg 2s | 0.5 | 0.6 | 0.0 | 0.3 |
| Al 2p | 2.6 | 3.0 | 4.1 | 2.8 |
| $Y_{Ni,Si}$ | 0.0 | 3.4 | 1.9 | 0.0 |
| $Y_{Mo,Si}$ | 0.0 | 0.0 | 0.9 | 0.9 |

Table A.2d: 'Per silicon' compositions of the Series 2 reduced at 300°C in the R300 experiment.

| RR300 | Composition normalized with respect to Si content; $(X_{Mass, Si})_i$ | | | |
|---|---|---|---|---|
| Name | HCHA | NiHCHA | NiMoHCHA | MoHCHA |
| Na 1s | 0.8 | 0.2 | 0.1 | 0.3 |
| Zn 2p | 0.0 | 0.0 | 2.3 | 0.0 |
| Ni 2p | 0.0 | 0.5 | 0.2 | 0.0 |
| Fe 2p | 0.5 | 0.7 | 0.5 | 0.4 |
| O 1s | 13.0 | 14.0 | 15.0 | 12.0 |
| N 1s | 0.0 | 0.0 | 0.3 | 0.1 |
| Ca 2p | 0.6 | 0.0 | 0.4 | 0.2 |
| C 1s | 1.3 | 2.0 | 0.0 | 1.5 |
| Mo 3d | 0.0 | 0.0 | 0.3 | 0.2 |
| Si 2p | 10.0 | 10.0 | 10.0 | 10.0 |
| Mg 2s | 0.6 | 0.5 | 0.0 | 0.0 |
| Al 2p | 2.9 | 3.6 | 4.2 | 2.9 |
| $Y_{Ni,Si}$ | 0.0 | 2.4 | 0.1 | 0.0 |
| $Y_{Mo,Si}$ | 0.0 | 0.0 | 0.9 | 0.6 |

Table A.2e: 'Per silicon' compositions of the Series 2 in the as made state in the R340 experiment.

| AMR340 | Composition normalized with respect to Si content; $(X_{Mass, Si})_i$ | | | |
|---|---|---|---|---|
| Name | HCHA | NiHCHA | NiMoHCHA | MoHCHA |
| Na 1s | 0.9 | 0.2 | 0.1 | 0.3 |
| Zn 2p | 0.0 | 0.0 | 0.0 | 0.0 |
| Ni 2p | 0.0 | 0.7 | 0.3 | 0.0 |
| Fe 2p | 0.3 | 0.4 | 0.3 | 0.3 |
| O 1s | 12.4 | 13.5 | 15.6 | 13.4 |
| N 1s | 0.0 | 0.2 | 0.2 | 0.1 |
| Ca 2p | 0.7 | 0.5 | 0.4 | 0.3 |
| C 1s | 1.9 | 2.9 | 2.8 | 1.6 |
| Mo 3d | 0.0 | 0.0 | 0.3 | 0.2 |
| Si 2p | 10.0 | 10.0 | 10.0 | 10.0 |
| Mg 2s | 0.7 | 0.4 | 0.0 | 0.2 |
| Al 2p | 2.8 | 2.5 | 3.1 | 2.5 |
| $Y_{Ni,Si}$ | 0.0 | 3.4 | 1.4 | 0.0 |
| $Y_{Mo,Si}$ | 0.0 | 0.0 | 0.9 | 0.5 |

Table A.2f: 'Per silicon' compositions of the Series 2 reduced at 340°C in the R340 experiment.

| R340 | Composition normalized with respect to Si content; $(X_{Mass, Si})_i$ | | | |
|---|---|---|---|---|
| Name | HCHA | NiHCHA | NiMoHCHA | MoHCHA |
| Na 1s | 0.8 | 0.1 | 0.1 | 0.3 |
| Zn 2p | 0.0 | 0.0 | 0.0 | 0.0 |
| Ni 2p | 0.0 | 0.3 | 0.2 | 0.0 |
| Fe 2p | 0.4 | 0.5 | 0.5 | 0.3 |
| O 1s | 13.6 | 14.5 | 13.6 | 12.7 |
| N 1s | 0.0 | 0.1 | 0.2 | 0.0 |
| Ca 2p | 0.7 | 0.4 | 0.3 | 0.3 |
| C 1s | 1.3 | 1.6 | 1.6 | 1.2 |
| Mo 3d | 0.0 | 0.0 | 0.2 | 0.2 |
| Si 2p | 10.0 | 10.0 | 10.0 | 10.0 |
| Mg 2s | 0.5 | 0.4 | 0.0 | 0.0 |
| Al 2p | 2.8 | 3.6 | 4.1 | 2.6 |
| $Y_{Ni,Si}$ | 0.0 | 1.4 | 1.0 | 0.0 |
| $Y_{Mo,Si}$ | 0.0 | 0.0 | 0.6 | 0.6 |

# Appendix B

## Transmission Electron Microscopy Results

This Appendix contains a wide array of TEM images of Series 1, (Na-, Ni-, Mo- and NiMo-CHA) and Series 2 (Ni-, Mo- and NiMoHCHA), in the as made, reduced and sulfided states. These images were the basis for the discussion of the TEM results found in "Structure of supports and catalysts (TEM and XRD)", in Chapter 4. Results and Discussion, which contains excerpts from this appendix.

Series 1: Na-CHA, Ni-CHA, Mo-CHA and NiMo-CHA.

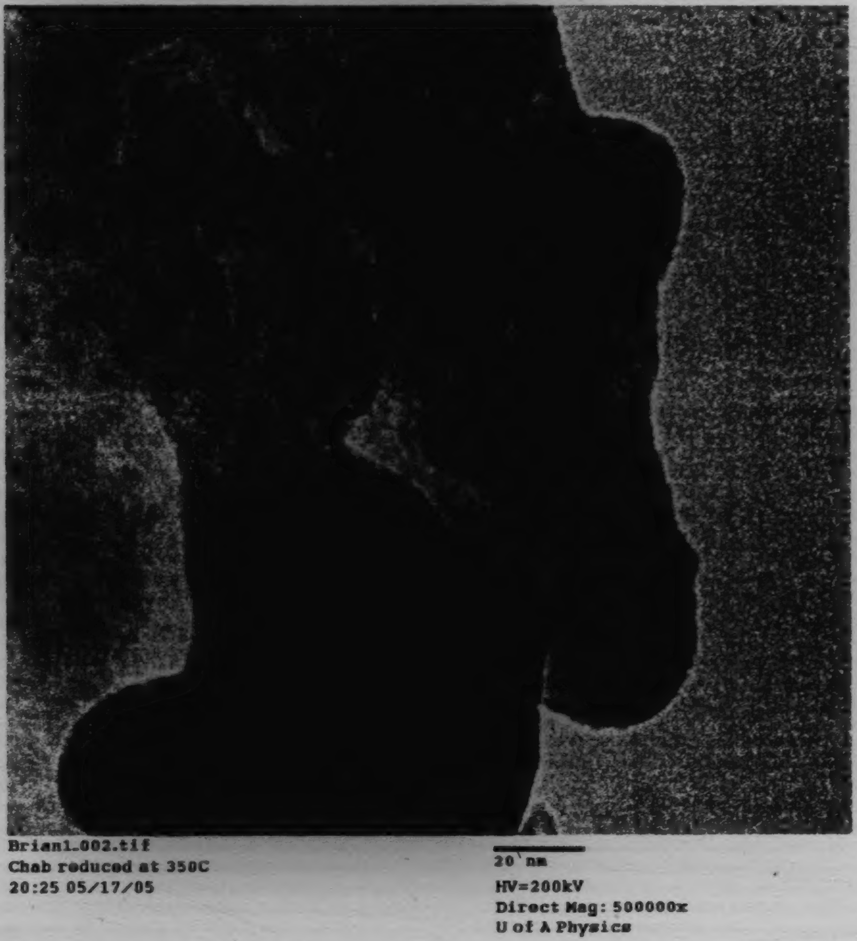
Brian1.002.tif
Chab reduced at 350C
20:25 05/17/05
20 nm
HV=200kV
Direct Mag: 500000x
U of A Physics

Figure B.1: Na-CHA reduced at 350°C in $H_2$.

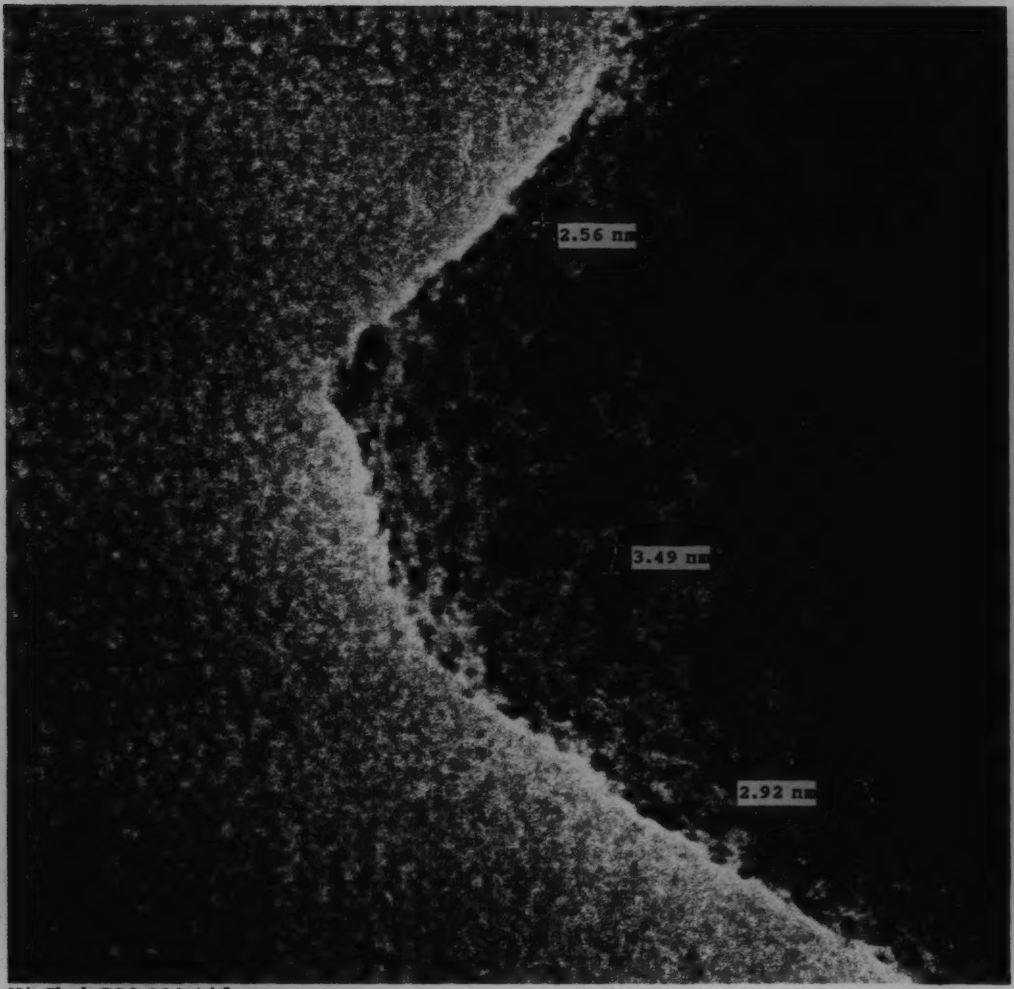

Ni_Chab_R50_010.tif
Ni Chab R50C
Print Mag: 653000x @ 3. in
23:56 09/12/05
TEM Mode: Imaging

20 nm
HV=200kV
Direct Mag: 800000x
U of A Physics

Figure B.2: Ni-CHA reduced at 50°C in $H_2$.

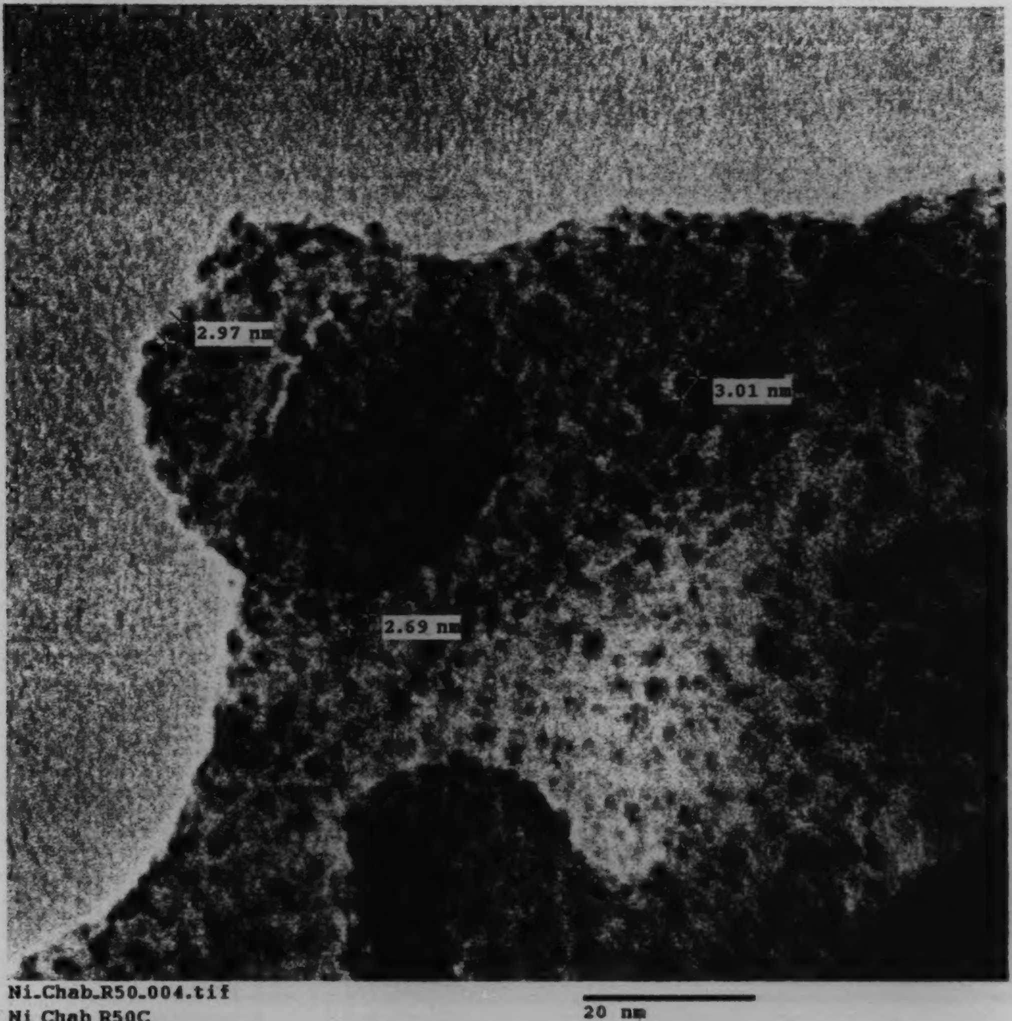
2.97 nm
3.01 nm
2.69 nm
20 nm

Ni_Chab_R50_004.tif
Ni Chab R50C
Print Mag: 653000x @ 3. in
23:41 09/12/05
TEM Mode: Imaging

HV=200kV
Direct Mag: 800000x
U of A Physics

Figure B.3: Ni-CHA reduced at 50°C in $H_2$.

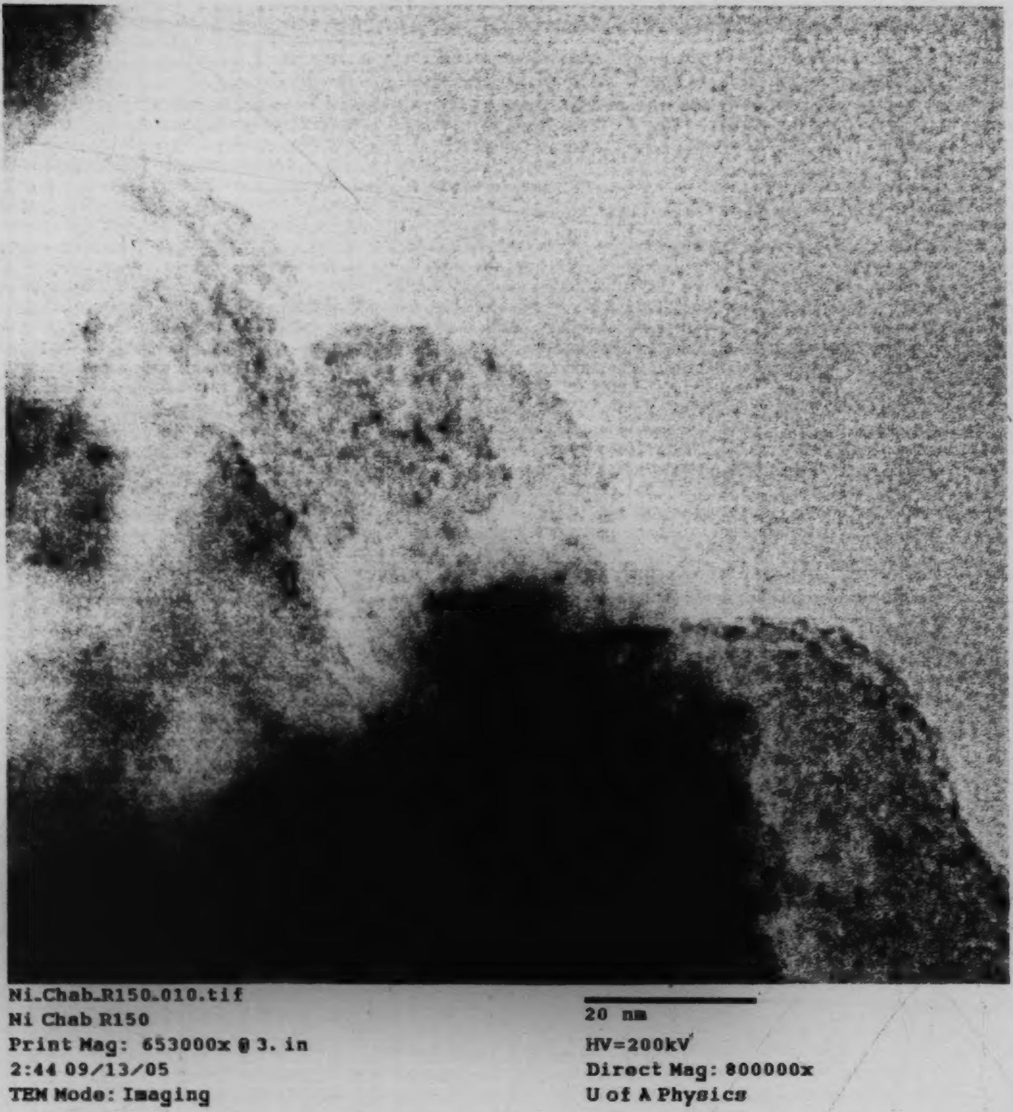
Ni_Chab_R150_010.tif
Ni Chab R150
Print Mag: 653000x @ 3. in
2:44 09/13/05
TEM Mode: Imaging
20 nm
HV=200kV
Direct Mag: 800000x
U of A Physics

Figure B.4: Ni-CHA reduced at 150°C in $H_2$.

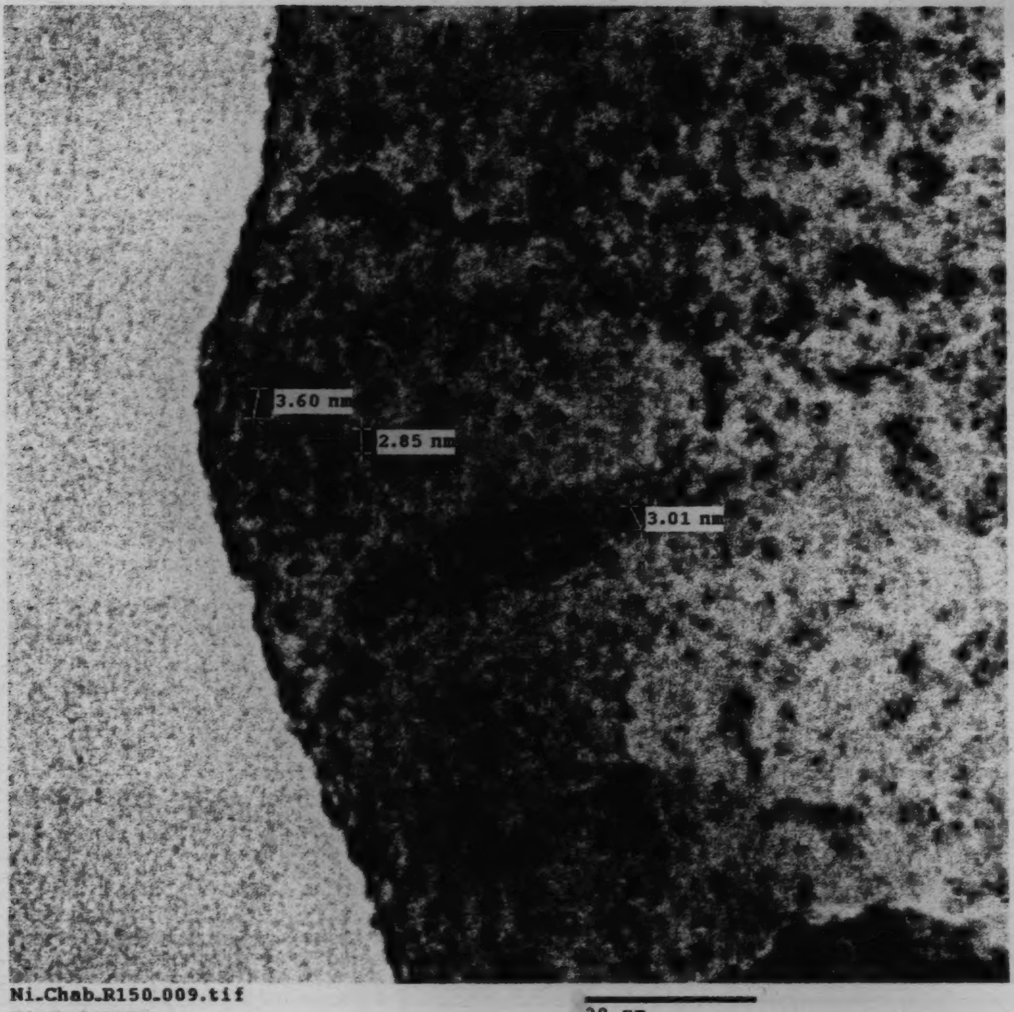
3.60 nm
2.85 nm
3.01 nm
20 nm

Ni_Chab_R150_009.tif
Ni Chab R150
Print Mag: 653000x @ 3. in
2:42 09/13/05
TEM Mode: Imaging

HV=200kV
Direct Mag: 800000x
U of A Physics

Figure B.5: Ni-CHA reduced at 150°C in $H_2$.

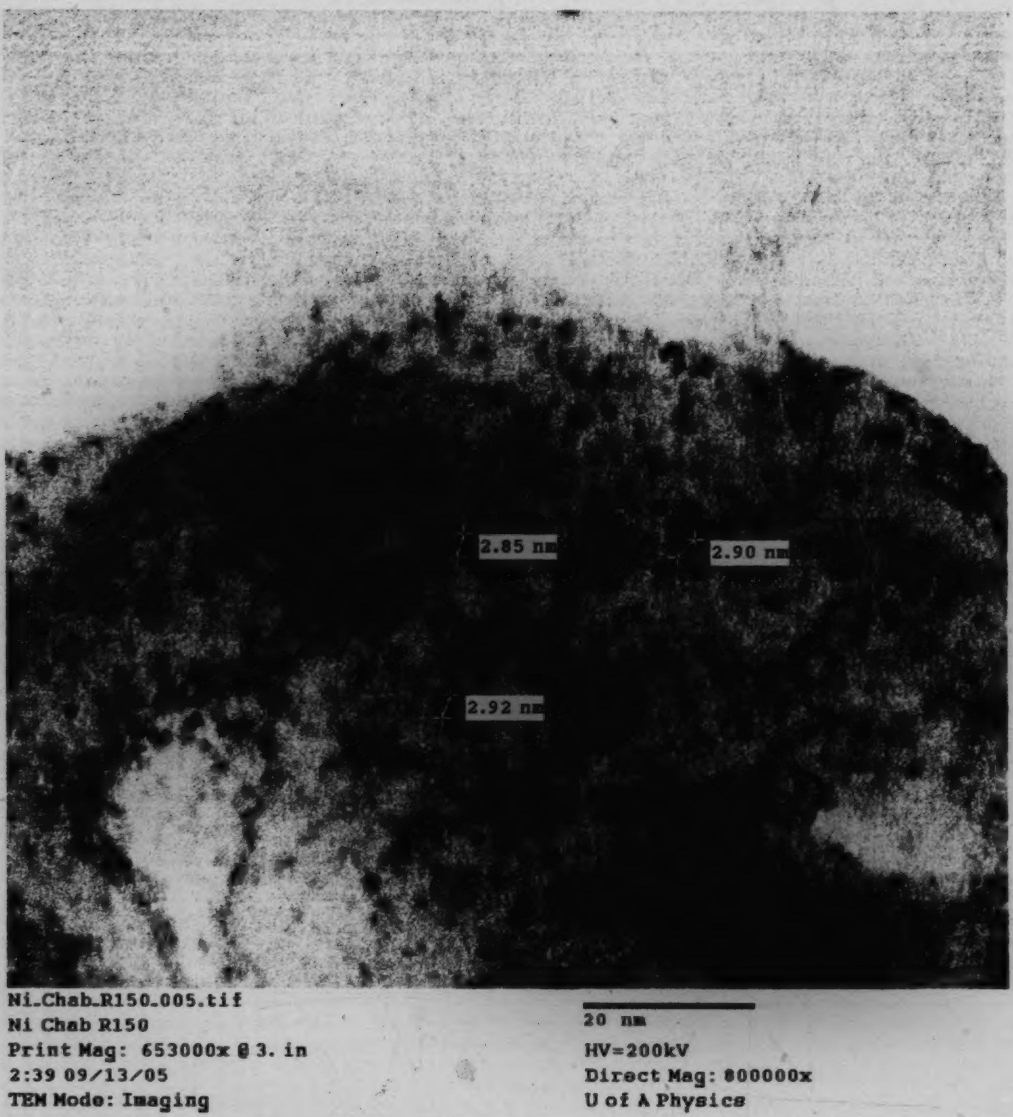
2.85 nm
2.90 nm
2.92 nm
Ni_Chab_R150_005.tif
Ni Chab R150
Print Mag: 653000x @ 3. in
2:39 09/13/05
TEM Mode: Imaging
20 nm
HV=200kV
Direct Mag: 800000x
U of A Physics

Figure B.6: Ni-CHA reduced at 150°C in $H_2$.

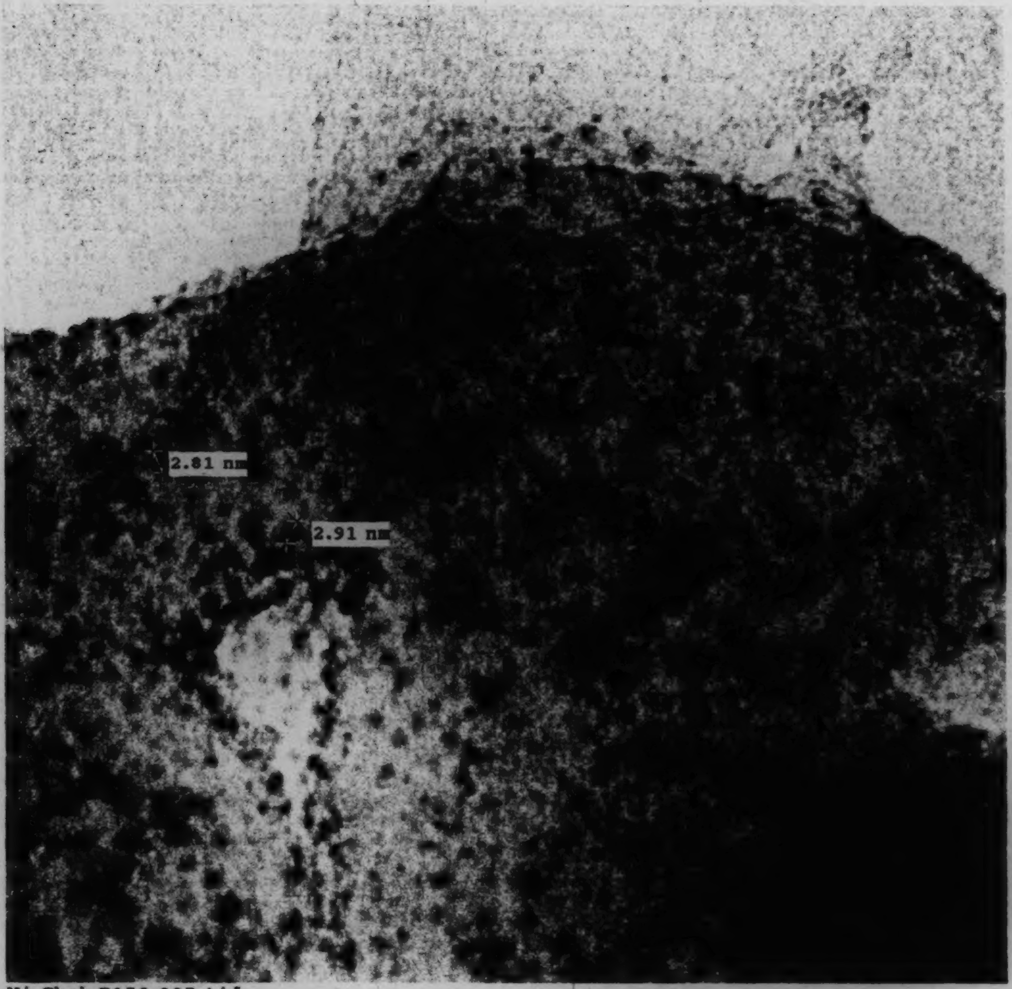

Ni_Chab_R150_007.tif
Ni Chab R150
Print Mag: 653000x @ 3. in
2:40 09/13/05
TEM Mode: Imaging

20 nm
HV=200kV
Direct Mag: 800000x
U of A Physics

Figure B.7: Ni-CHA reduced at 150°C in $H_2$.

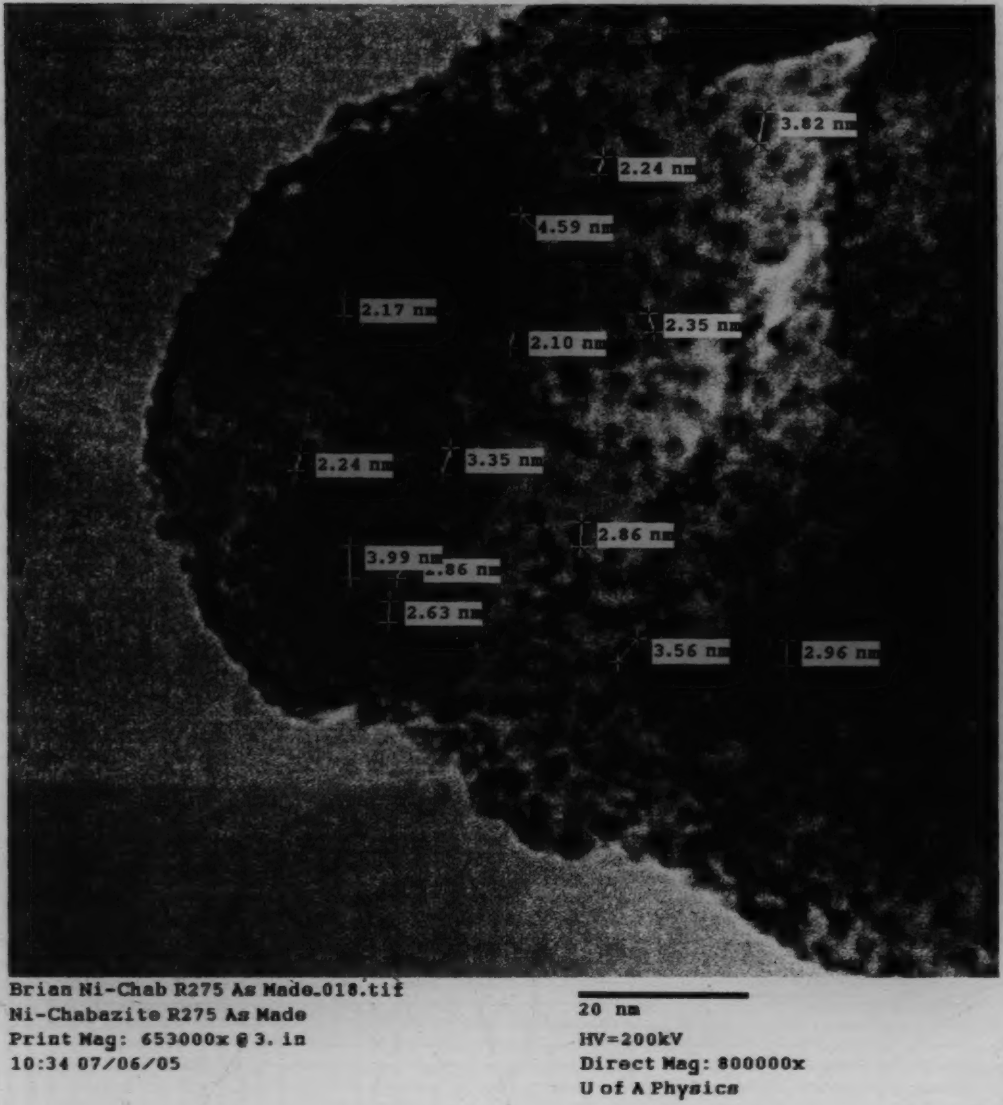
3.82 nm
2.24 nm
4.59 nm
2.17 nm
2.35 nm
2.10 nm
2.24 nm
3.35 nm
2.86 nm
3.99 nm
.86 nm
2.63 nm
3.56 nm
2.96 nm
Brian Ni-Chab R275 As Made_018.tif
Ni-Chabazite R275 As Made
Print Mag: 653000x @ 3. in
10:34 07/06/05
20 nm
HV=200kV
Direct Mag: 800000x
U of A Physics

Figure B.8: Ni-CHA reduced at 275°C in $H_2$.

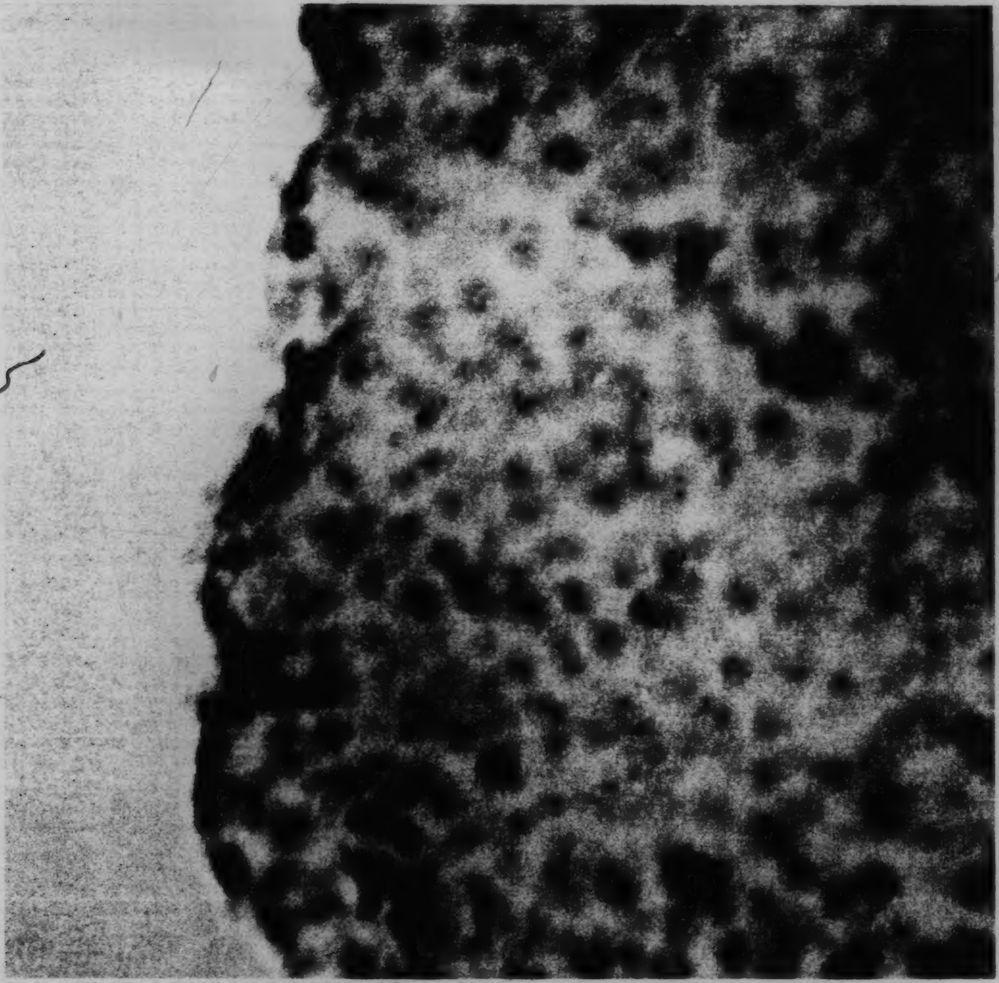

Brian Ni-Chab R275 As Made_012.tif
Ni-Chabazite R275 As Made
Print Mag: 816000x @ 3. in
10:46 07/06/05

5 nm
HV=200kV
Direct Mag: 1000000x
U of A Physics

Figure B.9: Ni-CHA reduced at 275°C in $H_2$.

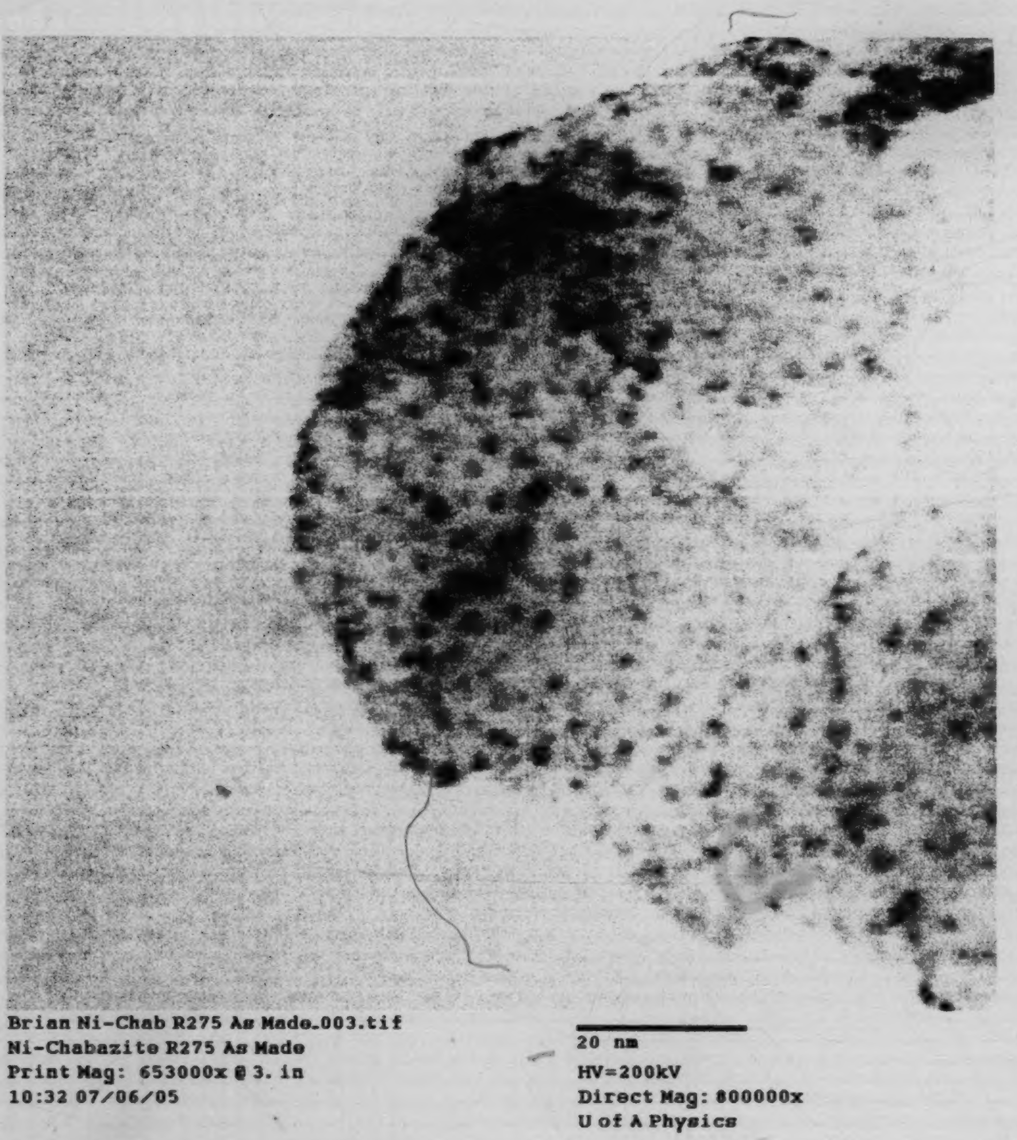
Brian Ni-Chab R275 As Made_003.tif
Ni-Chabazite R275 As Made
Print Mag: 653000x @ 3. in
10:32 07/06/05
20 nm
HV=200kV
Direct Mag: 800000x
U of A Physics

Figure B.10: Ni-CHA reduced at 275°C in $H_2$.

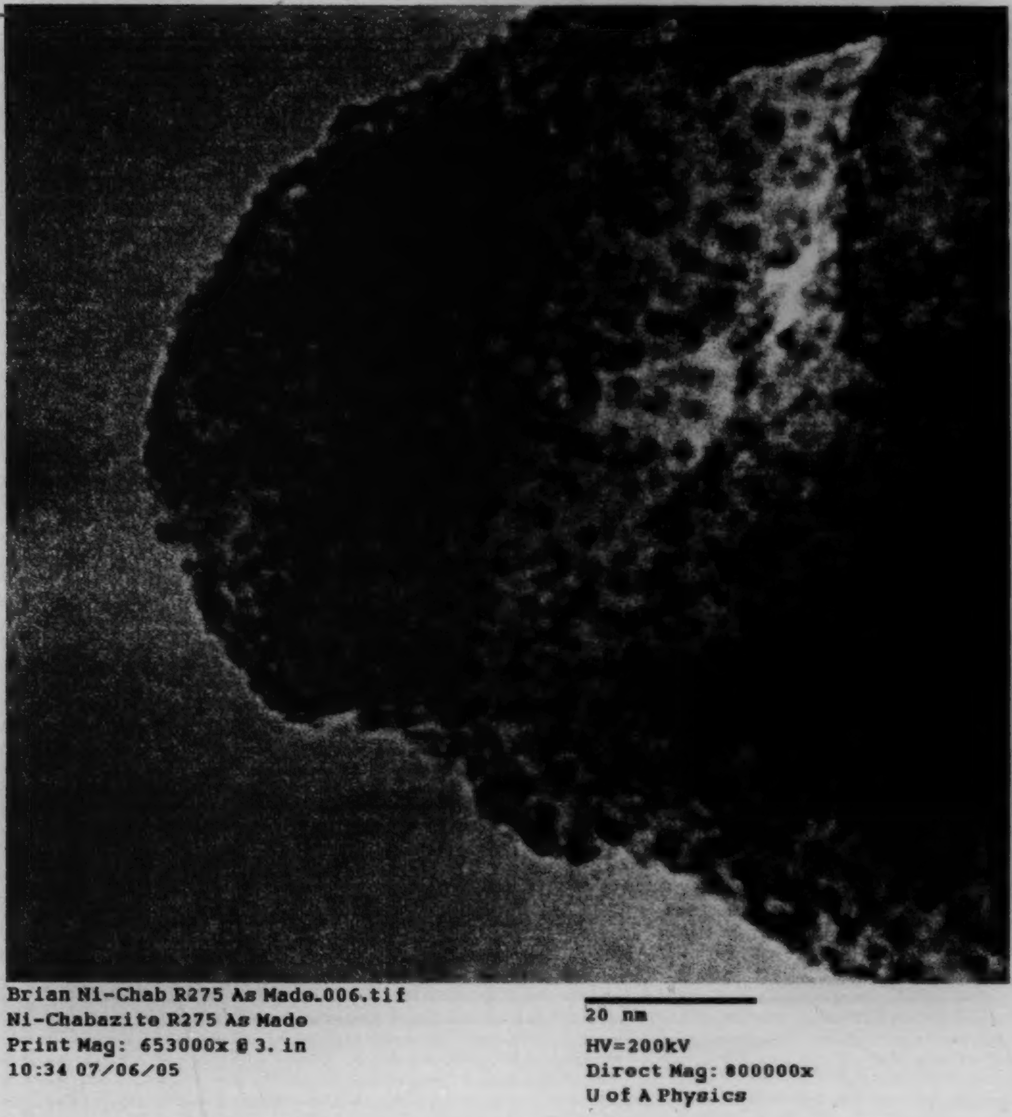
Brian Ni-Chab R275 As Made_006.tif
Ni-Chabazite R275 As Made
Print Mag: 653000x @ 3. in
10:34 07/06/05
20 nm
HV=200kV
Direct Mag: 800000x
U of A Physics

Figure B.11: Ni-CHA reduced at 275°C in $H_2$.

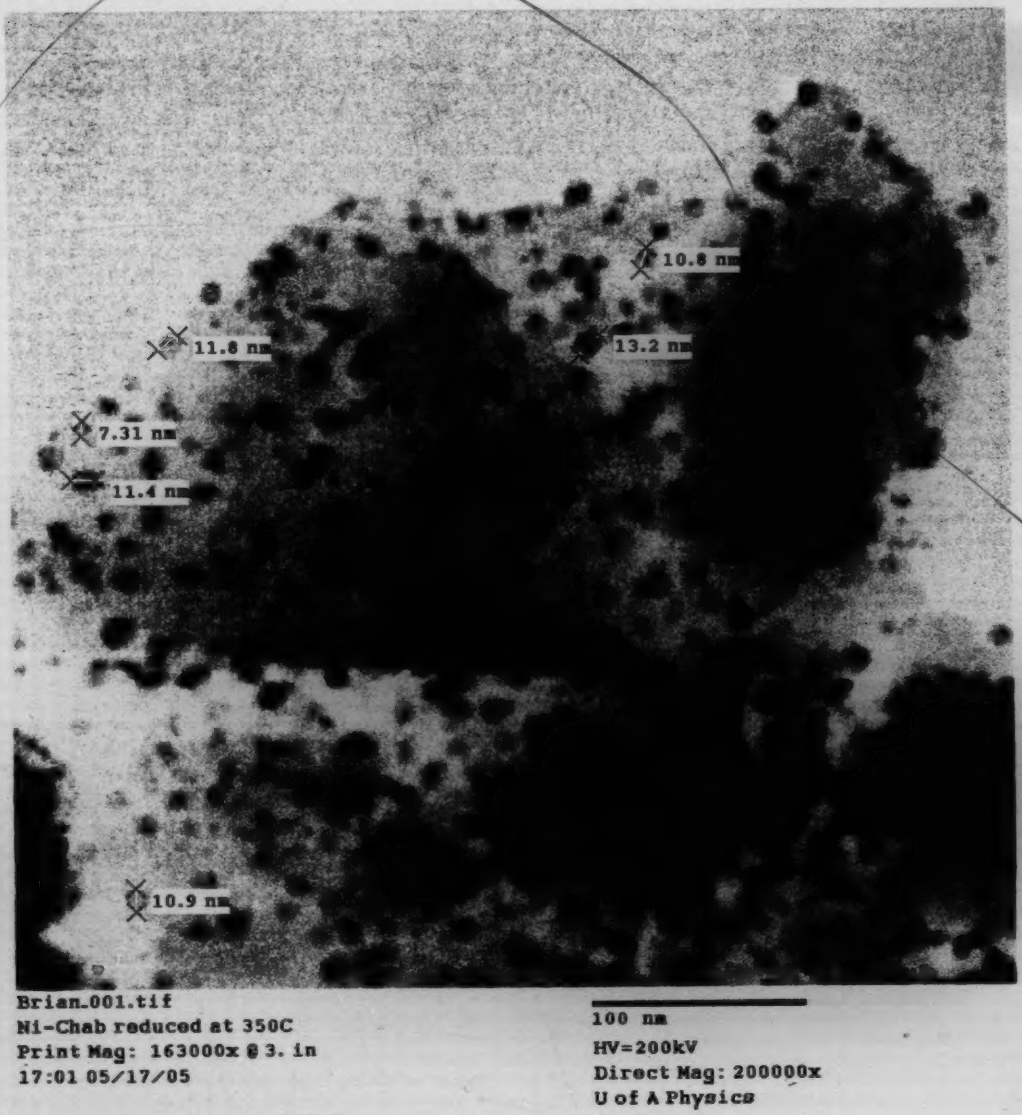
10.8 nm
11.8 nm
13.2 nm
7.31 nm
11.4 nm
10.9 nm
Brian_001.tif
Ni-Chab reduced at 350C
Print Mag: 163000x @ 3. in
17:01 05/17/05
100 nm
HV=200kV
Direct Mag: 200000x
U of A Physics

Figure B.12: Ni-CHA reduced at 350°C in $H_2$.

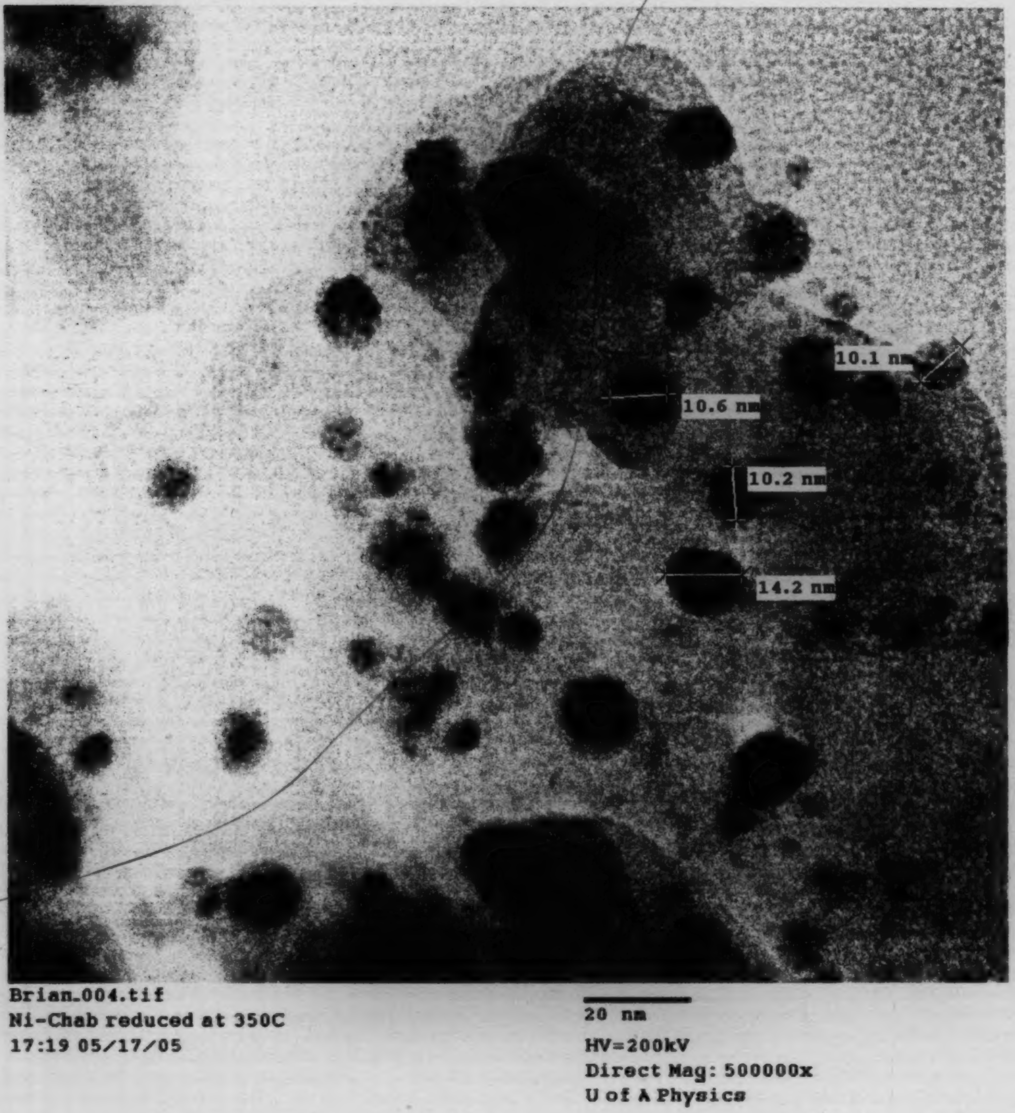
10.1 nm
10.6 nm
10.2 nm
14.2 nm
Brian_004.tif
Ni-Chab reduced at 350C
17:19 05/17/05
20 nm
HV=200kV
Direct Mag: 500000x
U of A Physics

Figure B.13: Ni-CHA reduced at 350°C in $H_2$.

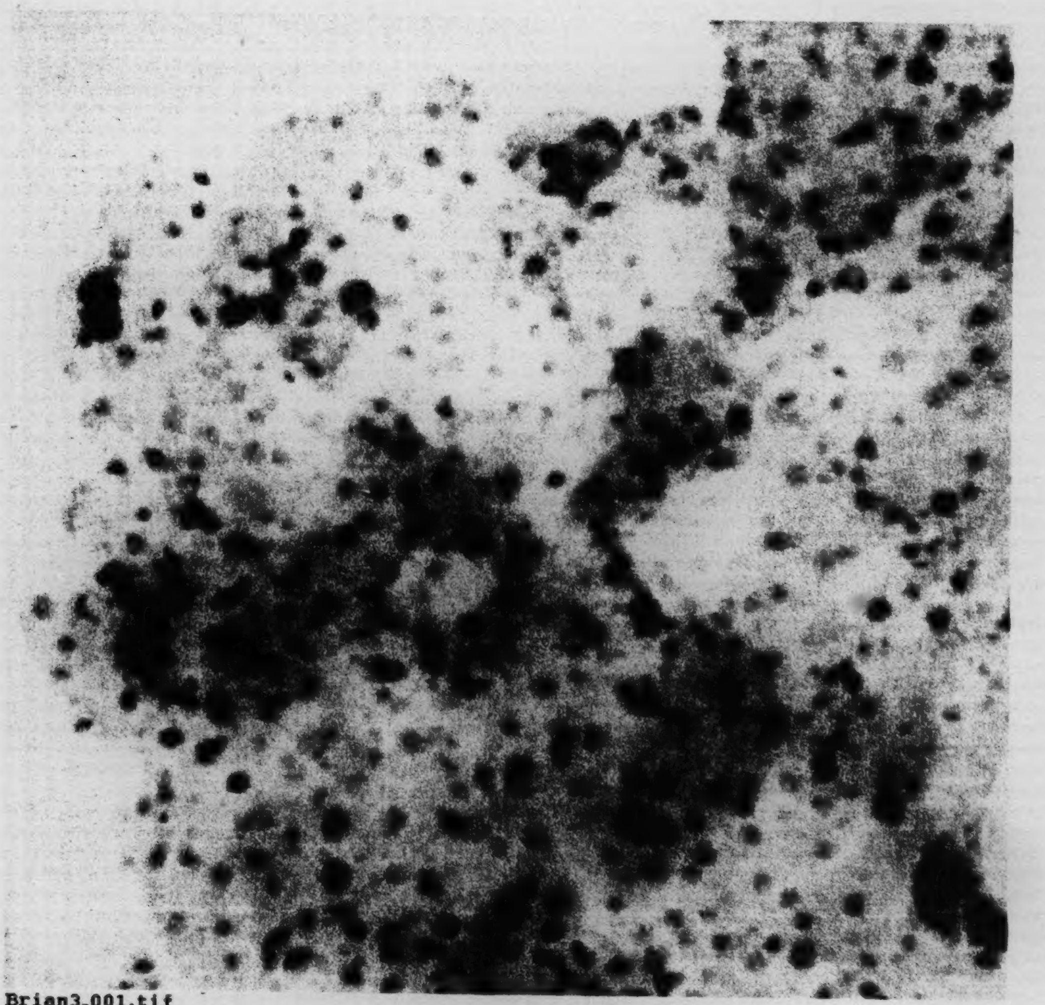
Brian3_001.tif
Ni-Chab reduced at 450C
18:14 05/17/05
100 nm
HV=200kV
Direct Mag: 200000x
U of A Physics

Figure B.14: Ni-CHA reduced at 450°C in $H_2$.

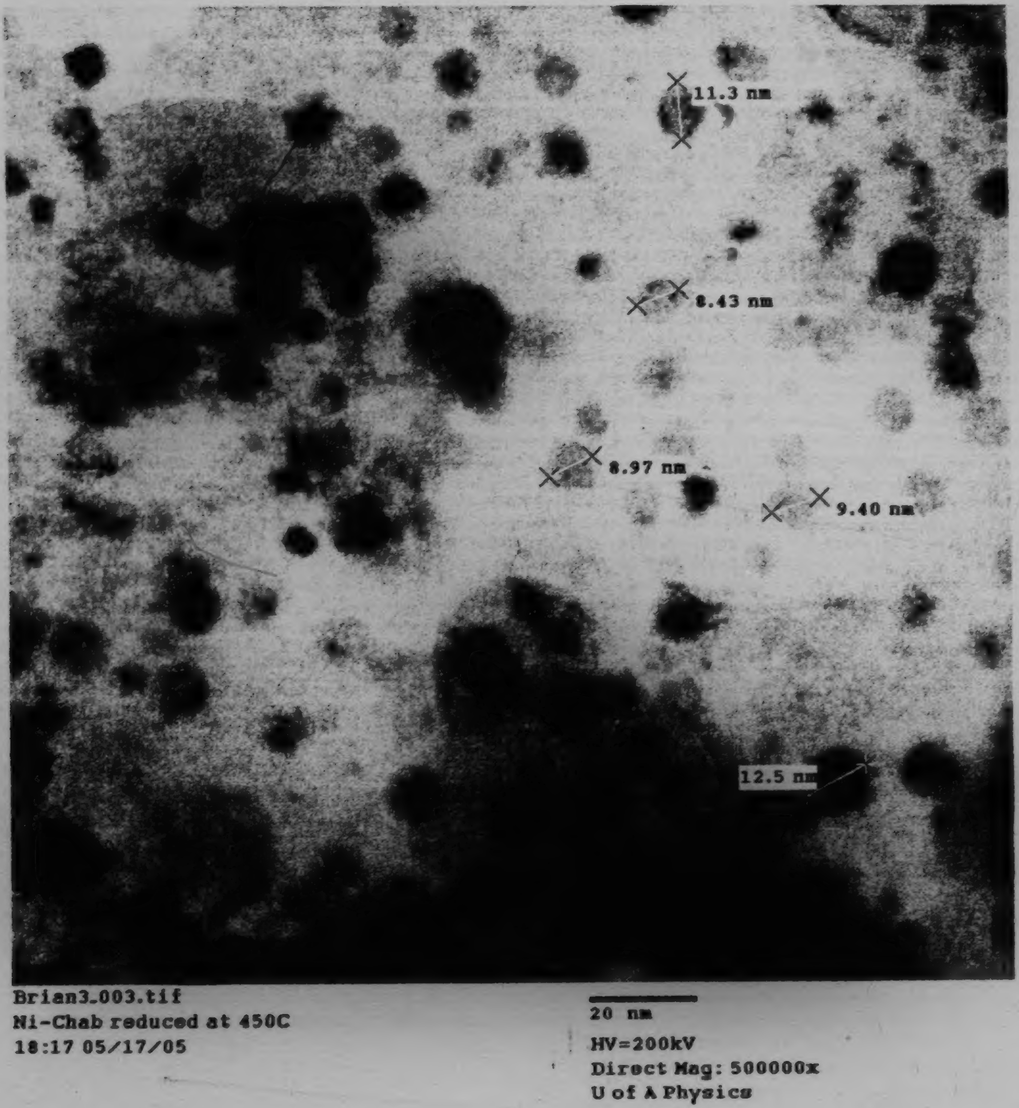
11.3 nm
8.43 nm
8.97 nm
9.40 nm
12.5 nm
Brian3_003.tif
Ni-Chab reduced at 450C
18:17 05/17/05
20 nm
HV=200kV
Direct Mag: 500000x
U of A Physics

Figure B.15: Ni-CHA reduced at 450°C in $H_2$.

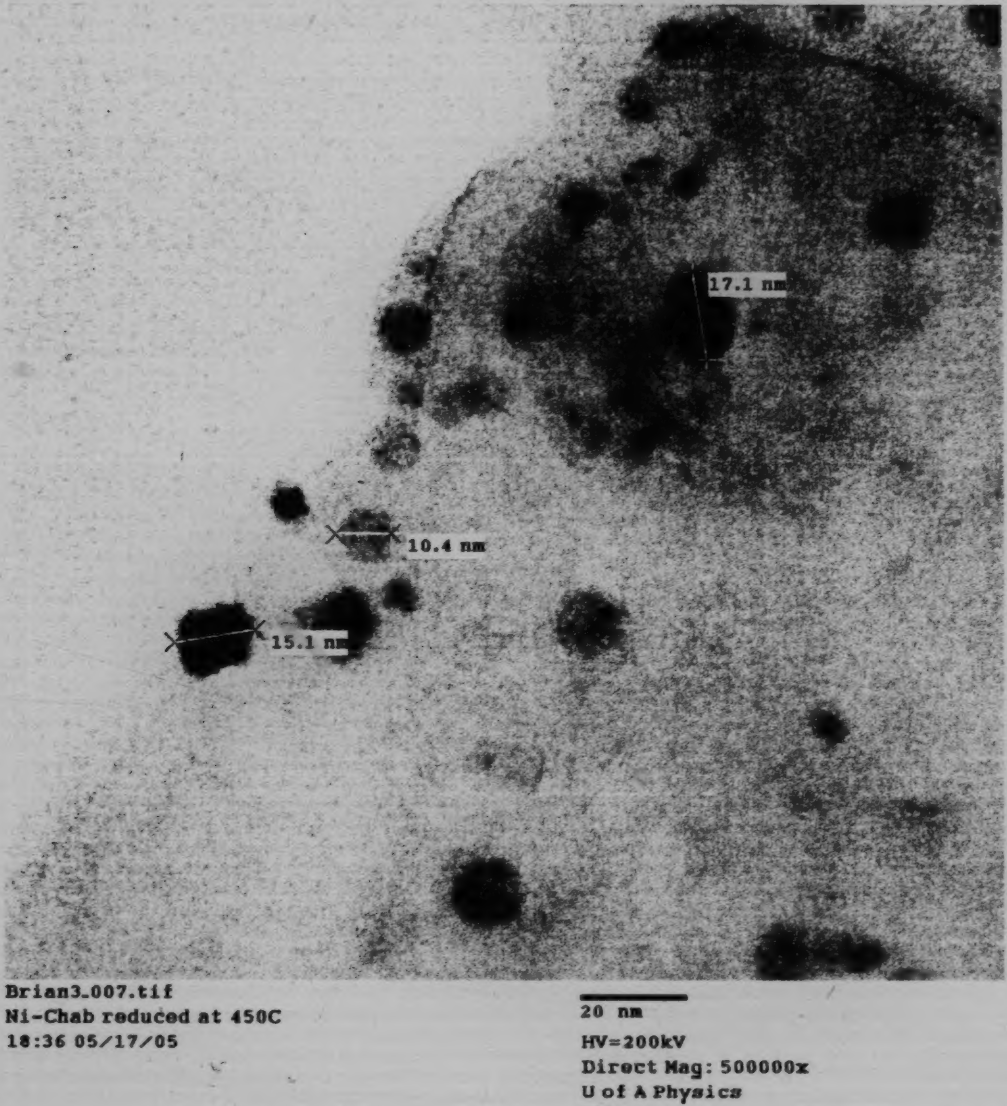
17.1 nm
10.4 nm
15.1 nm
Brian3_007.tif
Ni-Chab reduced at 450C
18:36 05/17/05
20 nm
HV=200kV
Direct Mag: 500000x
U of A Physics

Figure B.16: Ni-CHA reduced at 450°C in $H_2$.

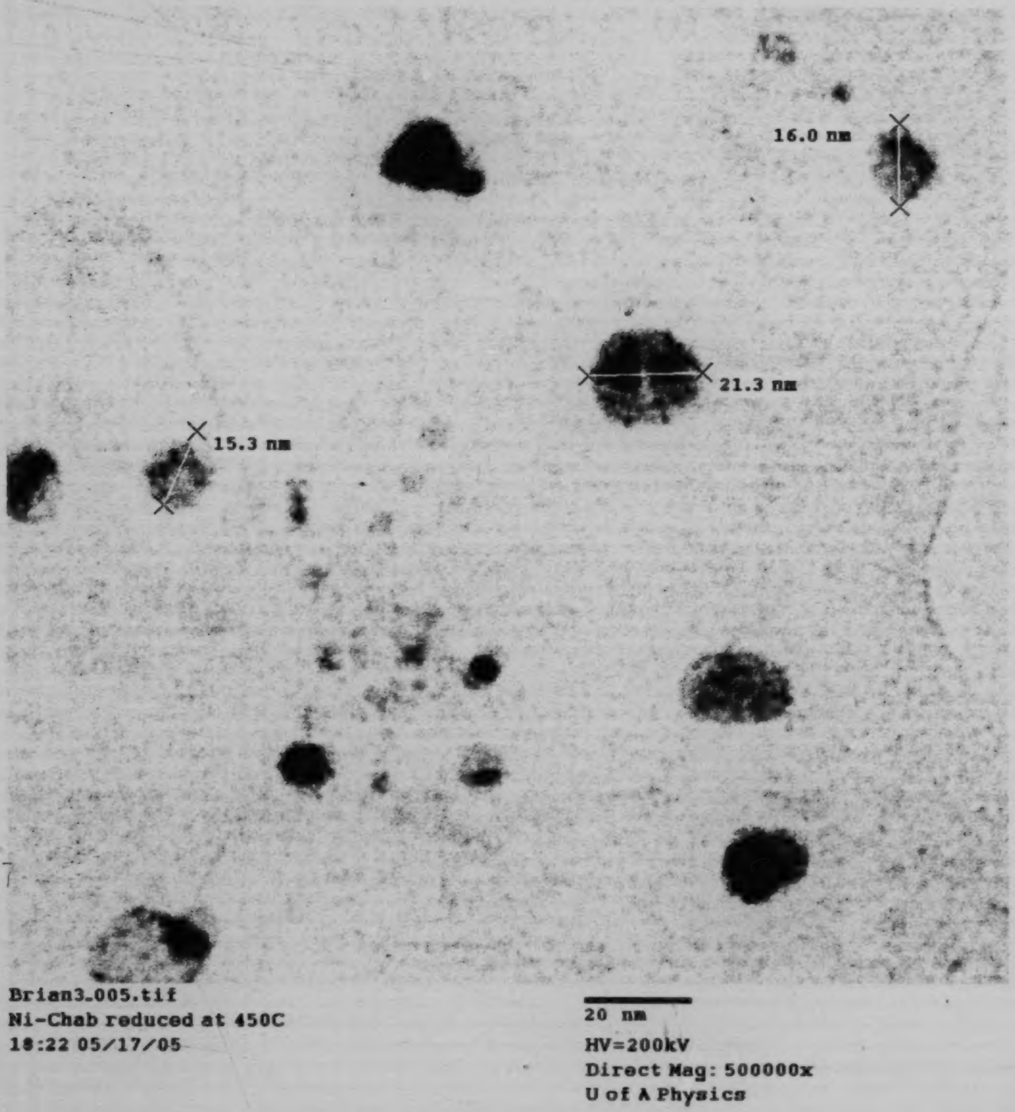
16.0 nm
21.3 nm
15.3 nm
Brian3_005.tif
Ni-Chab reduced at 450C
18:22 05/17/05
20 nm
HV=200kV
Direct Mag: 500000x
U of A Physics

Figure B.17: Ni-CHA reduced at 450°C in $H_2$.

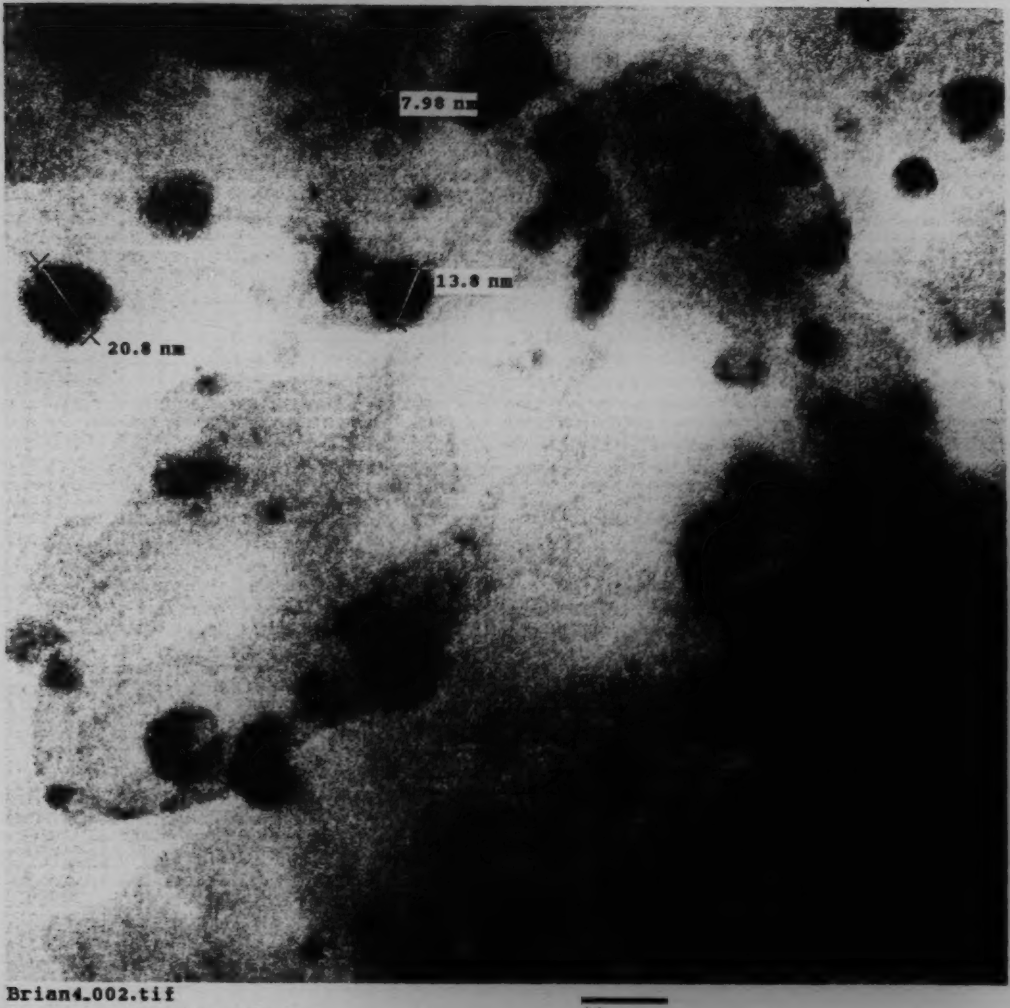
7.98 nm
13.8 nm
20.8 nm
20 nm

Brian4_002.tif
Ni-Chab reduced at 550C
19:08 05/17/05

HV=200kV
Direct Mag: 400000x
U of A Physics

Figure B.18: Ni-CHA reduced at 550°C in $H_2$.

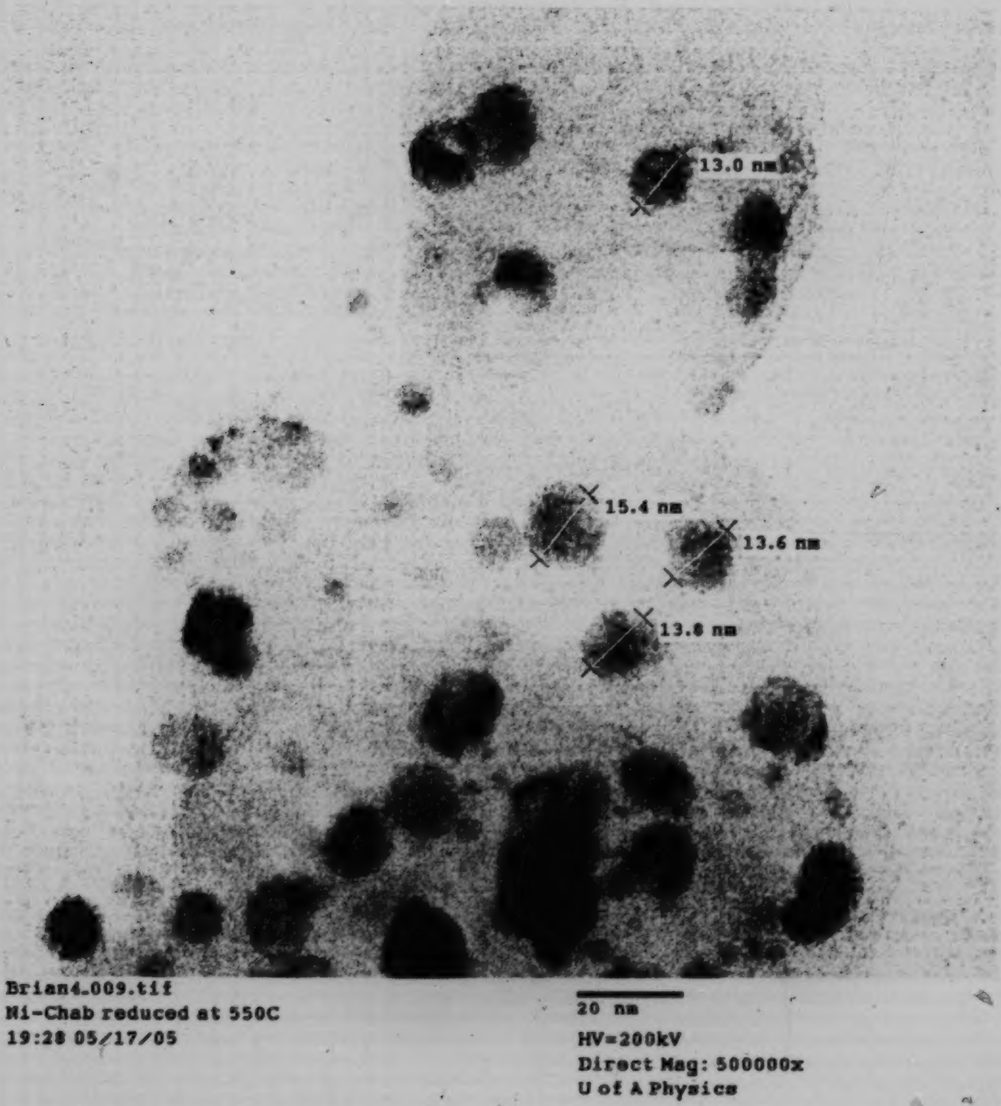
13.0 nm
15.4 nm
13.6 nm
13.8 nm
Brian4_009.tif
Ni-Chab reduced at 550C
19:28 05/17/05
20 nm
HV=200kV
Direct Mag: 500000x
U of A Physics

Figure B.19: Ni-CHA reduced at 550°C in $H_2$.

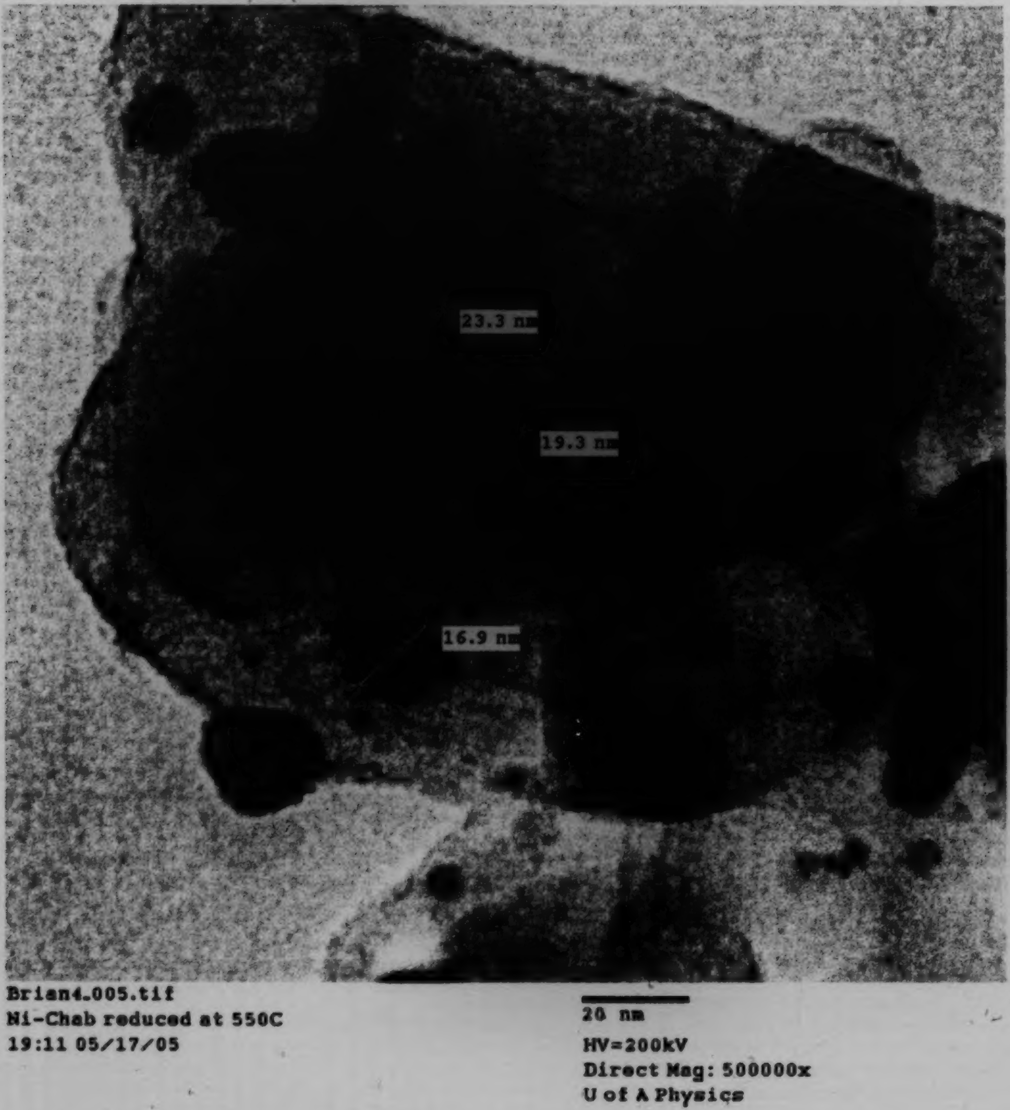
23.3 nm
19.3 nm
16.9 nm
Brian4_005.tif
Ni-Chab reduced at 550C
19:11 05/17/05
20 nm
HV=200kV
Direct Mag: 500000x
U of A Physics

Figure B.20: Ni-CHA reduced at 550°C in $H_2$.

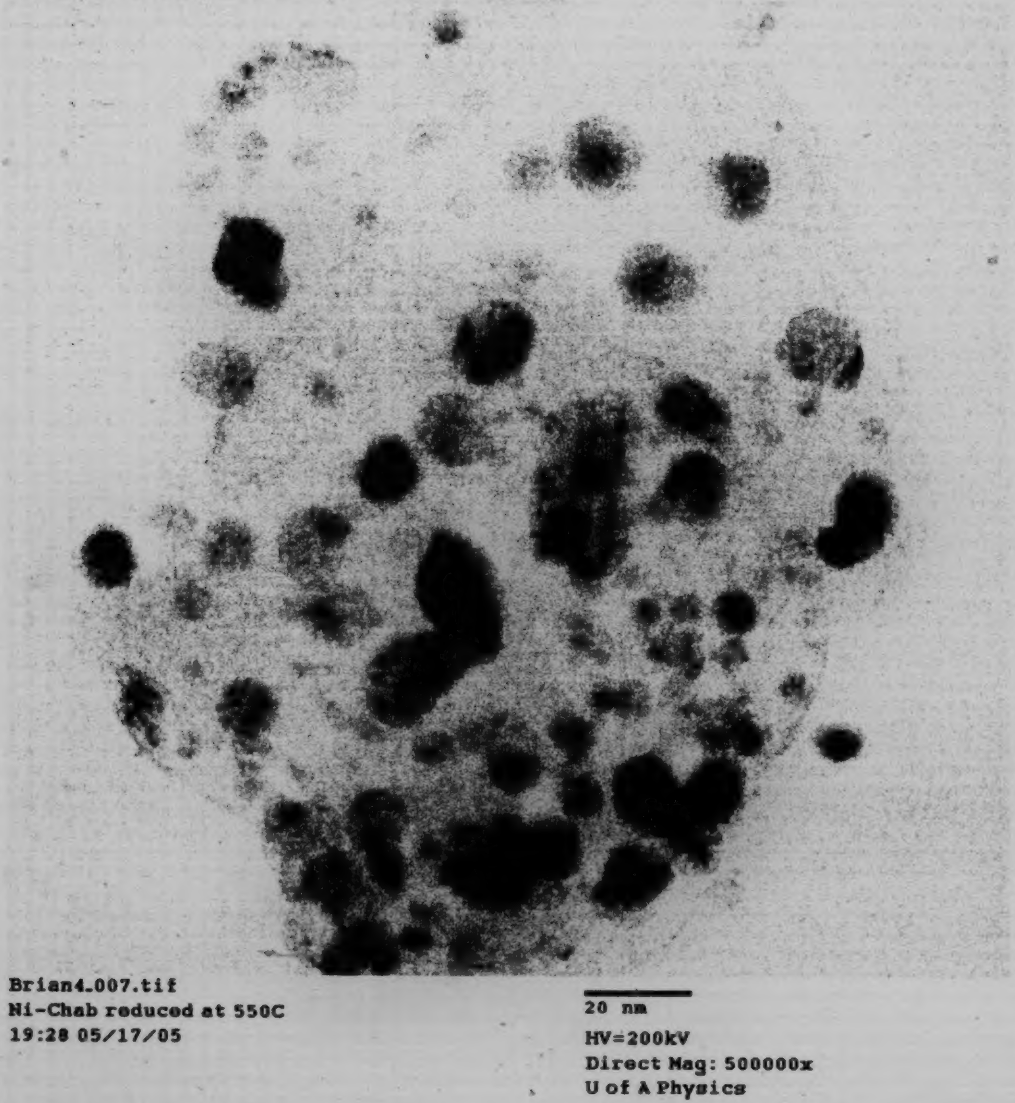
Brian4_007.tif
Ni-Chab reduced at 550C
19:28 05/17/05
20 nm
HV=200kV
Direct Mag: 500000x
U of A Physics

Figure B.21: Ni-CHA reduced at 550°C in $H_2$.

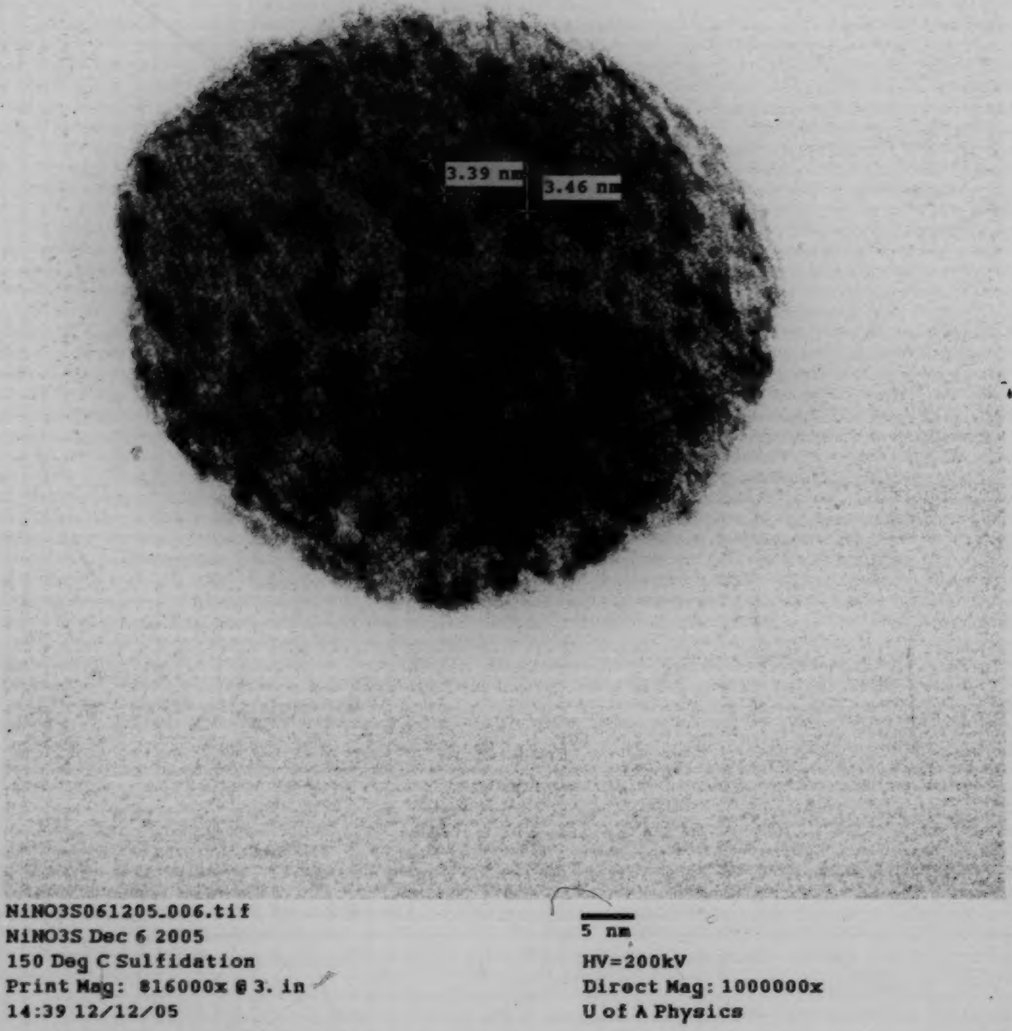
3.39 nm
3.46 nm
NiNO3S061205_006.tif
NiNO3S Dec 6 2005
150 Deg C Sulfidation
Print Mag: 816000x @ 3. in
14:39 12/12/05
5 nm
HV=200kV
Direct Mag: 1000000x
U of A Physics

Figure B.22: Ni-CHA sulfided at 150°C in 10% $H_2S/H_2$.

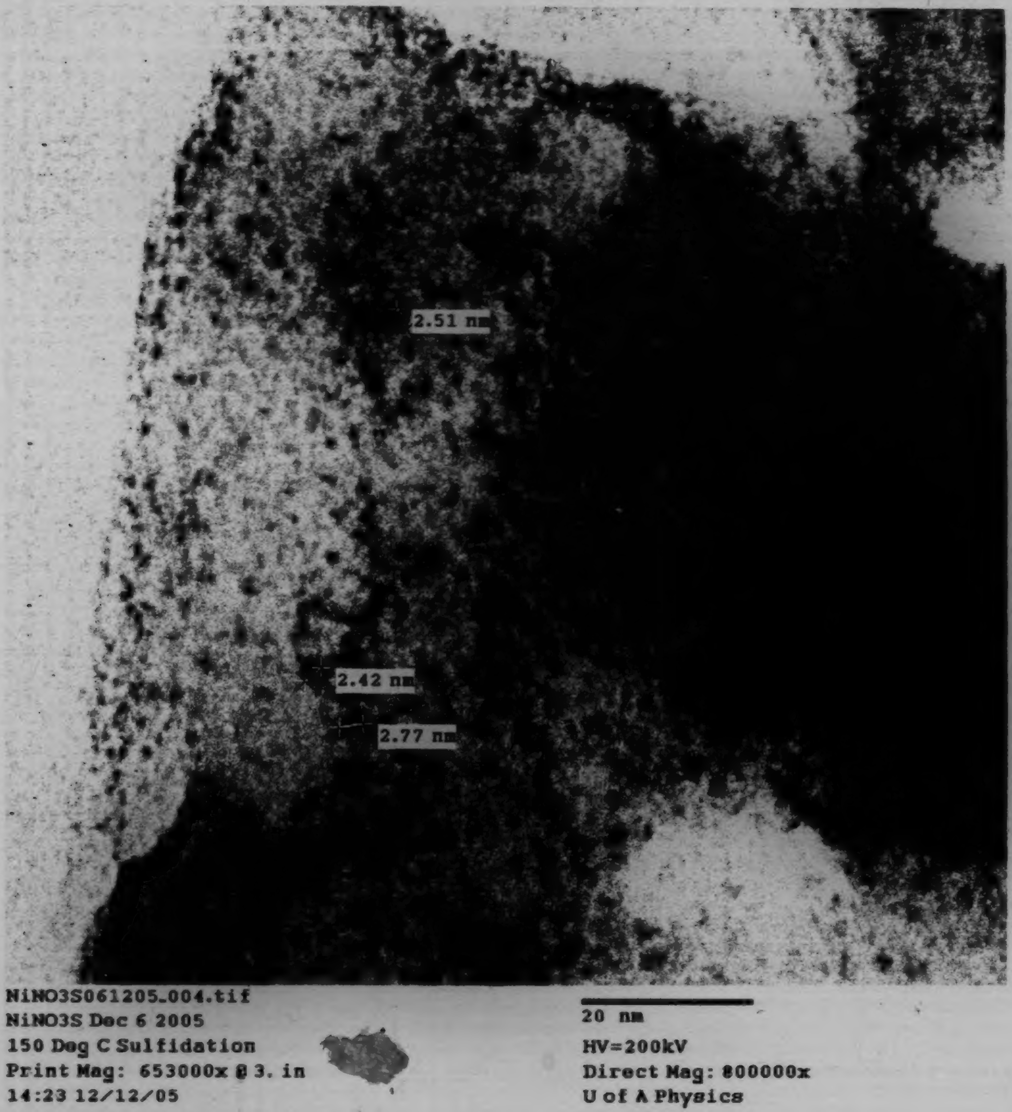
2.51 nm
2.42 nm
2.77 nm
NiNO3S061205_004.tif
NiNO3S Dec 6 2005
150 Deg C Sulfidation
Print Mag: 653000x @ 3. in
14:23 12/12/05
20 nm
HV=200kV
Direct Mag: 800000x
U of A Physics

Figure B.23: Ni-CHA sulfided at 150°C in 10% $H_2S/H_2$.

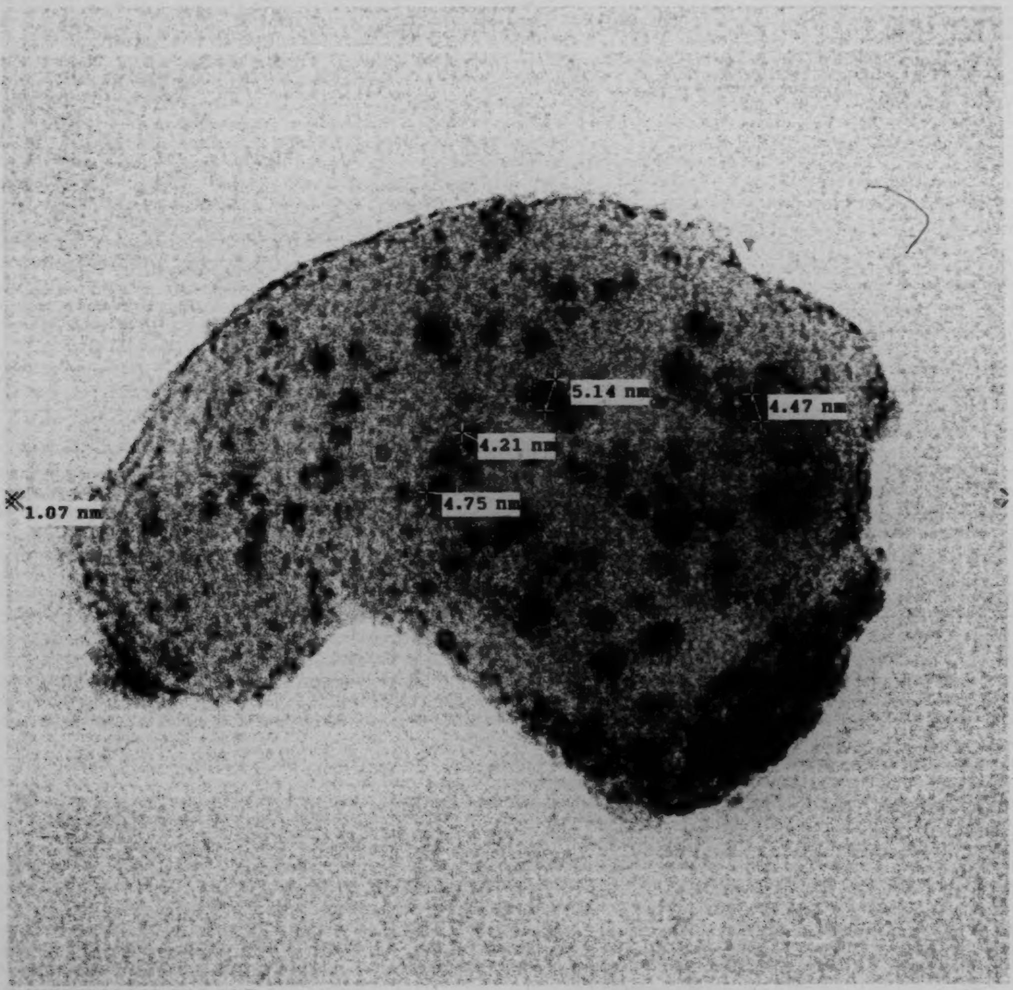
5.14 nm
4.47 nm
4.21 nm
4.75 nm
1.07 nm

NiNO3S051205_004.tif
NiNO3SCHA
Dec 5 05
Print Mag: 490000x @ 3. in
14:06 12/14/05

20 nm
HV=200kV
Direct Mag: 600000x
U of A Physics

Figure B.24: Ni-CHA sulfided at 250°C in 10% $H_2S/H_2$.

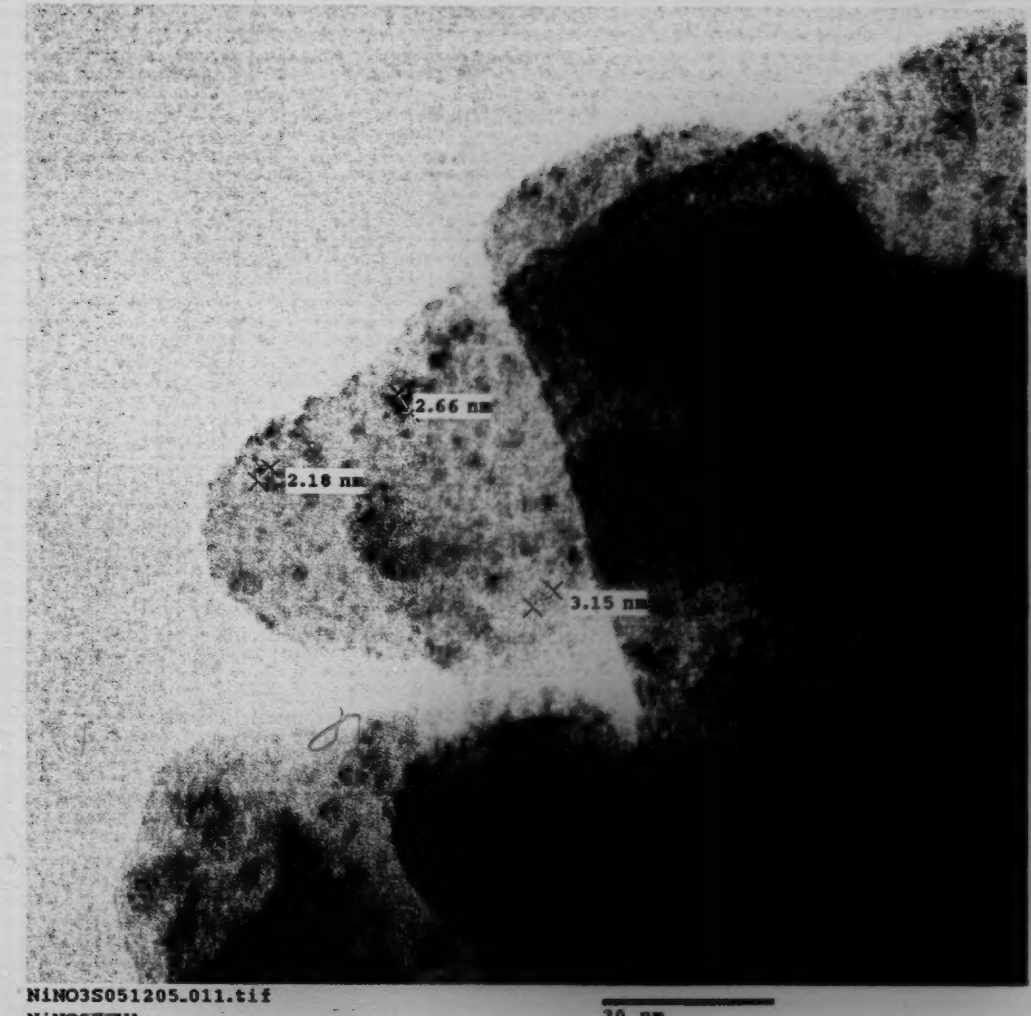
2.66 nm
2.18 nm
3.15 nm
20 nm

NiNO3S051205_011.tif
NiNO3SCHA
Dec 5 05
Print Mag: 653000x @ 3. in
14:46 12/14/05

HV=200kV
Direct Mag: 800000x
U of A Physics

Figure B.25: Ni-CHA sulfided at 250°C in 10% $H_2S/H_2$.

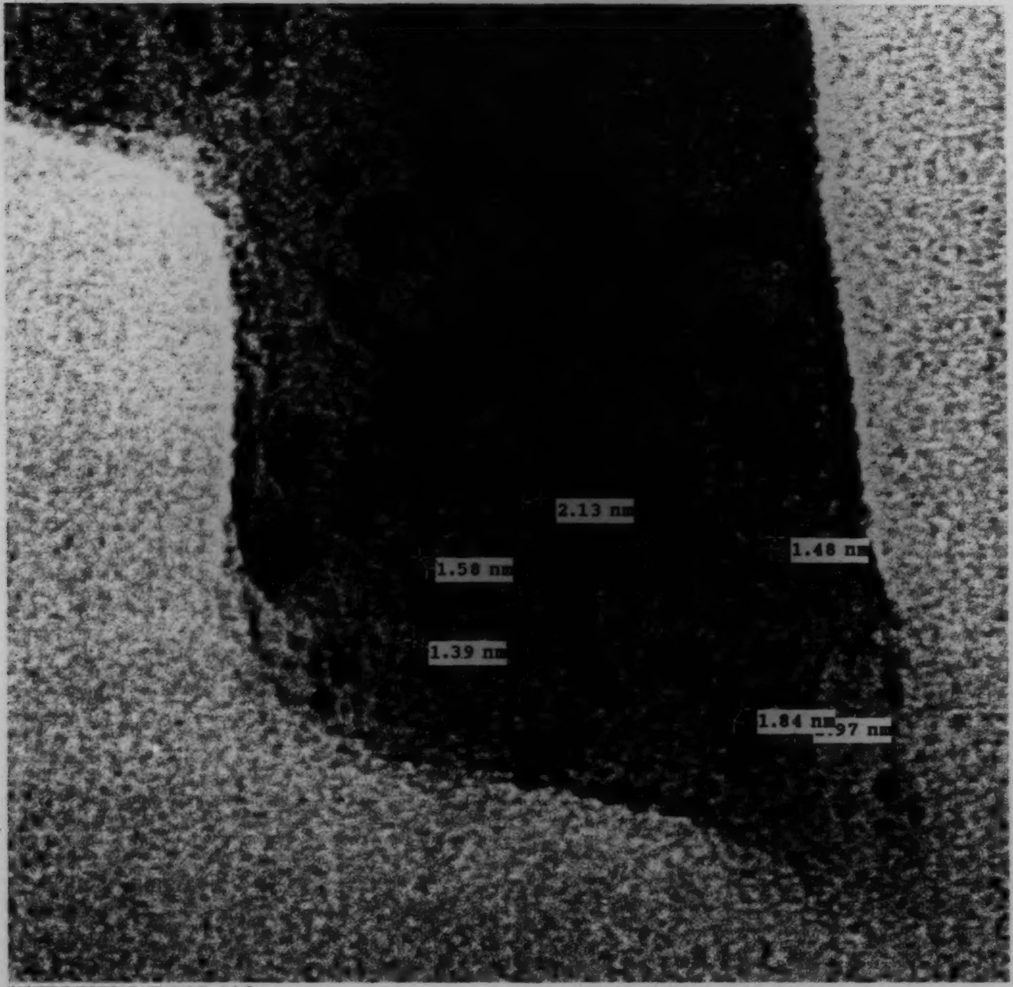
2.13 nm
1.48 nm
1.58 nm
1.39 nm
1.84 nm
.97 nm

NiNO3S051205_007.tif
NiNO3SCHA
Dec 5 05
Print Mag: 653000x @ 3. in
14:20 12/14/05

20 nm
HV=200kV
Direct Mag: 800000x
U of A Physics

Figure B.26: Ni-CHA sulfided at 250°C in 10% $H_2S/H_2$.

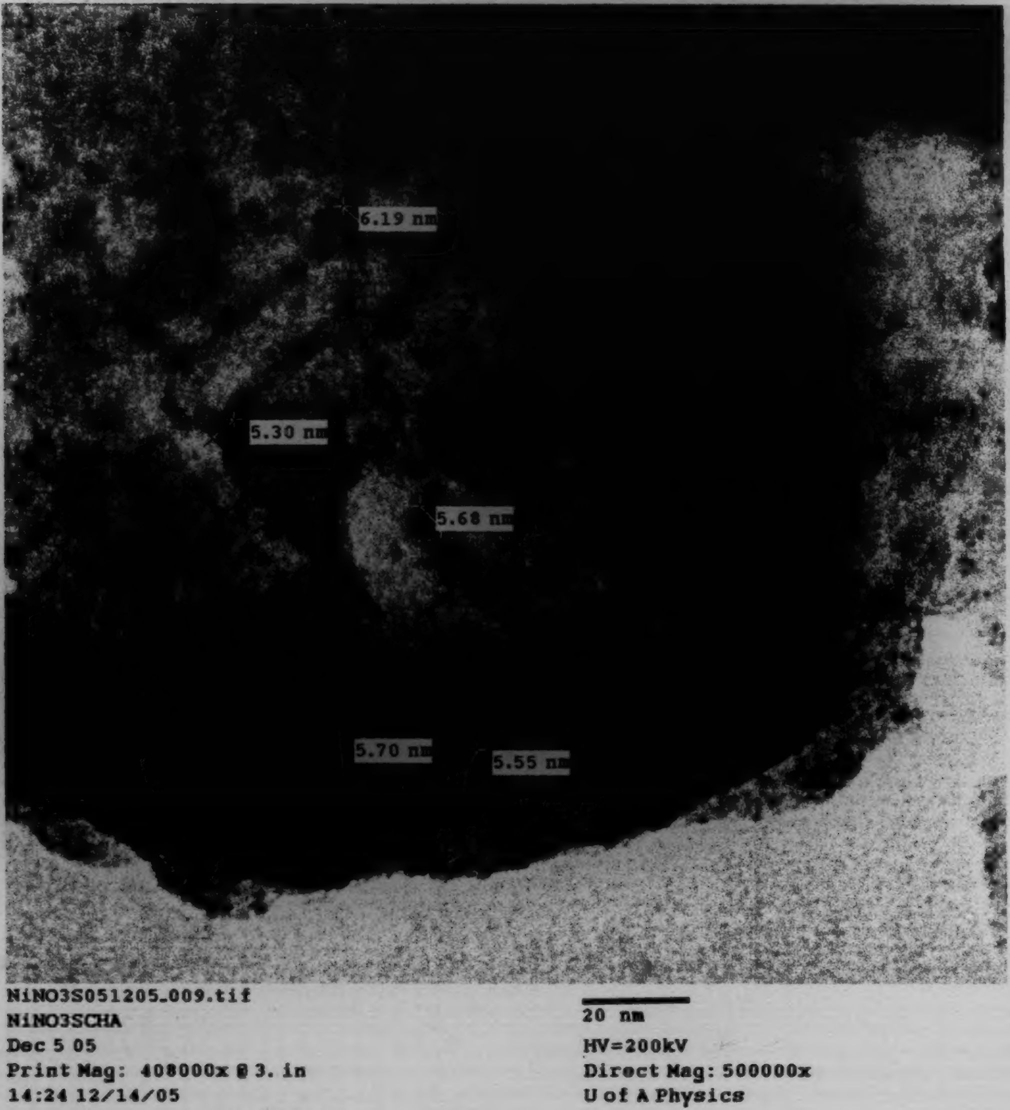
6.19 nm
5.30 nm
5.68 nm
5.70 nm
5.55 nm
NiNO3S051205_009.tif
NiNO3SCHA
Dec 5 05
Print Mag: 408000x @ 3. in
14:24 12/14/05
20 nm
HV=200kV
Direct Mag: 500000x
U of A Physics

Figure B.27: Ni-CHA sulfided at 250°C in 10% $H_2S/H_2$.

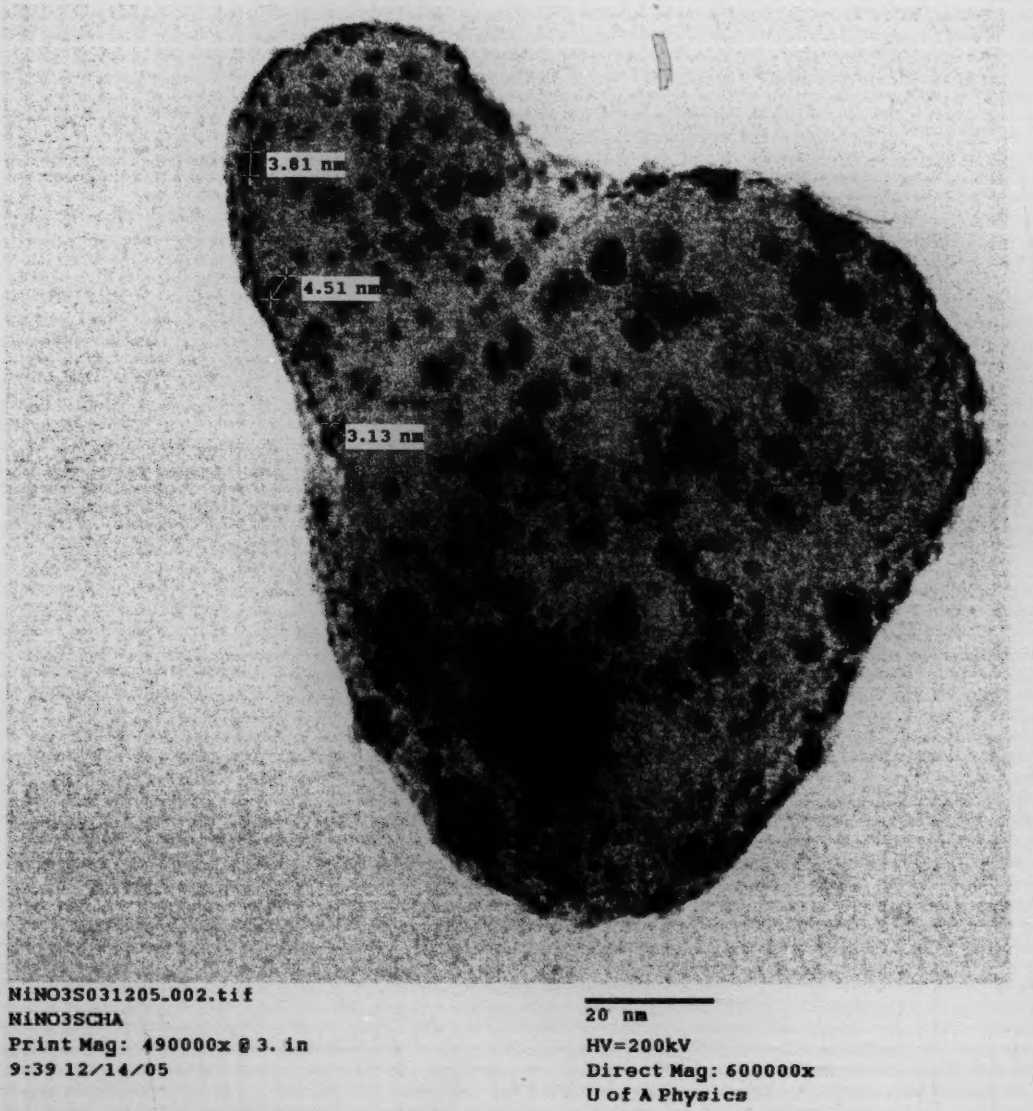
3.81 nm
4.51 nm
3.13 nm
NiNO3S031205_002.tif
NiNO3SCHA
Print Mag: 490000x @ 3. in
9:39 12/14/05
20 nm
HV=200kV
Direct Mag: 600000x
U of A Physics

Figure B.28: Ni-CHA sulfided at 350°C in 10% $H_2S/H_2$.

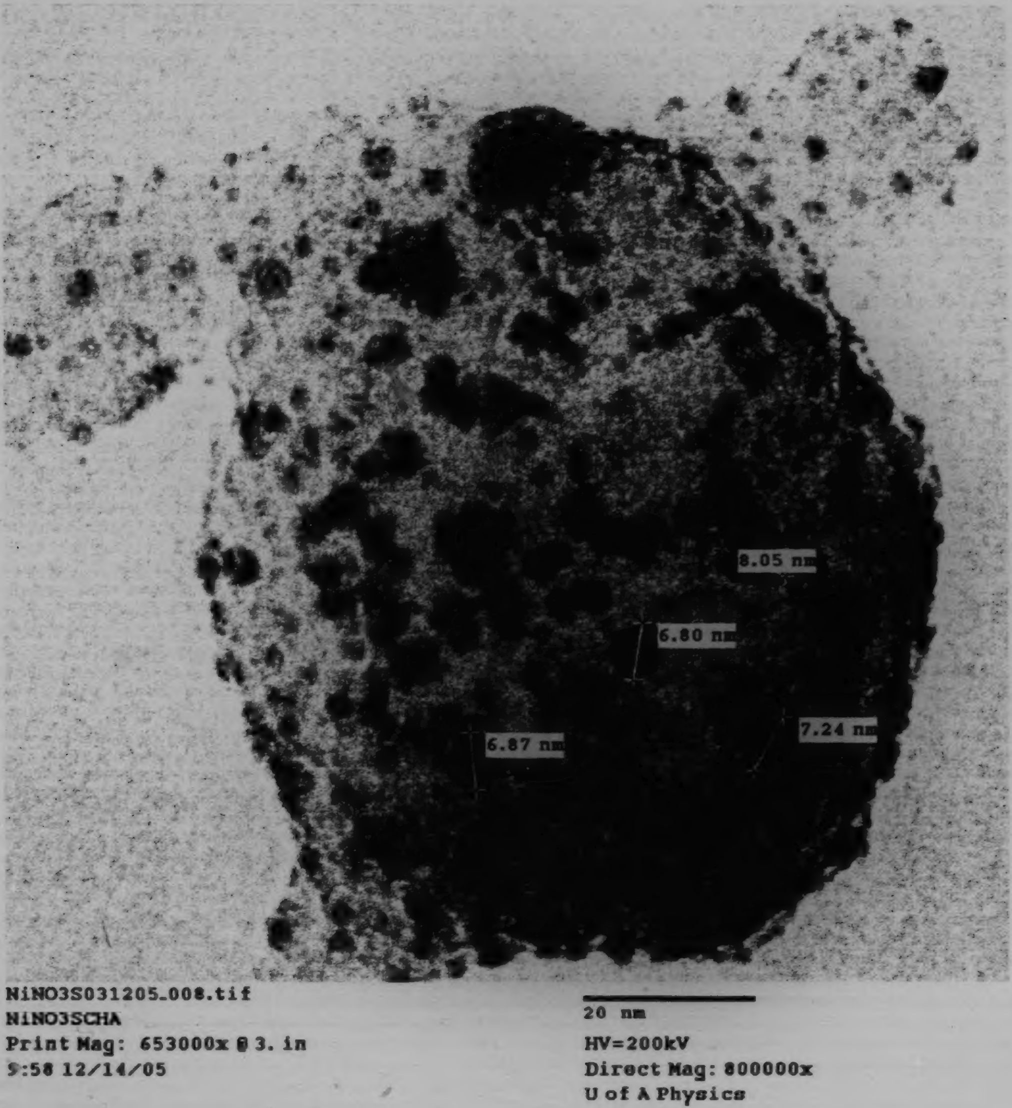
8.05 nm
6.80 nm
6.87 nm
7.24 nm
NiNO3S031205_008.tif
NiNO3SCHA
Print Mag: 653000x @ 3. in
9:58 12/14/05
20 nm
HV=200kV
Direct Mag: 800000x
U of A Physics

Figure B.29: Ni-CHA sulfided at 350°C in 10% $H_2S/H_2$.

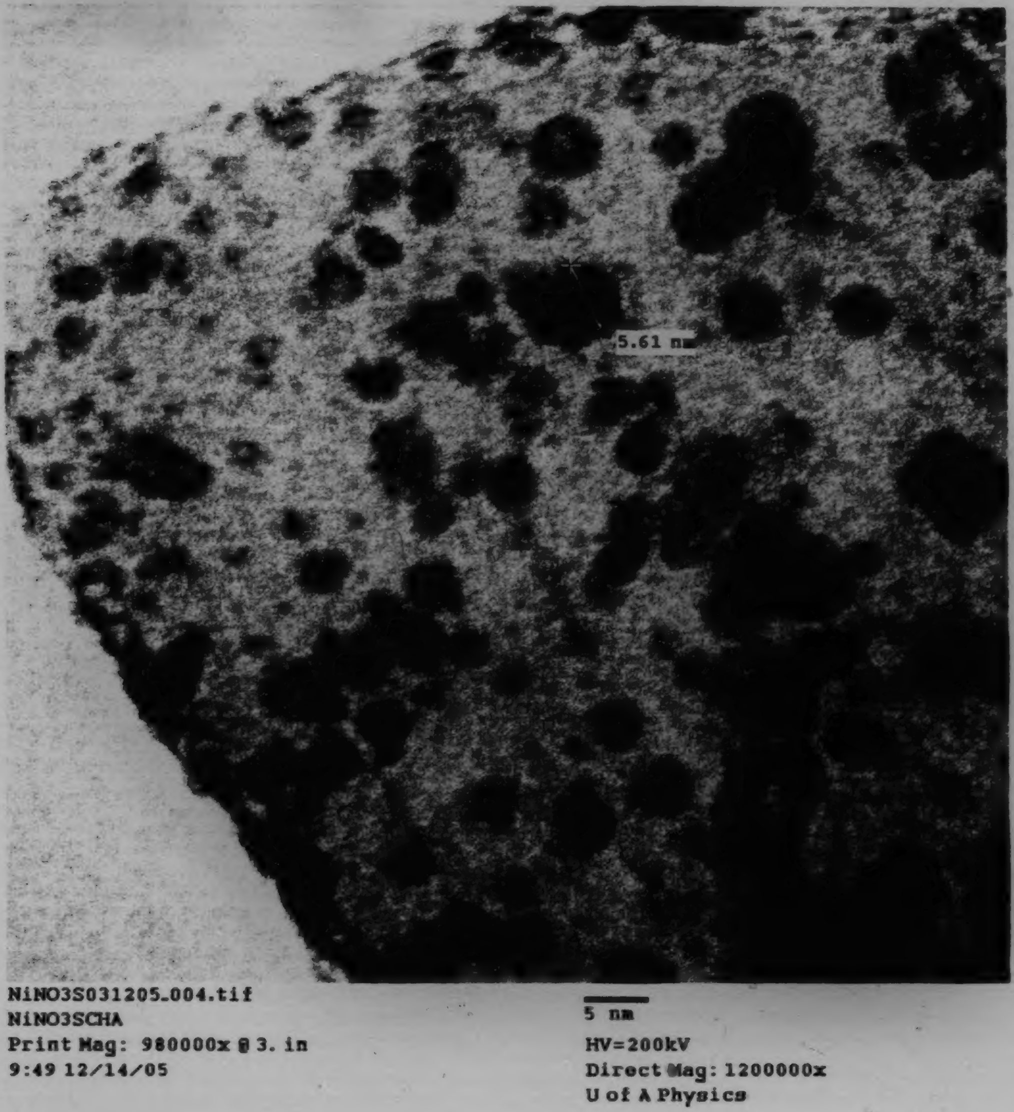
5.61 nm
NiNO3S031205_004.tif
NiNO3SCHA
Print Mag: 980000x @ 3. in
9:49 12/14/05
5 nm
HV=200kV
Direct Mag: 1200000x
U of A Physics

Figure B.30: Ni-CHA sulfided at 350°C in 10% $H_2S/H_2$.

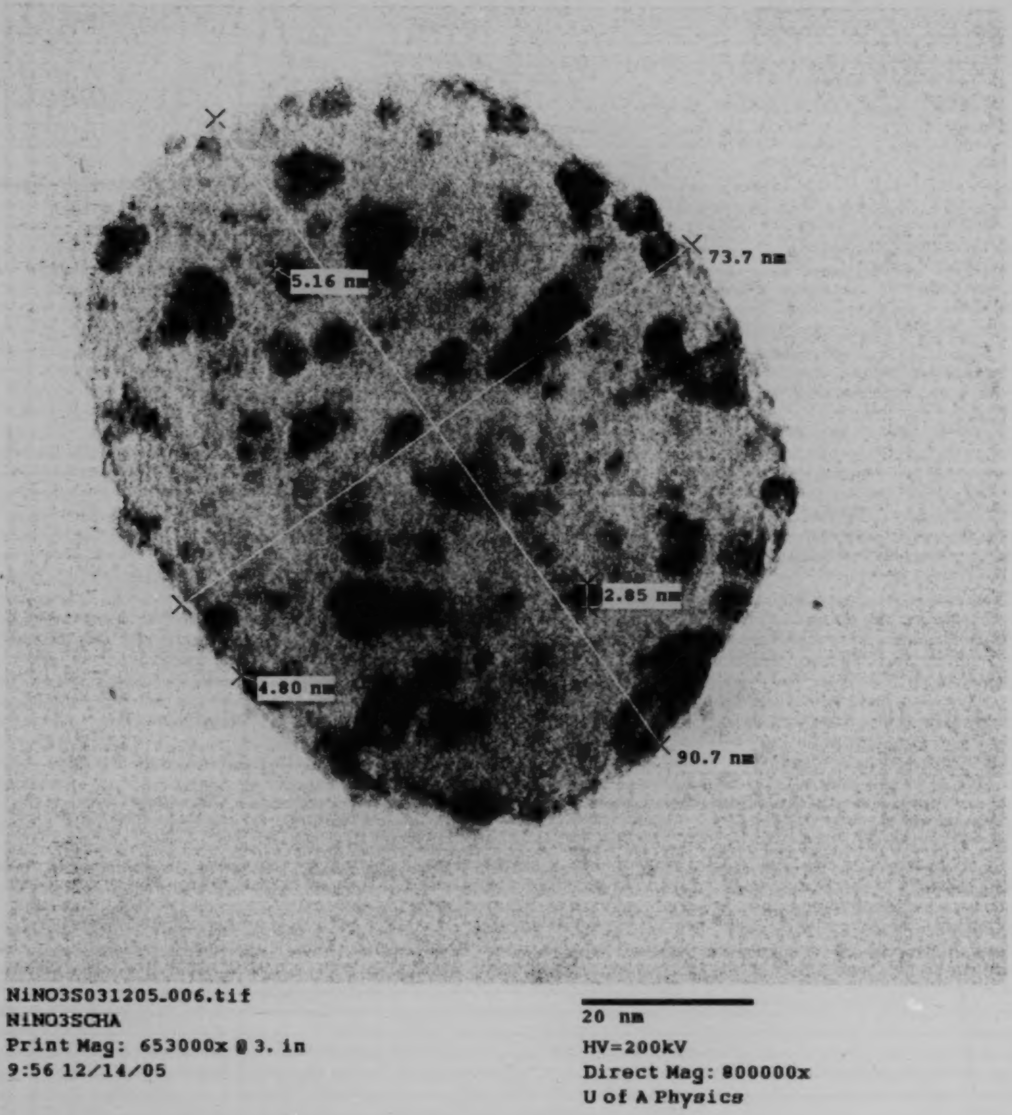
5.16 nm
73.7 nm
2.85 nm
4.80 nm
90.7 nm
NiNO3S031205_006.tif
NiNO3SCHA
Print Mag: 653000x @ 3. in
9:56 12/14/05
20 nm
HV=200kV
Direct Mag: 800000x
U of A Physics

Figure B.31: Ni-CHA sulfided at 350°C in 10% $H_2S/H_2$.

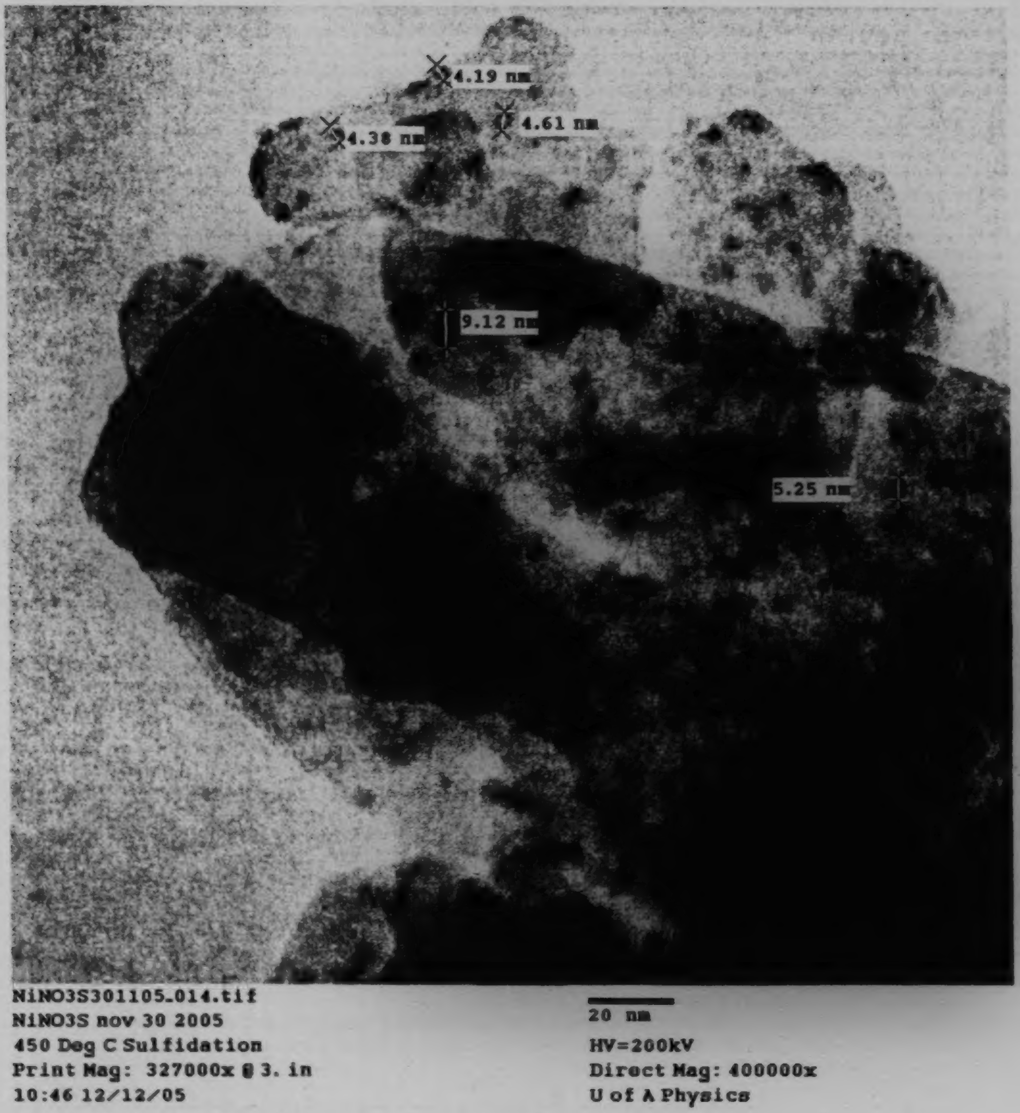
4.19 nm
4.38 nm
4.61 nm
9.12 nm
5.25 nm
NiNO3S301105_014.tif
NiNO3S nov 30 2005
450 Deg C Sulfidation
Print Mag: 327000x @ 3. in
10:46 12/12/05
20 nm
HV=200kV
Direct Mag: 400000x
U of A Physics

Figure B.32: Ni-CHA sulfided at 450°C in 10% $H_2S/H_2$.

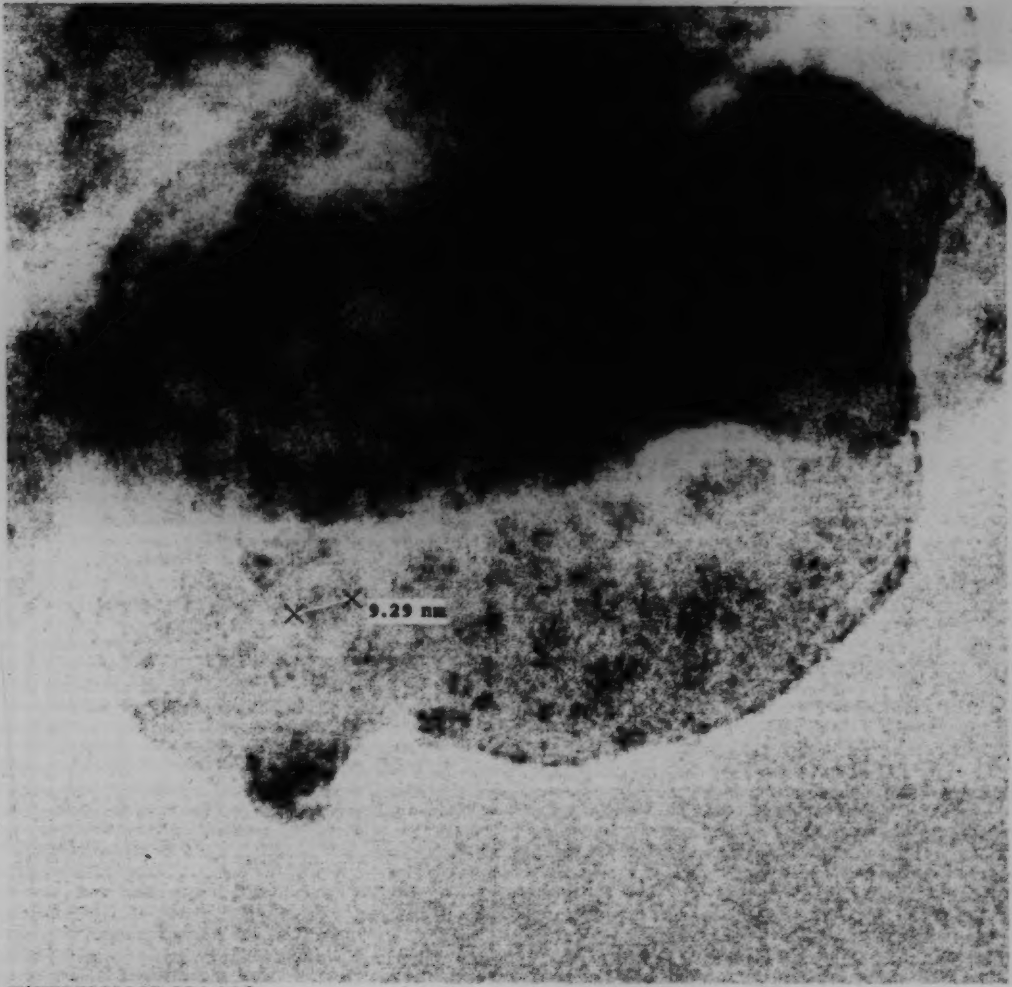

NiNO3S301105_004.tif
NiNO3S nov 30 2005
450 Deg C Sulfidation
Print Mag: 490000x @ 3. in
10:09 12/12/05

20 nm
HV=200kV
Direct Mag: 600000x
U of A Physics

Figure B.33: Ni-CHA sulfided at 450°C in 10% $H_2S/H_2$.

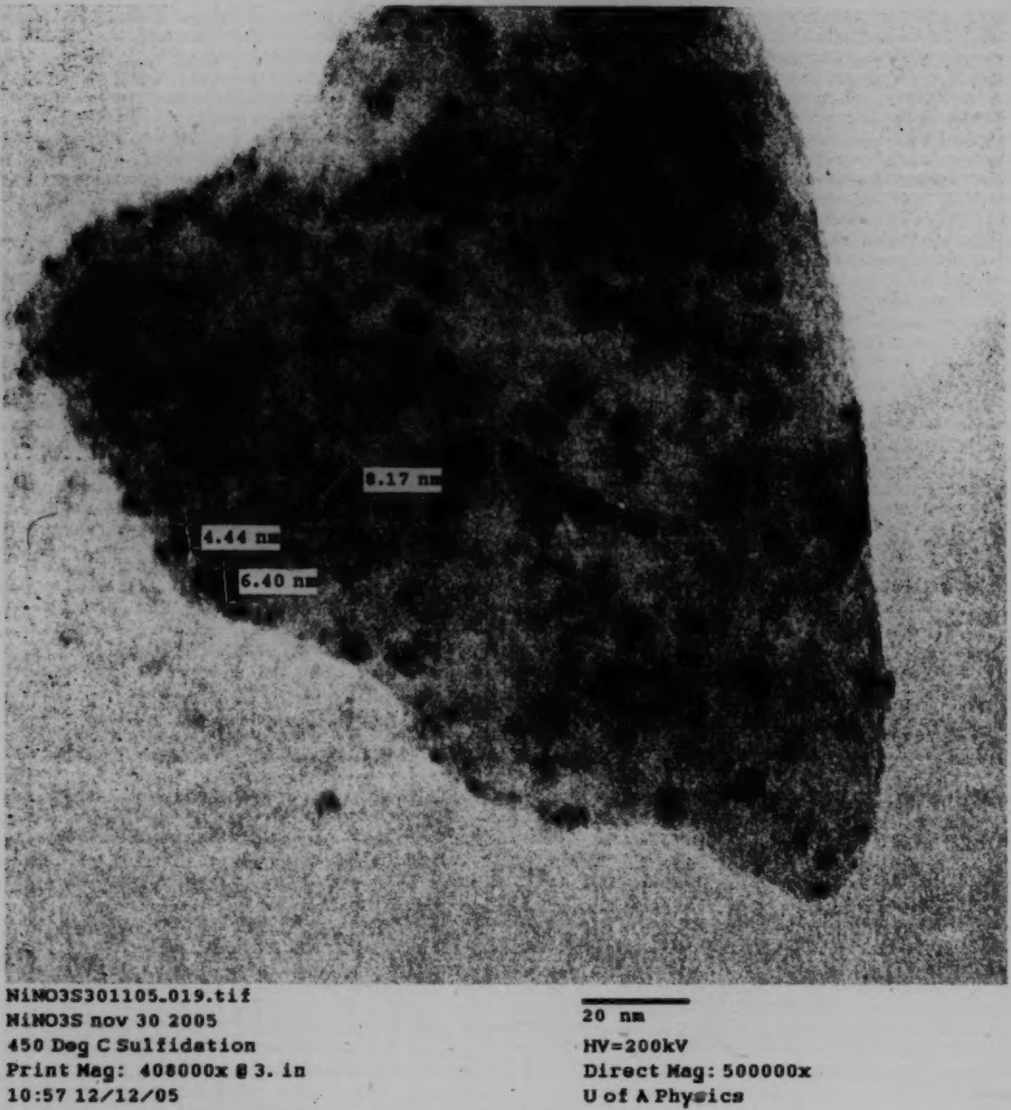
8.17 nm
4.44 nm
6.40 nm
NiNO3S301105_019.tif
NiNO3S nov 30 2005
450 Deg C Sulfidation
Print Mag: 408000x @ 3. in
10:57 12/12/05
20 nm
HV=200kV
Direct Mag: 500000x
U of A Physics

Figure B.34: Ni-CHA sulfided at 450°C in 10% $H_2S/H_2$.

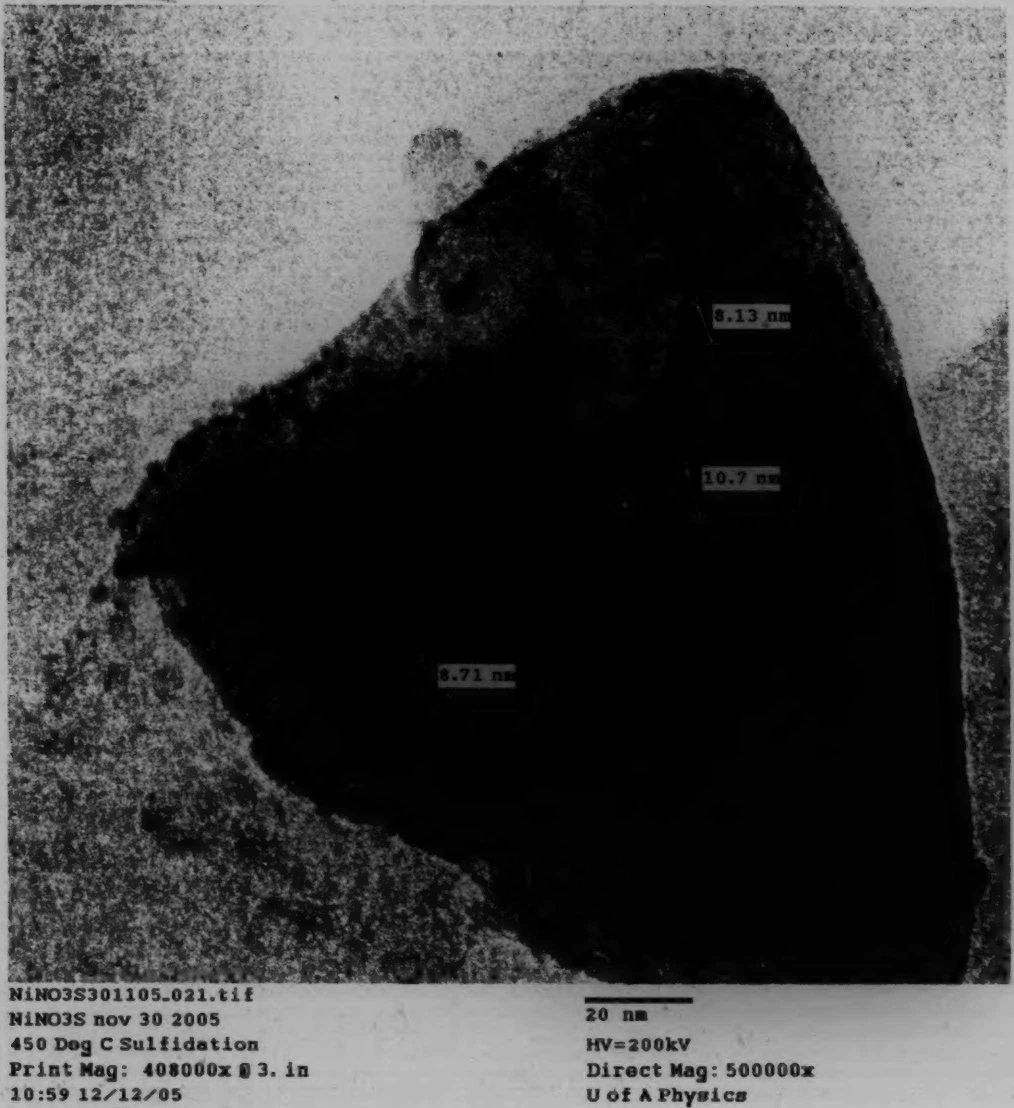
8.13 nm
10.7 nm
8.71 nm
NiNO3S301105_021.tif
NiNO3S nov 30 2005
450 Deg C Sulfidation
Print Mag: 408000x @ 3. in
10:59 12/12/05
20 nm
HV=200kV
Direct Mag: 500000x
U of A Physics

Figure B.35: Ni-CHA sulfided at 450°C in 10% $H_2S/H_2$.

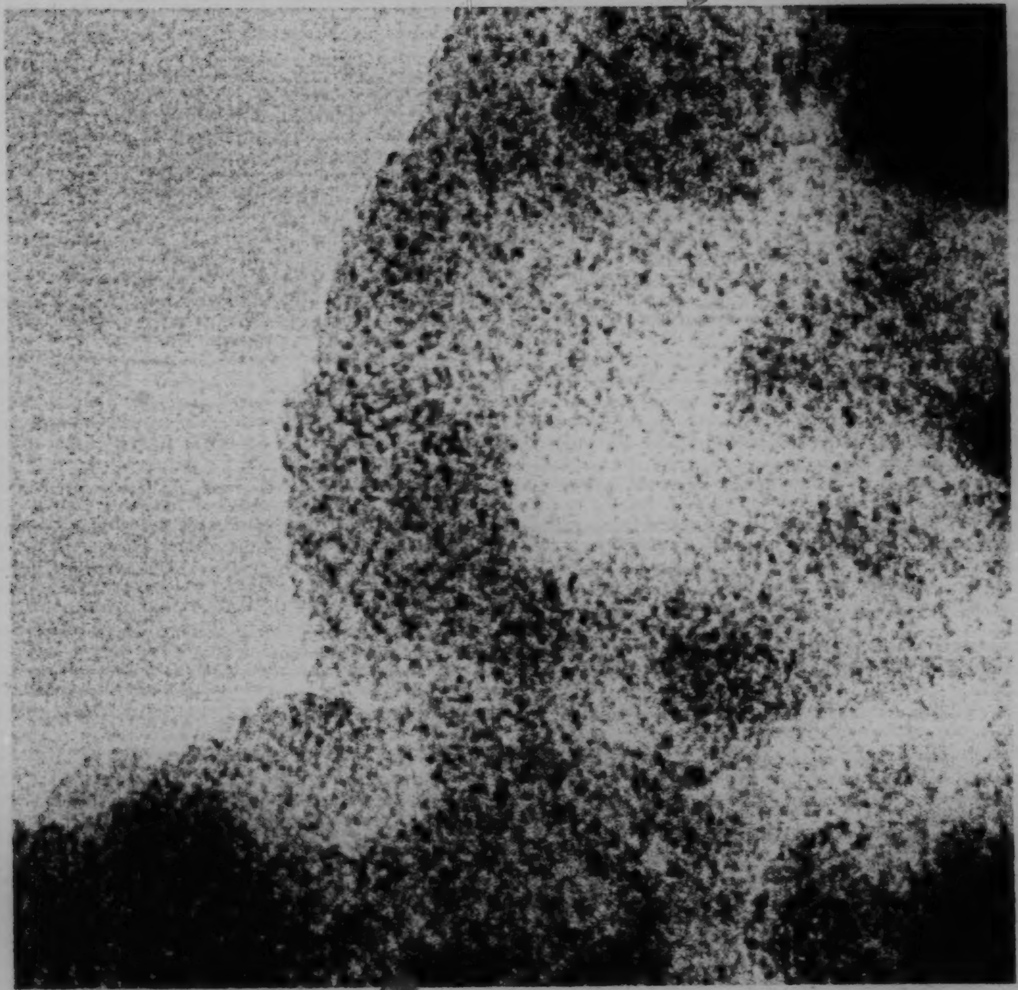
Mo.Chab 200905 2.006.tif
Mo.Chab R150 290805
Print Mag: 490000x @ 3. in
12:21 09/20/05
TEM Mode: Imaging
20 nm
HV=200kV
Direct Mag: 600000x
U of A Physics

Figure B.36: Mo-CHA reduced at 150°C in $H_2$.

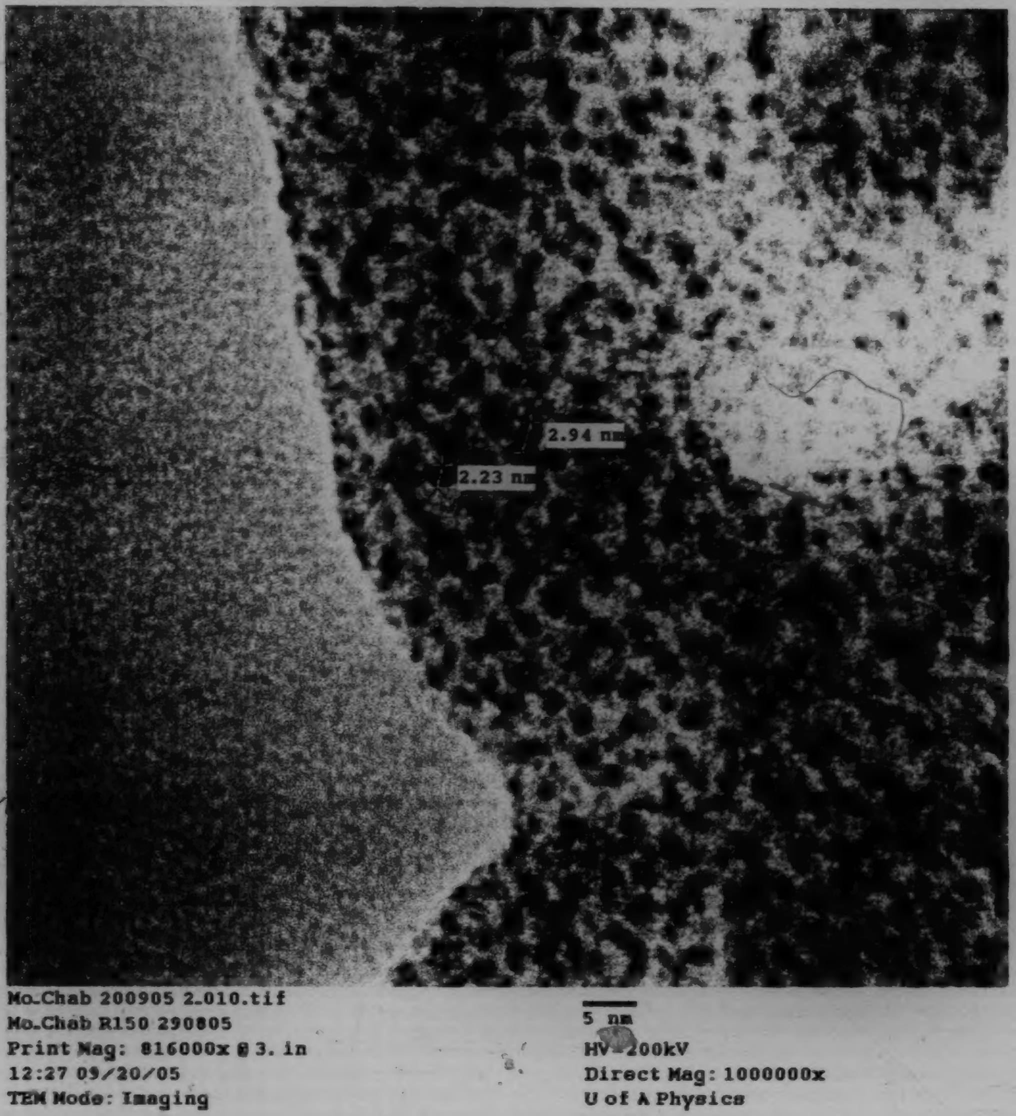
2.94 nm
2.23 nm
Mo-Chab 200905 2-010.tif
Mo-Chab R150 290805
Print Mag: 816000x @ 3. in
12:27 09/20/05
TEM Mode: Imaging
5 nm
HV=200kV
Direct Mag: 1000000x
U of A Physics

Figure B.37: Mo-CHA reduced at 150°C in $H_2$.

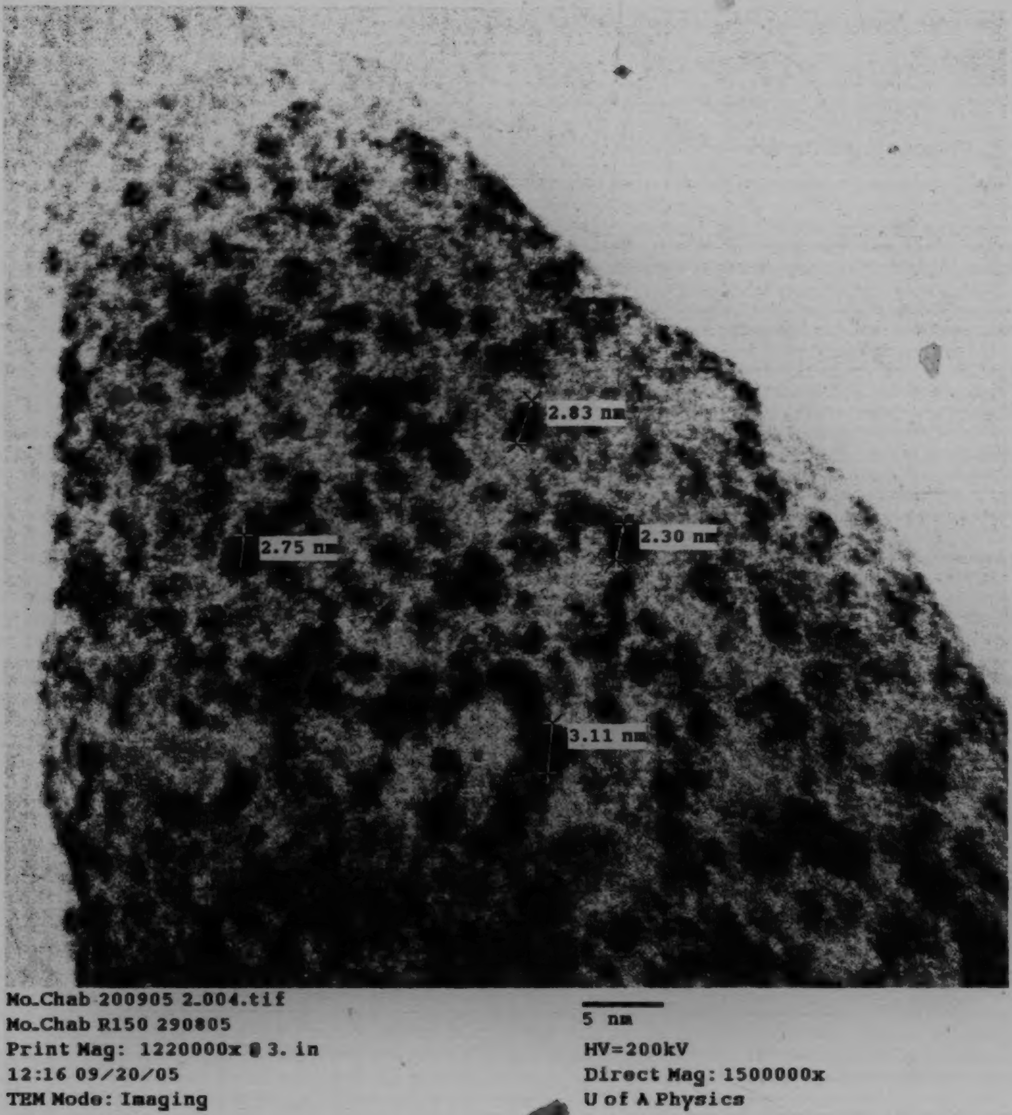
2.83 nm
2.75 nm
2.30 nm
3.11 nm
Mo_Chab 200905 2_004.tif
Mo_Chab R150 290805
Print Mag: 1220000x @ 3. in
12:16 09/20/05
TEM Mode: Imaging
5 nm
HV=200kV
Direct Mag: 1500000x
U of A Physics

Figure B.38: Mo-CHA reduced at 150°C in $H_2$.

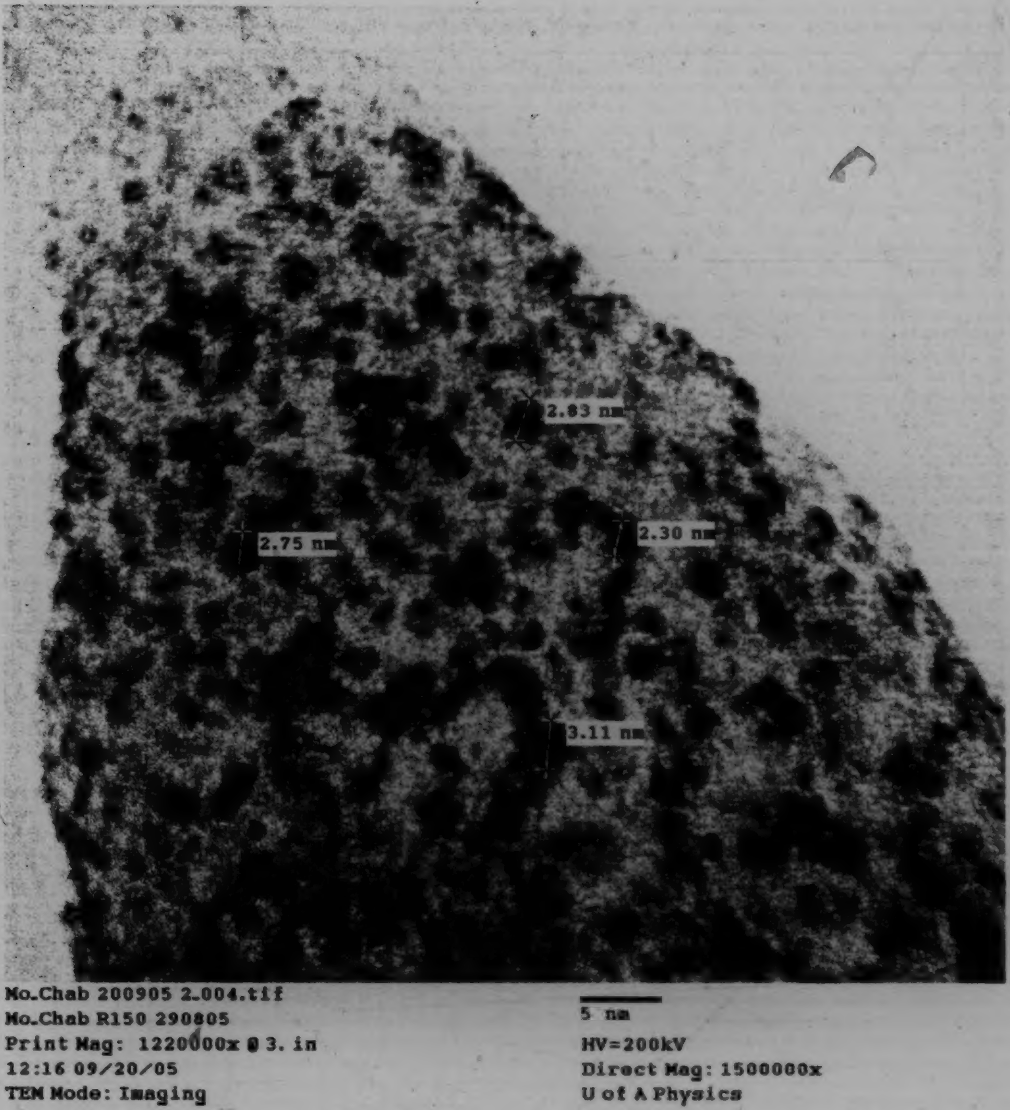
2.83 nm
2.75 nm
2.30 nm
3.11 nm
Mo.Chab 200905 2.004.tif
Mo.Chab R150 290805
Print Mag: 1220000x @ 3. in
12:16 09/20/05
TEM Mode: Imaging
5 nm
HV=200kV
Direct Mag: 1500000x
U of A Physics

Figure B.39: Mo-CHA reduced at 150°C in $H_2$.

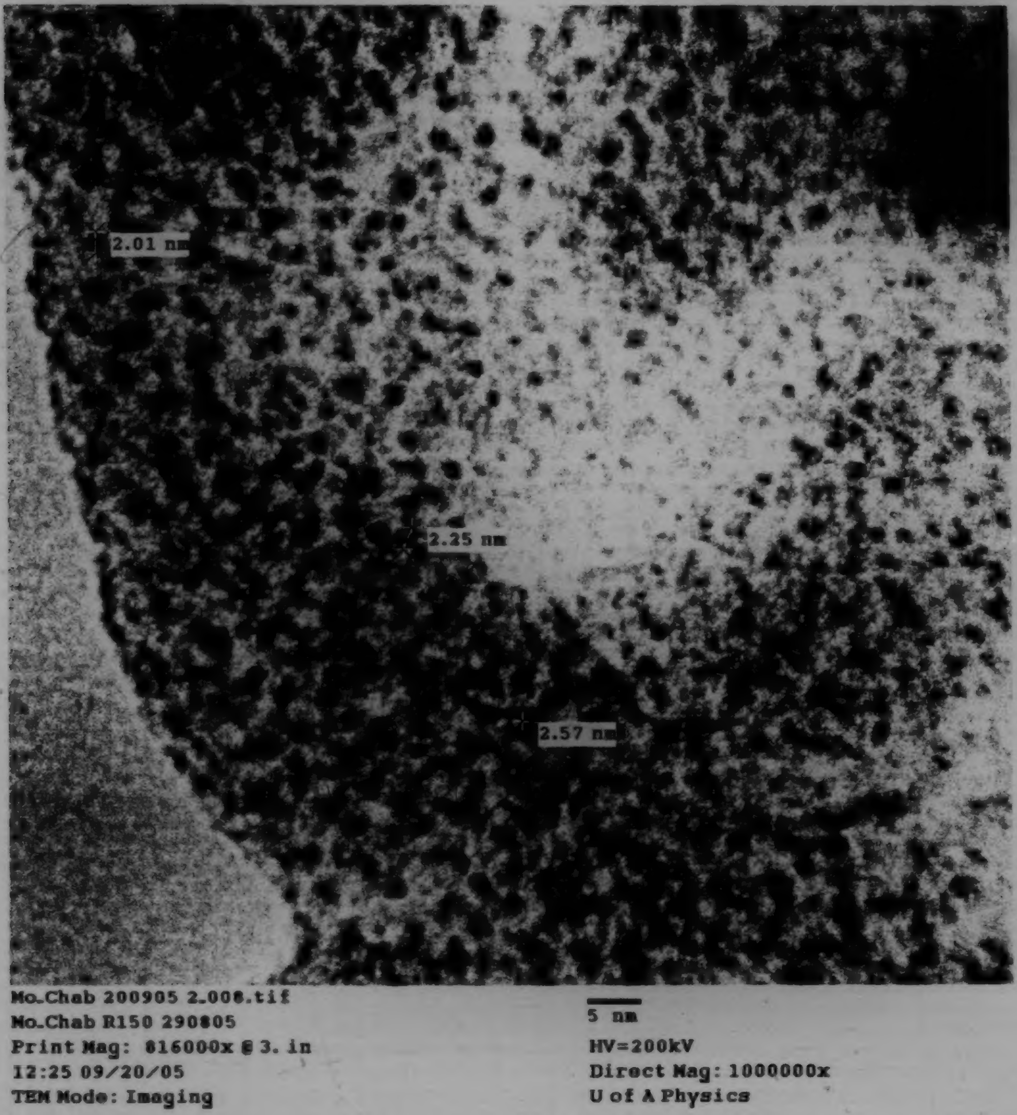
2.01 nm
2.25 nm
2.57 nm
Mo.Chab 200905 2.008.tif
Mo.Chab R150 290805
Print Mag: 816000x @ 3. in
12:25 09/20/05
TEM Mode: Imaging
5 nm
HV=200kV
Direct Mag: 1000000x
U of A Physics

Figure B.40: Mo-CHA reduced at 150°C in $H_2$.

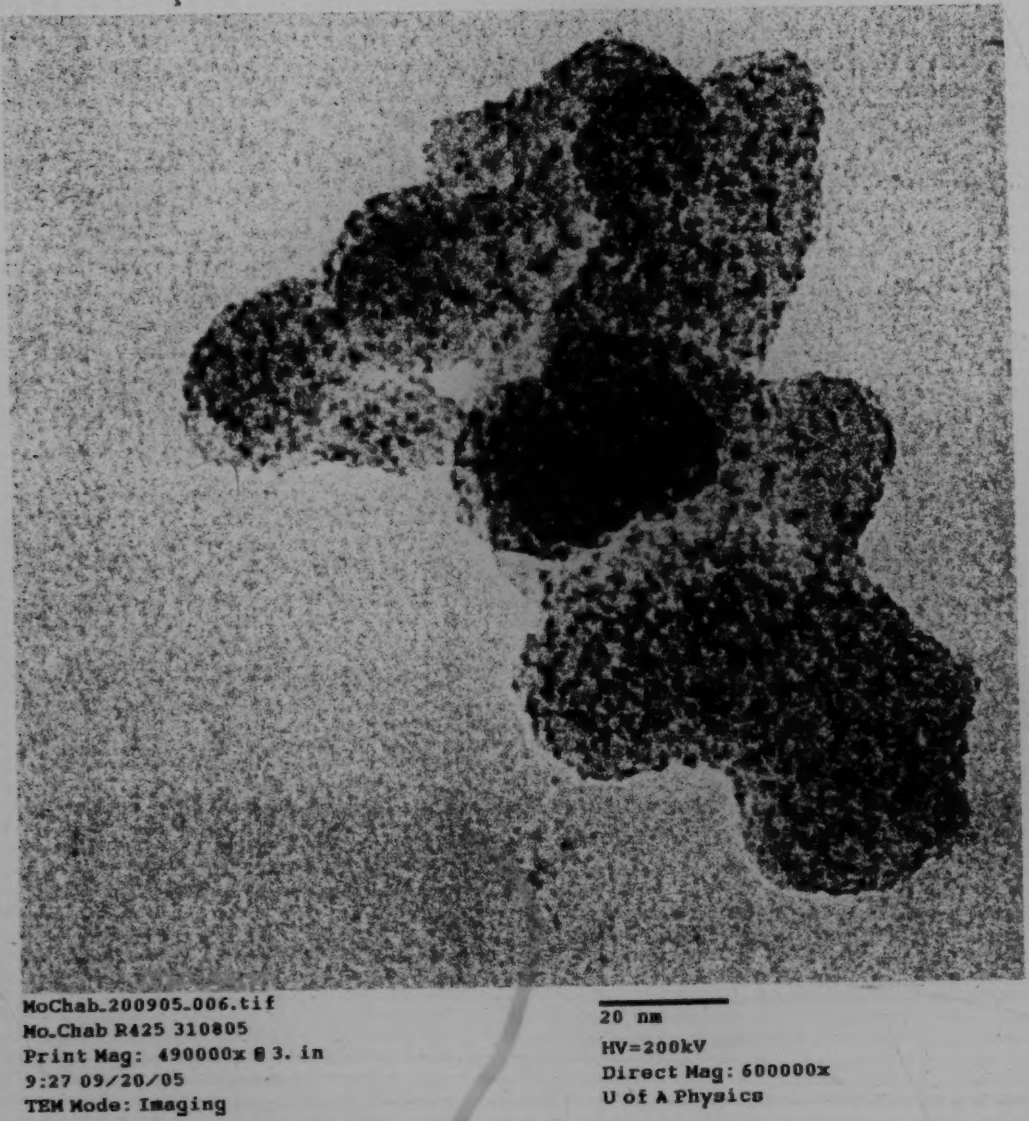
MoChab_200905_006.tif
Mo_Chab R425 310805
Print Mag: 490000x @ 3. in
9:27 09/20/05
TEM Mode: Imaging
20 nm
HV=200kV
Direct Mag: 600000x
U of A Physics

Figure B.41: Mo-CHA reduced at 425°C in $H_2$.

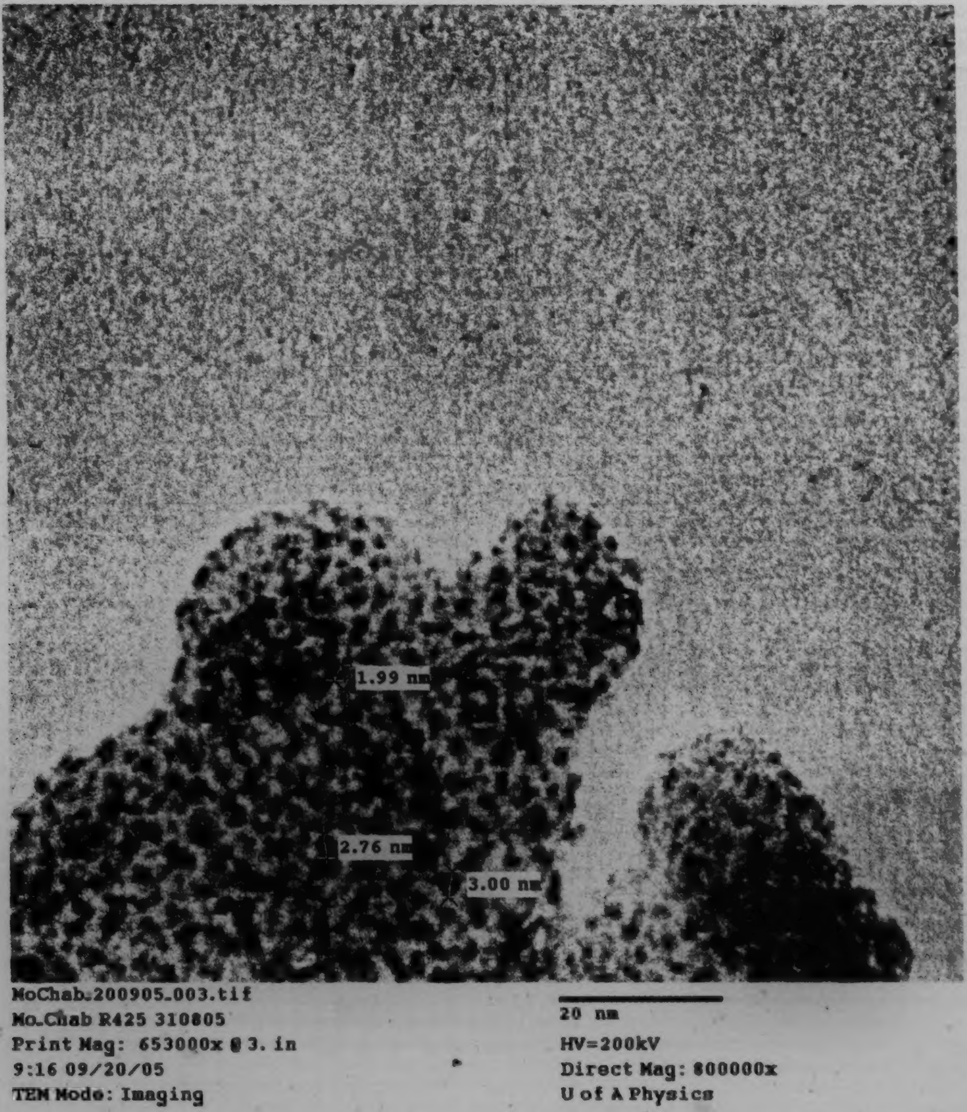
1.99 nm
2.76 nm
3.00 nm
MoChab_200905_003.tif
Mo_Chab R425 310805
Print Mag: 653000x @ 3. in
9:16 09/20/05
TEM Mode: Imaging
20 nm
HV=200kV
Direct Mag: 800000x
U of A Physics

Figure B.42: Mo-CHA reduced at 425°C in $H_2$.

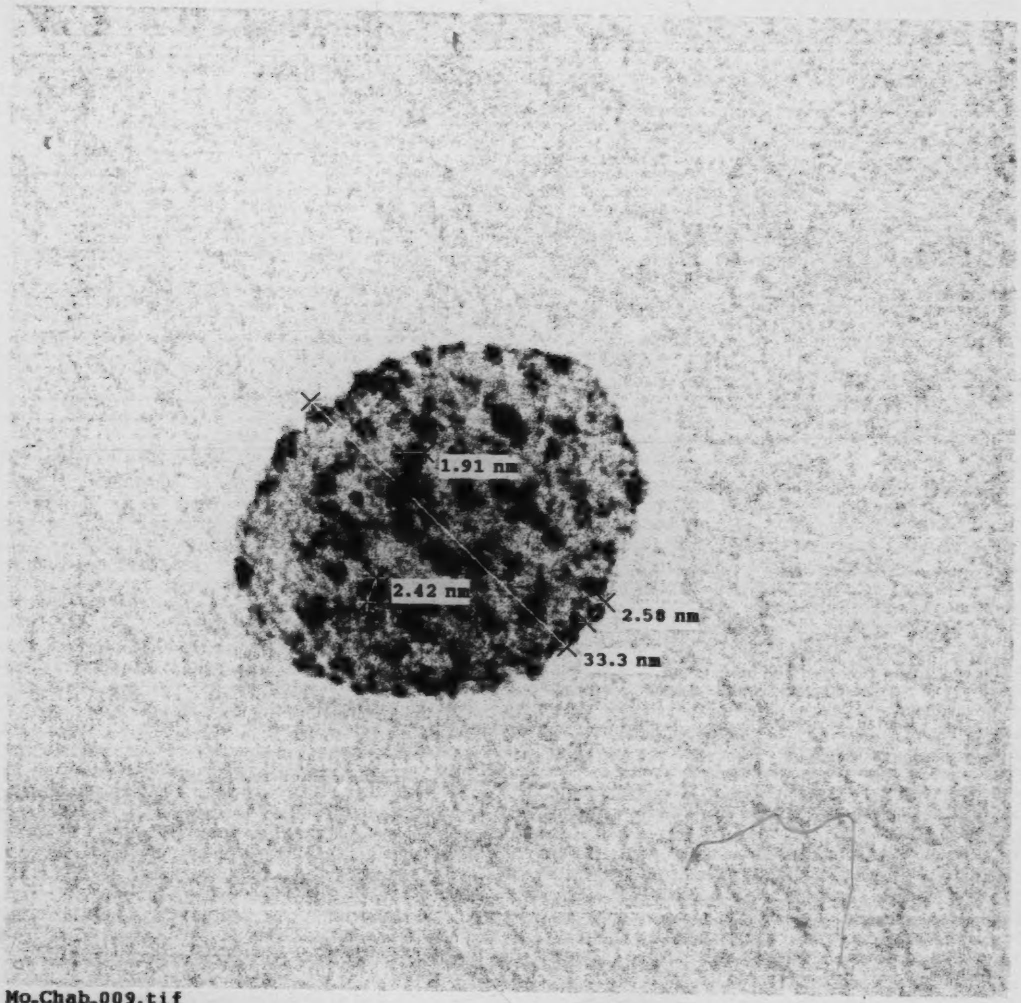
1.91 nm
2.42 nm
2.58 nm
33.3 nm

Mo_Chab_009.tif
MoChab Reduced to 450C
3108052
Print Mag: 816000x @ 3. in
4:44 09/01/05
TEM Mode: Imaging

5 nm
HV=200kV
U of A Physics

Figure B.43: Mo-CHA reduced at 450°C in $H_2$.

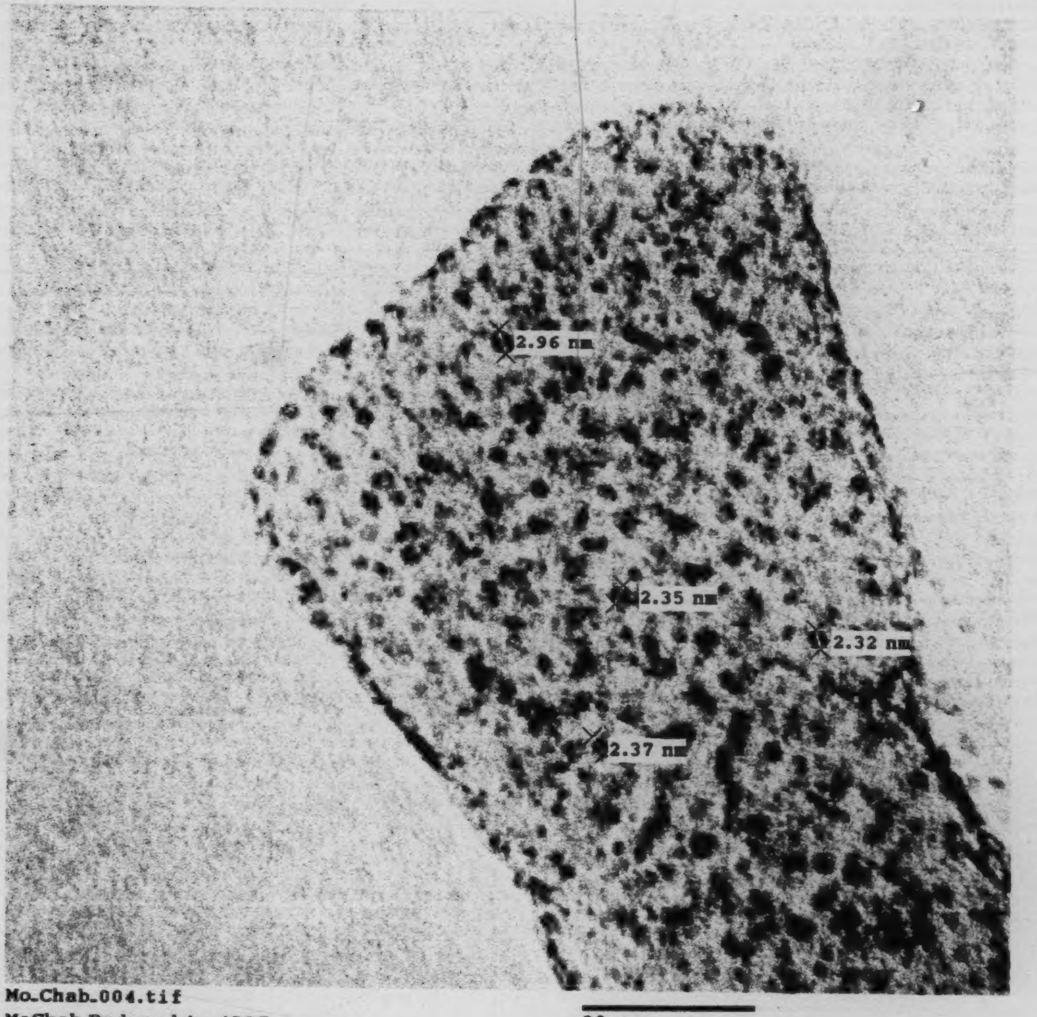
2.96 nm
2.35 nm
2.32 nm
2.37 nm
20 nm

Mo_Chab_004.tif
MoChab Reduced to 450C
3108052
Print Mag: 653000x @ 3. in
4:08 09/01/05
TEM Mode: Imaging

HV=200kV
U of A Physics

Figure B.44: Mo-CHA reduced at 450°C in $H_2$.

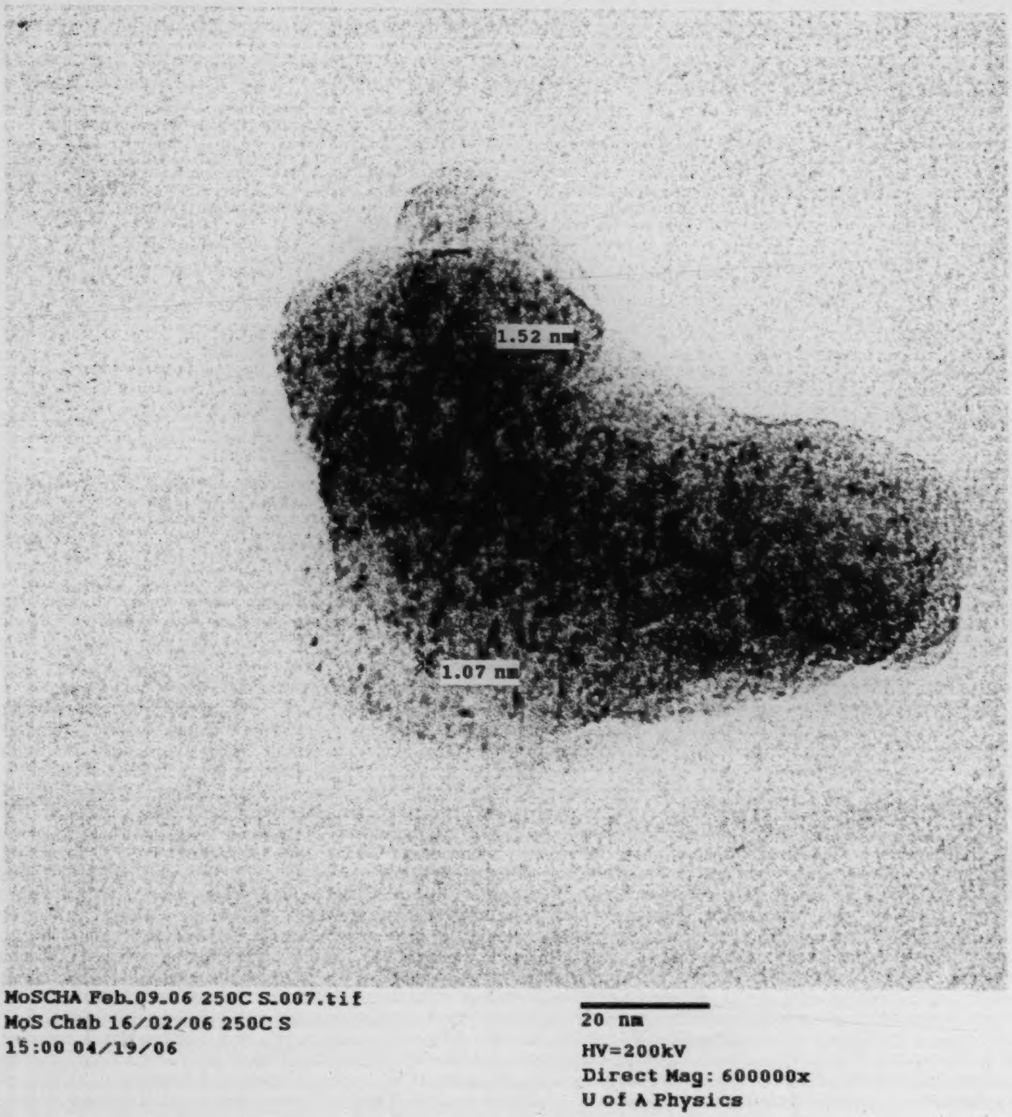
1.52 nm
1.07 nm
MoSCHA Feb_09_06 250C S_007.tif
MoS Chab 16/02/06 250C S
15:00 04/19/06
20 nm
HV=200kV
Direct Mag: 600000x
U of A Physics

Figure B.45: Mo-CHA sulfided at 250°C in 10% $H_2S/H_2$.

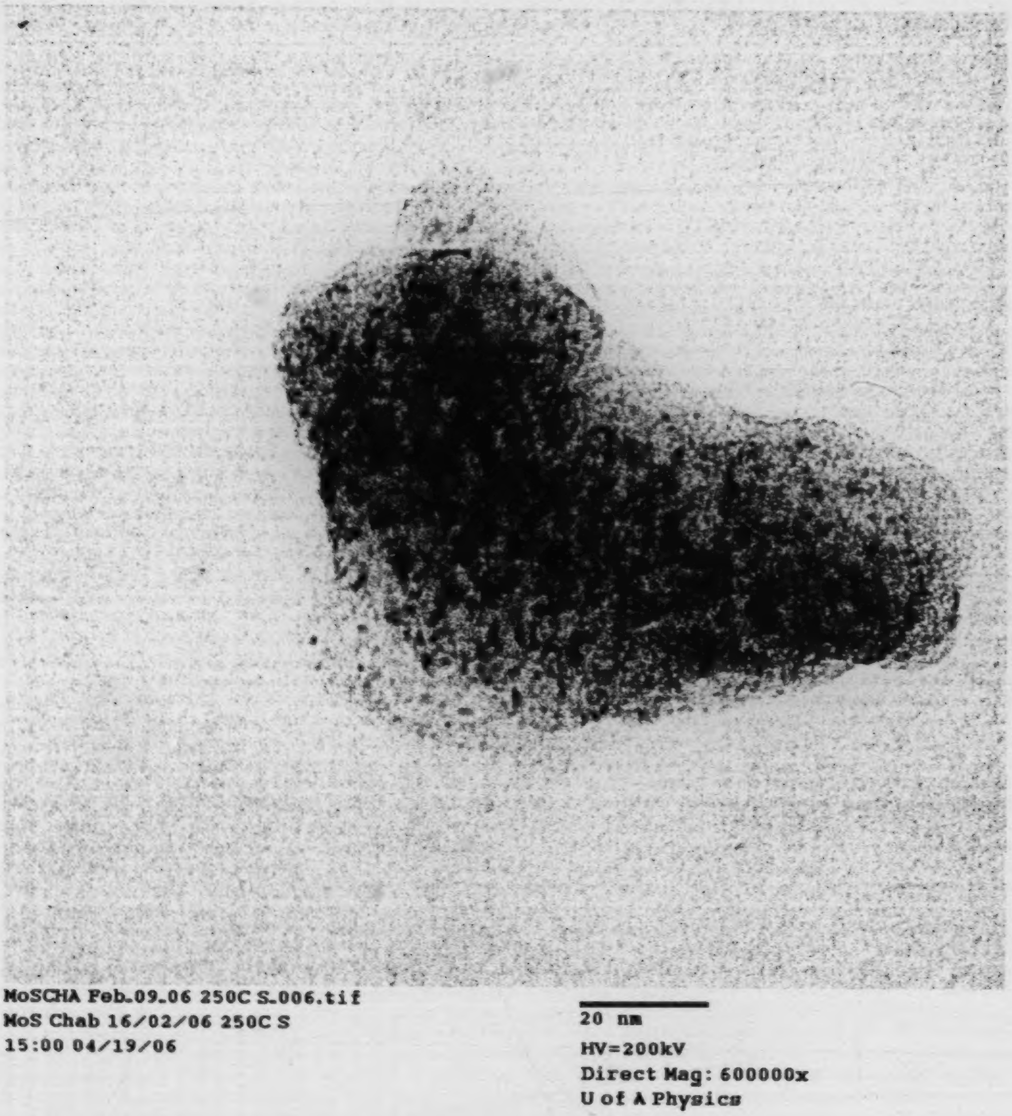
MoSCHA Feb_09_06 250C S_006.tif
MoS Chab 16/02/06 250C S
15:00 04/19/06
20 nm
HV=200kV
Direct Mag: 600000x
U of A Physics

Figure B.46: Mo-CHA sulfided at 250°C in 10% $H_2S/H_2$.

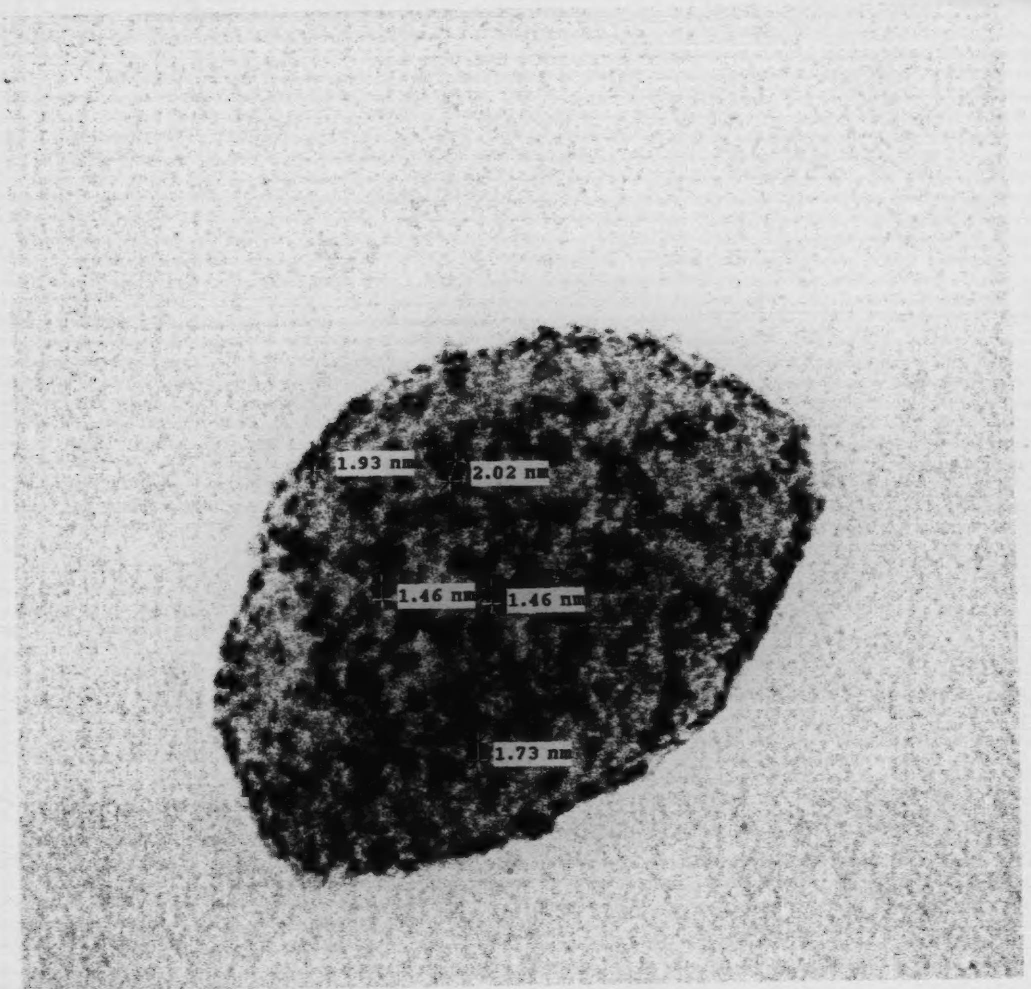
1.93 nm
2.02 nm
1.46 nm
1.46 nm
1.73 nm
5 nm

MoSCHA Feb_09_06 250C S_005.tif
MoS Chab 16/02/06 250C S
14:55 04/19/06

HV=200kV
Direct Mag: 1000000x
U of A Physics

Figure B.47: Mo-CHA sulfided at 250°C in 10% $H_2S/H_2$.

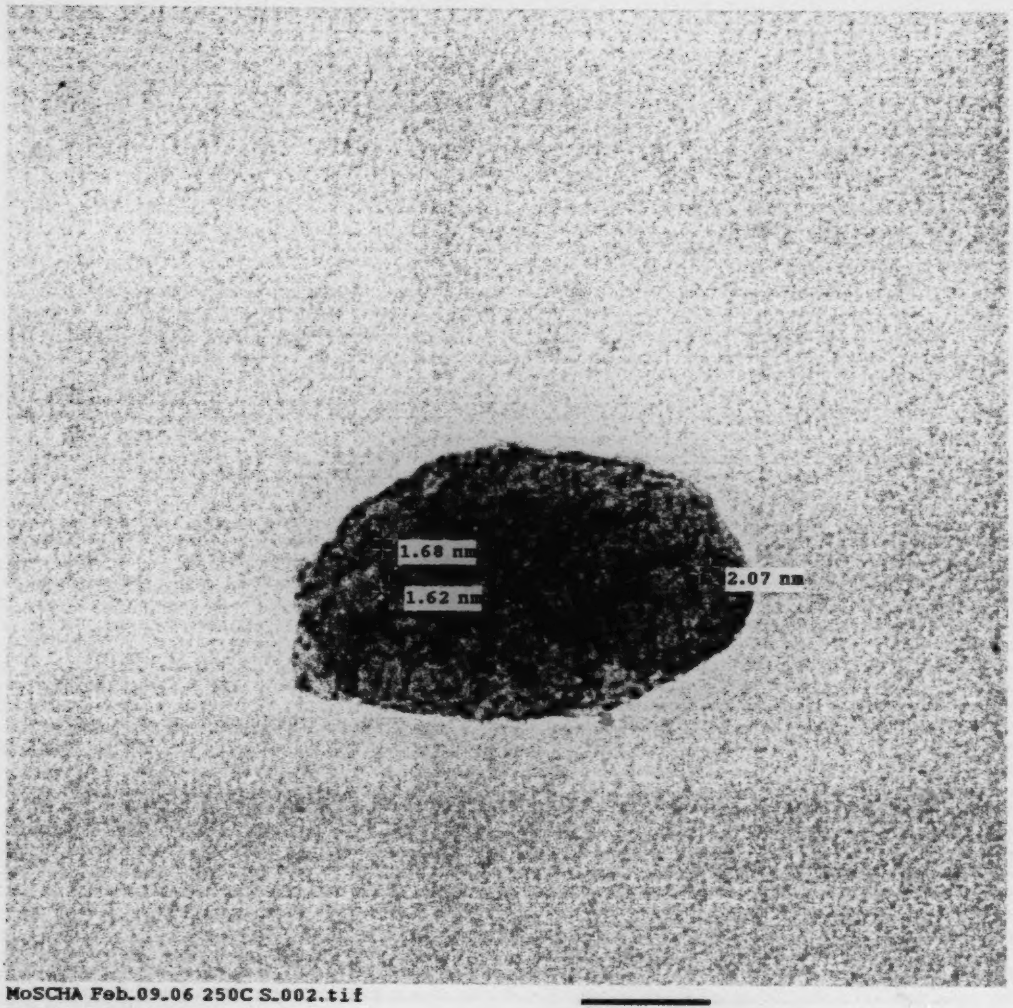
1.68 nm
1.62 nm
2.07 nm

MoSCHA Feb_09_06 250C S_002.tif
MoS Chab 16/02/06 250C S
14:51 04/19/06

20 nm
HV=200kV
Direct Mag: 600000x
U of A Physics

Figure B.48: Mo-CHA sulfided at 250°C in 10% $H_2S/H_2$.

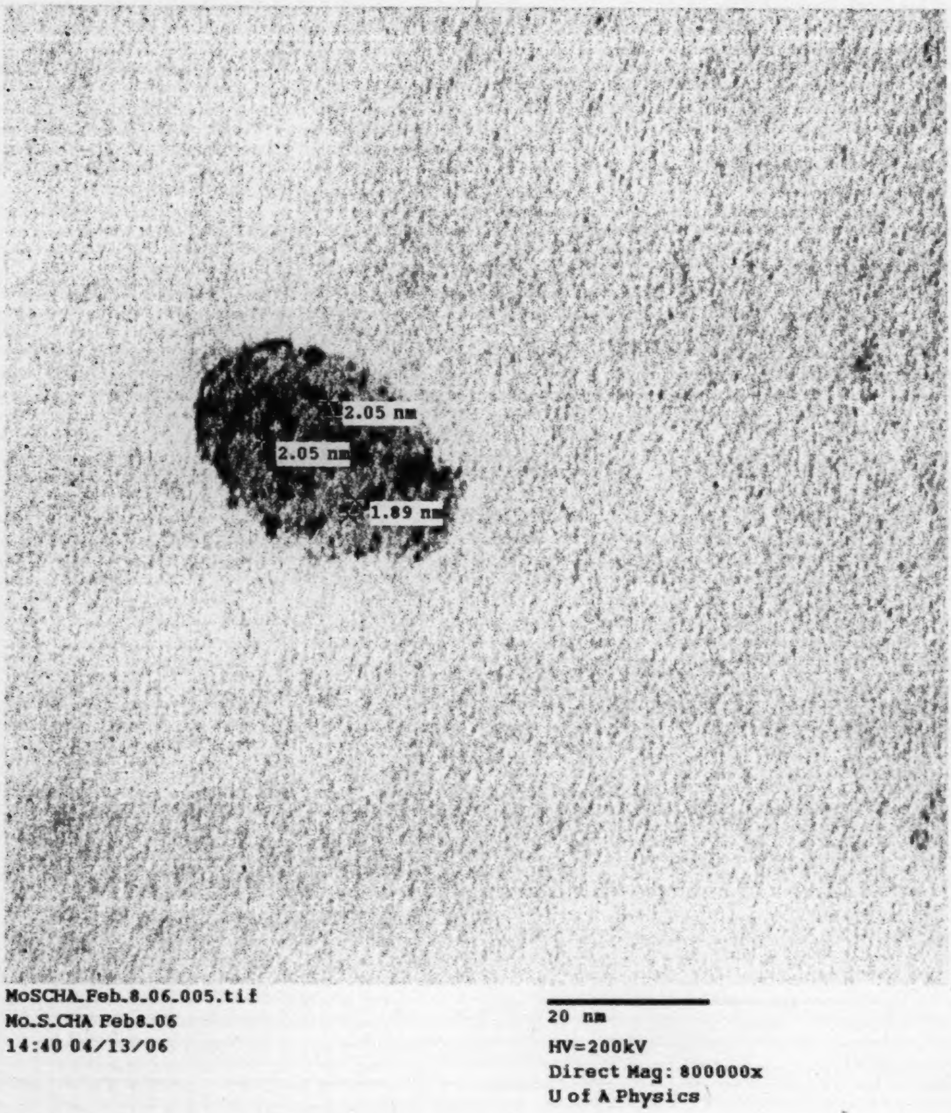
2.05 nm
2.05 nm
1.89 nm
MoSCHA_Feb_8_06_005.tif
Mo_S_CHA Feb8_06
14:40 04/13/06
20 nm
HV=200kV
Direct Mag: 800000x
U of A Physics

Figure B.49: Mo-CHA sulfided at 350°C in 10% $H_2S/H_2$.

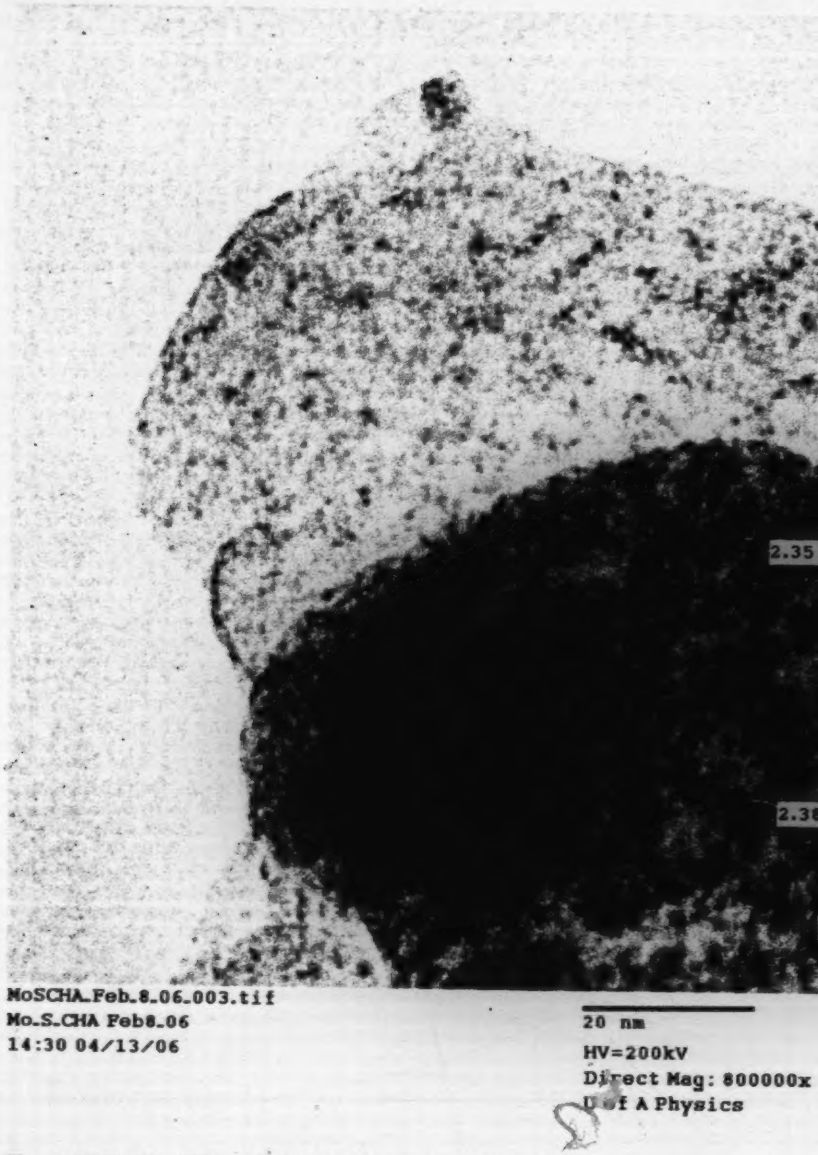
2.35 nm
2.71 nm
2.38 nm
2.51 nm
MoSCHA_Feb_8_06_003.tif
Mo_S_CHA Feb8_06
14:30 04/13/06
20 nm
HV=200kV
Direct Mag: 800000x
U of A Physics

Figure B.50: Mo-CHA sulfided at 350°C in 10% $H_2S/H_2$.

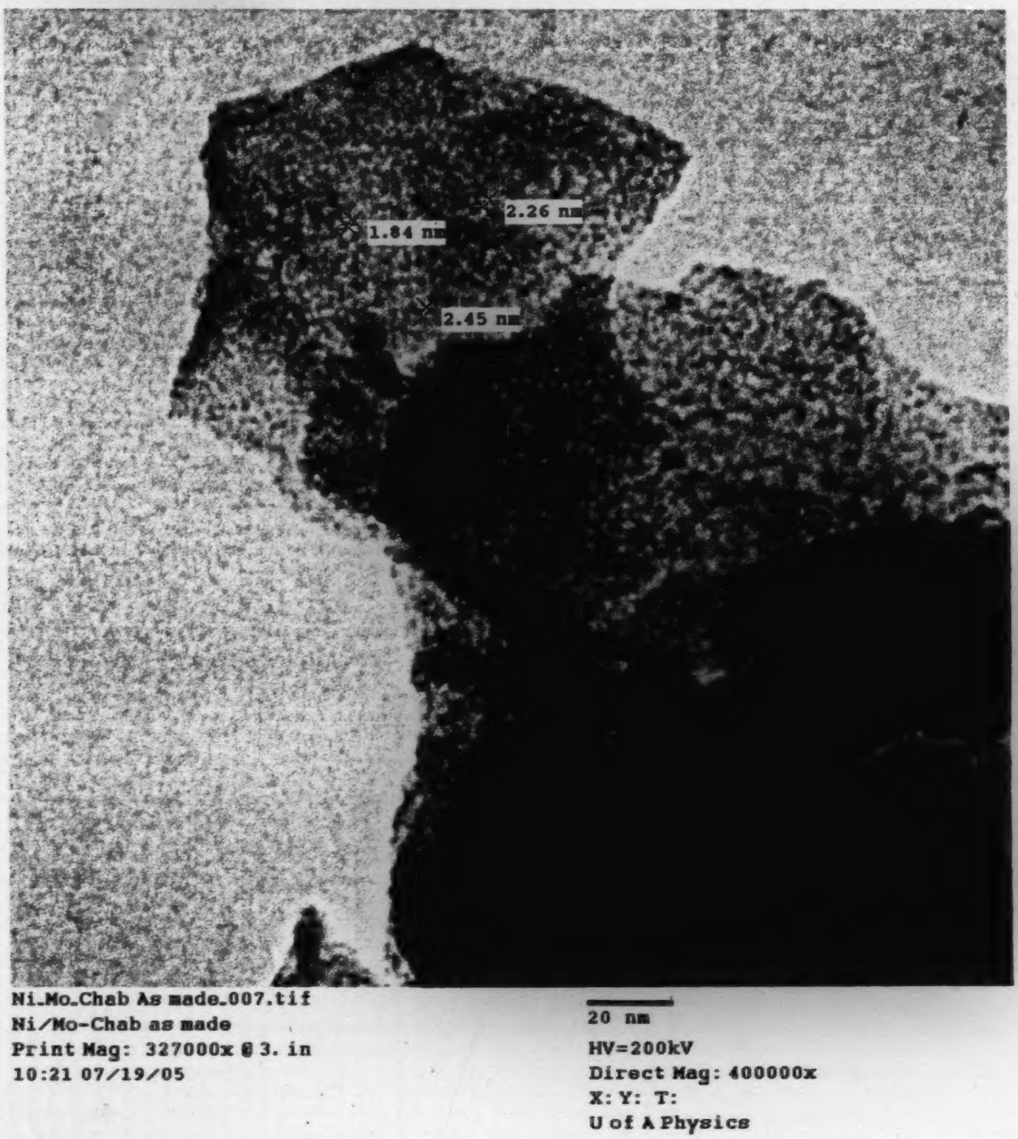
1.84 nm
2.26 nm
2.45 nm
20 nm

Ni_Mo_Chab As made_007.tif
Ni/Mo-Chab as made
Print Mag: 327000x @ 3. in
10:21 07/19/05

HV=200kV
Direct Mag: 400000x
X: Y: T:
U of A Physics

Figure B.51: NiMo-CHA As made.

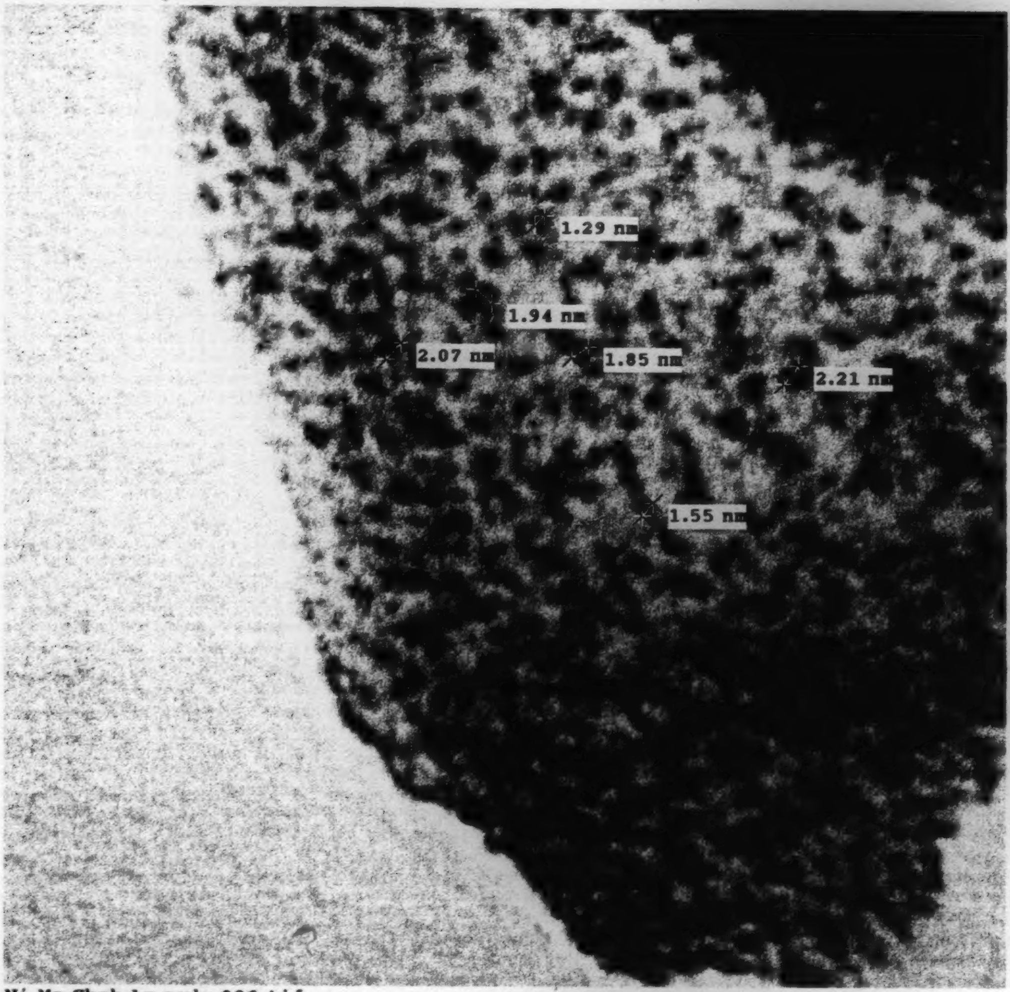
1.29 nm
1.94 nm
2.07 nm
1.85 nm
2.21 nm
1.55 nm

Ni_Mo_Chab As made_006.tif
Ni/Mo-Chab as made
Print Mag: 816000x @ 3. in
11:31 07/19/05

5 nm
HV=200kV
Direct Mag: 1000000x
X: Y: T:
U of A Physics

Figure B.52: NiMo-CHA As made.

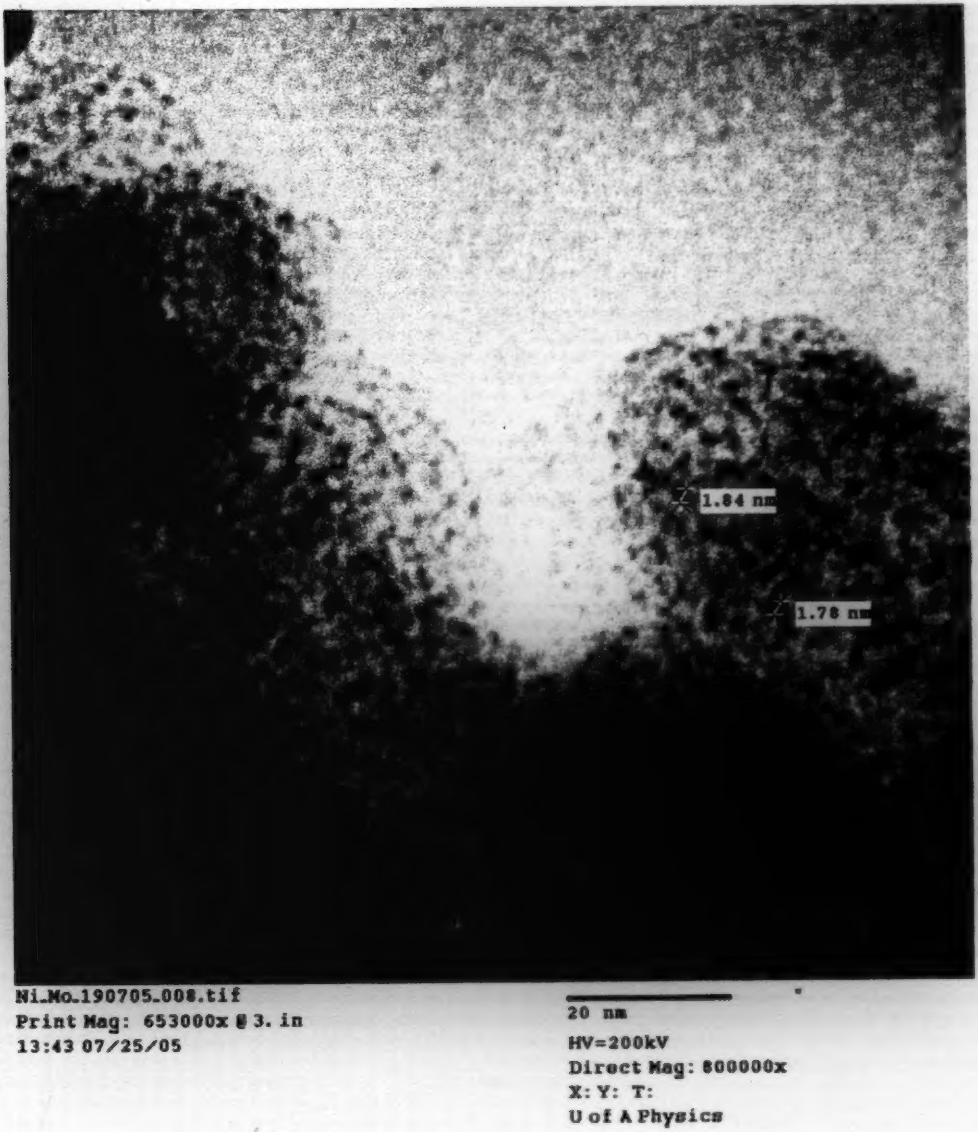
1.84 nm
1.78 nm
Ni_Mo_190705_008.tif
Print Mag: 653000x @ 3. in
13:43 07/25/05
20 nm
HV=200kV
Direct Mag: 800000x
X: Y: T:
U of A Physics

Figure B.53: NiMo-CHA reduced at 450°C in $H_2$.

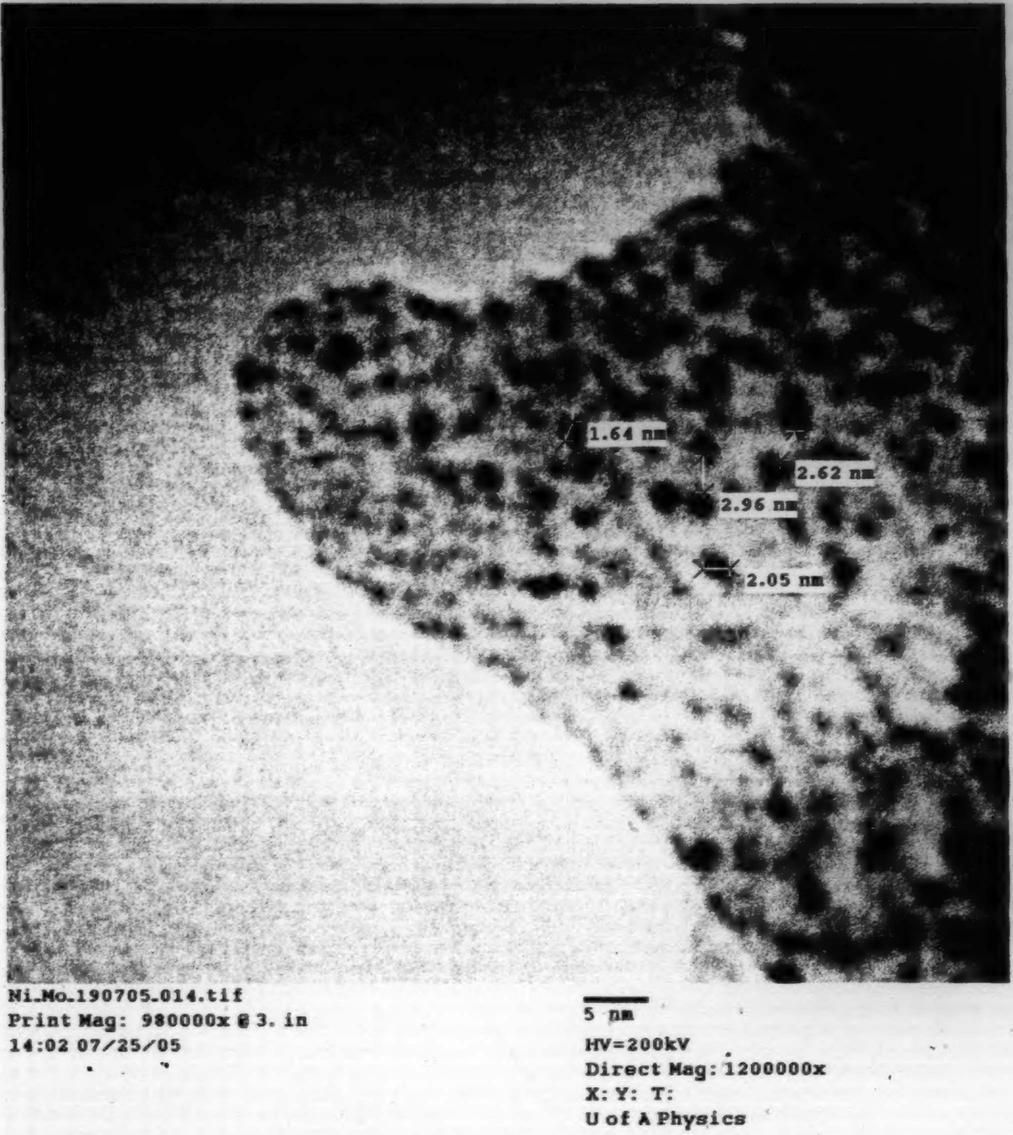
1.64 nm
2.62 nm
2.96 nm
2.05 nm
Ni_Mo_190705_014.tif
Print Mag: 980000x @ 3. in
14:02 07/25/05
5 nm
HV=200kV
Direct Mag: 1200000x
X: Y: T:
U of A Physics

Figure B.54: NiMo-CHA reduced at 450°C in $H_2$.

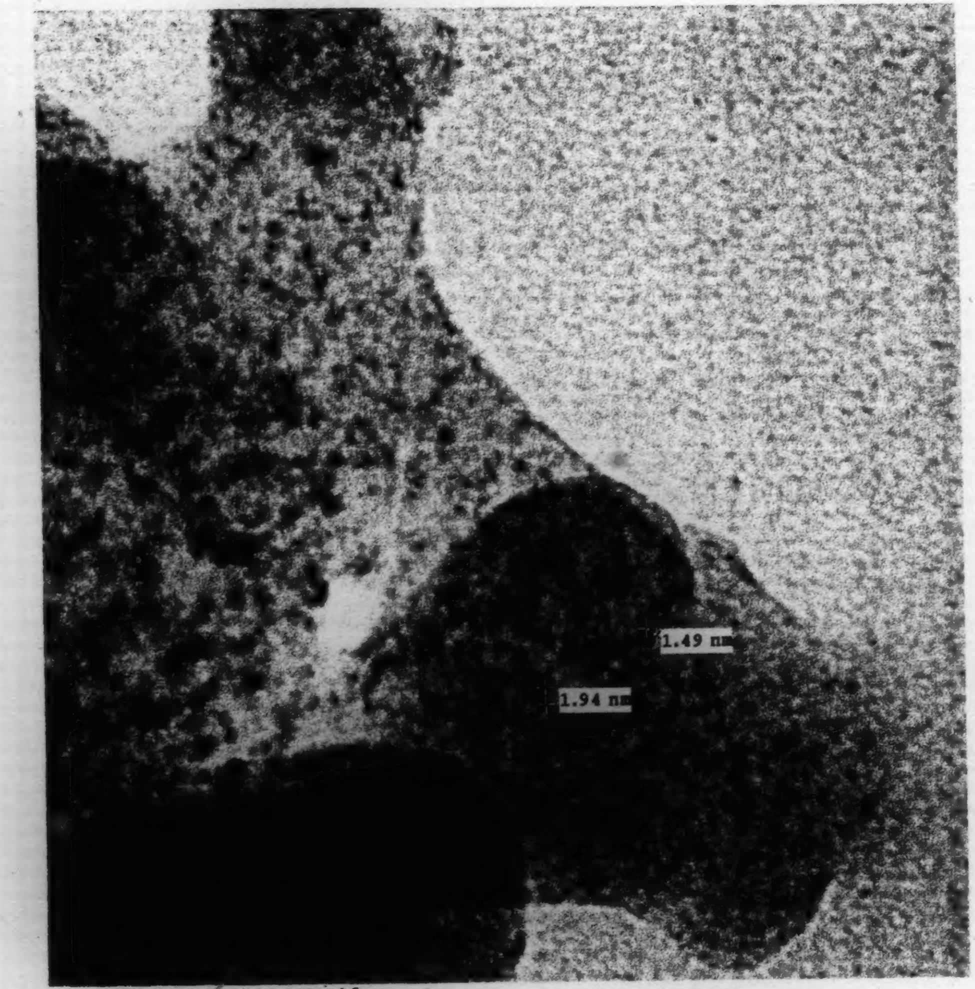
1.49 nm
1.94 nm
NiMoSCHA_250S_190206_005.tif
NiMoSCHA 250S
13:44 04/26/06
20 nm
HV=200kV
Direct Mag: 800000x
U of A Physics

Figure B.55: NiMo-CHA Sulfided at 250°C in 10% $H_2S/H_2$.

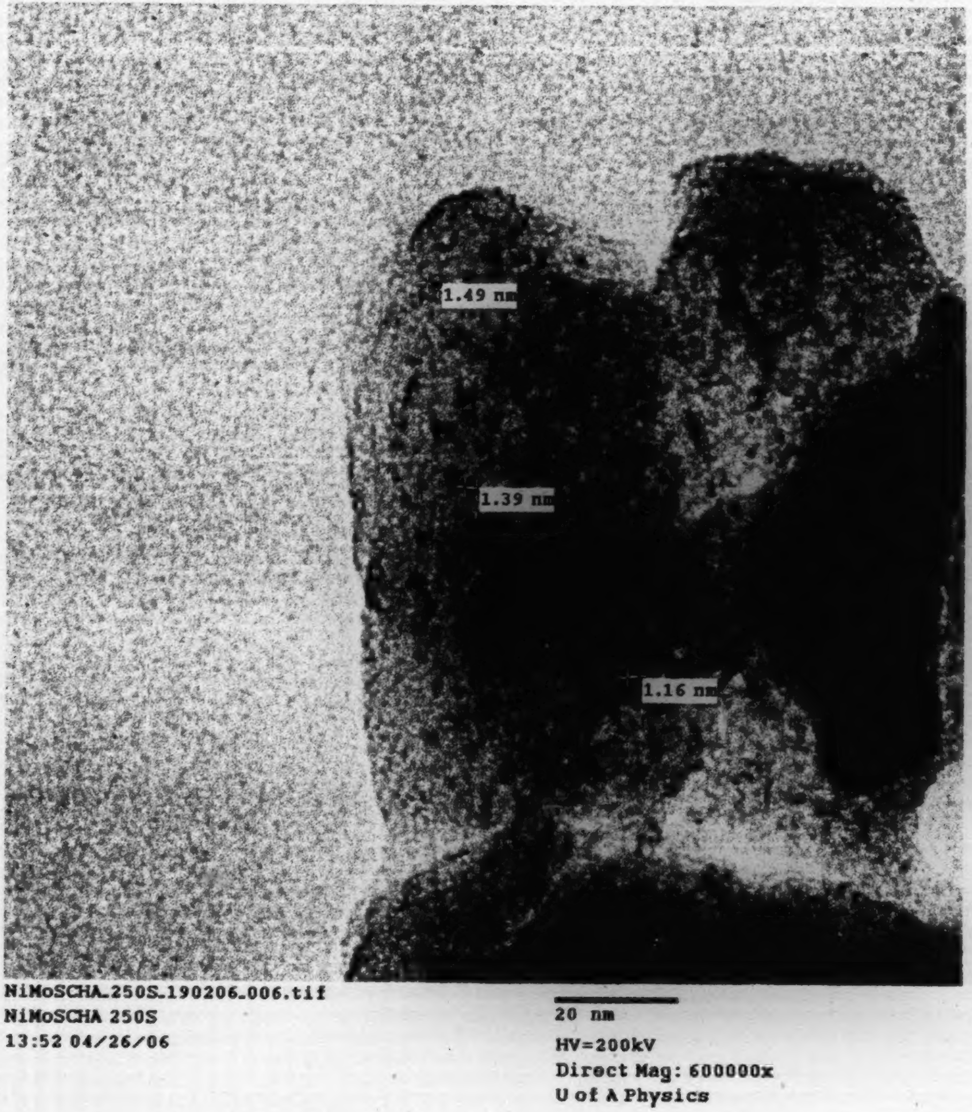
1.49 nm
1.39 nm
1.16 nm
NiMoSCHA_250S_190206_006.tif
NiMoSCHA 250S
13:52 04/26/06
20 nm
HV=200kV
Direct Mag: 600000x
U of A Physics

Figure B.56: NiMo-CHA Sulfided at 250°C in 10% $H_2S$/ $H_2$.

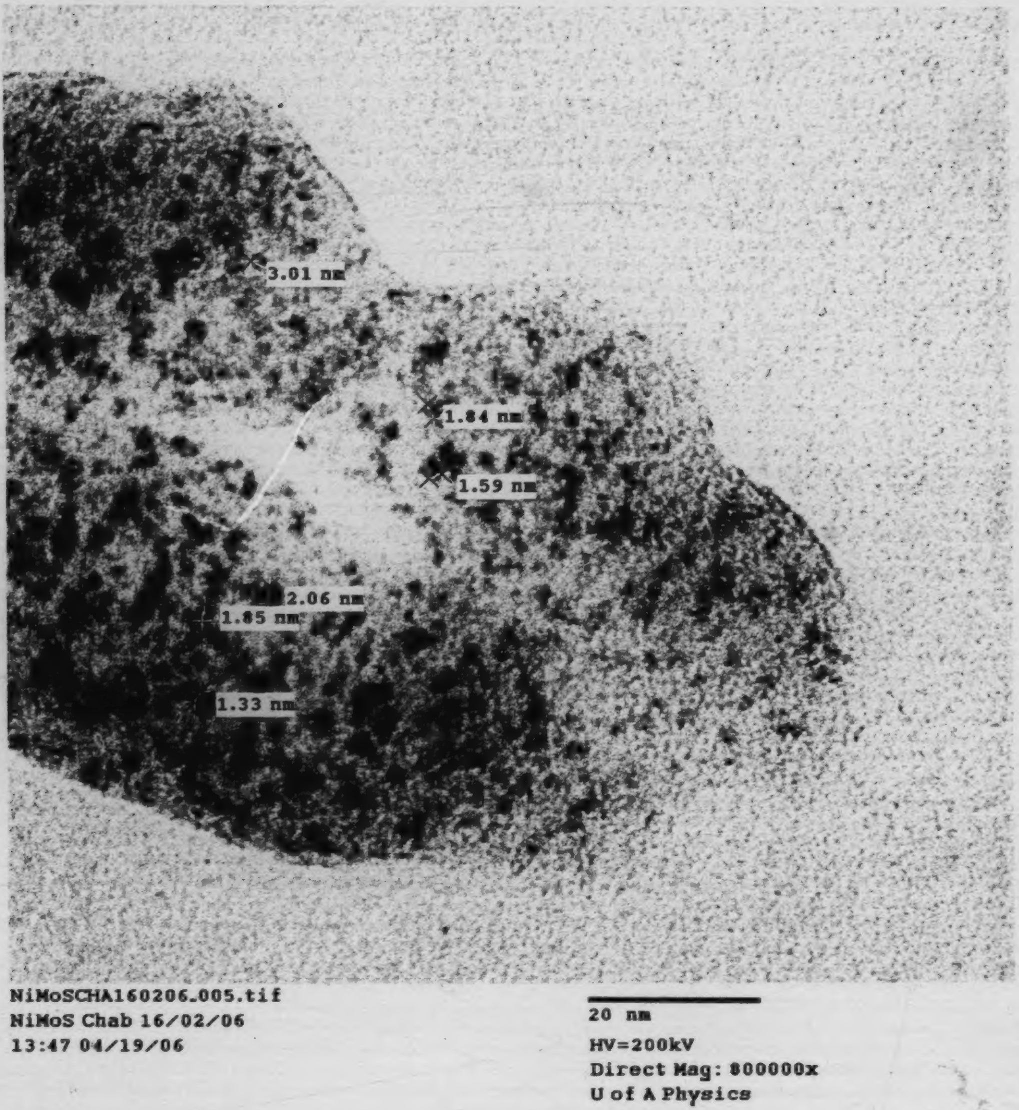
3.01 nm
1.84 nm
1.59 nm
2.06 nm
1.85 nm
1.33 nm
NiMoSCHA160206_005.tif
NiMoS Chab 16/02/06
13:47 04/19/06
20 nm
HV=200kV
Direct Mag: 800000x
U of A Physics

Figure B.57: NiMo-CHA Sulfided at 350°C in 10% $H_2S$/ $H_2$.

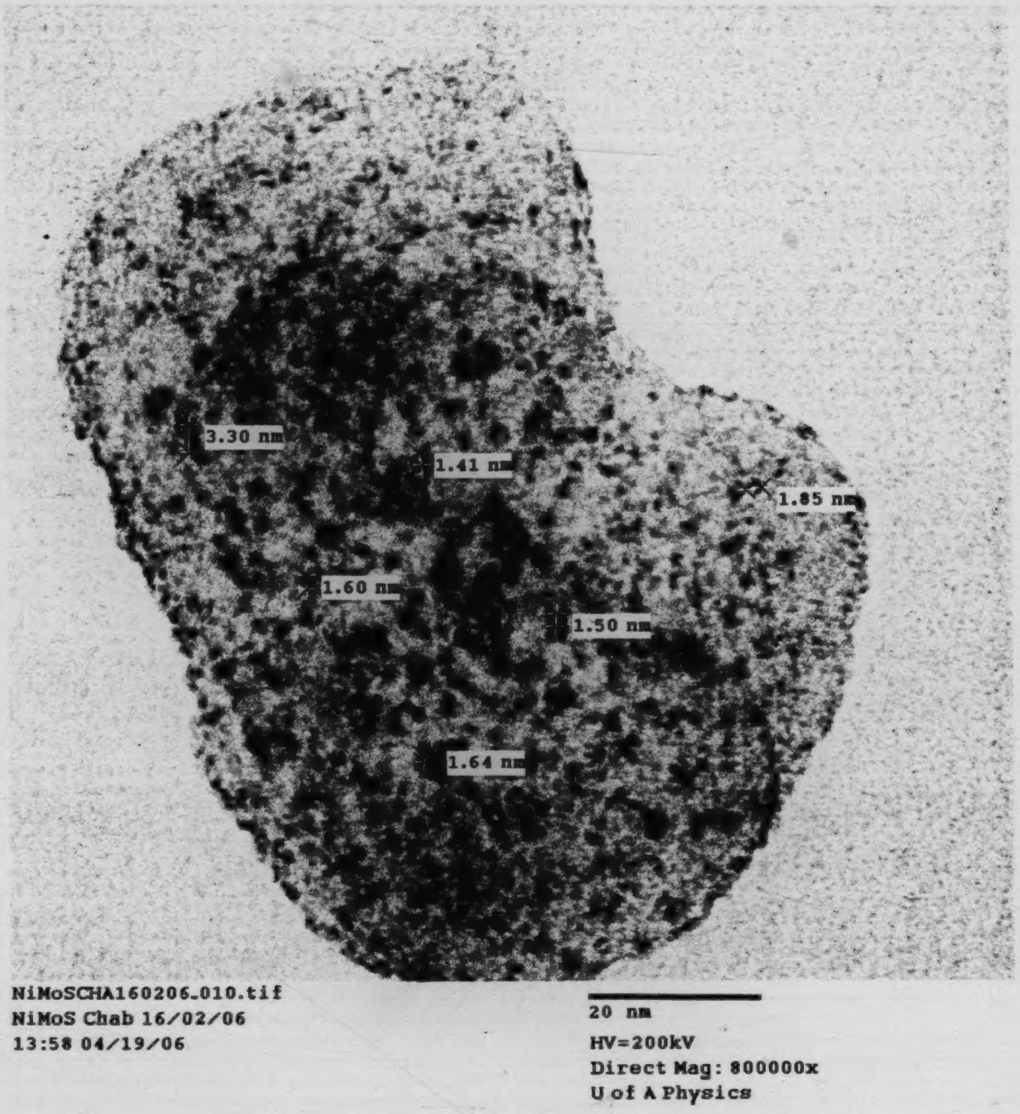
3.30 nm
1.41 nm
1.85 nm
1.60 nm
1.50 nm
1.64 nm
NiMoSCHA160206_010.tif
NiMoS Chab 16/02/06
13:58 04/19/06
20 nm
HV=200kV
Direct Mag: 800000x
U of A Physics

Figure B.58: NiMo-CHA Sulfided at 350°C in 10% $H_2S$/ $H_2$.

Series 2: NiHCHA, MoHCHA and NiMoHCHA.

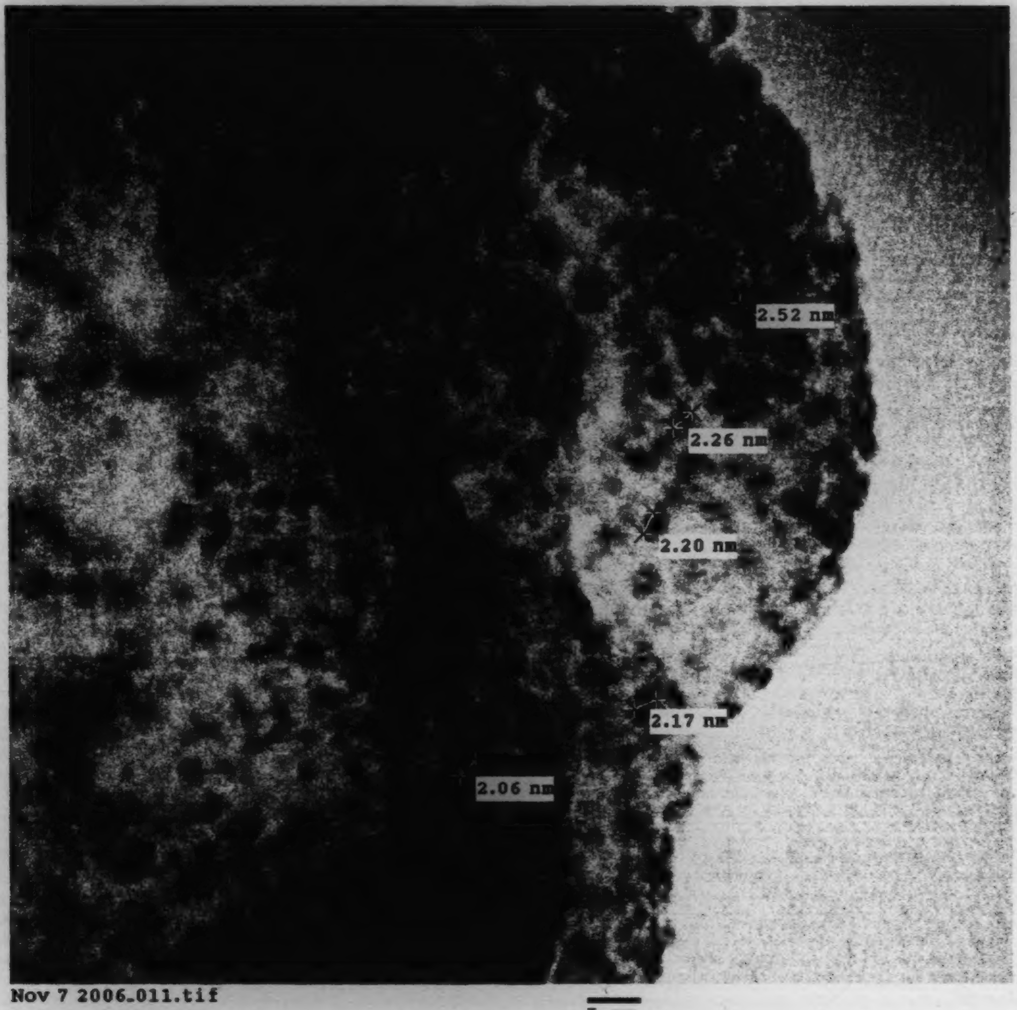
2.52 nm
2.26 nm
2.20 nm
2.17 nm
2.06 nm
5 nm

Nov 7 2006_011.tif
Calcined Ni H CHA
Print Mag: 816000x @ 3.0 in
8:56 11/07/06

HV=200kV
Direct Mag: 1000000x
U of A Physics

Figure B.59: NiHCHA As made.

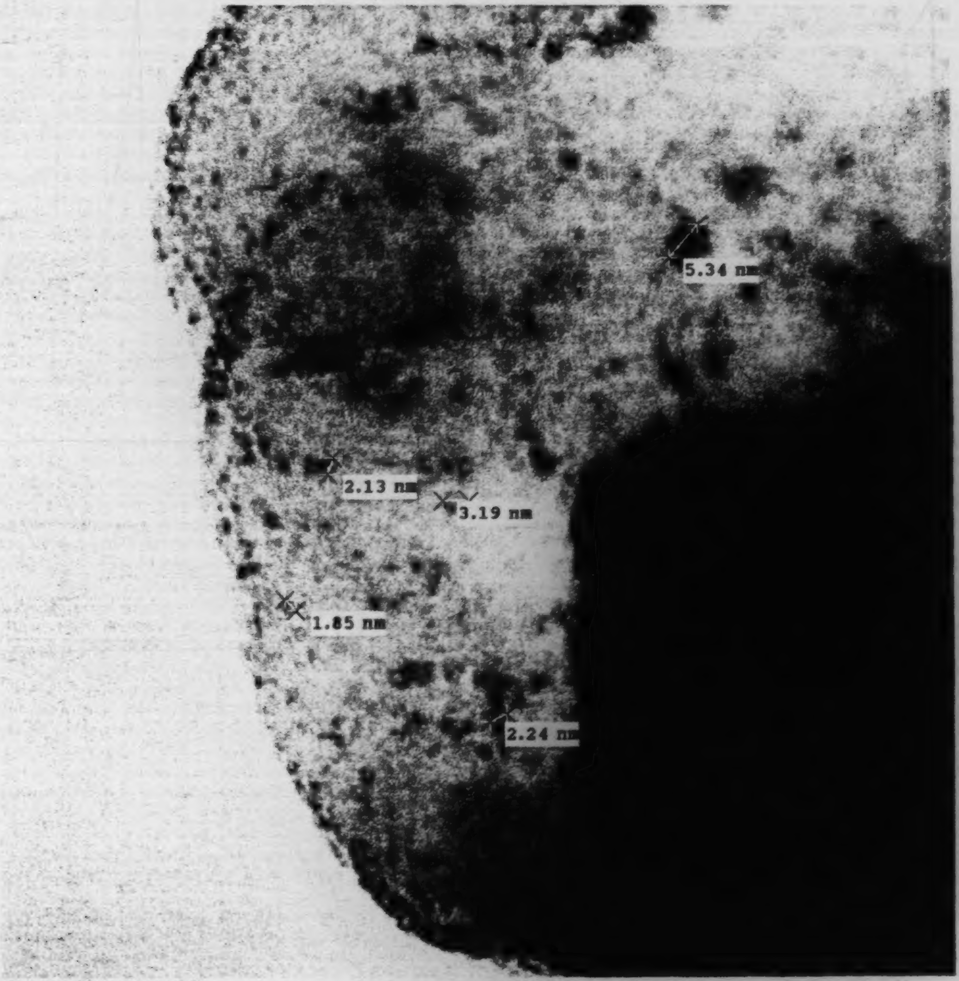
5.34 nm
2.13 nm
3.19 nm
1.85 nm
2.24 nm

Nov 7 2006.032.tif
Calcined Ni H CHA
Print Mag: 653000x @ 3.0 in
9:28 11/07/06

20 nm
HV=200kV
Direct Mag: 600000x
U of A Physics

Figure B.60: NiHCHA As made.

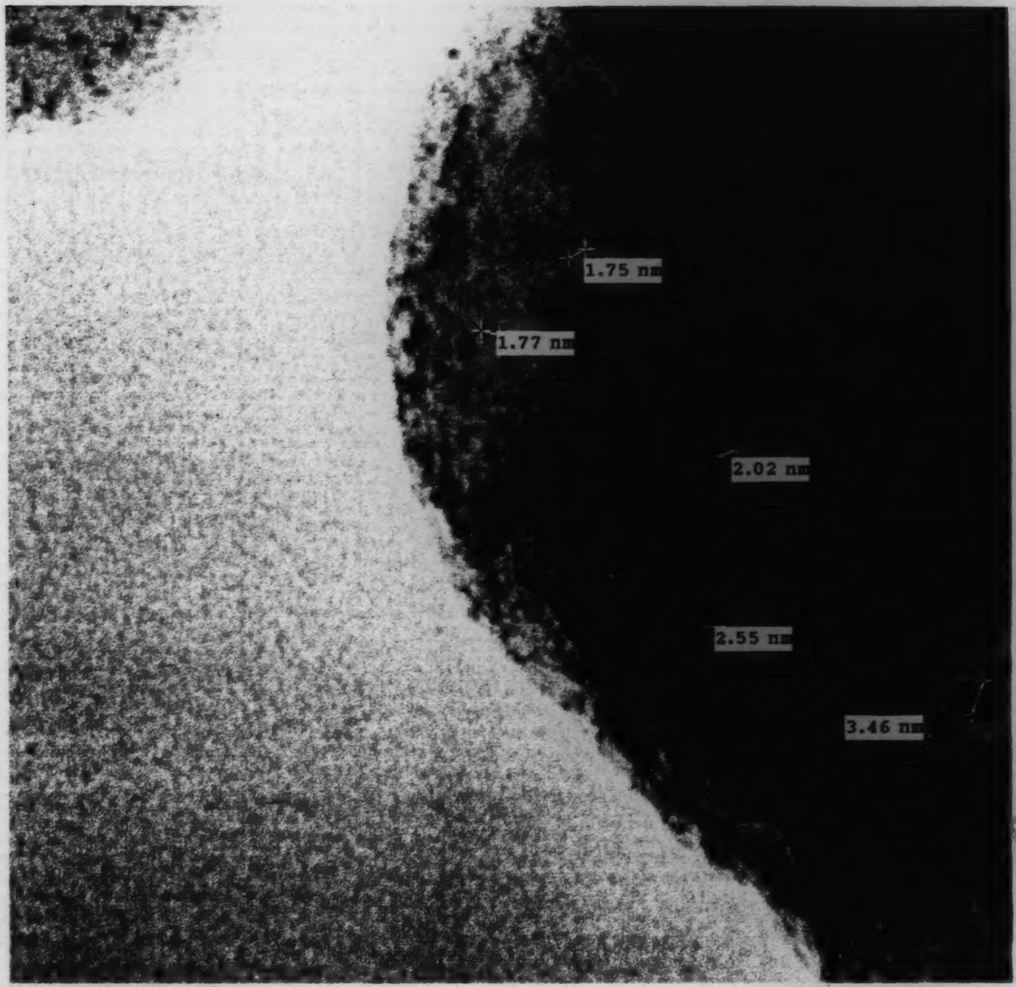
1.75 nm
1.77 nm
2.02 nm
2.55 nm
3.46 nm
5 nm

Nov 7 2006_034.tif
Calcined Ni H CHA
Print Mag: 816000x @ 3.0 in
9:30 11/07/06

HV=200kV
Direct Mag: 1000000x
U of A Physics

Figure B.61: NiHCHA As made.

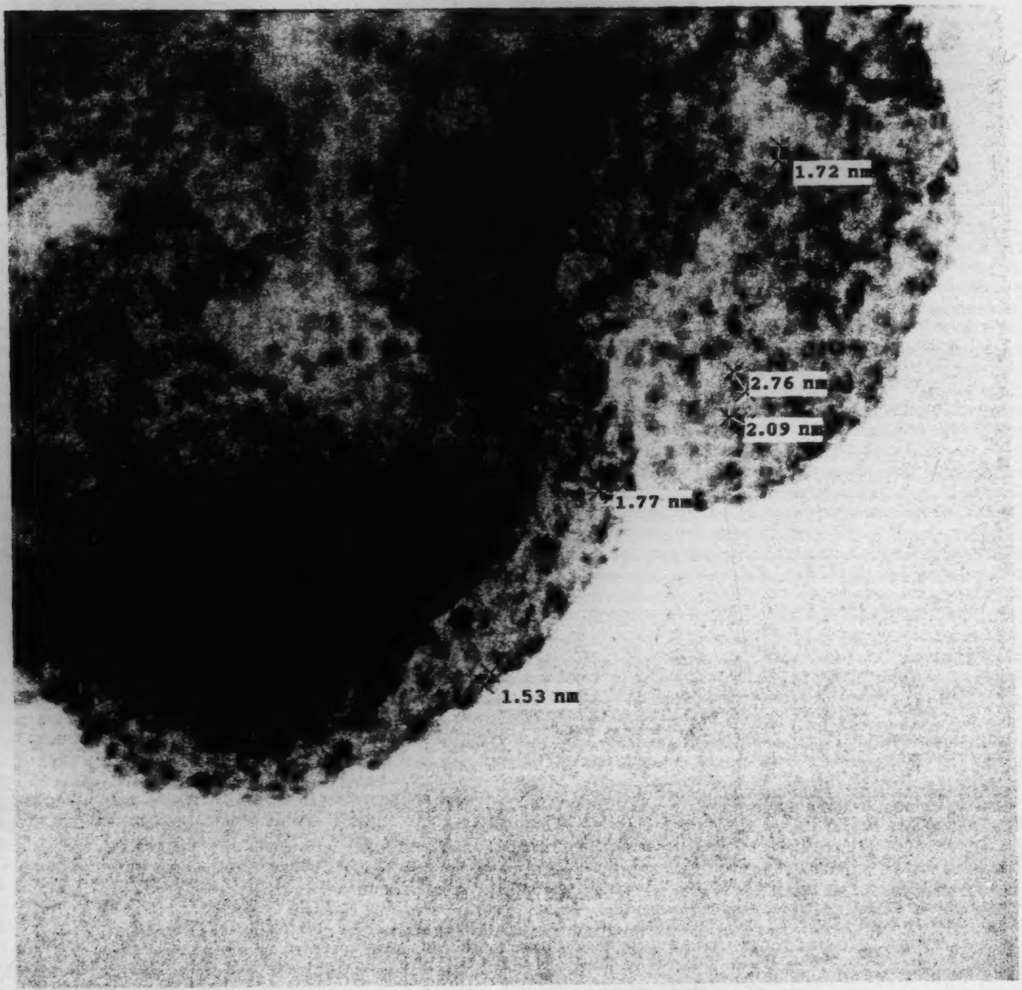
1.72 nm
2.76 nm
2.09 nm
1.77 nm
1.53 nm

Nov 7 2006_009.tif
Calcined Ni H CHA
Print Mag: 653000x @ 3.0 in
8:54 11/07/06

20 nm
HV=200kV
Direct Mag: 800000x
U of A Physics

Figure B.62: NiHCHA As made.

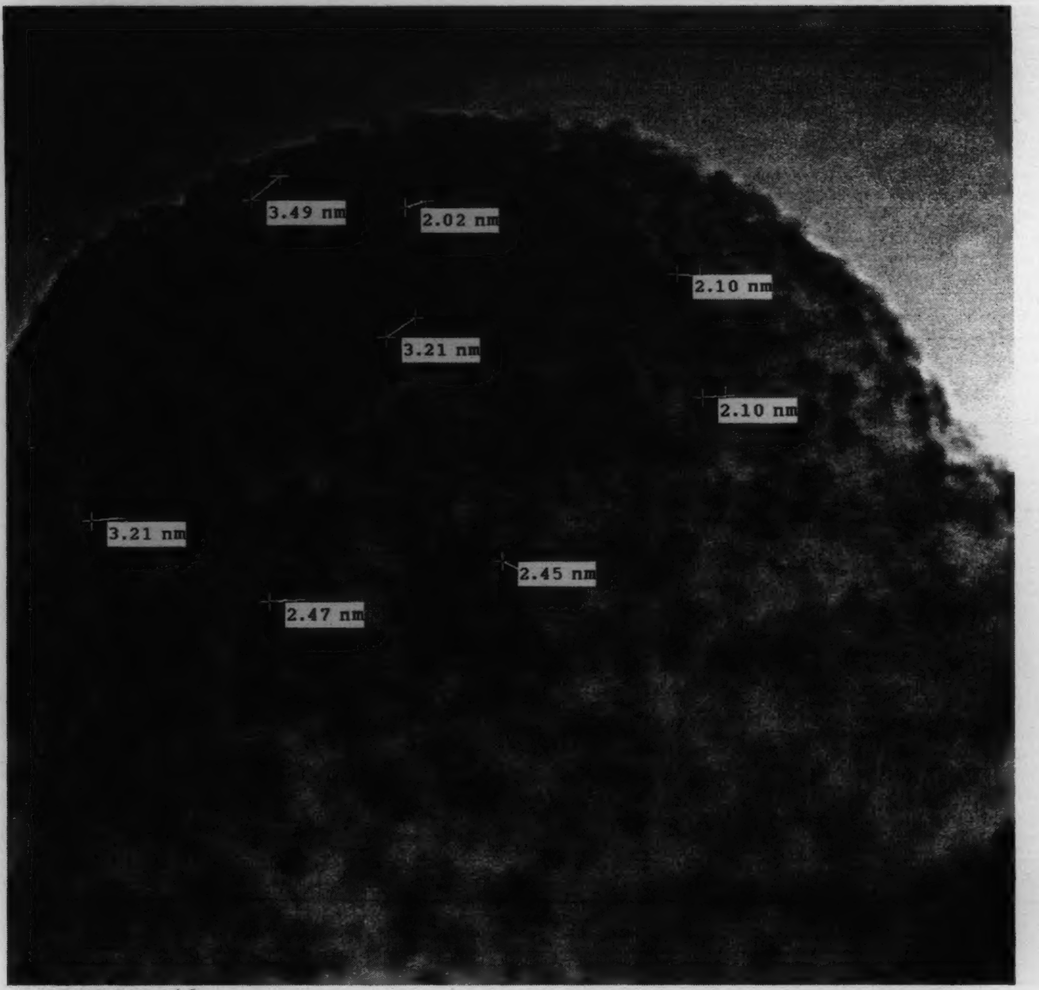
3.49 nm
2.02 nm
2.10 nm
3.21 nm
2.10 nm
3.21 nm
2.45 nm
2.47 nm
5 nm

oct13_06_013.tif
focus - 48nm
Print Mag: 816000x @ 3. in
9:56 10/13/06

HV=200kV
Direct Mag: 1000000x
U of A Physics

Figure B.63: NiHCHA reduced at 200°C in $H_2$.

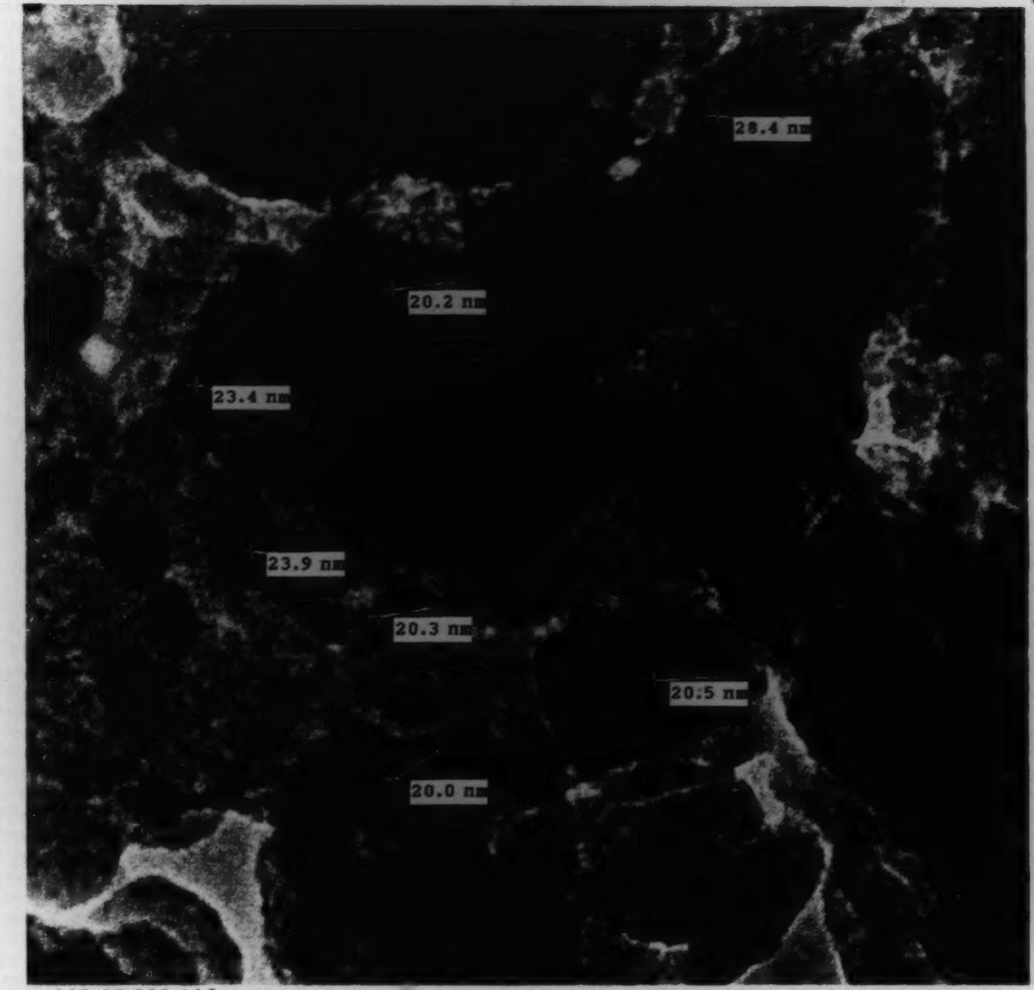
28.4 nm
20.2 nm
23.4 nm
23.9 nm
20.3 nm
20.5 nm
20.0 nm

oct13_06_023.tif
focus -976nm
Print Mag: 204000x @ 3. in
10:19 10/13/06

20 nm
HV=200kV
Direct Mag: 250000x
U of A Physics

Figure B.64: NiHCHA reduced at 200°C in $H_2$.

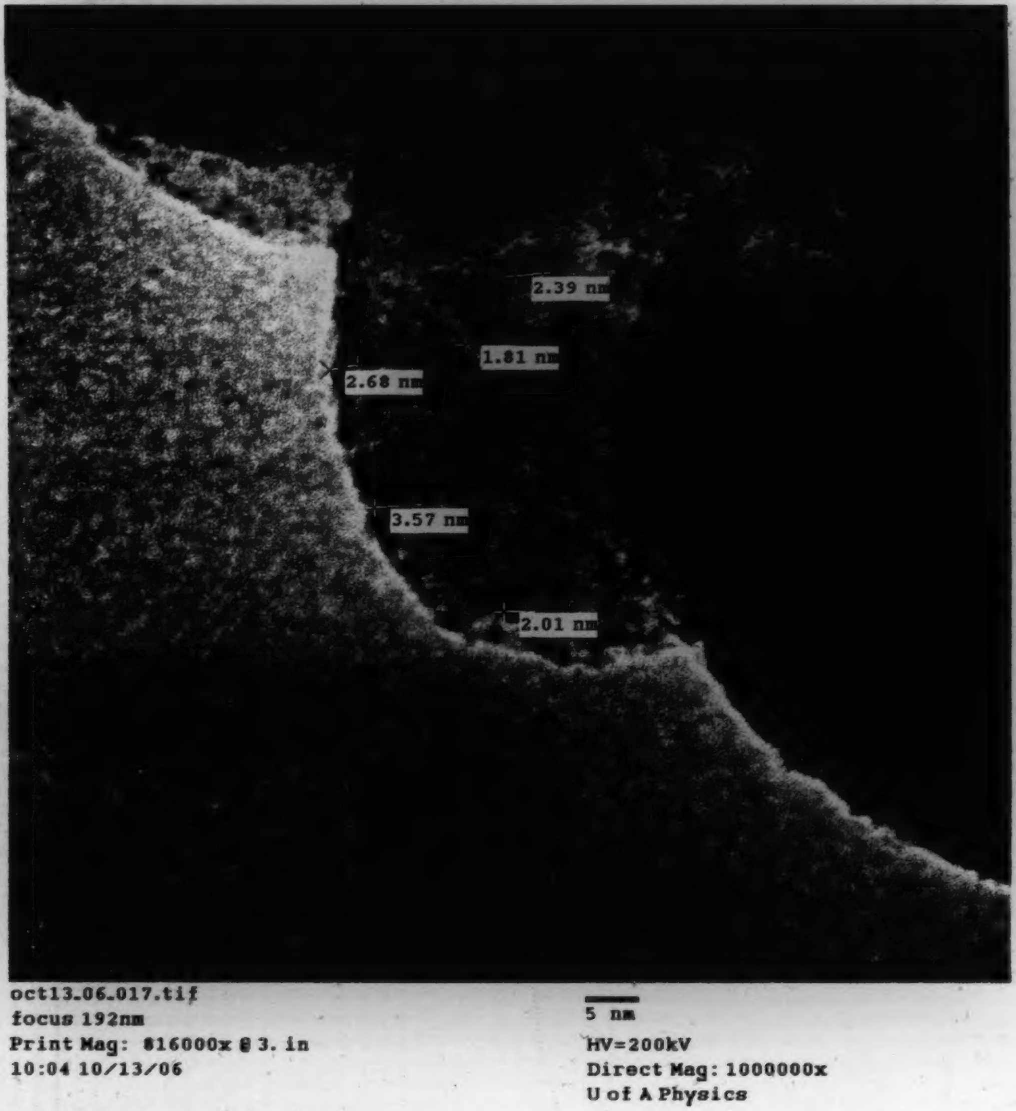
2.39 nm
1.81 nm
2.68 nm
3.57 nm
2.01 nm
oct13_06_017.tif
focus 192nm
Print Mag: 816000x @ 3. in
10:04 10/13/06
5 nm
HV=200kV
Direct Mag: 1000000x
U of A Physics

Figure B.65: NiHCHA reduced at 200°C in $H_2$.

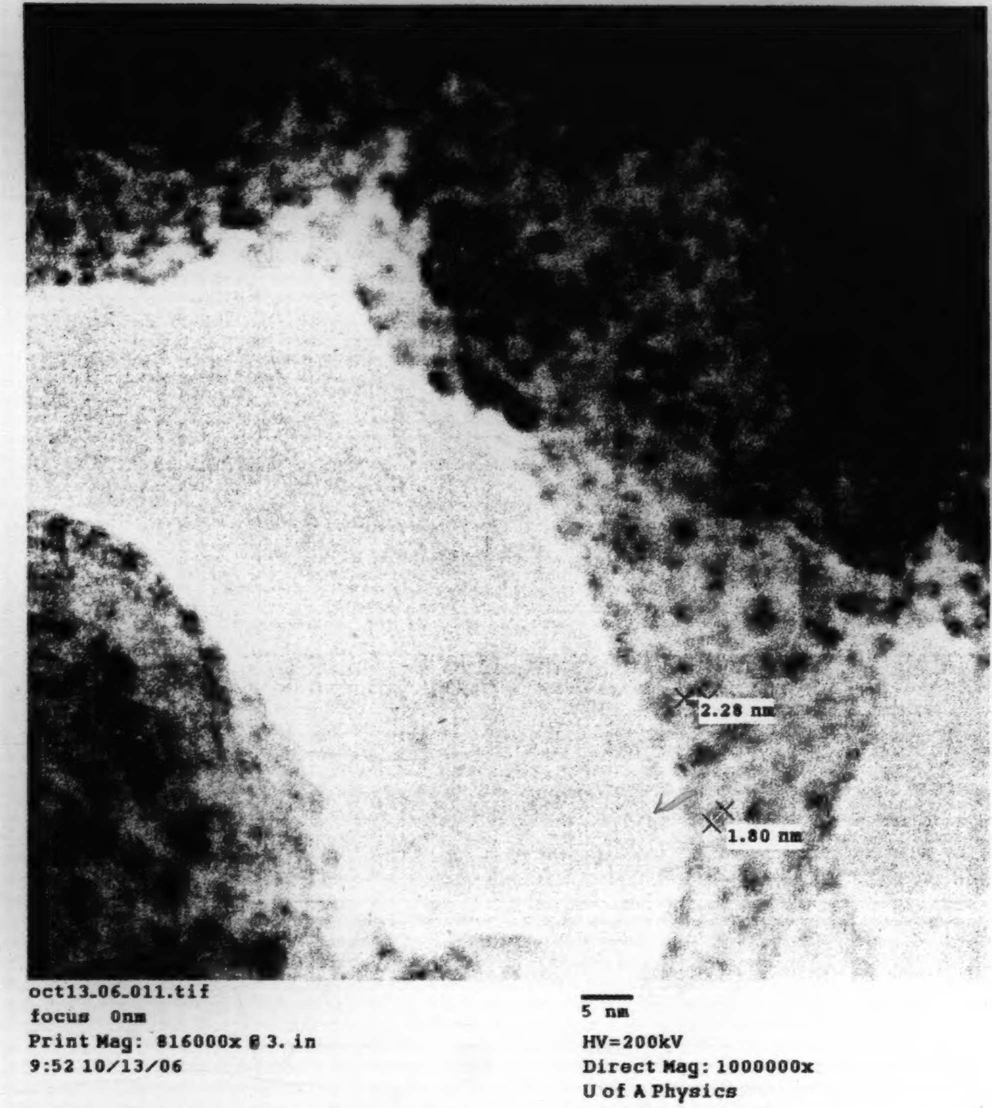
2.28 nm
1.80 nm
oct13_06_011.tif
focus 0nm
Print Mag: 816000x @ 3. in
9:52 10/13/06
5 nm
HV=200kV
Direct Mag: 1000000x
U of A Physics

Figure B.66: NiHCHA reduced at 200°C in $H_2$.

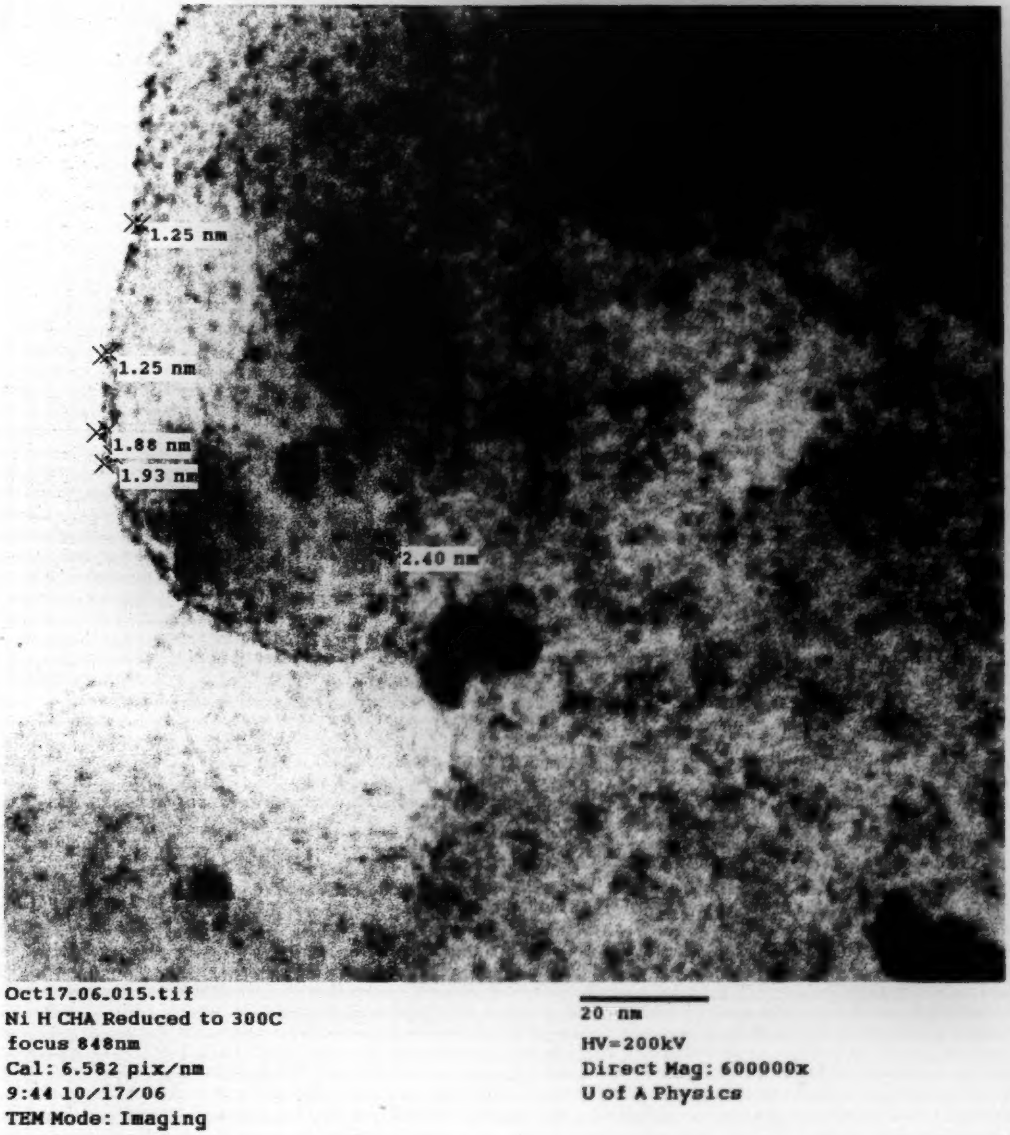
1.25 nm
1.25 nm
1.88 nm
1.93 nm
2.40 nm
Oct17_06_015.tif
Ni H CHA Reduced to 300C
focus 848nm
Cal: 6.582 pix/nm
9:44 10/17/06
TEM Mode: Imaging
20 nm
HV=200kV
Direct Mag: 600000x
U of A Physics

Figure B.67: NiHCHA reduced at 300°C in $H_2$.

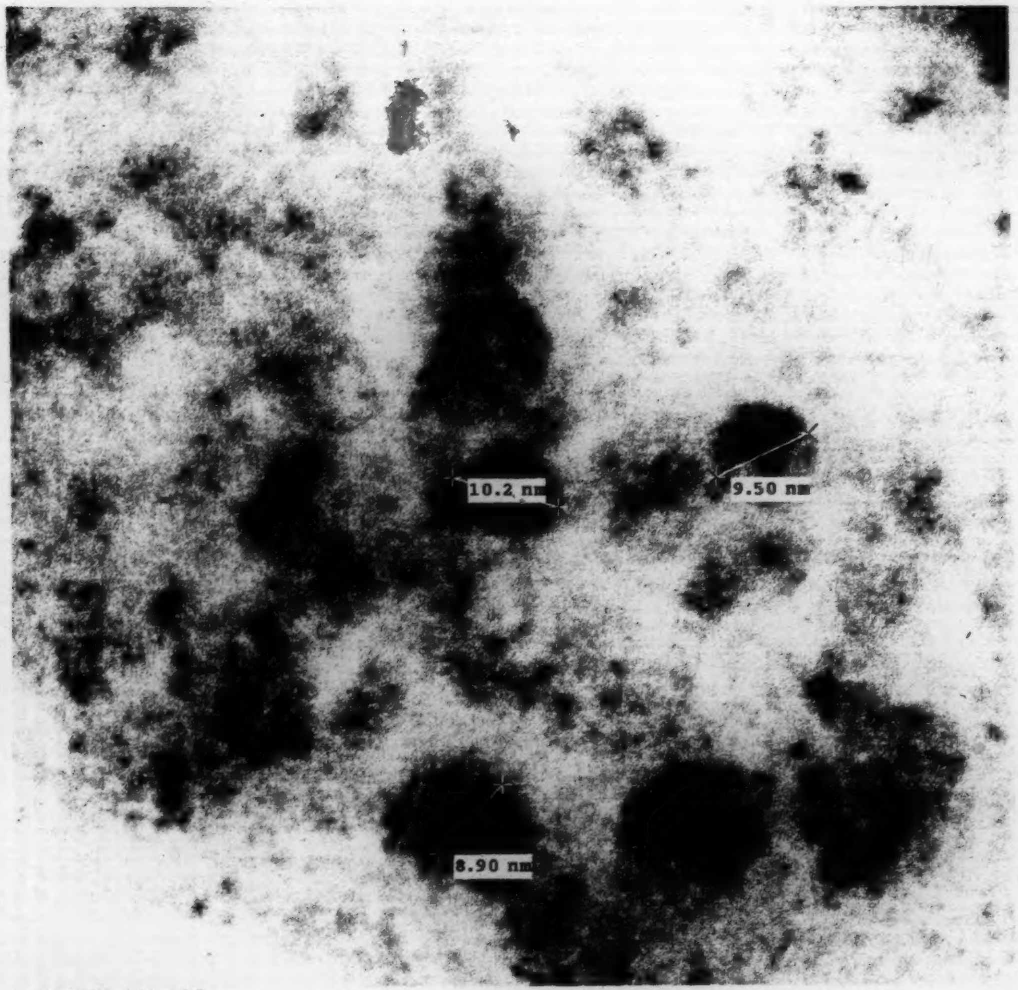

Oct17_06_031.tif
Ni H CHA Reduced to 300C
focus 2493
Cal: 10.97 pix/nm
10:31 10/17/06
TEM Mode: Imaging

5 nm
HV=200kV
Direct Mag: 1000000x
U of A Physics

Figure B.68: NiHCHA reduced at 300°C in $H_2$.

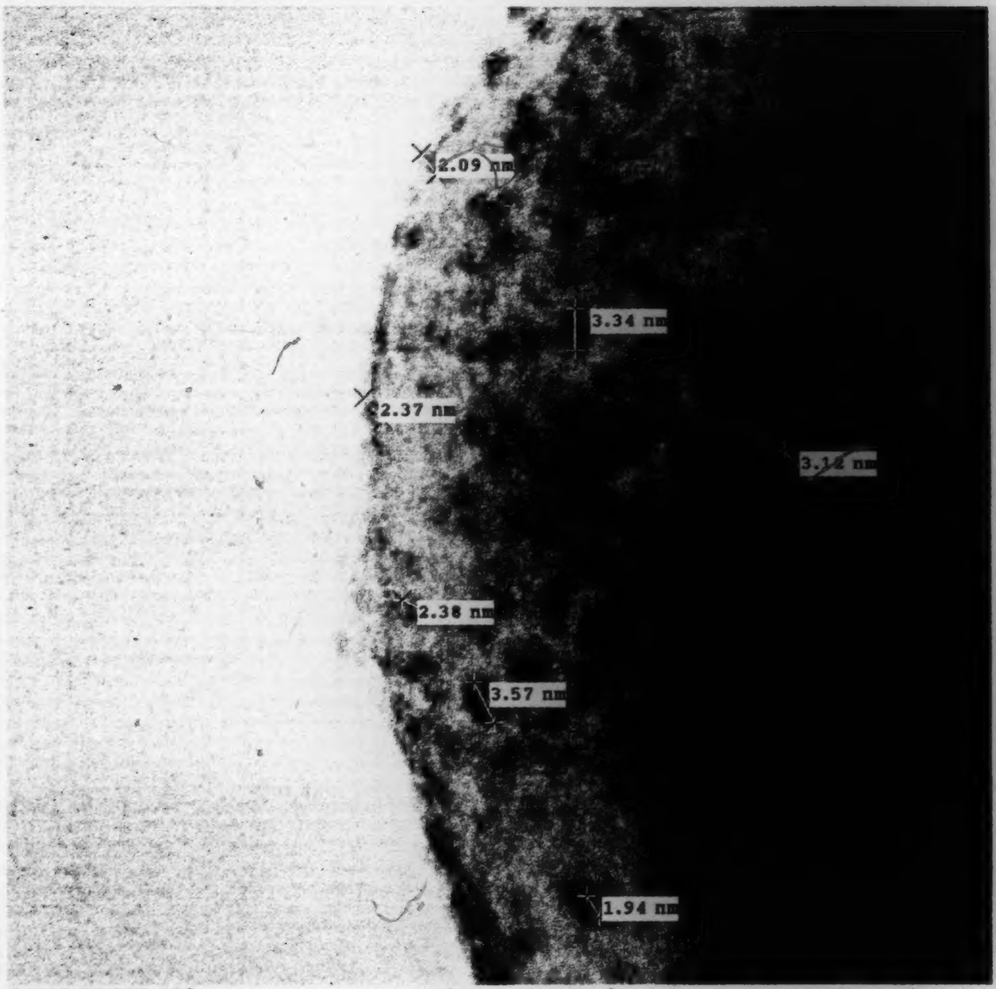
2.09 nm
3.34 nm
2.37 nm
3.12 nm
2.38 nm
3.57 nm
1.94 nm

Oct17_06_017.tif
Ni H CHA Reduced to 300C
focus -304
Cal: 13.164 pix/nm
9:50 10/17/06
TEM Mode: Imaging

5 nm
HV=200kV
Direct Mag: 1200000x
U of A Physics

Figure B.69: NiHCHA reduced at 300°C in $H_2$.

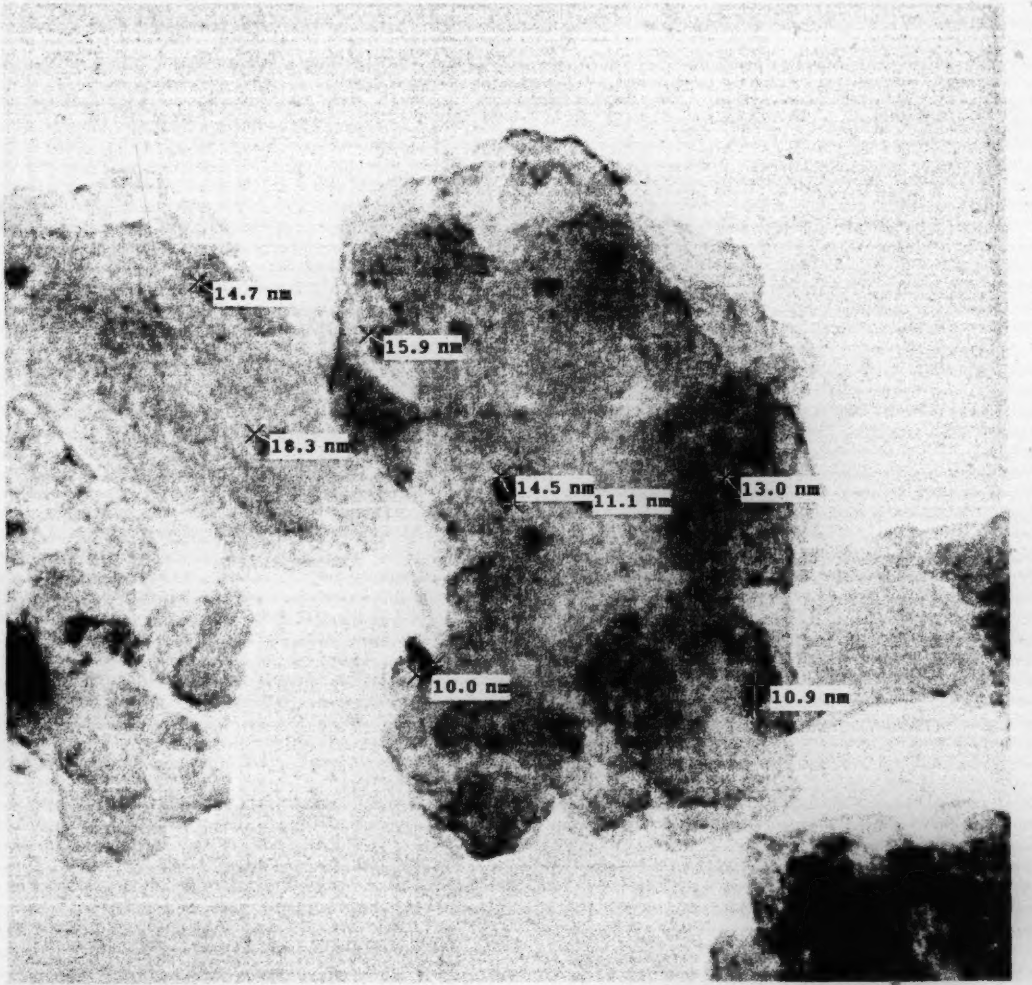
14.7 nm
15.9 nm
18.3 nm
14.5 nm
11.1 nm
13.0 nm
10.0 nm
10.9 nm

Oct17_06_033.tif
Ni H CHA Reduced to 300C
focus 1344
Cal: 2.194 pix/nm
10:35 10/17/06
TEM Mode: Imaging

100 nm
HV=200kV
Direct Mag: 200000x
U of A Physics

Figure B.70: NiHCHA reduced at 300°C in $H_2$.

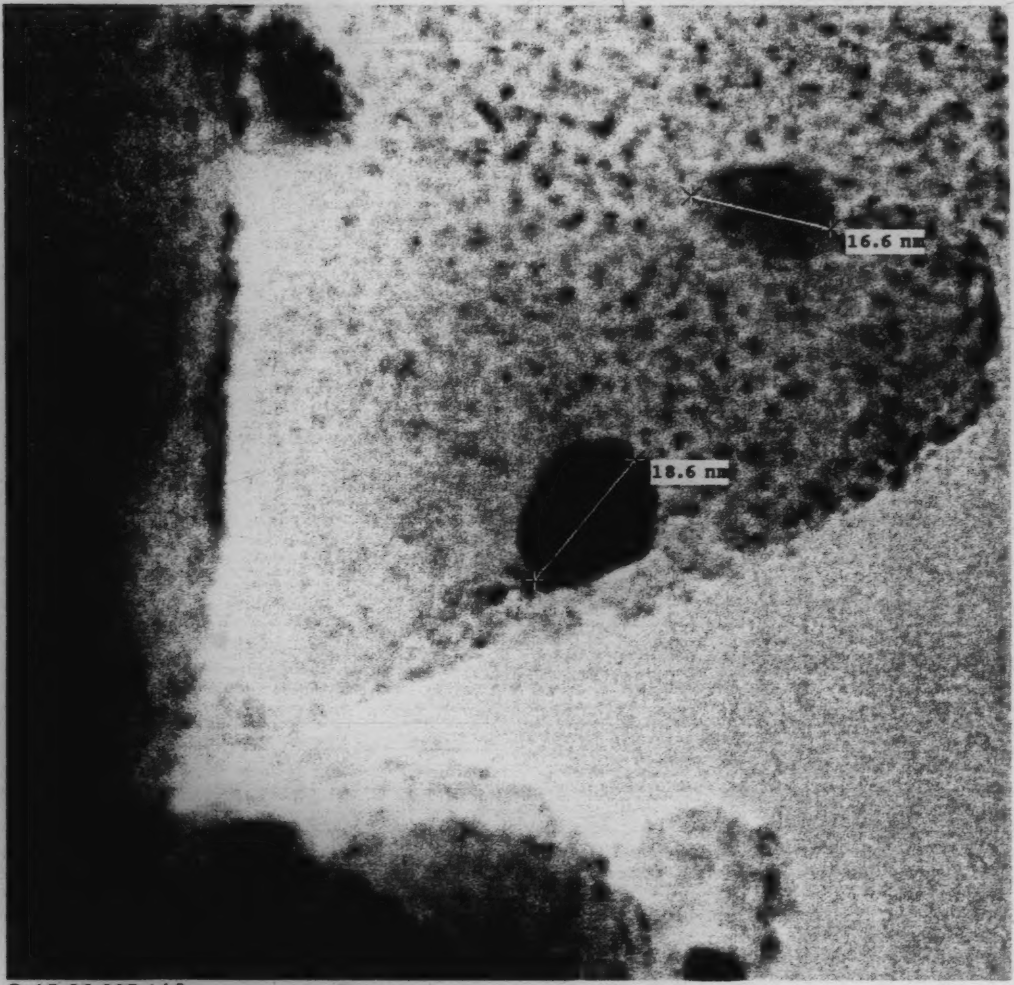

Oct5_06_007.tif
Calcined Ni-H-CHA R 400C
Print Mag: 653000x @ 3, in
10:21 10/05/06

20 nm
HV=200kV
Direct Mag: 800000x
U of A Physics

Figure B.71: NiHCHA reduced at 400°C in $H_2$.

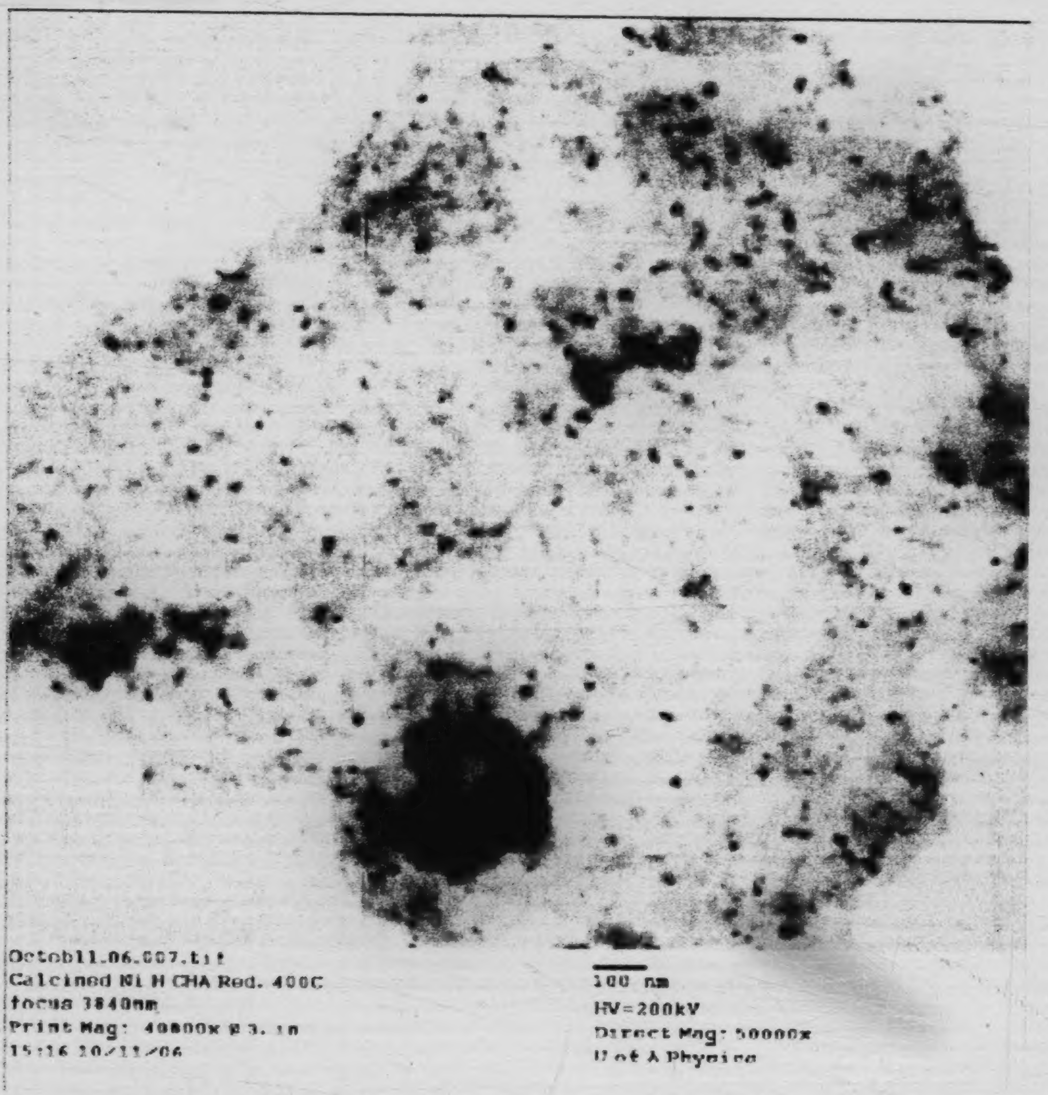
Octob11.06.007.tif
Calcined Ni H CHA Red. 400C
focus 3840nm
Print Mag: 40800x @ 3. in
15:16 10/11/06
100 nm
HV=200kV
Direct Mag: 50000x
U of A Physics

Figure B.72: NiHCHA reduced at 400°C in $H_2$.

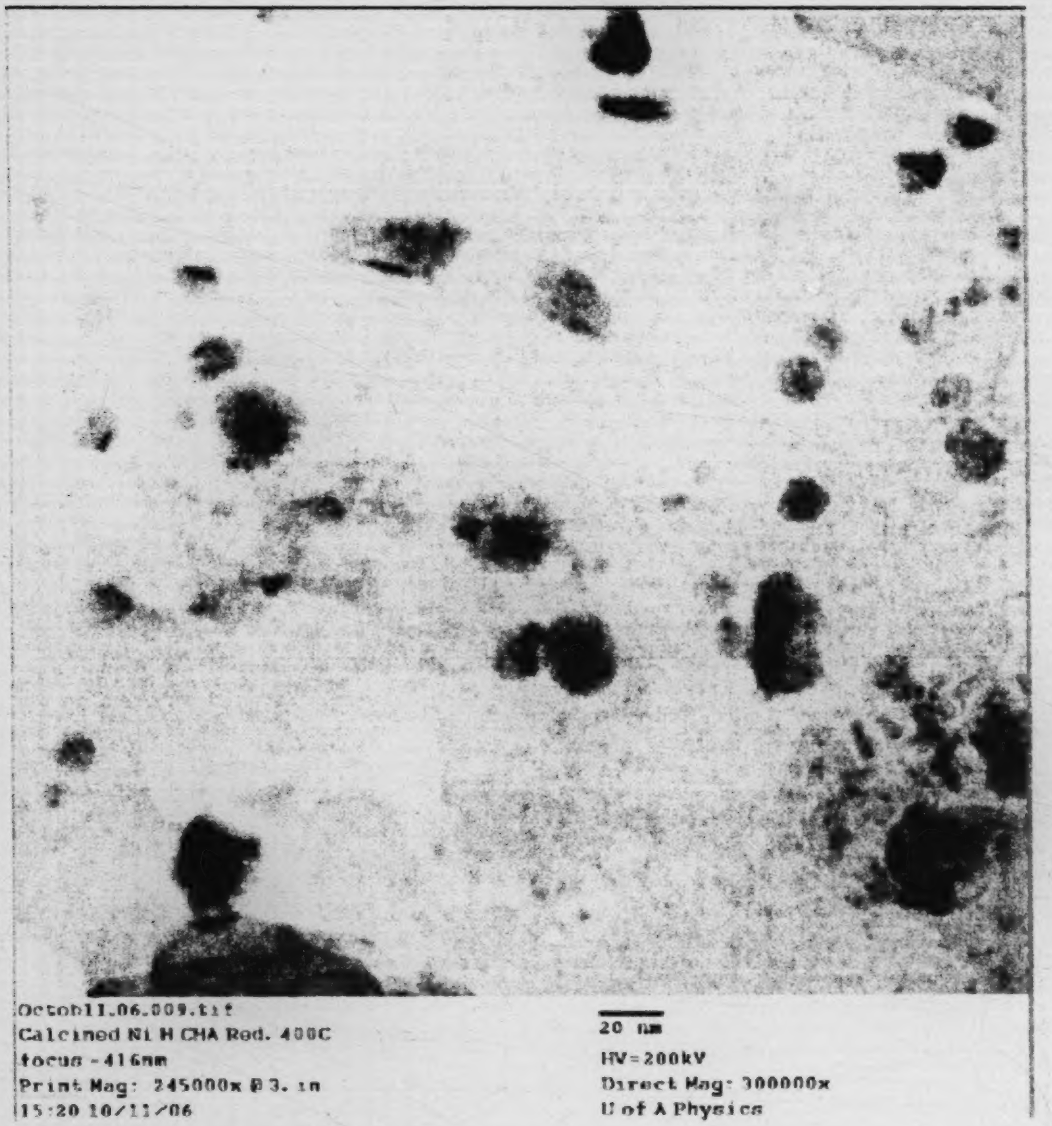
Octob11.06.009.tif
Calcined Ni H CHA Red. 400C
focus -416nm
Print Mag: 245000x @ 3. in
15:20 10/11/06
20 nm
HV=200kV
Direct Mag: 300000x
U of A Physics

Figure B.73: NiHCHA reduced at 400°C in $H_2$.

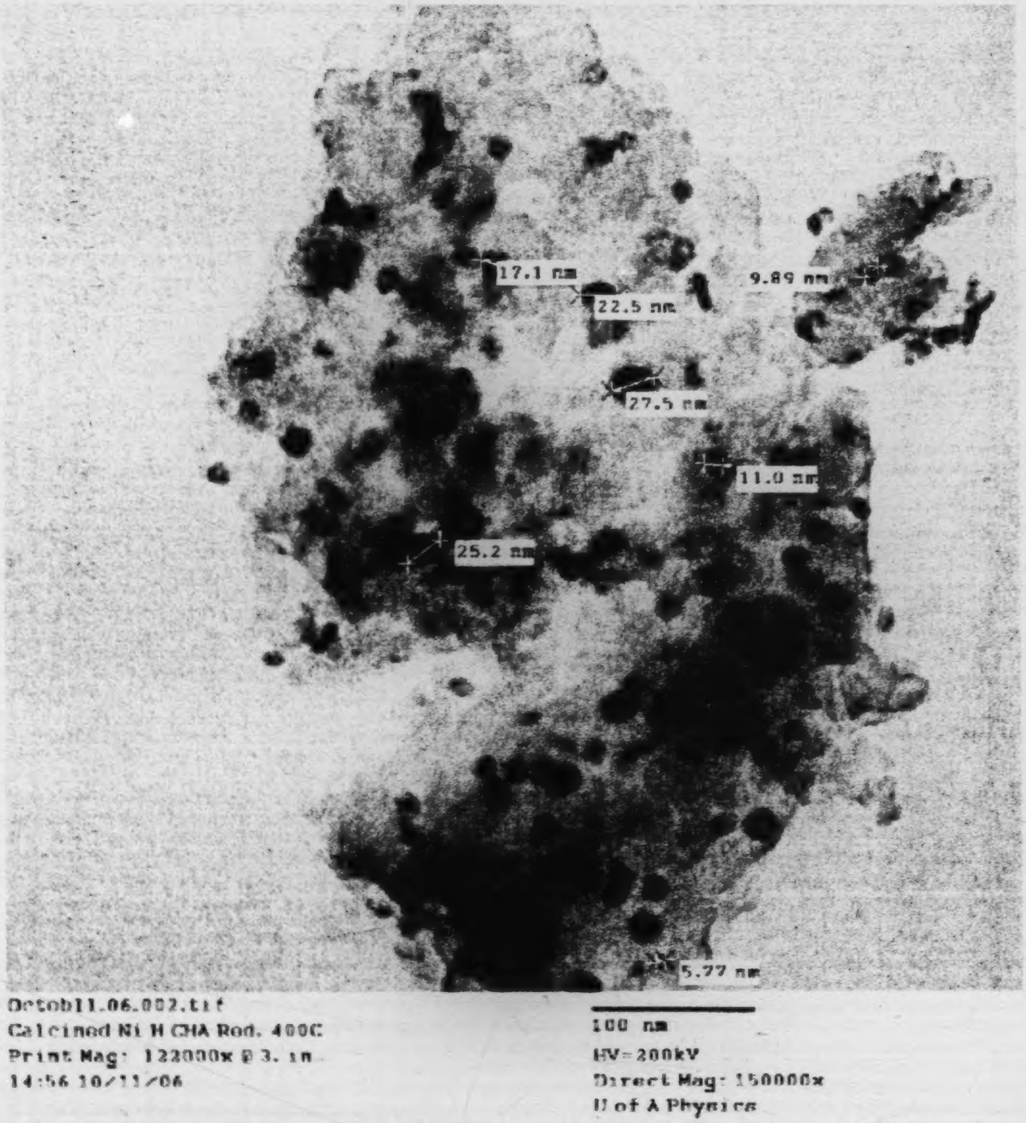
17.1 nm
22.5 nm
9.89 nm
27.5 nm
11.0 nm
25.2 nm
5.77 nm
Octob11.06.002.tif
Calcined Ni H CHA Red. 400C
Print Mag: 122000x @ 3. in
14:56 10/11/06
100 nm
HV=200kV
Direct Mag: 150000x
U of A Physics

Figure B.74: NiHCHA reduced at 400°C in $H_2$.

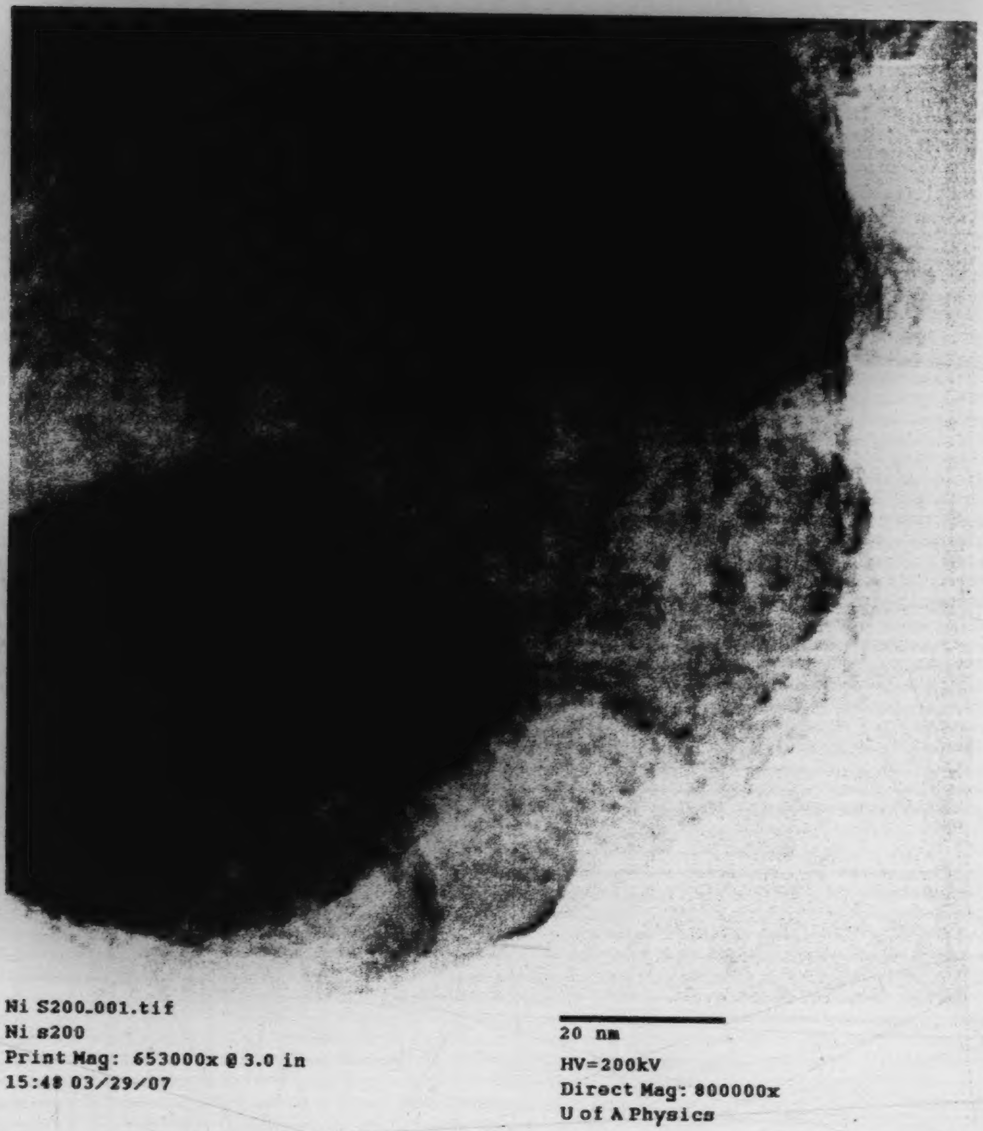
Ni S200_001.tif
Ni s200
Print Mag: 653000x @ 3.0 in
15:48 03/29/07
20 nm
HV=200kV
Direct Mag: 800000x
U of A Physics

Figure B.75: NiHCHA sulfided at 200°C in $H_2S/H_2$.

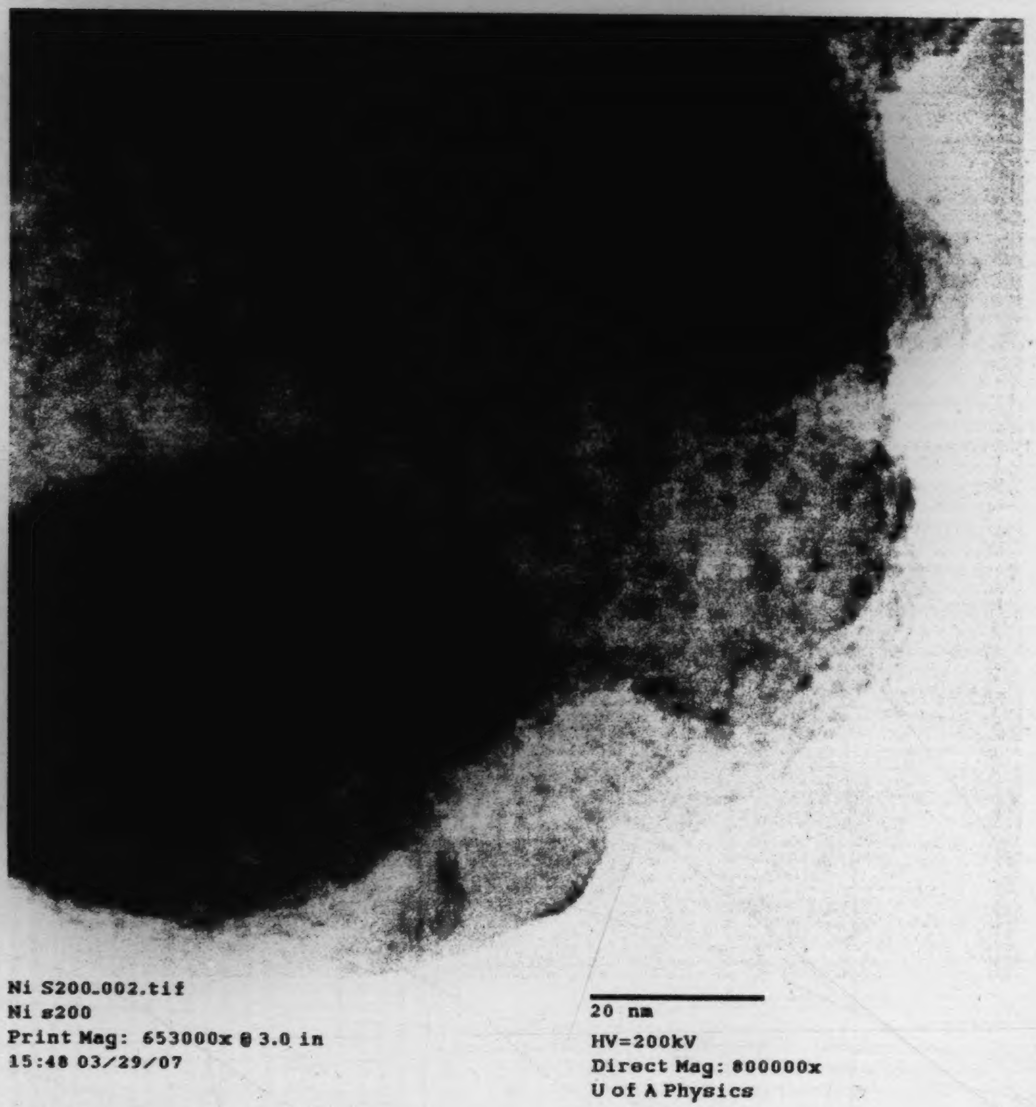
Ni S200_002.tif
Ni s200
Print Mag: 653000x @ 3.0 in
15:48 03/29/07
20 nm
HV=200kV
Direct Mag: 800000x
U of A Physics

Figure B.76: NiHCHA sulfided at 200°C in $H_2S/H_2$.

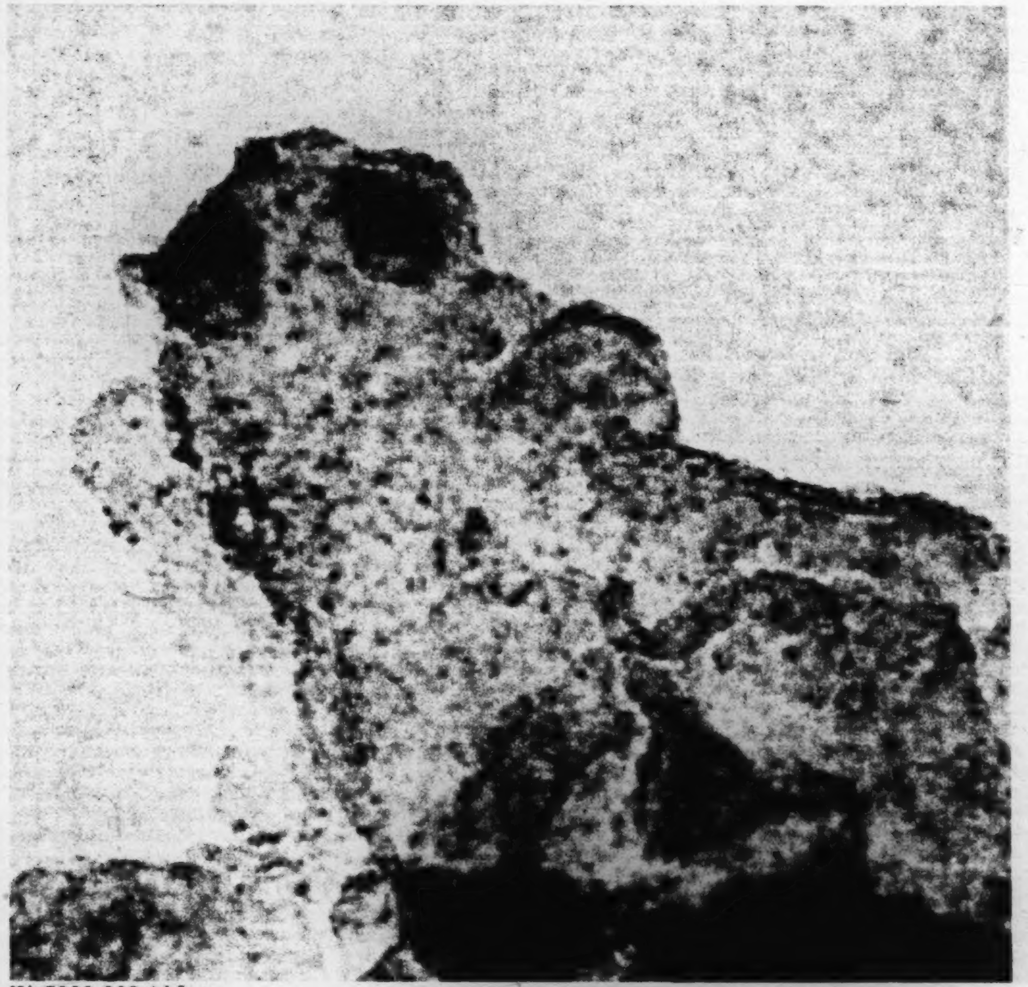

Ni S200_003.tif
Ni s200
Print Mag: 408000x @ 3.0 in
15:53 03/29/07

HV=200kV
Direct Mag: 500000x
U of A Physics

Figure B.77: NiHCHA sulfided at 200°C in $H_2S/H_2$.

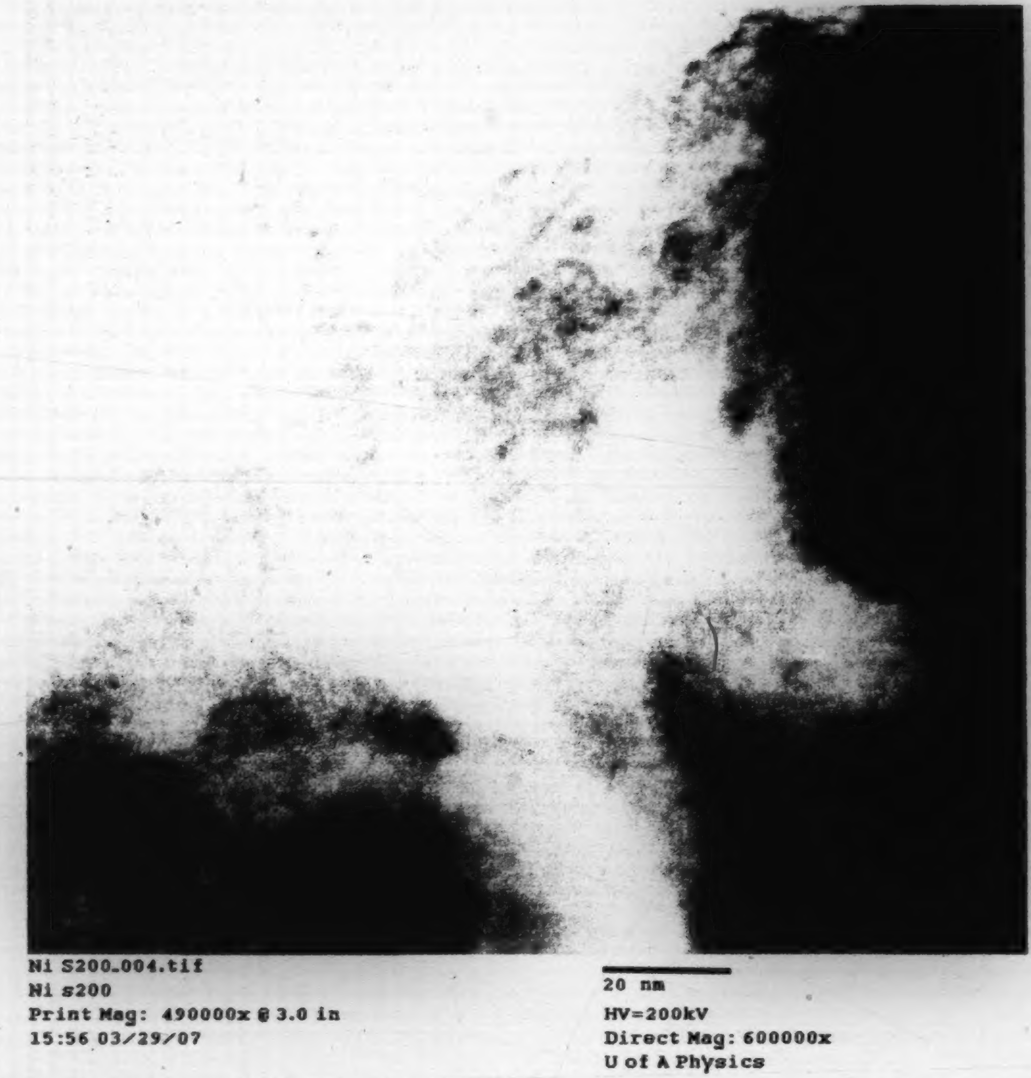
Ni S200_004.tif
Ni s200
Print Mag: 490000x @ 3.0 in
15:56 03/29/07
20 nm
HV=200kV
Direct Mag: 600000x
U of A Physics

Figure B.78: NiHCHA sulfided at 200°C in $H_2S/H_2$.

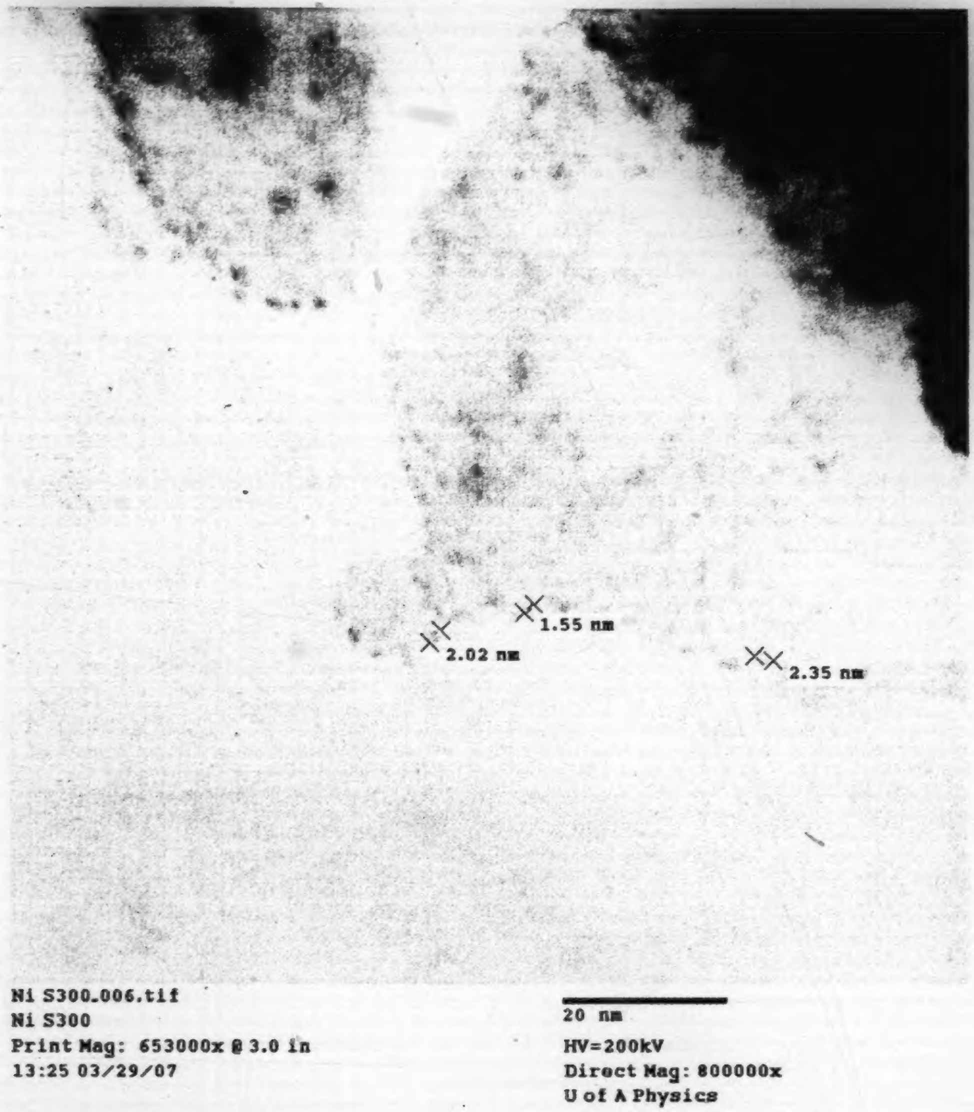
1.55 nm
2.02 nm
2.35 nm
Ni S300_006.tif
Ni S300
Print Mag: 653000x @ 3.0 in
13:25 03/29/07
20 nm
HV=200kV
Direct Mag: 800000x
U of A Physics

Figure B.79: NiHCHA sulfided at 300°C in $H_2S/H_2$.

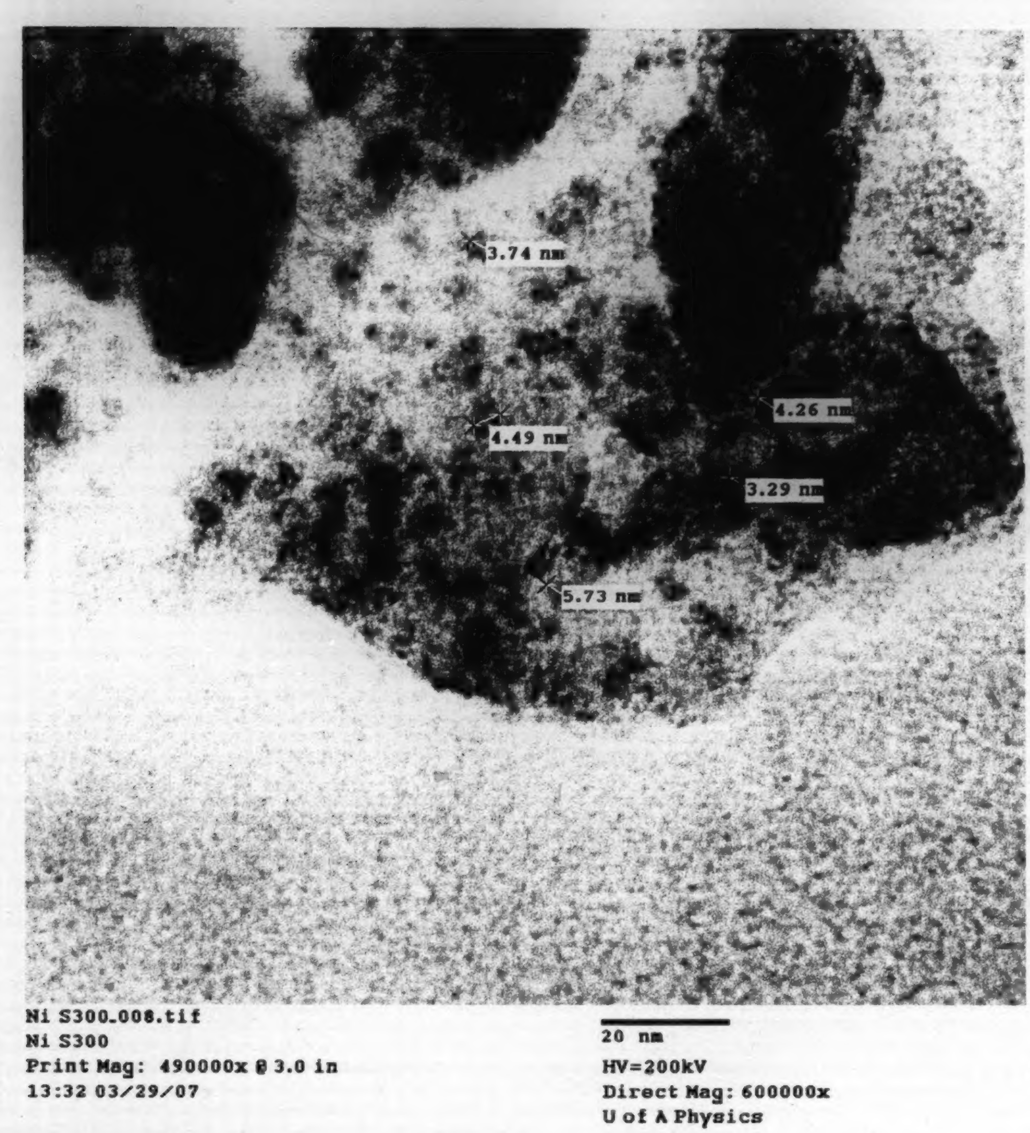
3.74 nm
4.26 nm
4.49 nm
3.29 nm
5.73 nm
Ni S300_008.tif
Ni S300
Print Mag: 490000x @ 3.0 in
13:32 03/29/07
20 nm
HV=200kV
Direct Mag: 600000x
U of A Physics

Figure B.80: NiHCHA sulfided at 300°C in $H_2S/H_2$.

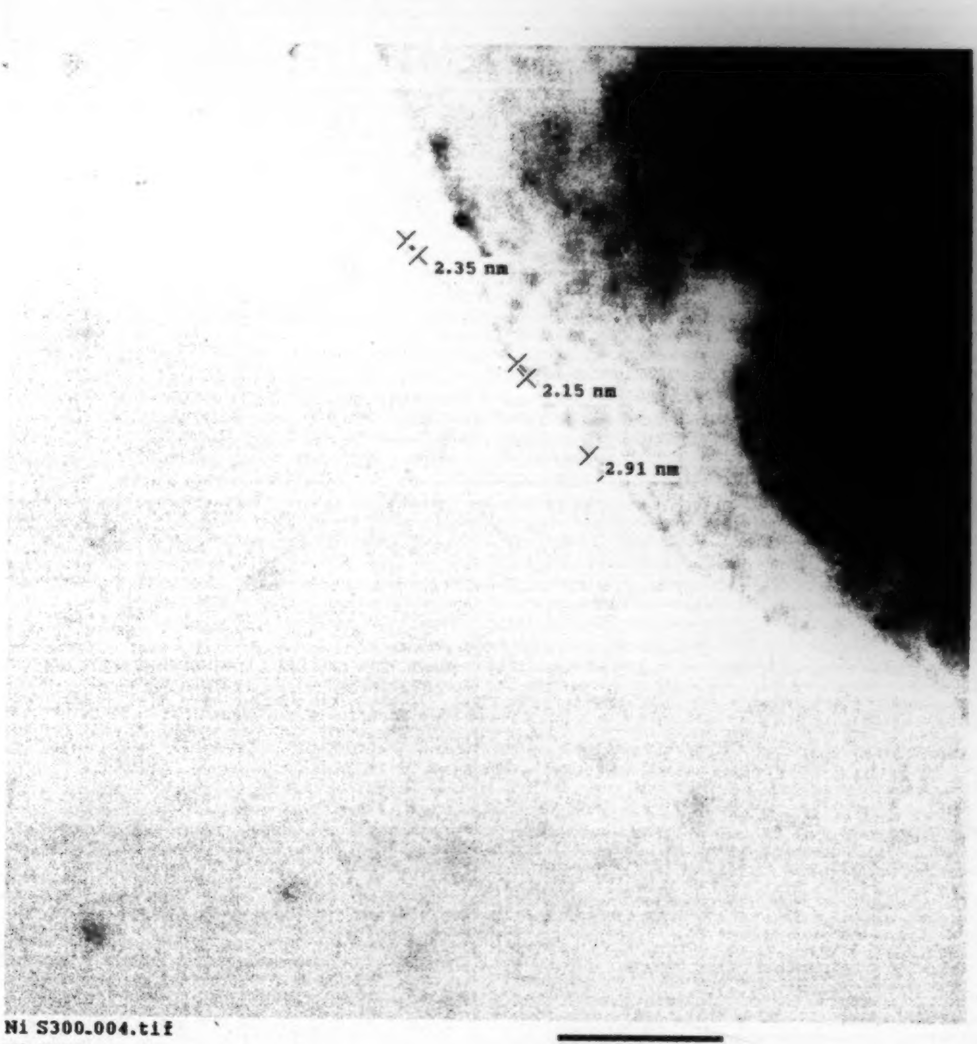
2.35 nm
2.15 nm
2.91 nm
Ni S300.004.tif
Ni S300
Print Mag: 653000x @ 3.0 in
13:23 03/29/07
20 nm
HV=200kV
Direct Mag: 800000x
U of A Physics

Figure B.81: NiHCHA sulfided at 300°C in $H_2S/H_2$.

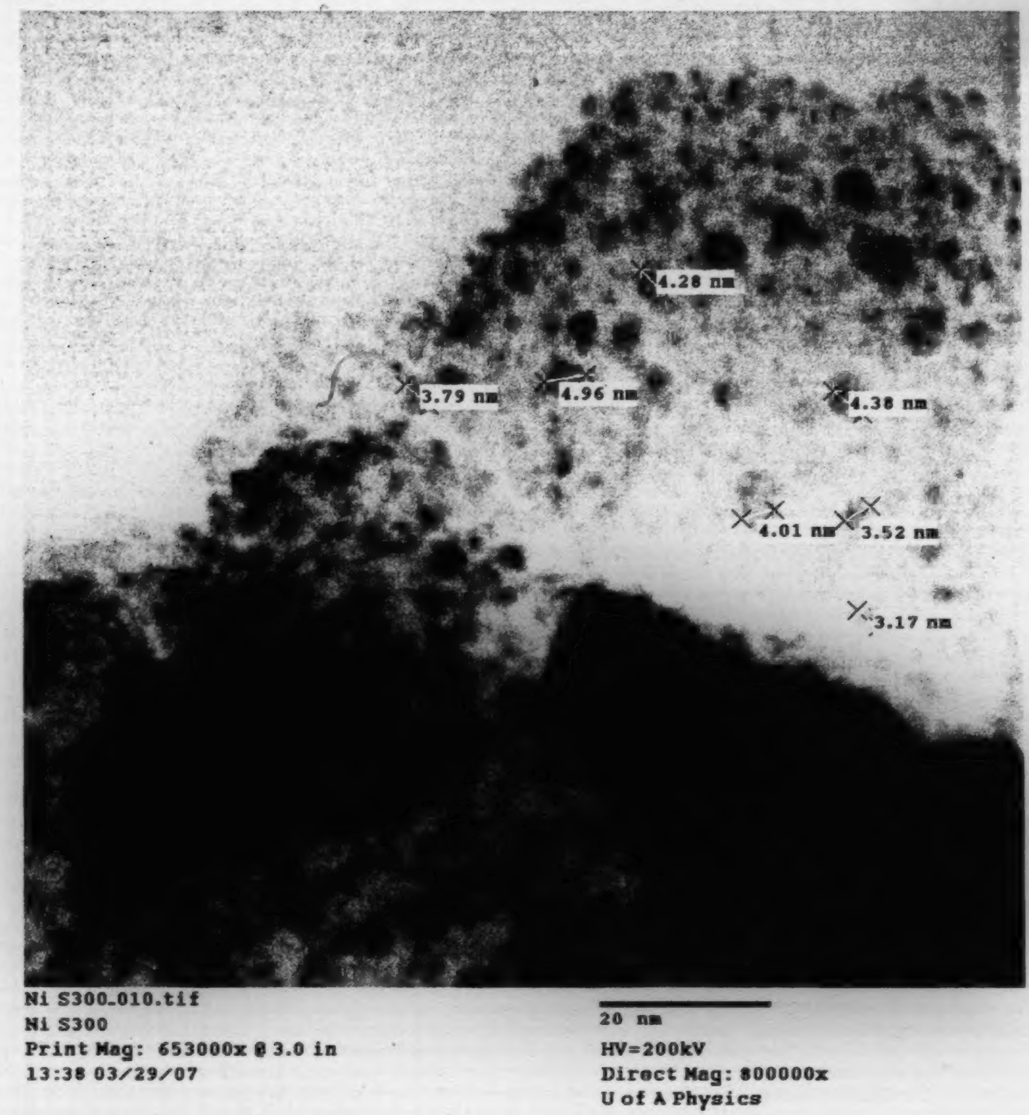
4.28 nm
3.79 nm
4.96 nm
4.38 nm
4.01 nm
3.52 nm
3.17 nm
Ni S300_010.tif
Ni S300
Print Mag: 653000x @ 3.0 in
13:38 03/29/07
20 nm
HV=200kV
Direct Mag: 800000x
U of A Physics

Figure B.82: NiHCHA sulfided at 300°C in $H_2S/H_2$.

Ni S400_001.tif
NiHCHA S400
Print Mag: 204000x @ 3.0 in
10:19 03/29/07
20 nm
HV=200kV
Direct Mag: 250000x
U of A Physics

Figure B.83: NiHCHA sulfided at 400°C in $H_2S/H_2$.

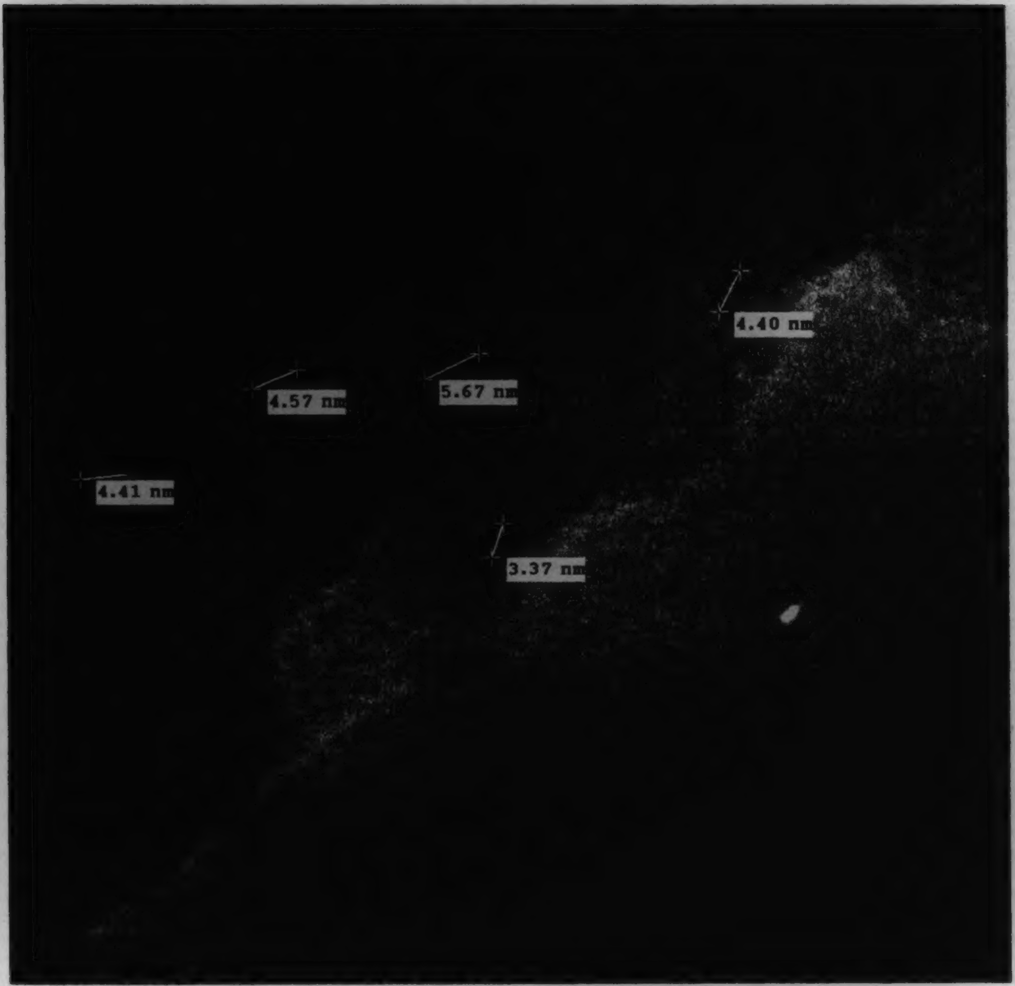
4.40 nm
4.57 nm
5.67 nm
4.41 nm
3.37 nm

Ni S400_007.tif
NiHCHA S400
Print Mag: 816000x @ 3.0 in
10:28 03/29/07

5 nm
HV=200kV
Direct Mag: 1000000x
U of A Physics

Figure B.84: NiHCHA sulfided at 400°C in $H_2S/H_2$.

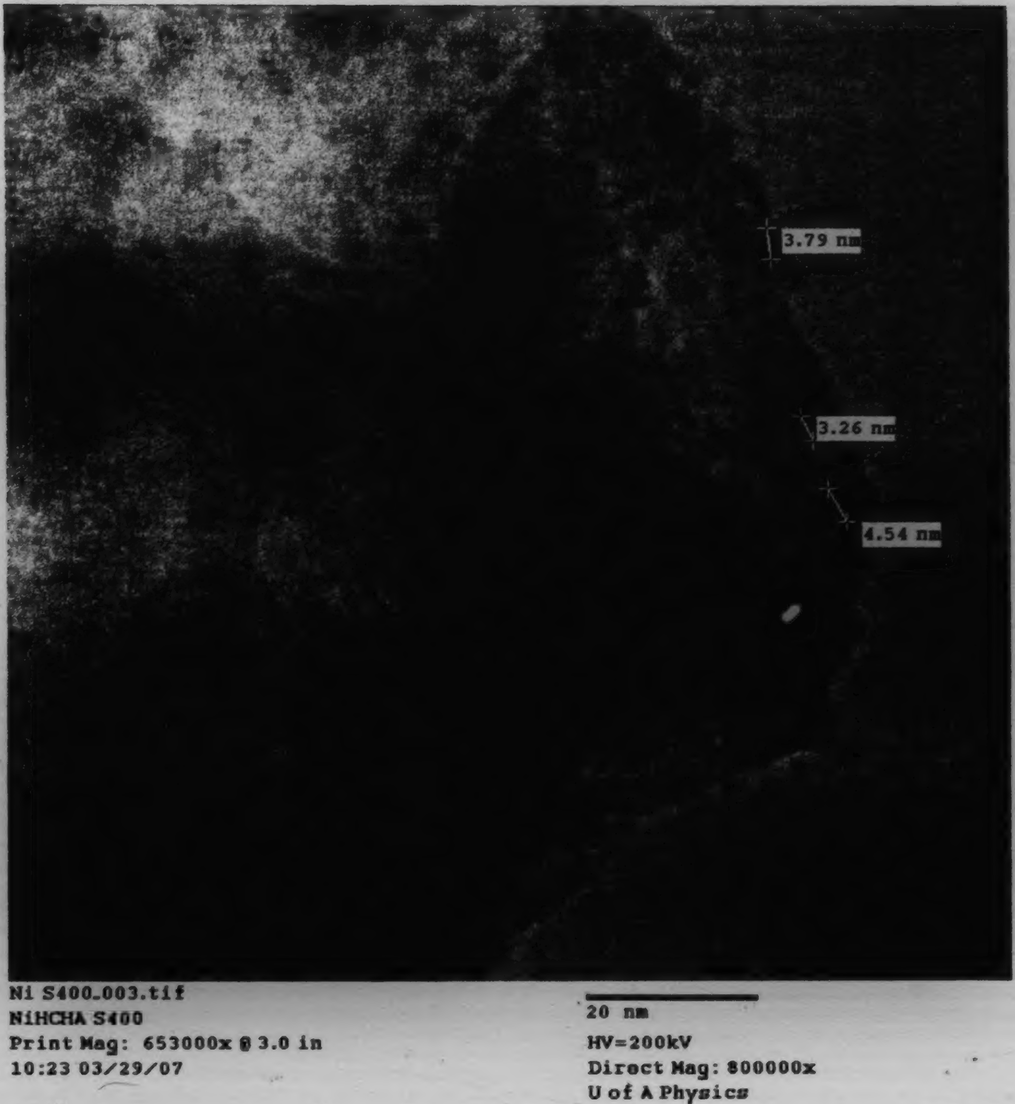
3.79 nm
3.26 nm
4.54 nm
Ni S400_003.tif
NiHCHA S400
Print Mag: 653000x @ 3.0 in
10:23 03/29/07
20 nm
HV=200kV
Direct Mag: 800000x
U of A Physics

Figure B.85: NiHCHA sulfided at 400°C in $H_2S/H_2$.

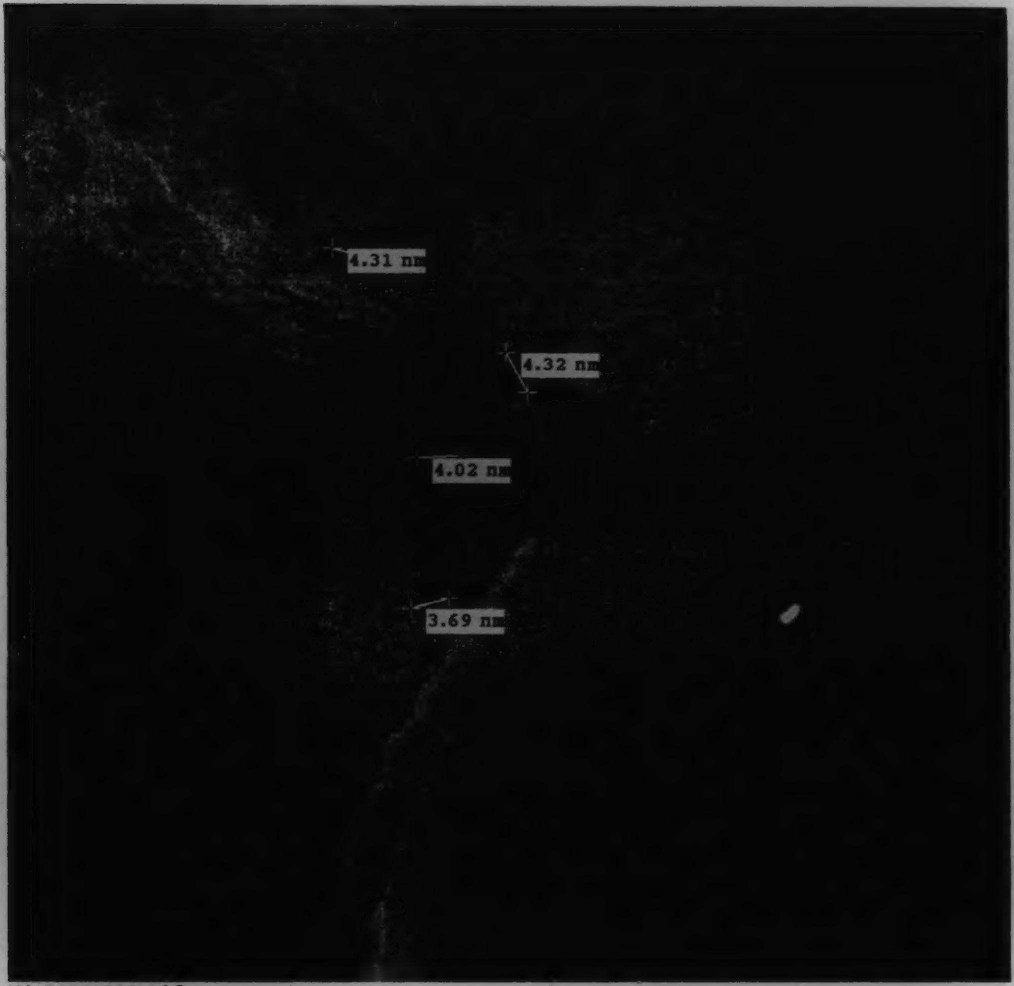
4.31 nm
4.32 nm
4.02 nm
3.69 nm
5 nm

Ni S400_005.tif
NiHCHA S400
Print Mag: 816000x @ 3.0 in
10:24 03/29/07

HV=200kV
Direct Mag: 1000000x
U of A Physics

Figure B.86: NiHCHA sulfided at 400°C in $H_2S/H_2$.

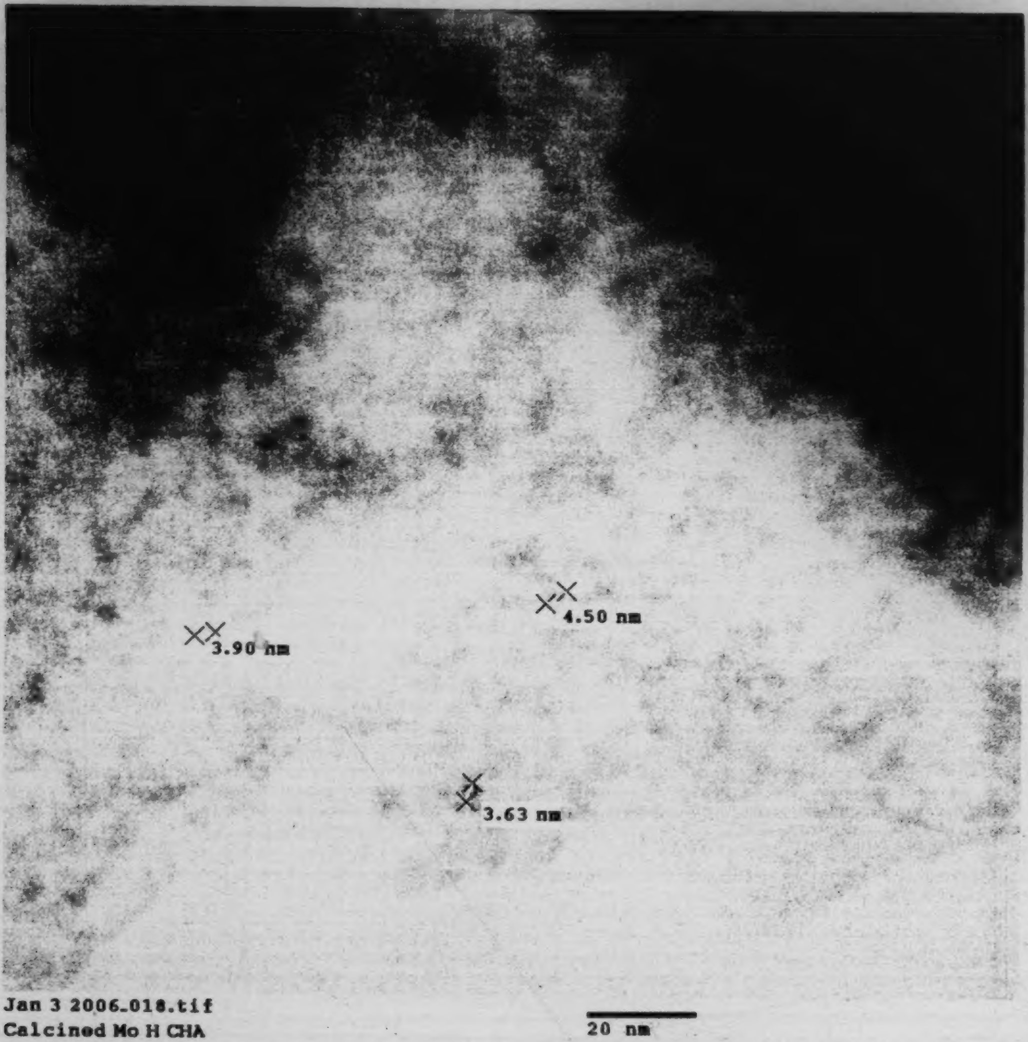
3.90 nm
4.50 nm
3.63 nm
20 nm

Jan 3 2006_018.tif
Calcined Mo H CHA
Print Mag: 273000x @ 51 mm
15:42 01/03/07

HV=200kV
Direct Mag: 500000x
U of A Physics

Figure B.87: MoHCHA As made.

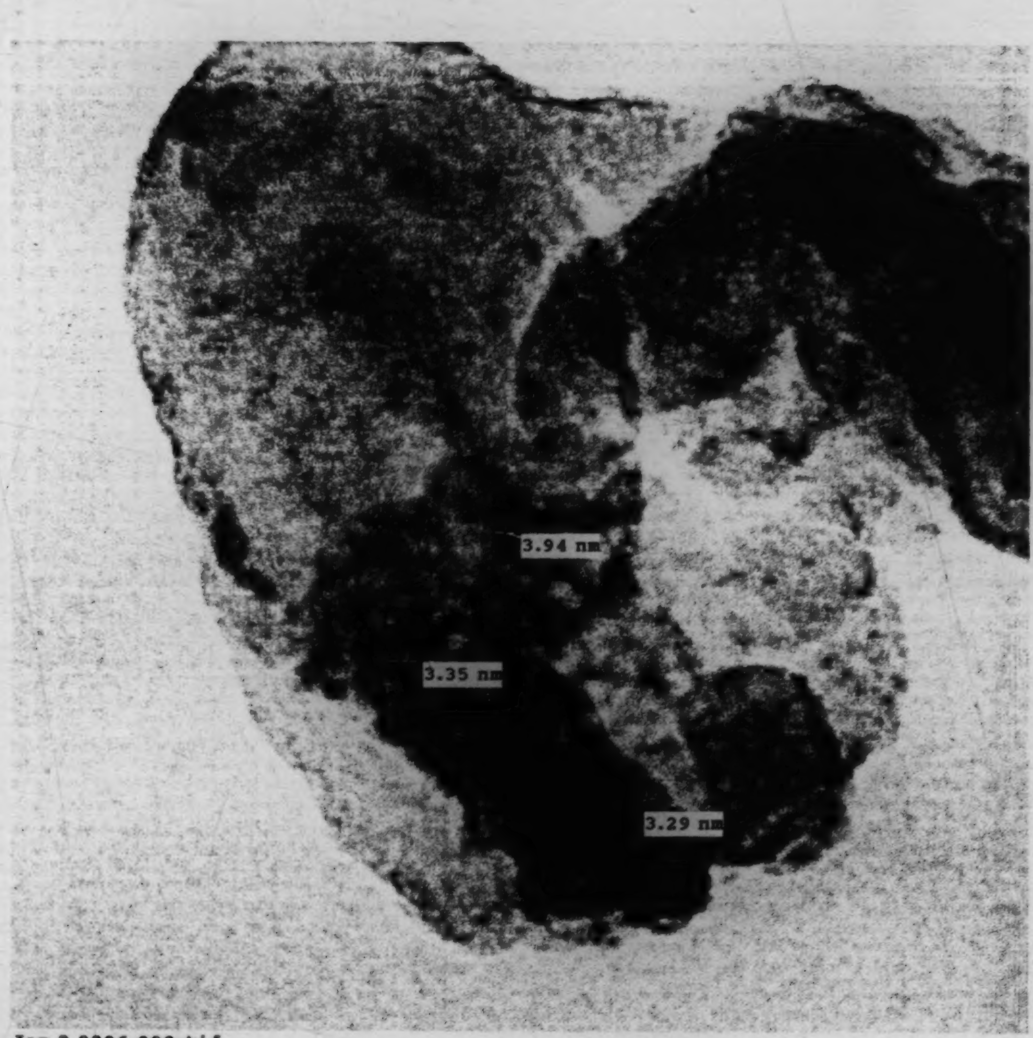
3.94 nm
3.35 nm
3.29 nm

Jan 3 2006_009.tif
Calcined Mo H CHA
Print Mag: 328000x @ 51 mm
15:31 01/03/07

20 nm
HV=200kV
Direct Mag: 600000x
U of A Physics

Figure B.88: MoHCHA As made.

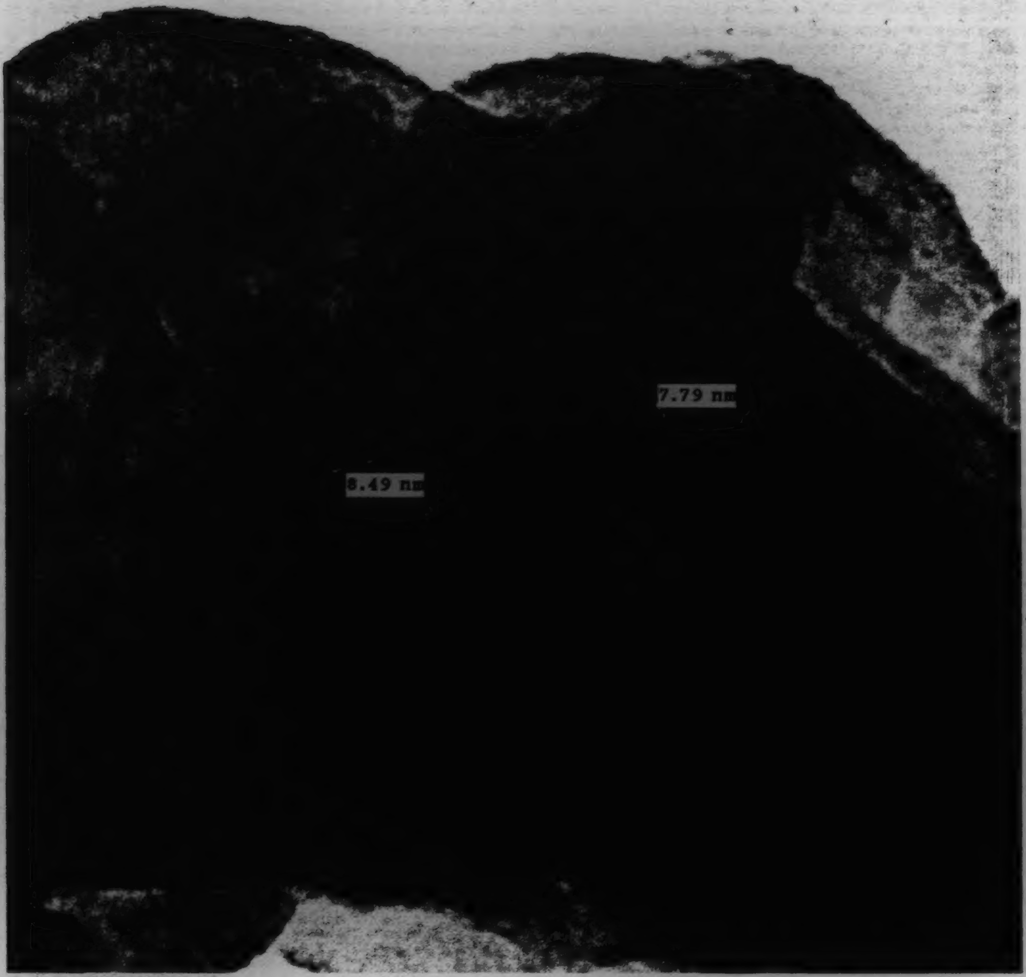

Jan 3 2006_007.tif
Calcined Mo H CHA
Print Mag: 273000x @ 51 mm
15:26 01/03/07

20 nm
HV=200kV
Direct Mag: 500000x
U of A Physics

Figure B.89: MoHCHA As made.

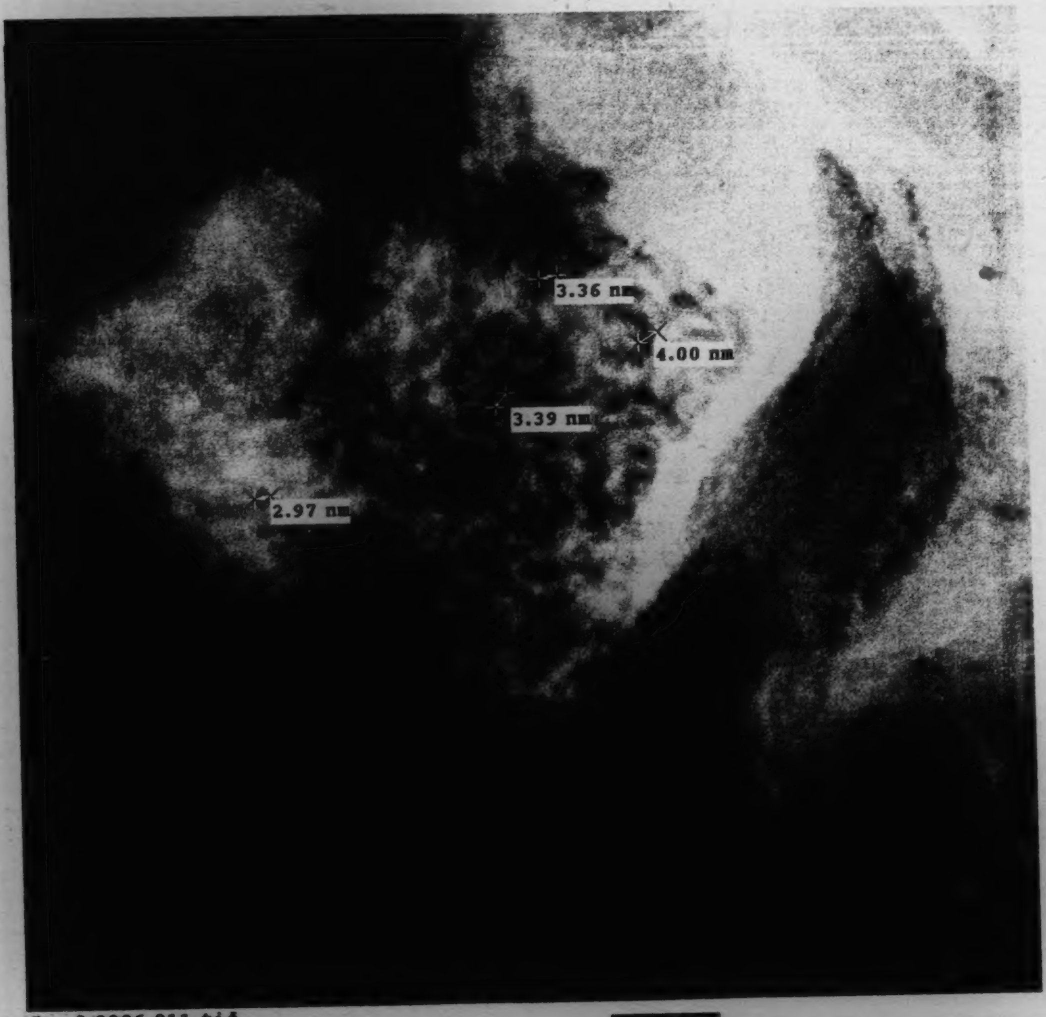
3.36 nm
4.00 nm
3.39 nm
2.97 nm

Jan 3 2006.011.tif
Calcined Mo H CHA
Print Mag: 273000x @ 51 mm
15:34 01/03/07

20 nm
HV=200kV
Direct Mag: 500000x
U of A Physics

Figure B.90: MoHCHA As made.

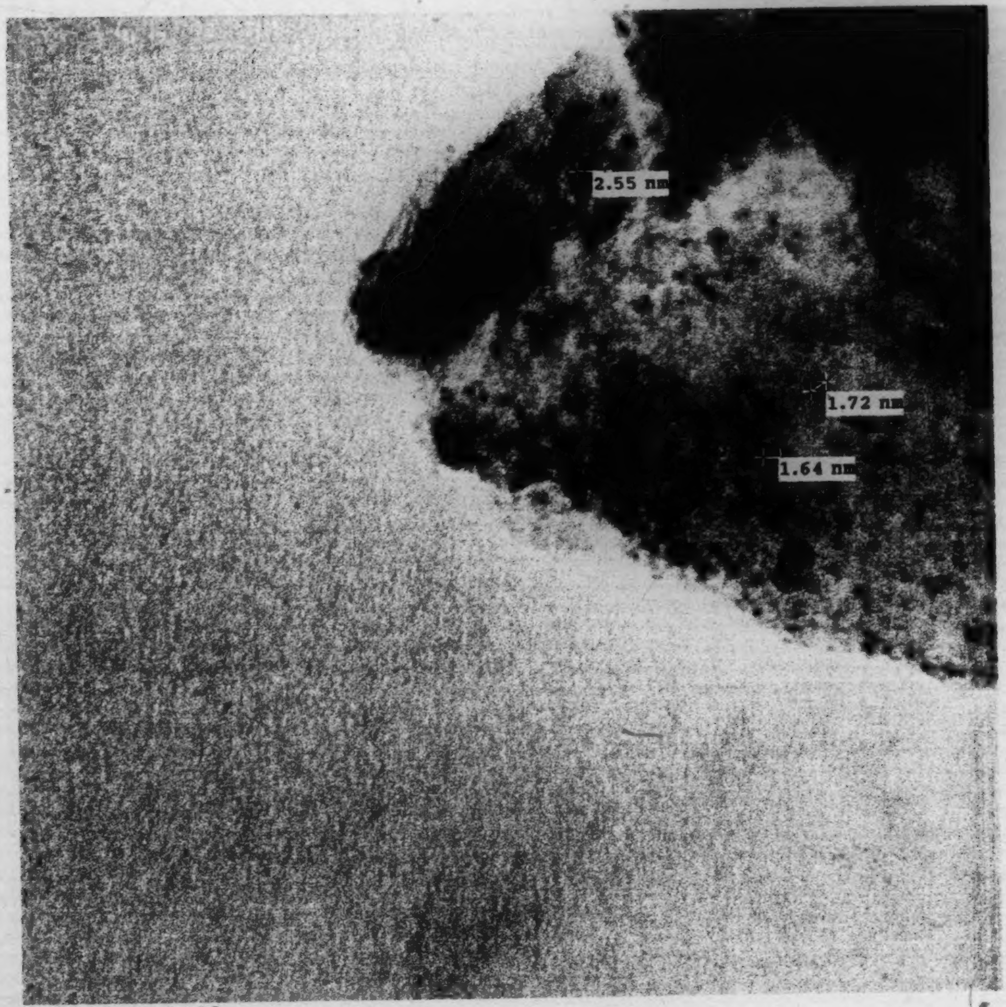
2.55 nm
1.72 nm
1.64 nm

March1 07_014.tif
MoHCHA 200R
Print Mag: 546000x @ 51 mm
11:28 03/01/07

5 nm
HV=200kV
Direct Mag: 1000000x
U of A Physics

Figure B.91: MoHCHA reduced at 200°C in $H_2$.

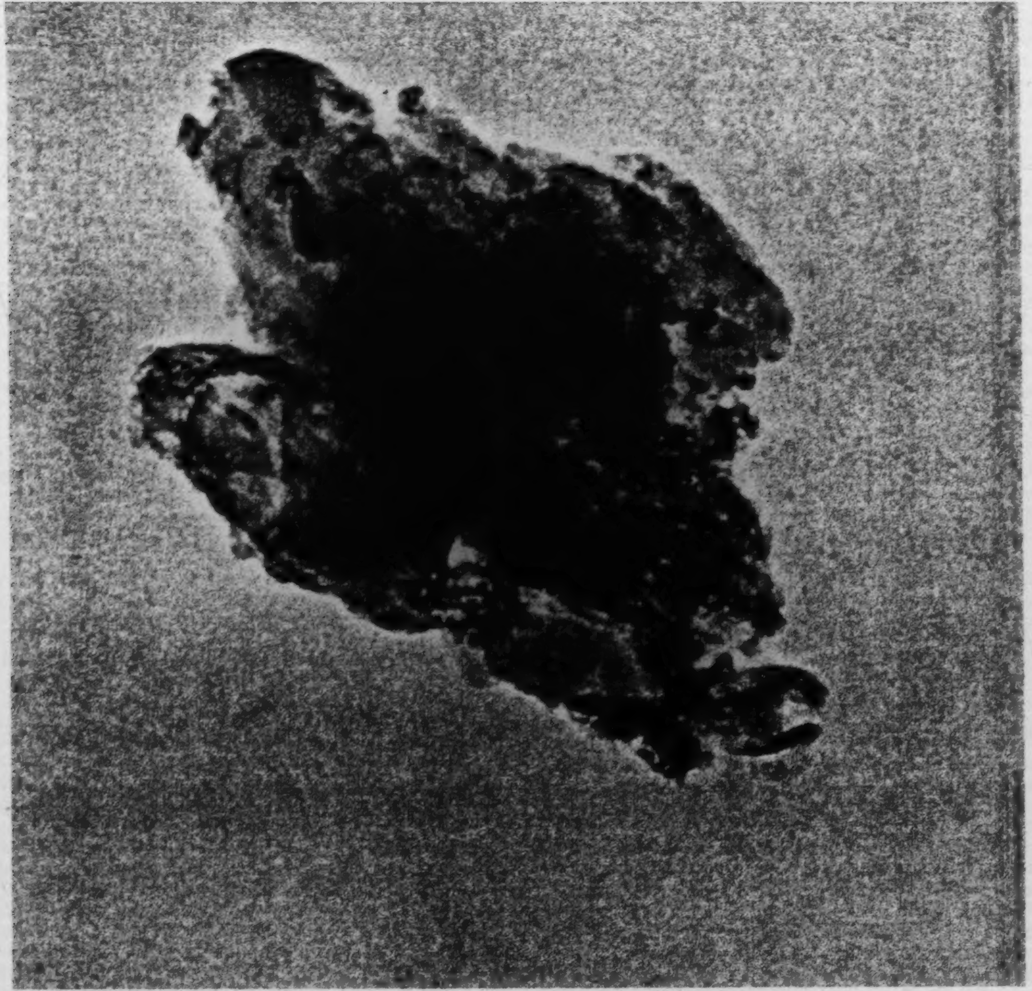

March1 07_011.tif
MoHCHA 200R
Print Mag: 137000x @ 51 mm
11:27 03/01/07

20 nm
HV=200kV
Direct Mag: 250000x
U of A Physics

Figure B.92: MoHCHA reduced at 200°C in $H_2$.

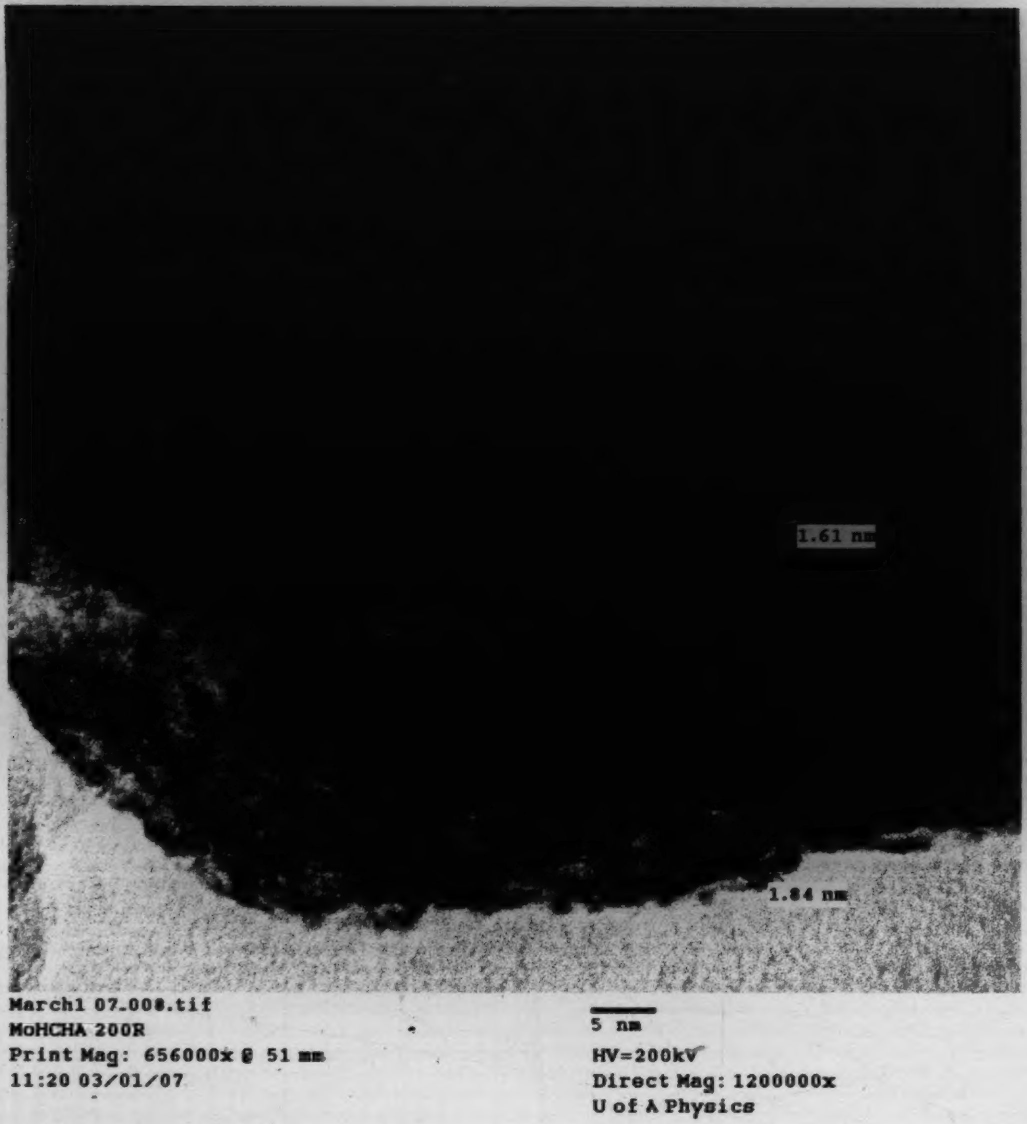
1.61 nm
1.84 nm
March1 07_008.tif
MoHCHA 200R
Print Mag: 656000x @ 51 mm
11:20 03/01/07
5 nm
HV=200kV
Direct Mag: 1200000x
U of A Physics

Figure B.93: MoHCHA reduced at 200°C in $H_2$.

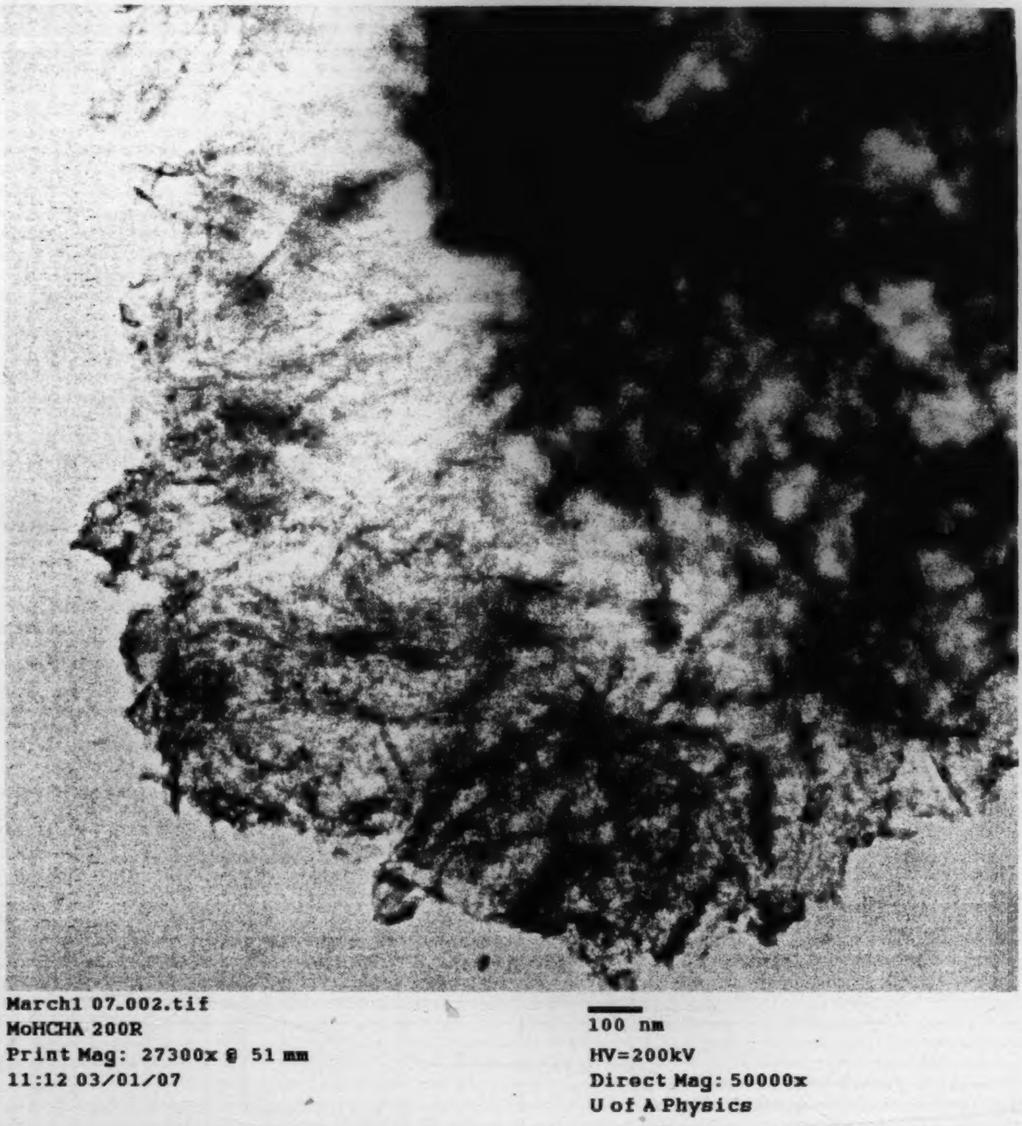
March1 07_002.tif
MoHCHA 200R
Print Mag: 27300x @ 51 mm
11:12 03/01/07
100 nm
HV=200kV
Direct Mag: 50000x
U of A Physics

Figure B.94: MoHCHA reduced at 200°C in $H_2$.

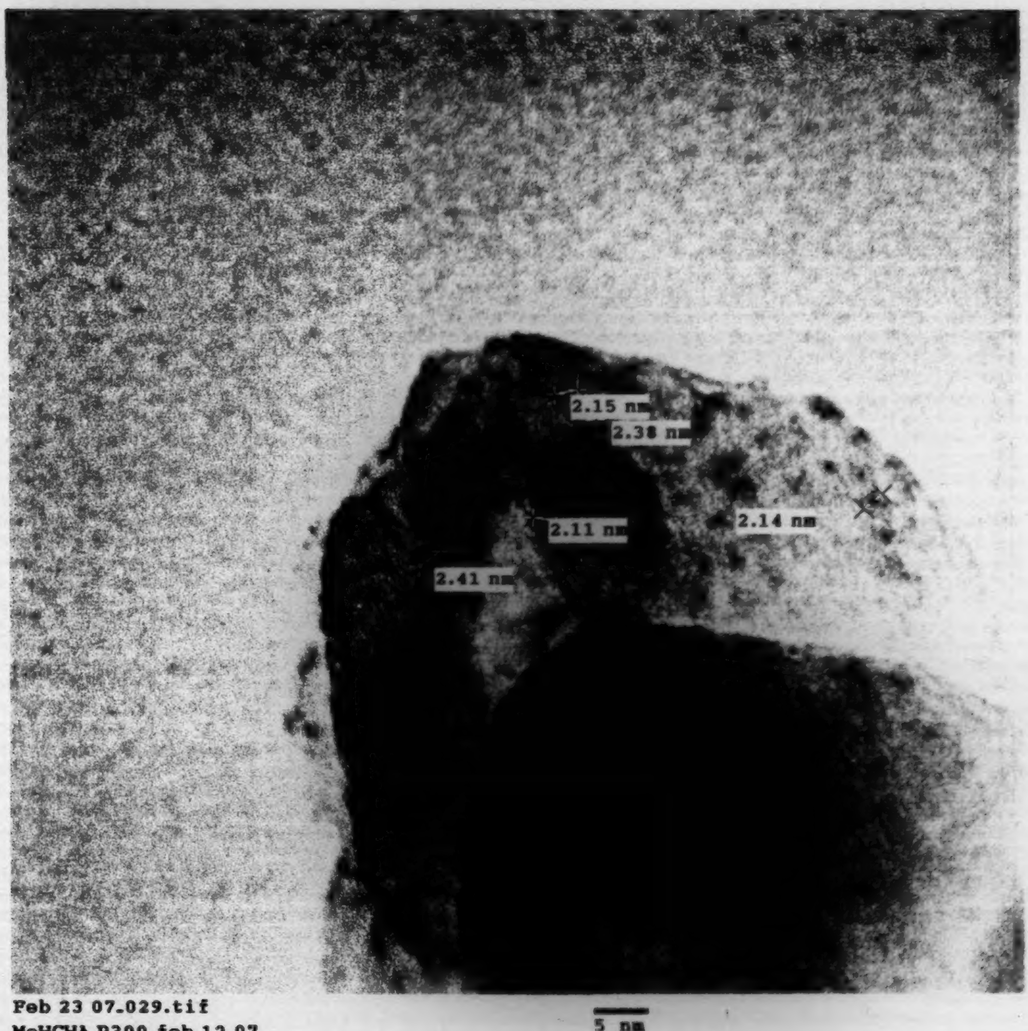
2.15 nm
2.38 nm
2.14 nm
2.11 nm
2.41 nm
5 nm

Feb 23 07_029.tif
MoHCHA R300 feb 12 07
Print Mag: 546000x @ 51 mm
11:45 02/23/07

HV=200kV
Direct Mag: 1000000x
U of A Physics

Figure B.95: MoHCHA reduced at 300°C in $H_2$.

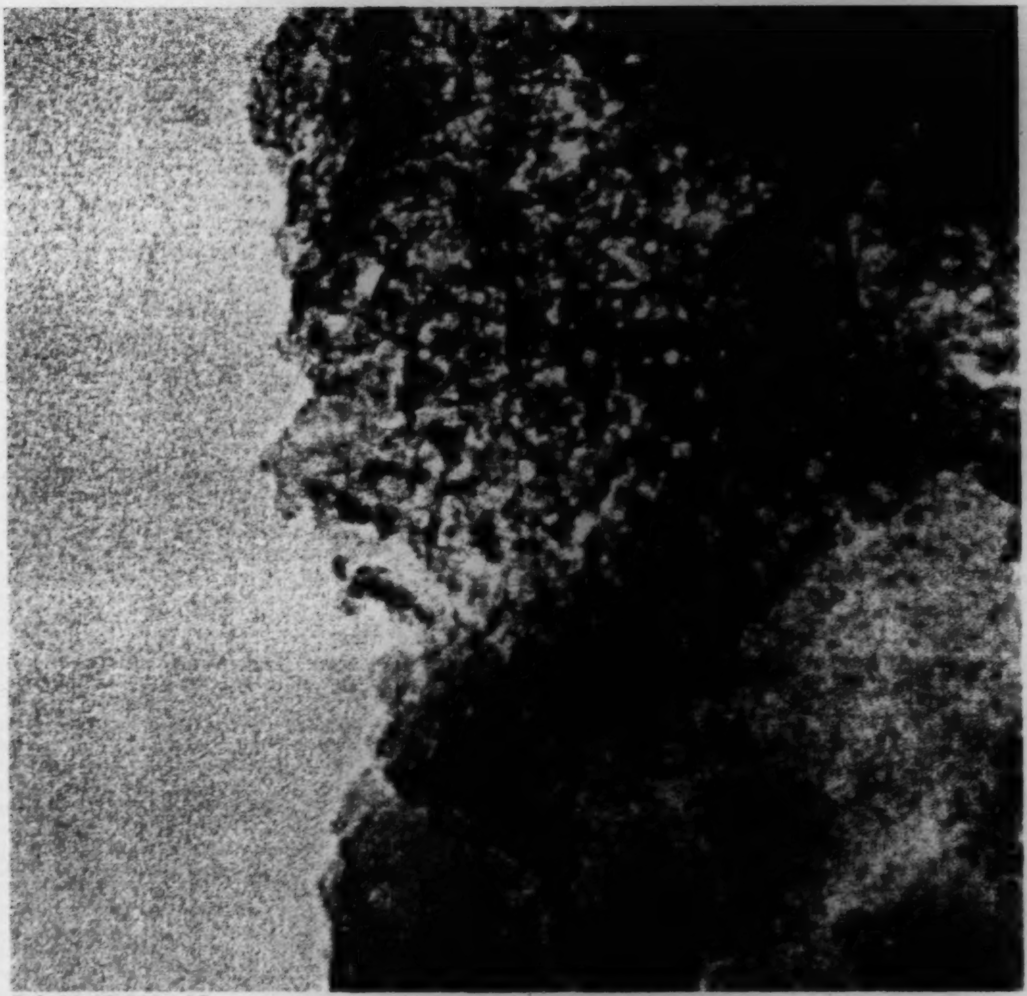

Feb 23 07_037.tif
MoHCHA R300 feb 12 07
Print Mag: 273000x @ 51 mm
11:56 02/23/07

20 nm
HV=200kV
Direct Mag: 500000x
U of A Physics

Figure B.96: MoHCHA reduced at 300°C in $H_2$.

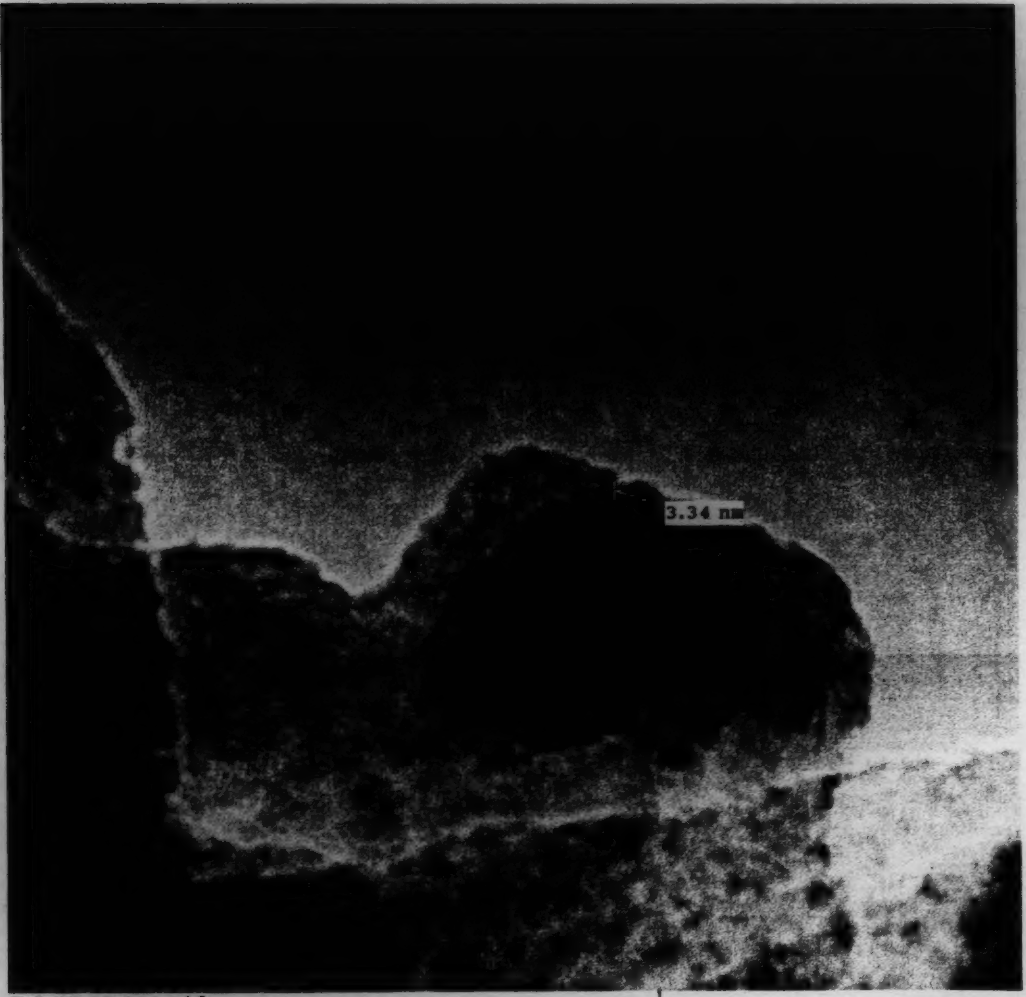

Feb 23 07_034.tif
MoHCHA R300 feb 12 07
Print Mag: 546000x @ 51 mm
11:50 02/23/07

5 nm
HV=200kV
Direct Mag: 1000000x
U of A Physics

Figure B.97: MoHCHA reduced at 300°C in $H_2$.

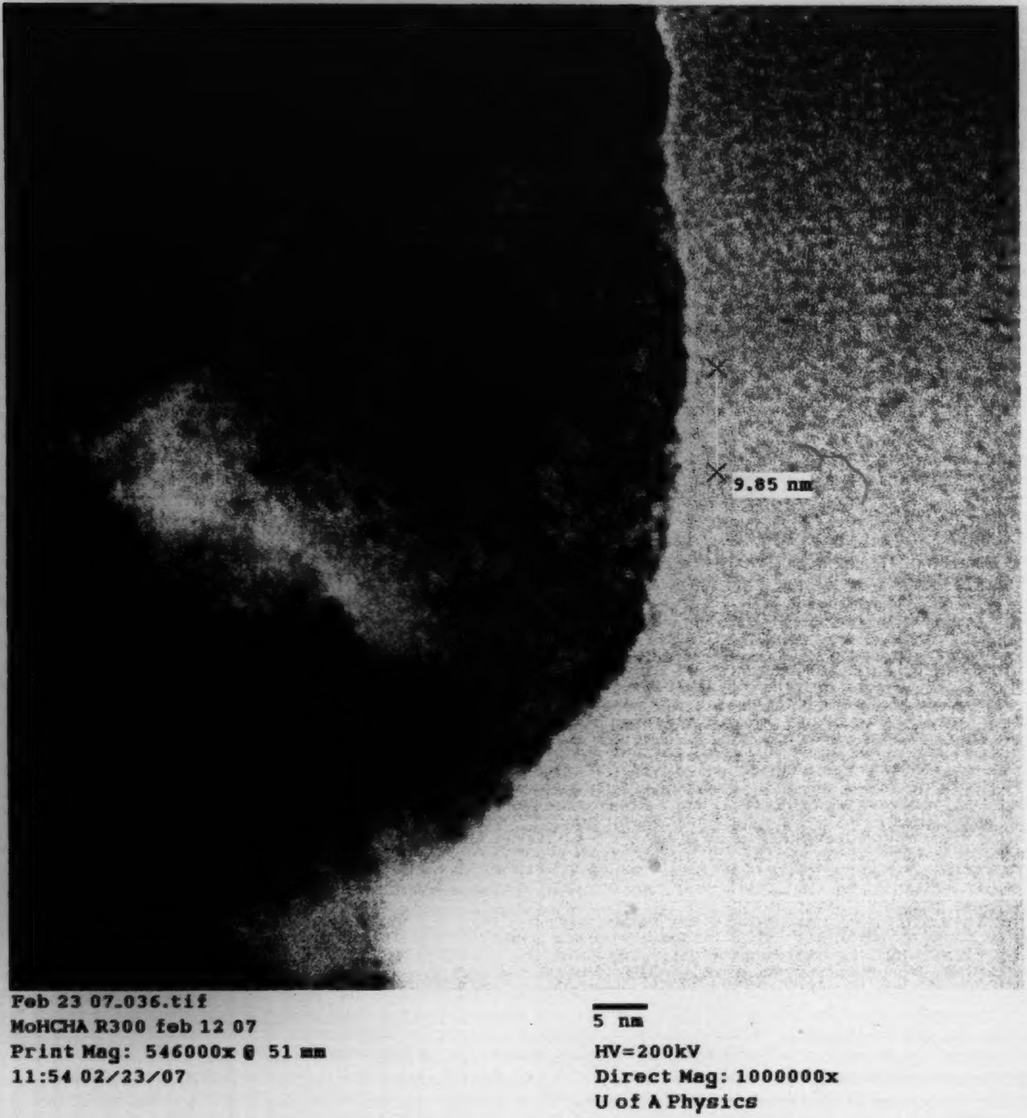
9.85 nm
Feb 23 07_036.tif
MoHCHA R300 feb 12 07
Print Mag: 546000x @ 51 mm
11:54 02/23/07
5 nm
HV=200kV
Direct Mag: 1000000x
U of A Physics

Figure B.98: MoHCHA reduced at 300°C in $H_2$.

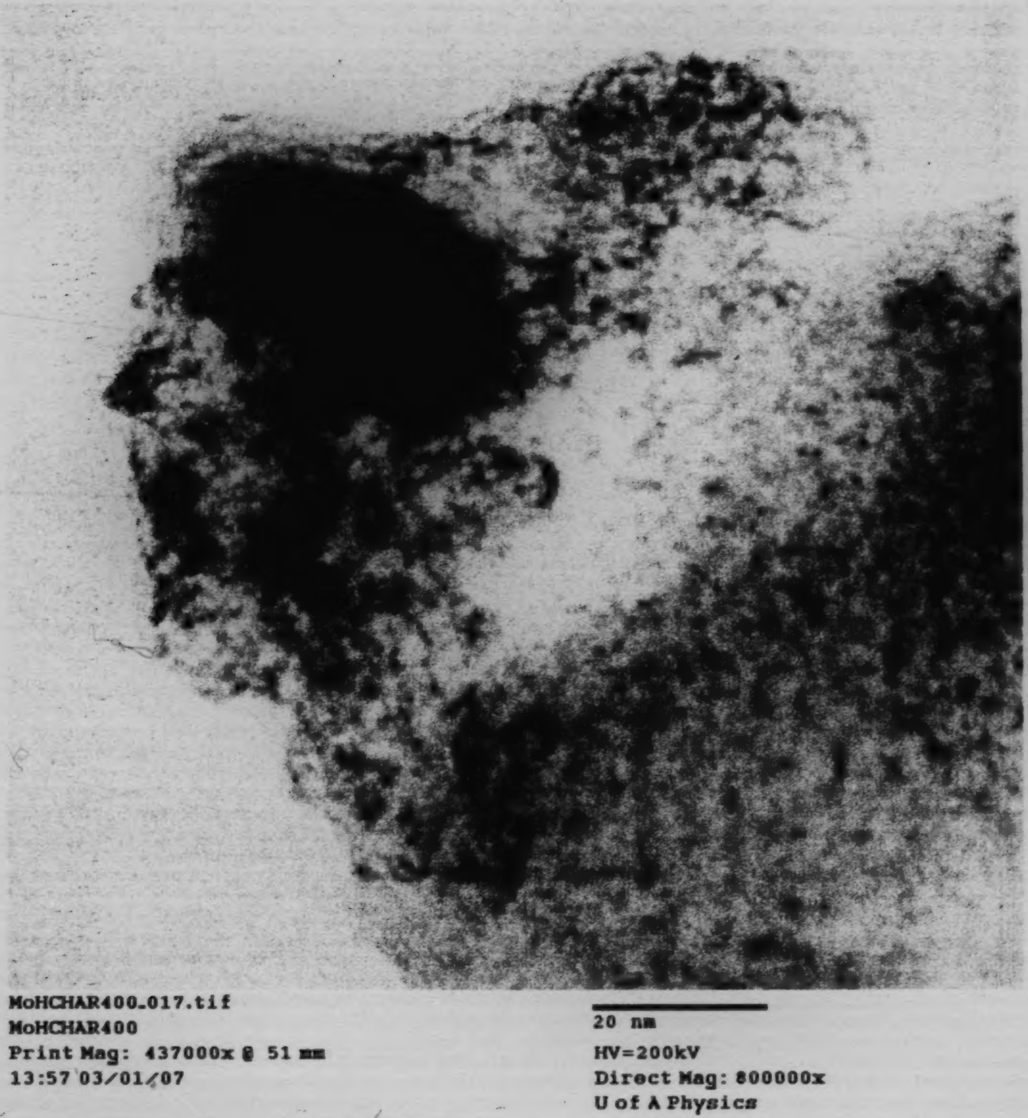
MoHCHAR400_017.tif
MoHCHAR400
Print Mag: 437000x @ 51 mm
13:57 03/01/07
20 nm
HV=200kV
Direct Mag: 800000x
U of A Physics

Figure B.99: MoHCHA reduced at 400°C in $H_2$.

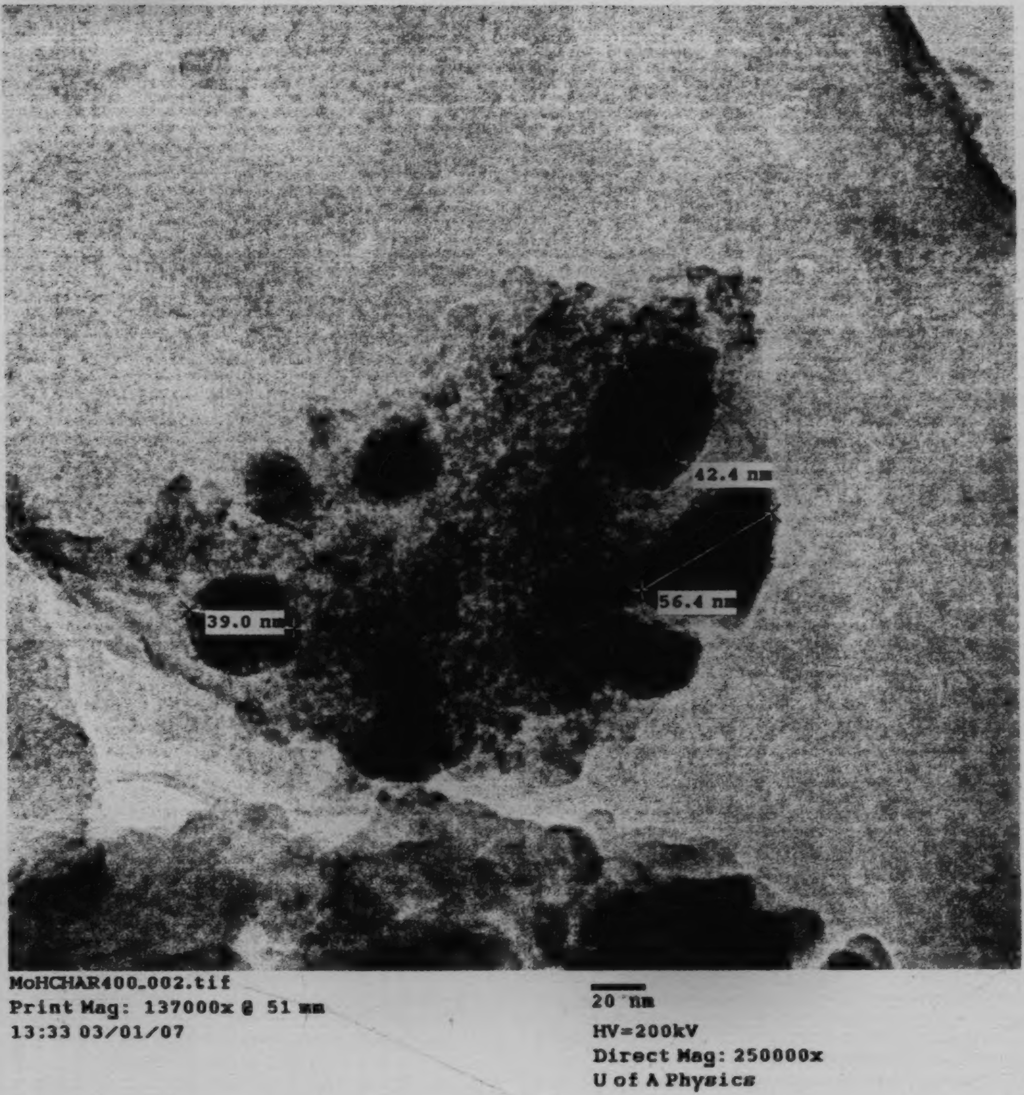
42.4 nm
56.4 nm
39.0 nm
MoHCHAR400_002.tif
Print Mag: 137000x @ 51 mm
13:33 03/01/07
20 nm
HV=200kV
Direct Mag: 250000x
U of A Physics

Figure B.100: MoHCHA reduced at 400°C in $H_2$.

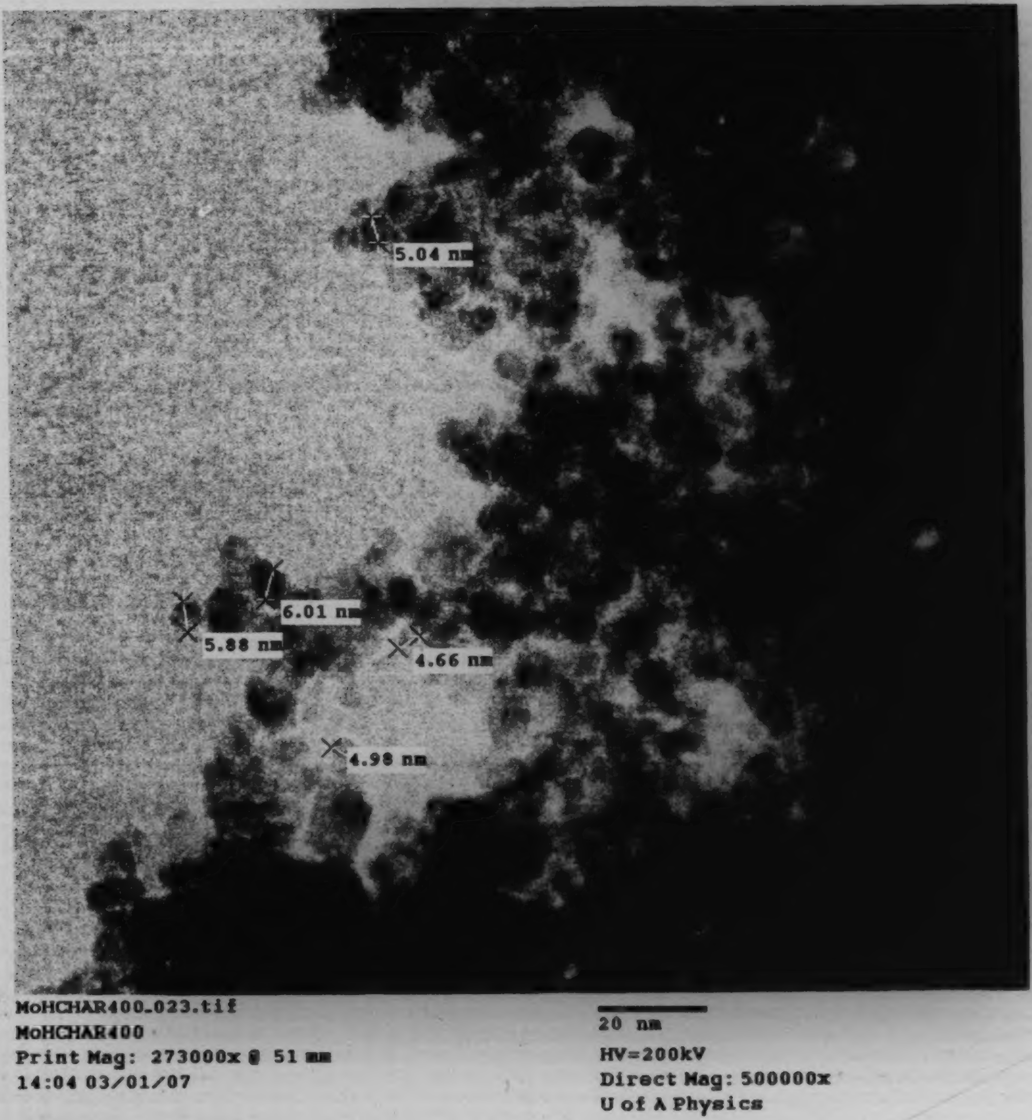
5.04 nm
6.01 nm
5.88 nm
4.66 nm
4.98 nm
MoHCHAR400_023.tif
MoHCHAR400
Print Mag: 273000x @ 51 mm
14:04 03/01/07
20 nm
HV=200kV
Direct Mag: 500000x
U of A Physics

Figure B.101: MoHCHA reduced at 400°C in $H_2$.

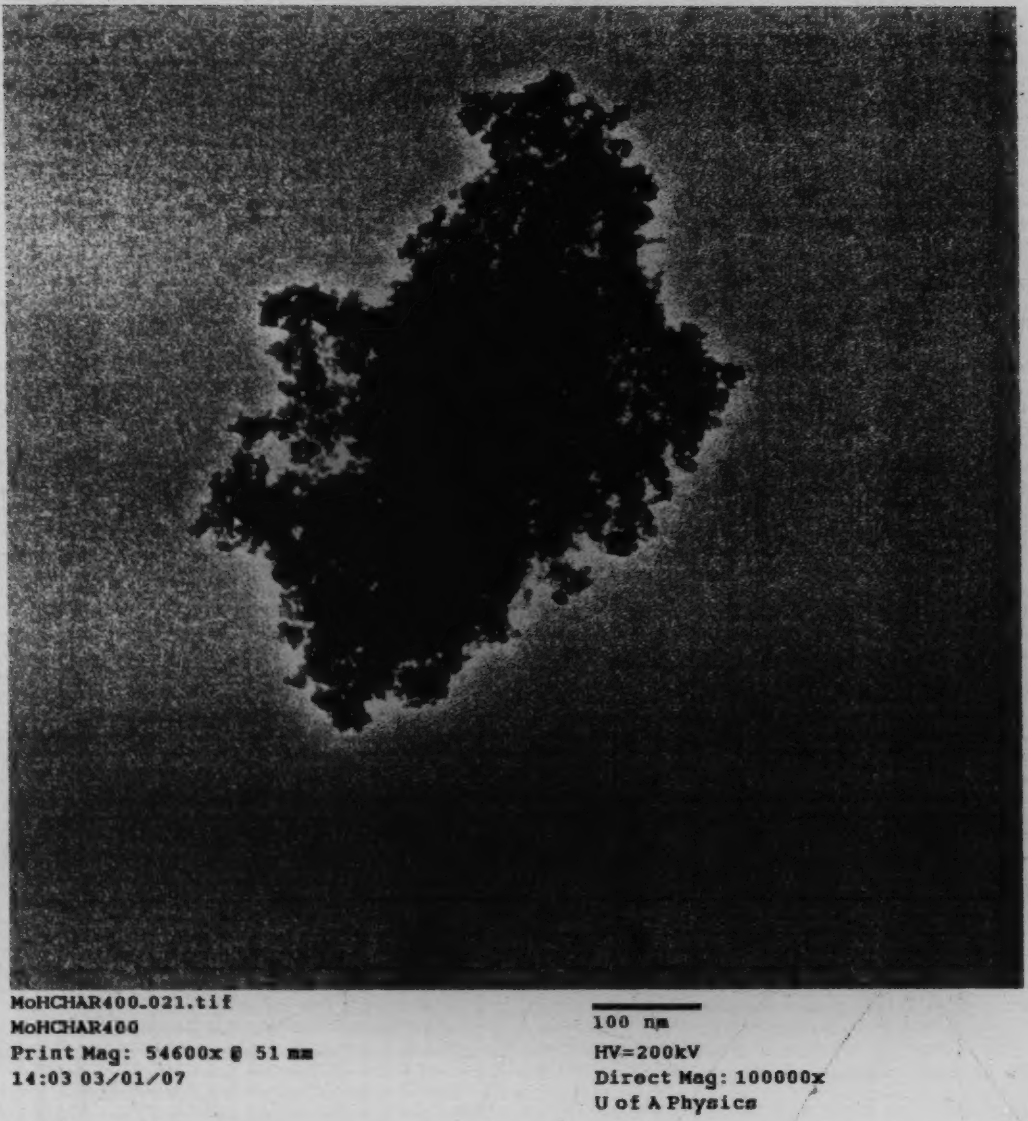
MoHCHAR400_021.tif
MoHCHAR400
Print Mag: 54600x @ 51 mm
14:03 03/01/07
100 nm
HV=200kV
Direct Mag: 100000x
U of A Physics

Figure B.102: MoHCHA reduced at 400°C in $H_2$.

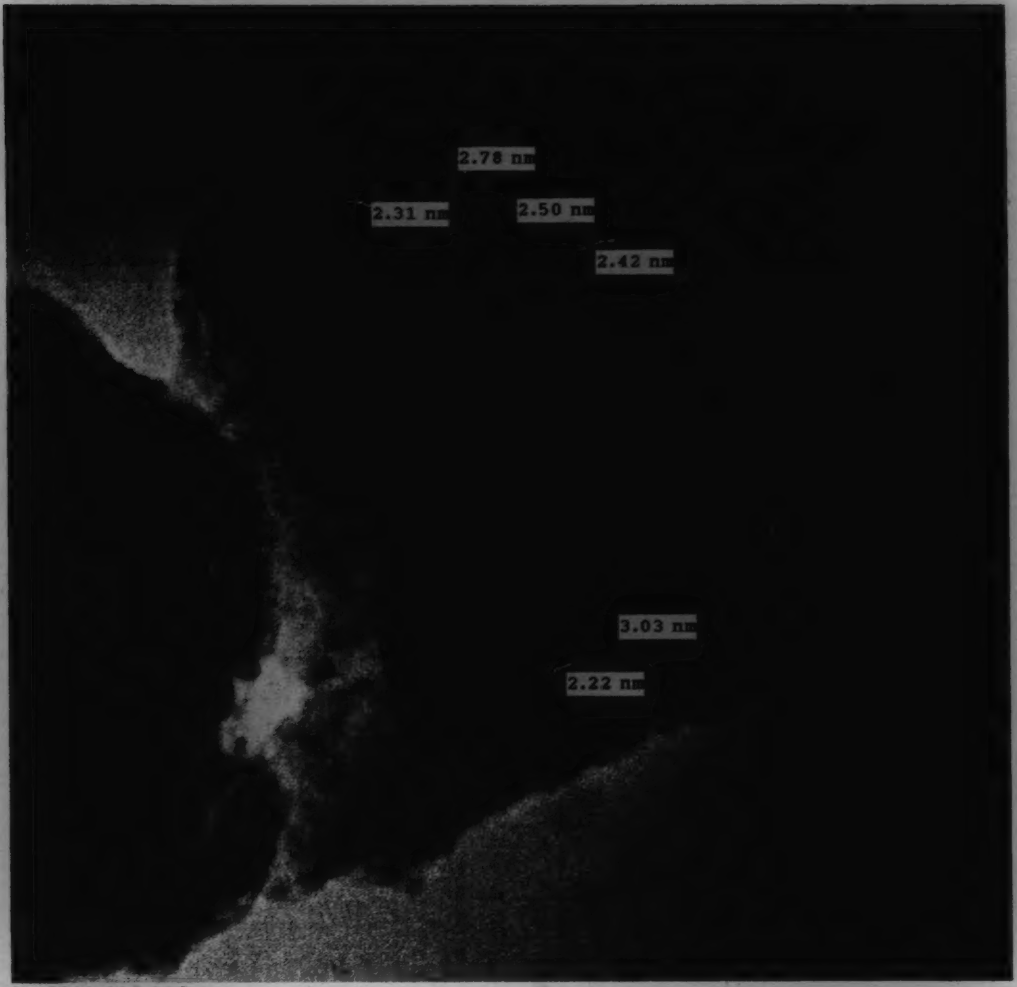
2.78 nm
2.31 nm
2.50 nm
2.42 nm
3.03 nm
2.22 nm

Mo S200.006.tif
Mo HCHA S200
Print Mag: 816000x @ 3.0 in
14:29 03/30/07

5 nm
HV=200kV
Direct Mag: 1000000x
U of A Physics

Figure B.103: MoHCHA sulfided at 200°C in $H_2S/H_2$

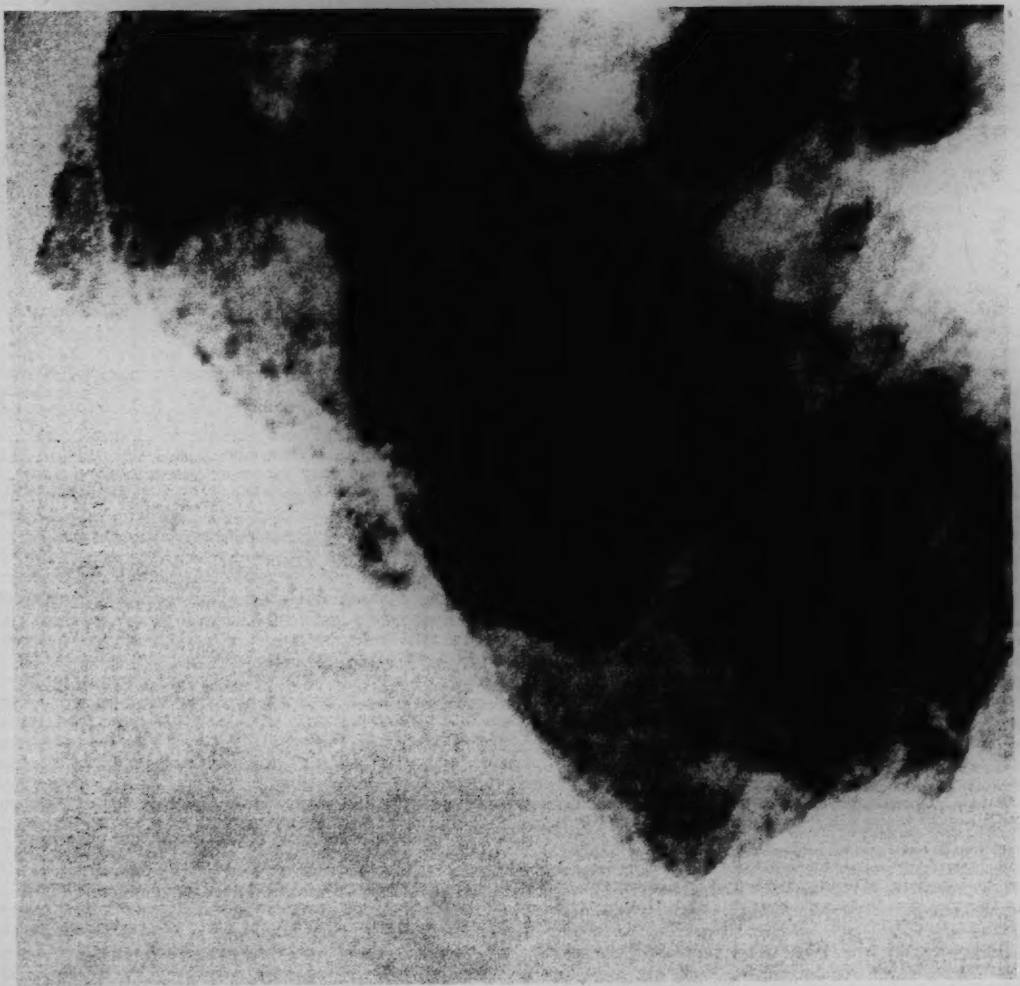

Mo S200_001.tif
Mo HCHA S200
Print Mag: 408000x @ 3.0 in
14:24 03/30/07

20 nm
HV=200kV
Direct Mag: 500000x
U of A Physics

Figure B.104: MoHCHA sulfided at 200°C in $H_2S/H_2$.

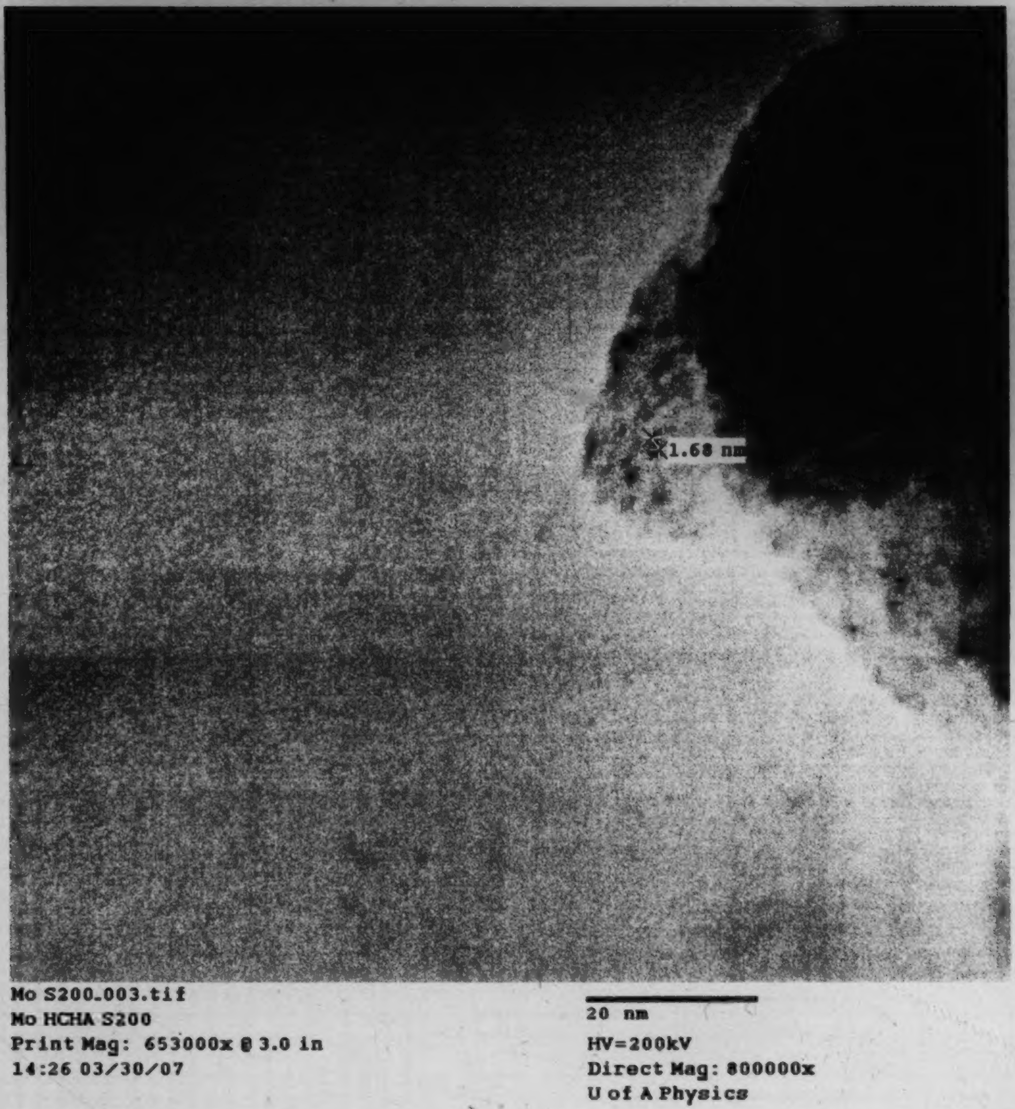
1.68 nm
Mo S200_003.tif
Mo HCHA S200
Print Mag: 653000x @ 3.0 in
14:26 03/30/07
20 nm
HV=200kV
Direct Mag: 800000x
U of A Physics

Figure B.105: MoHCHA sulfided at 200°C in $H_2S/H_2$.

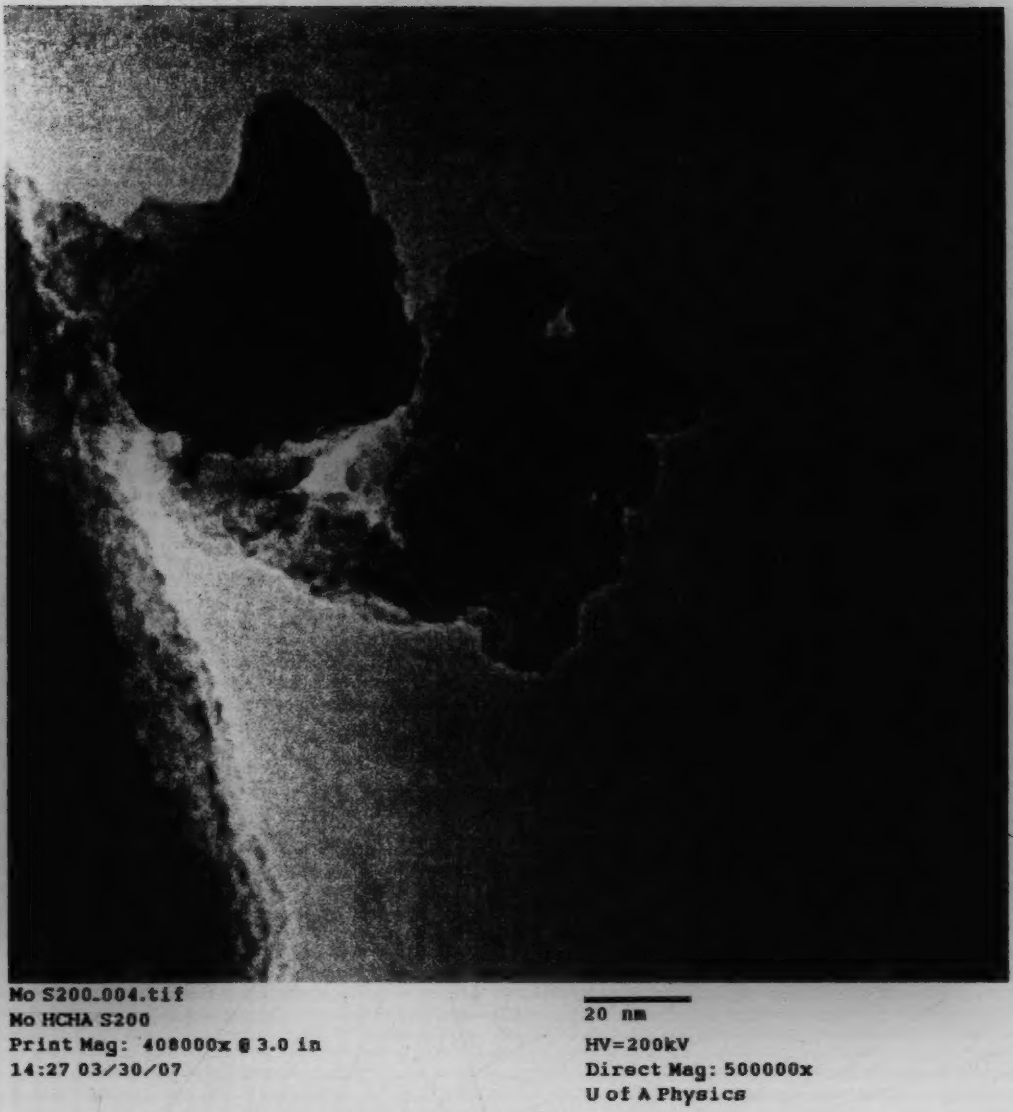
Mo S200_004.tif
Mo HCHA S200
Print Mag: 408000x @ 3.0 in
14:27 03/30/07
20 nm
HV=200kV
Direct Mag: 500000x
U of A Physics

Figure B.106: MoHCHA sulfided at 200°C in $H_2S/H_2$.

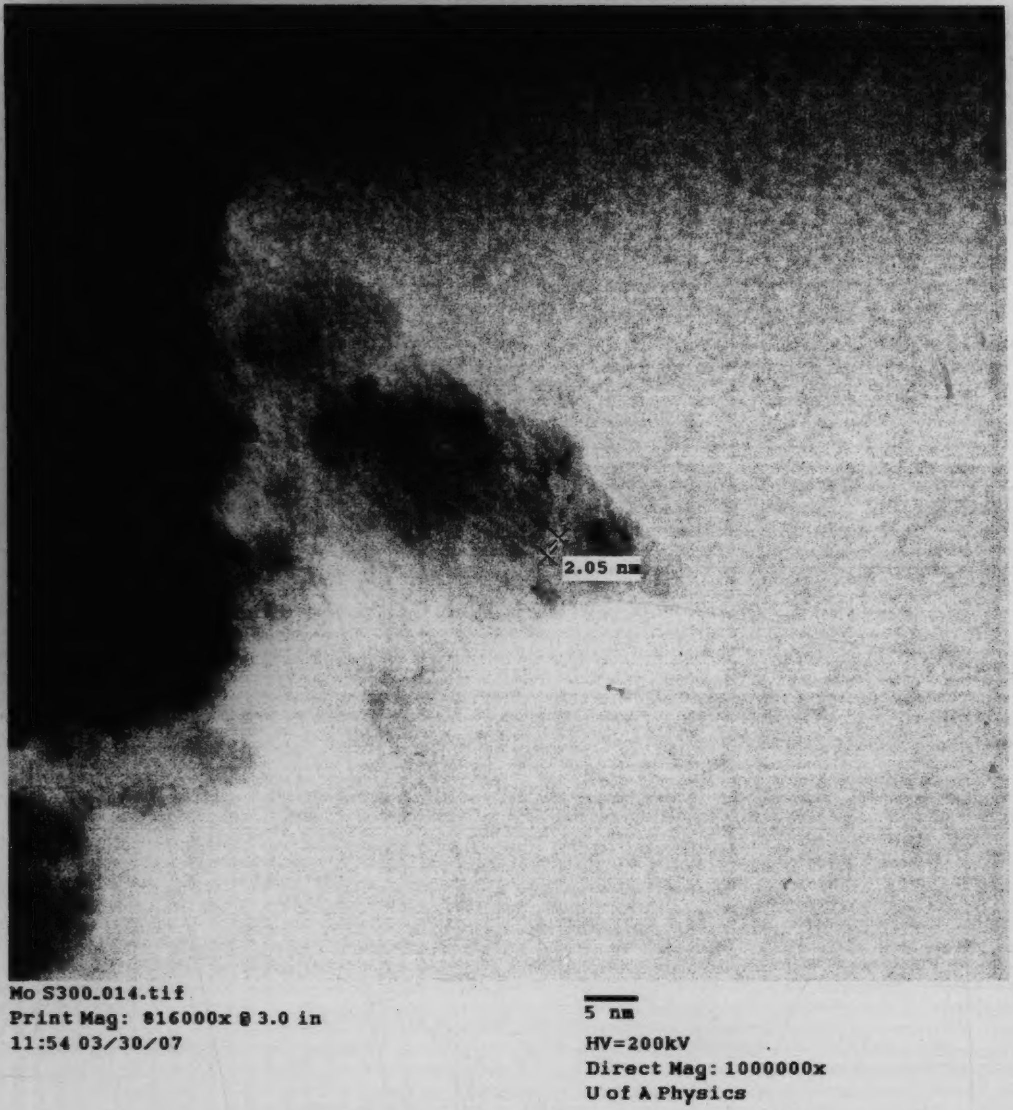
2.05 nm
Mo S300_014.tif
Print Mag: 816000x @ 3.0 in
11:54 03/30/07
5 nm
HV=200kV
Direct Mag: 1000000x
U of A Physics

Figure B.107: MoHCHA sulfided at 300°C in $H_2S/H_2$.

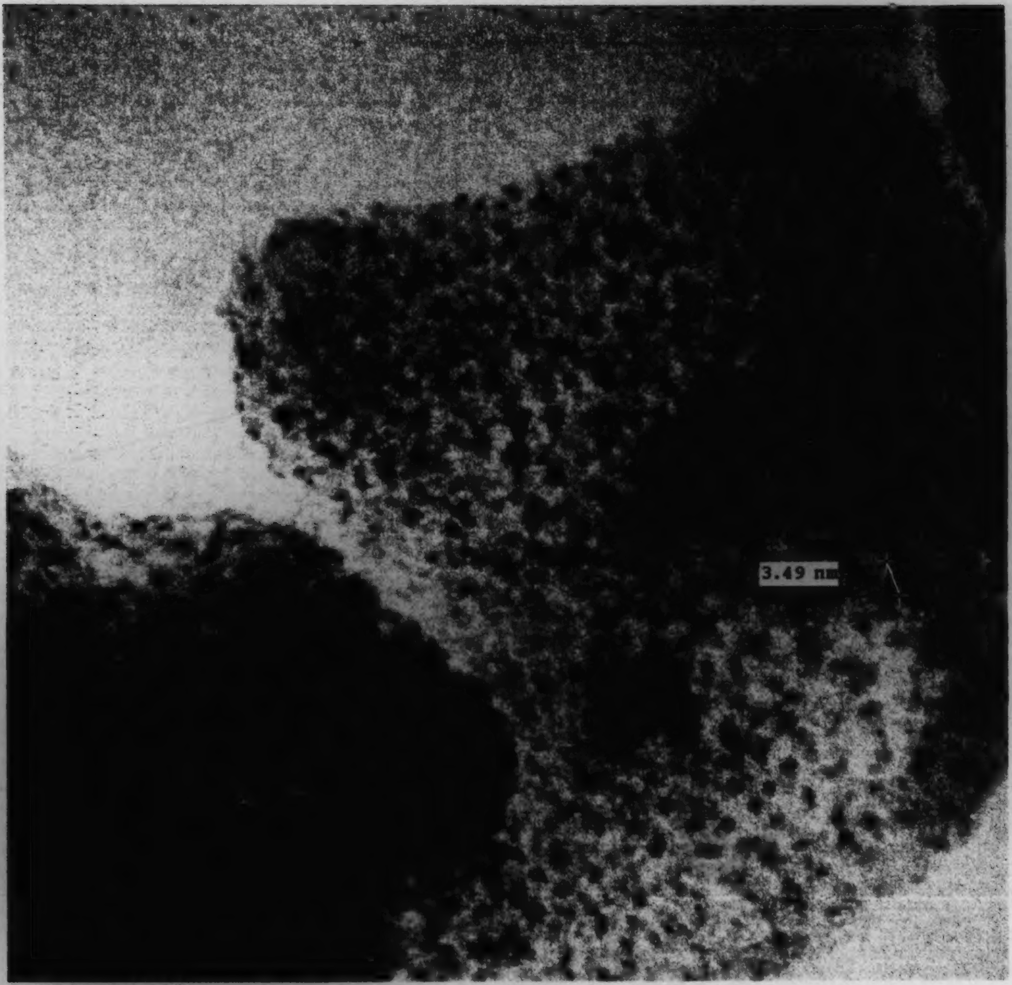
3.49 nm
Mo S300_008.tif
Print Mag: 816000x @ 3.0 in
11:39 03/30/07
5 nm
HV=200kV
Direct Mag: 1000000x
U of A Physics

Figure B.108: MoHCHA sulfided at 300°C in $H_2S/H_2$.

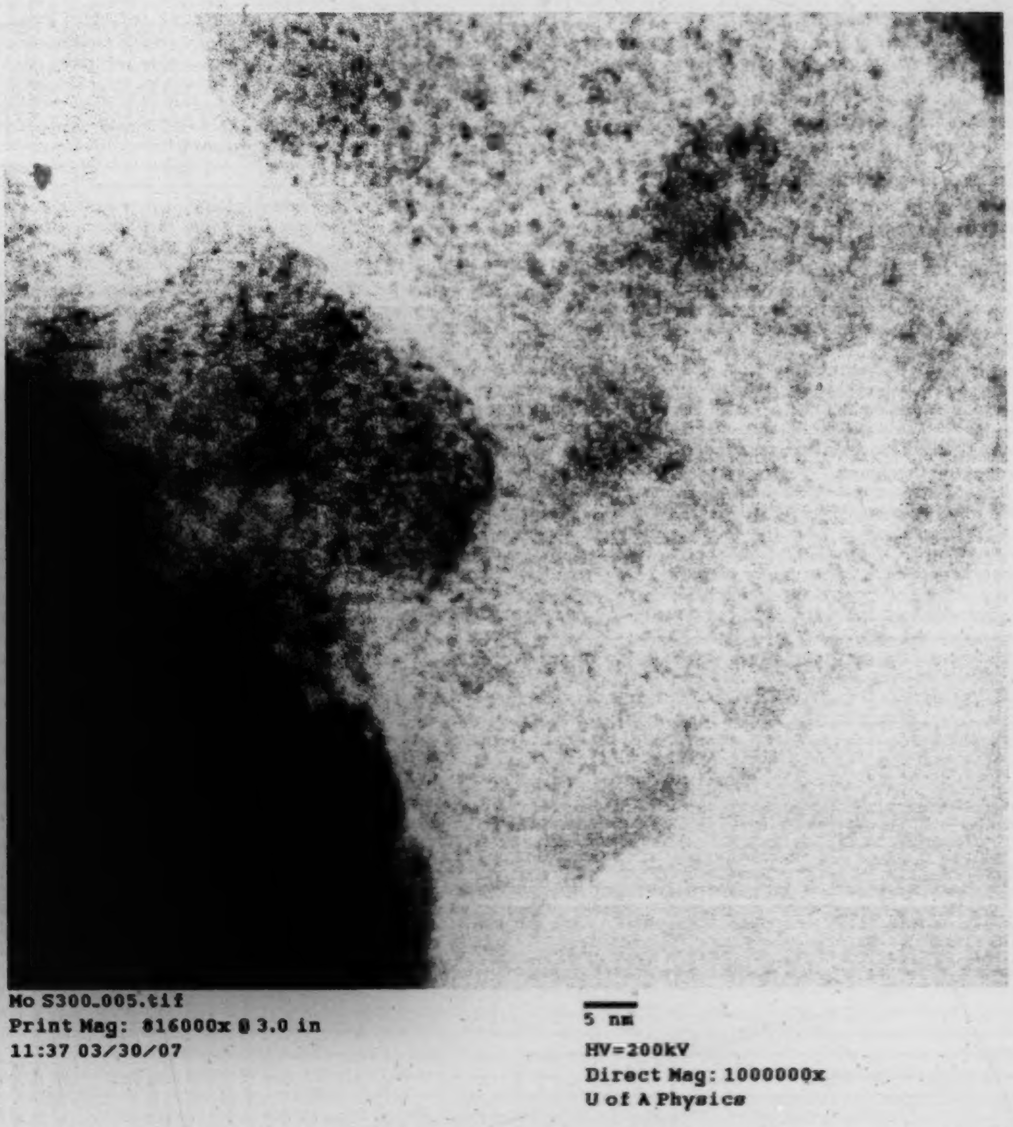
Mo S300_005.tif
Print Mag: 816000x @ 3.0 in
11:37 03/30/07
5 nm
HV=200kV
Direct Mag: 1000000x
U of A Physics

Figure B.109: MoHCHA sulfided at 300°C in $H_2S/H_2$.

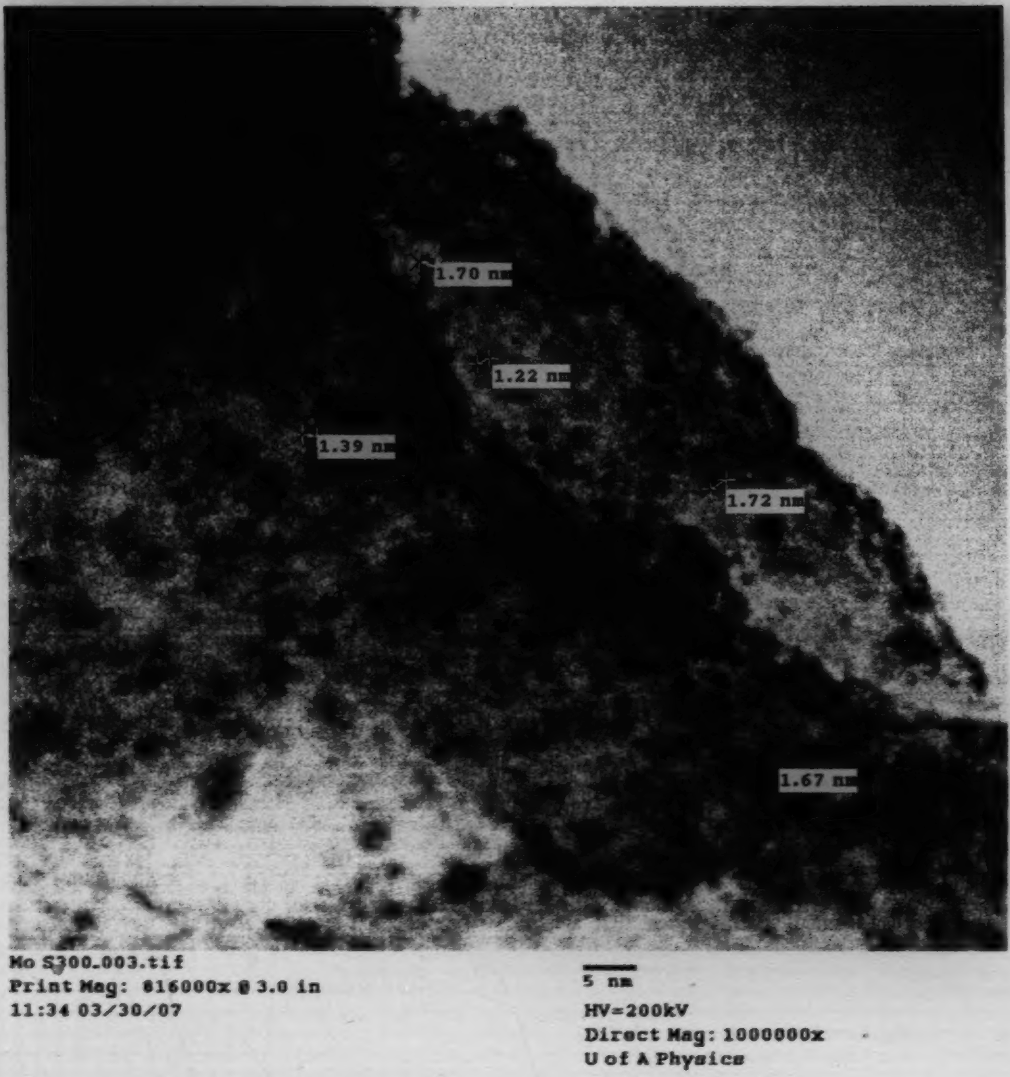
1.70 nm
1.22 nm
1.39 nm
1.72 nm
1.67 nm
Mo S300_003.tif
Print Mag: 816000x @ 3.0 in
11:34 03/30/07
5 nm
HV=200kV
Direct Mag: 1000000x
U of A Physics

Figure B.110: MoHCHA sulfided at 300°C in $H_2S/H_2$.

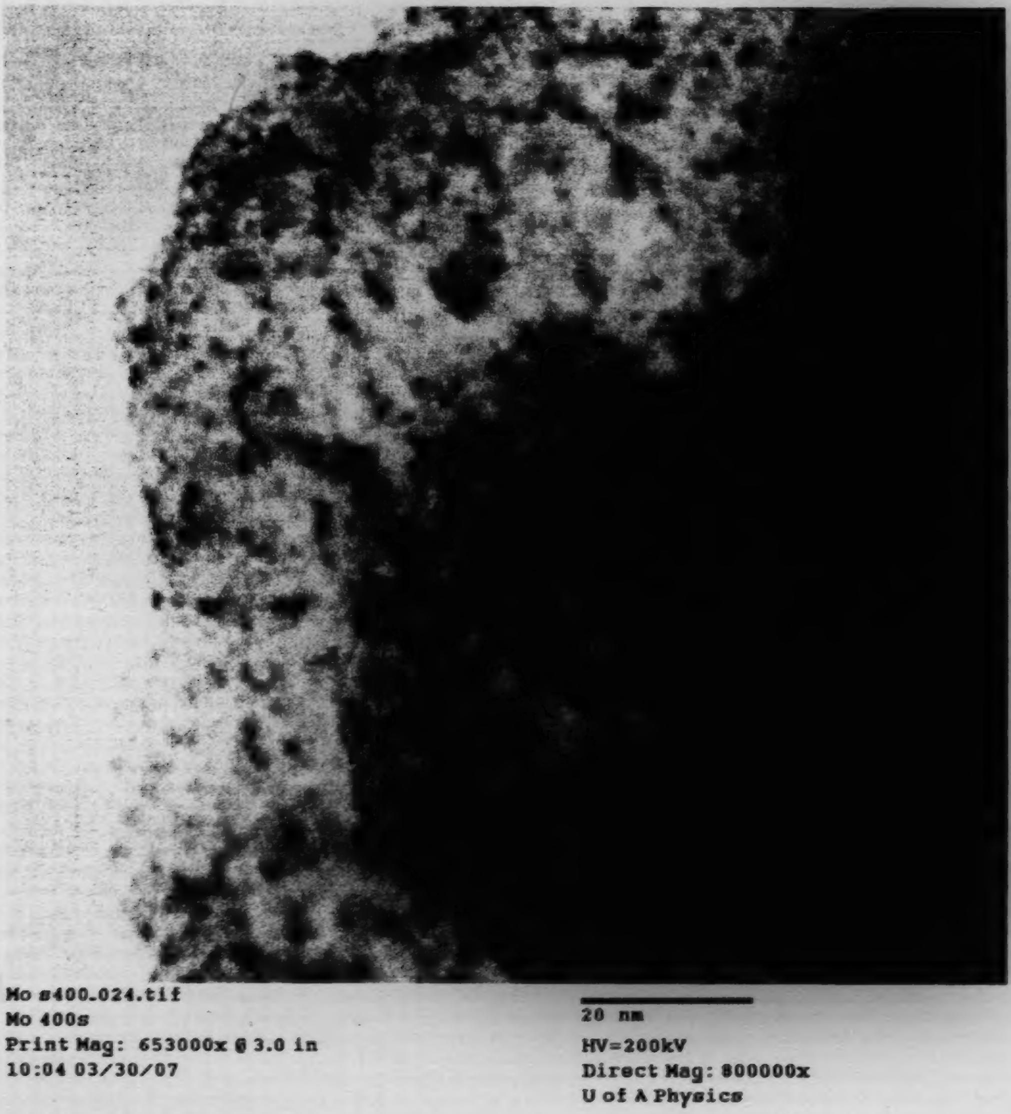
Mo s400_024.tif
Mo 400s
Print Mag: 653000x @ 3.0 in
10:04 03/30/07
20 nm
HV=200kV
Direct Mag: 800000x
U of A Physics

Figure B.111: MoHCHA sulfided at 300°C in $H_2S/H_2$.

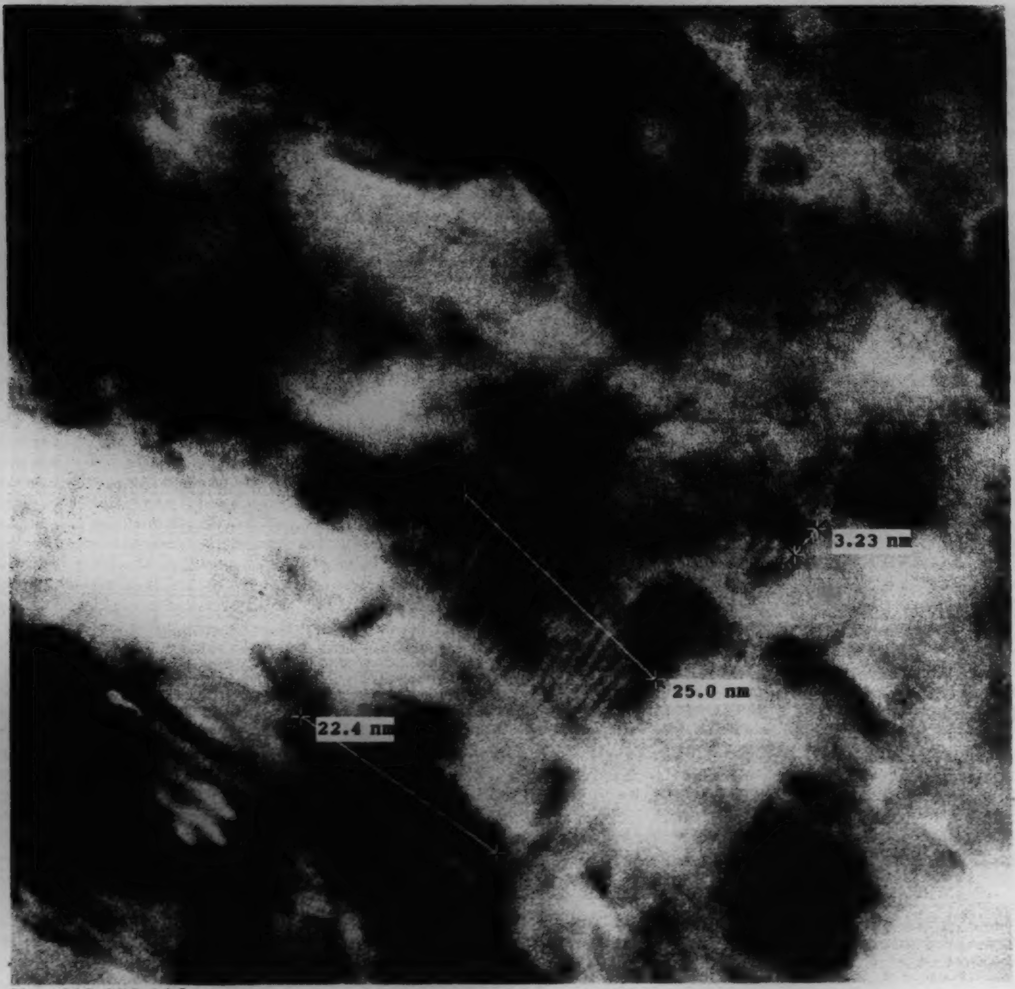
3.23 nm
25.0 nm
22.4 nm

Mo s400_020.tif
Mo 400s
Print Mag: 816000x @ 3.0 in
9:49 03/30/07

5 nm
HV=200kV
Direct Mag: 1000000x
U of A Physics

Figure B.112: MoHCHA sulfided at 300°C in $H_2S/H_2$.

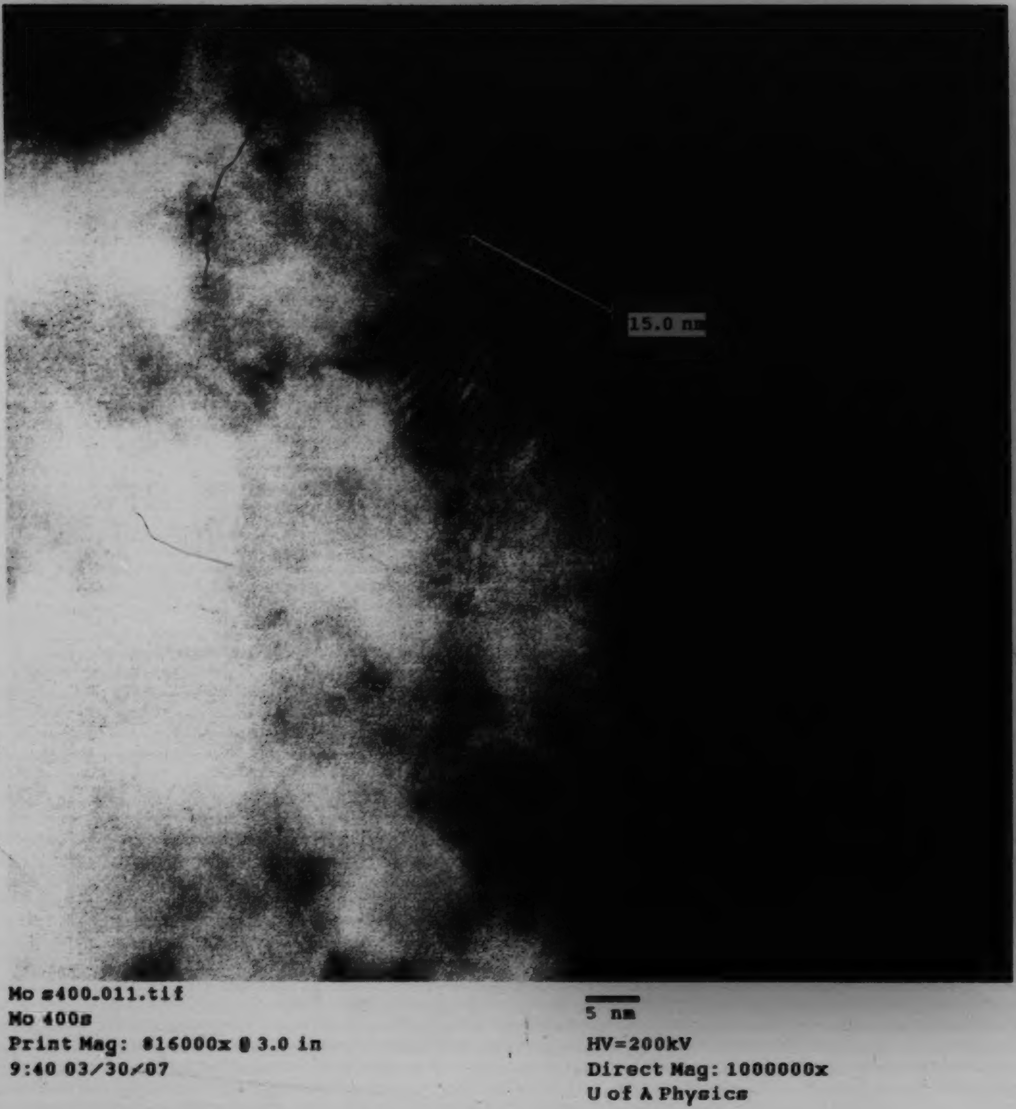
15.0 nm
Mo s400_011.tif
Mo 400s
Print Mag: 816000x @ 3.0 in
9:40 03/30/07
5 nm
HV=200kV
Direct Mag: 1000000x
U of A Physics

Figure B.113: MoHCHA sulfided at 300°C in $H_2S/H_2$.

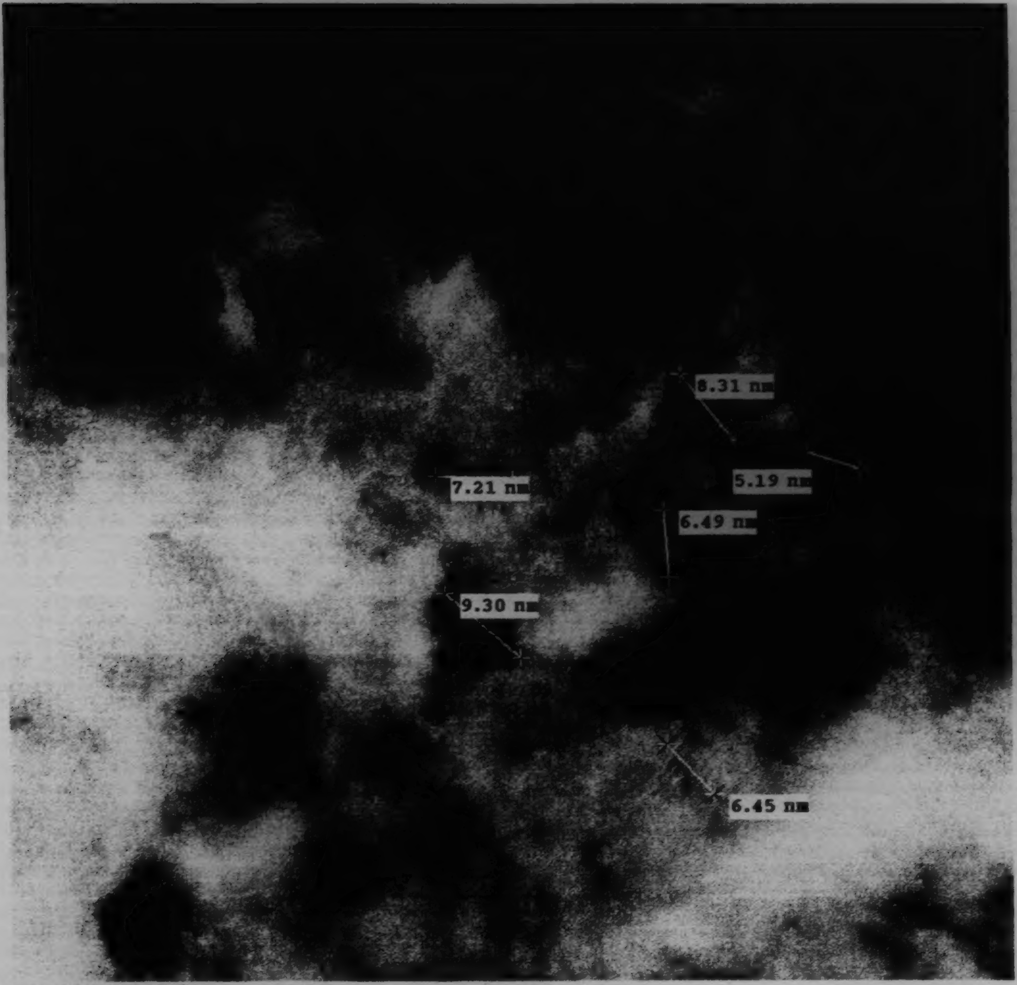
8.31 nm
5.19 nm
7.21 nm
6.49 nm
9.30 nm
6.45 nm

Mo s400_008.tif
Mo 400s
Print Mag: 816000x @ 3.0 in
9:38 03/30/07

5 nm
HV=200kV
Direct Mag: 1000000x
U of A Physics

Figure B.114: MoHCHA sulfided at 300°C in $H_2S/H_2$.

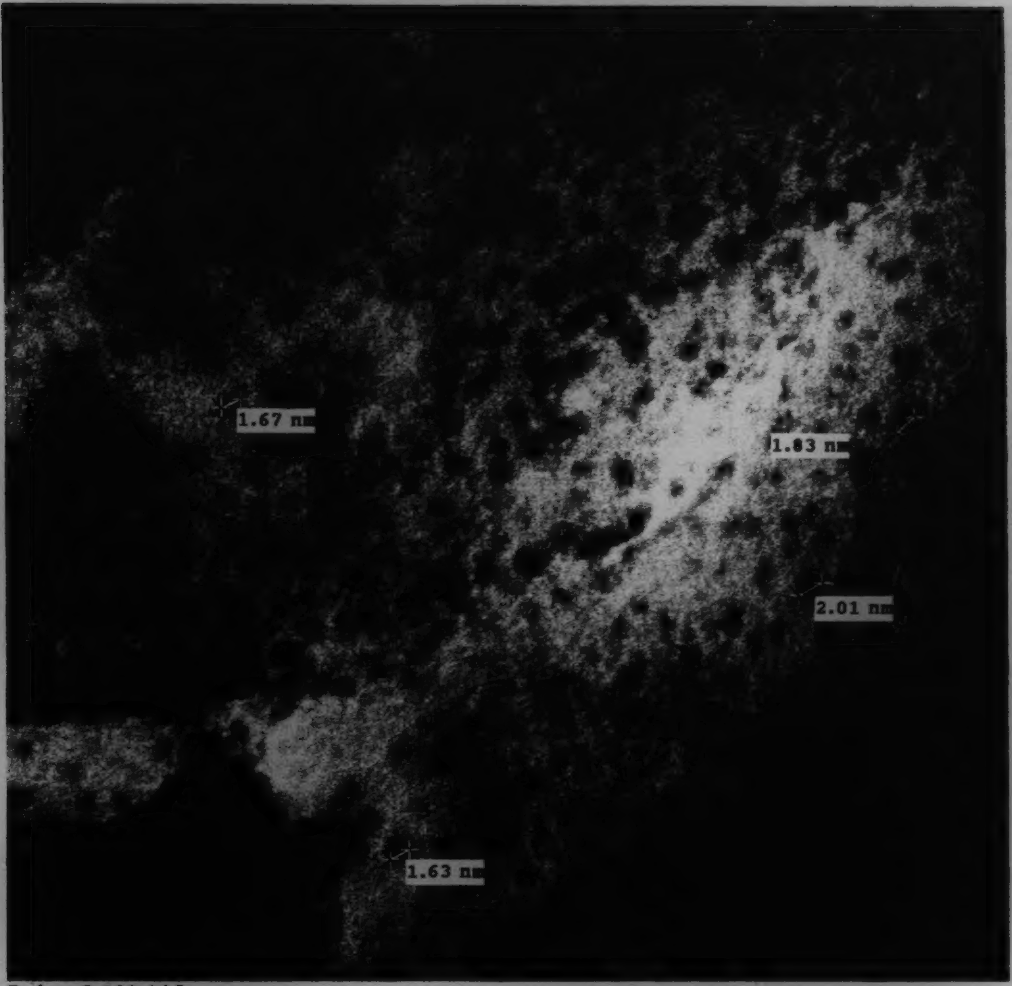
1.67 nm
1.83 nm
2.01 nm
1.63 nm

Brian_G.008.tif
Calcined NiMo H CHA
Print Mag: 980000x @ 3.0 in
9:23 11/02/06

5 nm
HV=200kV
Direct Mag: 1200000x
U of A Physics

Figure B.115: NiMoHCHA As made.

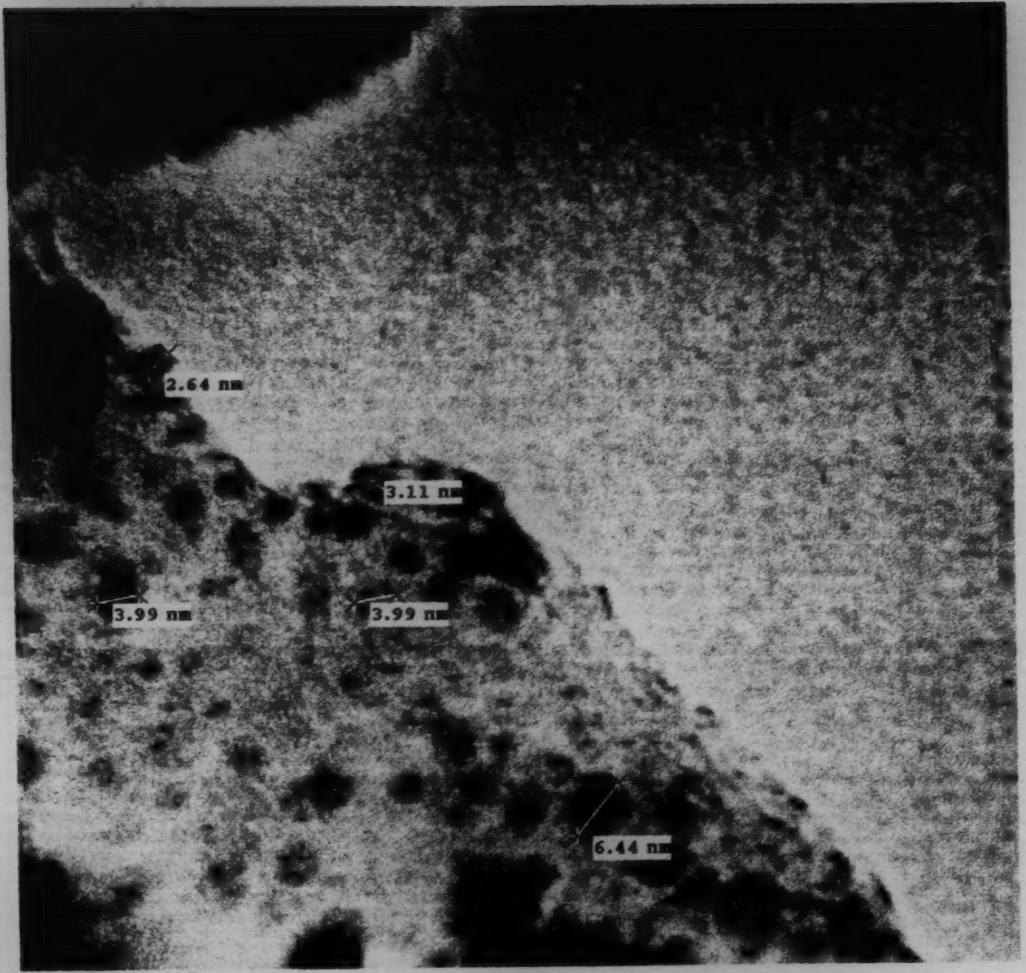
2.64 nm
3.11 nm
3.99 nm
3.99 nm
6.44 nm

Brian_G_015.tif
Calcined NiMo H CHA
Print Mag: 816000x @ 3.0 in
9:38 11/02/06

5 nm
HV=200kV
Direct Mag: 1000000x
U of A Physics

Figure B.116: NiMoHCHA As made.

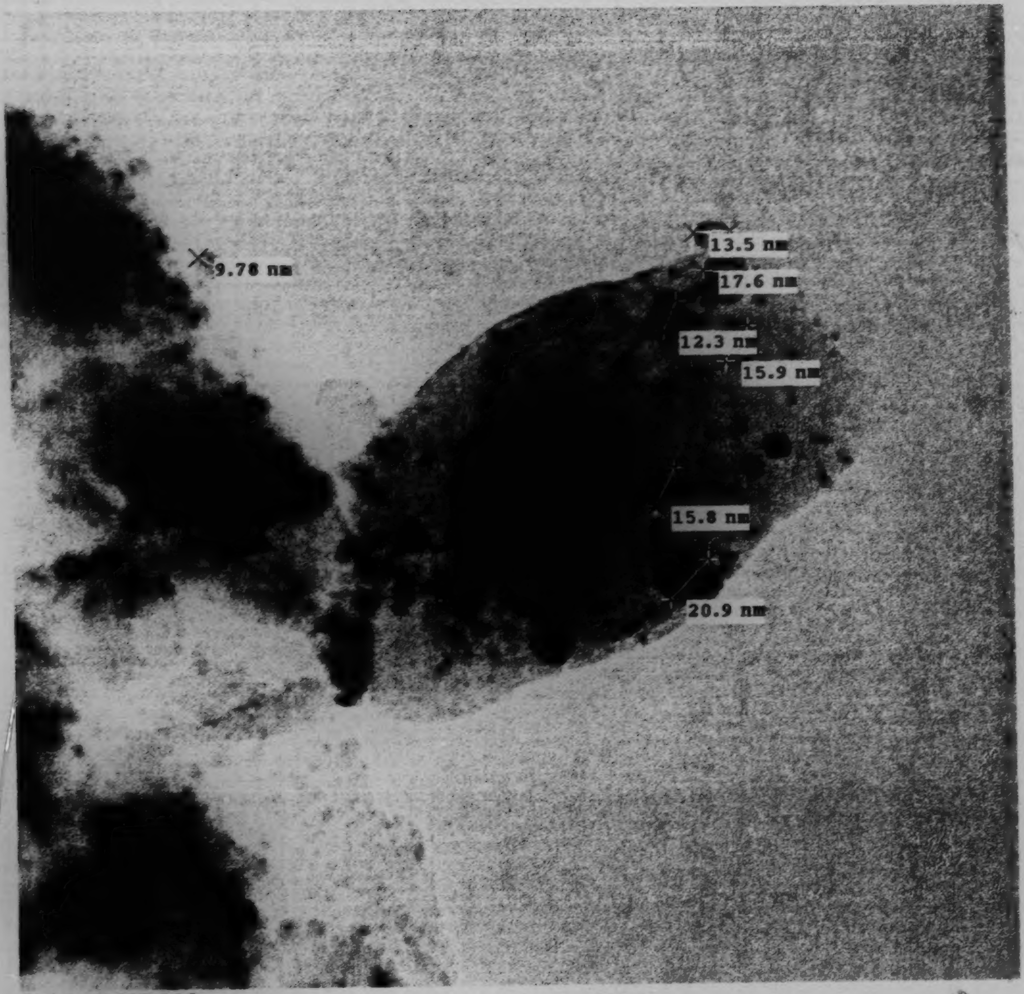
9.78 nm
13.5 nm
17.6 nm
12.3 nm
15.9 nm
15.8 nm
20.9 nm

Brian_G_017.tif
Calcined NiMo H CHA
Print Mag: 204000x @ 3.0 in
9:39 11/02/06

20 nm
HV=200kV
Direct Mag: 250000x
U of A Physics

Figure B.117: NiMoHCHA As made.

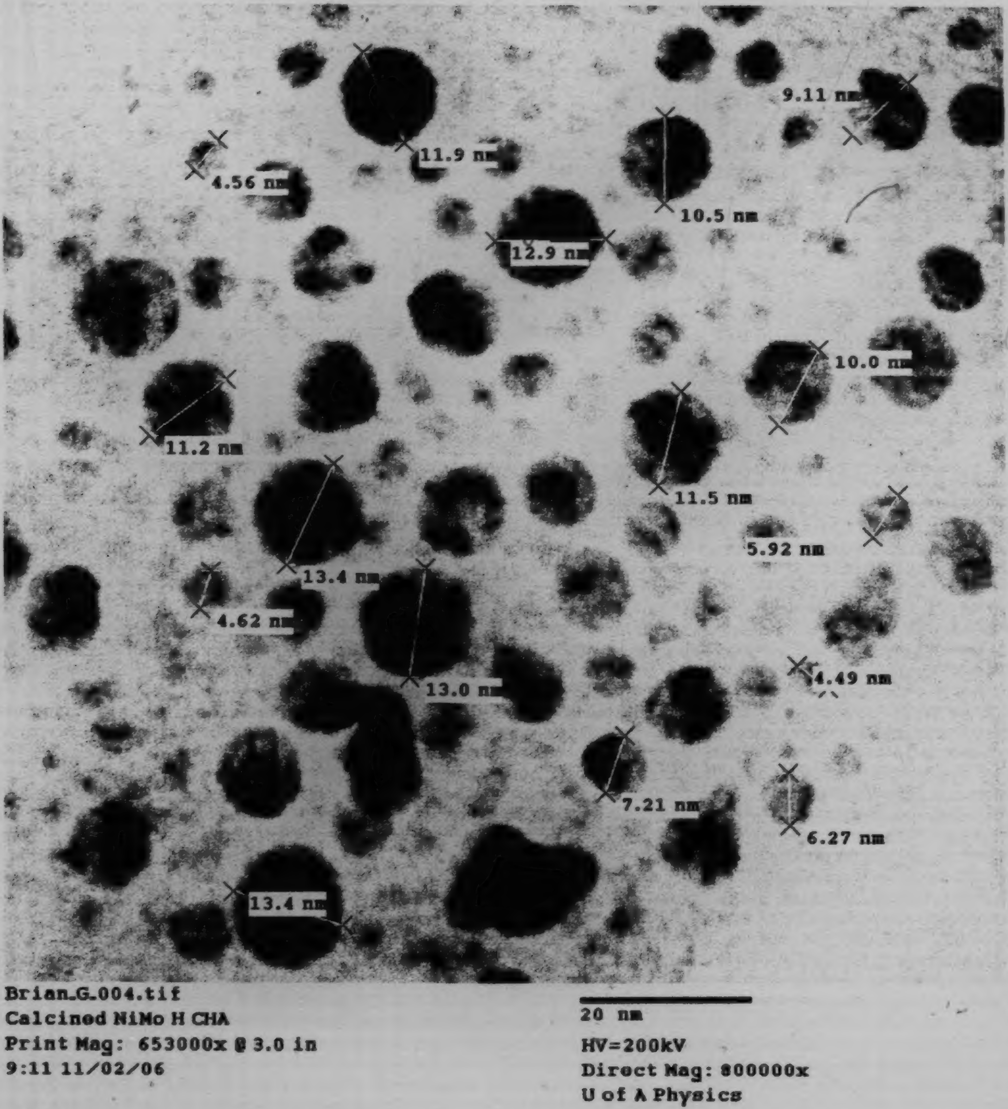
9.11 nm
11.9 nm
4.56 nm
10.5 nm
12.9 nm
10.0 nm
11.2 nm
11.5 nm
5.92 nm
13.4 nm
4.62 nm
13.0 nm
4.49 nm
7.21 nm
6.27 nm
13.4 nm
Brian_G_004.tif
Calcined NiMo H CHA
Print Mag: 653000x @ 3.0 in
9:11 11/02/06
20 nm
HV=200kV
Direct Mag: 800000x
U of A Physics

Figure B.118: NiMoHCHA As made.

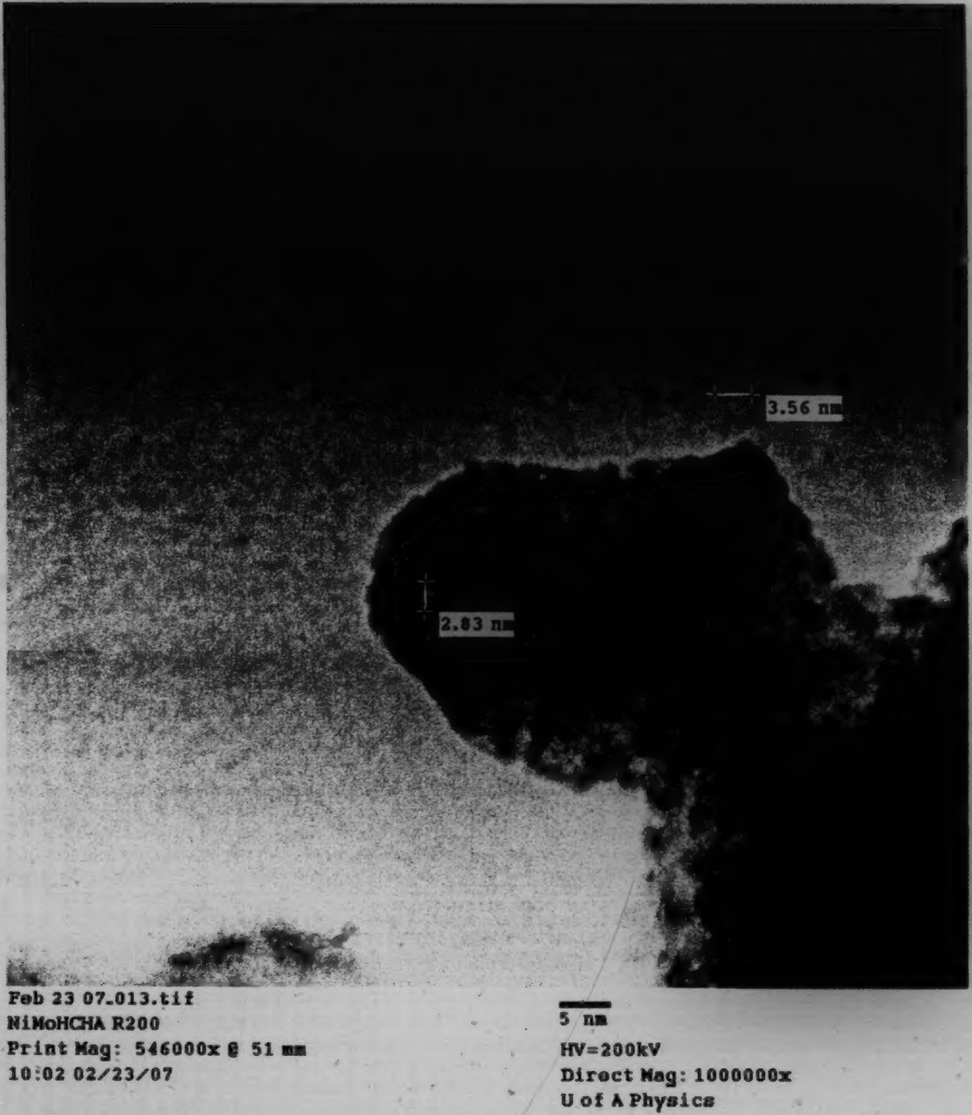
3.56 nm
2.83 nm
Feb 23 07_013.tif
NiMoHCHA R200
Print Mag: 546000x @ 51 mm
10:02 02/23/07
5 nm
HV=200kV
Direct Mag: 1000000x
U of A Physics

Figure B.119: NiMo[illegible]HA reduced at 200°C in $H_2$.

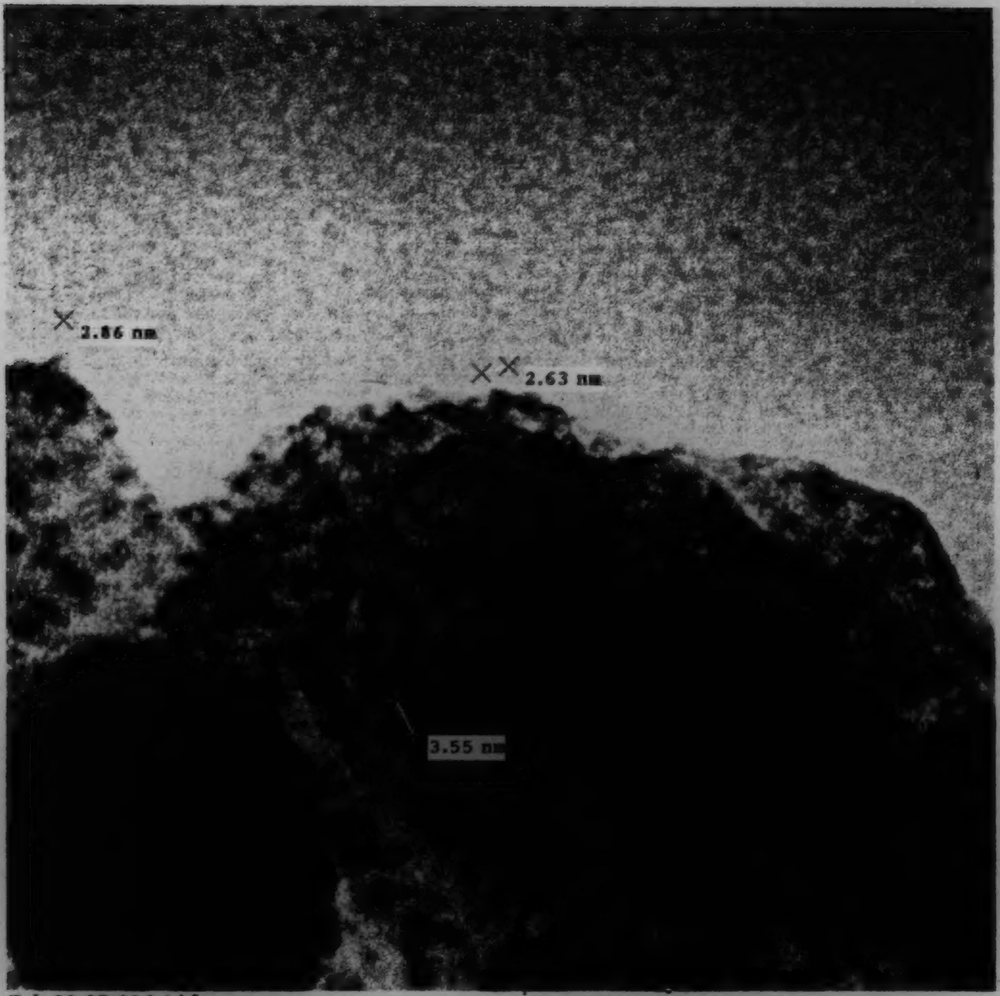
2.86 nm
2.63 nm
3.55 nm

Feb 23 07_016.tif
NiMoHCHA R200
Print Mag: 546000x @ 51 mm
10:06 02/23/07

5 nm
HV=200kV
Direct Mag: 1000000x
U of A Physics

Figure B.120: NiMoHCHA reduced at 200°C in $H_2$.

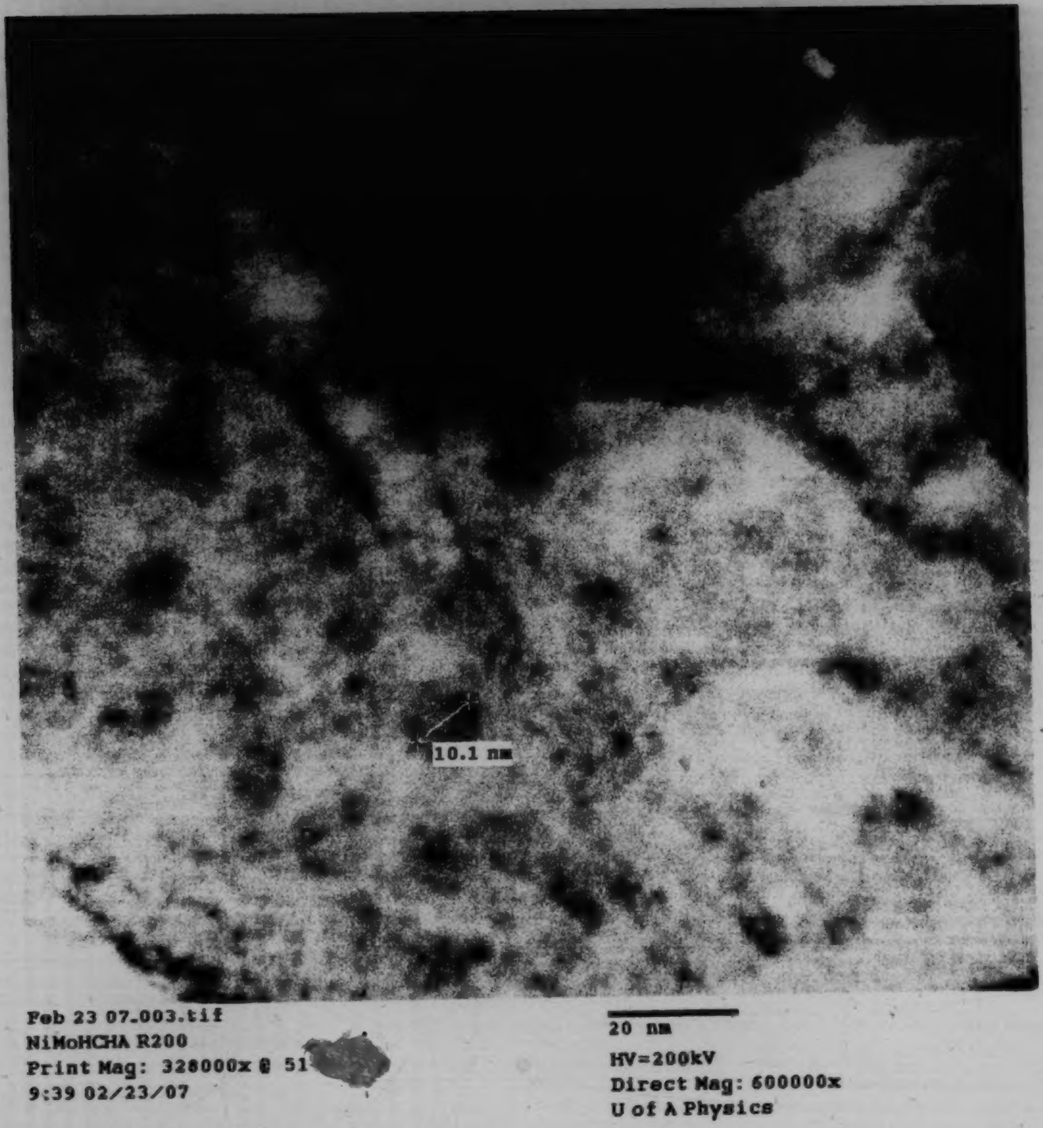
10.1 nm
Feb 23 07_003.tif
NiMoHCHA R200
Print Mag: 328000x @ 51
9:39 02/23/07
20 nm
HV=200kV
Direct Mag: 600000x
U of A Physics

Figure B.121: NiMoHCHA reduced at 200°C in $H_2$.

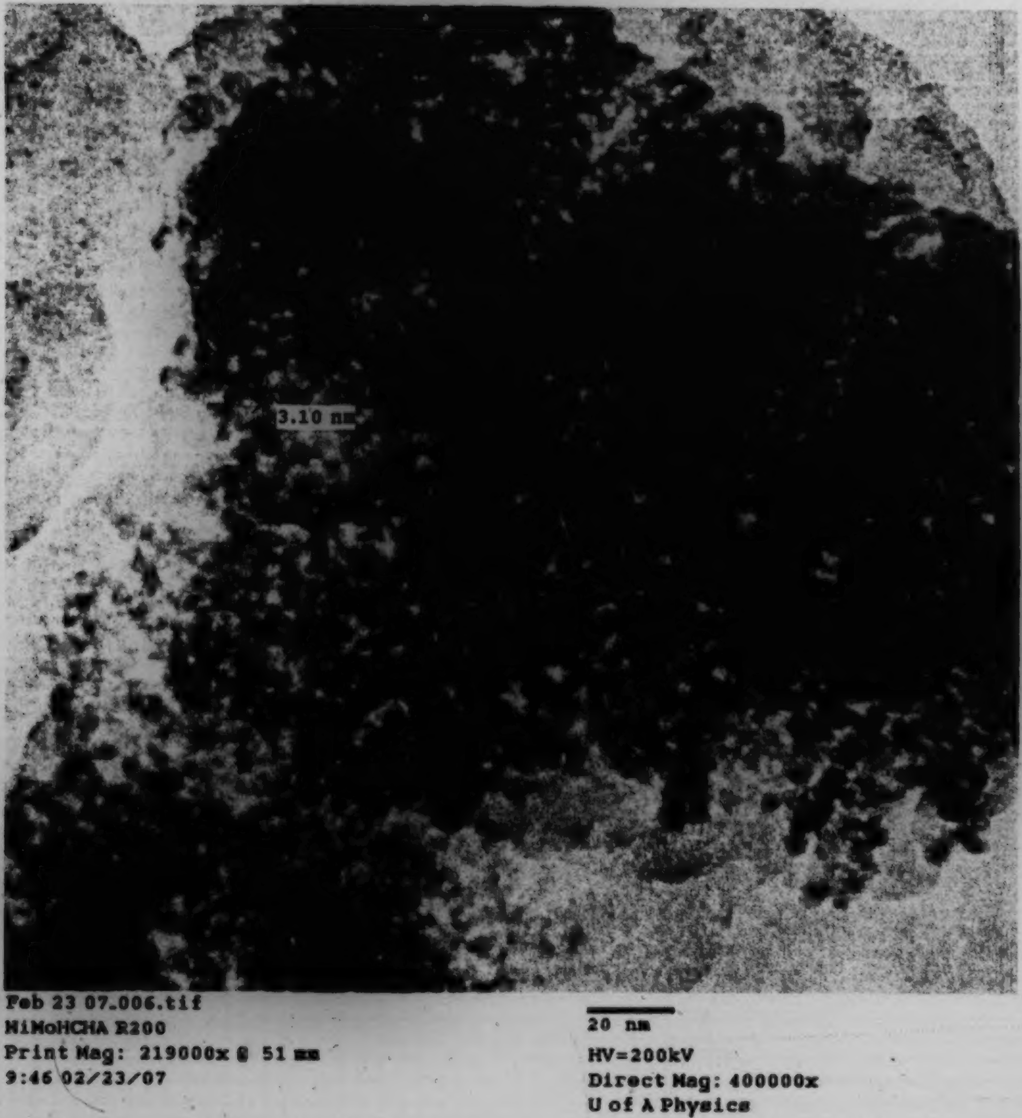
3.10 nm
Feb 23 07.006.tif
NiMoHCHA R200
Print Mag: 219000x @ 51 mm
9:46 02/23/07
20 nm
HV=200kV
Direct Mag: 400000x
U of A Physics

Figure B.122: NiMoHCHA reduced at 200°C in $H_2$.

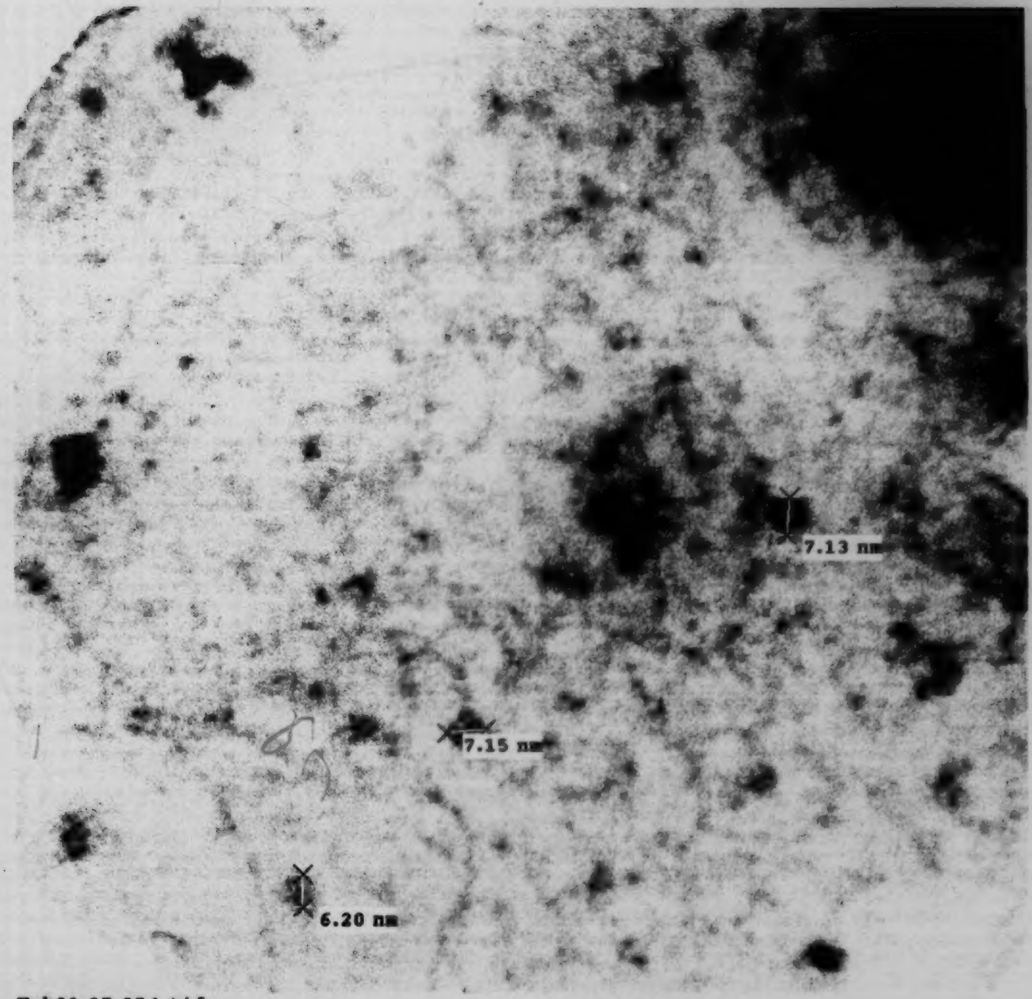
7.13 nm
7.15 nm
6.20 nm

Feb21 07_054.tif
NiMoHCHA 300R
Print Mag: 273000x @ 51 mm
11:55 02/21/07

20 nm
HV=200kV
Direct Mag: 500000x
U of A Physics

Figure B.123: NiMoHCHA reduced at 300°C in $H_2$.

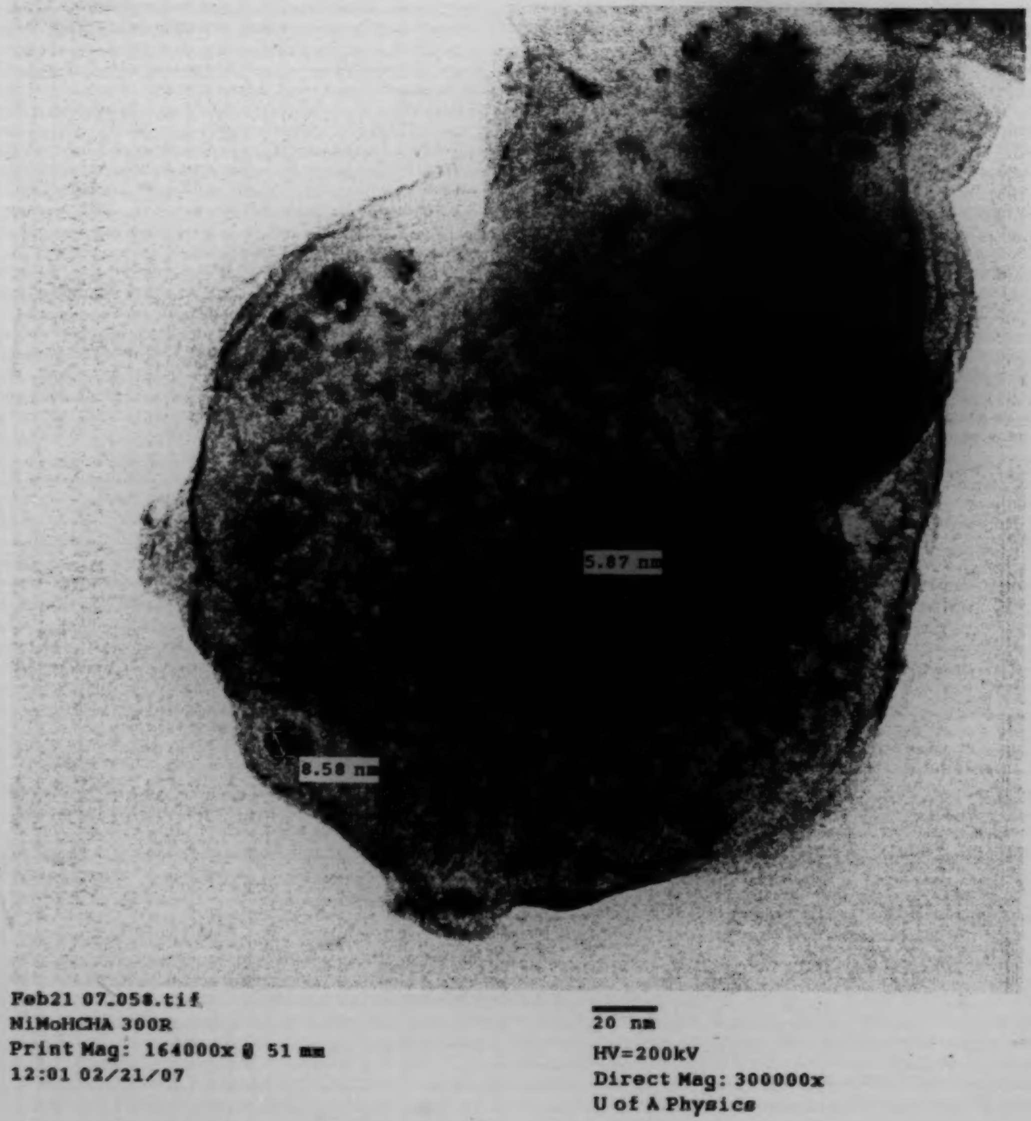
5.87 nm
8.58 nm
Feb21 07_058.tif
NiMoHCHA 300R
Print Mag: 164000x @ 51 mm
12:01 02/21/07
20 nm
HV=200kV
Direct Mag: 300000x
U of A Physics

Figure B.124: NiMoHCHA reduced at 300°C in $H_2$.

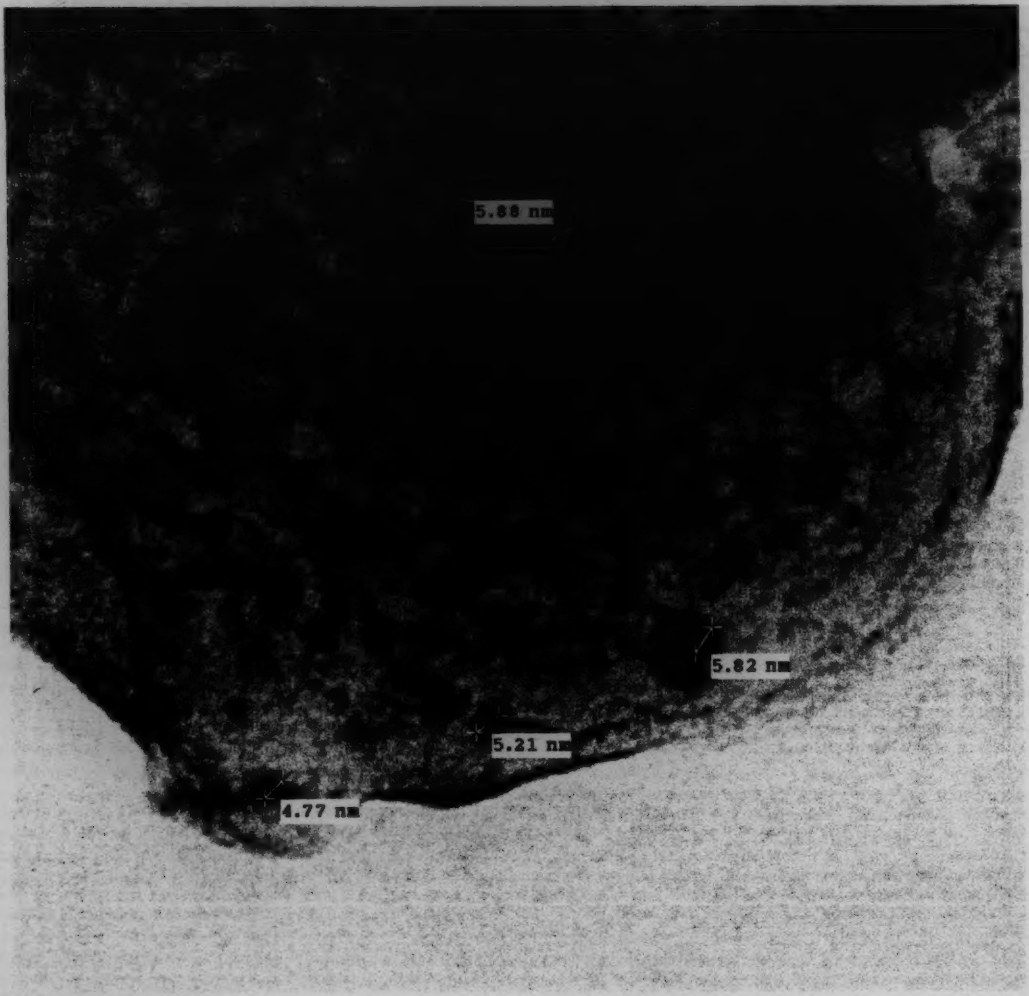
5.88 nm
5.82 nm
5.21 nm
4.77 nm

Feb21 07_060.tif
NiMoHCHA 300R
Print Mag: 273000x @ 51 mm
12:02 02/21/07

20 nm
HV=200kV
Direct Mag: 500000x
U of A Physics

Figure B.125: NiMoHCHA reduced at 300°C in $H_2$.

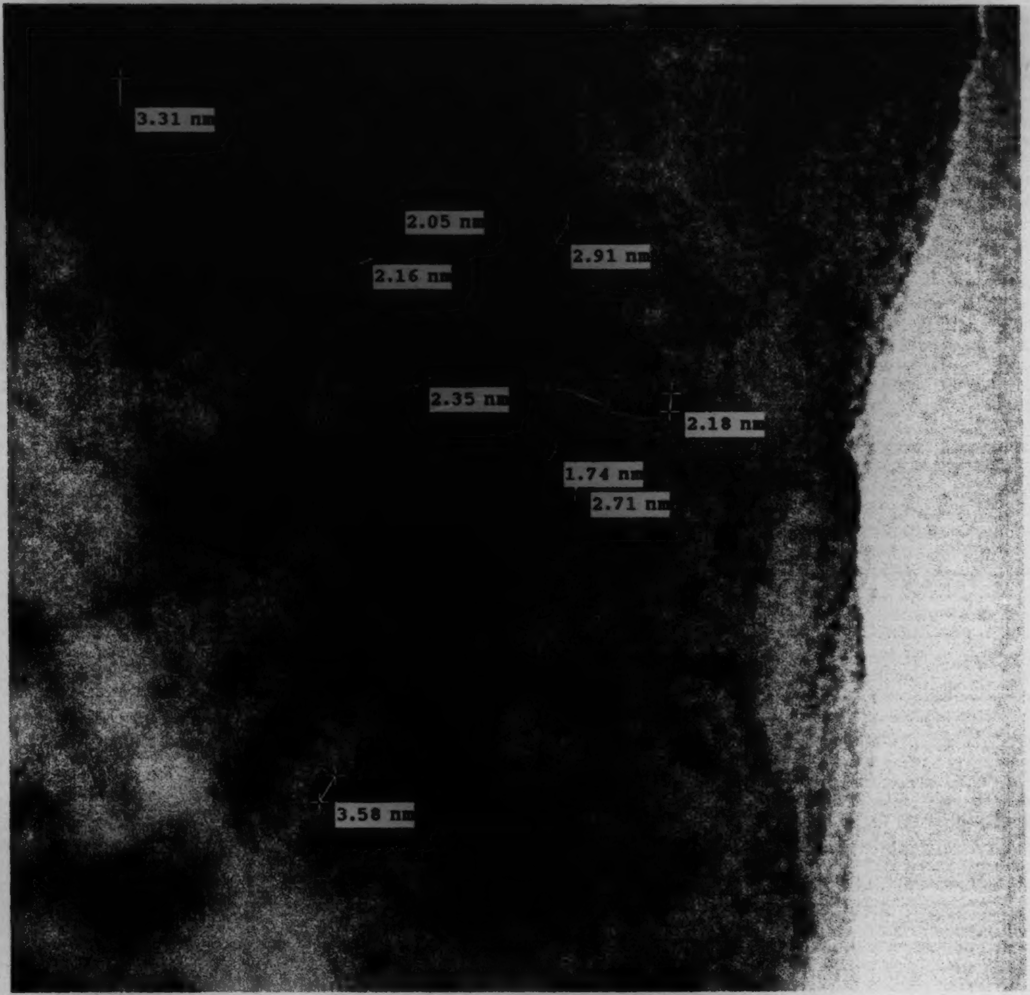
3.31 nm
2.05 nm
2.91 nm
2.16 nm
2.35 nm
2.18 nm
1.74 nm
2.71 nm
3.58 nm

Feb21 07_048.tif
NiMoHCHA 300R
Print Mag: 437000x @ 51 mm
11:51 02/21/07

20 nm
HV=200kV
Direct Mag: 800000x
U of A Physics

Figure B.126: NiMoHCHA reduced at 300°C in $H_2$.

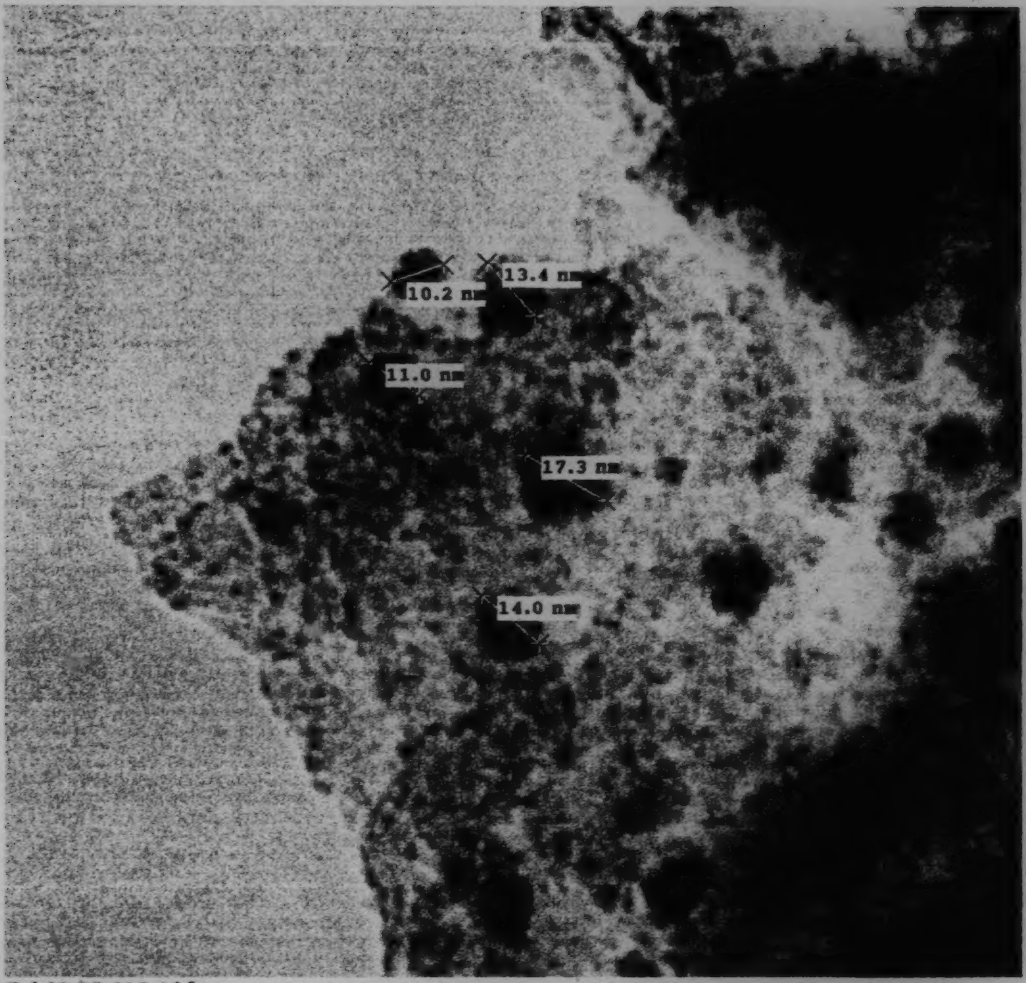
10.2 nm
13.4 nm
11.0 nm
17.3 nm
14.0 nm

Feb21 07_010.tif
NiMoHCHA R400
Print Mag: 273000x @ 51 mm
9:18 02/21/07

20 nm
HV=200kV
Direct Mag: 500000x
U of A Physics

Figure B.127: NiMoHCHA reduced at 400°C in $H_2$.

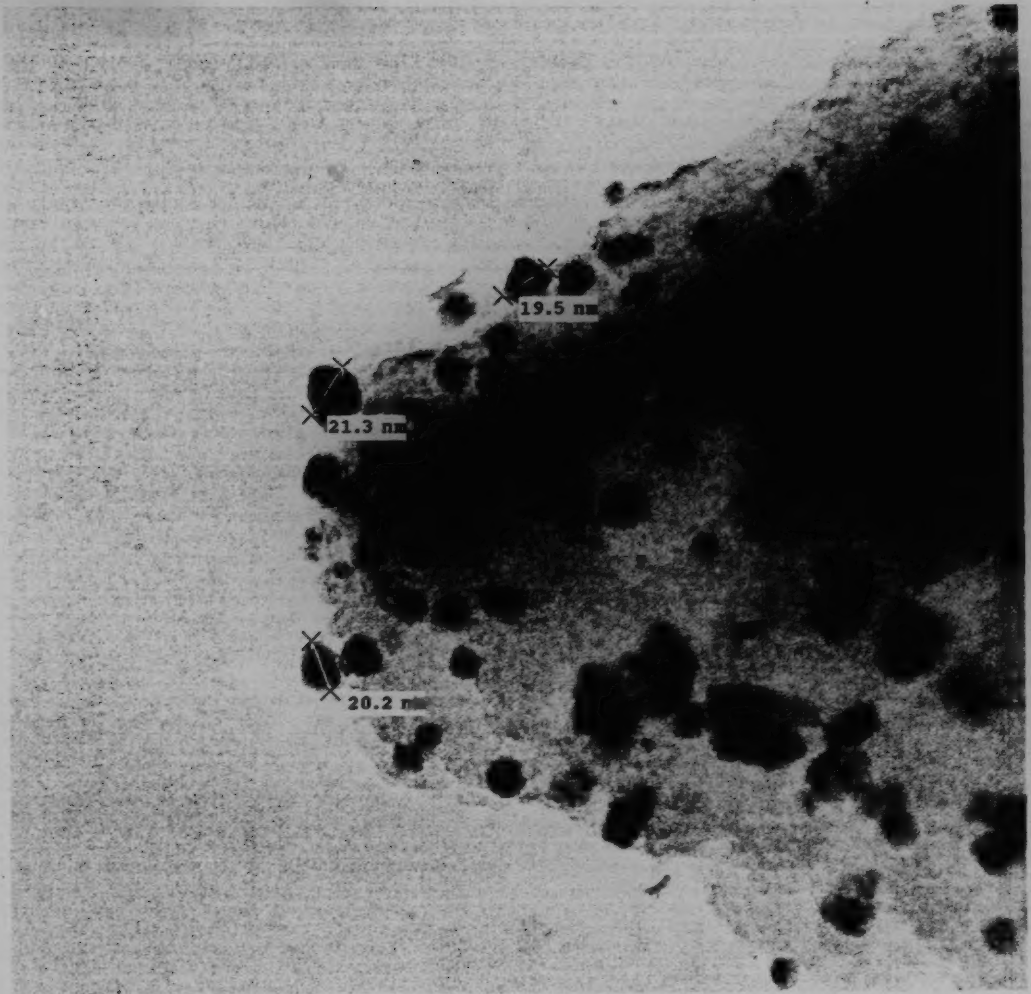
19.5 nm
21.3 nm
20.2 nm

Feb21 07_020.tif
NiMoHCHA R400
Print Mag: 137000x @ 51 mm
9:36 02/21/07

20 nm
HV=200kV
Direct Mag: 250000x
U of A Physics

Figure B.128: NiMoHCHA reduced at 400°C in $H_2$.

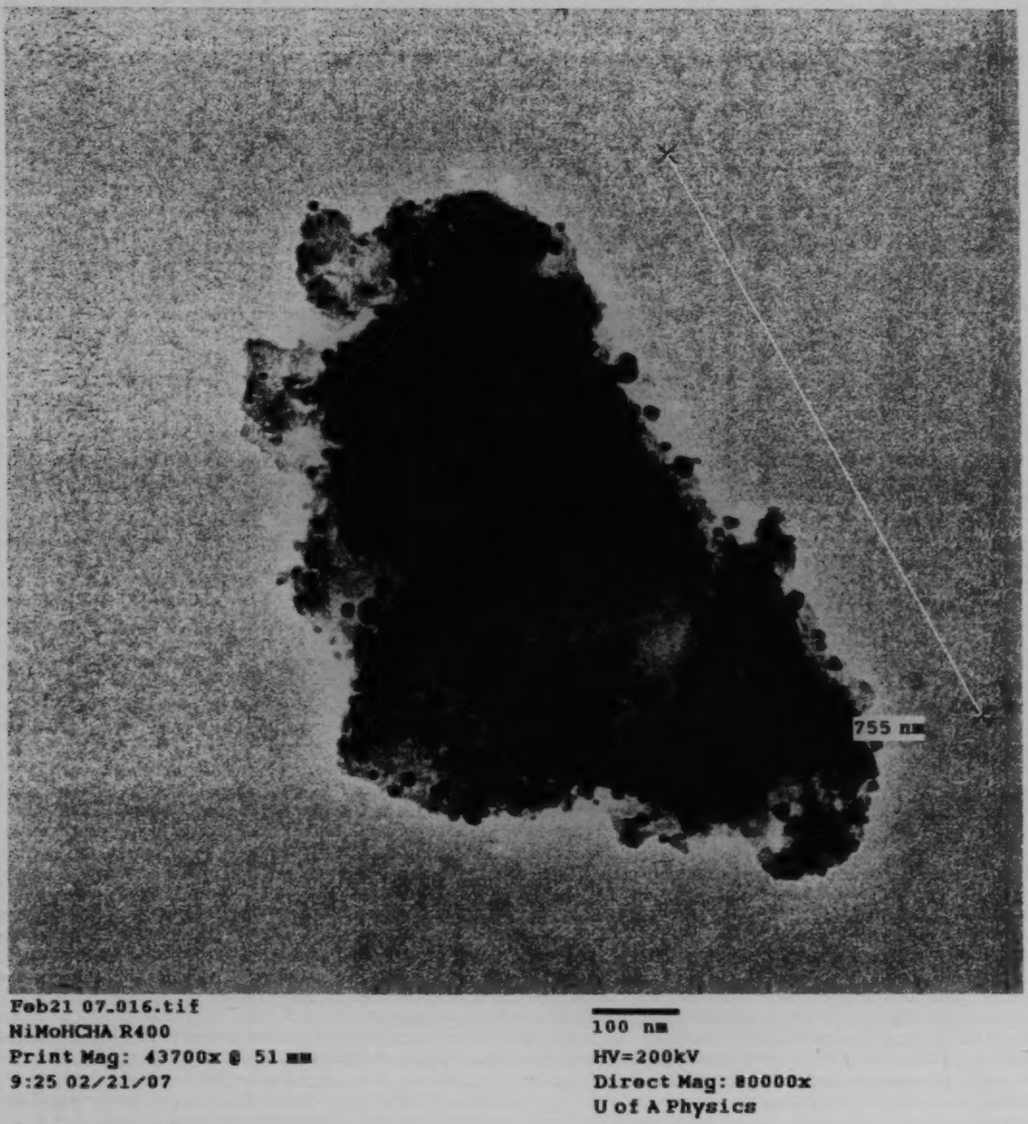
755 nm
Feb21 07_016.tif
NiMoHCHA R400
Print Mag: 43700x @ 51 mm
9:25 02/21/07
100 nm
HV=200kV
Direct Mag: 80000x
U of A Physics

Figure B.129: NiMoHCHA reduced at 400°C in $H_2$.

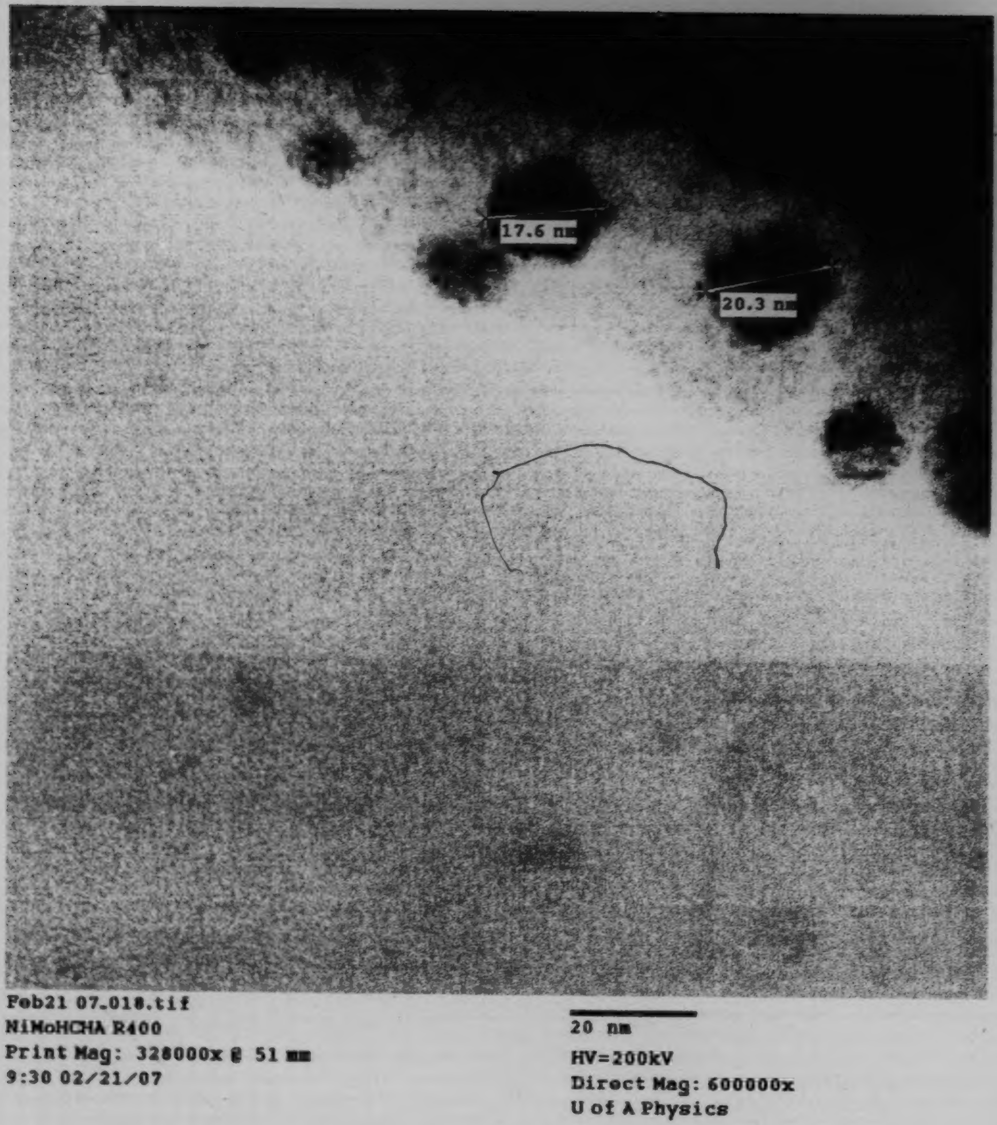
17.6 nm
20.3 nm
Feb21 07_018.tif
NiMoHCHA R400
Print Mag: 328000x @ 51 mm
9:30 02/21/07
20 nm
HV=200kV
Direct Mag: 600000x
U of A Physics

Figure B.130: NiMoHCHA reduced at 400°C in $H_2$.

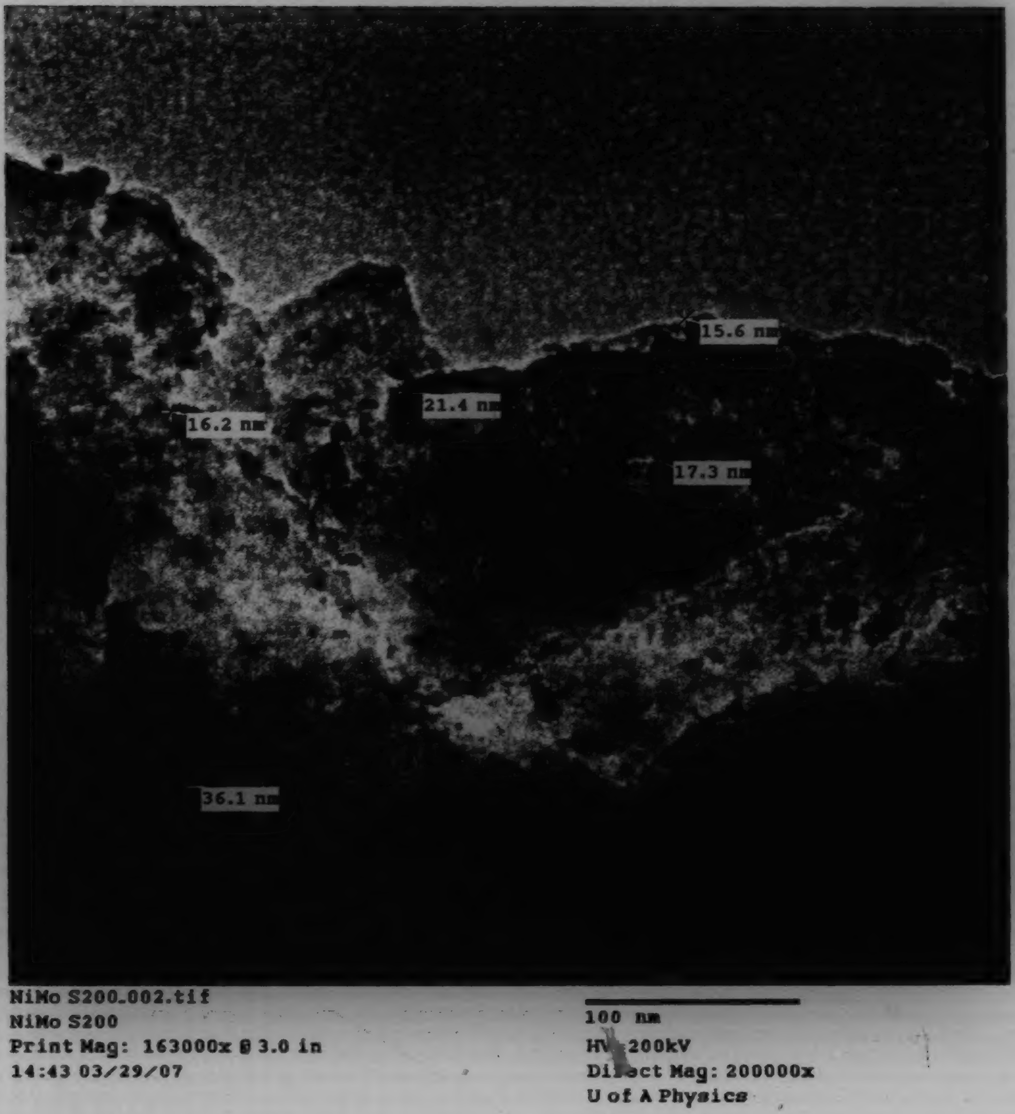
15.6 nm
21.4 nm
16.2 nm
17.3 nm
36.1 nm
NiMo S200_002.tif
NiMo S200
Print Mag: 163000x @ 3.0 in
14:43 03/29/07
100 nm
HV=200kV
Direct Mag: 200000x
U of A Physics

Figure B.131: NiMoHCHA sulfided at 200°C in $H_2S/H_2$.

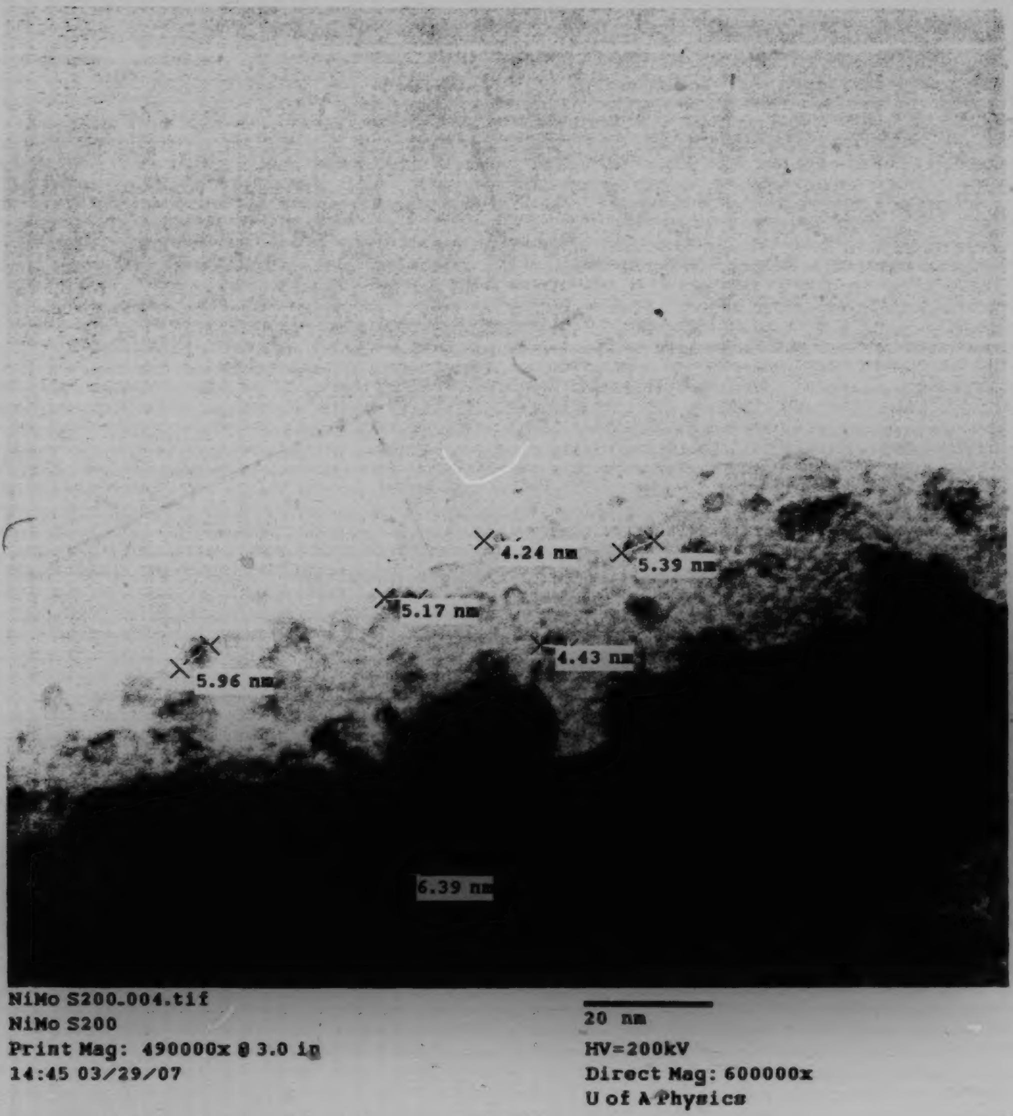
4.24 nm
5.39 nm
5.17 nm
4.43 nm
5.96 nm
6.39 nm
NiMo S200_004.tif
NiMo S200
Print Mag: 490000x @ 3.0 in
14:45 03/29/07
20 nm
HV=200kV
Direct Mag: 600000x
U of A Physics

Figure B.132: NiMoHCHA sulfided at 200°C in $H_2S/H_2$.

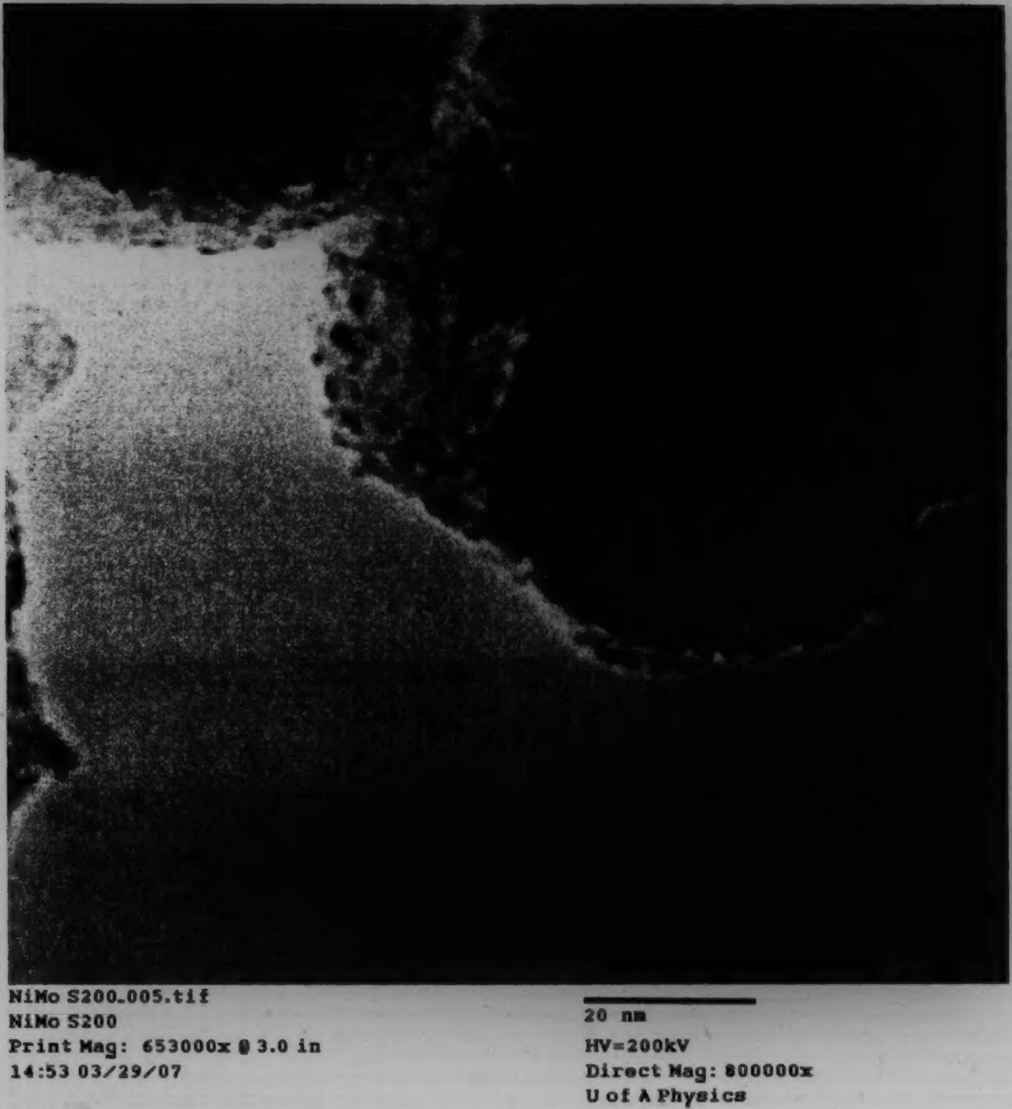
NiMo S200_005.tif
NiMo S200
Print Mag: 653000x @ 3.0 in
14:53 03/29/07
20 nm
HV=200kV
Direct Mag: 800000x
U of A Physics

Figure B.133: NiMoHCHA sulfided at 200°C in $H_2S/H_2$.

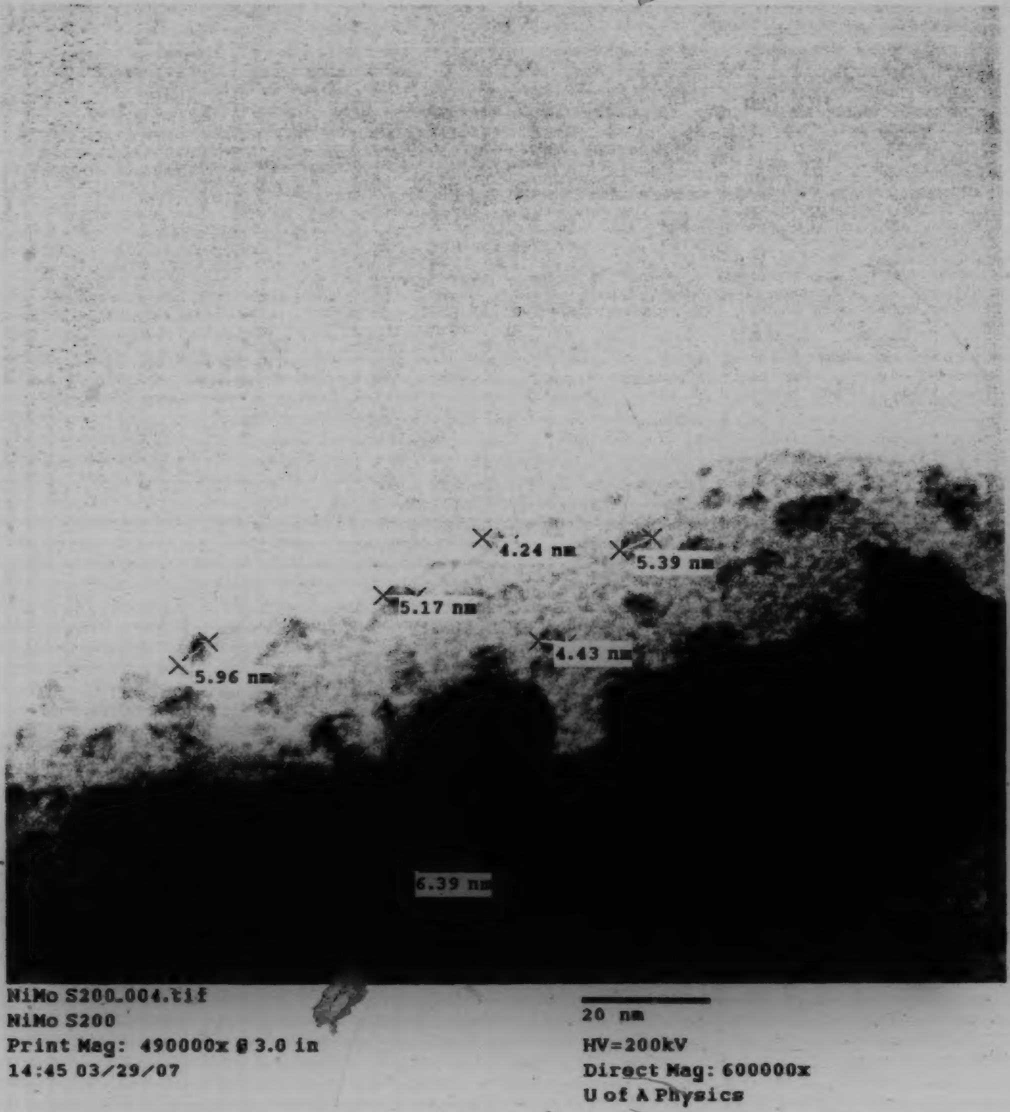
4.24 nm
5.39 nm
5.17 nm
4.43 nm
5.96 nm
6.39 nm
NiMo S200_004.tif
NiMo S200
Print Mag: 490000x @ 3.0 in
14:45 03/29/07
20 nm
HV=200kV
Direct Mag: 600000x
U of A Physics

Figure B.134: NiMoHCHA sulfided at 200°C in $H_2S/H_2$.

NiMo S300_006.tif
NiMo S300
Print Mag: 327000x @ 3.0 in
12:02 03/29/07
20 nm
HV=200kV
Direct Mag: 400000x
U of A Physics

Figure B.135: NiMoHCHA sulfided at 300°C in $H_2S/H_2$.

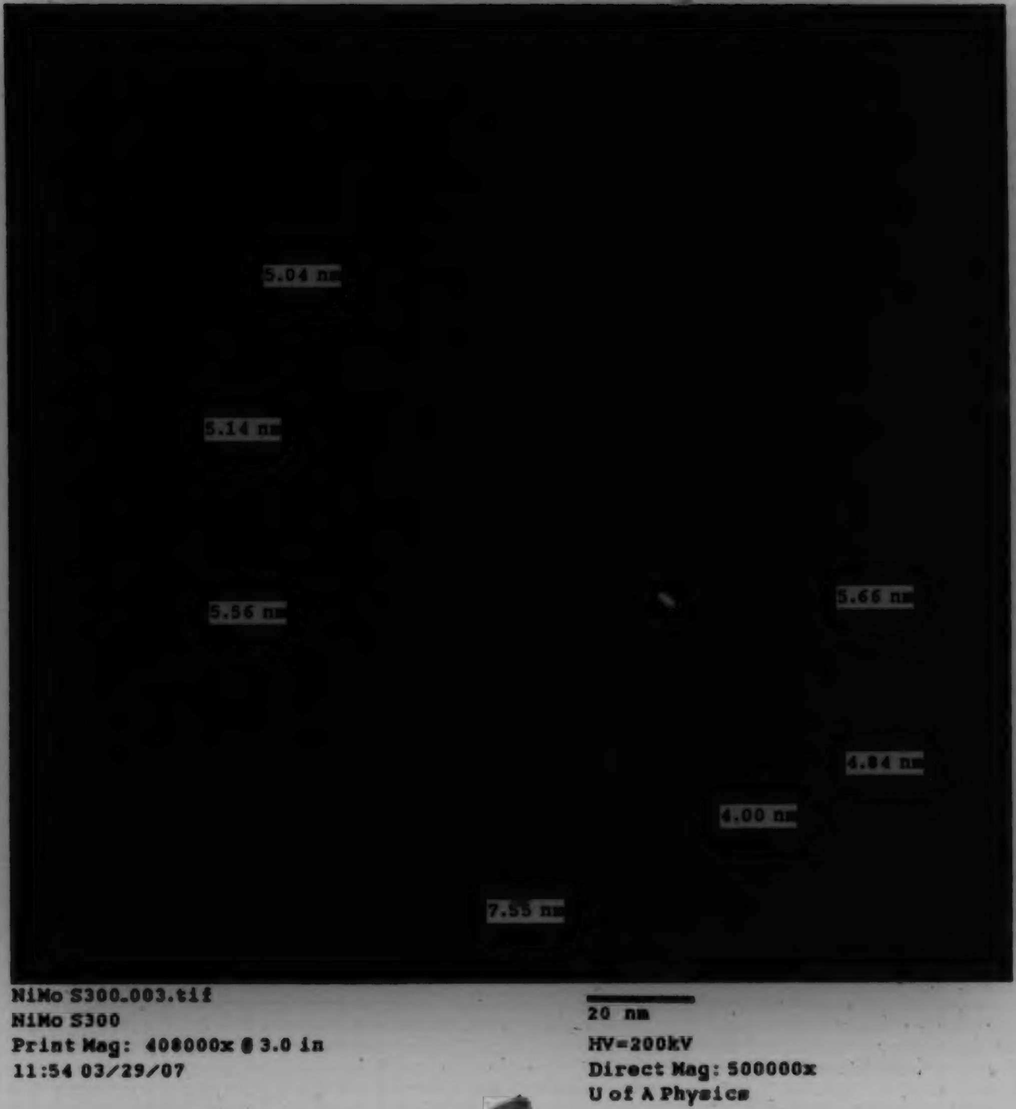
5.04 nm
5.14 nm
5.56 nm
5.66 nm
4.84 nm
4.00 nm
7.55 nm
NiMo S300_003.tif
NiMo S300
Print Mag: 408000x @ 3.0 in
11:54 03/29/07
20 nm
HV=200kV
Direct Mag: 500000x
U of A Physics

Figure B.136: NiMoHCHA sulfided at 300°C in $H_2S/H_2$.

2.45 nm
3.12 nm
4.30 nm
3.02 nm

NiMo S300.005.tif
NiMo S300
Print Mag: 490000x @ 3.0 in
11:58 03/29/07

20 nm
HV=200kV
Direct Mag: 600000x
U of A Physics

Figure B.137: NiMoHCHA sulfided at 300°C in $H_2S/H_2$.

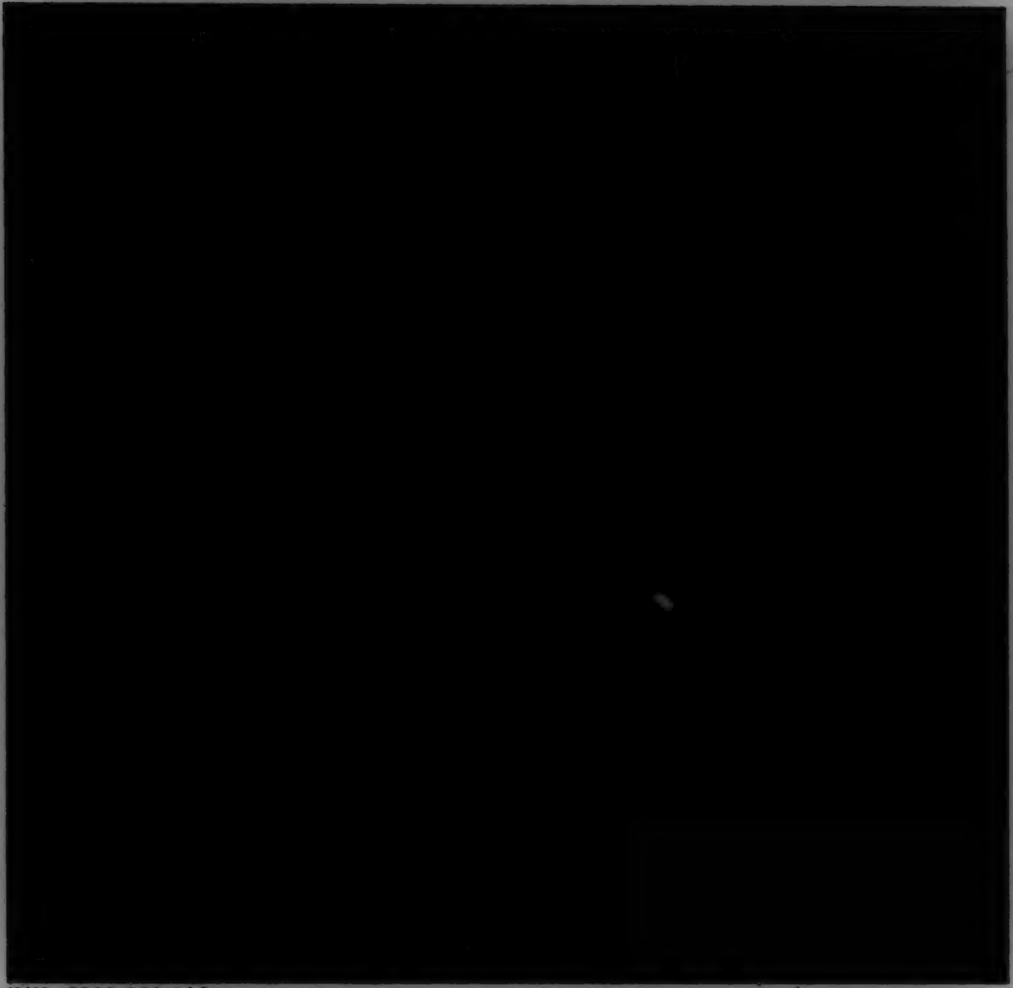

NiMo S300.009.tif
NiMo S300
Print Mag: 816000x @ 3.0 in
12:14 03/29/07
5 nm
HV=200kV
Direct Mag: 1000000x
U of A Physics

Figure B.138: NiMoHCHA sulfided at 300°C in $H_2S/H_2$.

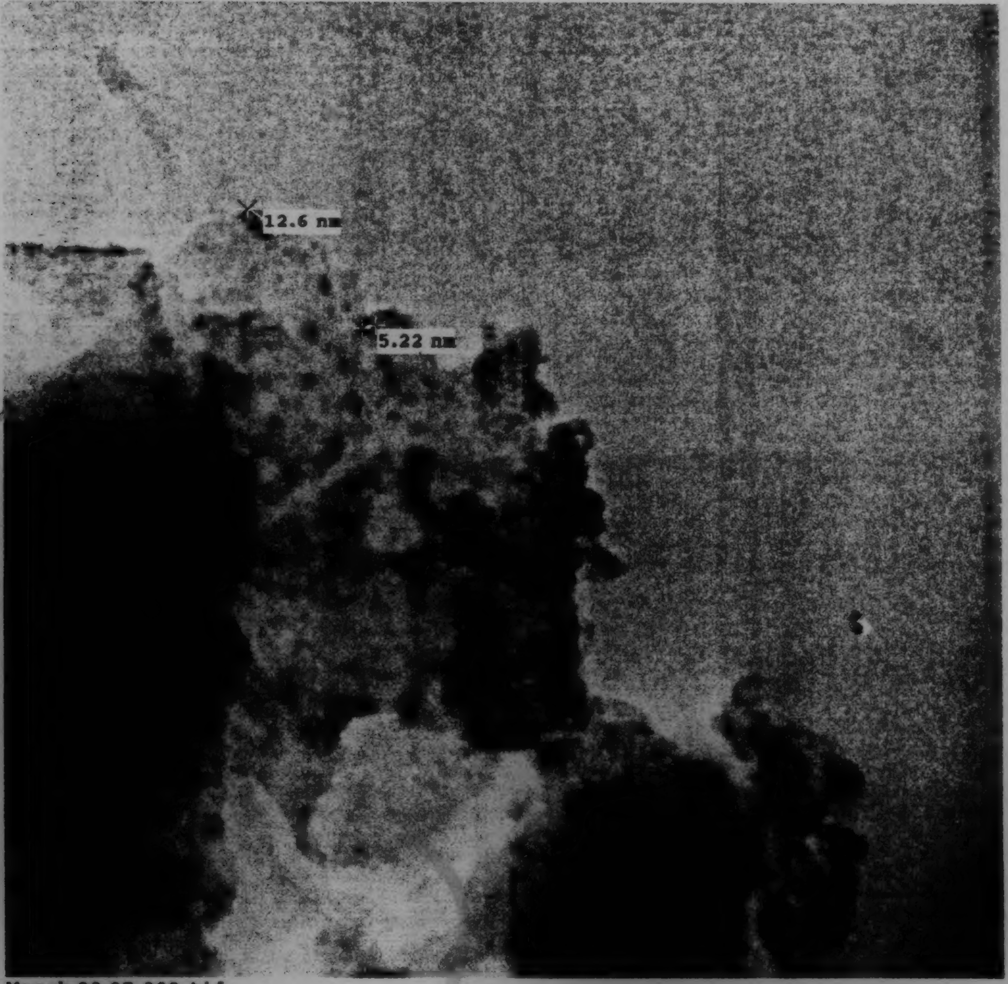

March 29 07_002.tif
NiMo CHA 400S
Print Mag: 204000x @ 3.0 in
8:47 03/29/07

20 nm
HV=200kV
Direct Mag: 250000x
U of A Physics

Figure B.139: NiMoHCHA sulfided at 400°C in $H_2S/H_2$.

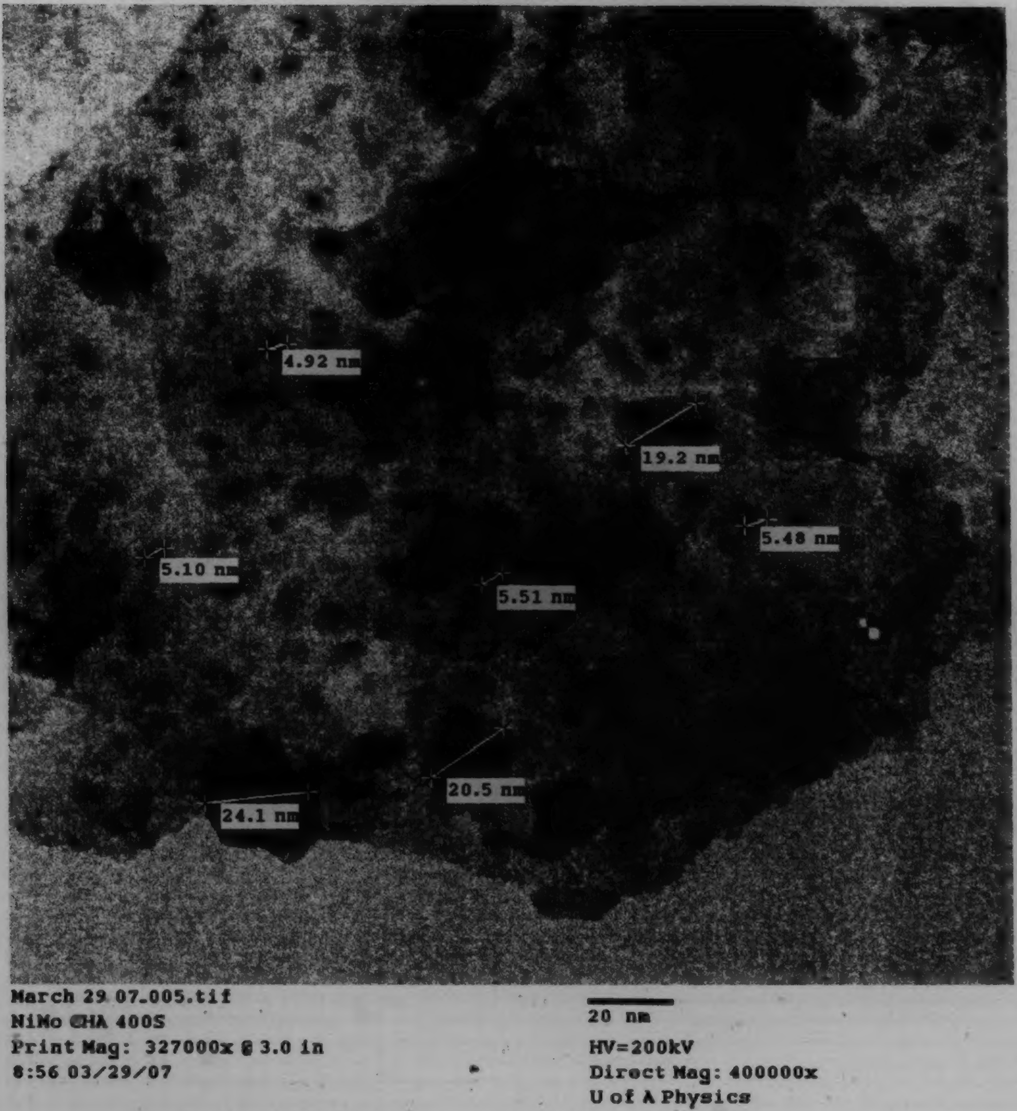
4.92 nm
19.2 nm
5.48 nm
5.10 nm
5.51 nm
20.5 nm
24.1 nm
March 29 07_005.tif
NiMo CHA 400S
Print Mag: 327000x @ 3.0 in
8:56 03/29/07
20 nm
HV=200kV
Direct Mag: 400000x
U of A Physics

Figure B.140: NiMoHCHA sulfided at 400°C in $H_2S/H_2$.

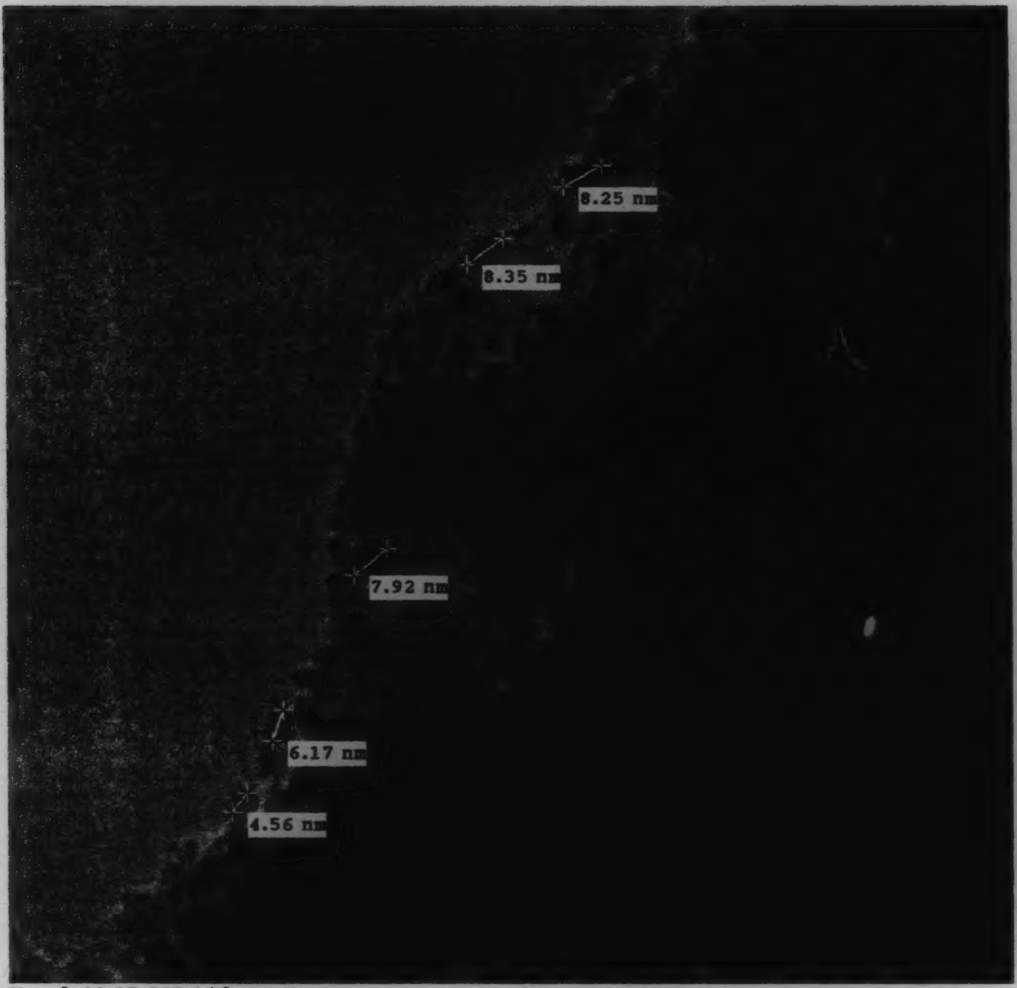
8.25 nm
8.35 nm
7.92 nm
6.17 nm
4.56 nm
20 nm

March 29 07_013.tif
NiMo CHA 400S
Print Mag: 408000x @ 3.0 in
9:20 03/29/07

HV=200kV
Direct Mag: 500000x
U of A Physics

Figure B.141: NiMoHCHA sulfided at 400°C in $H_2S/H_2$.

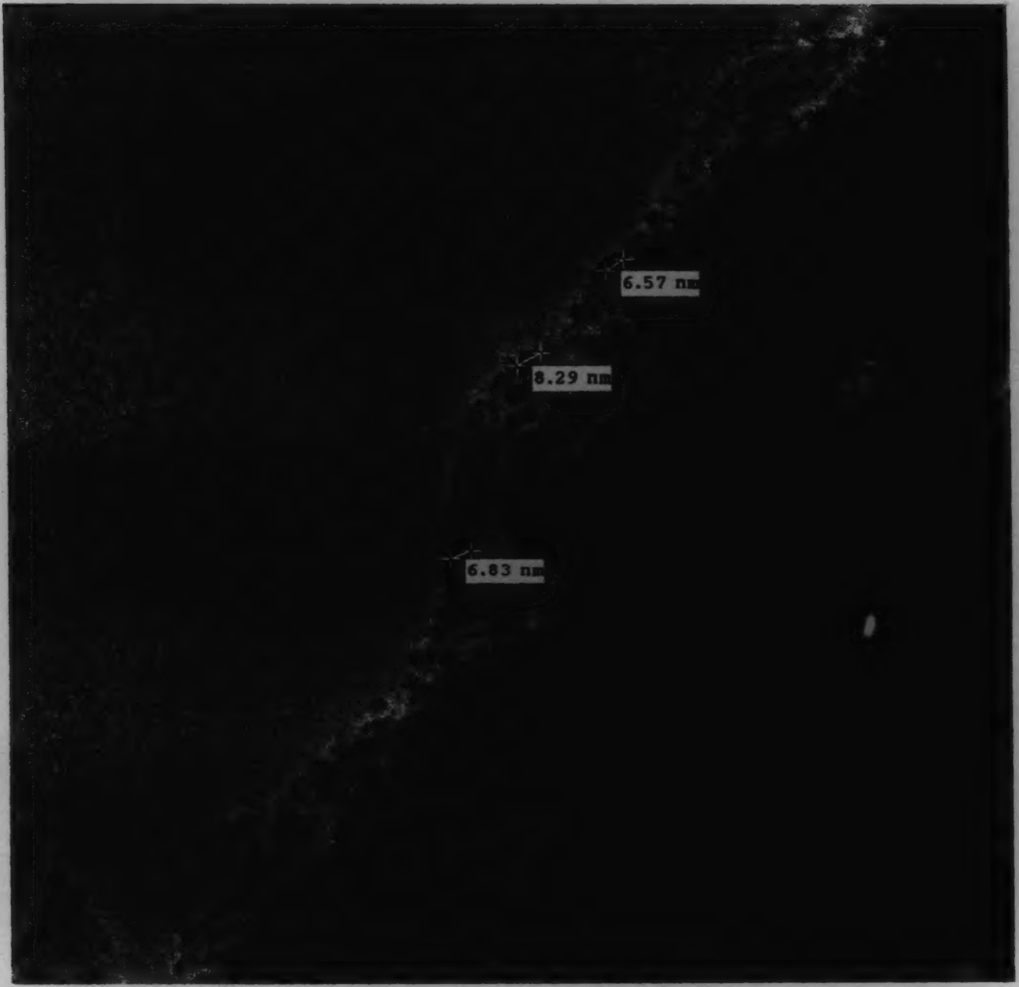
6.57 nm
8.29 nm
6.83 nm

March 29 07_011.tif
NiMo CHA 400S
Print Mag: 245000x @ 3.0 in
9:19 03/29/07

20 nm
HV=200kV
Direct Mag: 300000x
U of A Physics

Figure B.142: NiMoHCHA sulfided at 400°C in $H_2S/H_2$.

# Appendix C
## NH3-TPD Results

This Appendix contains $NH_3$ TPD spectra of Series 1, (Na-, Ni-, Mo- and NiMo-CHA), $NH_4$ exchanged chabazite and Series 2 (Ni-, Mo- and NiMoHCHA), in the as made states, as well as a selected reduced samples. This data was the basis for the discussion found in "Acidity of supports and catalysts ($NH_3$-TPD)", in Chapter 4. Results and Discussion, which contains excerpts from this appendix.

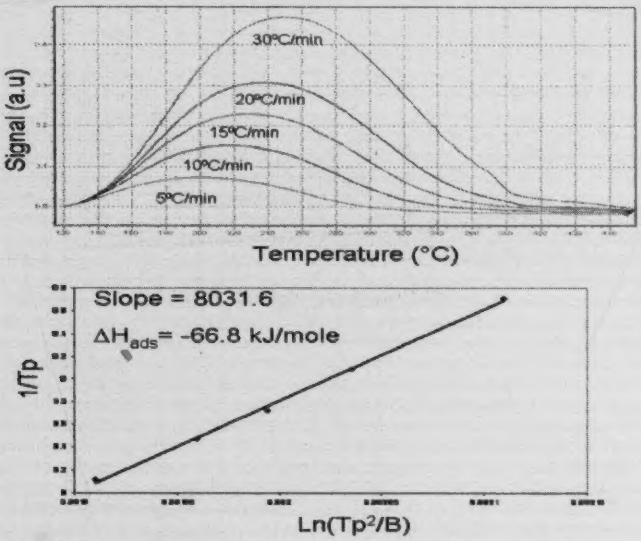

Figure C.1: $NH_3$-TPD data for Na-CHA.

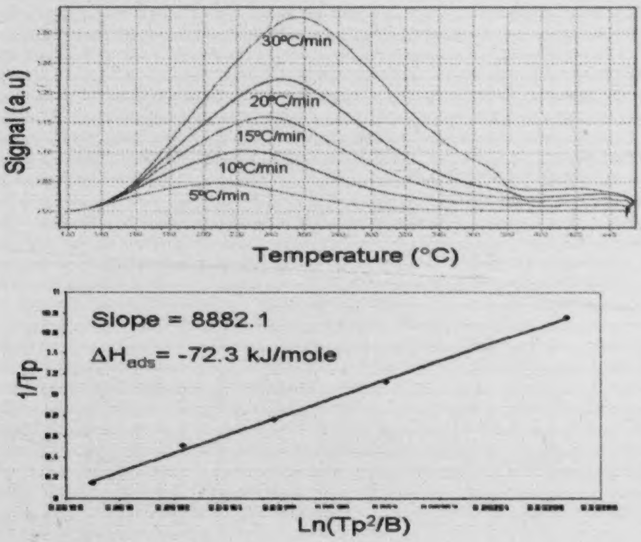

Figure C.2: $NH_3$-TPD data for Ni-CHA.

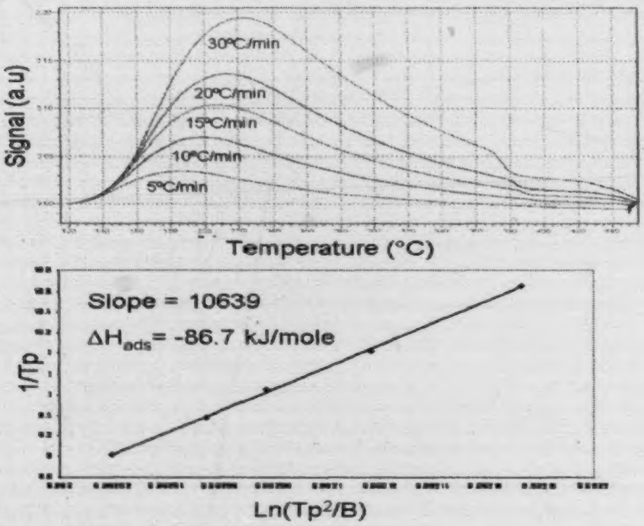

Figure C.3: $NH_3$-TPD data for NiMo-CHA.

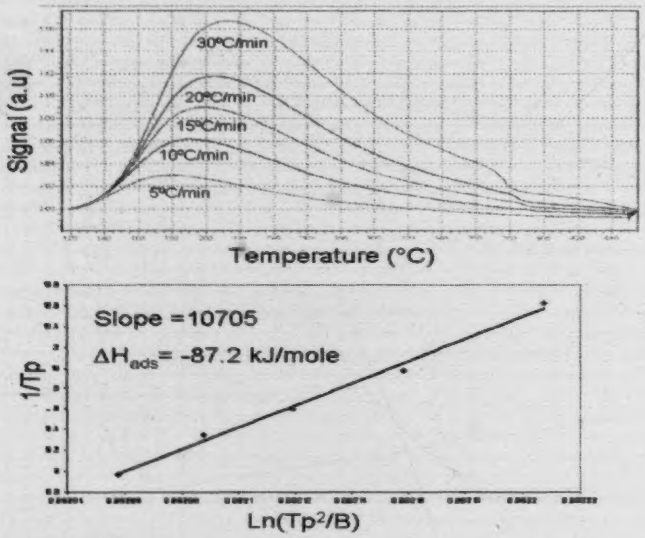

Figure C.4: $NH_3$-TPD data for Mo-CHA.

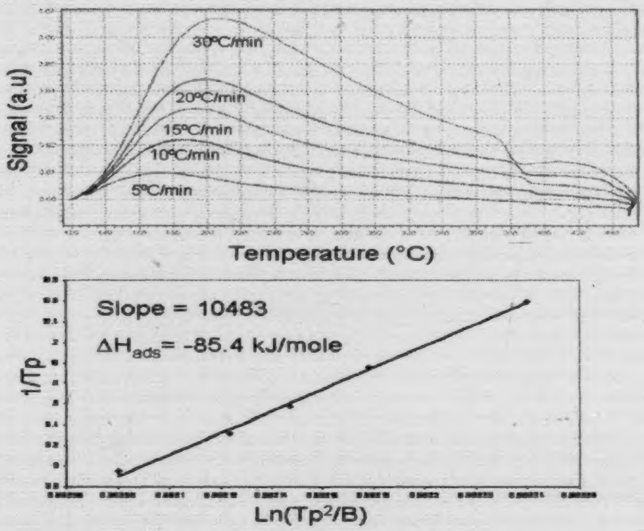

Figure C.5: $NH_3$-TPD data for NiMo-CHA reduced at 400 ºC in $H_2$/

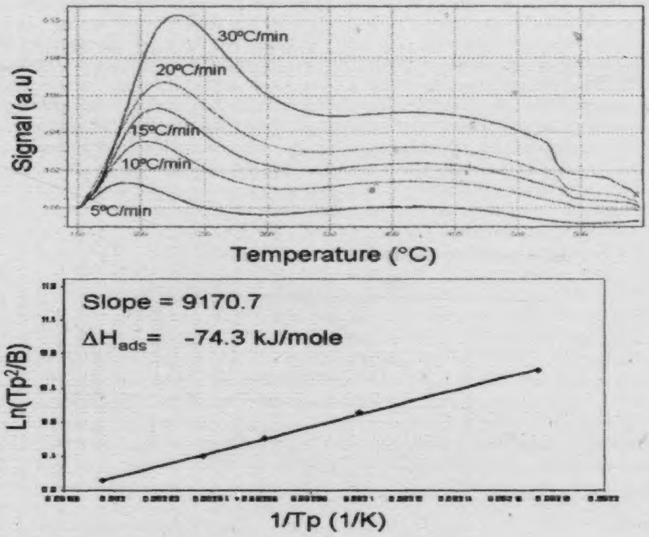

Figure C.6: $NH_3$-TPD data for $NH_4$-CHA(1).

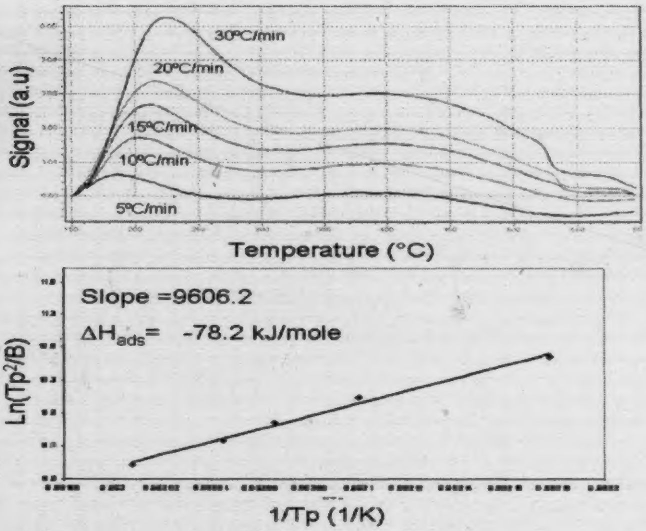

Figure C.7: $NH_3$-TPD data for $NH_4$-CHA(2).

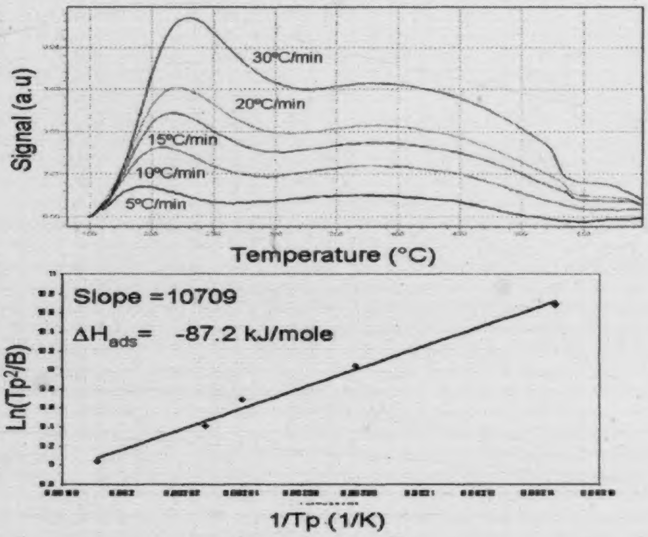

Figure C.8: $NH_3$-TPD data for $NH_4$-CHA(3).

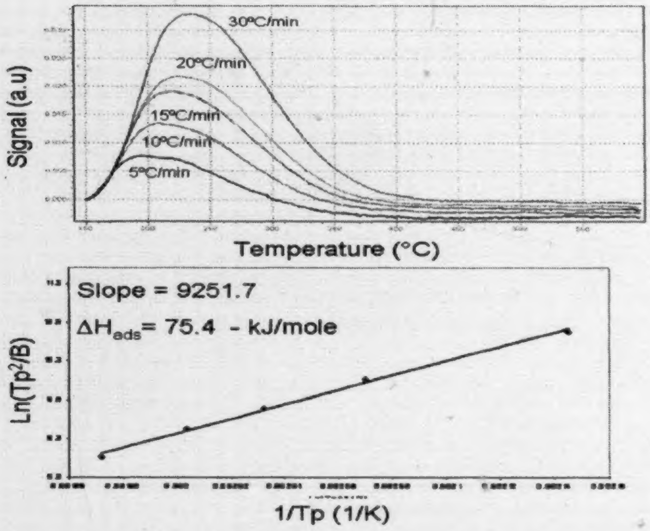

Figure C.9: $NH_3$-TPD data for NiMo-CHA prepared for $NH_4^+$ incorporation.

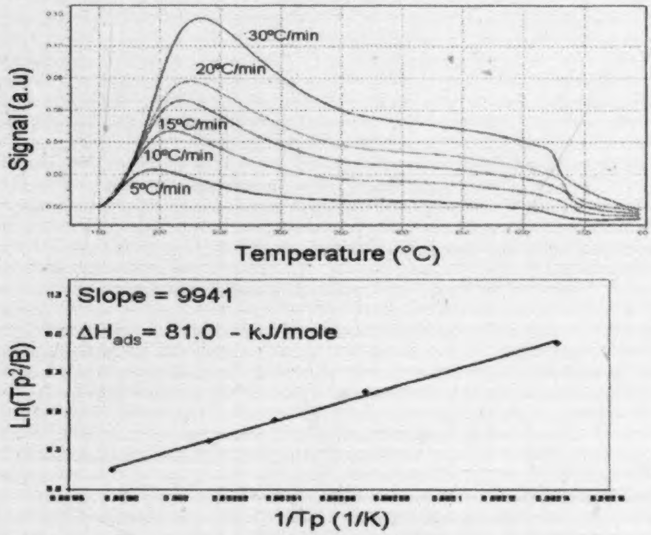

Figure C.10: $NH_3$-TPD data for $NH_4^+$ exchanged into NiMo-CHA.

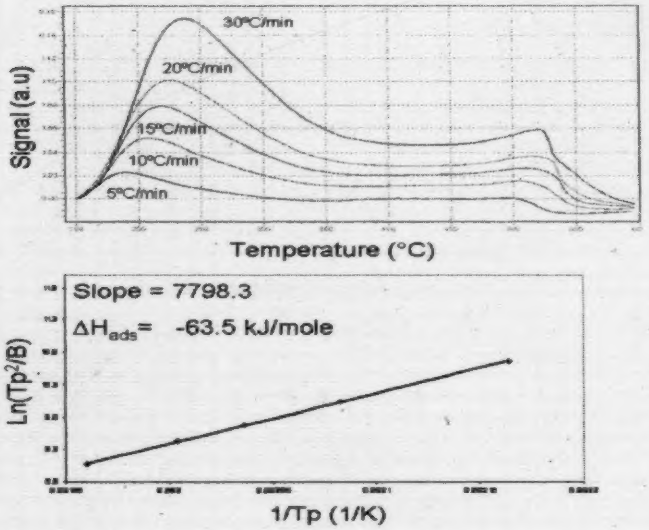

Figure C.11: $NH_3$-TPD data for NiMo exchanged into $NH_4$-CHA.

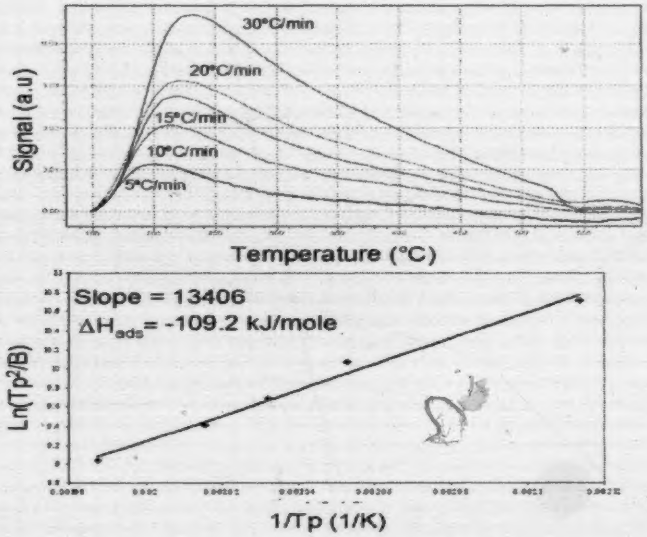

Figure C.12: $NH_3$-TPD data for low temperature (450°C) calcined NiMo exchanged into $NH_4$-CHA.

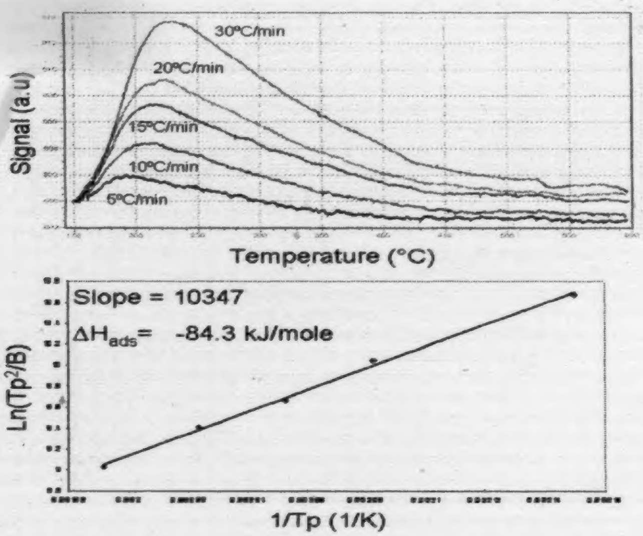

Figure C.13: $NH_3$-TPD data for high temperature (600°C) calcined NiMo exchanged into $NH_4$-CHA.

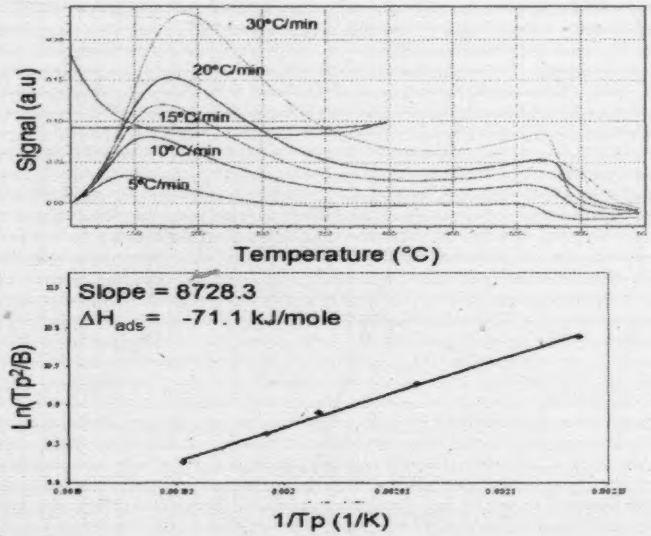

Figure C.14: $NH_3$-TPD data for NiMo exchanged into $NH_4$-CHA reduced at 400°C in $H_2$.

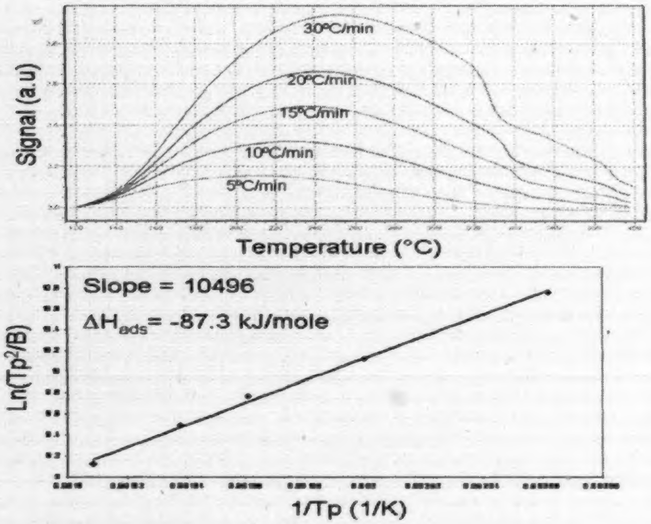

Figure C.15: $NH_3$-TPD data for HCHA.

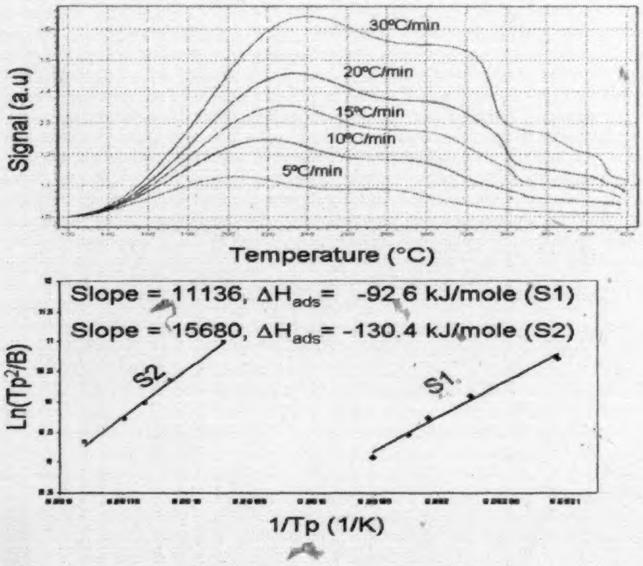

Figure C.16: $NH_3$-TPD data for NiHCHA (S2 represents the higher temperature peaks).

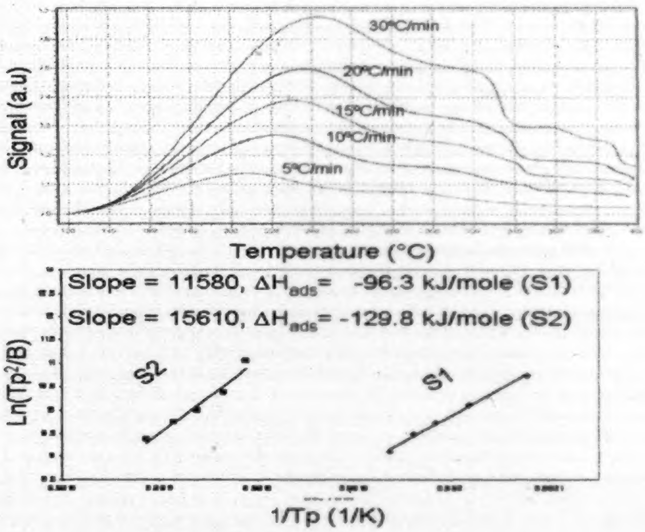

Figure C.17: $NH_3$-TPD data for NiMoHCHA (S2 represents the higher temperature peaks).

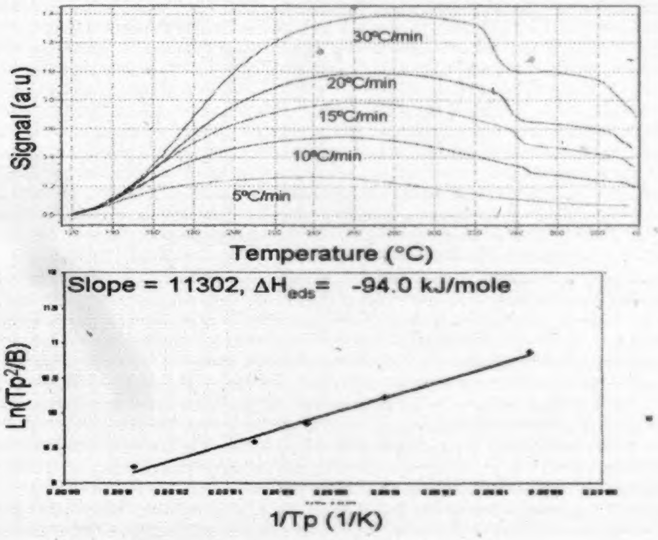

Figure C.18: $NH_3$-TPD data for MoHCHA.

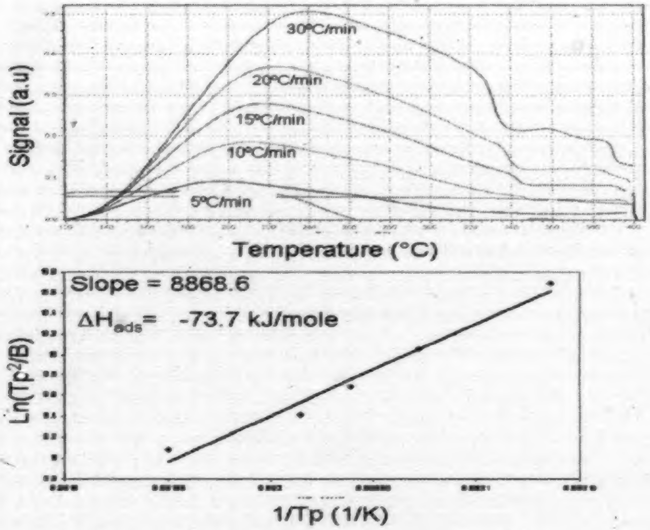

Figure C.19: $NH_3$-TPD data for NiHCHA reduced at 400°C in $H_2$.

# Appendix D

## Ethylene Hydrogenation Results

This Appendix contains a wide array of ethylene hydrogenation results of Series 2 (Ni-, Mo- and NiMoHCHA), in the presence and absence of hydrogen sulfide. This data was the basis for the discussion of the activity and selectivity results found in "Ethylene Hydrogenation Activities", in Chapter 4. Results and Discussion, which contains excerpts from this appendix.

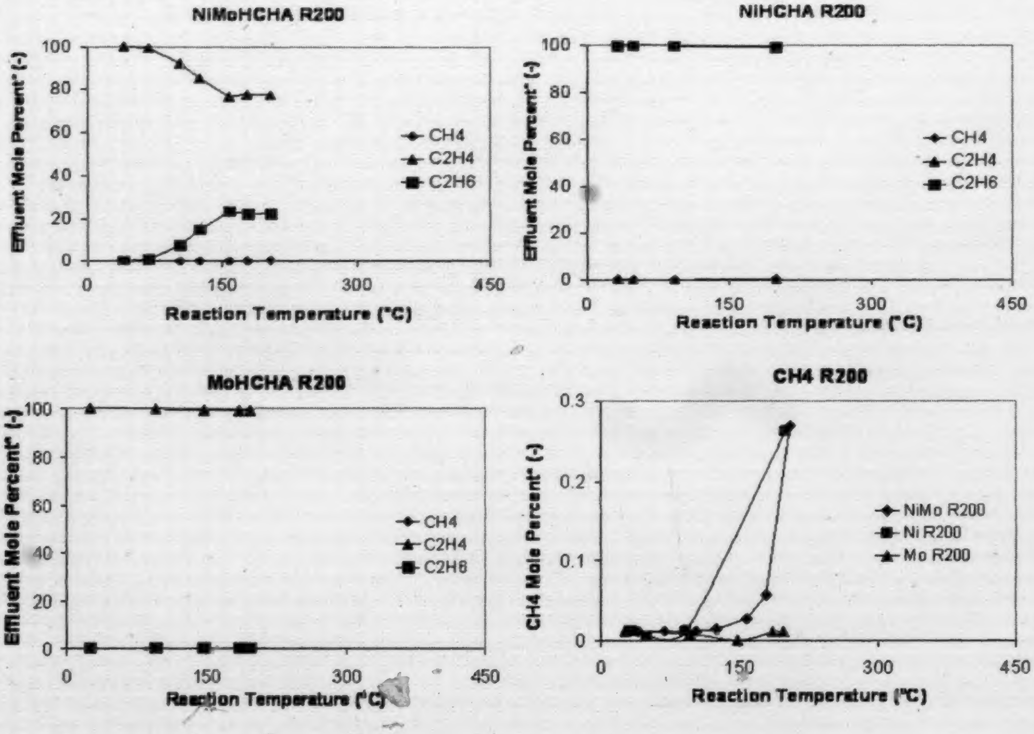

Figure D.1: Catalytic results for the metal loaded acidified chabazites reduced at 200°C.

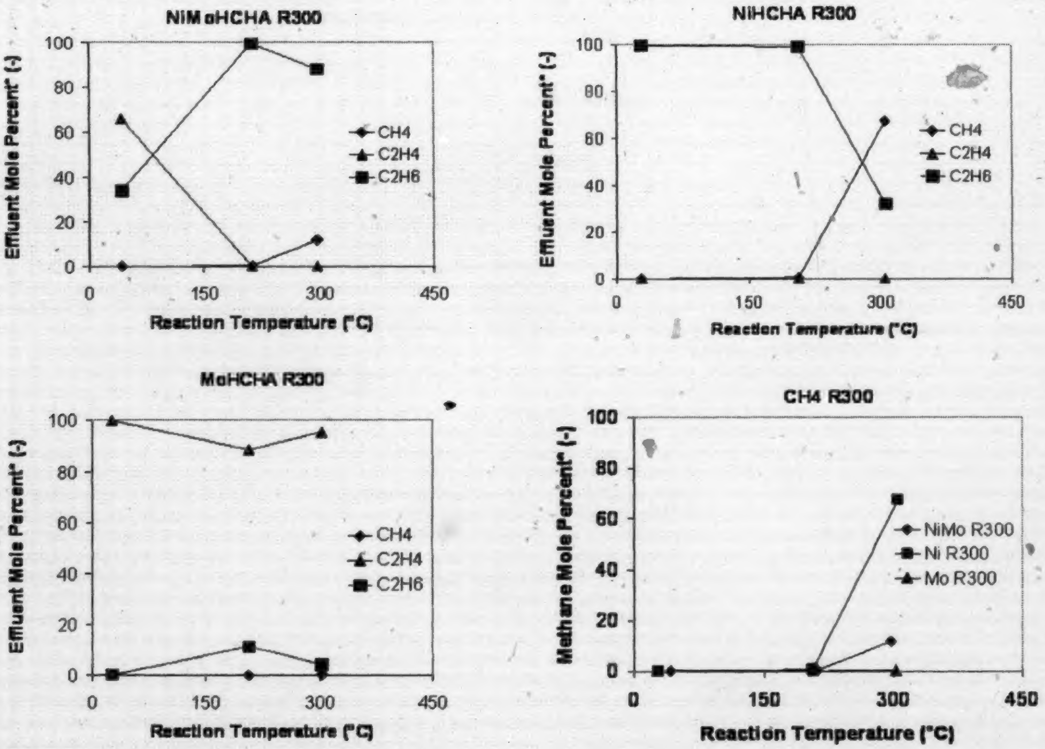

Figure D.2: Catalytic results for the metal loaded acidified chabazites reduced at 300°C.

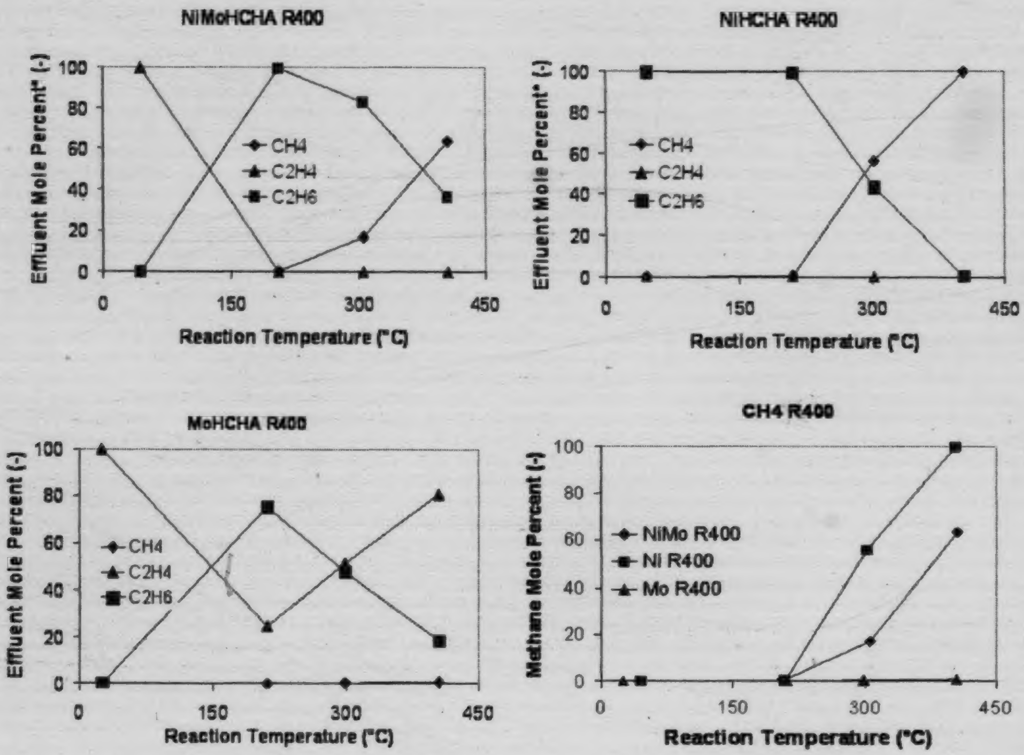

Figure D.3: Catalytic results for the metal loaded acidified chabazites reduced at 400°C.

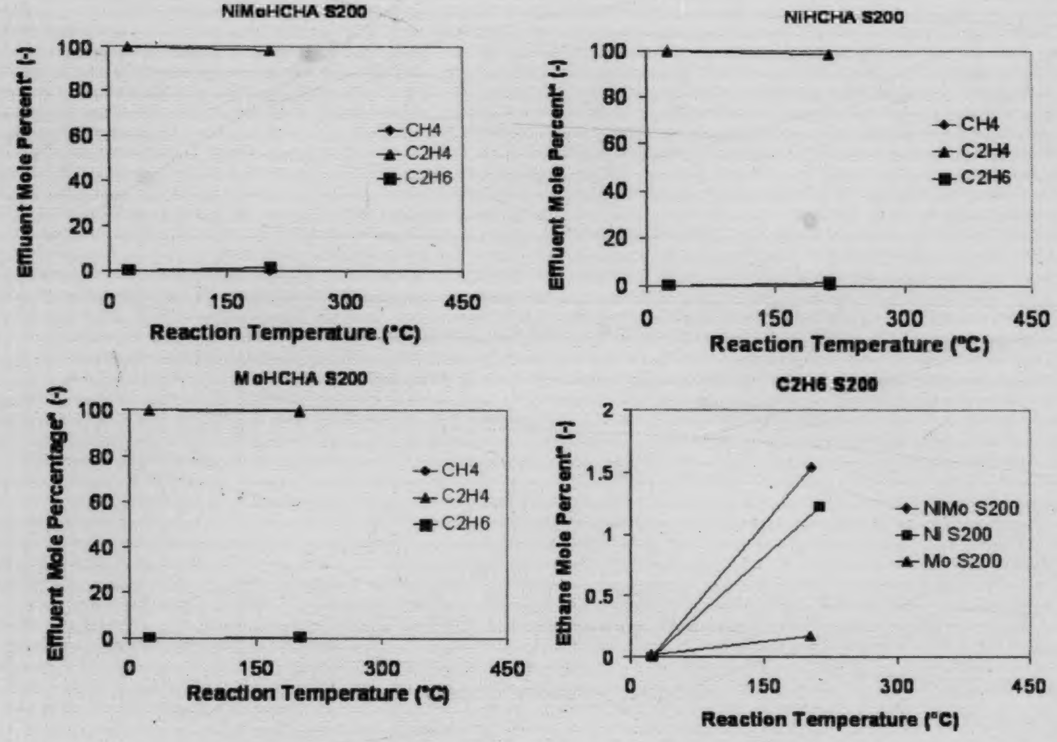

Figure D.4: Catalytic results for the metal loaded acidified chabazites sulfided at 200°C.

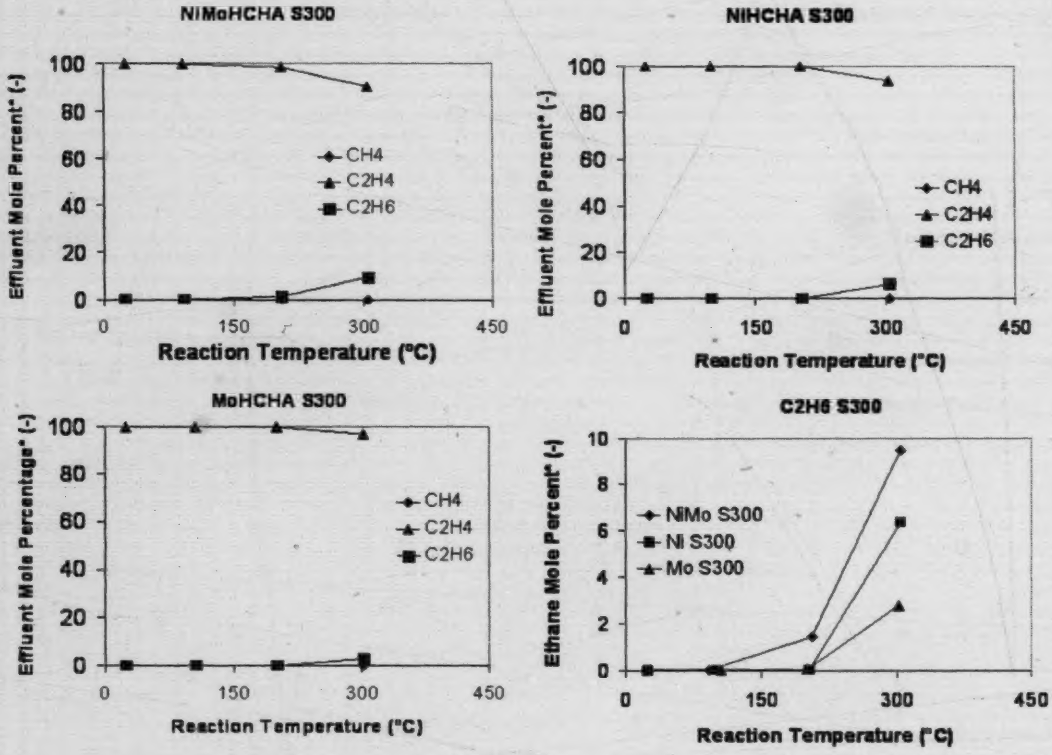

Figure D.5: Catalytic results for the metal loaded acidified chabazites sulfided at 300°C.

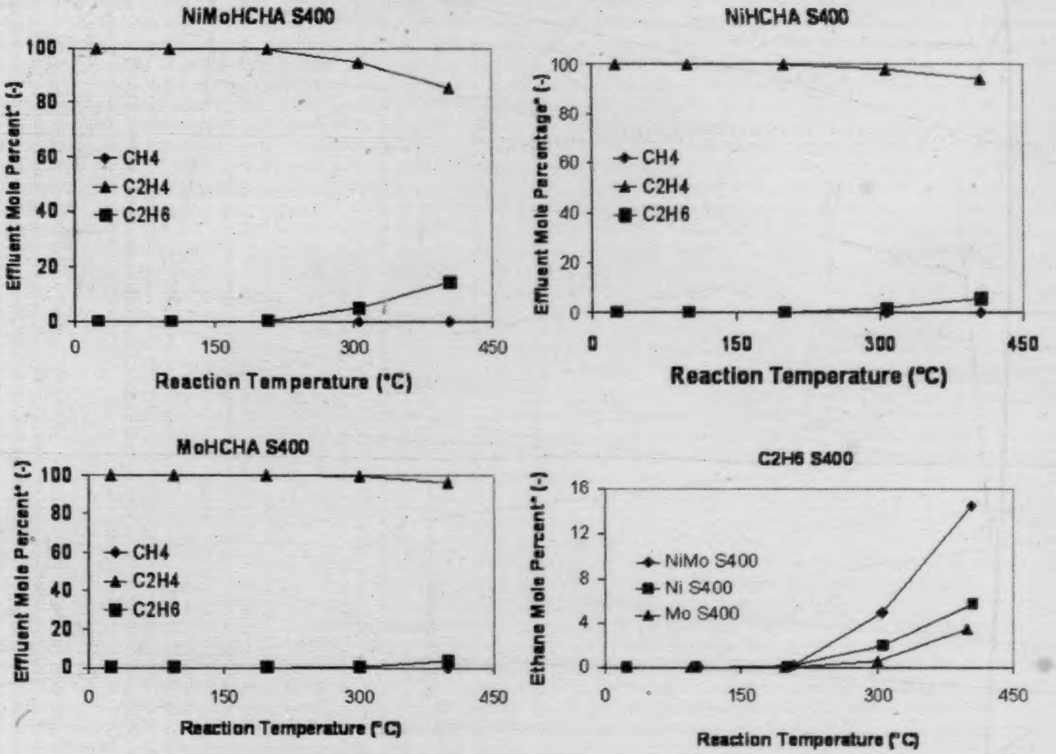

Figure D.6: Catalytic results for the metal loaded acidified chabazites sulfided at 400°C.